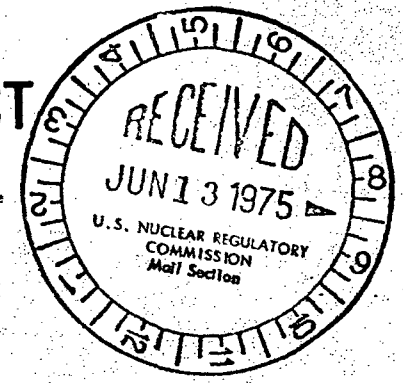


**CLINCH RIVER  
BREEDER REACTOR PROJECT**

50-537

**PRELIMINARY  
SAFETY ANALYSIS  
REPORT**



**VOLUME 4 A**

**PROJECT MANAGEMENT CORPORATION**

6428

## TABLE OF CONTENTS

	<u>Section</u>	<u>Page</u>
34	1.0 <u>INTRODUCTION AND GENERAL DESCRIPTION OF THE PLANT</u>	1.1-1
	1.1 <u>INTRODUCTION</u>	1.1-1
	1.1.1 General Information	1.1-2
	1.1.2 Overview of Safety Design Approach	1.1-3
44	1.1.3 Applicability of Regulatory Guides	1.1-5 11
	1.2 <u>GENERAL PLANT DESCRIPTION</u>	1.2-1
	1.2.1 Site	1.2-1 11
	1.2.2 Engineered Safety Features	1.2-2
	1.2.3 Reactor, Heat Transport and Related Systems	1.2-2
	1.2.4 Steam Generator - Turbine and Related Systems	1.2-3
34	1.2.5 Offsite and Onsite Power	1.2-5
	1.2.6 Instrumentation, Control, and Protection	1.2-6
	1.2.7 Auxiliary Systems	1.2-7
	1.2.8 Refueling System	1.2-8
	1.2.9 Radwaste Disposal System	1.2-9 22
	1.2.10 Reactor Confinement/Containment System	1.2-9
	1.2.11 Major Structures	1.2-10
	1.3 <u>COMPARISON TABLES</u>	1.3-1
	1.3.1 Comparisons with Similar Designs	1.3-1
	1.3.2 Detailed Comparison with Fast Flux Test Facility	1.3-2
	1.4 <u>IDENTIFICATION OF PROJECT PARTICIPANTS</u>	1.4-1
	1.4.1 Functions, Responsibilities, and Authorities of Project Participants	1.4-2
	1.4.2 Description of Organizations	1.4-3
	1.4.3 Interrelationships with Contractors and Suppliers	1.4-21a
34	1.4.4 General Qualification Requirement of CRBRP Project Participants	1.4-22
	1.5 <u>REQUIREMENTS FOR FURTHER TECHNICAL INFORMATION</u>	1.5-1
	1.5.1 Information Concerning the Adequacy of a New Design	1.5-2
	1.5.2 Information Concerning Margin of Conservatism of Proven Design	1.5-28
	1.5.3 References	1.5-47 22

TABLE OF CONTENTS (Cont'd.)

<u>Section</u>	<u>Page</u>
1.6	<u>MATERIAL INCORPORATED BY REFERENCE</u> 1.6-1
1.6.1	Introduction 1.6-1
1.6.2	References 1.6-1
	Appendix 1-A Flow Diagram Symbols 22
34 2.0	<u>SITE CHARACTERISTICS</u> 2.1-1
2.1	<u>GEOGRAPHY AND DEMOGRAPHY</u> 2.1-1
2.1.1	Site Location and Layout 2.1-1
2.1.2	Site Description 2.1-2
2.1.3	Population and Population Distribution 2.1-4
2.1.4	Uses of Adjacent Lands and Waters 2.1-8
	22
2.2	<u>NEARBY INDUSTRIAL, TRANSPORTATION AND MILITARY FACILITIES</u> 2.2-1
2.2.1	Locations, Routes, and Descriptions 2.2-1
2.2.2	Evaluations 2.2-3
34 2.2.3	New Facility/Land Use Requirements 2.2-4c
	22
2.3	<u>METEOROLOGY</u> 2.3-1
2.3.1	Regional Climatology 2.3-1
2.3.2	Local Meteorology 2.3-6
34 2.3.3	On-site Meteorological Monitoring Program 2.3-15
2.3.4	Short-Term (Accident) Diffusion Estimates 2.3-15
44 2.3.5	Long-Term (Routine) Diffusion Estimates 2.3-19
2.4	<u>HYDROLOGIC ENGINEERING</u> 2.4-1
	22
2.4.1	Hydrologic Description 2.4-1
2.4.2	Floods 2.4-6
2.4.3	Probable Maximum Flood (PMF) on Streams and Rivers 2.4-10
2.4.4	Potential Dam Failures (Seismically and Otherwise Induced) 2.4-21
2.4.7	Ice Flooding 2.4-31
2.4.8	Cooling Water Canals and Reservoirs 2.4-31a
	22
2.4.9	Channel Diversions 2.4-32
2.4.10	Flooding Protection Requirements 2.4-32
2.4.11	Low Water Considerations 2.4-33
2.4.12	Environmental Acceptance of Effluents 2.4-42
2.4.13	Groundwater 2.4-44
2.4.14	Technical Specification and Emergency Operation Requirement 2.4-55
	22

TABLE OF CONTENTS (Cont'd.)

<u>Section</u>	<u>Page</u>
2.5	2.5-1
<u>GEOLOGY AND SEISMOLOGY</u>	
2.5.1	2.5-1
2.5.2	2.5-20
2.5.3	2.5-27
2.5.4	2.5-32
2.5.5	2.5-48a
Appendix 2-A	Field Investigative Procedures
Appendix 2-B	Laboratory Test Procedures
Appendix 2-C	Report of Test Grouting Program
Appendix 2-D	Reports of Engineering Properties for Crushed Stone Materials from Commercial Suppliers
Appendix 2-E	Extracts from U.S. Atomic Energy Commission AEC Manual
	11
3.0	22
<u>DESIGN CRITERIA - STRUCTURES, COMPONENTS EQUIPMENT AND SYSTEMS</u>	
	3.1-1
34	
3.1	3.1-1
<u>CONFORMANCE WITH GENERAL DESIGN CRITERIA</u>	
3.1.1	3.1-1
3.1.2	3.1-2
34	
3.1.3	3.1-8
	22
3.2	3.2-1
<u>CLASSIFICATIONS OF STRUCTURES, SYSTEMS, AND COMPONENTS</u>	
3.2.1	3.2-1
3.2.2	3.2-2
	22
3.3	3.3-1
<u>WIND AND TORNADO LOADINGS</u>	
3.3.1	3.3-1
3.3.2	3.3-2
3.4	3.4-1
<u>WATER LEVEL (FLOOD) DESIGN</u>	
3.4.1	3.4-1
3.4.2	3.4-1a
	22
3.5	3.5-1
<u>MISSILE PROTECTION</u>	
3.5.1	3.5-4
3.5.2	3.5-4a
	22

TABLE OF CONTENTS (Cont'd.)

<u>Section</u>		<u>Page</u>
	3.5.3 Selected Missiles	3.5-7
	3.5.4 Barrier Design Procedures	3.5-10
34	3.5.5 Missile Barrier Features	3.5-13c 1
	3.6 <u>PROTECTION AGAINST DYNAMIC EFFECTS ASSOCIATED WITH THE POSTULATED RUPTURE OF PIPING</u>	3.6-1
	3.6.1 Systems in Which Pipe Breaks are Postulated	3.6-1
34	3.6.2 Pipe Break Criteria	3.6-2
	3.6.3 Design Loading Combinations	3.6-2
44	3.6.4 Dynamic Analyses	3.6-3
	3.6.5 Protective Measures	3.6-6g 22
	3.7 <u>SEISMIC DESIGN</u>	3.7-1
	3.7.1 Seismic Input	3.7-1
	3.7.2 Seismic System Analysis	3.7-4a
34	3.7.3 Seismic Subsystem Analysis	3.7-11
	3.7.4 Seismic Instrumentation Program	3.7-16
	3.7.5 Seismic Design Control	3.7-20
	Appendix to Section 3.7	
	3.8 <u>DESIGN OF CATEGORY I STRUCTURES</u>	3.8-1
	3.8.1 Concrete Containment (Not Applicable)	3.8-1
34	3.8.2 Steel Containment System	3.8-1
	3.8.3 Concrete and Structural Steel Internal Structures of Steel Containment	3.8-8
	3.8.4 Other Seismic Category I Structures	3.8-22a 1
	3.8.5 Foundations and Concrete Supports	3.8-35
	3.9 <u>MECHANICAL SYSTEMS AND COMPONENTS</u>	3.9-1
	3.9.1 Dynamic System Analysis and Testing	3.9-1
	3.9.2 ASME Code Class 2 and 3 Components	3.9-3a 1
	3.9.3 Components Not Covered by ASME Code	3.9-4a 2
	3.10 <u>SEISMIC DESIGN OF CATEGORY I INSTRUMENTATION AND ELECTRICAL EQUIPMENT</u>	3.10-1
	3.10.1 Seismic Design Criteria	3.10-1
	3.10.2 Analysis, Testing Procedures and Restraint Measures	3.10-3 1

TABLE OF CONTENTS (Cont'd.)

<u>Section</u>		<u>Page</u>
3.11	<u>ENVIRONMENTAL DESIGN OF MECHANICAL AND ELECTRICAL EQUIPMENT</u>	3.11-1
3.11.1	Equipment Identification	3.11-1
3.11.2	Qualification Test and Analysis	3.11-1
3.11.3	Qualification Test Results	3.11-1
3.11.4	Loss of Ventilation	3.11-2
3.11.5	Special Considerations	3.11-2
44   3.A.0	<u>SUPPLEMENTARY INFORMATION ON SEISMIC CATEGORY I STRUCTURES</u>	3.A.1-1
3.A.1	Inner Cell System	3.A.1-1 22
3.A.2	Head Access Area	3.A.2-1
3.A.3	Control Building	3.A.3-1
3.A.4	Reactor Service Building (RSB)	3.A.4-1
3.A.5	Steam Generator Building	3.A.5-1
3.A.6	Diesel Generator Building	3.A.6-1
3.A.7	Auxiliary Equipment Building	3.A.7-1
34   4.0	<u>REACTOR</u>	4.1-1
4.1	<u>SUMMARY DESCRIPTION</u>	4.1-1
4.1.1	Lower Internals	4.1-1
4.1.2	Upper Internals	4.1-3
34   4.1.3	Core Restraint	4.1-4
4.1.4	Core, Radial Blanket and Removable Radial Shield Regions	4.1-4
4.1.5	Design and Performance Characteristics	4.1-9
4.1.6	Loading Conditions and Analysis Techniques	4.1-9
4.1.7	List of Computer Codes	4.1-10
4.2	<u>MECHANICAL DESIGN</u>	4.2-1
4.2.1	Fuel and Radial Blanket Design	4.2-1
44   4.2.2	Reactor Vessels Internals	4.2-67b
4.2.3	Reactivity Control Systems	4.2-151
4.3	<u>NUCLEAR DESIGN</u>	4.3-1
4.3.1	Design Bases	4.3-1
4.3.2	Description	4.3-3
44   4.3.3	Analytical Methods	4.3-34b
4.3.4	Changes	4.3-39
4.3.5	FFTF vs LWR Plutonium in the CRBR	4.3-42

TABLE OF CONTENTS (Cont'd.)

<u>Section</u>	<u>Page</u>
4.4	4.4-1
<u>THERMAL AND HYDRAULIC DESIGN</u>	
4.4.1	4.4-1
4.4.2	4.4-4
4.4.3	4.4-22a   1
4.4.4	4.4-34
34   4.4.5	4.4-36
34   5.0	5.1-1
<u>HEAT TRANSPORT AND CONNECTED SYSTEMS</u>	
5.1	5.1-1a
<u>SUMMARY DESCRIPTION</u>	
5.1.1	5.1-1a   1
5.1.2	5.1-2
5.1.3	5.1-5
5.1.4	5.1-7
5.1.5	5.1-8
5.1.6	5.1-9
5.1.7	5.1-10   22
5.1.8	5.1-11
5.2	5.2-1
<u>REACTOR VESSEL, CLOSURE HEAD, AND GUARD VESSEL</u>	
5.2.1	5.2-1
1   5.2.2	5.2-4   22
34   5.2.3	5.2-7
5.2.4	5.2-8
34   5.2.5	5.2-10c   22
5.2.6	5.2-11
34   5.2.7	5.2-11a
5.3	5.3-1
<u>PRIMARY HEAT TRANSPORT SYSTEM (PHTS)</u>	
5.3.1	5.3-1
5.3.2	5.3-9
5.3.3	5.3-33
5.3.4	5.3-72
5.4	5.4-1
<u>INTERMEDIATE HEAT TRANSPORT SYSTEM (IHTS)</u>	
5.4.1	5.4-1
5.4.2	5.4-6
5.4.3	5.4-12

TABLE OF CONTENTS (Cont'd.)

<u>Section</u>		<u>Page</u>
7.2	<u>REACTOR SHUTDOWN SYSTEM</u>	7.2-1
7.2.1	Description	7.2-1
7.2.2	Analysis	7.2-13
7.3	<u>ENGINEERED SAFETY FEATURE INSTRUMENTATION AND CONTROL</u>	7.3-1
7.3.1	Containment Isolation System	7.3-1
7.3.2	Analysis	7.3-3
7.4	<u>INSTRUMENTATION AND CONTROL SYSTEMS REQUIRED FOR SAFE SHUTDOWN</u>	7.4-1
7.4.1	Steam Generator Auxiliary Heat Removal Instrumentation and Control Systems	7.4-1
7.4.2	Outlet Steam Isolation Instrumentation and Control System	7.4-6
34 7.5	<u>INSTRUMENTATION AND MONITORING SYSTEM</u>	7.5-1
7.5.1	Flux Monitoring System	7.5-1
7.5.2	Heat Transport Instrumentation System	7.5-5
7.5.3	Reactor and Vessel Instrumentation	7.5-13
7.5.4	Fuel Failure Monitoring System	7.5-14
7.5.5	Leak Detection Systems	7.5-18
7.5.6	Sodium-Water Reaction Pressure Relief System (SWRPRS) Instrumentation and Controls	7.5-30
7.5.7	Containment Hydrogen Monitoring	7.5-33b
7.5.8	Containment Vessel Temperature Monitoring	7.5-33b
44 7.5.9	Containment Pressure Monitoring	7.5-33b
7.6	<u>OTHER INSTRUMENTATION AND CONTROL SYSTEMS REQUIRED FOR SAFETY</u>	7.6-1
7.6.1	Plant Service Water and Chilled Water Instrumentation and Control Systems	7.6-1 22
7.6.2	Fuel Handling Safety Interlocks	7.6-1
26 7.6.3	Direct Heat Removal Service (DHRS) Instrumentation and Control System	7.6-3 22
34 7.6.4	Heating, Ventilating, and Air Conditioning Instrumentation and Control System	7.6-3e
7.7	<u>INSTRUMENTATION AND CONTROL SYSTEMS NOT REQUIRED FOR SAFETY</u>	7.7-1
7.7.1	Plant Control System Description	7.7-1
7.7.2	Design Analysis	7.7-16



TABLE OF CONTENTS (Cont'd.)

<u>Section</u>		<u>Page</u>
7.8	<u>PLANT DATA HANDLING AND DISPLAY SYSTEM</u>	7.8-1
7.8.1	Design Description	7.8-1
7.8.2	Design Analysis	7.8-2
7.9	<u>OPERATING CONTROL STATIONS</u>	7.9-1
7.9.1	Design Basis	7.9-1
7.9.2	Control Room	7.9-1
7.9.3	Local Control Stations	7.9-6
7.9.4	Communications	7.9-6
7.9.5	Design Evaluation	7.9-6
34 8.0	<u>ELECTRIC POWER</u>	8.1-1
8.1	<u>INTRODUCTION</u>	8.1-1
8.1.1	Utility Grid and Interconnections	8.1-1
8.1.2	Plant Electrical Power System	8.1-1
8.1.3	Criteria and Standards	8.1-3
8.2	<u>OFFSITE POWER SYSTEM</u>	8.2-1
8.2.1	Description	8.2-1
8.2.2	Analysis	8.2-4
8.3	<u>ON-SITE POWER SYSTEMS</u>	8.3-1
8.3.1	AC Power Systems	8.3-1
8.3.2	DC Power System	8.3-26
9.0	<u>AUXILIARY SYSTEMS</u>	9.1-1
9.1	<u>FUEL STORAGE AND HANDLING</u>	9.1-1
9.1.1	New Fuel Storage	9.1-3
9.1.2	Spent Fuel Storage	9.1-7
9.1.3	Spent Fuel Cooling and Cleanup System	9.1-18
9.1.4	Fuel Handling System	9.1-28

22

TABLE OF CONTENTS (Cont'd.)

<u>Section</u>		<u>Page</u>
9.2	<u>MAINTENANCE</u>	9.2-1
9.2.1	Maintenance System Facilities and Equipment, and Handling Equipment	9.2-1 22
9.2.2	Sodium Removal and Decontamination System	9.2-6b <sub>1</sub>
34		
9.3	<u>AUXILIARY LIQUID METAL SYSTEM</u>	9.3-1
44	9.3.1 Sodium and NaK Receiving System	9.3-1a
	9.3.2 Primary Na Storage and Processing	9.3-2
	9.3.3 EVS Sodium Processing	9.3-9
	9.3.4 Primary Cold Trap NaK Cooling System	9.3-10
	9.3.5 Intermediate Na Processing System	9.3-12
9.4	<u>PIPING AND EQUIPMENT ELECTRICAL HEATING</u>	9.4-1 22
9.4.1	Design Bases	9.4-1
9.4.2	Systems Description	9.4-2
9.4.3	Safety Evaluation	9.4-3a
9.4.4	Tests and Inspections	9.4-3b
9.4.5	Instrumentation Application	9.4-3b 22
9.5	<u>INERT GAS RECEIVING AND PROCESSING SYSTEM</u>	9.5-1
9.5.1	Argon Distribution Subsystem	9.5-1a
9.5.2	Nitrogen Distribution System	9.5-10 22
9.5.3	Vacuum Subsystem	9.5-14
9.5.4	Fueling Handling Cell Atmospheric Purification Unit	9.5-15
9.6	<u>HEATING, VENTILATING, AND AIR CONDITIONING SYSTEM</u>	9.6-1
9.6.1	Control Building HVAC System	9.6-1
9.6.2	Reactor Containment Building	9.6-12 22
9.6.3	Reactor Service Building HVAC System	9.6-22
9.6.4	Turbine Generator Building Ventilation System	9.6-30
9.6.5	Diesel Generator Building HVAC System	9.6-32
9.6.6	Steam Generator Building HVAC System	9.6-36 1
9.7	<u>CHILLED WATER SYSTEMS</u>	9.7-1
9.7.1	Normal Chilled Water System	9.7-1
9.7.2	Emergency Chilled Water System	9.7-3
15	9.7.3 Prevention of Sodium/Water Interactions	9.7-7

TABLE OF CONTENTS (Cont'd.)

<u>Section</u>		<u>Page</u>
9.8	<u>IMPURITY MONITORING AND ANALYSIS SYSTEM</u>	9.8-1
9.8.1	Design Basis	9.8-1
9.8.2	Design Description	9.8-2
9.8.3	Design Evaluation	9.8-5
45   9.8.4	Tests and Inspection	9.8-7
9.8.5	Instrumentation Requirements	9.8-8
9.9	<u>SERVICE WATER SYSTEMS</u>	9.9-1
9.9.1	Normal Plant Service Water System	9.9-1
9.9.2	Emergency Plant Service Water System	9.9-2
11   9.9.3	Secondary Service Closed Cooling Water System	9.9-4
9.9.5	River Water Service System	9.9-11
15   9.10	<u>COMPRESSED AIR SYSTEM</u>	9.10-1
9.10.1	Design Bases	9.10-1
9.10.2	System Description	9.10-1
9.10.3	Design Evaluation	9.10-2
9.10.4	Tests and Inspections	9.10-3
9.10.5	Instrumentation Application	9.10-3
9.11	<u>COMMUNICATIONS SYSTEM</u>	9.11-1
9.11.1	Design Bases	9.11-1
9.11.2	Description	9.11-2
9.12	<u>LIGHTING SYSTEMS</u>	9.12-1
9.12.1	Normal Lighting System	9.12-1
9.12.2	Emergency Lighting Systems	9.12-1
9.13	<u>PLANT FIRE PROTECTION SYSTEM</u>	9.13-1
9.13.1	Non-Sodium Fire Protection System	9.13-1
34   9.13.2	Sodium Fire Protection System	9.13-13
9.14	<u>DIESEL GENERATOR AUXILIARY SYSTEM</u>	9.14-1
9.14.1	Fuel Oil Storage and Transfer System	9.14-1
9.14.2	Cooling Water System	9.14-2
9.14.3	Starting Air Systems	9.14-4
9.14.4	Lubrication System	9.14-5
9.15	<u>EQUIPMENT AND FLOOR DRAINAGE SYSTEM</u>	9.15-1
9.15.1	Design Bases	9.15-1
9.15.2	System Description	9.15-1
9.15.3	Safety Evaluation	9.15-2
9.15.4	Tests and Inspections	9.15-2
9.15.5	Instrumentation Application	9.15-2

TABLE OF CONTENTS (Cont'd.)

<u>Section</u>	<u>Page</u>
34 10.0	<u>STEAM AND POWER CONVERSION SYSTEM</u> 10.1-1
10.1	<u>SUMMARY DESCRIPTION</u> 10.1-1
10.2	<u>TURBINE GENERATOR</u> 10.2-1
10.2.1	Design Bases 10.2-1
44  10.2.2	Description 10.2-1a
10.2.3	Turbine Missiles 10.2-5
10.2.4	Evaluation 10.2-9
	22
10.3	<u>MAIN STEAM SUPPLY SYSTEM</u> 10.3-1
10.3.1	Design Bases 10.3-1
44  10.3.2	Description 10.3-1
10.3.3	Evaluation 10.3-2
	1
10.3.4	Inspection and Testing Requirements 10.3-2
10.3.5	Water Chemistry 10.3-3
10.4	<u>OTHER FEATURES OF STEAM AND POWER CONVERSION SYSTEM</u> 10.4-1
10.4.1	Condenser 10.4-1
10.4.2	Condenser Air Removal System 10.4-2
10.4.3	Turbine Gland Sealing System 10.4.3
10.4.4	Turbine Bypass System 10.4-4
10.4.5	Circulating Water System 10.4-5
10.4.6	Condensate Cleanup System 10.4-7
10.4.7	Condensate and Feedwater Systems 10.4-9
10.4.8	Steam Generator Blowdown System 10.4-14
34 11.0	<u>RADIOACTIVE WASTE MANAGEMENT</u> 11.1-1
11.1	<u>SOURCE TERMS</u> 11.1-1
11.1.1	Modes of Radioactive Waste Production 11.1-1
11.1.2	Activation Product Source Strength Models 11.1-2
11.1.3	Fission Product and Plutonium Release Models 11.1-5
11.1.4	Tritium Production Sources 11.1-7
11.1.5	Summary of Design Bases for Deposition of Radio- activity in Primary Sodium on Reactor and Primary Heat Transfer Surfaces and Within Reactor Auxiliary Systems 11.1-7
11.1.6	Leakage Rates 11.1-10
	22

TABLE OF CONTENTS (Cont'd.)

<u>Section</u>		<u>Page</u>
11.2	<u>LIQUID WASTE SYSTEM</u>	11.2-1
11.2.1	Design Objectives	11.2-1
11.2.2	System Description	11.2-2
11.2.3	System Design	11.2-4
11.2.4	Operating Procedures and Performance Tests	11.2-5
11.2.5	Estimated Releases	11.2-6
11.2.6	Release Points	11.2-6
11.2.7	Dilution Factors	11.2-7
11.2.8	Estimated Doses	11.2-8
34	Appendix 11.2A Dose Models: Liquid Effluents	11.2A-1
11.3	<u>GASEOUS WASTE SYSTEM</u>	11.3-1
11.3.1	Design	11.3-1
11.3.2	System Description	11.3-1
11.3.3	System Design	11.3-8
11.3.4	Operating Procedures and Performance Tests	11.3-9
11.3.5	Estimated Releases	11.3-12
11.3.6	Release Points	11.3-12
34 11.3.7	Dilution Factors	11.3-13a
11.3.8	Dose Estimates	11.3-14
34	Appendix 11.3A Dose Models: Gaseous Effluents	11.3A-1
11.4	<u>PROCESS AND EFFLUENT RADIOLOGICAL MONITORING SYSTEM</u>	11.4-1
11.4.1	Design Objectives	11.4-1
11.4.2	Continuous Monitoring/Samples	11.4-2      22
34 11.5	<u>SOLID WASTE SYSTEM</u>	11.5-1
11.5.1	Design Objectives	11.5-1
11.5.2	System Inputs	11.5-1
11.5.3	Equipment Description	11.5-1
11.5.4	Expected Volumes	11.5-3      22
11.5.5	Packaging	11.5-4
11.5.6	Storage Facilities	11.5-4      1
11.5.7	Shipment	11.5-4

TABLE OF CONTENTS (Cont'd.)

<u>Section</u>		<u>Page</u>
11.6	<u>OFF-SITE RADIOLOGICAL MONITORING PROGRAM</u>	11.6-1
11.6.1	Expected Background	11.6-1
11.6.2	Critical Pathways to Man	11.6-2
11.6.3	Sampling Media, Locations, and Frequencies	11.6-4
11.6.4	Analytical Sensitivity	11.6-4
11.6.5	Data Analysis and Presentation	11.6-5
11.6.6	Program Statistical Sensitivity	11.6-6
12.0	<u>RADIATION PROTECTION</u>	12.1-1
34 12.1	<u>SHIELDING</u>	12.1-1
12.1.1	Design Objectives	12.1-1
12.1.2	Design Description	12.1-3
44 12.1.3	Source Terms	12.1-13
12.1.4	Area Radiation Monitoring	12.1-23
12.1.5	Estimates of Exposure	12.1-24
34	Appendix to Section 12.1	12.1A-1
12.2	<u>VENTILATION</u>	12.2-1
12.2.1	Design Objectives	12.2-1
12.2.2	Design Description	12.2-1
12.2.3	Source Terms	12.2-3
12.2.4	Airborne Radioactivity Monitoring	12.2-3
12.2.5	Inhalation Doses	12.2-5
12.3	<u>HEALTH PHYSICS PROGRAM</u>	12.3-1
12.3.1	Program Objectives	12.3-1
12.3.2	Facilities and Equipment	12.3-1
12.3.3	Personnel Dosimetry	12.3-3
34 12.3.4	Estimated Occupancy Times	12.3-4
44	Appendix A to Chapter 12	12.A-1
13.0	<u>CONDUCT OF OPERATIONS</u>	13.1-1
34 13.1	<u>ORGANIZATIONAL STRUCTURE OF THE APPLICANT</u>	13.1-1
13.1.1	Project Organization	13.1-1
13.1.2	Operating Organization	13.1-4
13.1.3	Qualification Requirements for Nuclear Plant Personnel	13.1-11
13.2	<u>TRAINING PROGRAM</u>	13.2-1
13.2.1	Program Description	13.2-1
13.2.2	Retraining Program	13.2-6
13.2.3	Replacement Training	13.2-6
13.2.4	Records	13.2-6

TABLE OF CONTENTS (Cont'd.)

<u>Section</u>		<u>Page</u>
13.3	<u>EMERGENCY PLANNING</u>	13.3-1
13.3.1	General	13.3-1
13.3.2	Emergency Organization	13.3-2
13.3.3	Coordination with Offsite Groups	13.3-4
13.3.4	Protective Action Levels	13.3-4
13.3.5	Protective Measures	13.3-5
13.3.6	Review and Updating	13.3-5
13.3.7	Medical Support	13.3-5
13.3.8	Drills	13.3-6
13.3.9	Training	13.3-6
13.3.10	Recovery and Reentry	13.3-6
13.3.11	Implementation	13.3-6
13.4	<u>REVIEW AND AUDIT</u>	13.4-1
13.4.1	Review and Audit - Construction	13.4-1
13.4.2	Review and Audit - Test and Operation	13.4-1
13.5	<u>PLANT PROCEDURES</u>	13.5-1
13.5.1	General	13.5-1
13.5.2	Normal Operating Instructions	13.5-1
13.5.3	Abnormal Operating Instructions	13.5-2
13.5.4	Emergency Operating Instructions	13.5-2
13.5.5	Maintenance Instructions	13.5-3
13.5.6	Surveillance Instructions	13.5-4
13.5.7	Technical Instructions	13.5-4
13.5.8	Sections Instruction Letters	13.5-4
13.6	<u>PLANT RECORDS</u>	13.6-1
13.6.1	Plant History	13.6-1
13.6.2	Operating Records	13.6-1
13.6.3	Event Records	13.6-1
13.7	<u>INDUSTRIAL SECURITY</u>	13.7-1
13.7.1	Organization and Personnel	13.7-1
13.7.2	Plant Design	13.7-4
13.7.3	Security Plan	13.7-7

TABLE OF CONTENTS (Cont'd.)

<u>Section</u>		<u>Page</u>
34	14.0	<u>INITIAL TESTS AND OPERATION</u> 14.1-1
	14.1	<u>DESCRIPTION OF TEST PROGRAMS</u> 14.1-1
	14.1.1	Preoperational Test Programs 14.1-2
	14.1.2	Startup Test Program 14.1-2
	14.1.3	Administration of Testing Program 14.1-3
44	14.1.4	Test Objectives of First-of-a-Kind Design Features 14.1-7a 22
	14.2	<u>AUGMENTATION OF OPERATOR'S STAFF FOR INITIAL TESTS AND OPERATION</u> 14.2-1
34	15.0	<u>ACCIDENT ANALYSES</u> 15.1-1
	15.1	<u>INTRODUCTION</u> 15.1-1
	15.1.1	Design Approach to Safety 15.1-1
	15.1.2	Fuel, Blanket and Control Assembly Integrity Limits and Control Rod Shutdown Rate 15.1-50
	15.1.3	Plant Protection System Trip Levels Design Events and Duty Cycles 15.1-93
	15.2	<u>REACTIVITY INSERTION DESIGN EVENTS - INTRODUCTION</u> 15.2-1
	15.2.1	Anticipated Events 15.2-5
	15.2.2	Unlikely Events 15.2-34
	15.2.3	Extremely Unlikely Events 15.2-51
	15.3	<u>UNDERCOOLING DESIGN EVENTS - INTRODUCTION</u> 15.3-1
	15.3.1	Anticipated Events 15.3-6
	15.3.2	Unlikely Events 15.3-29
	15.3.3	Extremely Unlikely Events 15.3-38
	15.4	<u>LOCAL FAILURE EVENTS - INTRODUCTION</u> 15.4-1
	15.4.1	Fuel Assembly 15.4-2
	15.4.2	Control Assemblies 15.4-42
	15.4.3	Radial Blanket Assembly 15.4-51
	15.5	<u>FUEL HANDLING AND STORAGE EVENTS - INTRODUCTION</u> 15.5-1
	15.5.1	Anticipated Events (None) 15.5-4
	15.5.2	Unlikely Events 15.5-4
	15.5.3	Extremely Unlikely Events 15.5-23



TABLE OF CONTENTS (Cont'd.)

<u>Section</u>	<u>Page</u>
15.6	<u>SODIUM SPILLS - INTRODUCTION</u> 15.6-1
15.6.1	Extremely Unlikely Events 15.6-5
15.7	<u>OTHER EVENTS - INTRODUCTION</u> 15.7-1
15.7.1	Anticipated Events 15.7-3
15.7.2	Unlikely Events 15.7-9
15.7.3	Extremely Unlikely Events 15.7-18
	Appendix 15.A - CRBRP Reference Design Radiological Source Term For Assessment of Site Suitability 22 11
34 16.0	<u>TECHNICAL SPECIFICATIONS</u> 16.1-1
16.1	<u>DEFINITIONS</u> 16.1-1
16.1.1	Reactor Operating Condition 16.1-1
16.1.2	Reactor Core 16.1-2
16.1.3	Plant Protection System Instrumentation 16.1-3
16.1.4	Safety Limit 16.1-5
16.1.5	Limiting Safety System Setting (LSSS) 16.1-5
16.1.6	Limiting Conditions for Operation (LCO) 16.1-6
16.1.7	Surveillance Requirements 16.1-6
16.1.8	Containment Integrity 16.1-6
16.1.9	Abnormal Occurrence 16.1-6
16.2	<u>SAFETY LIMITS AND LIMITING SAFETY SYSTEM SETTINGS</u> 16.2-1
16.2.1	Safety Limit, Reactor Core 16.2-1
16.2.2	Limiting Safety System Settings 16.2-1
16.3	<u>LIMITING CONDITIONS FOR OPERATION</u> 16.3-1
16.3.1	Reactor Operating Conditions 16.3-1
16.3.2	Primary Heat Transport System (PHTS) 16.3-2
16.3.3	Intermediate Heat Transport Coolant System 16.3-6
16.3.4	Steam Generation System (SGS) 16.3-7
16.3.5	Auxiliary Liquid Metal System 16.3-12
16.3.6	Inert Gas System Cover Gas Purification System 16.3-13
16.3.7	Auxiliary Cooling System 16.3-14
16.3.8	Containment Integrity 16.3-21
16.3.9	Auxiliary Electrical System 16.3-21
16.3.10	Refueling 16.3-24
16.3.11	Effluent Release 16.3-27
16.3.12	Reactivity and Control Rod Limits 16.3-31
16.3.13	Plant Protection System 16.3-34

TABLE OF CONTENTS (Cont'd.)

<u>Section</u>		<u>Page</u>
16.4	<u>SURVEILLANCE REQUIREMENTS</u>	16.4-1
16.4.1	Operational Safety Review	16.4-1
16.4.2	Reactor Coolant System Surveillance	16.4-1
16.4.3	Containment Tests	16.4-3
16.4.4	HVAC and Radioactive Effluents	16.4-6
16.4.5	Emergency Power System Periodic Tests	16.4-10
16.4.6	Inert Gas System	16.4-13
16.4.7	Reactivity Anomalies	16.4-13
16.4.8	Pressure and Leakage Rate Test of RAPS Surge Tank Cell	16.4-15
16.5	<u>DESIGN FEATURES</u>	16.5-1
16.5.1	Site	16.5-1
16.5.2	Confinement/Containment	16.5-1   22
16.5.3	Reactor	16.5-2
16.5.4	Heat Transport System	16.5-5
16.5.5	Fuel Storage	16.5-7
16.6	<u>ADMINISTRATIVE CONTROLS</u>	16.6-1
16.6.1	Organization	16.6-1
16.6.2	Review and Audit	16.6-1
16.6.3	Instructions	16.6-4
16.6.4	Actions to be Taken in the Event of an Abnormal Occurrence in Plant Operation	16.6-7
16.6.5	Action to be Taken in the Event a Safety Limit is Exceeded	16.6-8
16.6.6	Station Operating Room	16.6-8
16.6.7	Reporting Requirements	16.6-9
16.6.8	Minimum Staffing	16.6-10
17.0	<u>QUALITY ASSURANCE - INTRODUCTION</u>	17.0-1
17.0.1	Scope	17.0-1
17.0.2	Quality Philosophy	17.0-1
17.0.3	Participants	17.0-2
17.0.4	Project Phase Control	17.0-3
17.0.5	Applicability	17.0-3
17.1	<u>QUALITY ASSURANCE DURING DESIGN AND CONSTRUCTION</u>	17.1-1
17.1.1	Organization	17.1-1
17.1.2	Quality Assurance Program	17.1-2
17.1.3	References Referred to in the Text	17.1-6
17.1.4	Acronyms Used in Chapter 17 Text and Appendices	17.1-6a   22

TABLE OF CONTENTS (Cont'd.)

Section

Appendix 17A A Description of the Owner Quality Assurance Program

45 | Appendix 17B A Description of the FS Quality Assurance Program

Appendix 17C A Description of the Balance of Plant Supply Quality Assurance Program

Appendix 17D A Description of the ARD Lead Reactor Manufacturer Quality Assurance Program

Appendix 17E A Description of the Architect-Engineer Quality Assurance Program

Appendix 17F A Description of the Constructor Quality Assurance Program

Appendix 17G RDT Standard F2-2, 1973, Quality Assurance Program Requirements

Appendix 17H A Description of the ARD Reactor Manufacturer Quality Assurance Program

Appendix 17I A Description of the GE-FBRD-RM Quality Assurance Program

Appendix 17J A Description of the AI-RM Quality Assurance Program

11

Appendix A Computer Codes

Appendix B General Plant Transient Data

Appendix C Reliability Program

Appendix F Core Disruptive Accident Accommodation

34

1764-32

4.2-506

Amend. 51  
Sept. 1975

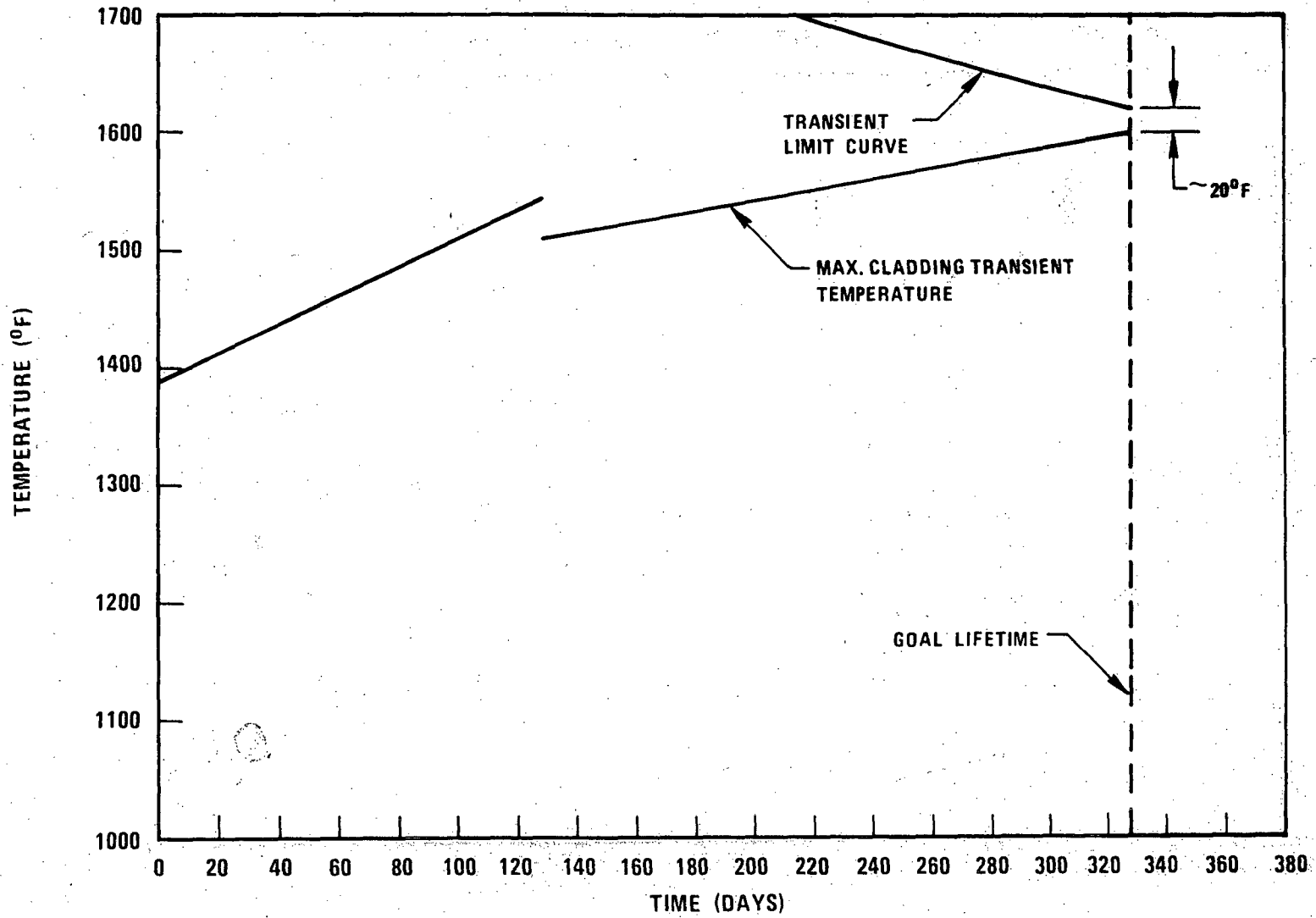


Figure 4.2-28A Blanket Assembly 67 Transient Limit Evaluation

1764-33

4.2-507

Amend. 51  
Sept. 1979

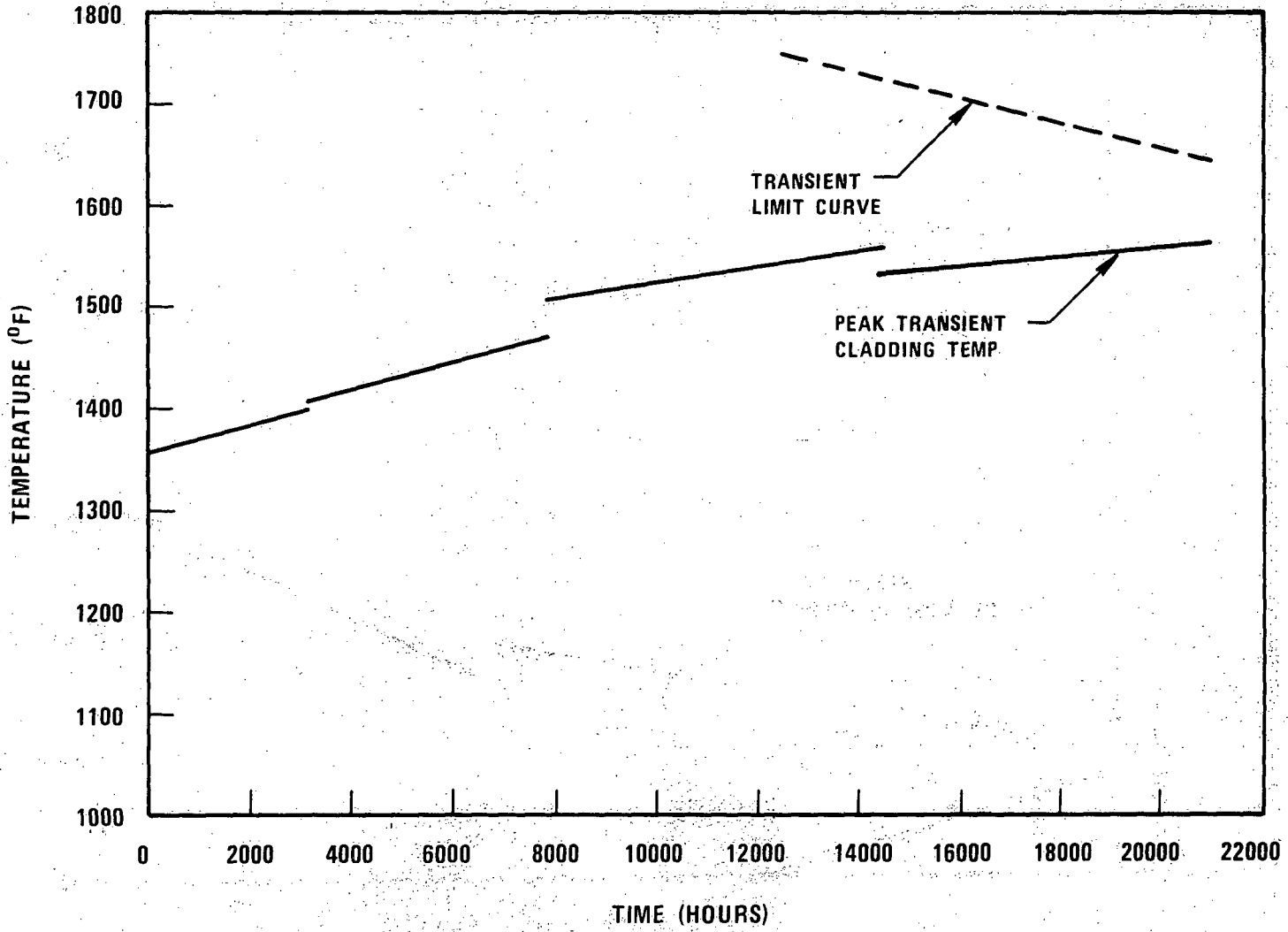


Figure 4.2-28B Radial Blanket Assembly 201 Transient Limit Evaluation

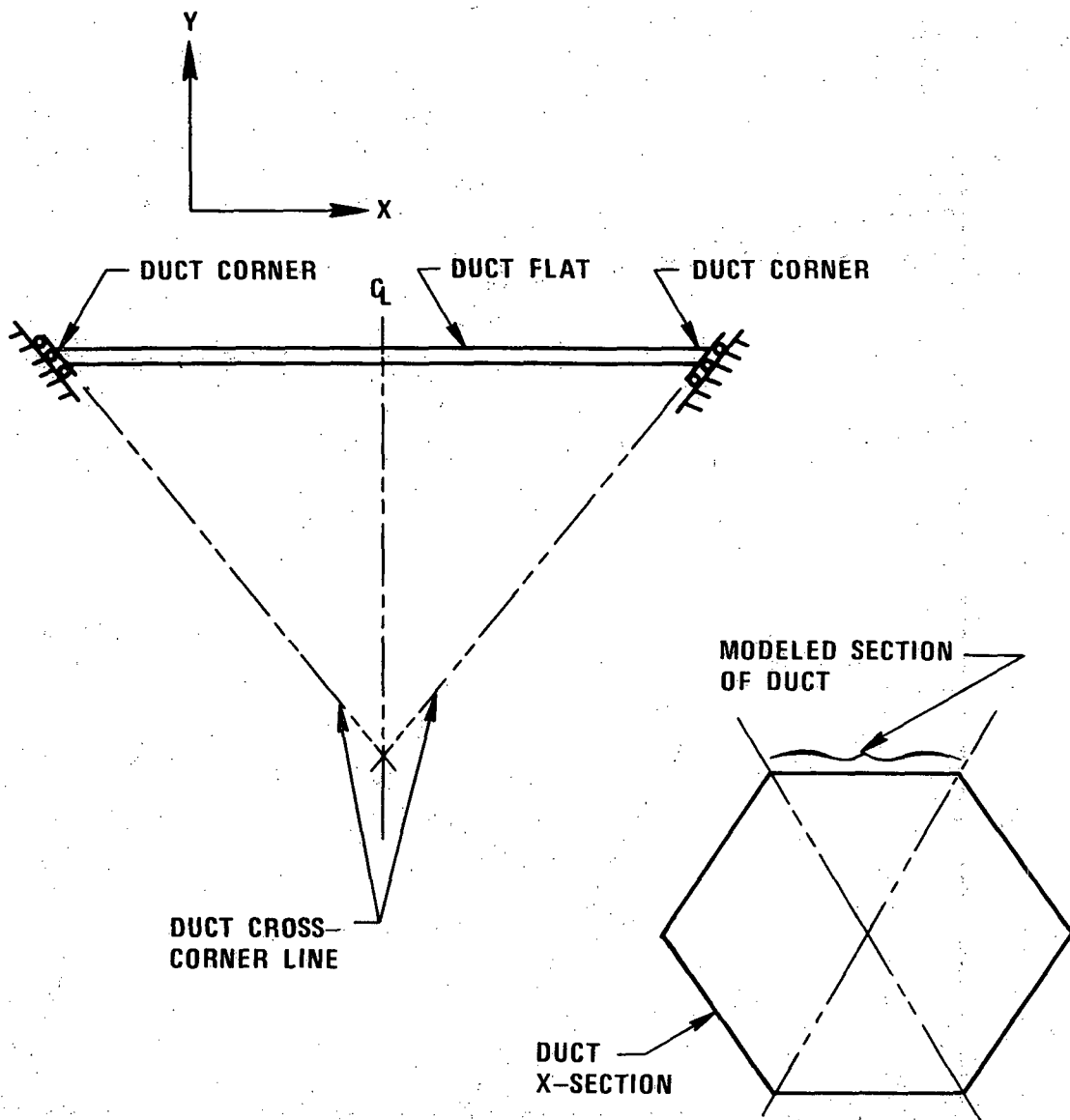


Figure 4.2-29 Model for Duct Swelling Calculation

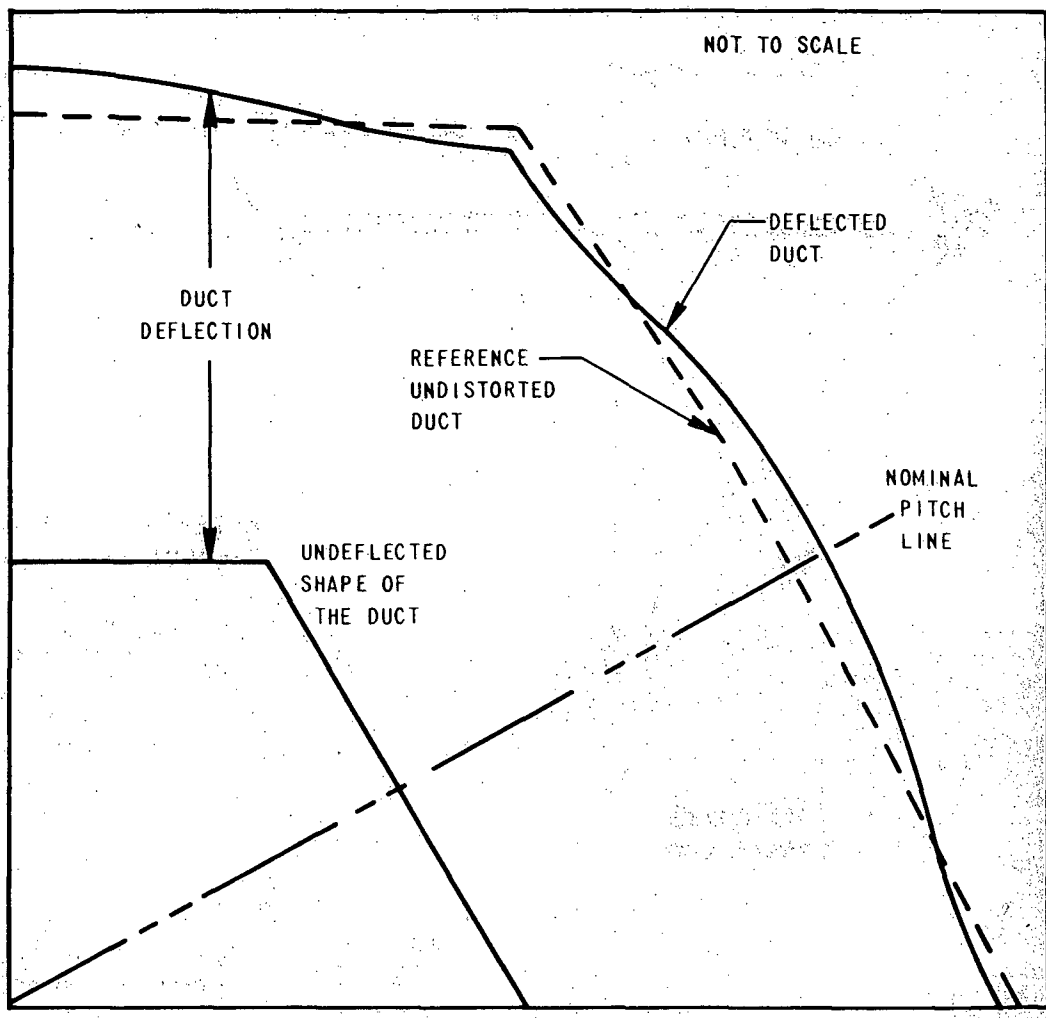


Figure 4.2-30 Deflected Shape of the Duct after Irradiation Creep and Swelling

1764-35

4.2-509

Amend. 51  
Sept. 1979

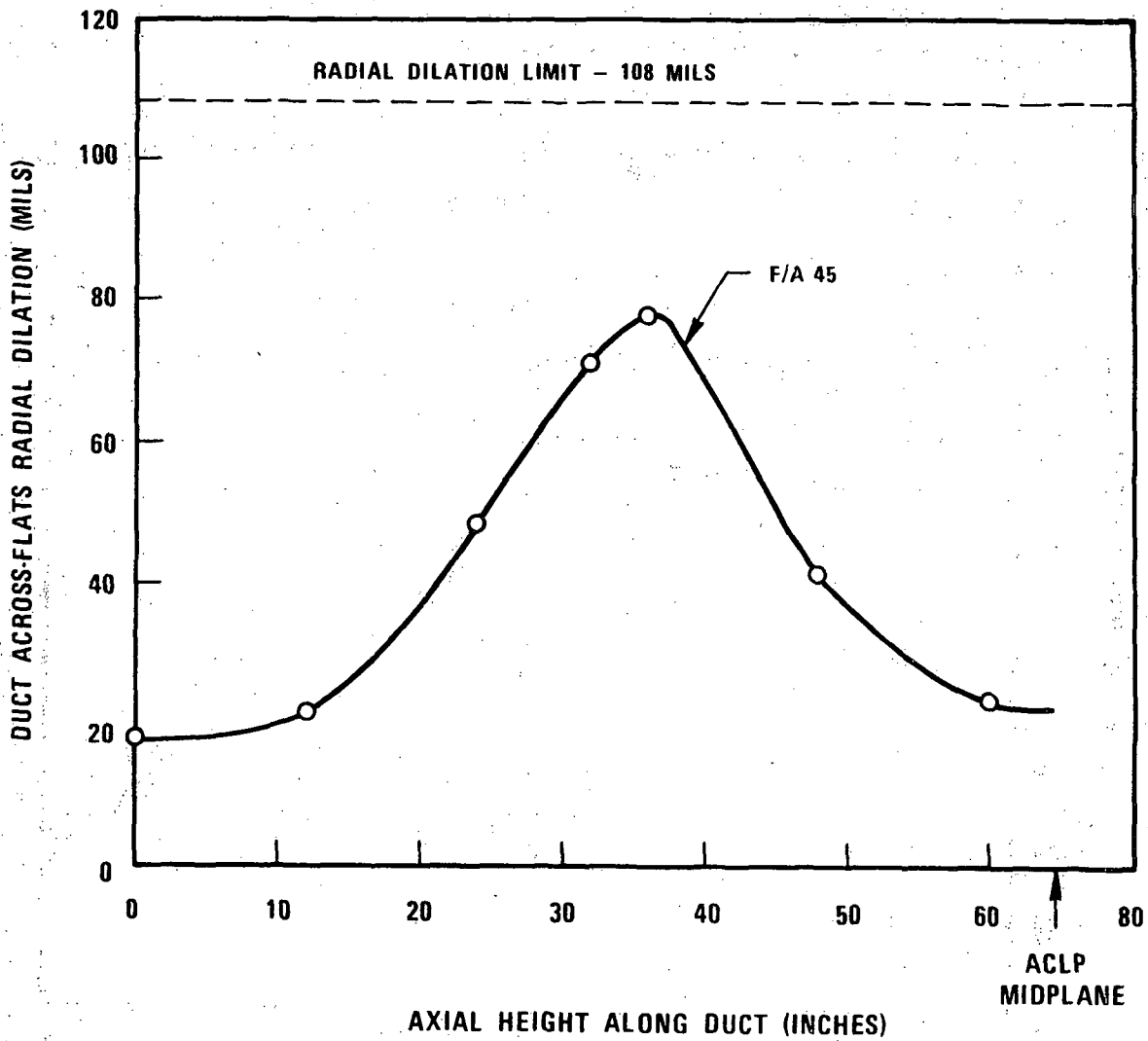


Figure 4.2-31A Maximum Duct Radial Dilation Across Flats Versus Axial Location at End-of-Life. For F/A 45

1764-36

4.2-510

Amend. 51  
Sept. 1979



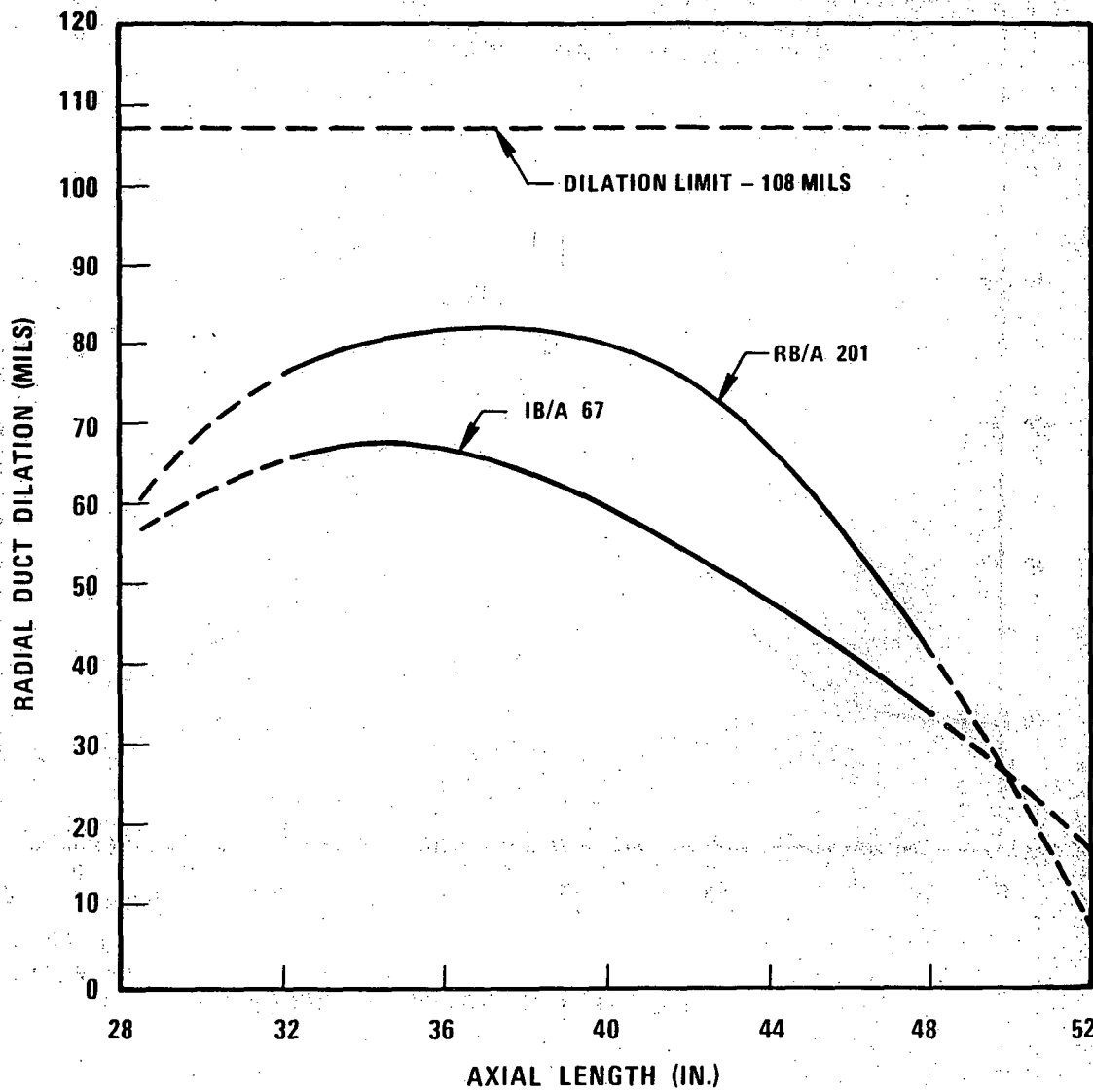


Figure 4.2-31B Duct Dilation vs. Axial Height for IB/A 67 and RB/A 201

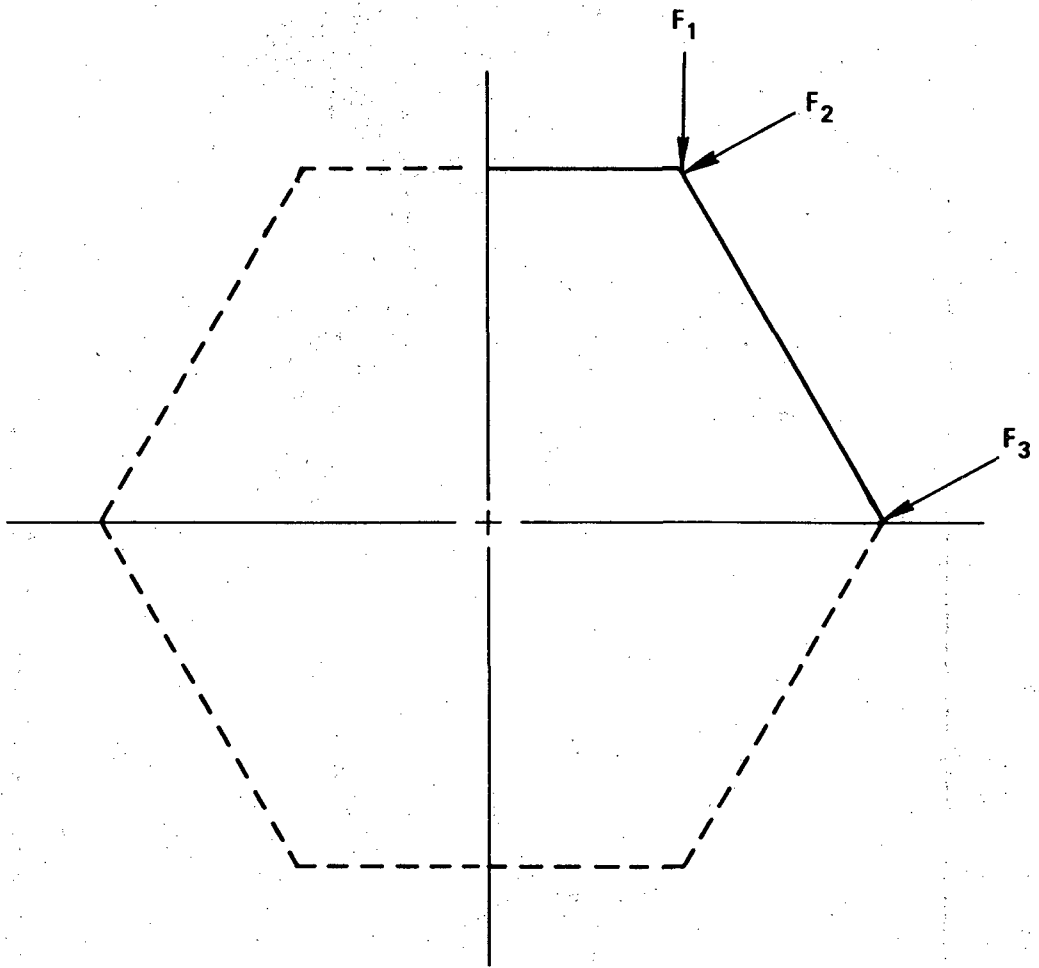


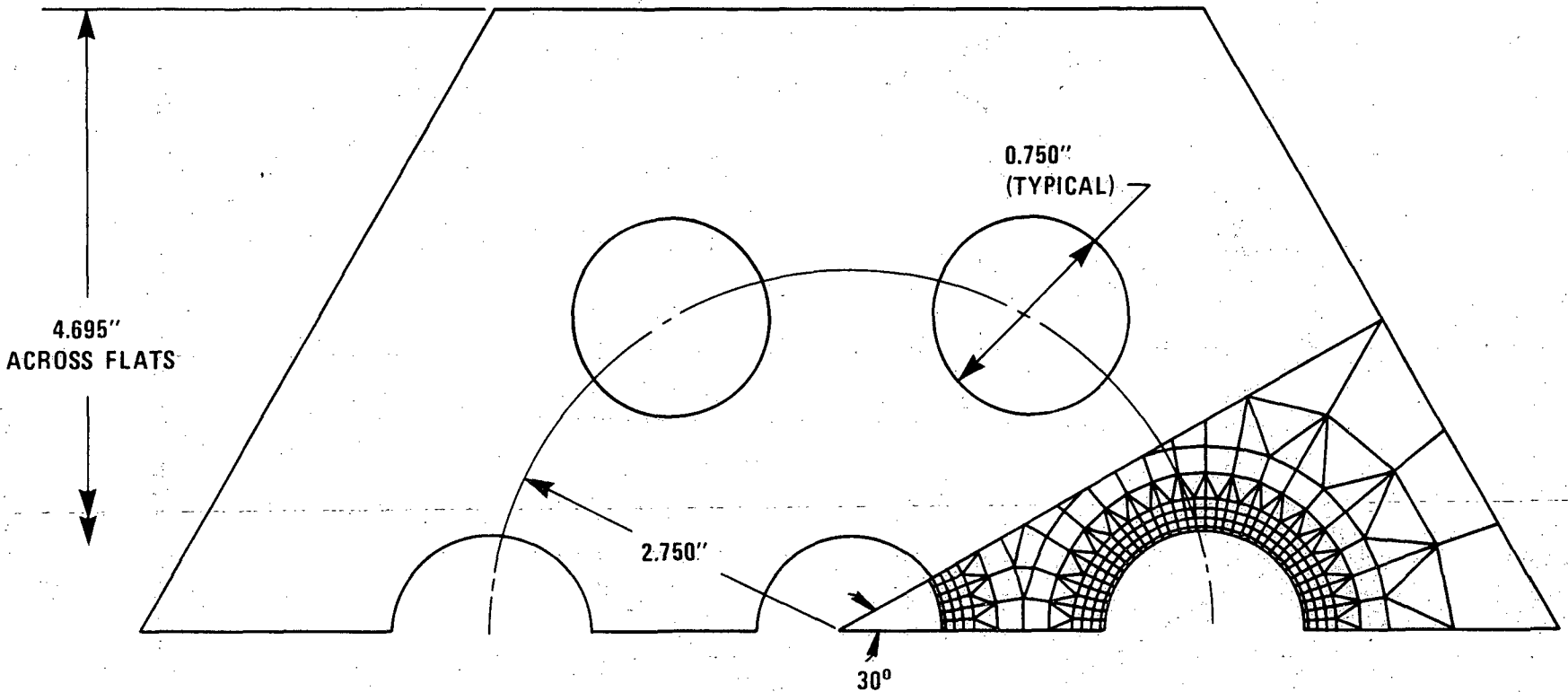
Figure 4.2-33A. Designation Scheme for Seismic and Core Restraint Loads

1789-1

4.2-514

Amend. 51  
Sept. 1979

1789-2



Amend. 51  
Sept. 1979

Figure 4.2-33B. F/A Shield Block Thermal/Mechanical Model Dimensional Extent and Finite Element Detail

1764-40

4.2-516

Amend. 51  
Sept. 1979

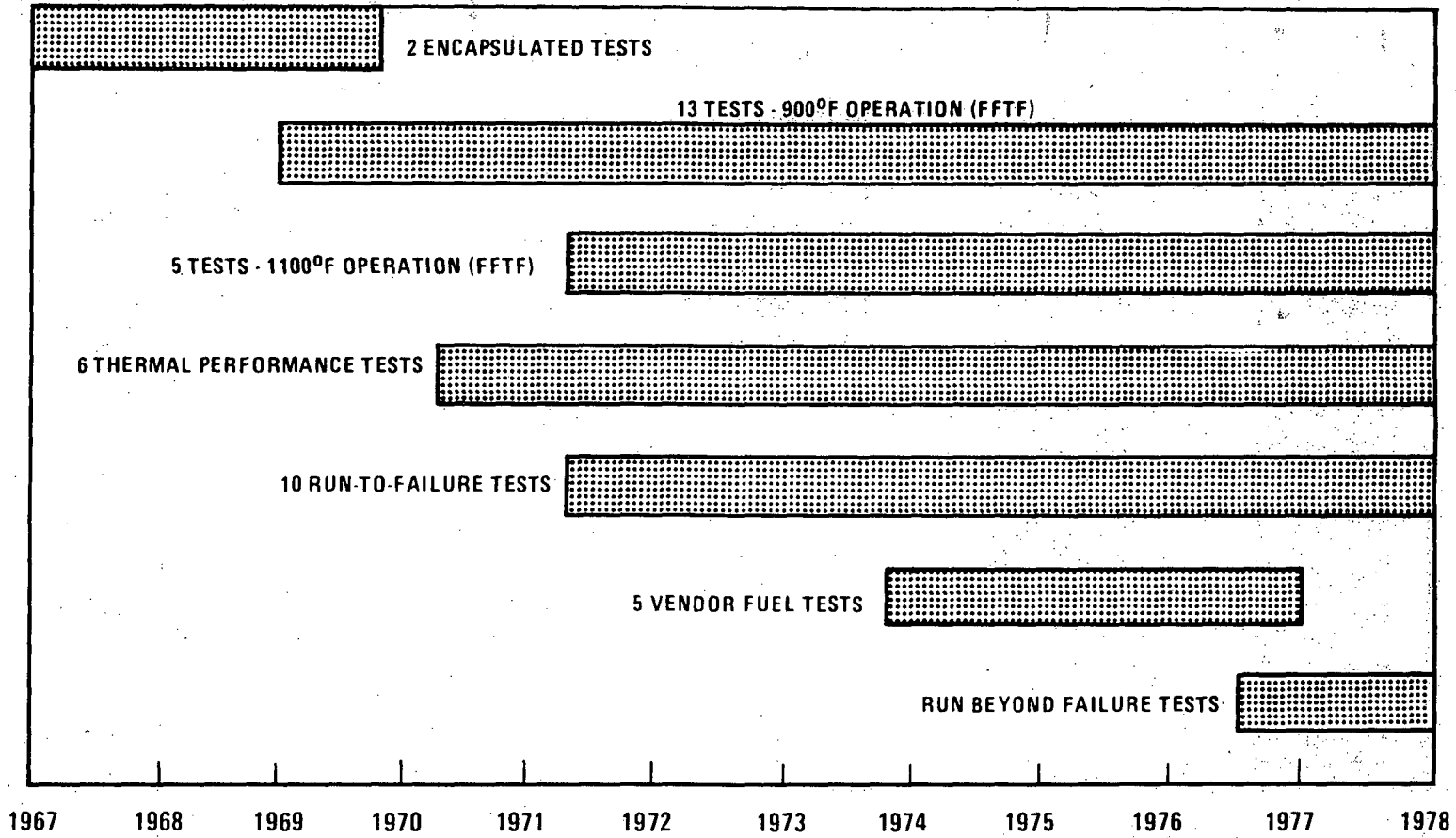
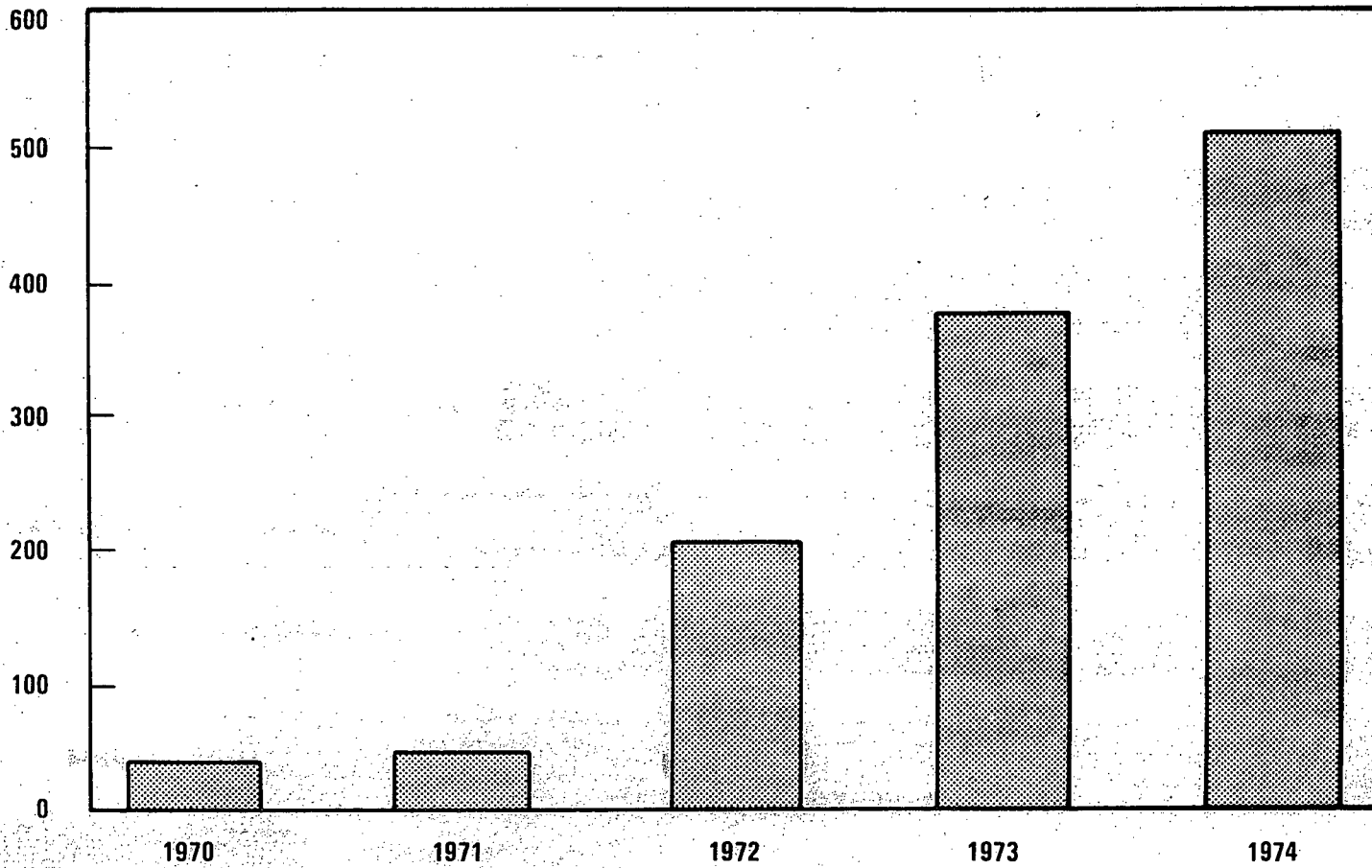


Figure 4.2-34 LMFBR Fuel Development Steady State Irradiation Testing Program

4.2-517

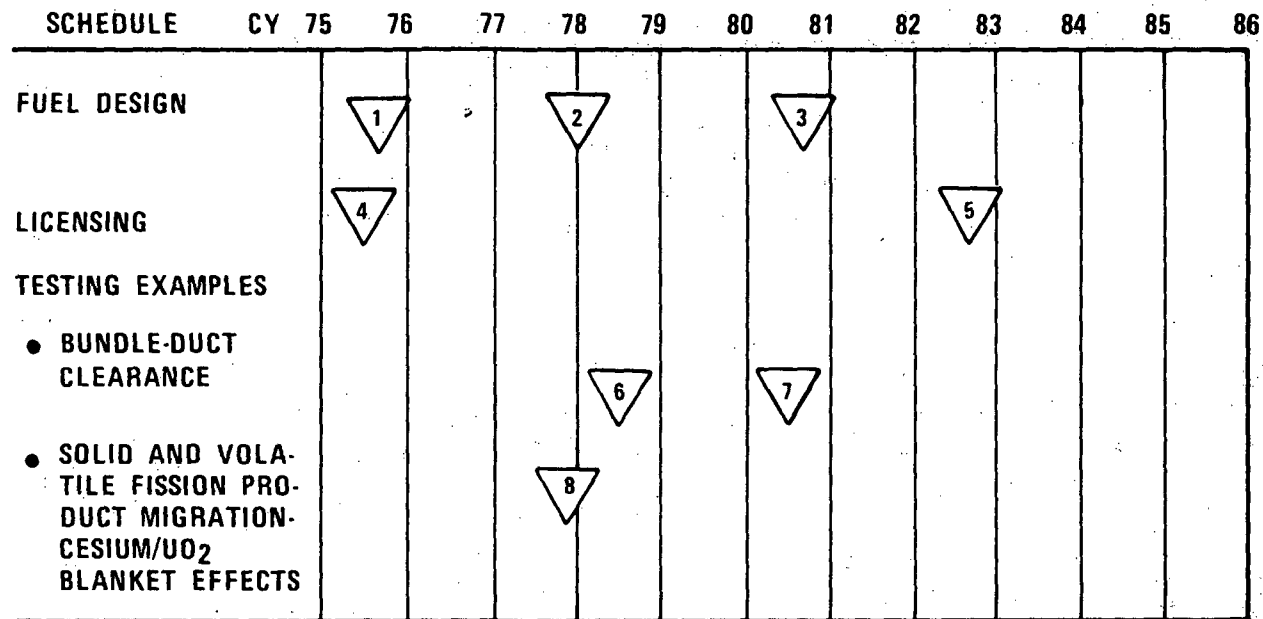
Amend.  
Sept.



4.2-35 Number of Fuel Rods Exceeding FFTF/CRBRP Goal Burnup

1764-42

4.2-518



**FALLBACK EXAMPLES**

- BUNDLE-DUCT INTERACTION - CHANGE THE INITIAL POROSITY BY SMALL CHANGES IN WIRE WRAP DIAMETER AND/OR SELECTIVE ASSEMBLY
- CESIUM/UO<sub>2</sub> BKT. EFFECTS - FOR THE FIRST SEVERAL AXIAL BLANKET PELLETS AT EACH END, INCREASE THE DIAMETRAL GAP.

**LEGEND:**

1 PRELIMINARY DESIGN REVIEW

4 PSAR SUBMITTAL

6 P13,P14 EXAMINATION COMPLETE

2 FINAL DESIGN REVIEW

5 START FSAR

7 VALIDATE DESIGN FIX FOR BUNDLE VIBRATION AND WEAR

3 RELEASE TO FABRICATION

8 ESTABLISH EFFECT WITH LOW O/M FUEL

Figure 4.2-35A Design Fallback Positions

Amend. 51  
Sept. 1979

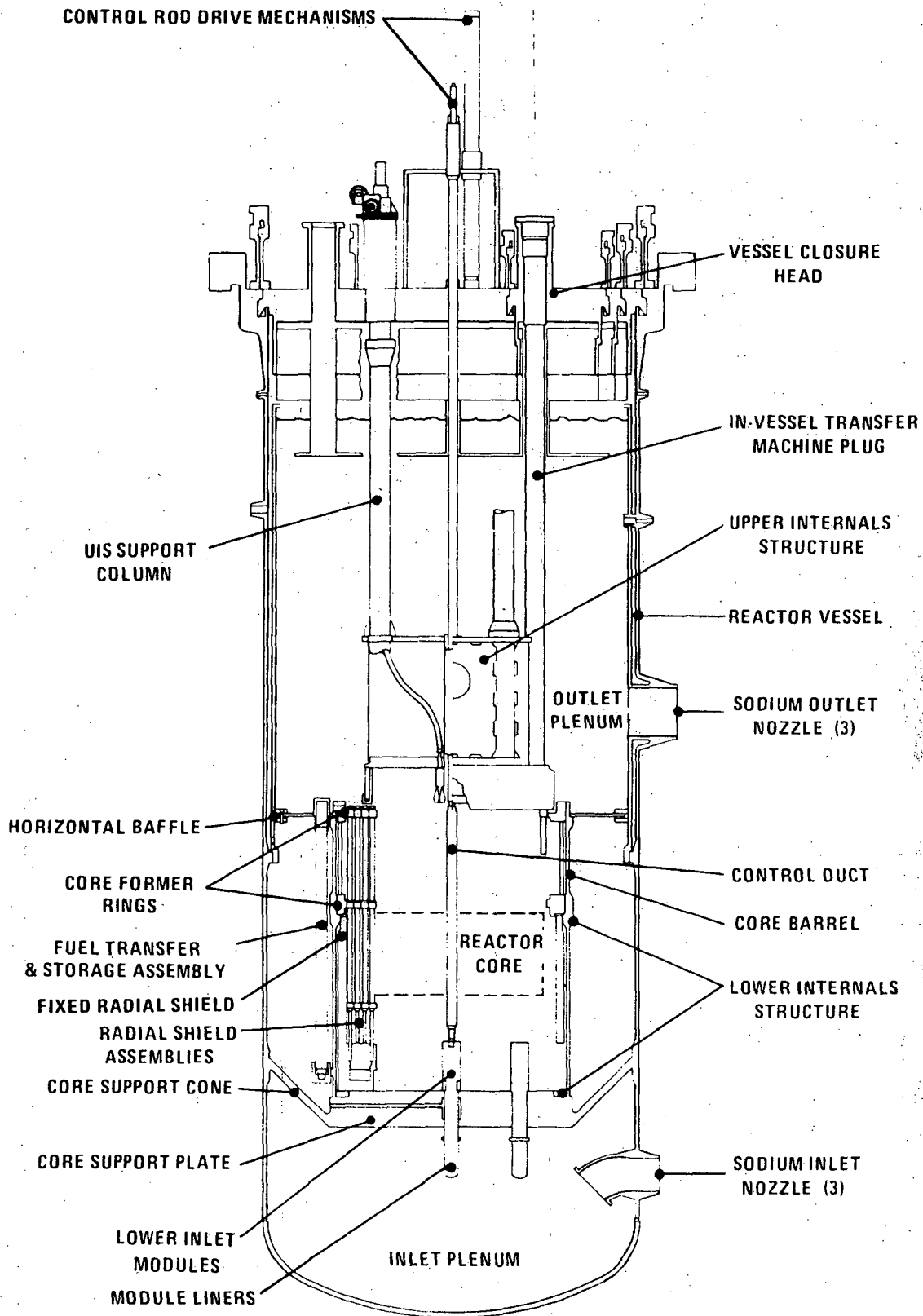


Figure 4.2-36. Reactor Elevation

4419-4

4.2-519

Amend. 58  
Nov. 1980

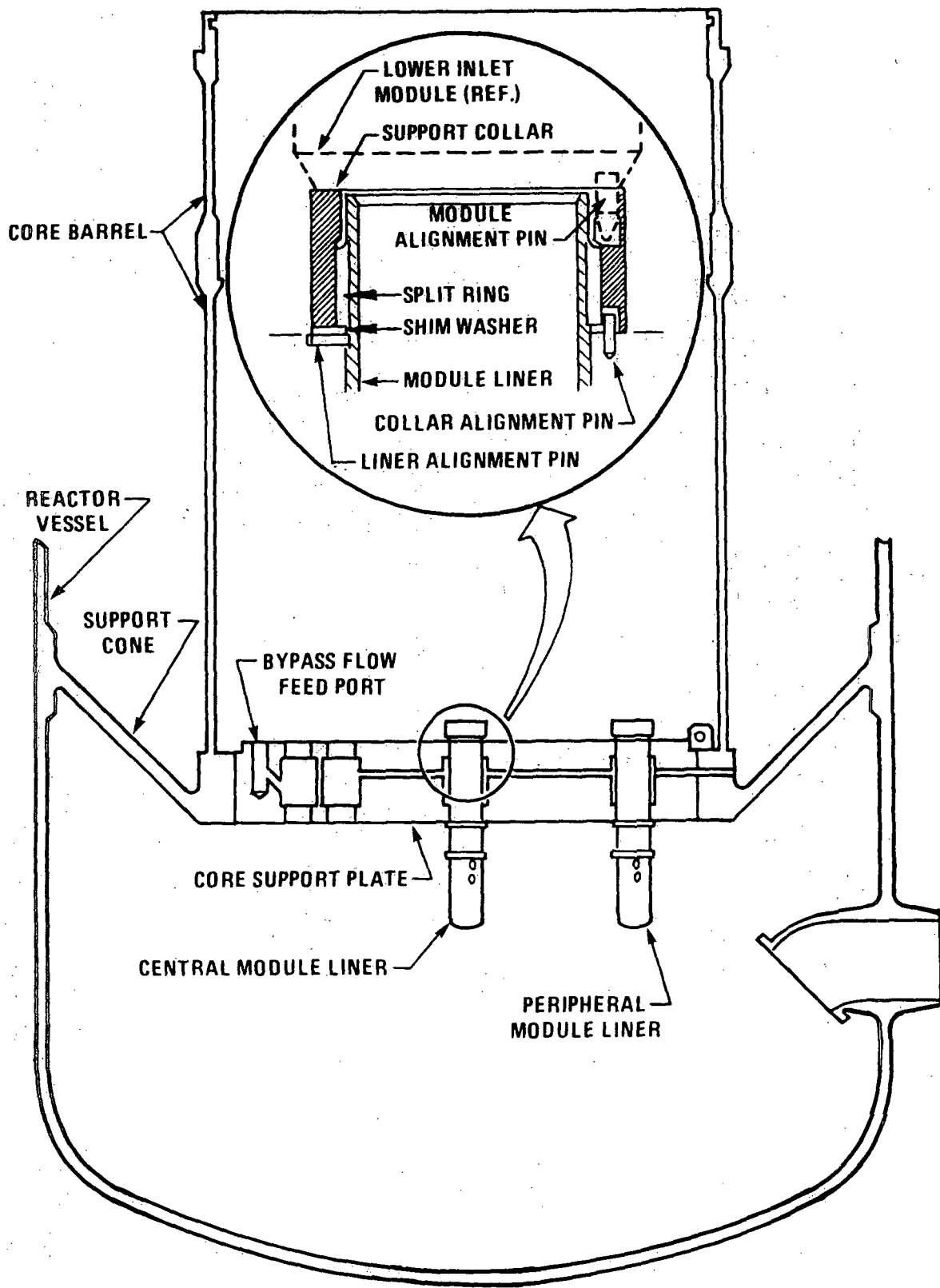


Figure 4.2-37. 304 Stainless Steel Core Support Structure

4419-3



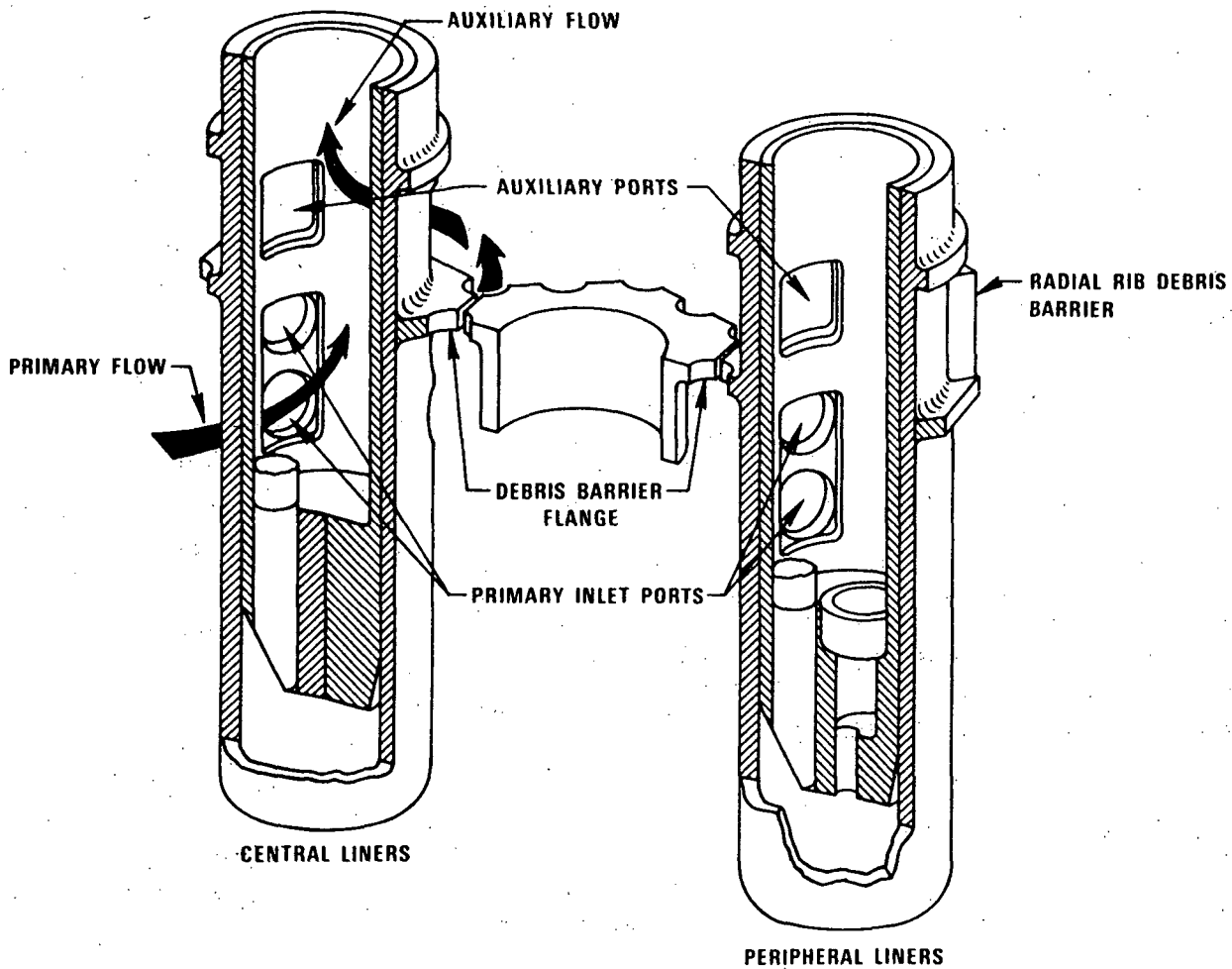


Figure 4.2-38. Core Module Liner

6664-68

4.2-521

Amend. 51  
Sept. 1979

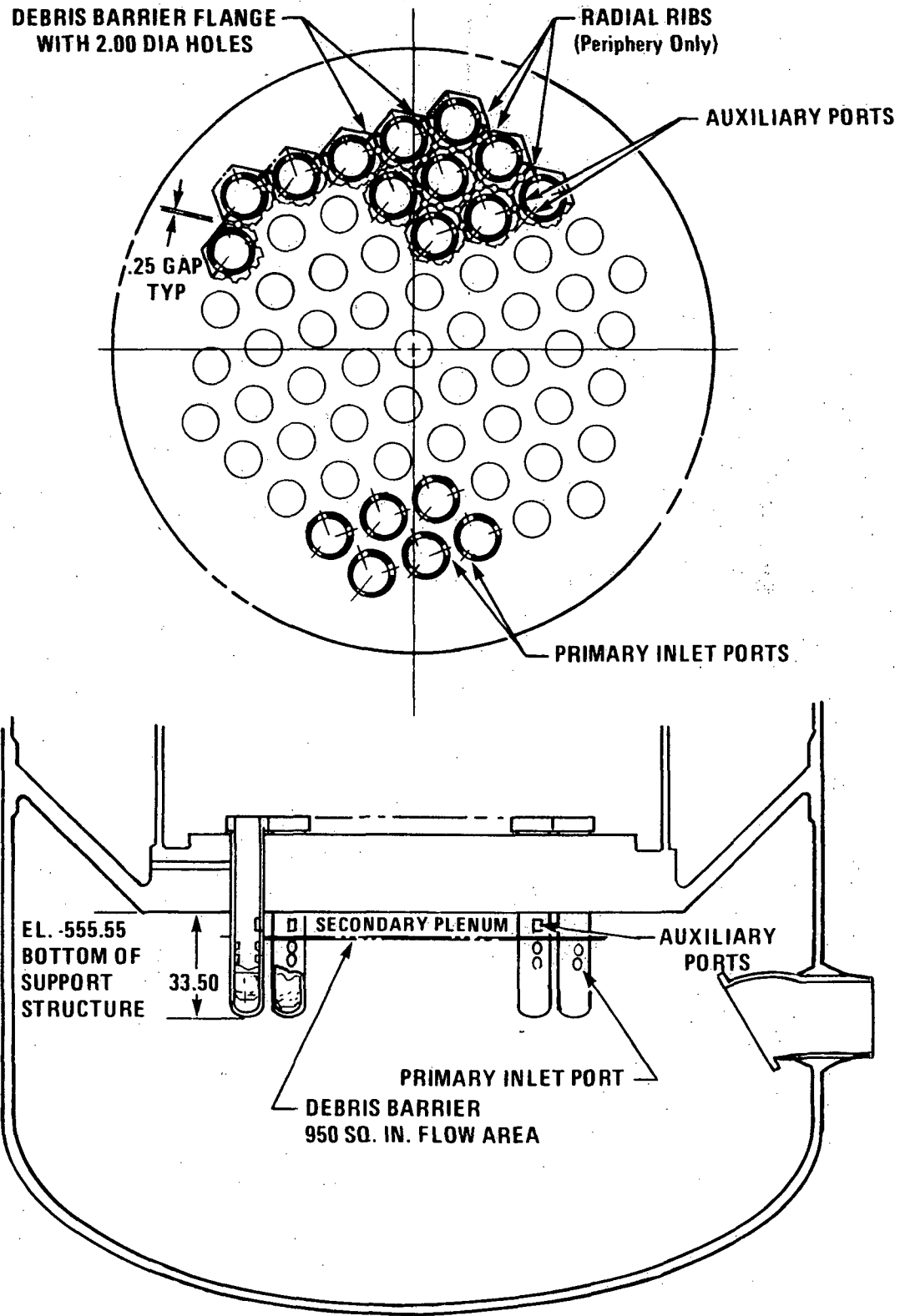


Figure 4.2-39. Core Support Structure Secondary Plenum Concept

4419-1

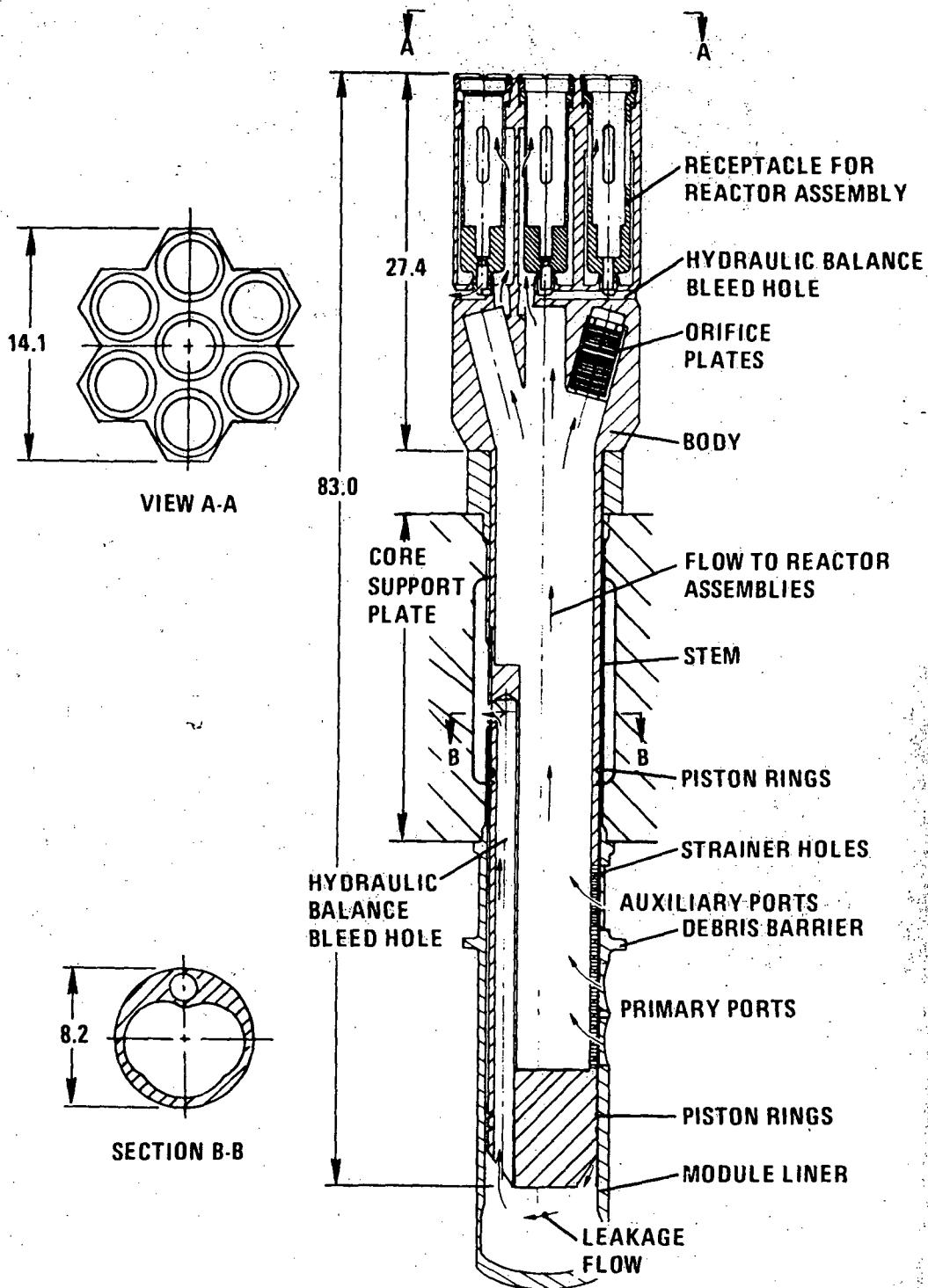


Figure 4.2-40 Elevation of Typical Lower Inlet Module

9826

4.2-523

Amend. 51  
Sept. 1979

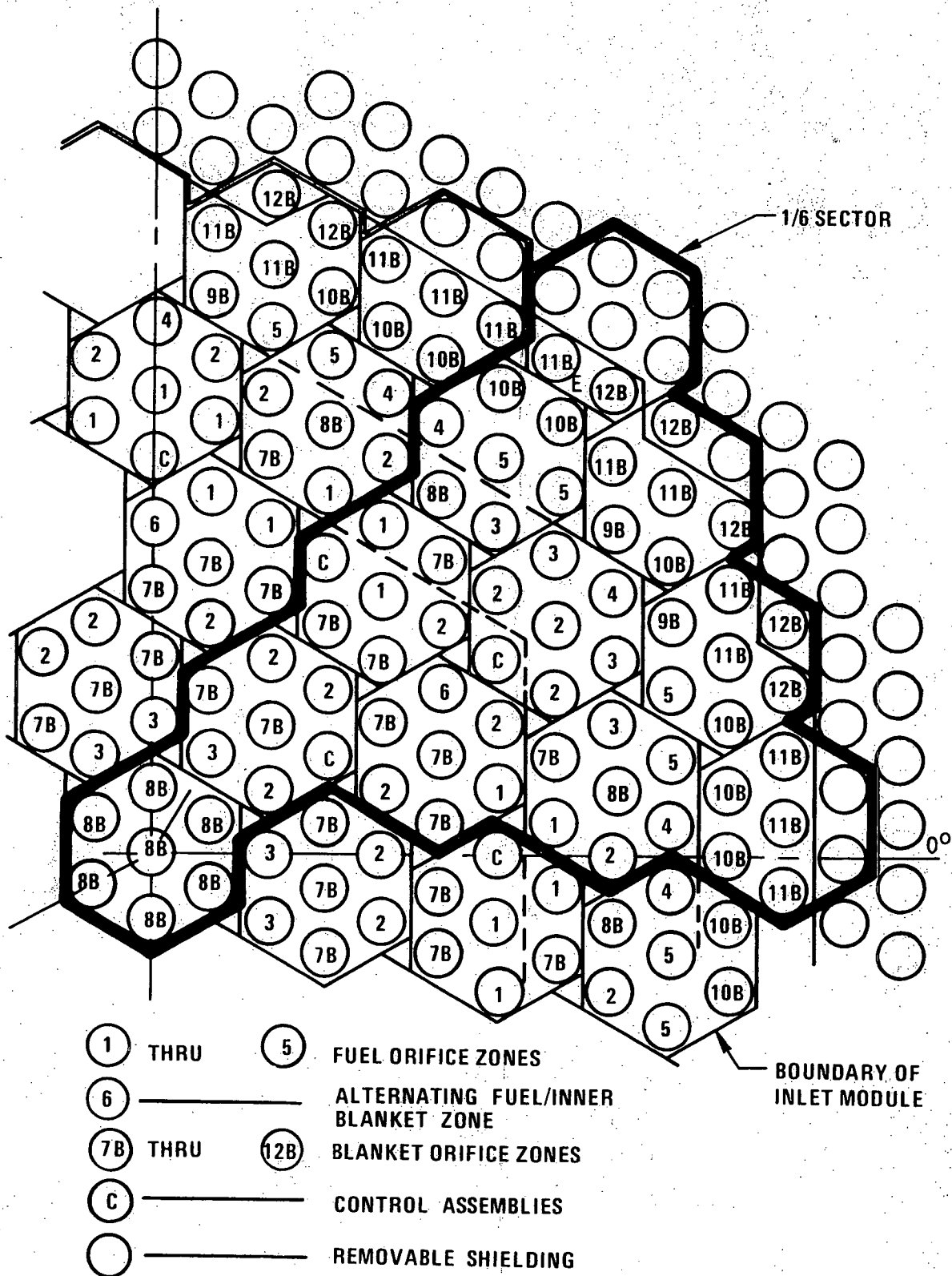
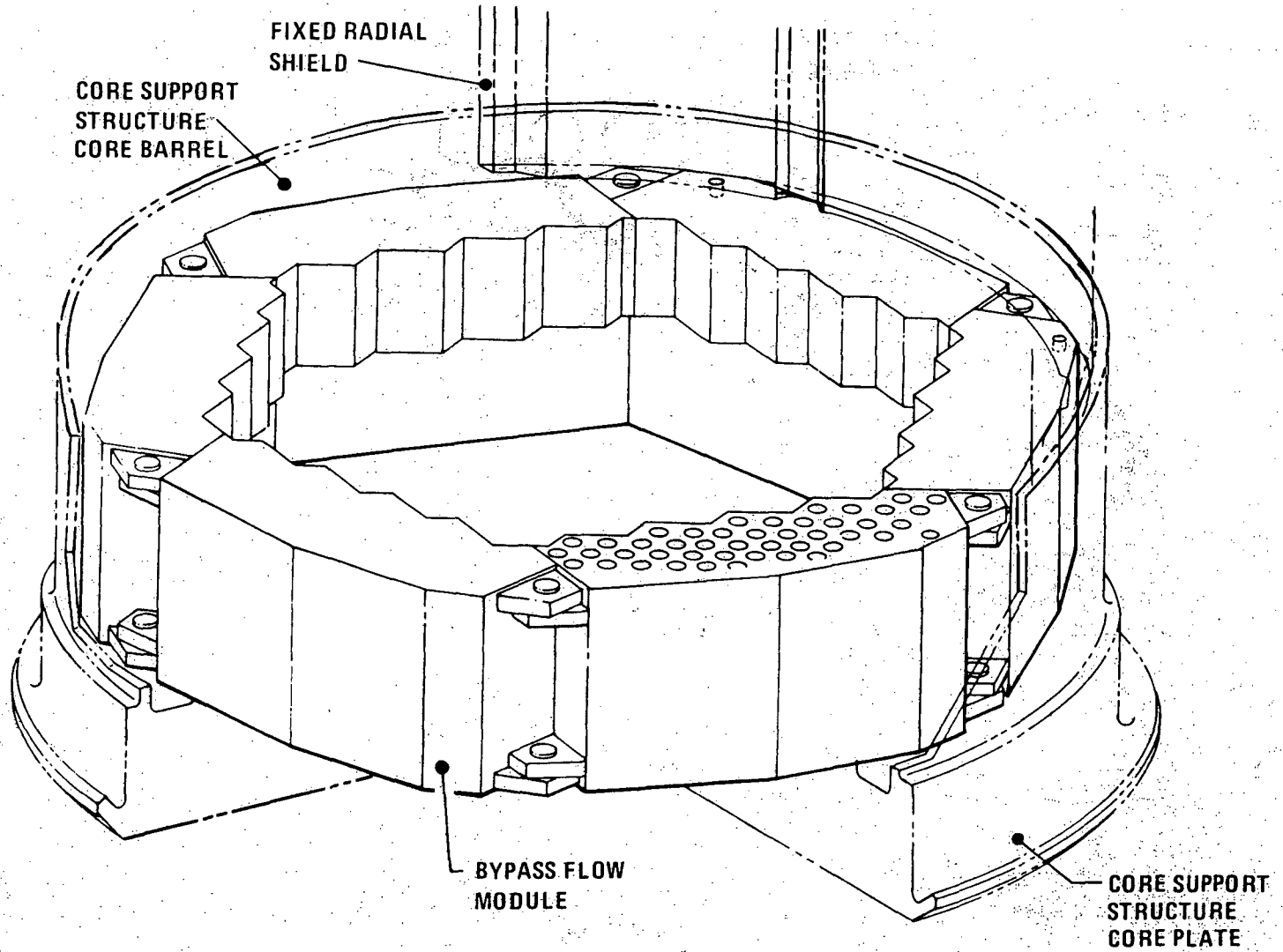


FIGURE 4.2-41. Inlet Module Core Map Showing the Orificing Plan for Compactor Assemblies 5894-7

4419-2



4.2-525

Amend. 58  
Nov. 1980

Figure 4.2-41A. Bypass Flow Module Assembly

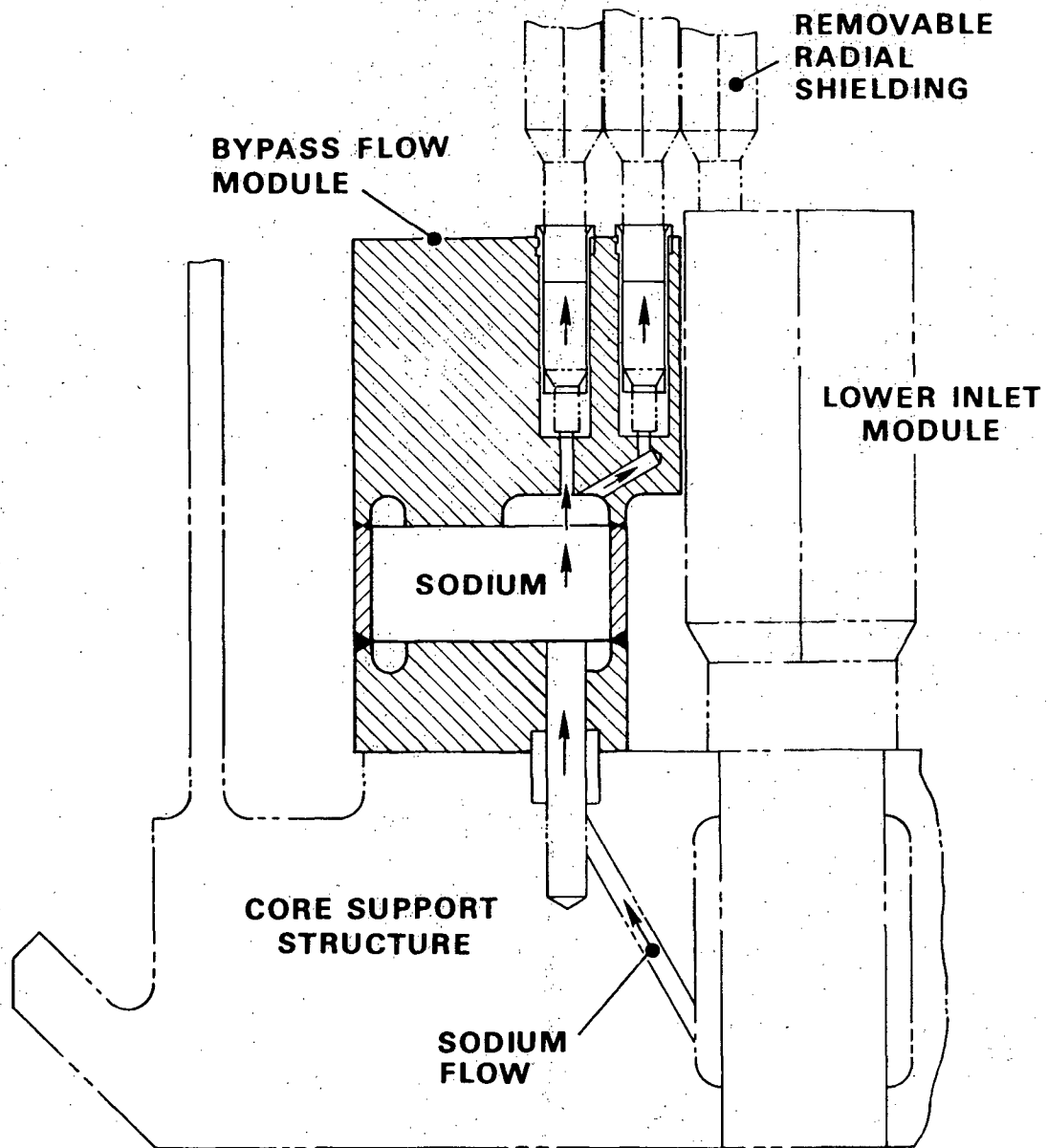


Figure 4.2-41B. Bypass Flow Module Section View

8791-4

4.2-526

Amend. 51  
 Sept. 1979

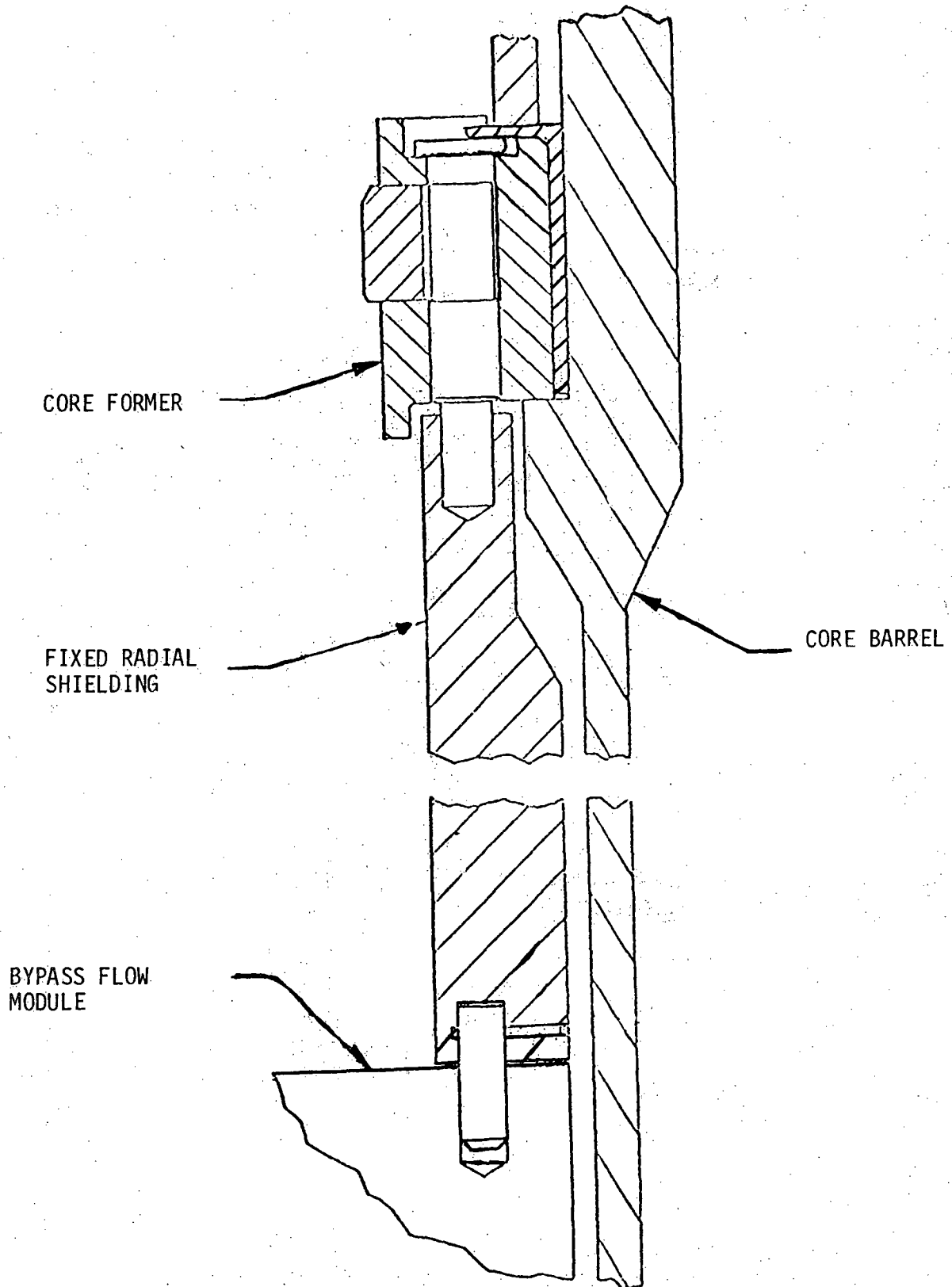


Figure 4.2-42. Fixed Radial Shielding

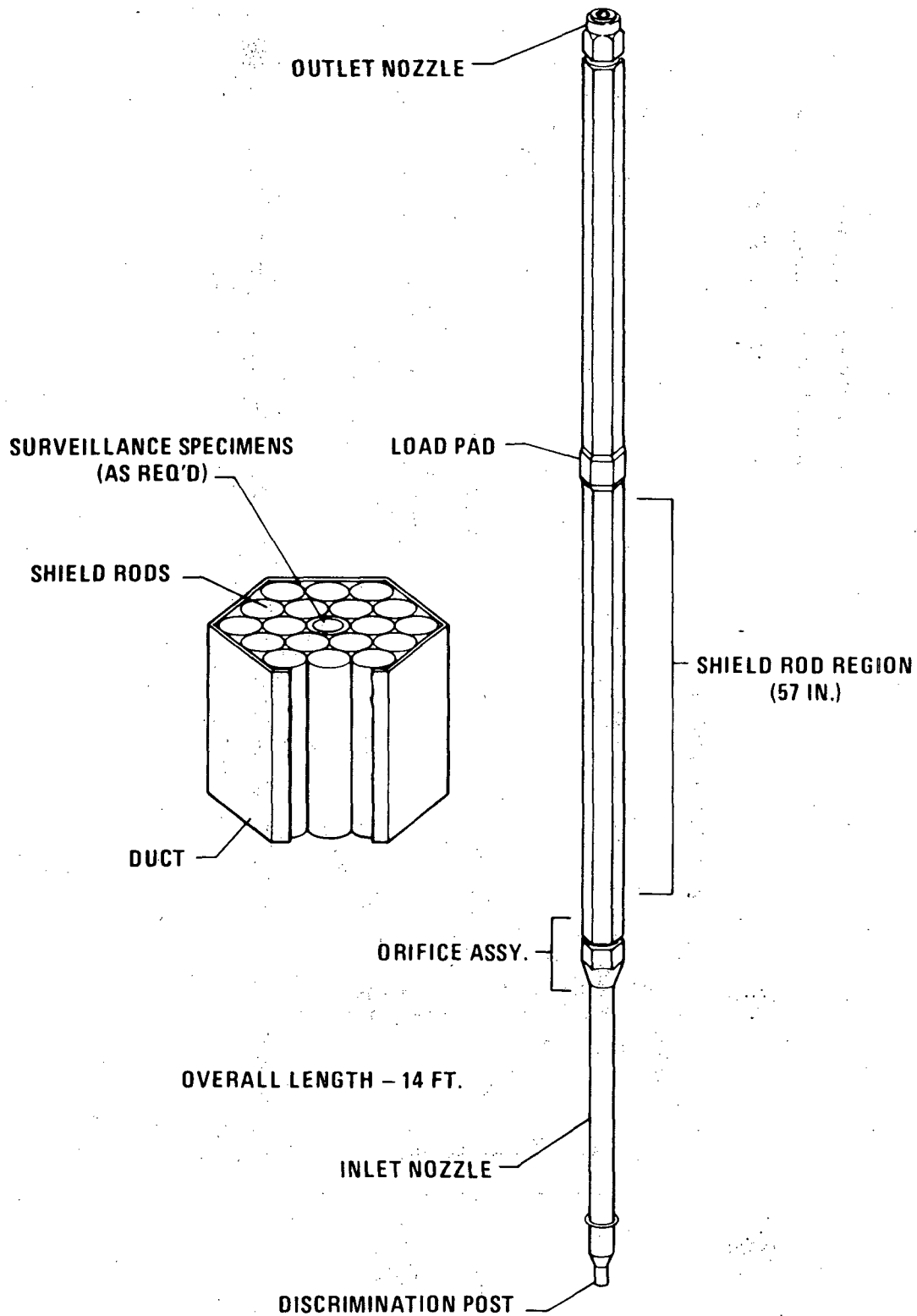


Figure 4.2-43. Removable Radial Shield Assembly

79544



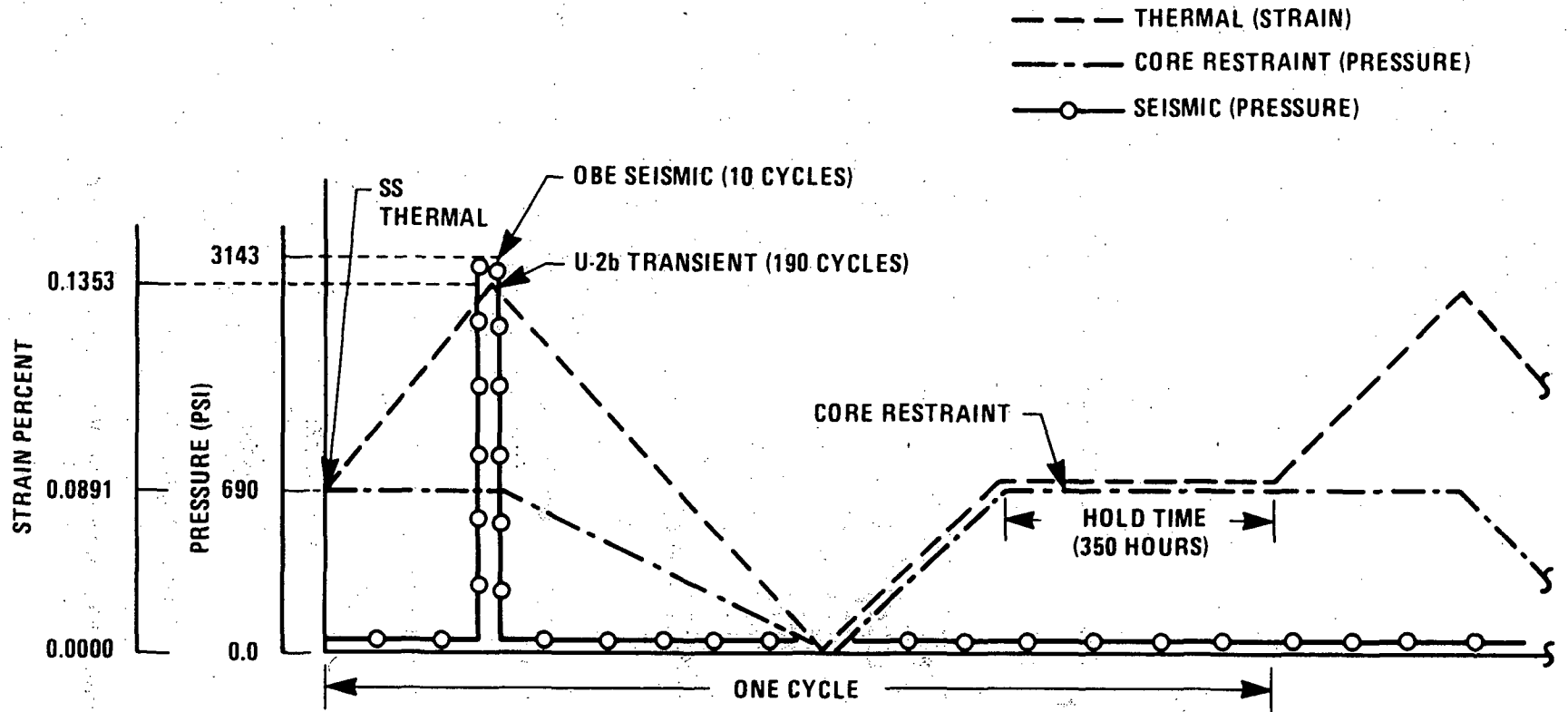


FIGURE 4.2-43A. LOADING HISTOGRAM USED IN INELASTIC ANALYSES OF RRS ACLP

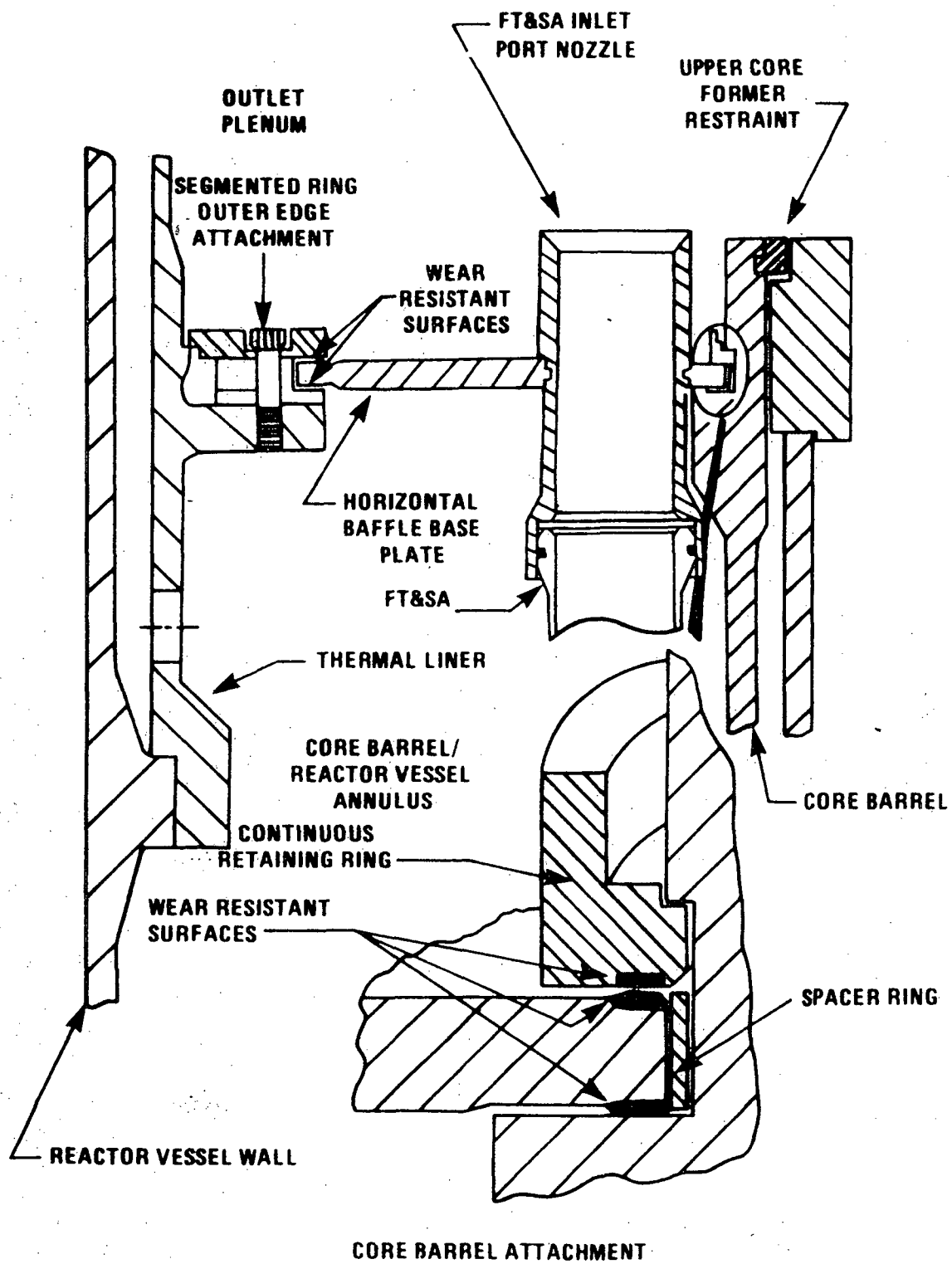


Figure 4.2-44. Horizontal Baffle

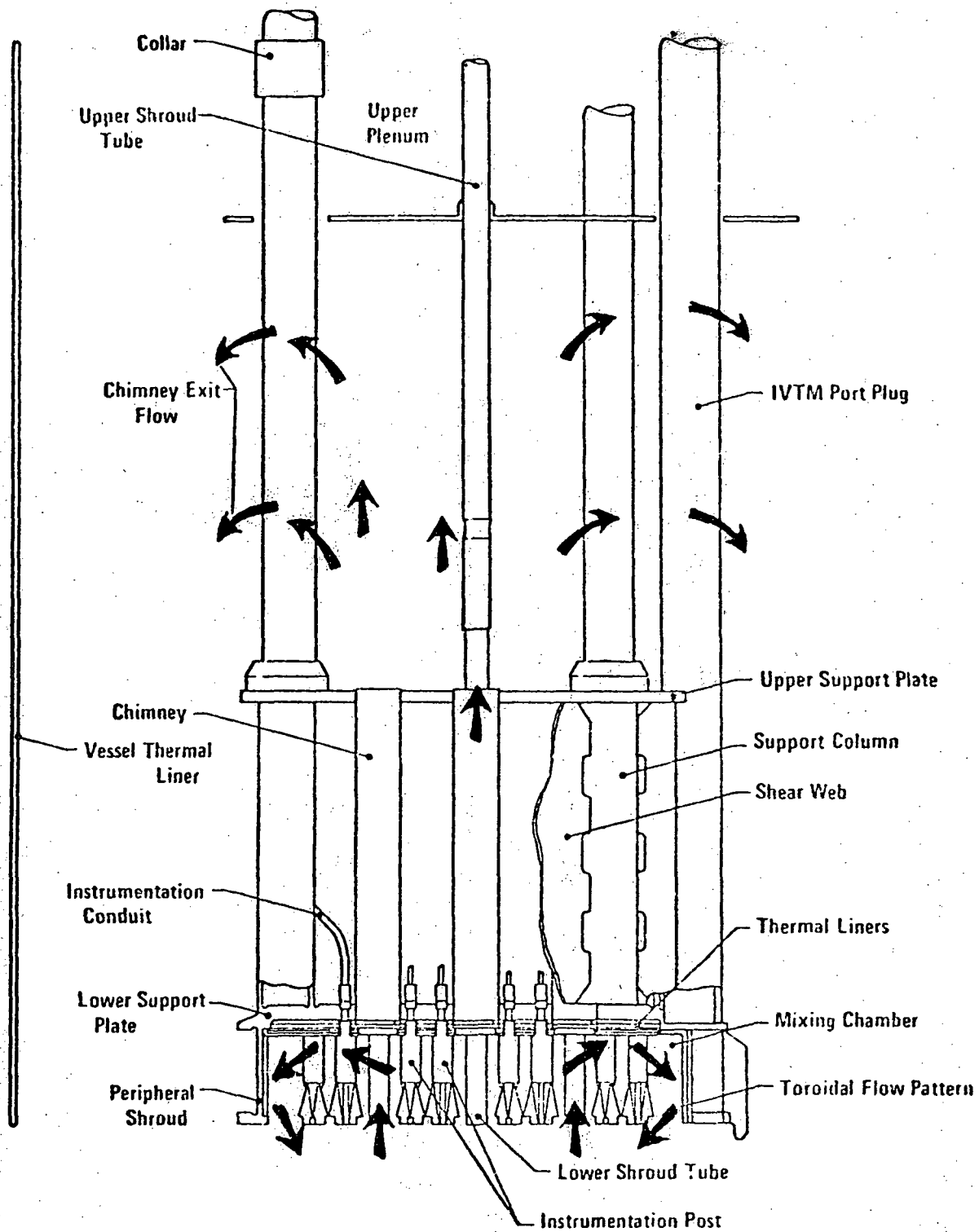


Figure 4.2-45 Elevation of the UIS In The CRBRP

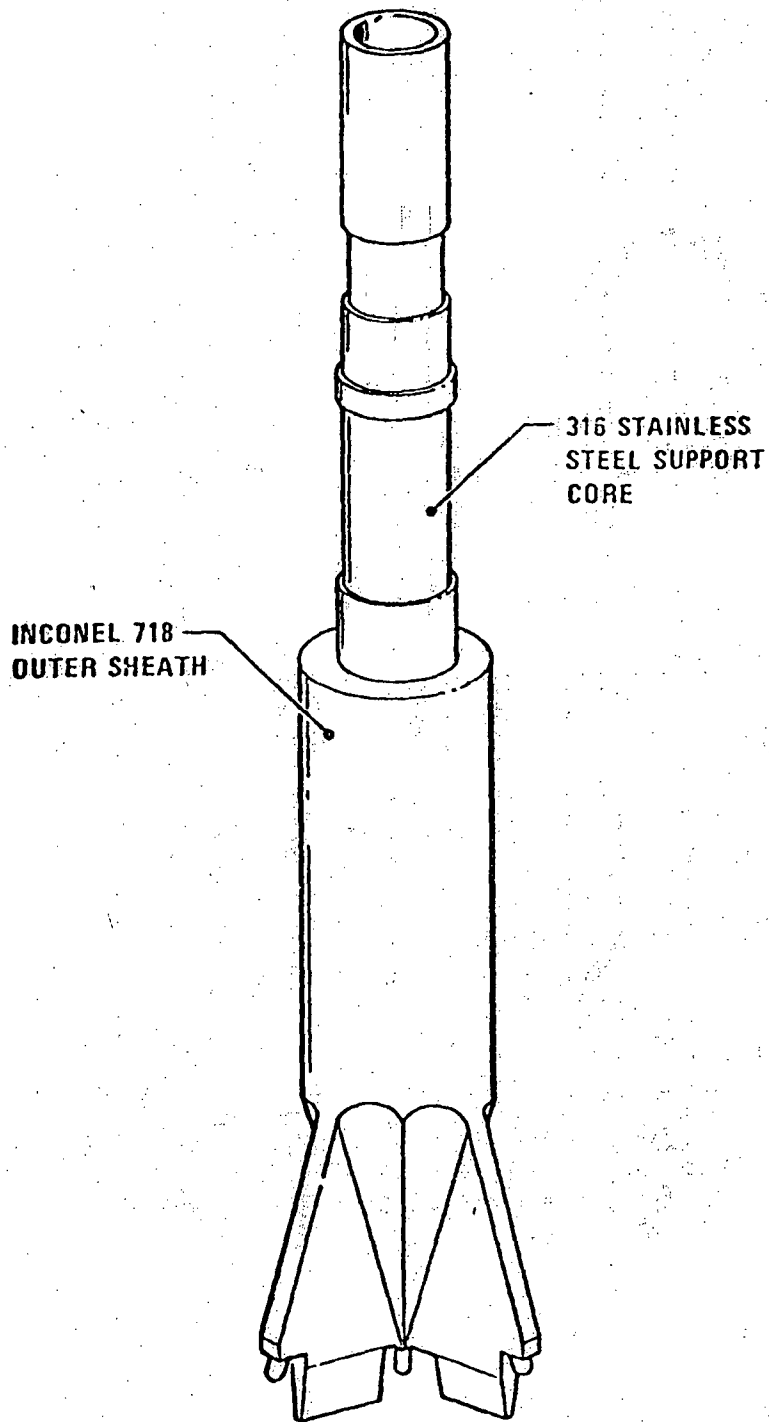


Figure 4.2-45A Instrumentation Post (Bench Assembly)

4.2-531

Amend. 51  
Sept. 1979

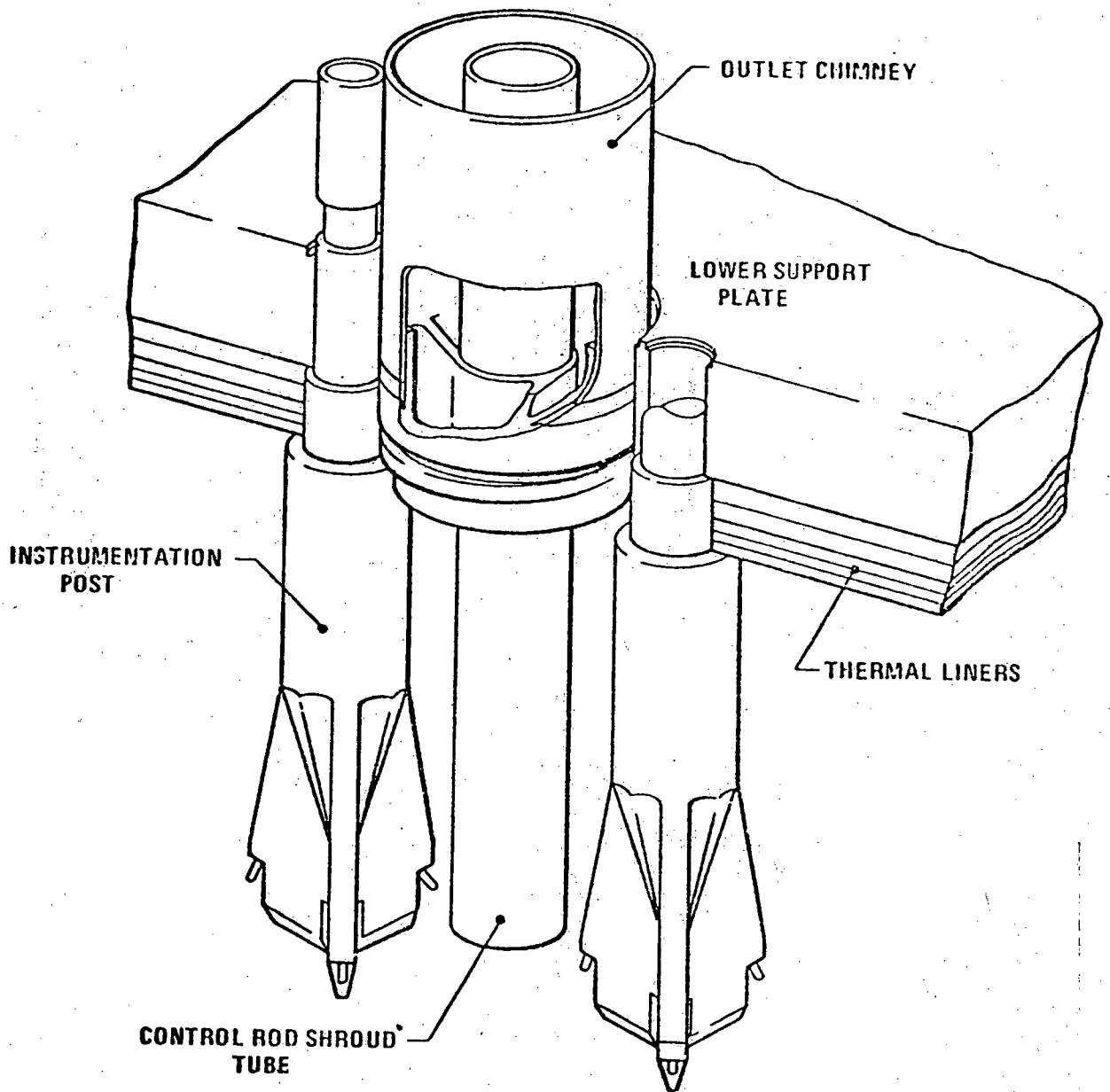


Figure 4.2-45B Method of Positioning Control Rod Shroud Tube

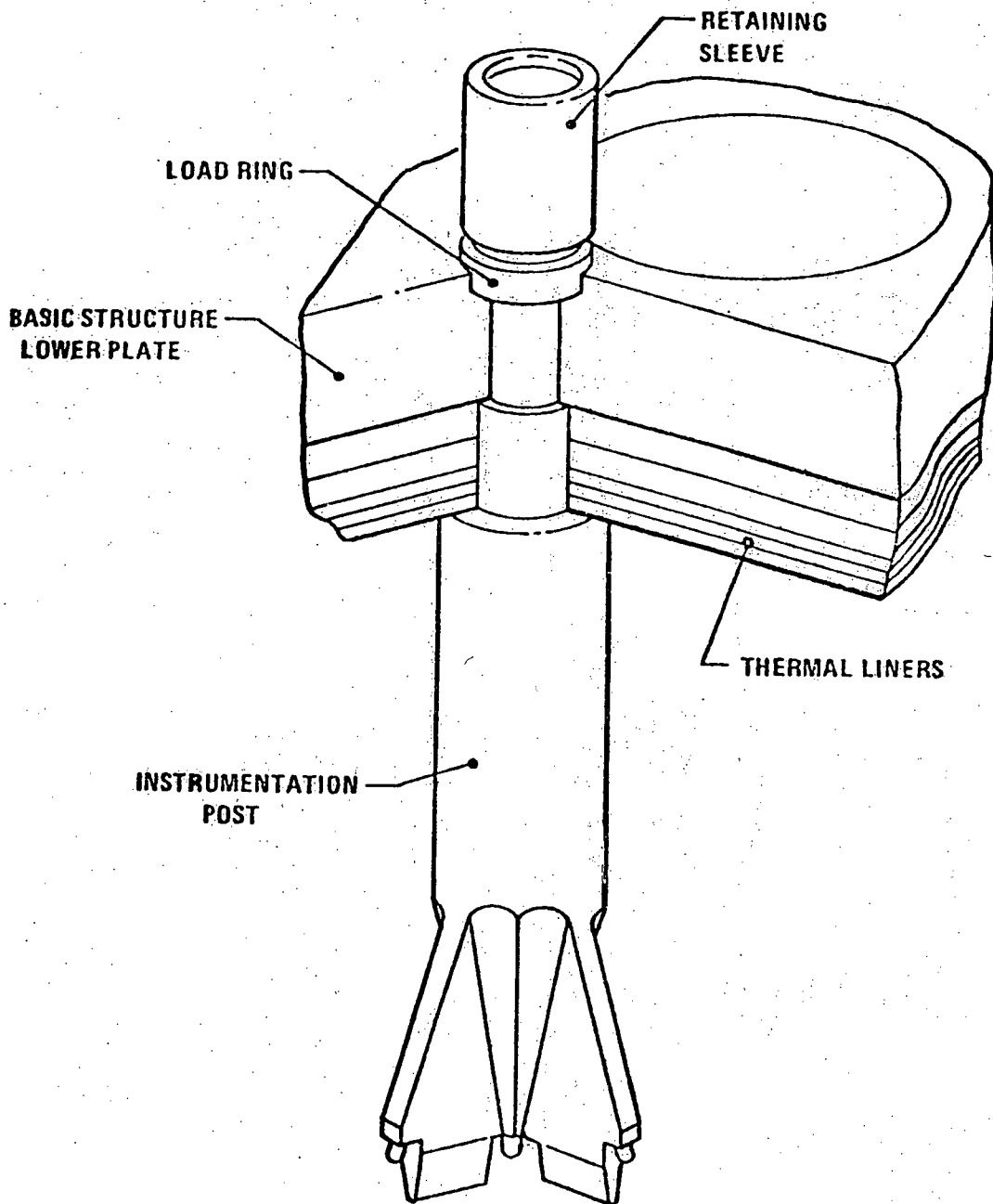


Figure 4.2-45C Instrumentation Post Installation

Amend. 51  
Sept. 1979

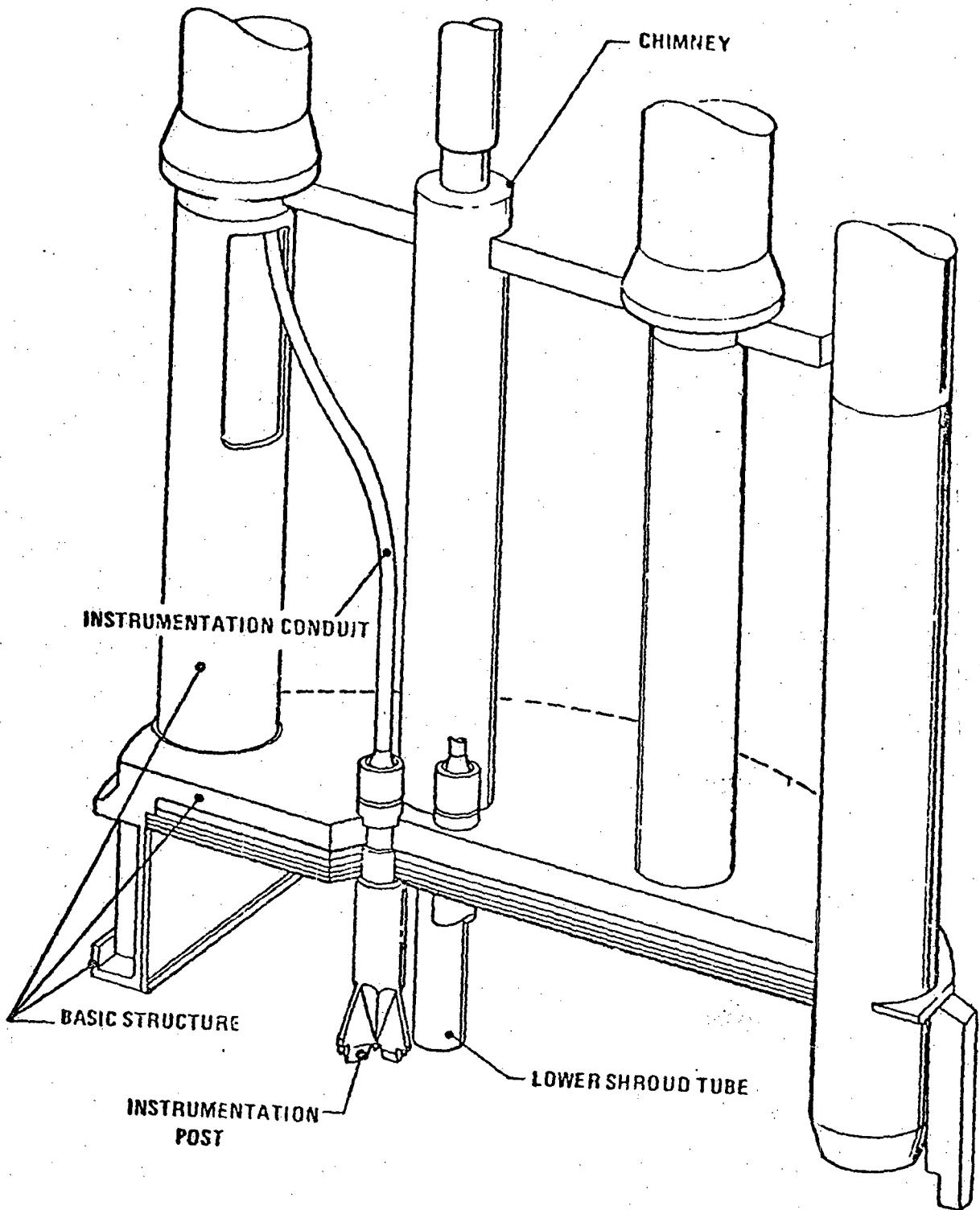


Figure 4.2-45D. Instrumentation Post Installation

Amend. 51  
Sept. 1979

5315-1

4.2-535

Amend. 61  
Sept. 1981

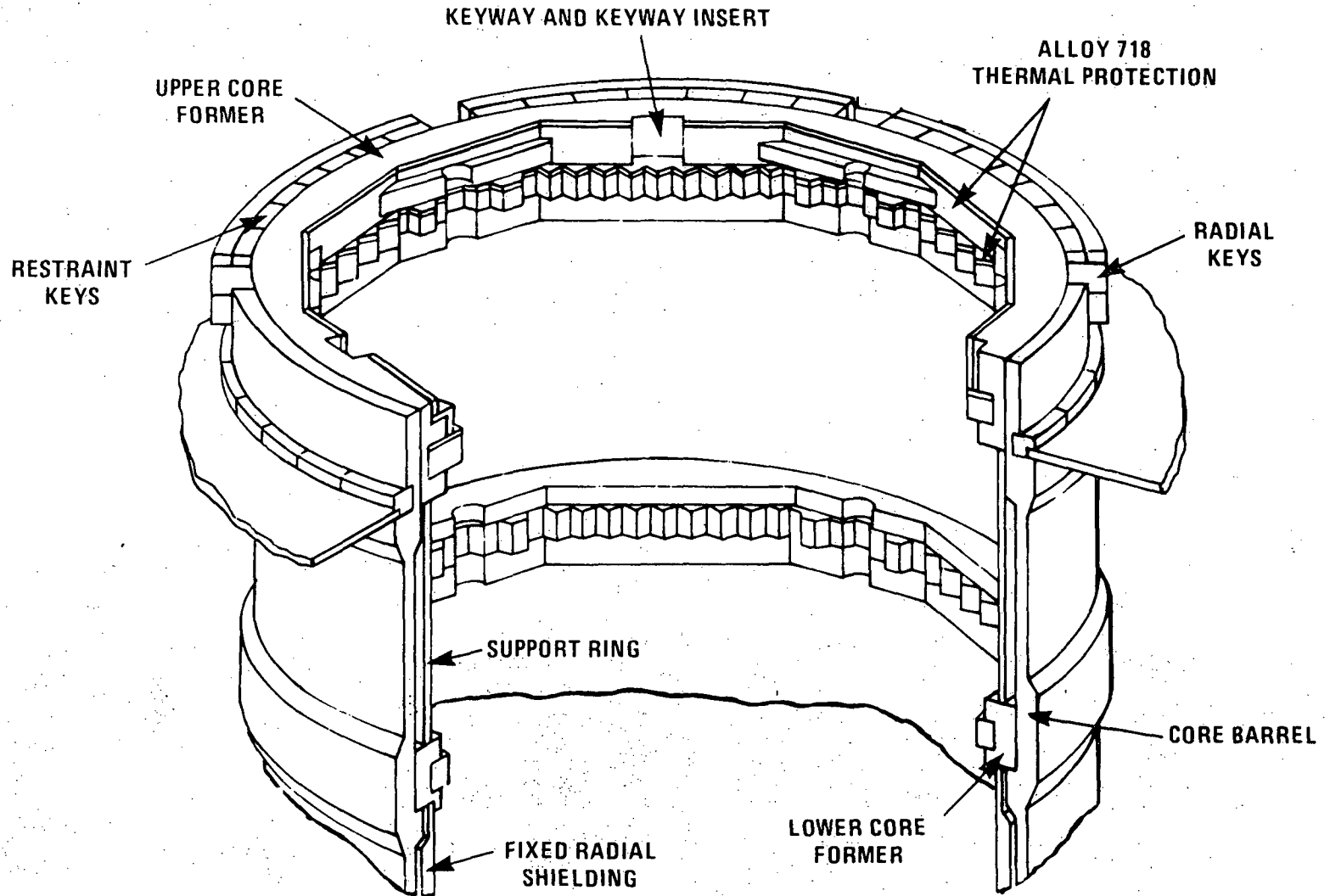
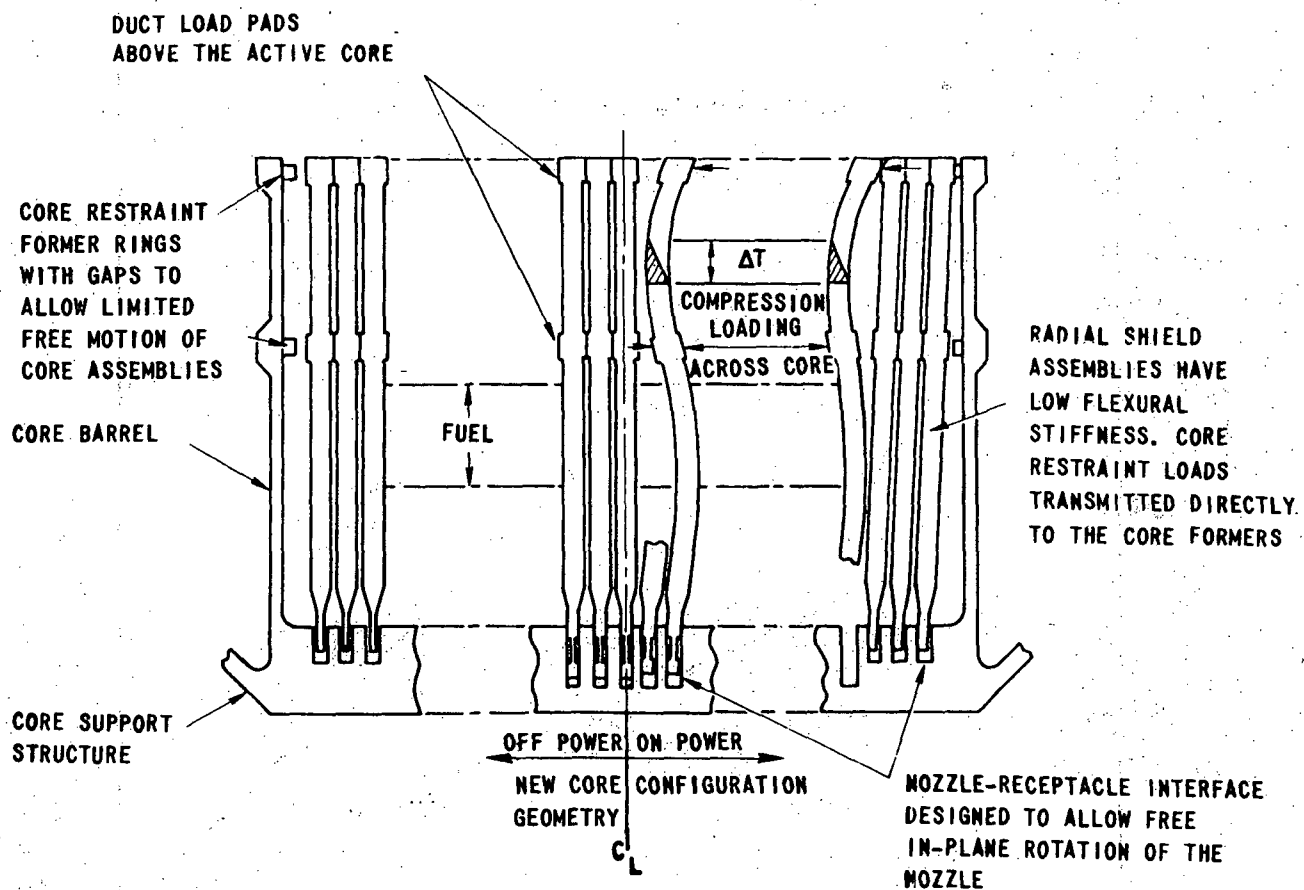


Figure 4.2-46. Core Former Structure





THIS FIGURE UTILIZES AN EXAGGERATED SCALE TO ILLUSTRATE THE FUEL ASSEMBLY DISTORTIONS

Figure 4.2-47. Limited Free Bow Core Restraint Concept

666472

4.2-536

Amend. 51  
Sept. 1979

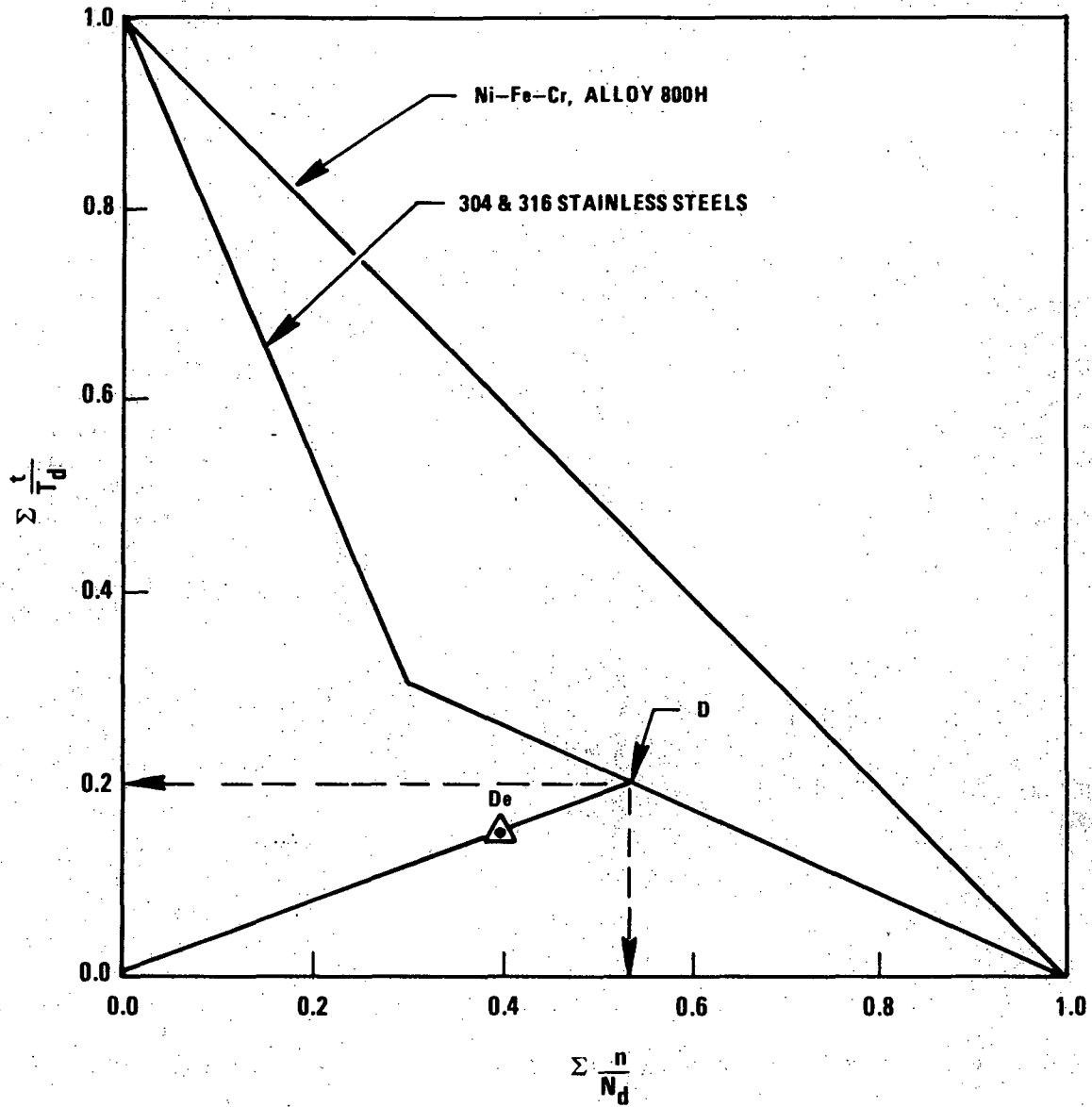


Figure 4.2-47A. Creep-Fatigue Damage Envelope

3417-1

Amend. 53  
Jan. 1980

4.2-536a

3238-1

4.2-536b

Amend. 57  
Nov. 1980

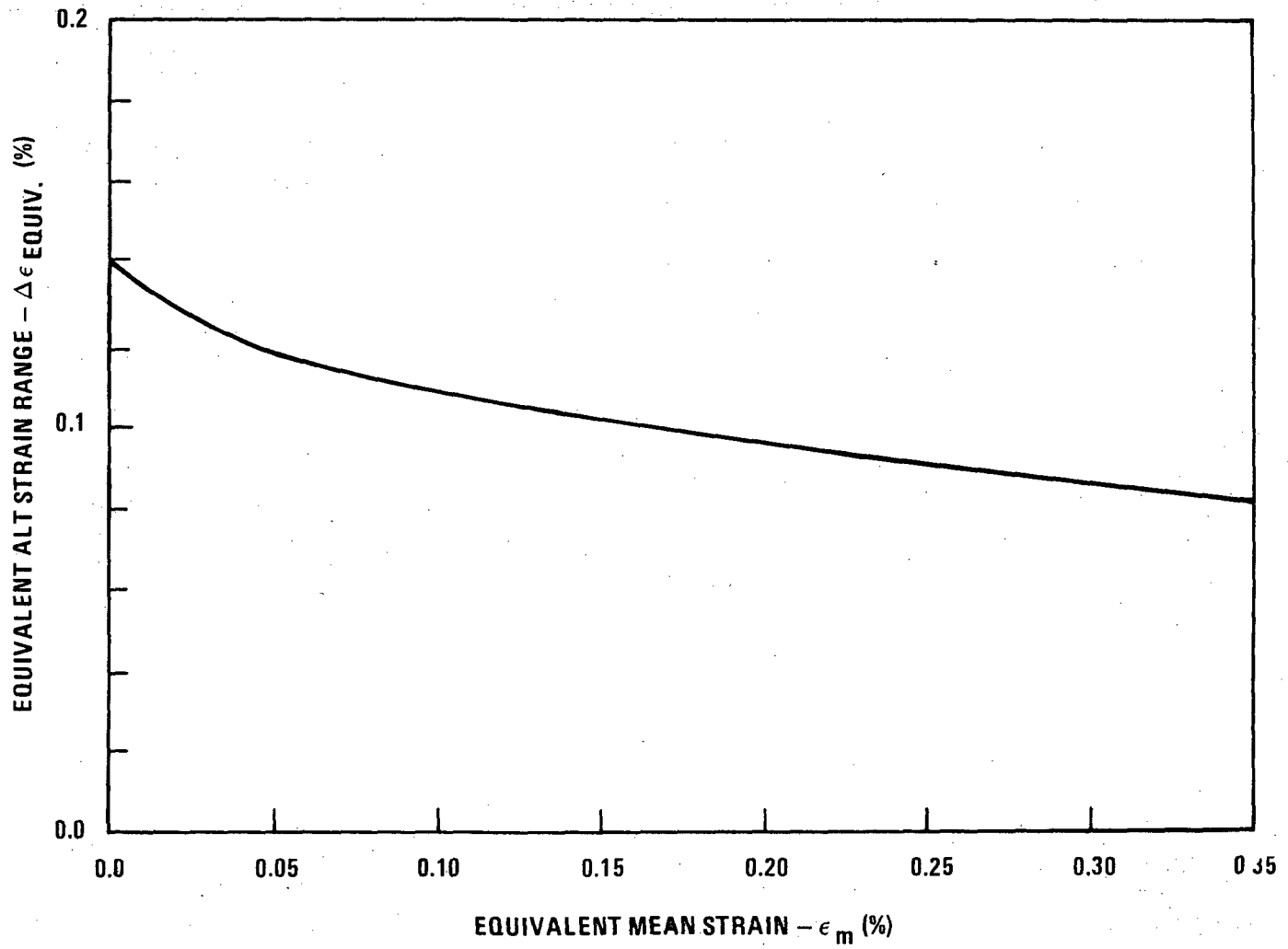
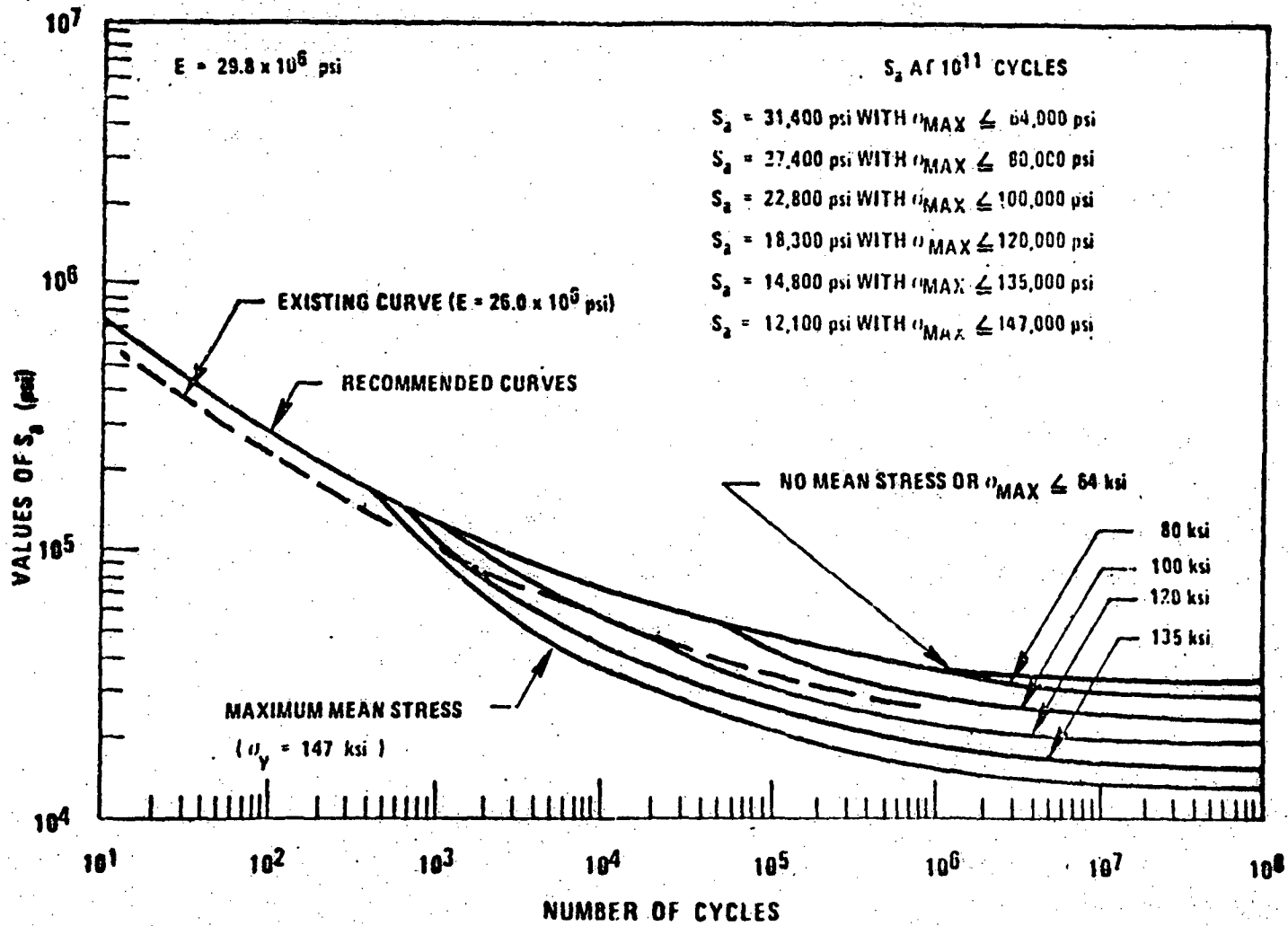


Figure 4.2-47B Allowable Alternating Strain Range Versus Mean Strain for T ≤ 1100°F

4.2-537



Amend. 51  
Sept. 1979

Figure 4.2-48 Design Fatigue Curve for Nickel-Chromium Alloy 718

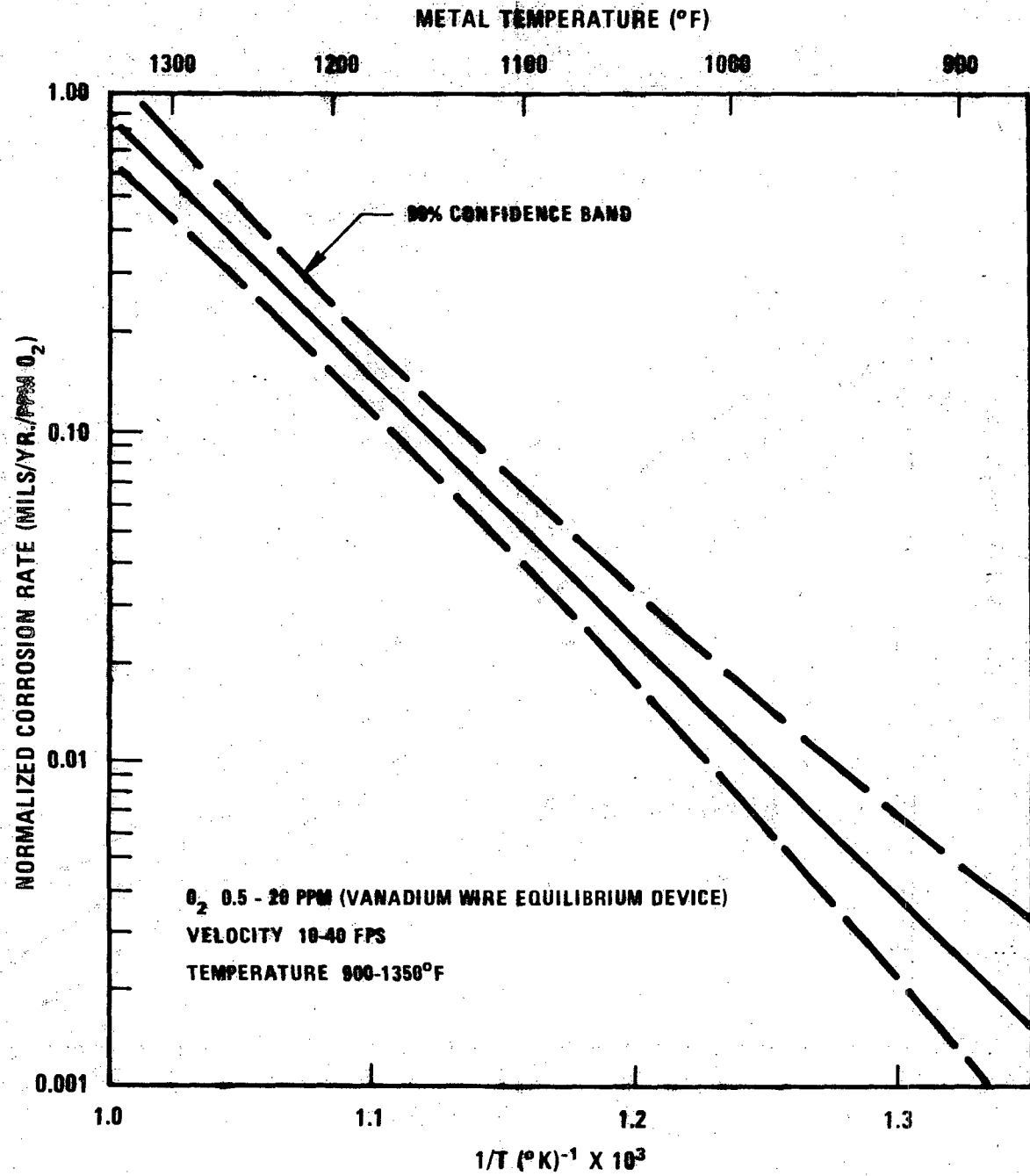


Figure 4.2-48A. Corrosion Rate of Types 304 and 316 Stainless Steel in Flowing Sodium.

7683-8

4.2-538

Amend. 51  
Sept. 1979

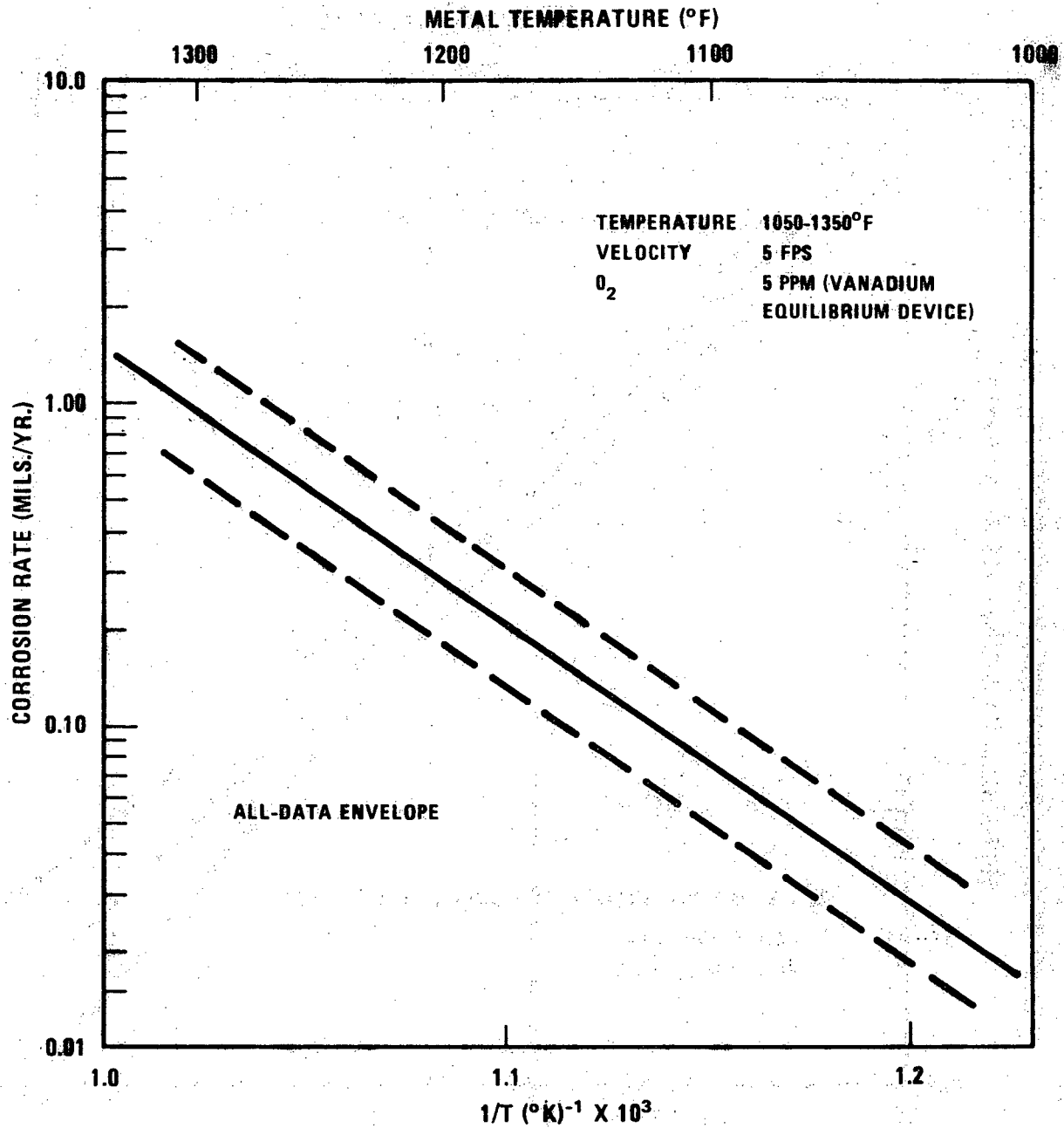


Figure 4.2-48B. Corrosion Rate of Inconel 718 in Sodium.

4685-1

4.2-540

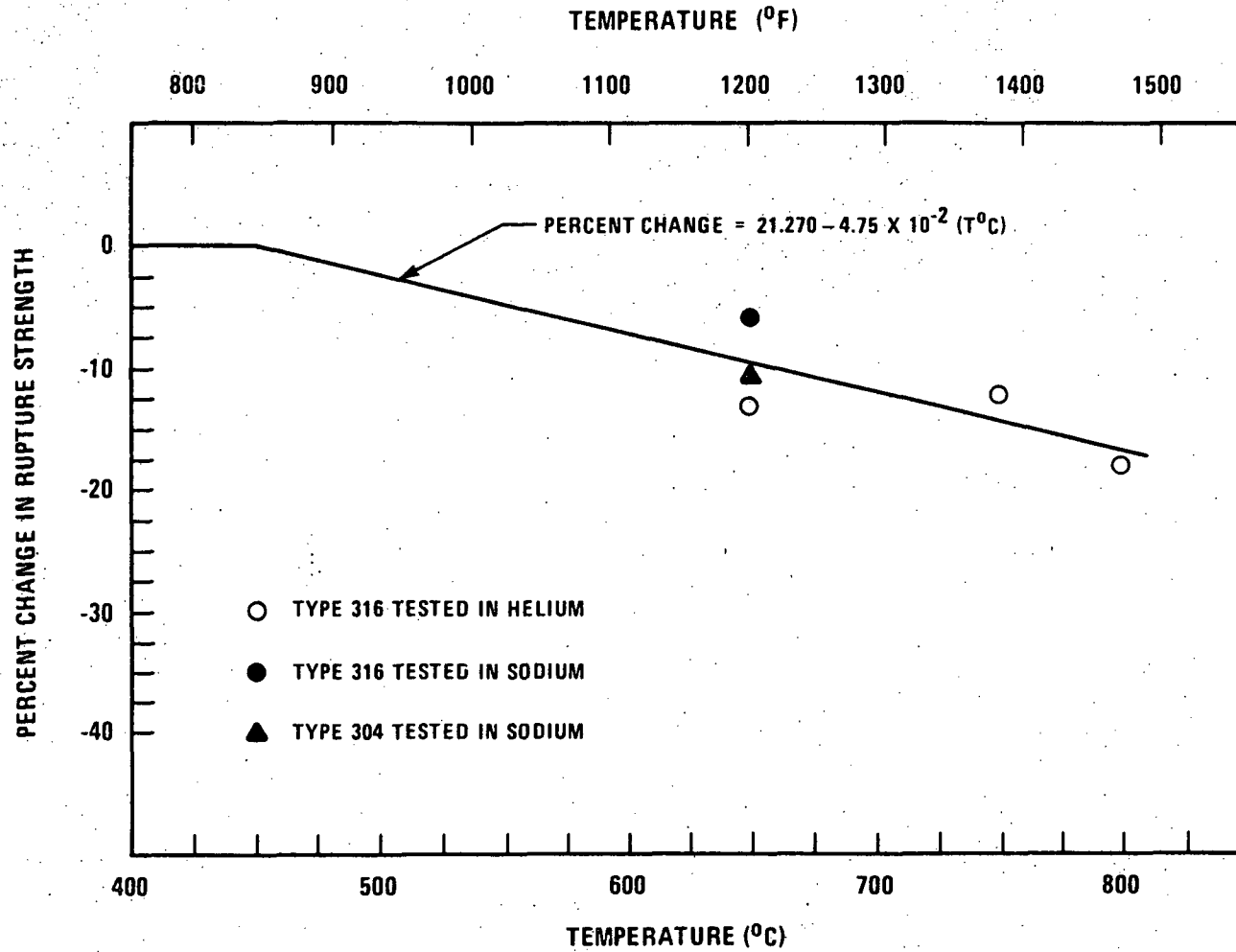


Figure 4.2-48C Design Factor for Estimating the Decrease in Rupture Strength of Type 316 Stainless Steel from Surface Interactions with Sodium (Reference.183)

Amend. 66  
Mar. 1982

FIGURES 4.2-48D, 48E and 48F HAVE BEEN DELETED.

4.2-541  
(Next Page is 4.2-544)

Amend. 66  
Mar. 1982



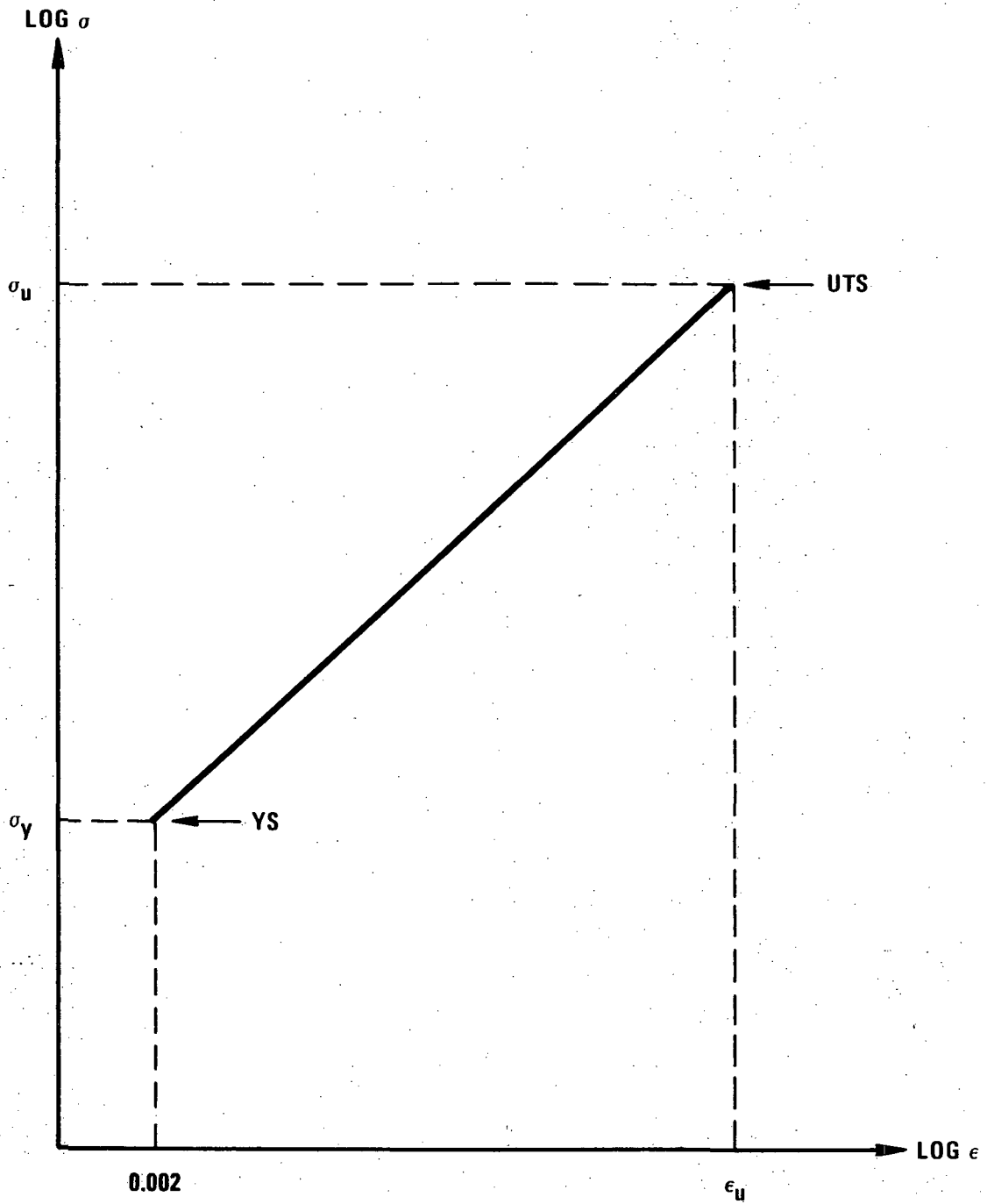


Figure 4.2-48G. Calculation of Stress-Strain Curves for Type 304 and 316 Stainless Steel.

7683-17

4.2-544

Amend. 51  
Sept. 1979

FIGURE 4.2-48H HAS BEEN DELETED.

7683-19

4.2-546

Amend. 51  
Sept. 1979

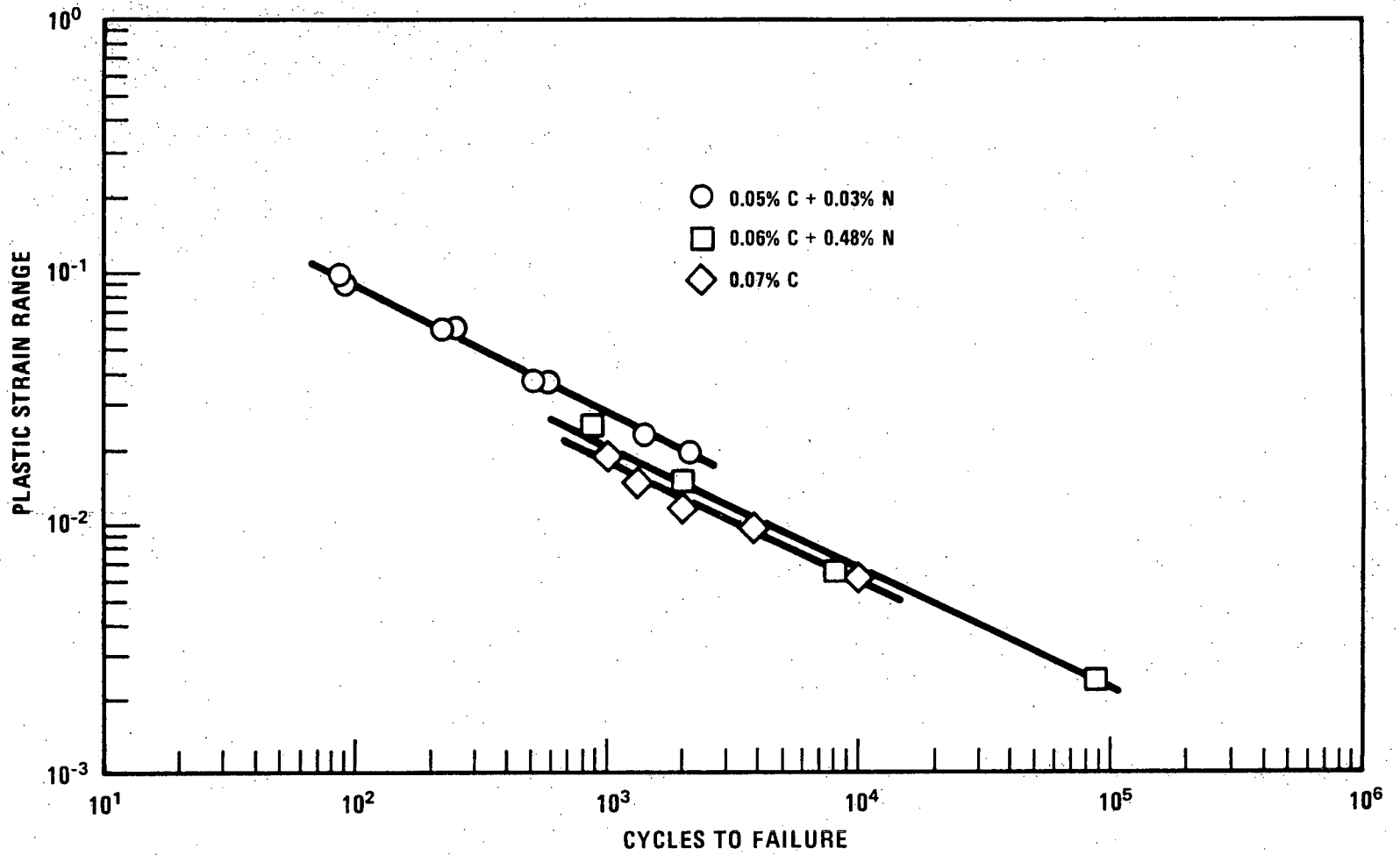


Figure 4.2-48I. Effect of Carbon and Nitrogen Concentration on the Fatigue Strength of Type 316 Stainless Steel at Room Temperature.

FIGURE 4.2-48J HAS BEEN DELETED.

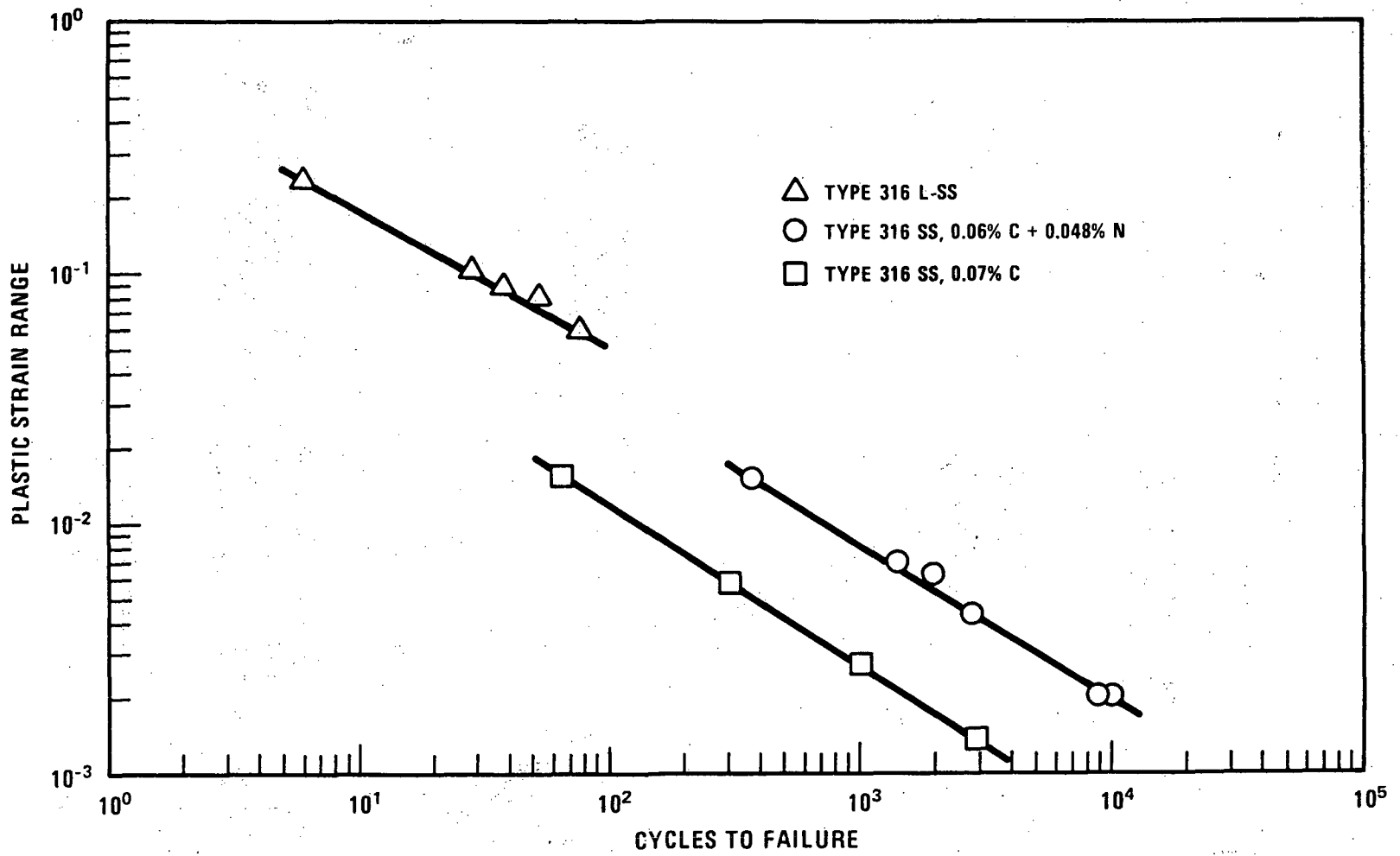
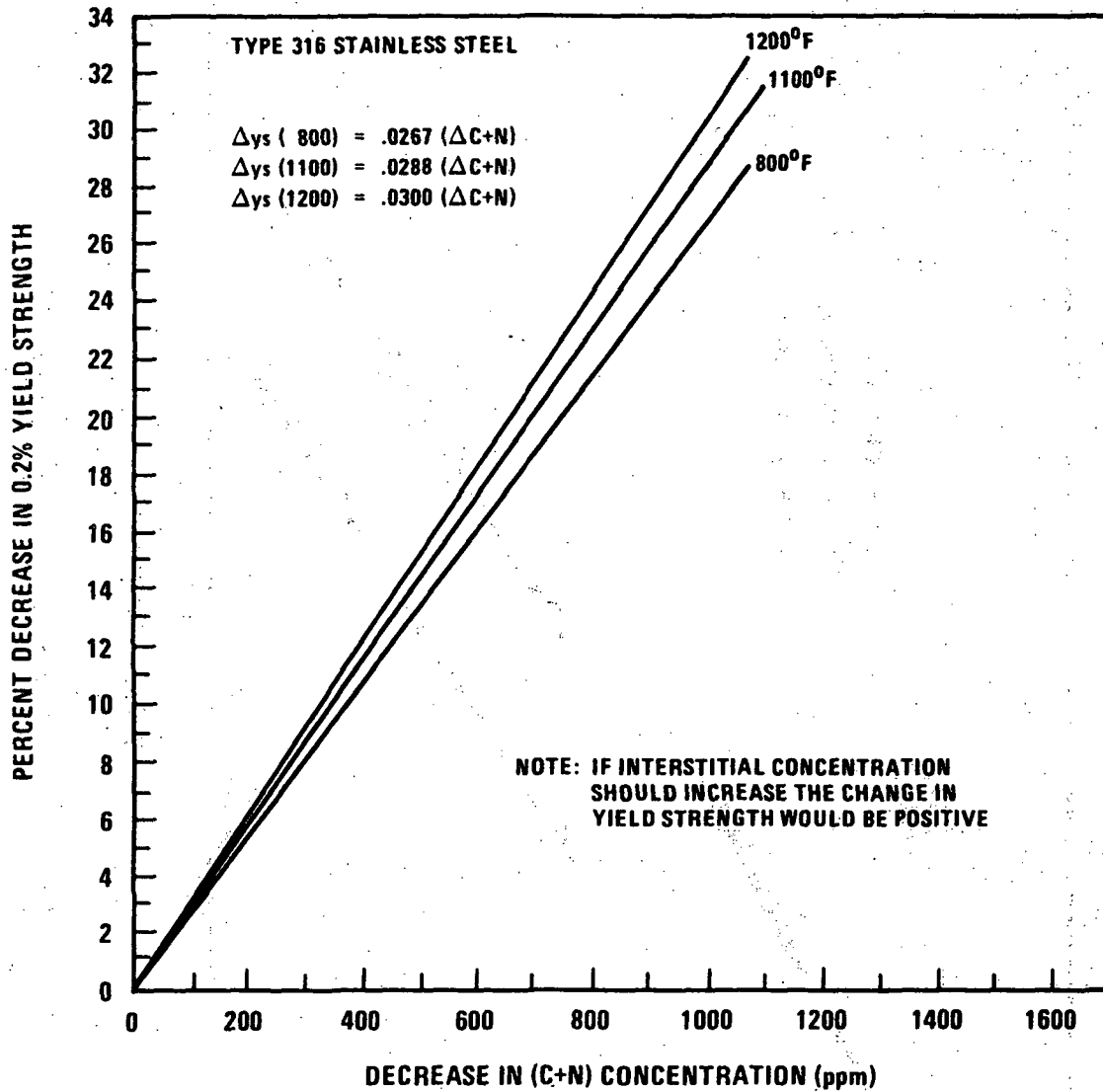


Figure 4.2-48K. Effect of Carbon Concentration on the Fatigue Strength of Type 316 Stainless Steel at 1200°F.



FOR TEMPERATURES BETWEEN THOSE FOR WHICH CURVES ARE GIVEN, REDUCTION FACTORS COULD BE DETERMINED BY STRAIGHT LINE INTERPOLATION BETWEEN 800 AND 1100°F OR BETWEEN 1100 AND 1200°F. MORE CONSERVATIVE VALUES COULD BE OBTAINED BY INTERPOLATING BETWEEN 800 AND 1200°F.

Figure 4.2-48L Decrease in Yield Strength of Type 316 SS as a Function of Decrease in C+N Concentration (Reference 185)

4685-2

4.2-548a

Amend. 69  
July 1982

4685-3

4.2-548b

Amend. 69  
July 1982

FOR TEMPERATURES BETWEEN THOSE FOR WHICH CURVES ARE GIVEN, REDUCTION FACTORS COULD BE DETERMINED BY STRAIGHT LINE INTERPOLATION BETWEEN 800 AND 1100°F OR BETWEEN 1100 AND 1200°F. MORE CONSERVATIVE VALUES COULD BE OBTAINED BY INTERPOLATING BETWEEN 800 AND 1200°F

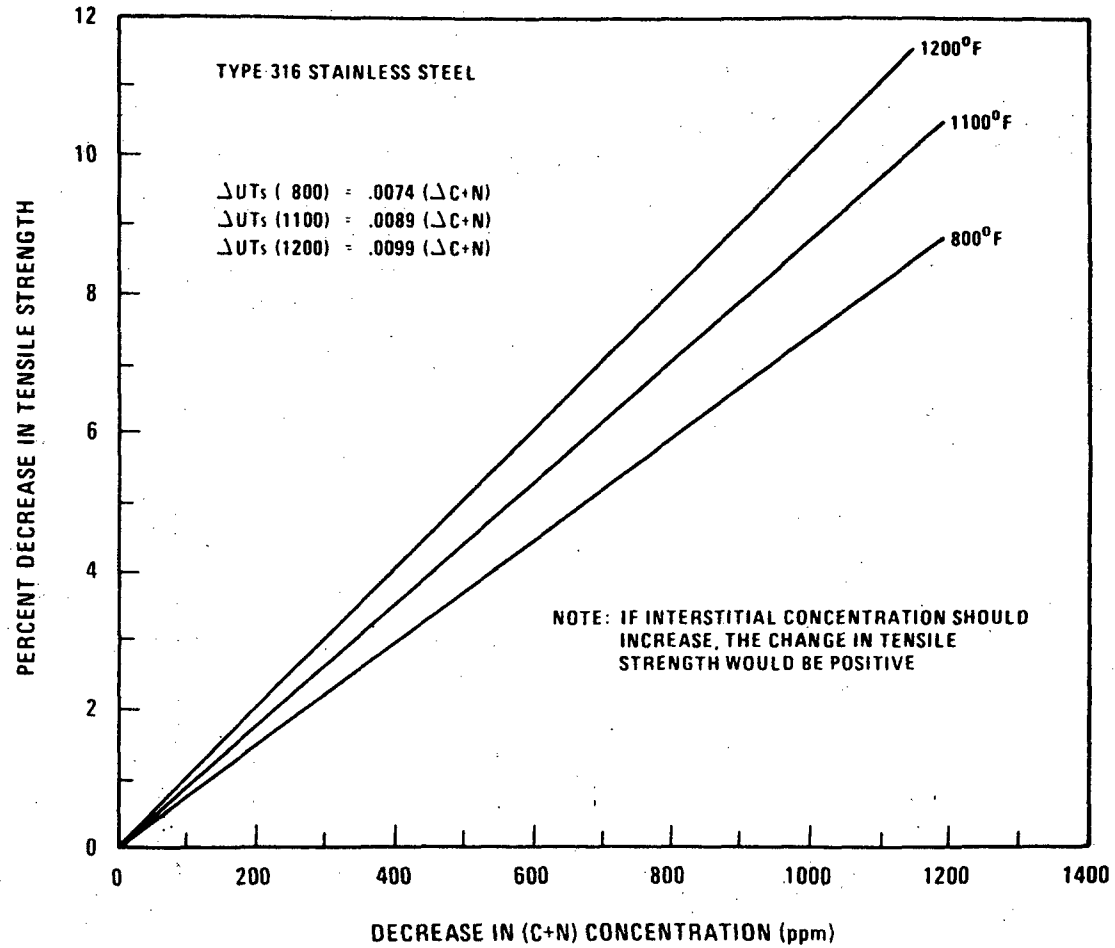


Figure 4.2-48M Decrease in Tensile Strength of Type 316 SS as a Function of Decrease in C+N Concentration (Reference 185)

5310-1

4.2-549

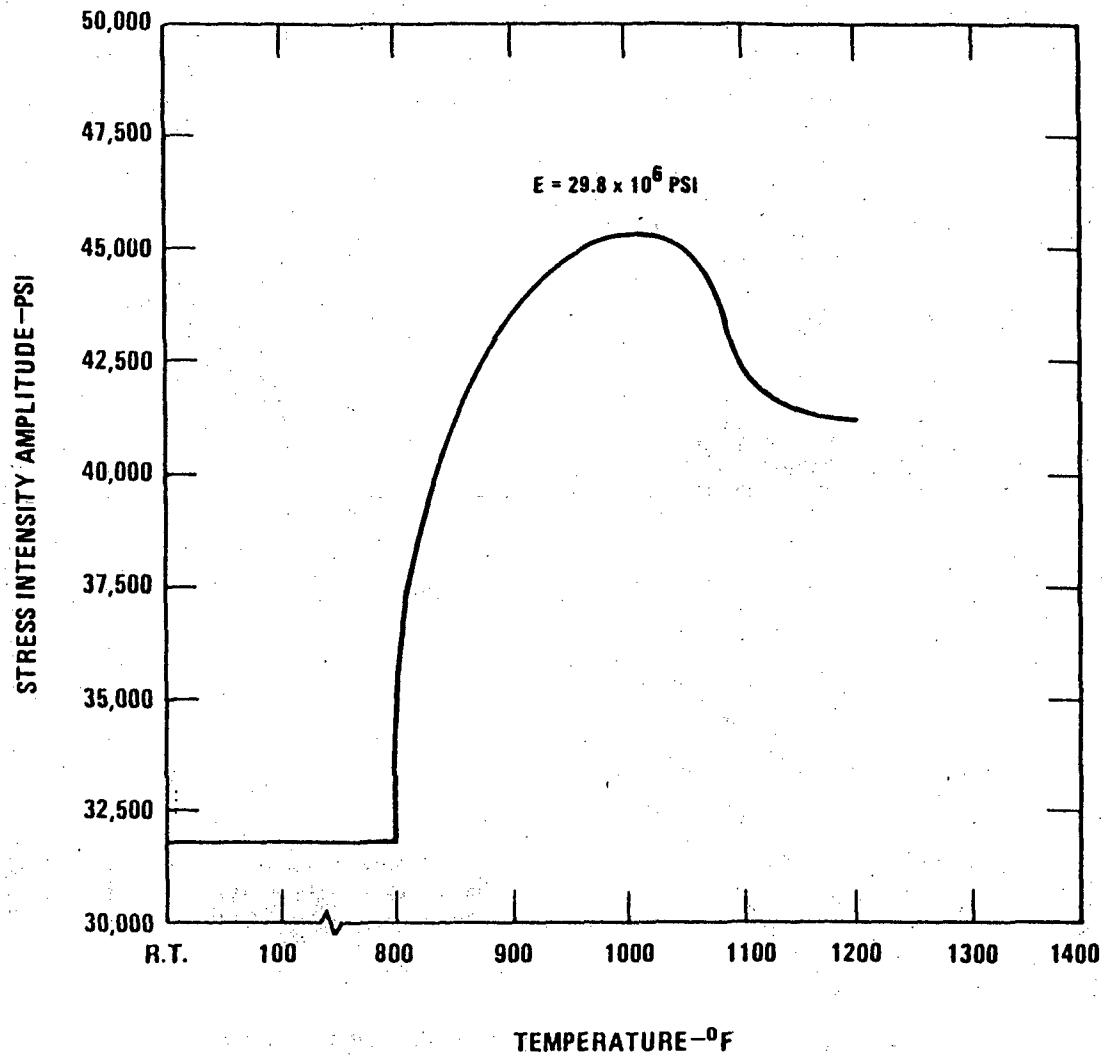


Figure 4.2-49. Design Fatigue Strength ( $10^8$  Cycles or More) for Alloy 718  
(Reference 184 Proprietary DOE)

Amend. 64  
Jan. 1982



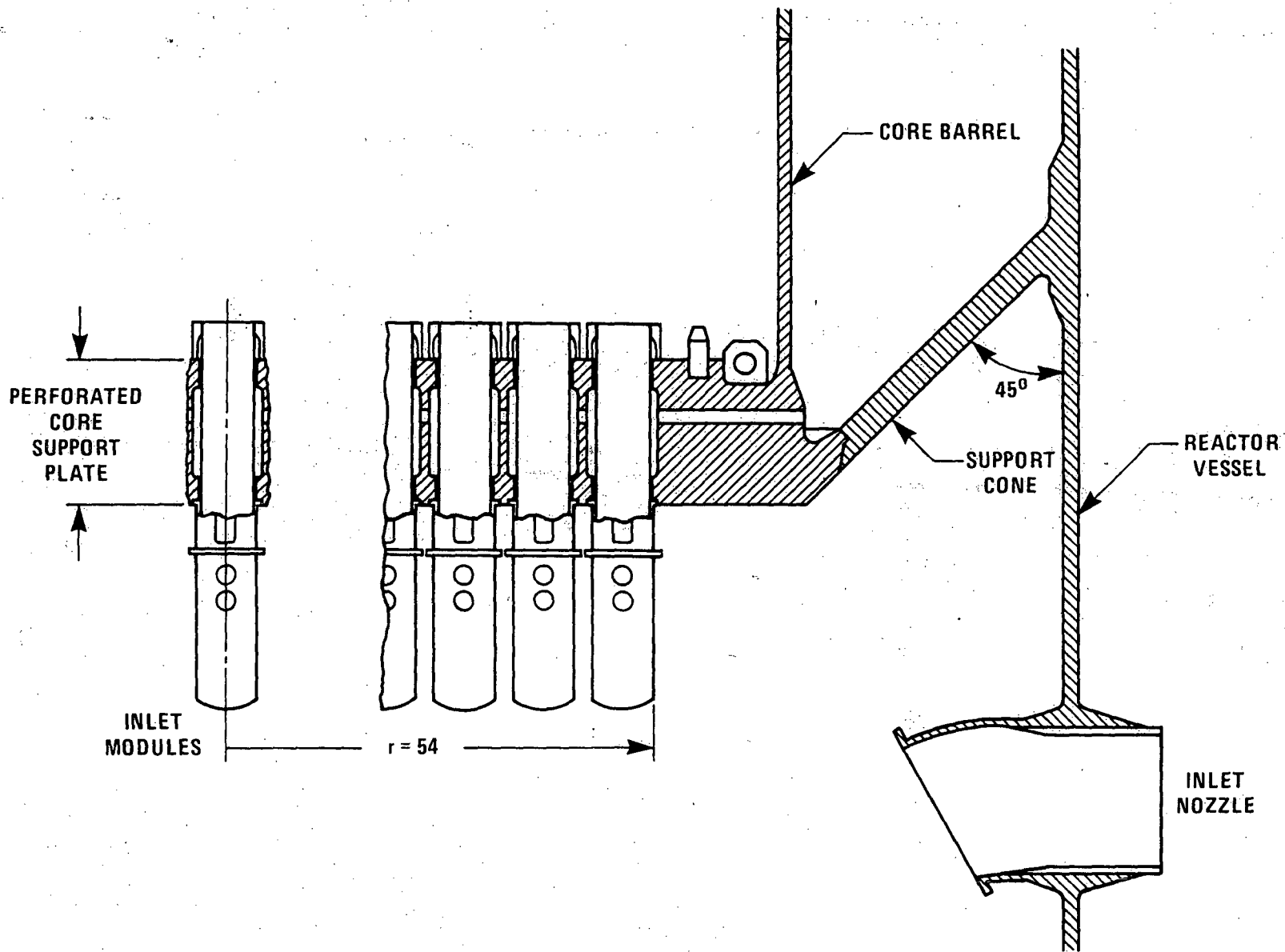


Figure 4.2-50. Core Support Structure (CSS)

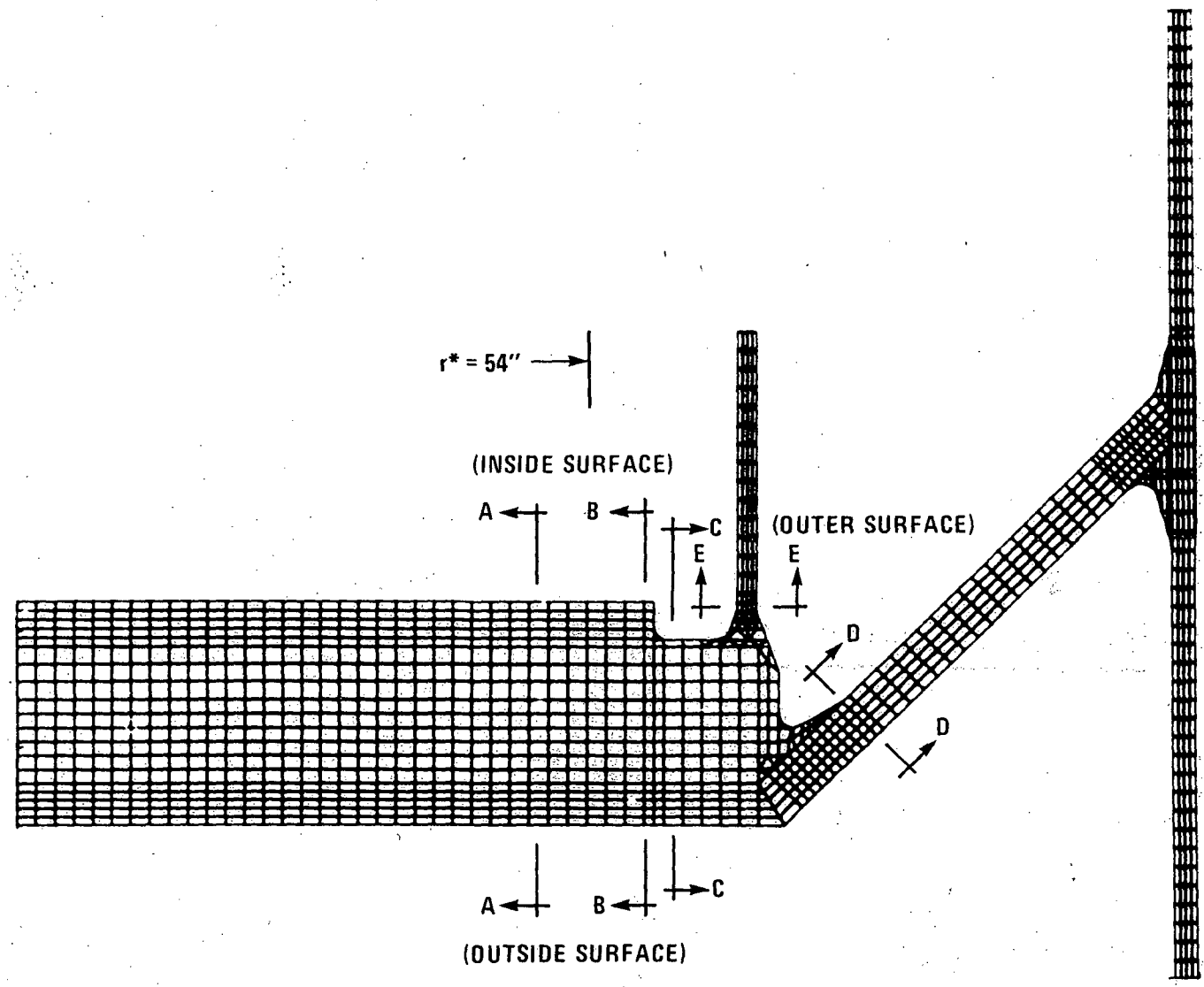


Figure 4.2-51 Core Support Structure Axisymmetric Thermal Stress Model

4685-6

4.2-552

Amend. 59  
Dec. 1980

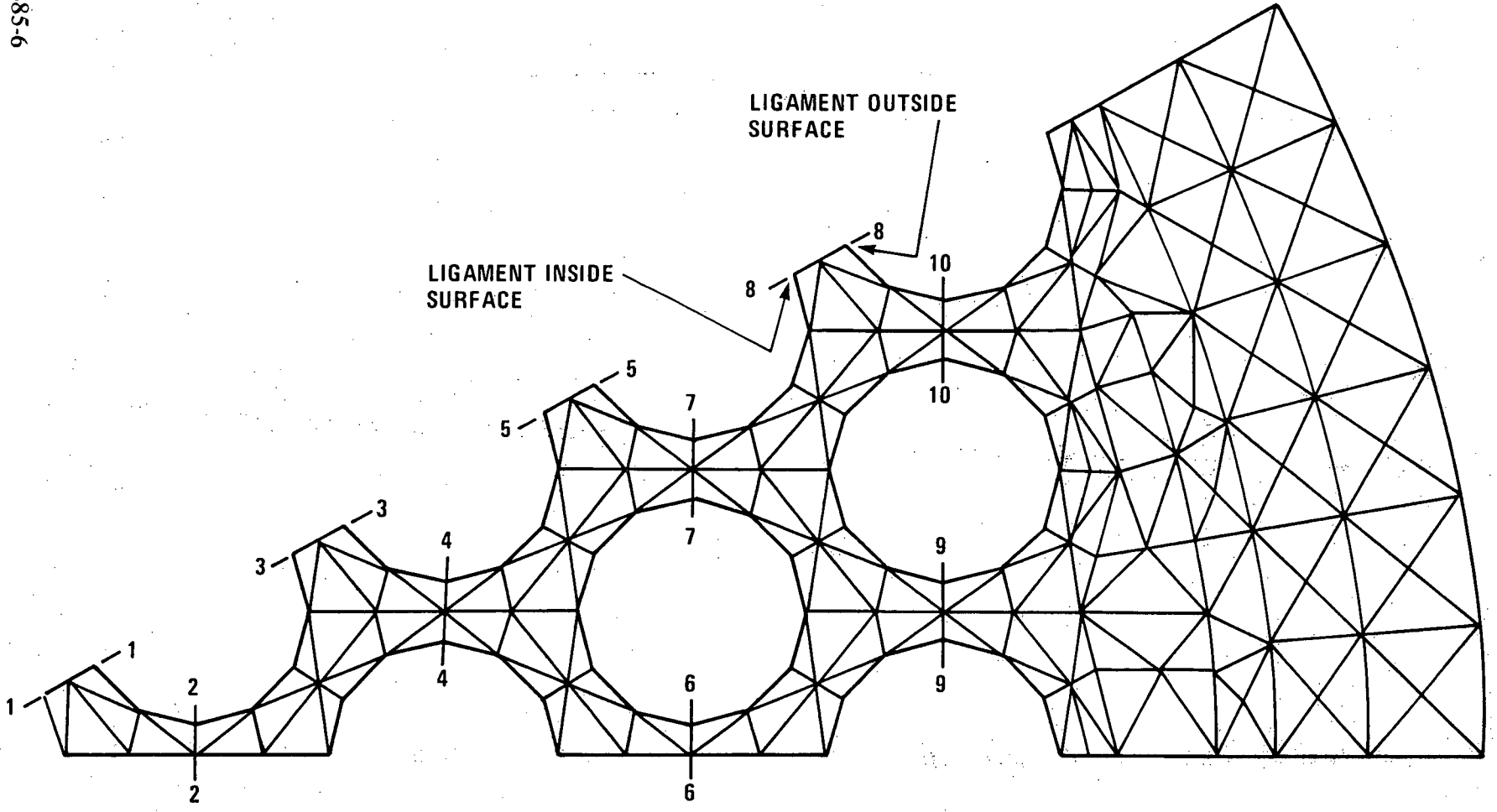


Figure 4.2-52 Identifying Cut Numbers in Sector of the Lower Support Structure Central Region

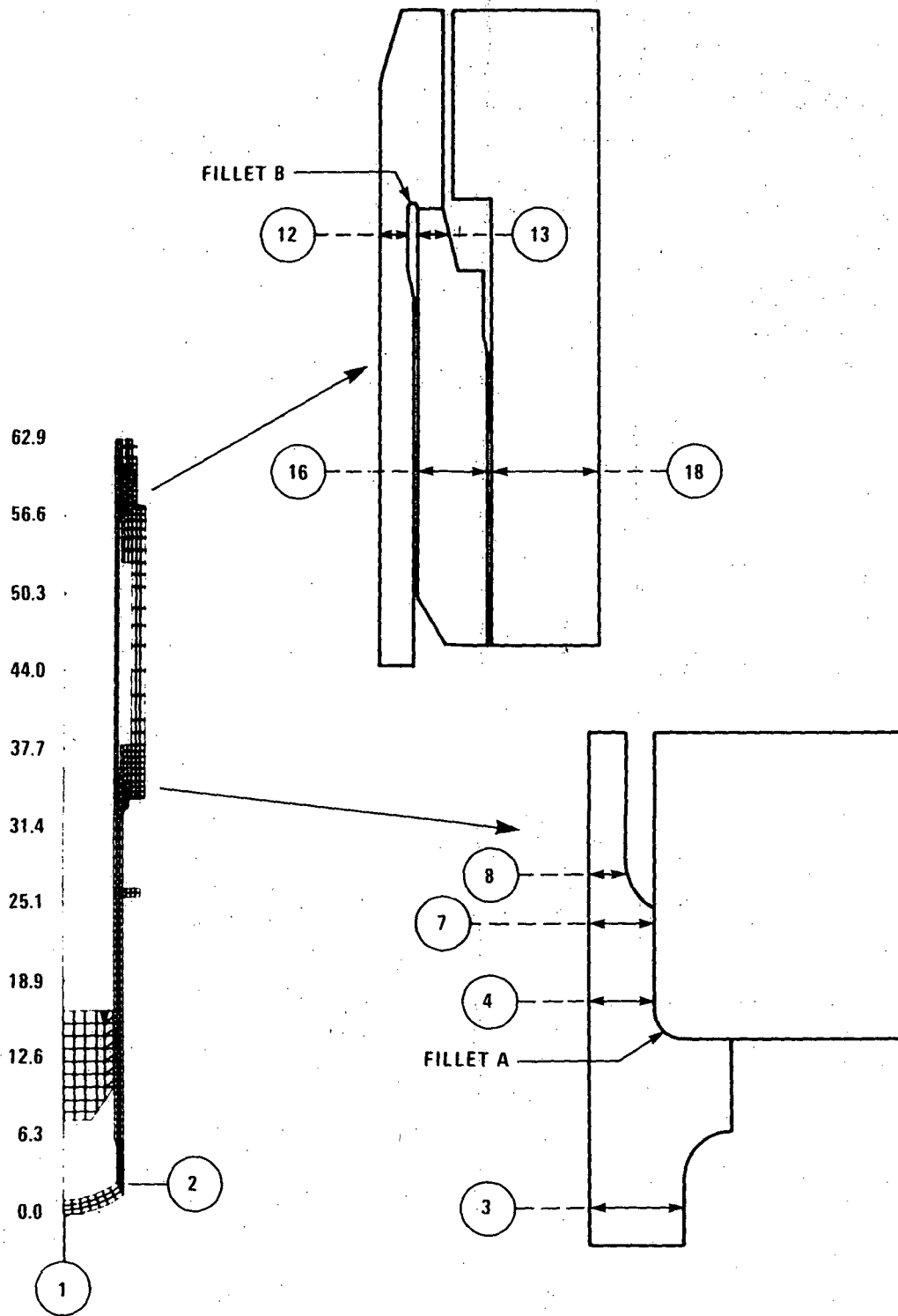


Figure 4.2-53 Lim Liner Finite Element Stress Model with Key Structural Evaluation Sections

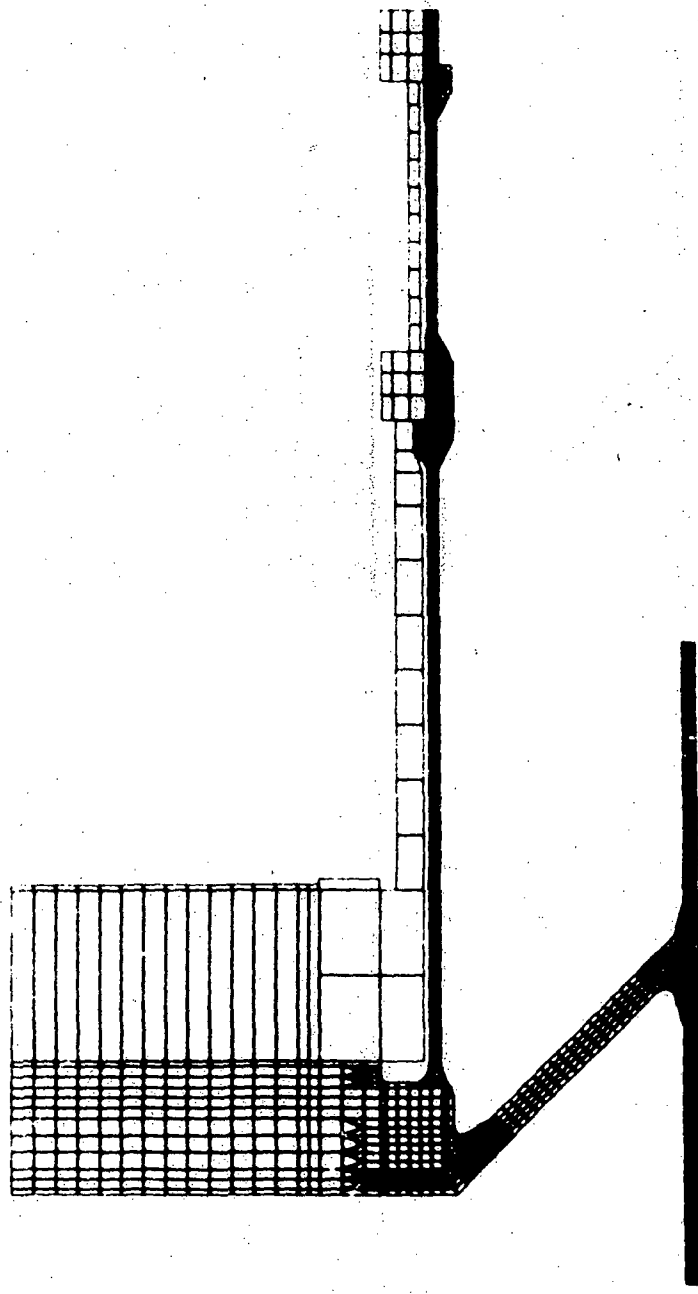


Figure 4.2-54 Core Support Structure Seismic and Deadweight Model

4685-8

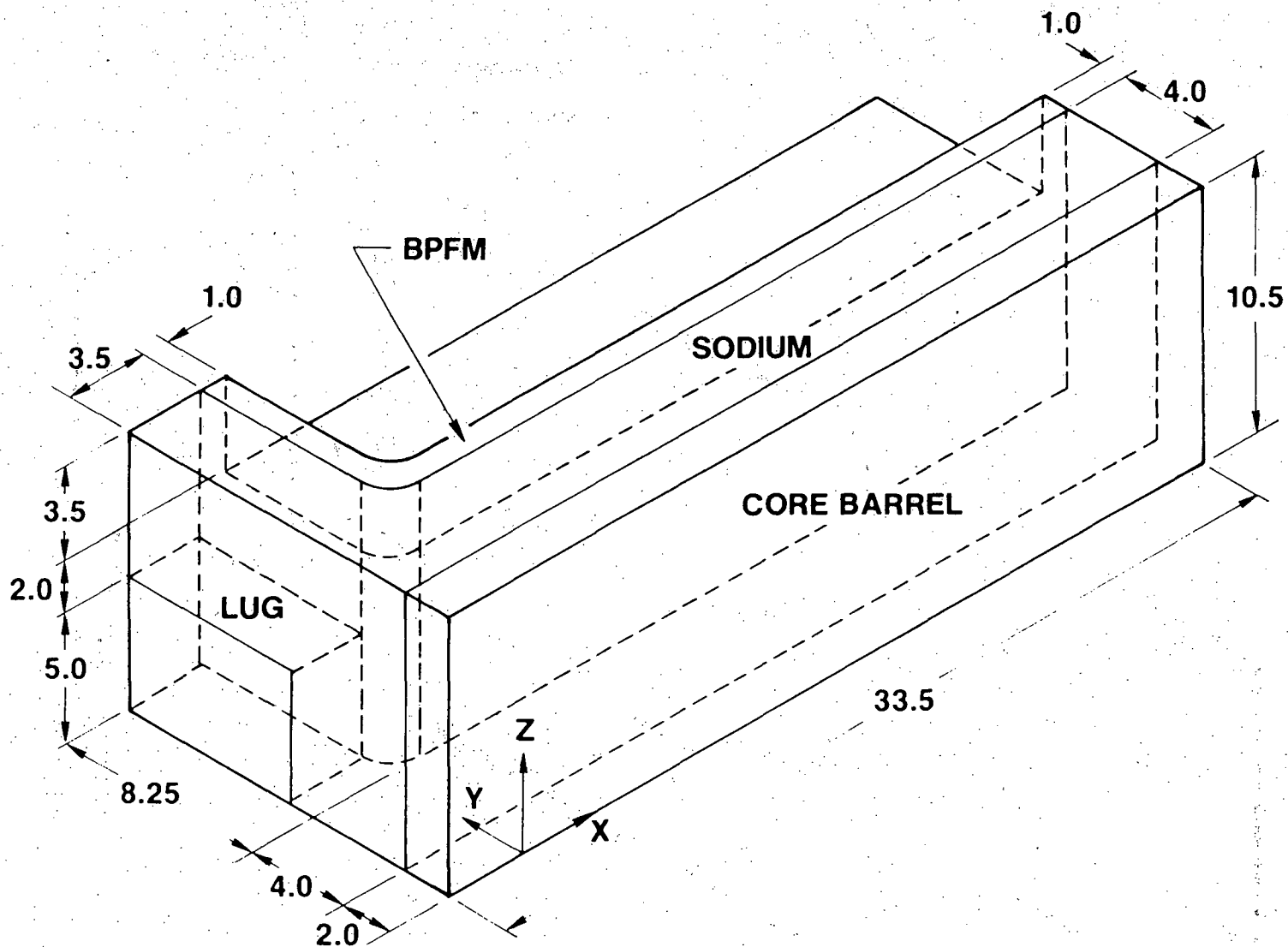
4.2-554

Amend. 59  
Dec. 1980

FIGURES 4.2-55 through -63  
HAVE BEEN DELETED

4.2-555  
(next page is 4.2-564)

9169-1



4.2-564

Amend. 53  
Jan. 1980

Figure 4.2-63A. One-Eighth BPFM 3-D Finite Element Thermal Molded Geometry

(all dimensions in inches)

9222-6

4.2-565

Amend. 51  
Sept. 1979

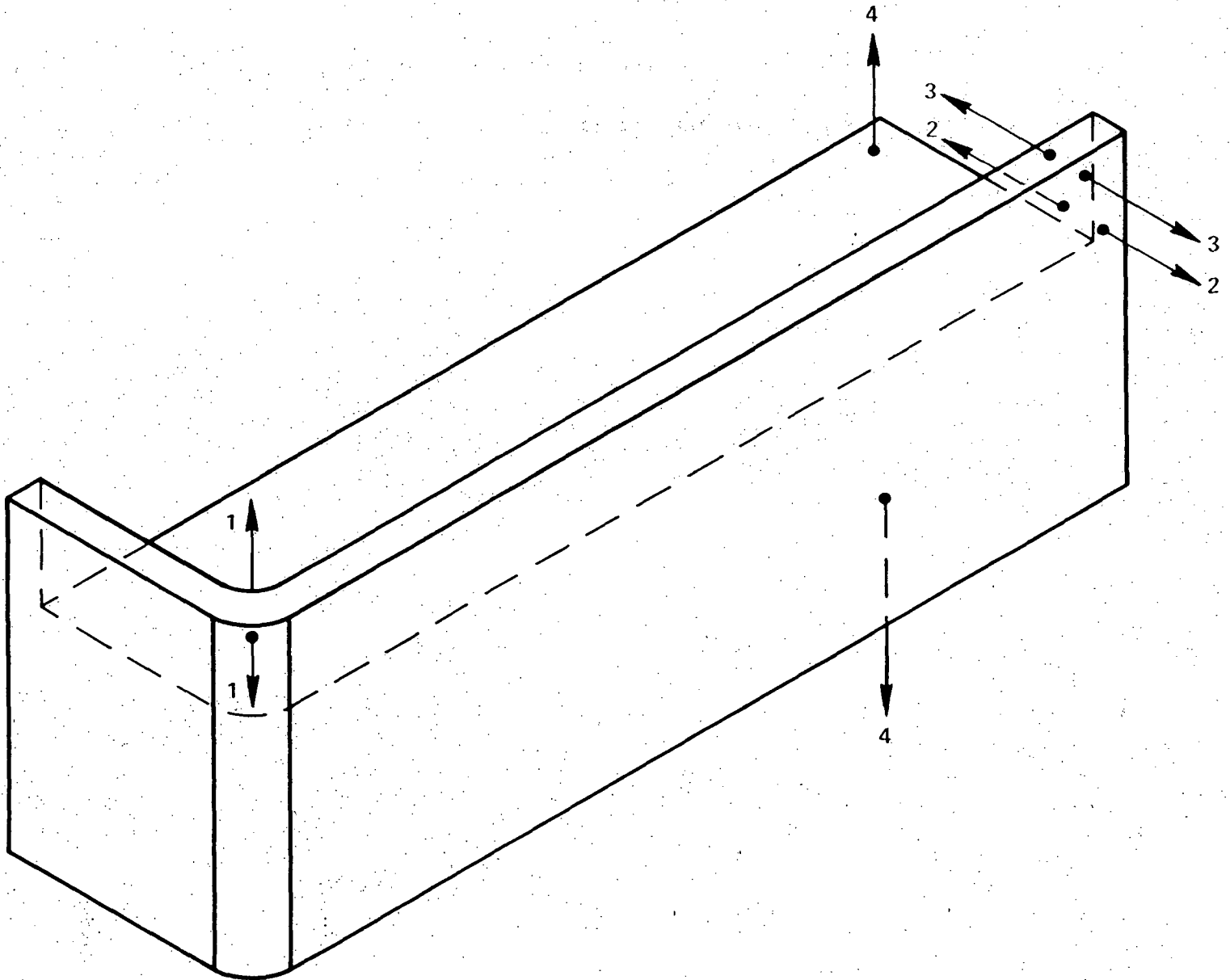


Figure 4.2-63B. BPFM Critical Sections in the One-Eight BPFM 3-D Finite Element Stress Module



51|

FIGURE 4.2-64, 65 and 66 DELETED

4.2-566

Amend. 51  
Sept. 1979

FIGURES 4.2-67 through -74  
HAVE BEEN DELETED

4.2-567  
(next page is 4.2-574a)

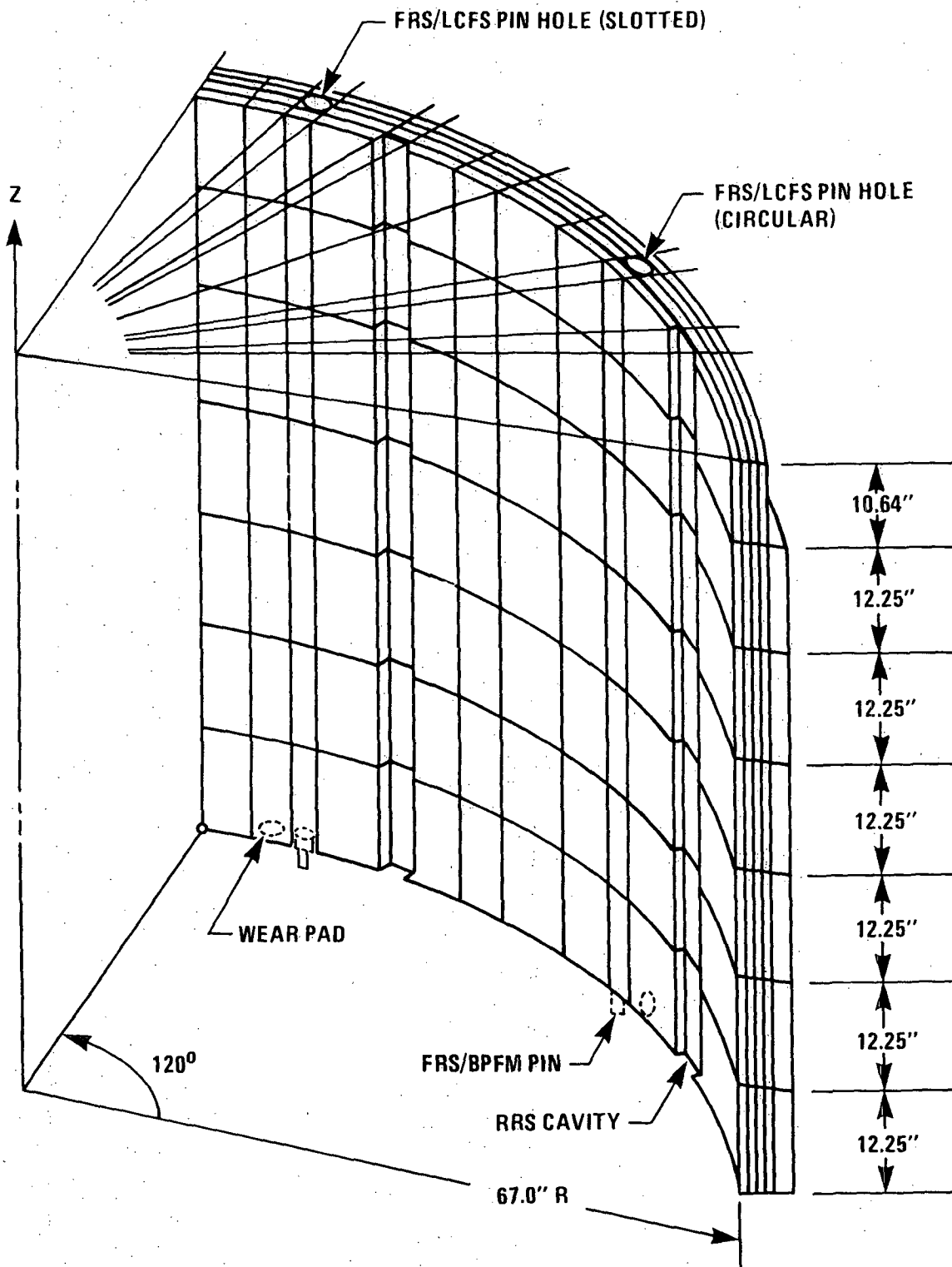


Figure 4.2-75. FRS Computer Model W/8 Node Isoparametric Elements

4756-2

4.2-574a

Amend. 59  
Dec. 1980

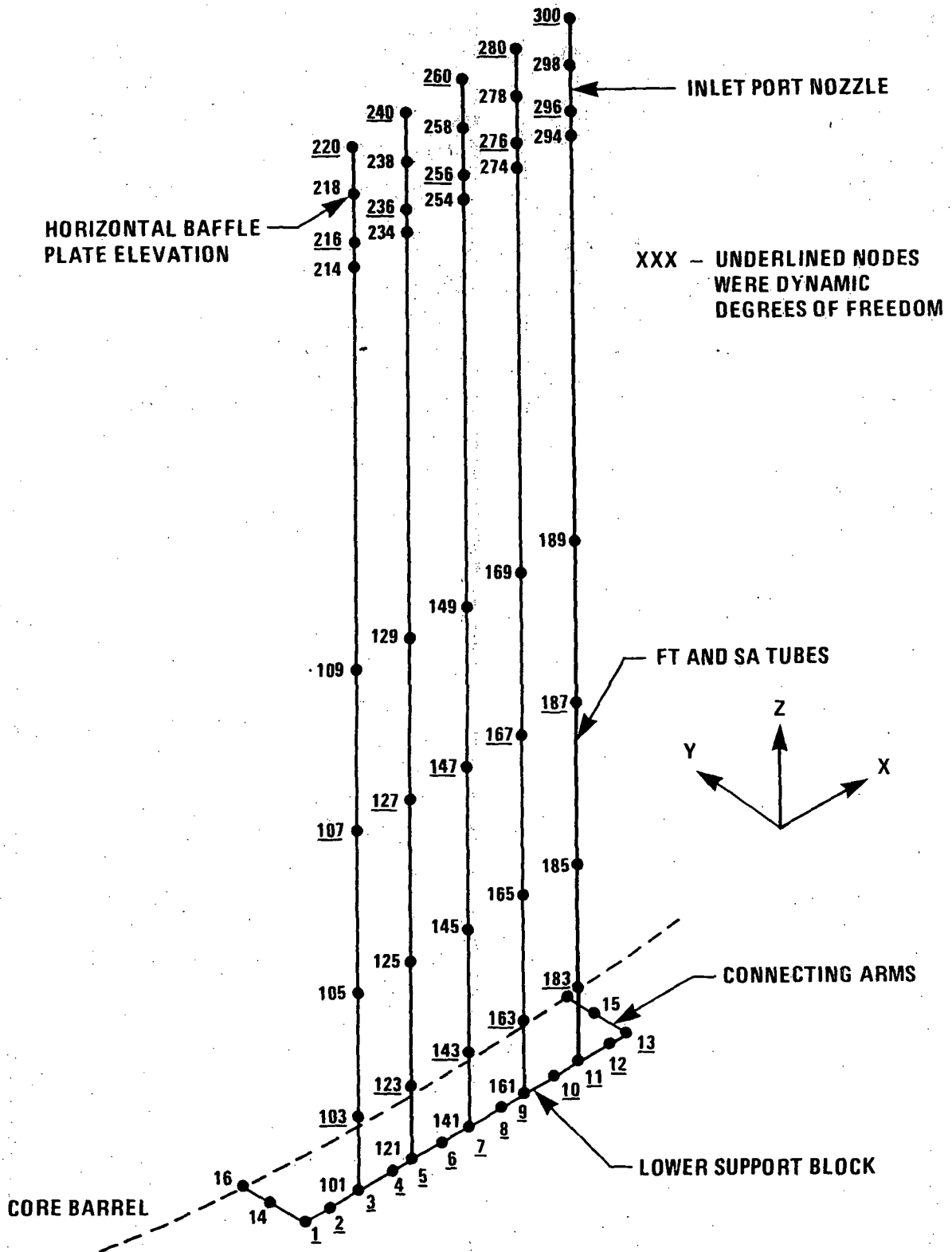


Figure 4.2-76. Finite Element Model of FT and SA Assembly

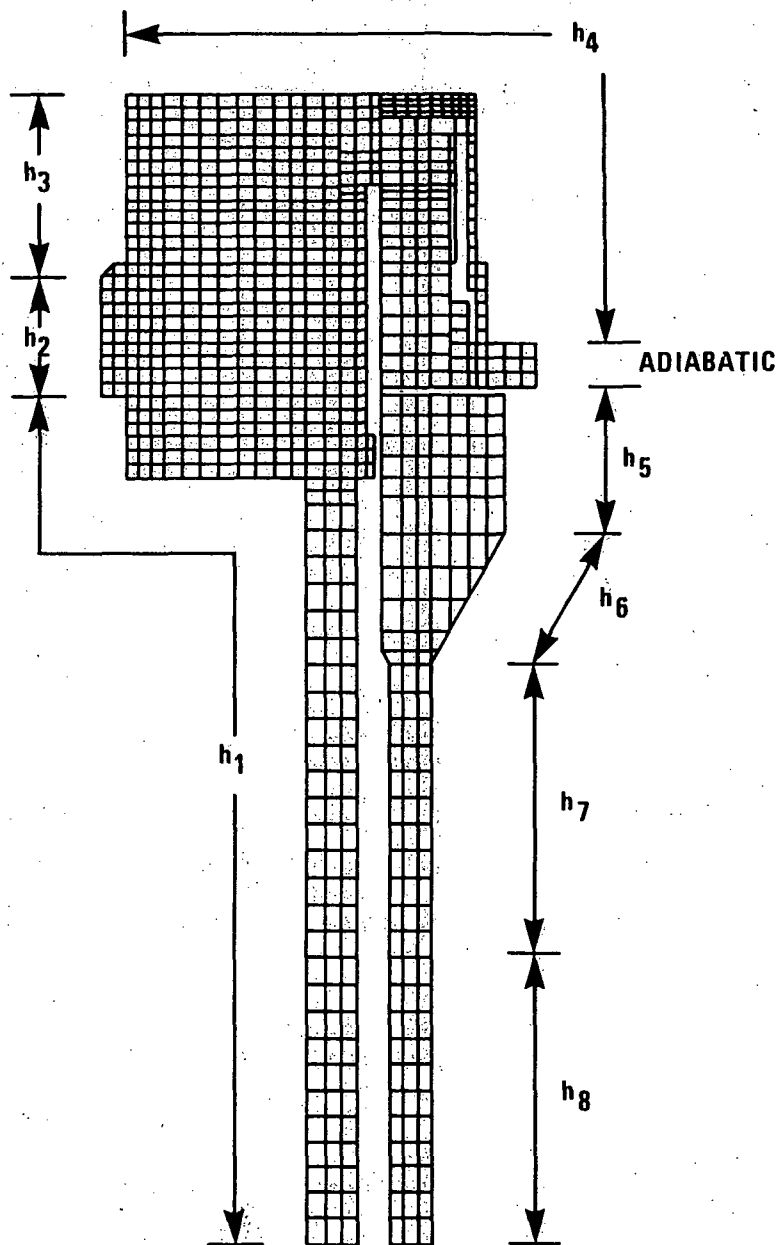


Figure 4.2-77. Heat Transfer Coefficient Regions for the CFS

4756-1

4.2-574c

Amend. 59  
Dec. 1980

59

FIGURES 4.2-78 THROUGH 4.2-83 DELETED

4.2-575

Amend. 59  
Dec. 1980

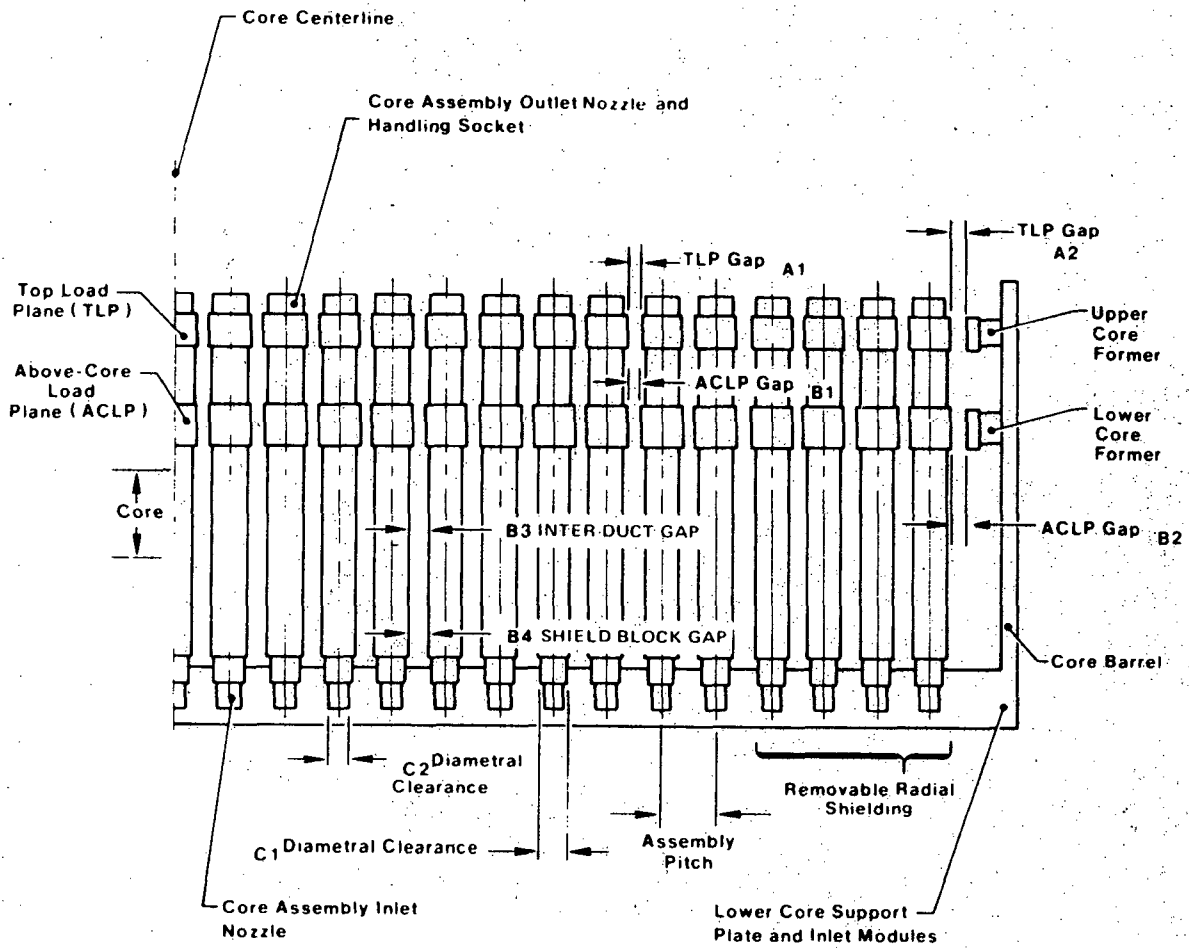
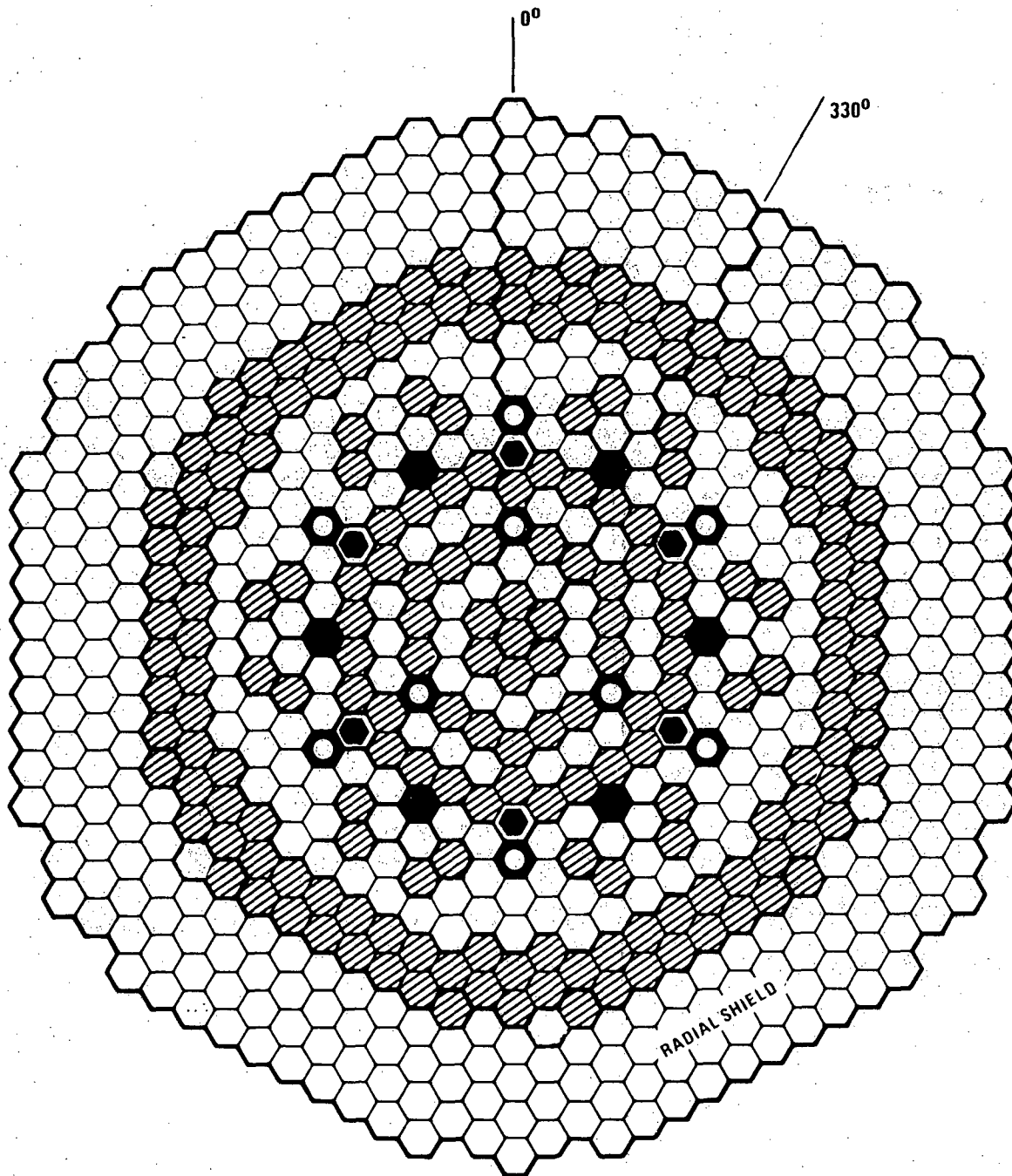






Figure 4.2-84. CRBRP Core Restraint System.

4655-4

4.2-576

Amend. 59  
Dec. 1980



-  FUEL ASSEMBLIES
-  BLANKET ASSEMBLIES
-  CONTROL ASSEMBLIES
-  ALTERNATE FUEL BLANKET ASSEMBLIES

ROW NO. = RADIAL ROW FROM CENTER  
ASSEMBLY (CENTER = ROW 1)

FIGURE 4.2-85. Schematic View of Reactor Core Showing Sector of Core Simulated in NUBOW-3D Model

4655-1a



59

THIS PAGE INTENTIONALLY BLANK

4.2-578

Amend. 59  
Dec. 1980

59

THIS PAGE INTENTIONALLY BLANK

Amend. 59  
Dec. 1980

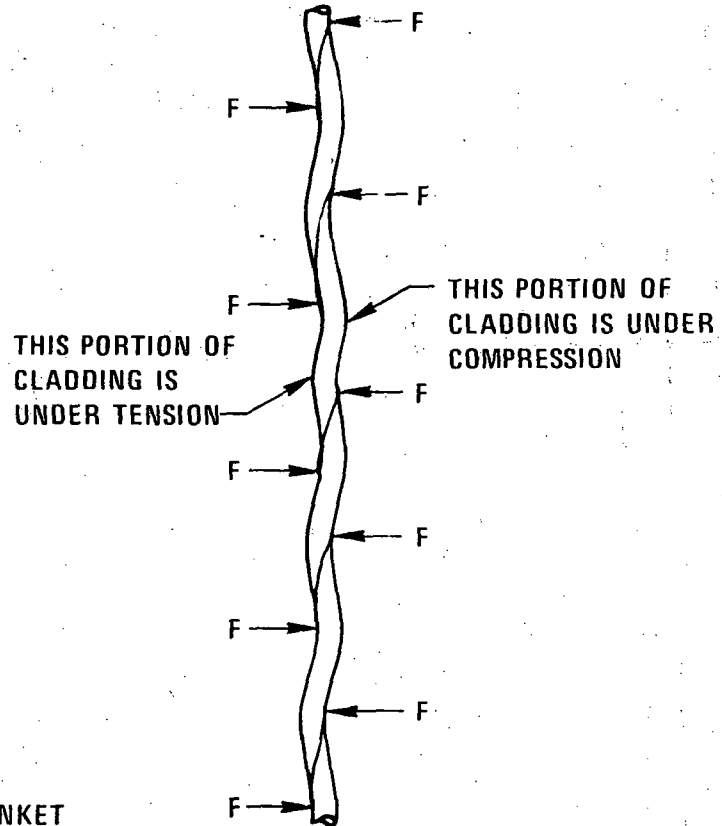
4.2-579

CORE CENTER  
 →  
 (TEMPERATURE, FLUX INCREASE)



A. UNCONSTRAINED RADIAL BLANKET ROD AT BEGINNING OF LIFE SUBJECTED TO CORE FLUX AND THERMAL GRADIENTS

CORE CENTER  
 →



B. ROD IN (A.) SUBJECTED TO CONSTRAINT FORCES F AT WIRE WRAP CONTACT POINTS

Figure 4.2-87A. Illustration of Effects of Core Thermal and Flux Gradients in Radial Blanket Rod (not to scale)

7683-217

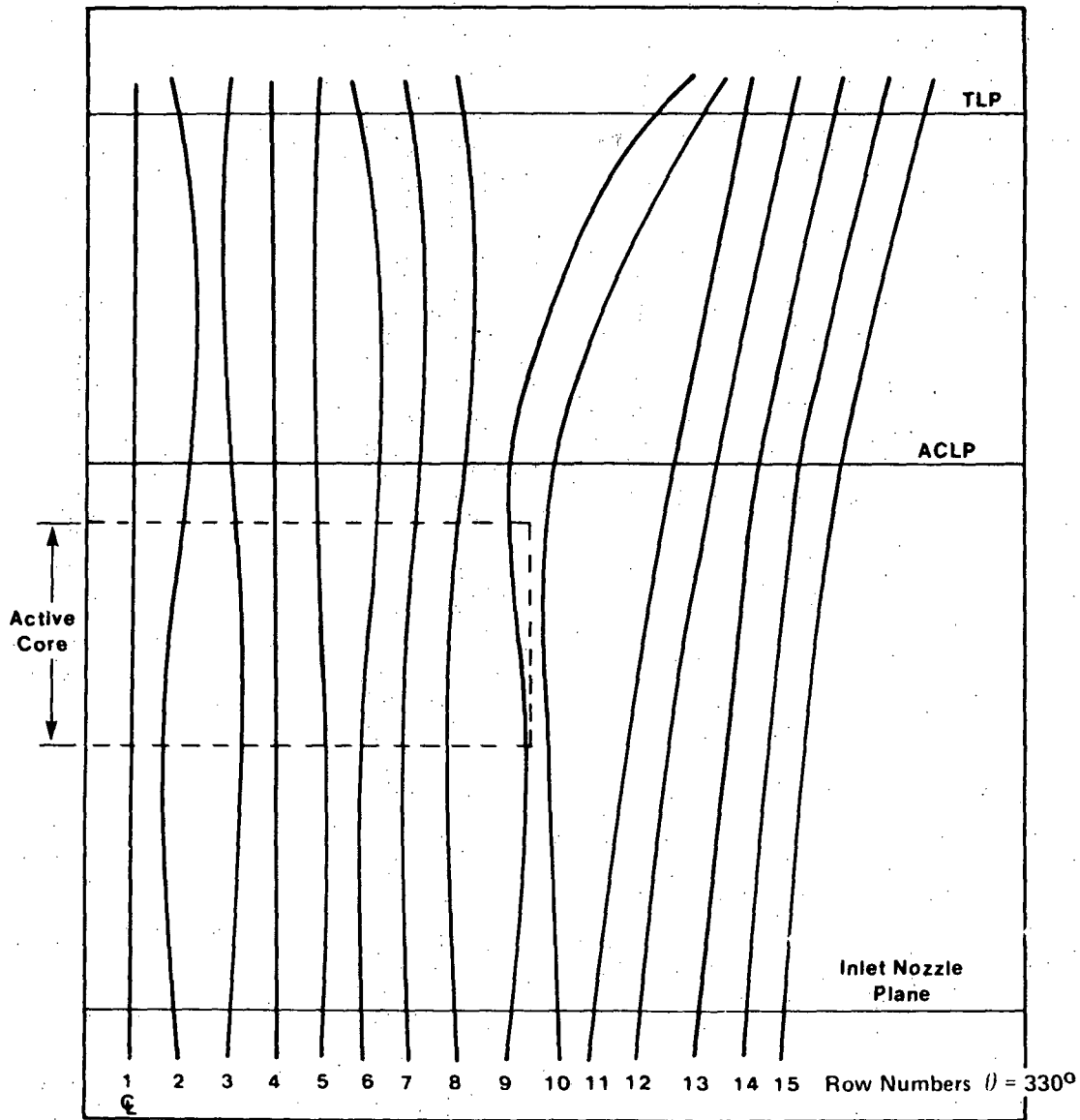
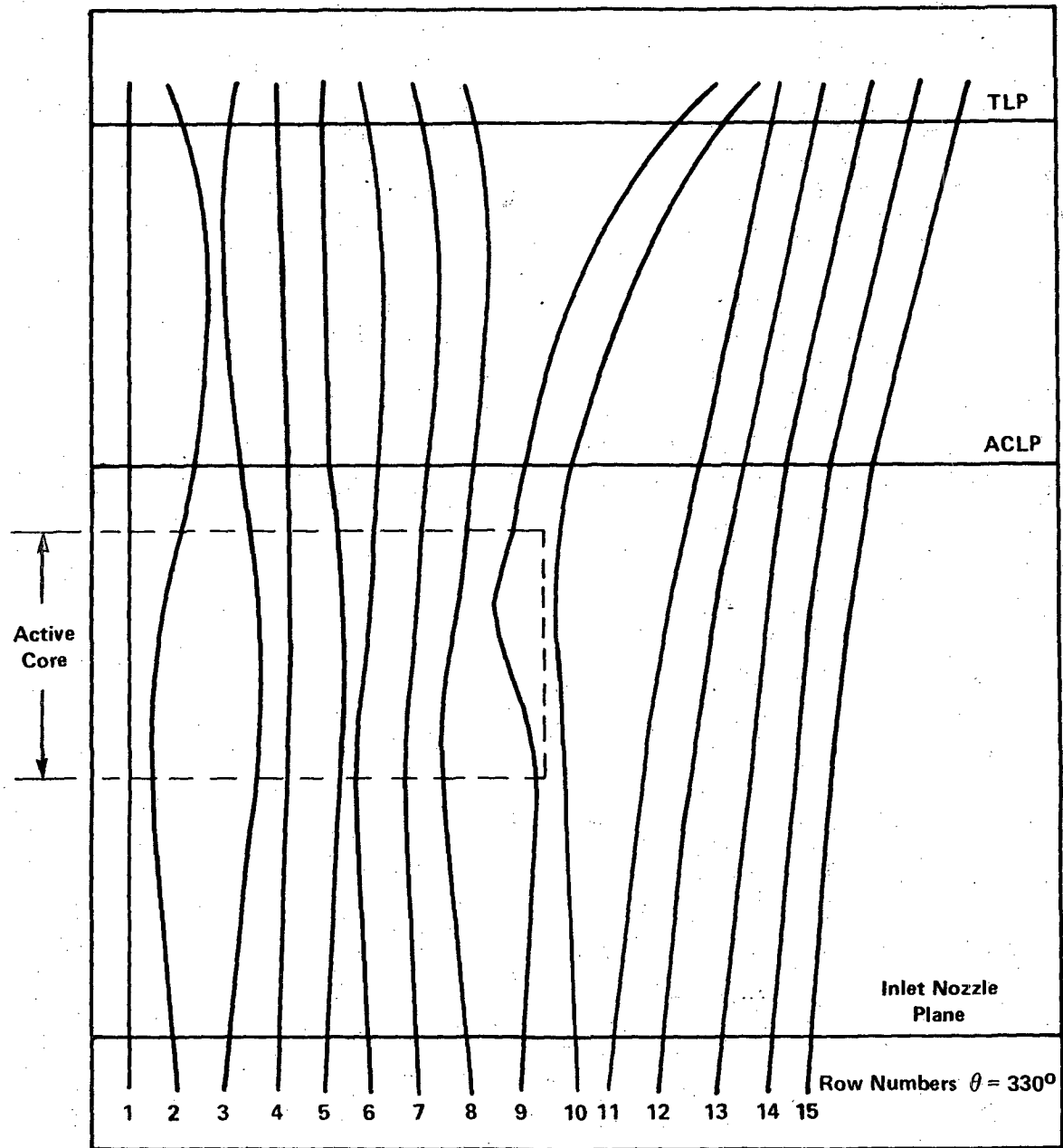


Figure 4.2-88. On-Power Bow Shapes at SOC1

4655-3

4.2-581

Amend. 59  
Dec. 1980



CORE CENTERLINE THRU LEFTMOST DUCT

FIGURE 4.2-89 On-Power Bow Shapes at EOC2

4655-10

Nominal Case, Time = 0.0 Days  
Contact Force Level 3, ACLP

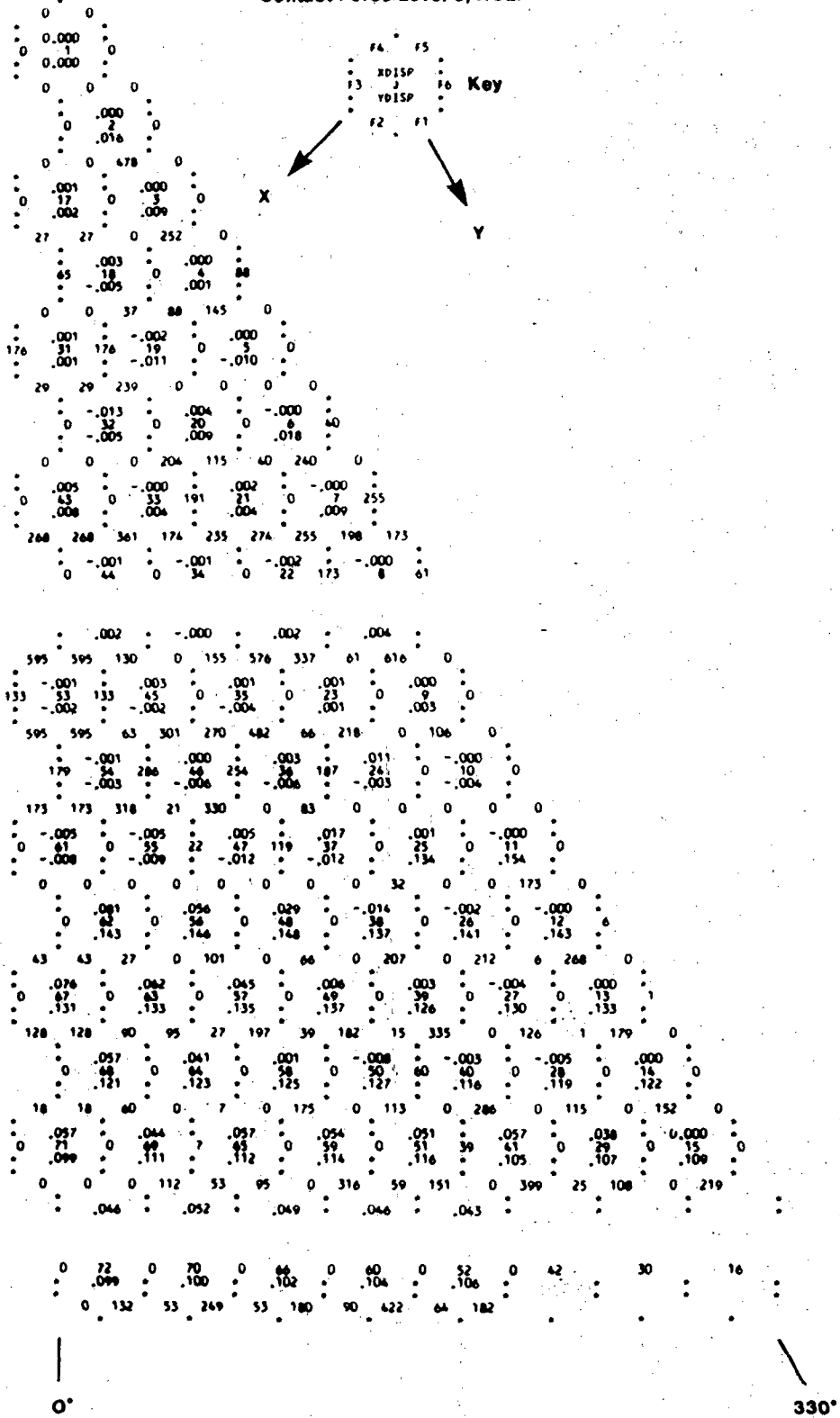


Figure 4.2-90. On-Power Forces and Displacements at the Above Core Load Plane at Start of Cycle 1.

59|

THIS PAGE INTENTIONALLY BLANK

4.2-584

Amend. 59  
Dec. 1980

59

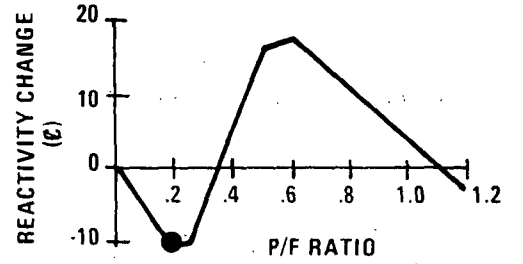
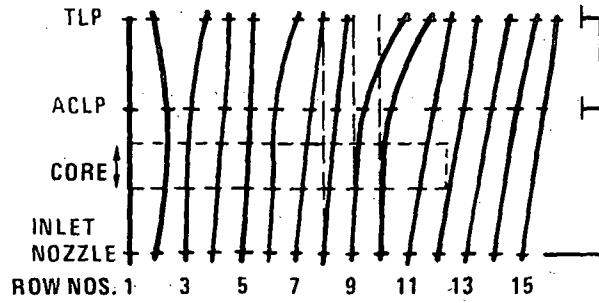
THIS PAGE INTENTIONALLY BLANK

4.2-585

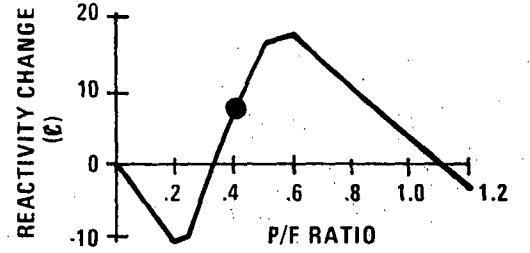
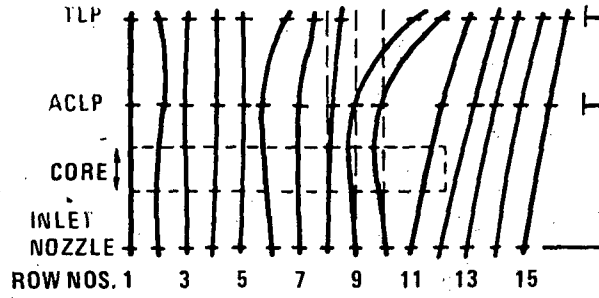
Amend. 59  
Dec. 1980



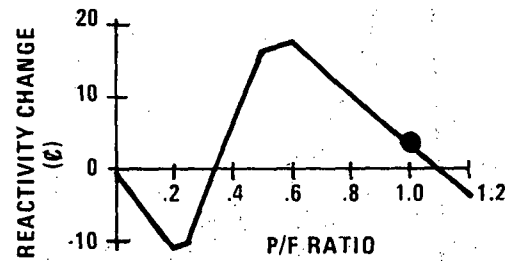
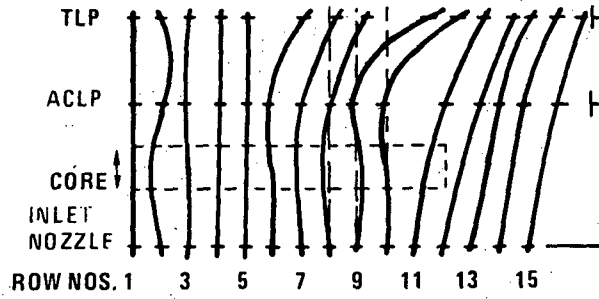
A: 0.2 P/F



B: 0.4 P/F



C: 1.0 P/F



CORE CL

CORE FORMER

Figure 4.2-92a. Bowing Displacements and Reactivity Change Versus Power to Flow Ratio

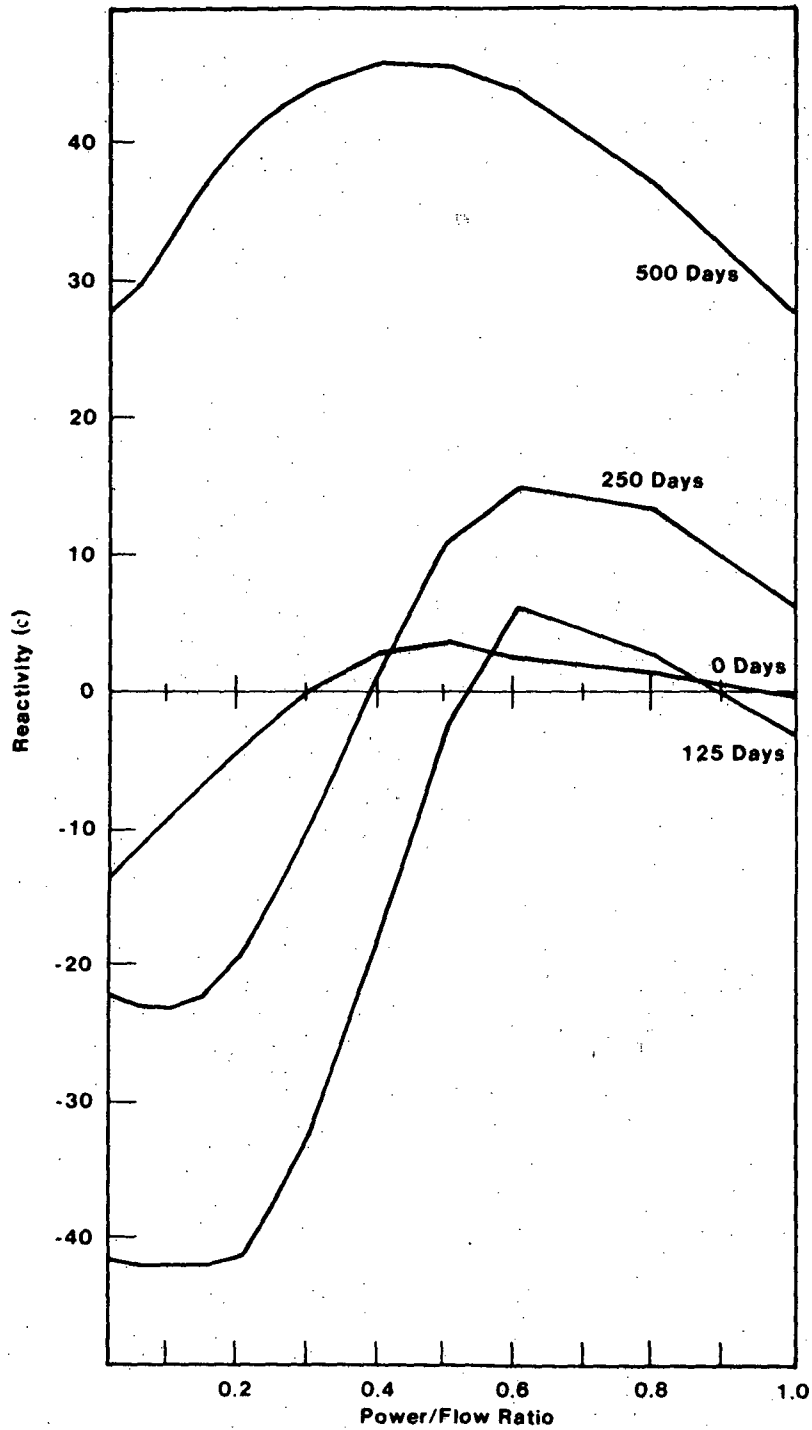


FIGURE 4.2-92B Bowing Reactivity Vs. Power-to-Flow Ratio at 40% Flow at Various Times in Fuel Assembly Life

4655-2

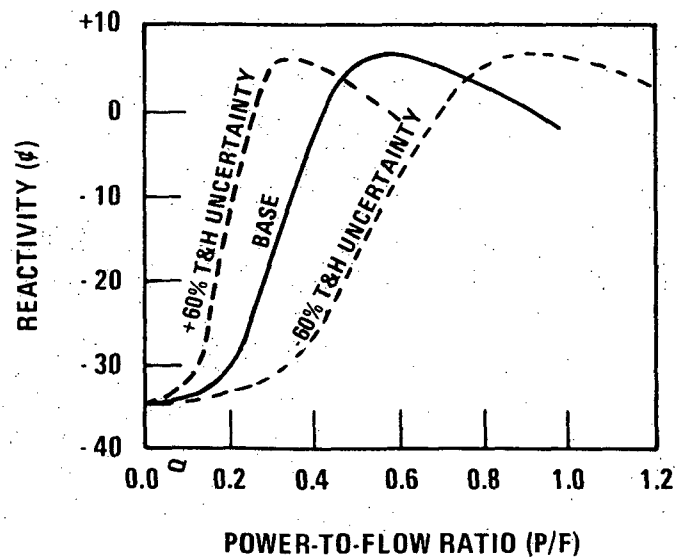
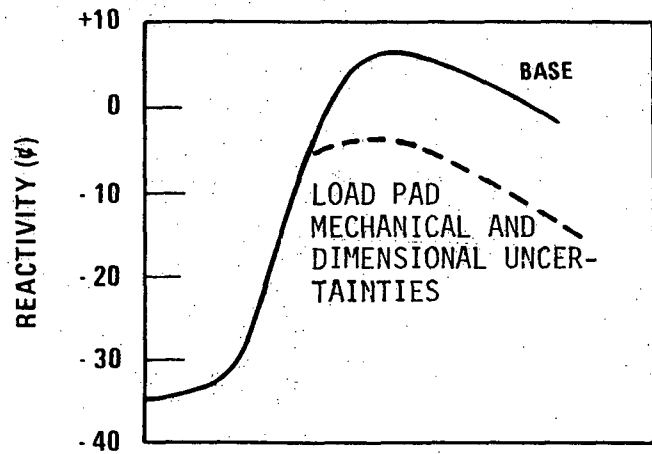
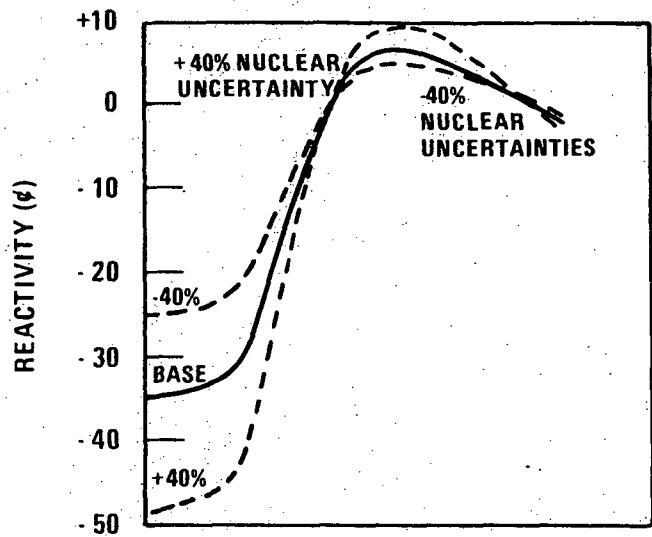


FIGURE 4.2-92C Bowing Reactivity vs. Power-to-Flow Ratio

4655-9

Amend. 59  
Dec. 1980

1746-43

4.2-588

Amend. 53  
Jan. 1980

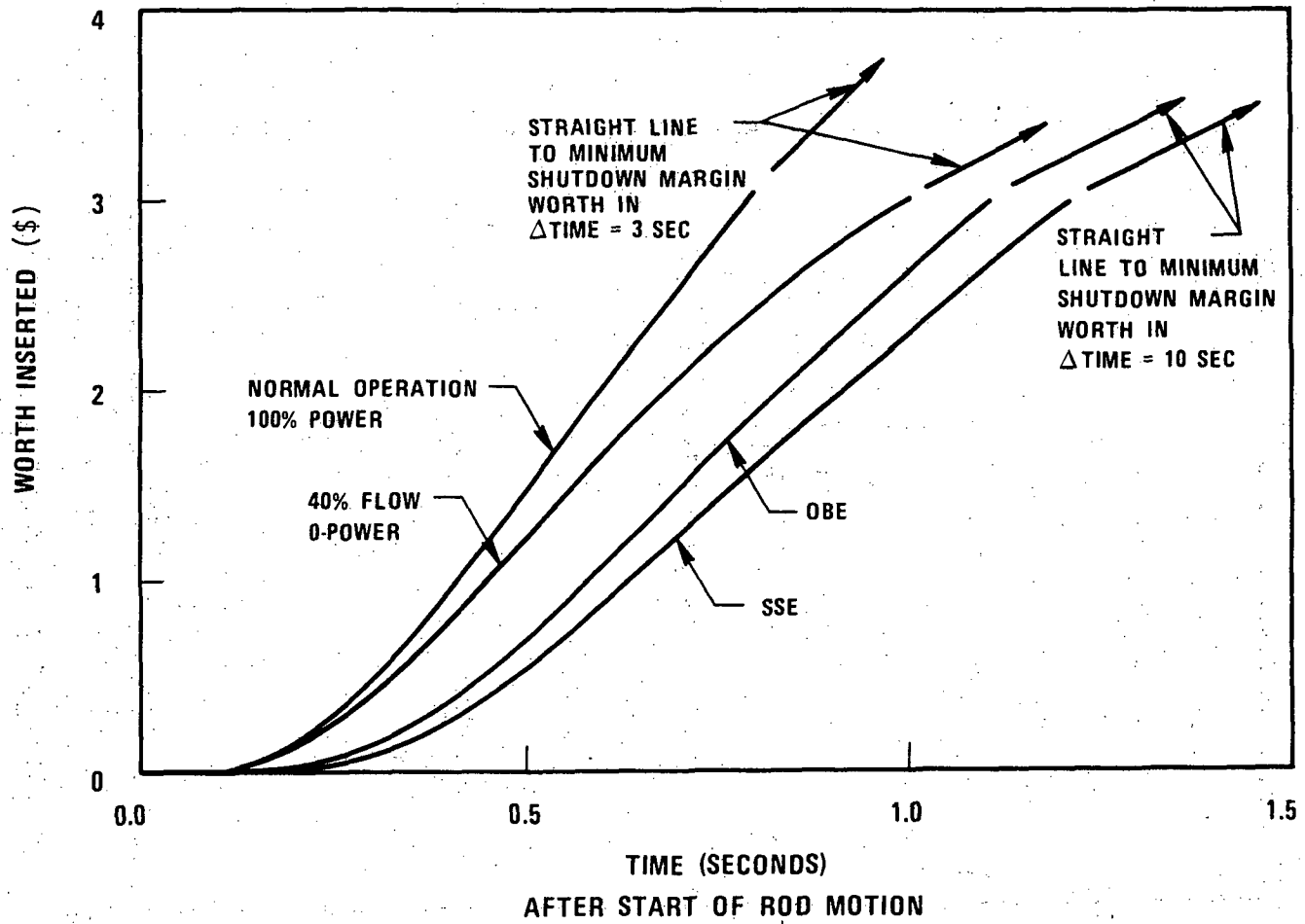


Figure 4.2-93 PCRS Scram Insertion Requirements for the Heterogeneous Core

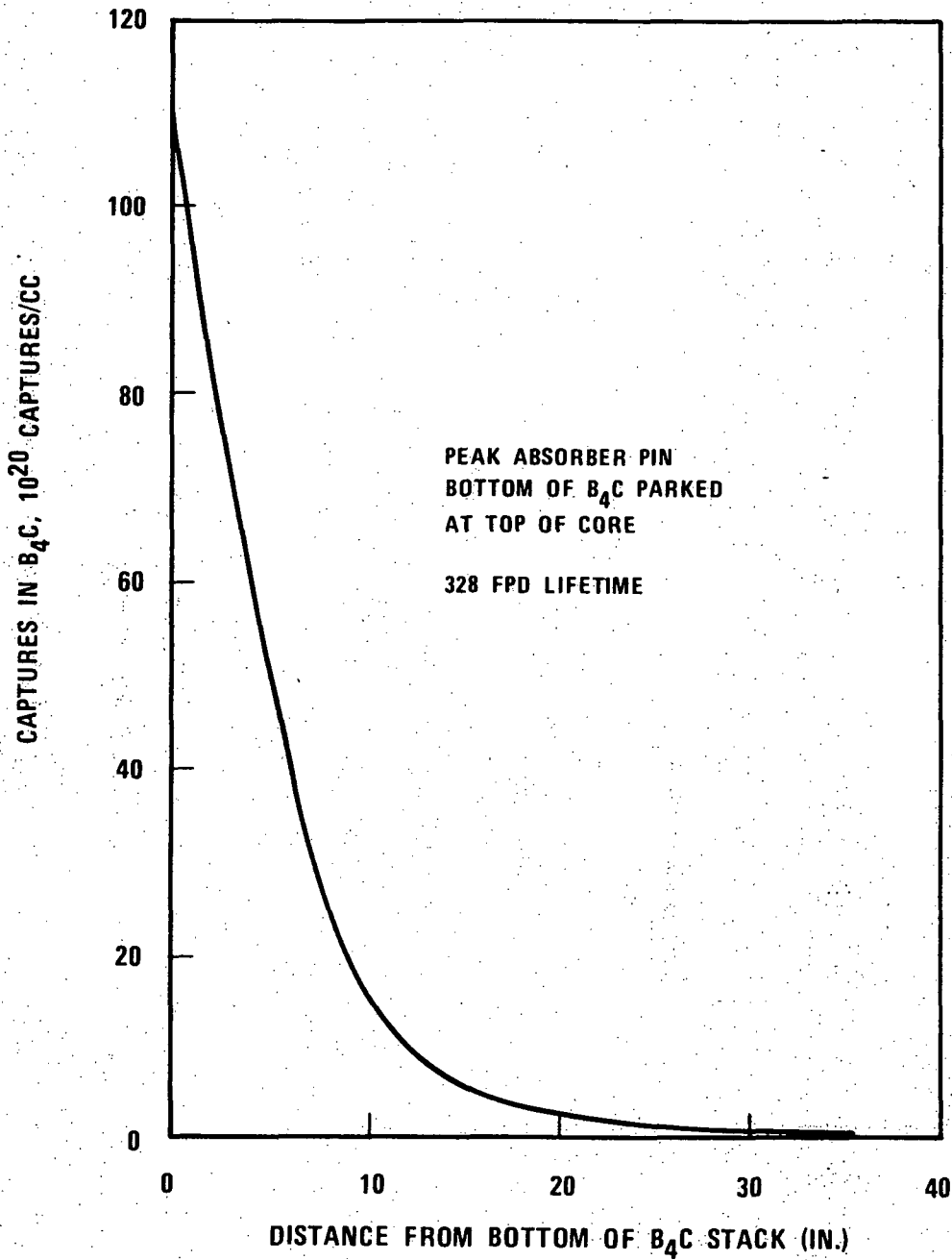


Figure 4.2-93a Calculated Axial Profile of B<sub>4</sub>C Captures in the Secondary Control Assembly

4.2-590

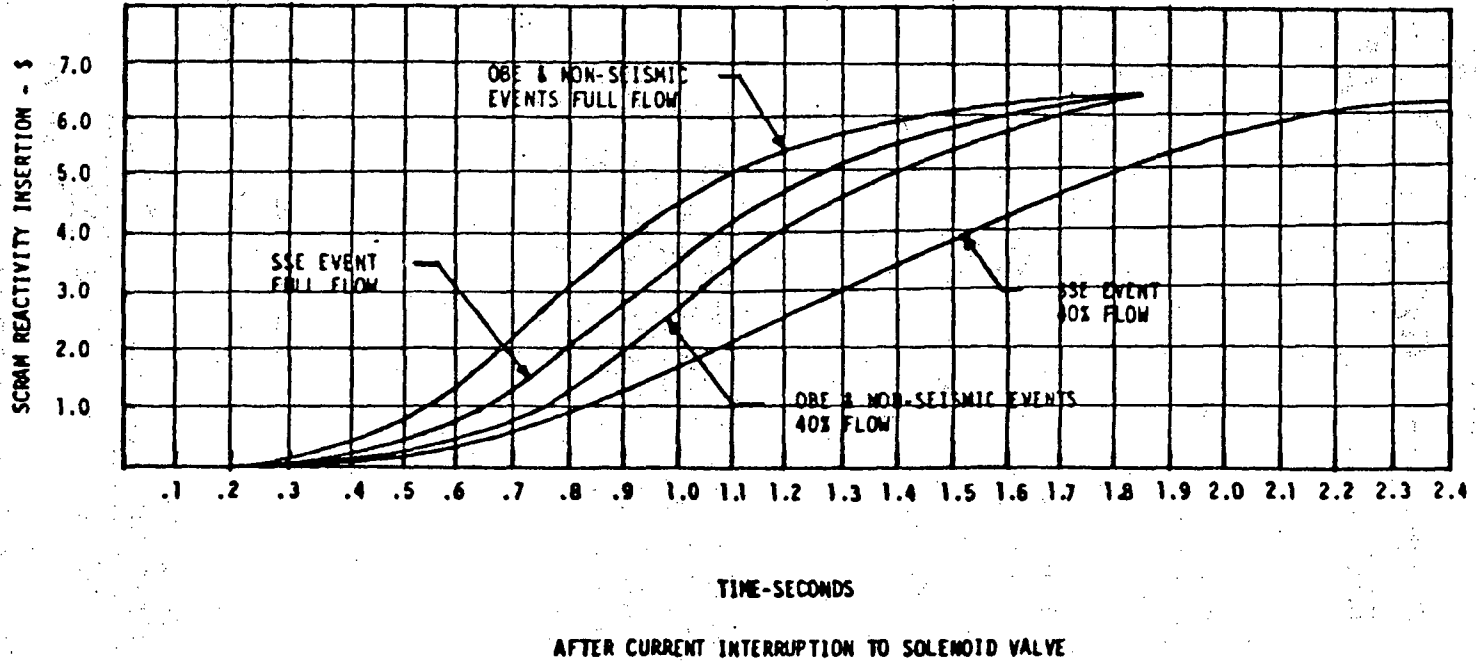
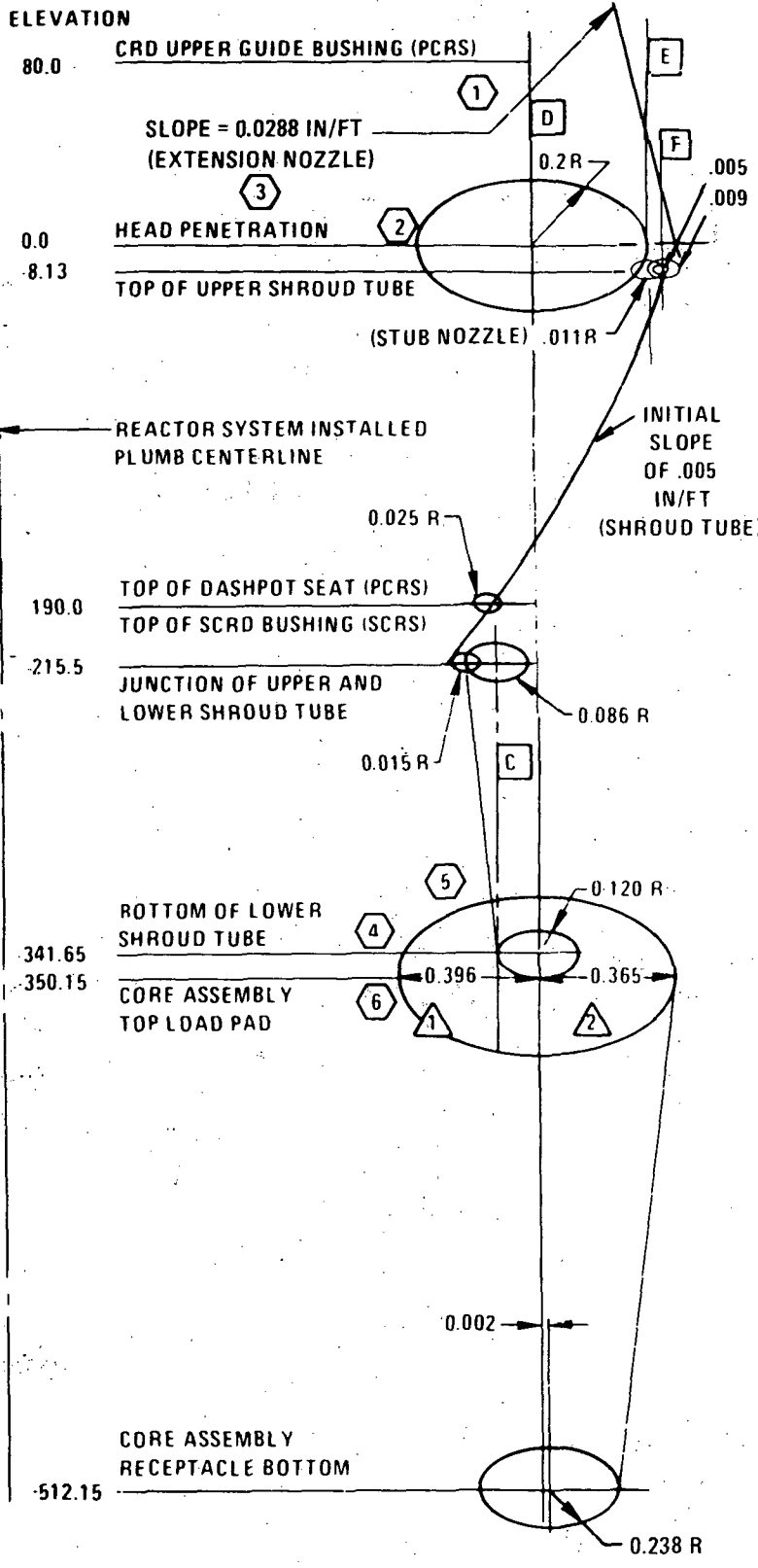


Figure 4.2-94 Secondary Control Rod System Minimum SCRAM Insertion Requirements

Amend. 71  
Sept. 1982



- NOTES:**
- ① DATUM D IS THE REACTOR SYSTEM INSTALLED PLUMB CENTERLINE FOR REFERENCE DATUM D HAS BEEN DRAWN THROUGH THE APPLICABLE PENETRATION IN HEAD
  - ② THE VALUES REPRESENT MAXIMUM RADIAL MISALIGNMENTS OF COMPONENT (FEATURE) CENTERLINES. ACTUAL MAGNITUDE AND ORIENTATION OF MISALIGNMENT AT EACH ELEVATION MAY BE ANYWHERE WITHIN A CIRCLE OF RADIUS AS INDICATED
  - ③ THE CENTERLINE OF THE PRIMARY CRDM GUIDE BUSHING IS TO BE WITHIN 0.048 INCHES OF THE INDICATED SLOPE AT ELEVATION 80.
  - ④ THE VALUES USED IN THE SKETCH ARE FOR A ROW SEVEN CORNER CONTROL ROD. ADDITIONAL DATA IS GIVEN IN THE TABLE BELOW
- |   | R7C   | R7F   | R4C   |
|---|-------|-------|-------|
| ① | 0.396 | 0.403 | 0.402 |
| ② | 0.365 | 0.377 | 0.388 |
- ⑤ LARGE DIMENSION IS ASSEMBLY TO CORE EDGE THROUGH CORE C. SMALL DIMENSION IS ASSEMBLY TO CORE EDGE.
  - ⑥ TO GET THE MISALIGNMENT FOR THE PCA HANDLING SOCKET ID AT ELEV. 344.15 ADD 0.008 IN. TO THE VALUES GIVEN AT ELEV. 350.15.
  - ⑦ DATUM A IS THE CENTERLINE OF THE DATUM B IS THE CENTERLINE OF THE LOWER SHROUD TUBE AT EL 341.65. DATUM C IS THE CENTERLINE OF THE LOWER SHROUD TUBE AT EL -215.5. DATUM E IS THE CENTERLINE OF THE HEAD STUB NOZZLE. DATUM F IS THE CENTERLINE OF THE UPPER SHROUD TUBE AND THE EXTENSION NOZZLE AT EL -8.13. DATUM A, B, C, E AND F ARE PARALLEL TO DATUM D.
  - ⑧ ALL DIMENSIONS ARE IN INCHES UNLESS OTHERWISE NOTED

Figure 4.2-95A Control Rod System Operating Misalignment Envelope

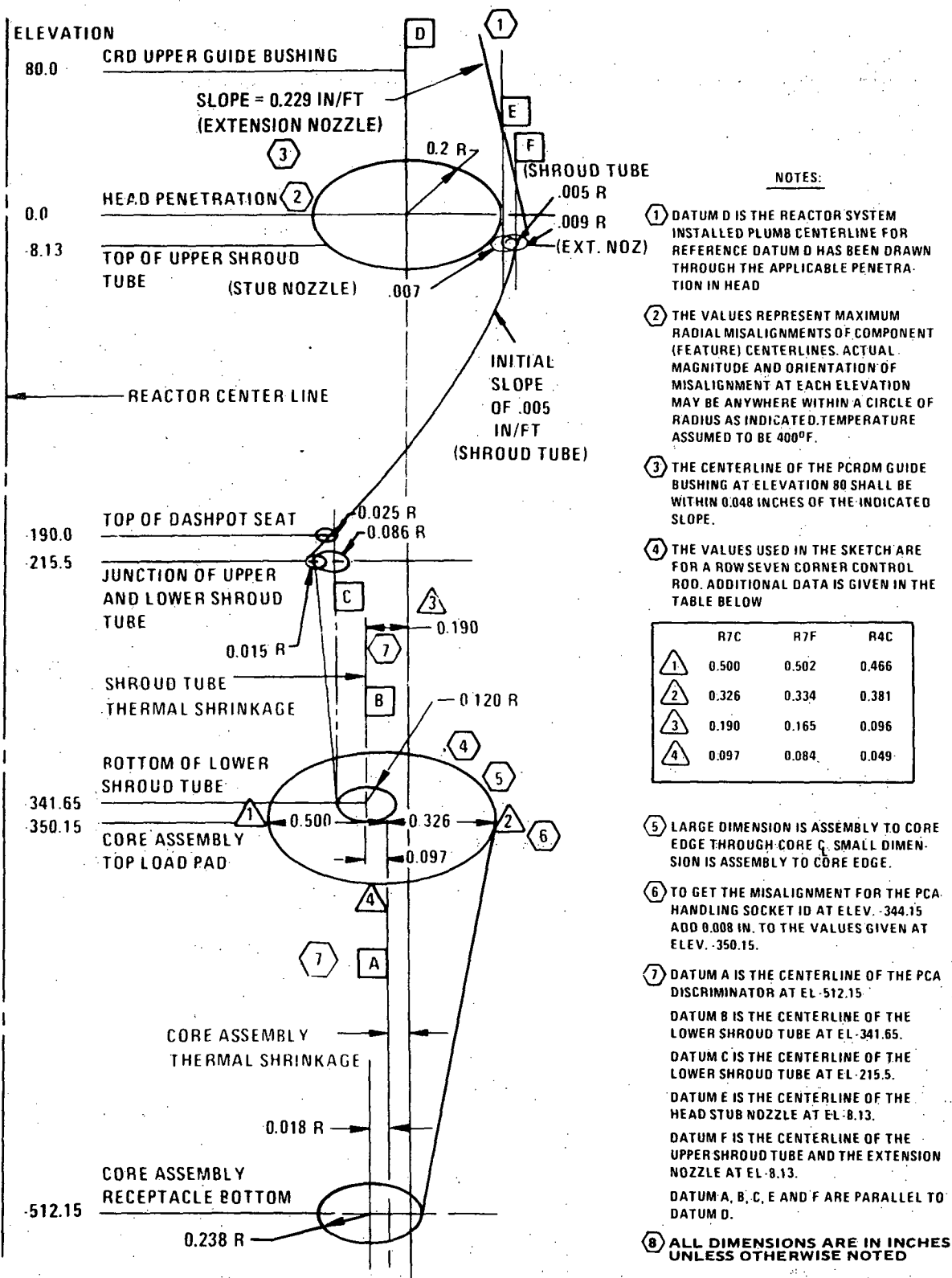


Figure 4.2-95B Control Rod System Refueling Misalignment Envelope



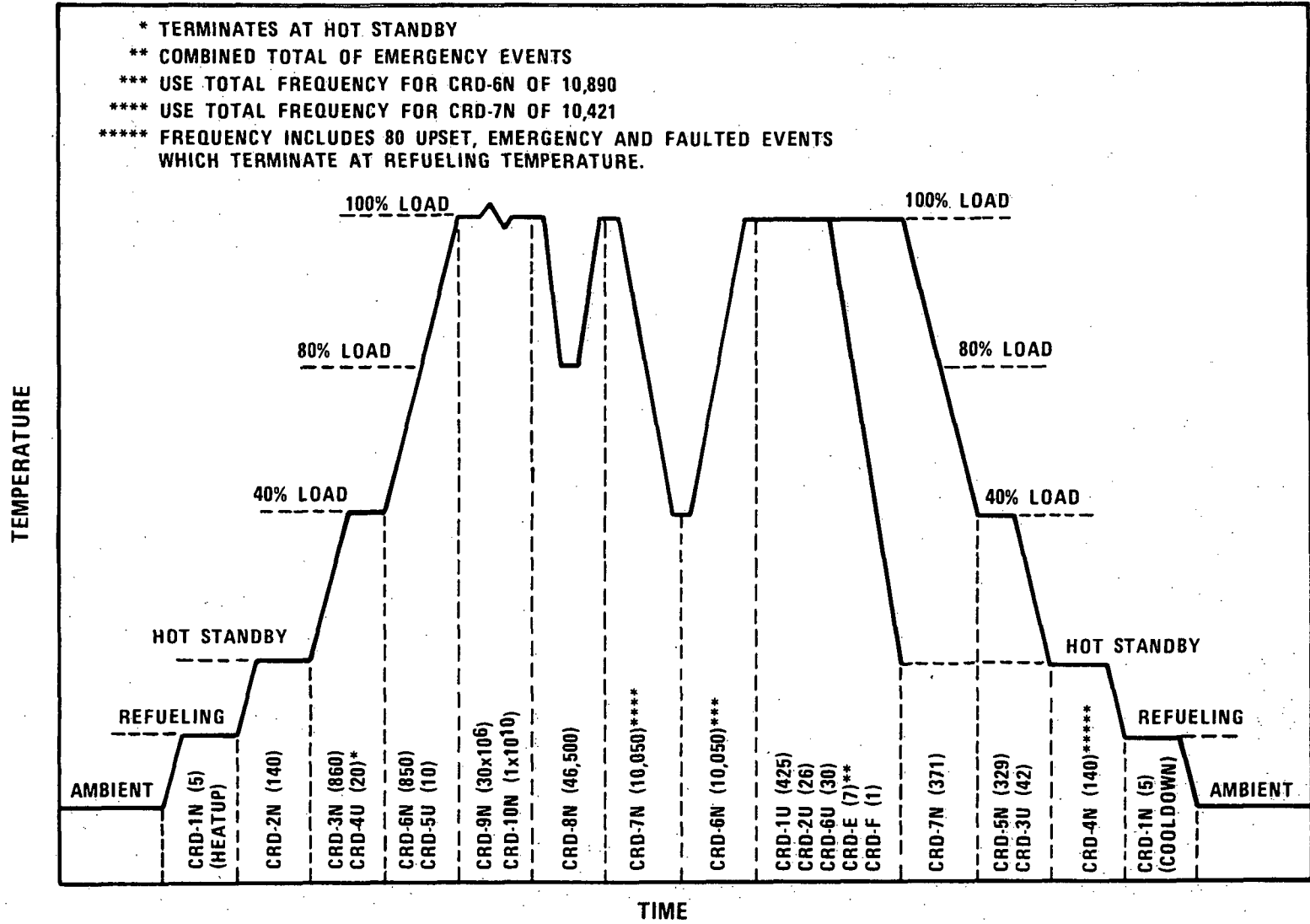


Figure 4.2-96 Control Rod Driveline 30 Year Histogram

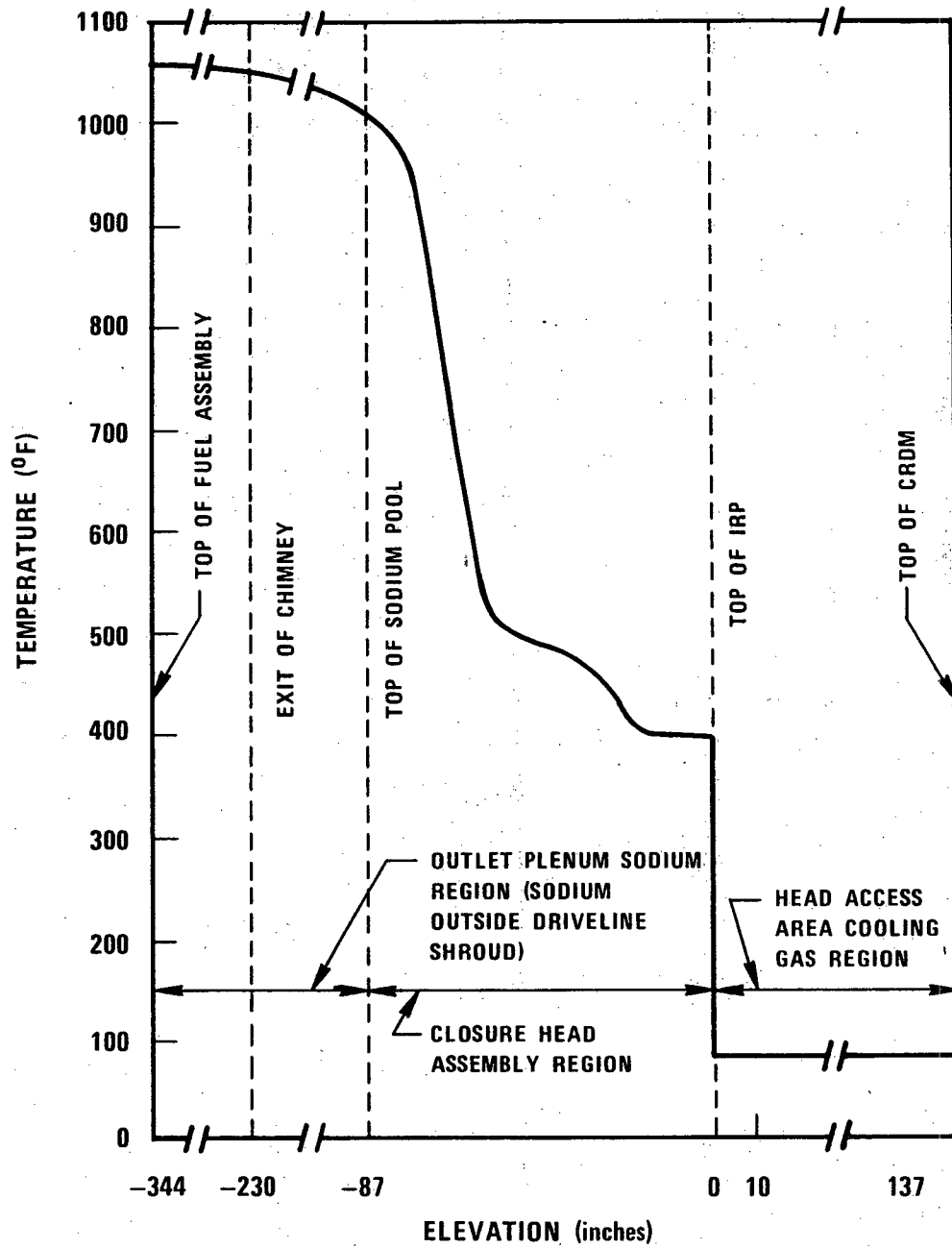


Figure 4.2-97 Reactor Steady State Thermal Environment

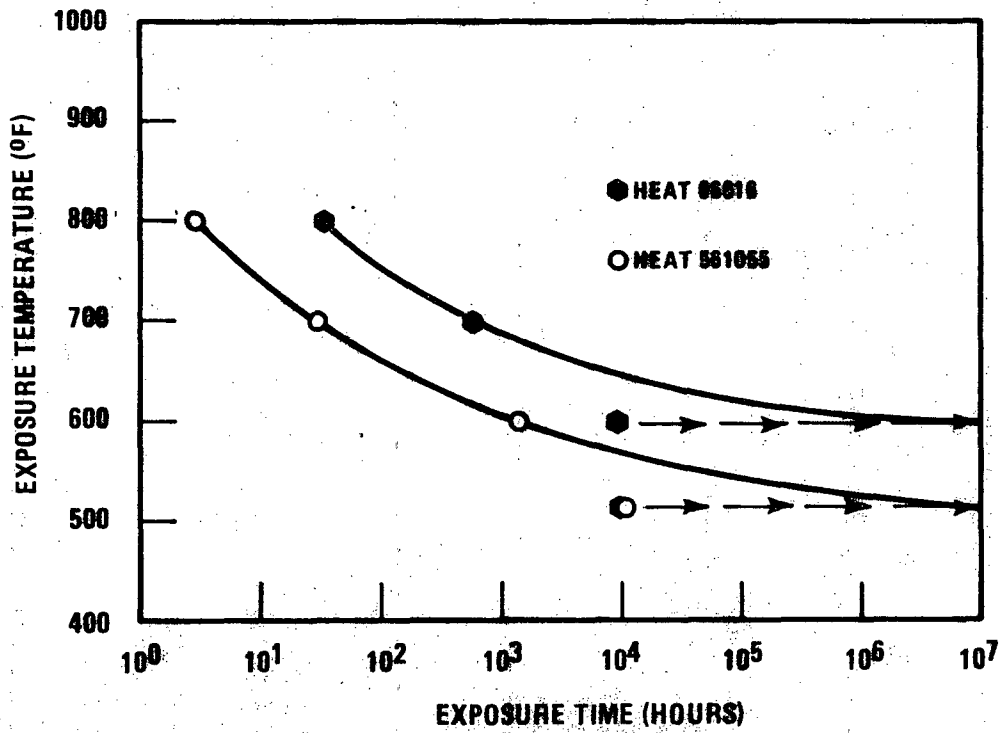


Figure 4.2-97A Exposure Time Required to Cause Room Temperature Toughness to Fall Below 15 Ft. Lbs.

7683-1

4.2-595

Amend. 51  
Sept. 1979

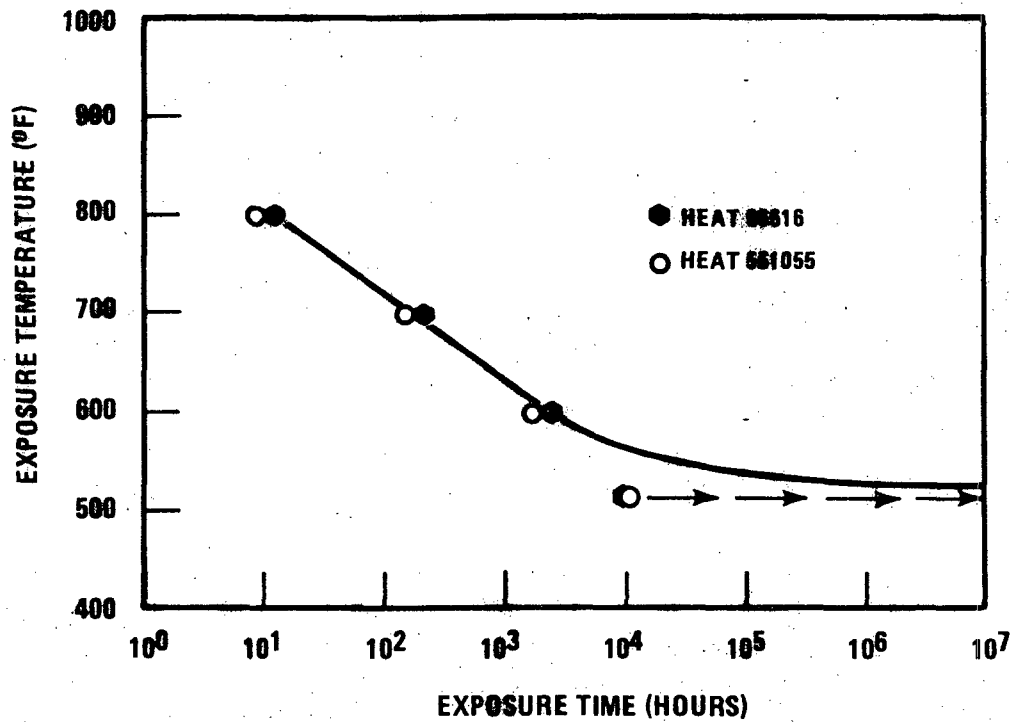


Figure 4.2-97B Exposure Time Required to Deplete Room Temperature Toughness by One Half

7683-2

4.2-596

Amend. 51  
Sept. 1979

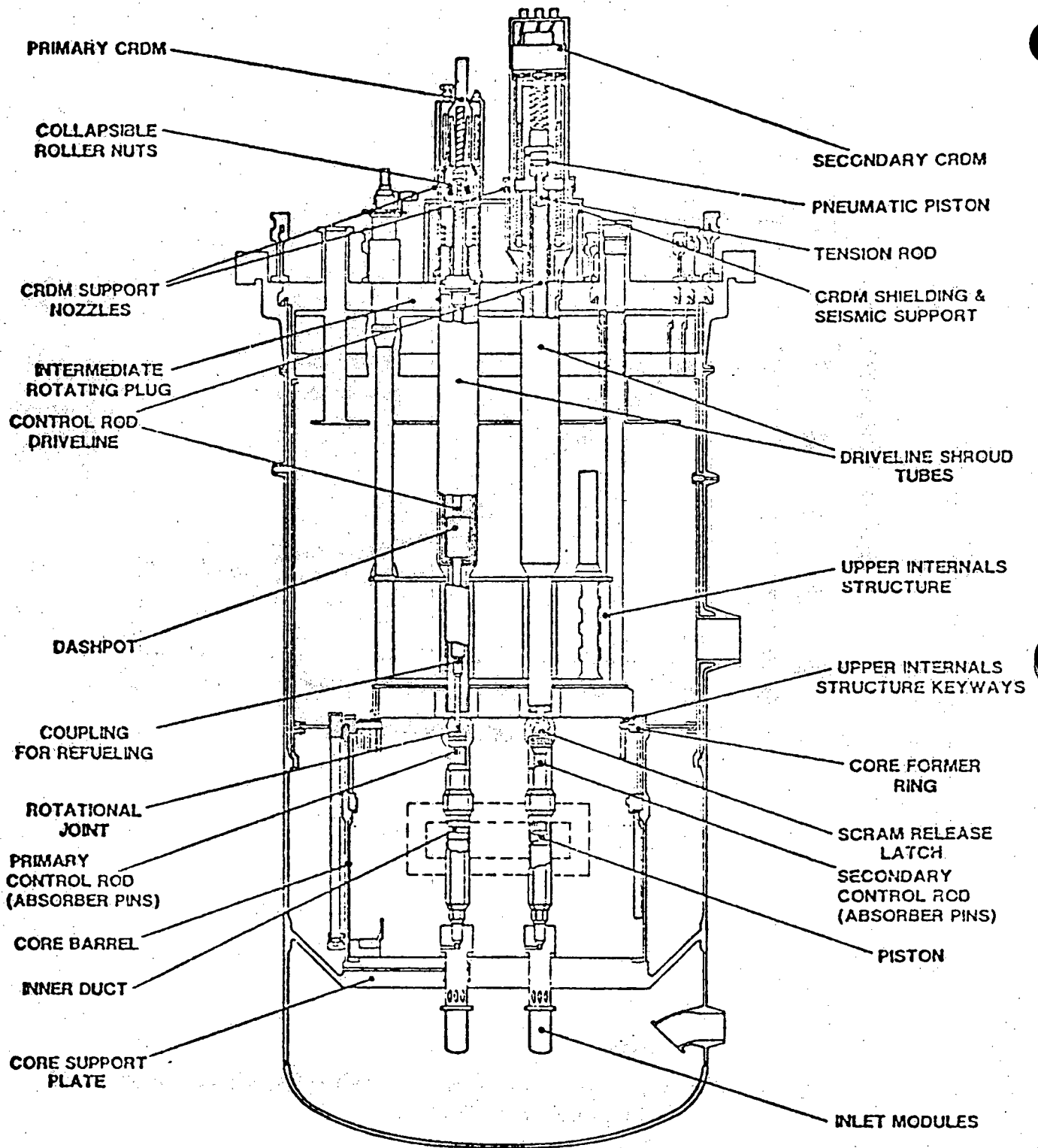


Figure 4.2-98 Control Rod Systems - Reactor Elevation

FIGURE 4.2-99 DELETED

Amend. 51  
Sept. 1979

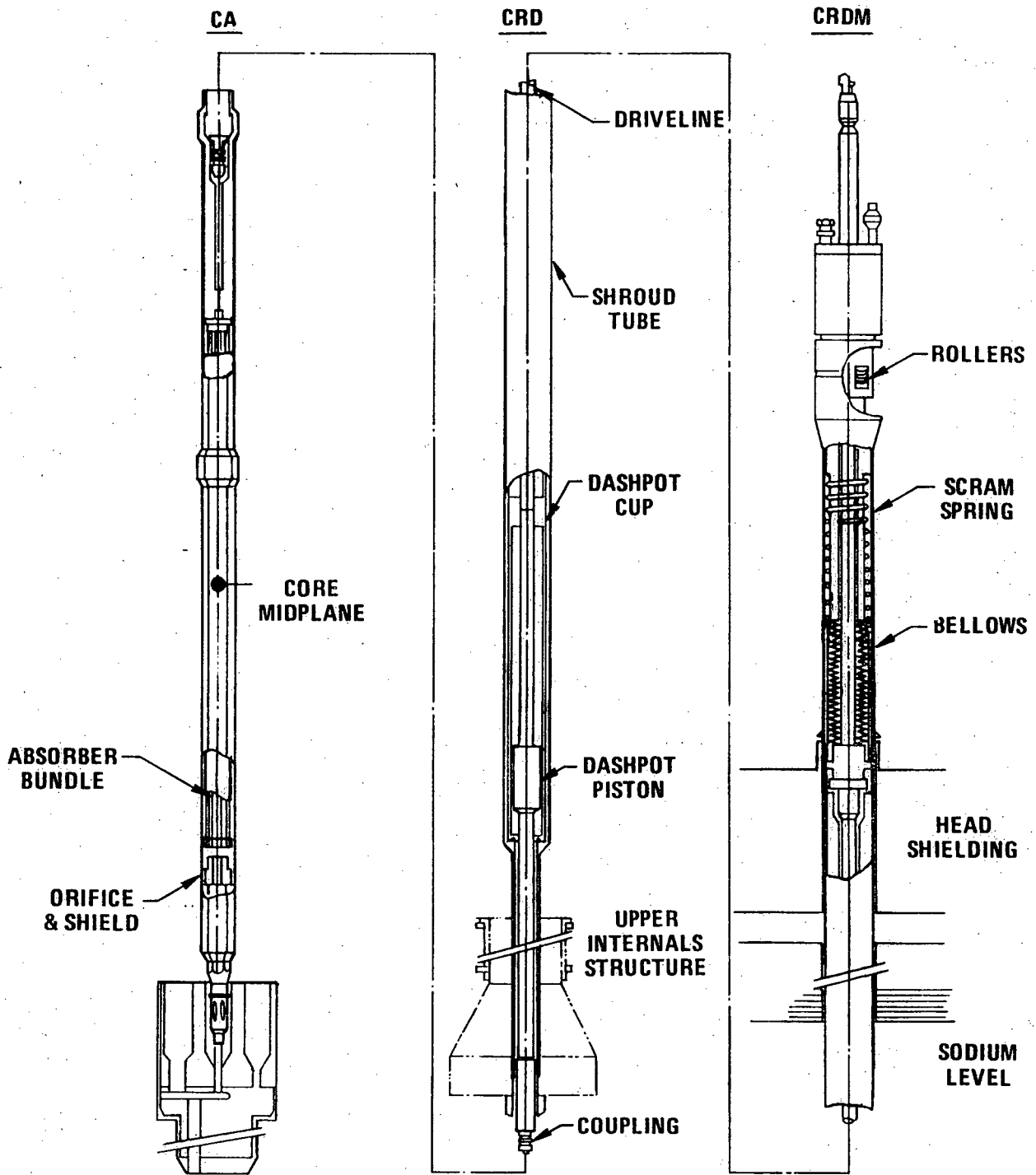


Figure 4.2-100. Primary Mechanical Sub-System

6664-83

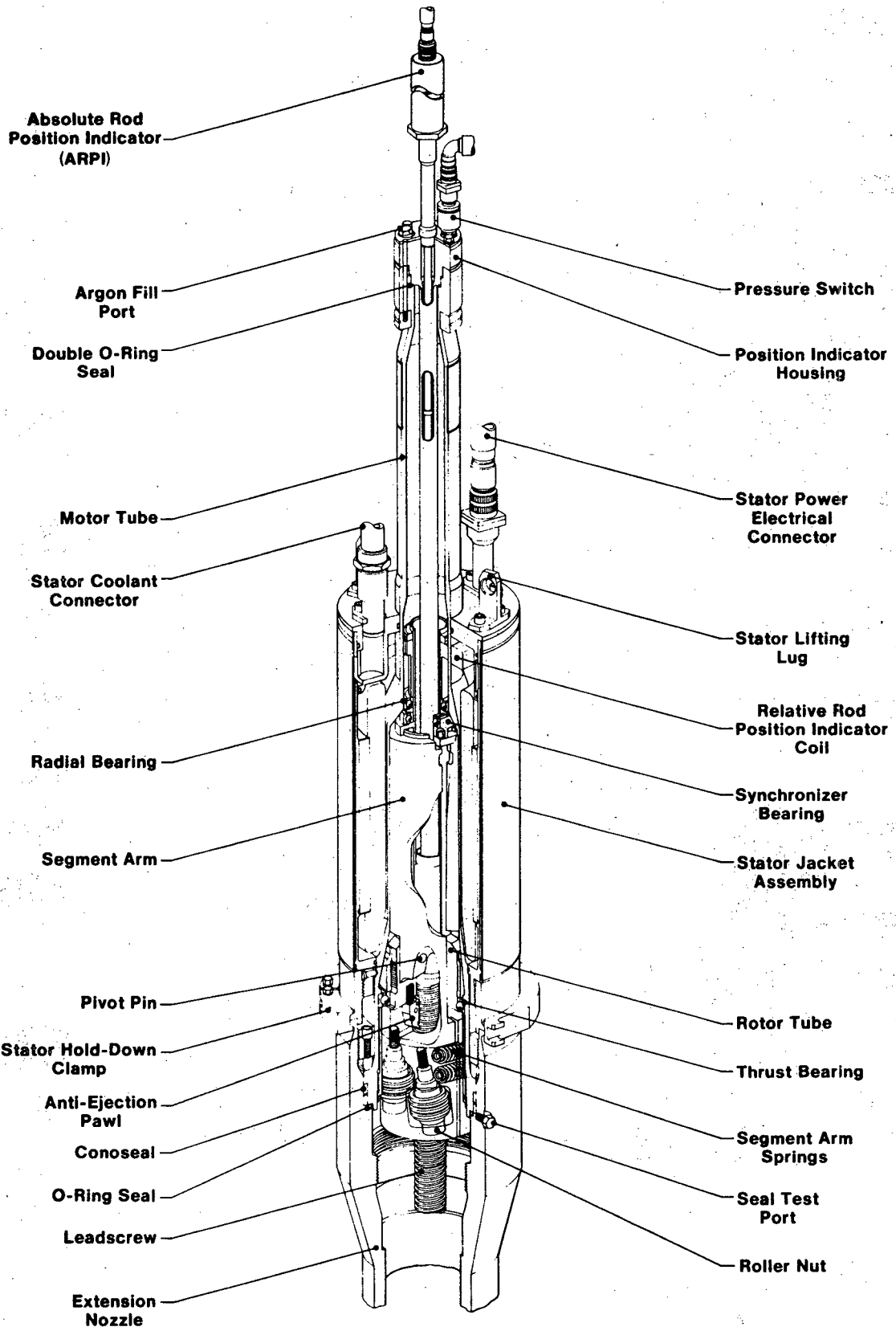


Figure 4.2-101 Primary Control Rod Drive Mechanism (PCRD) - Upper CRDM Assembly and Extension Nozzle

1764-50

Amend. 51  
Sept. 1979



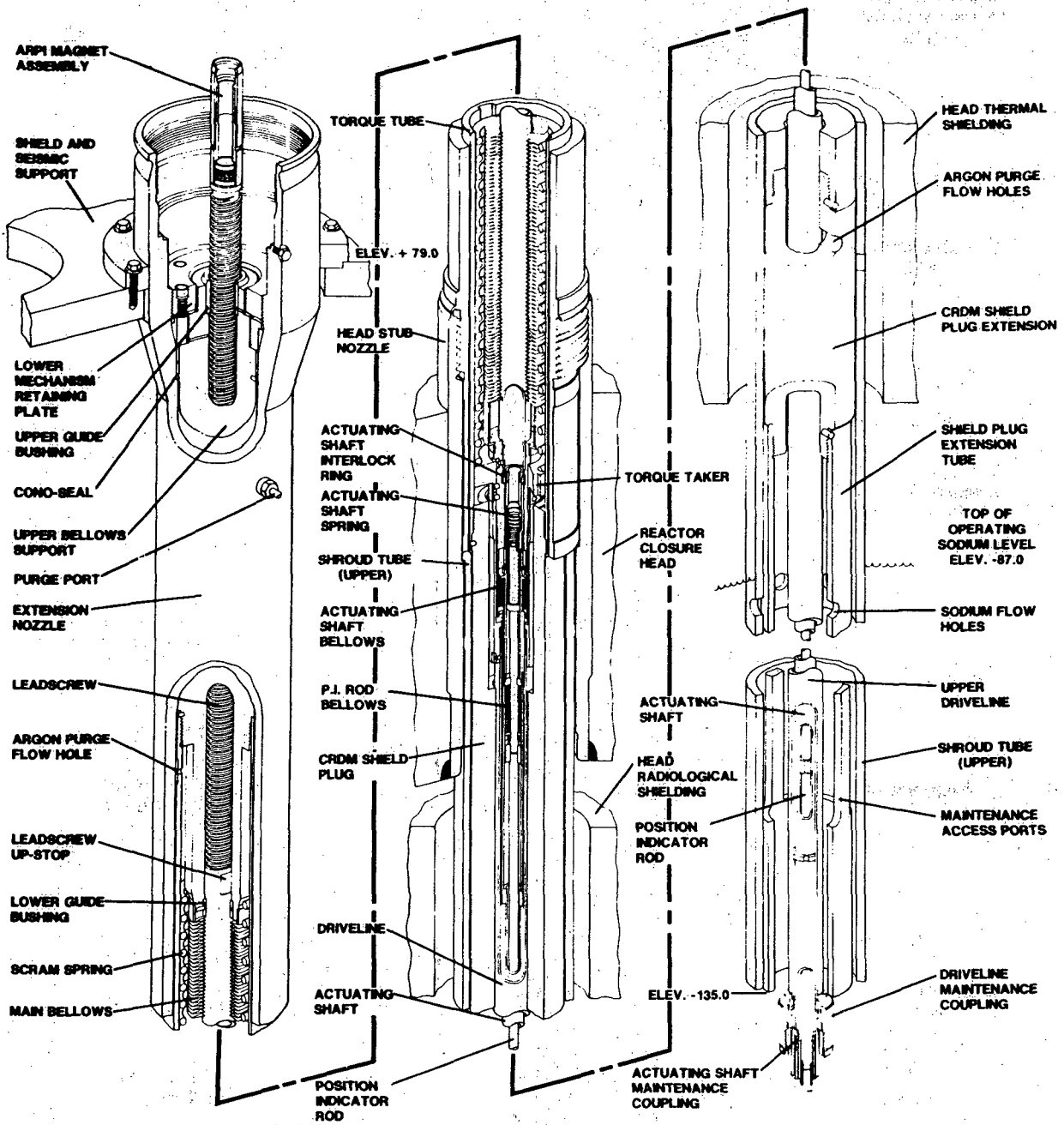


Figure 4.2-102 Lower CRDM Assembly, Extension Nozzle and Upper Shroud Tube

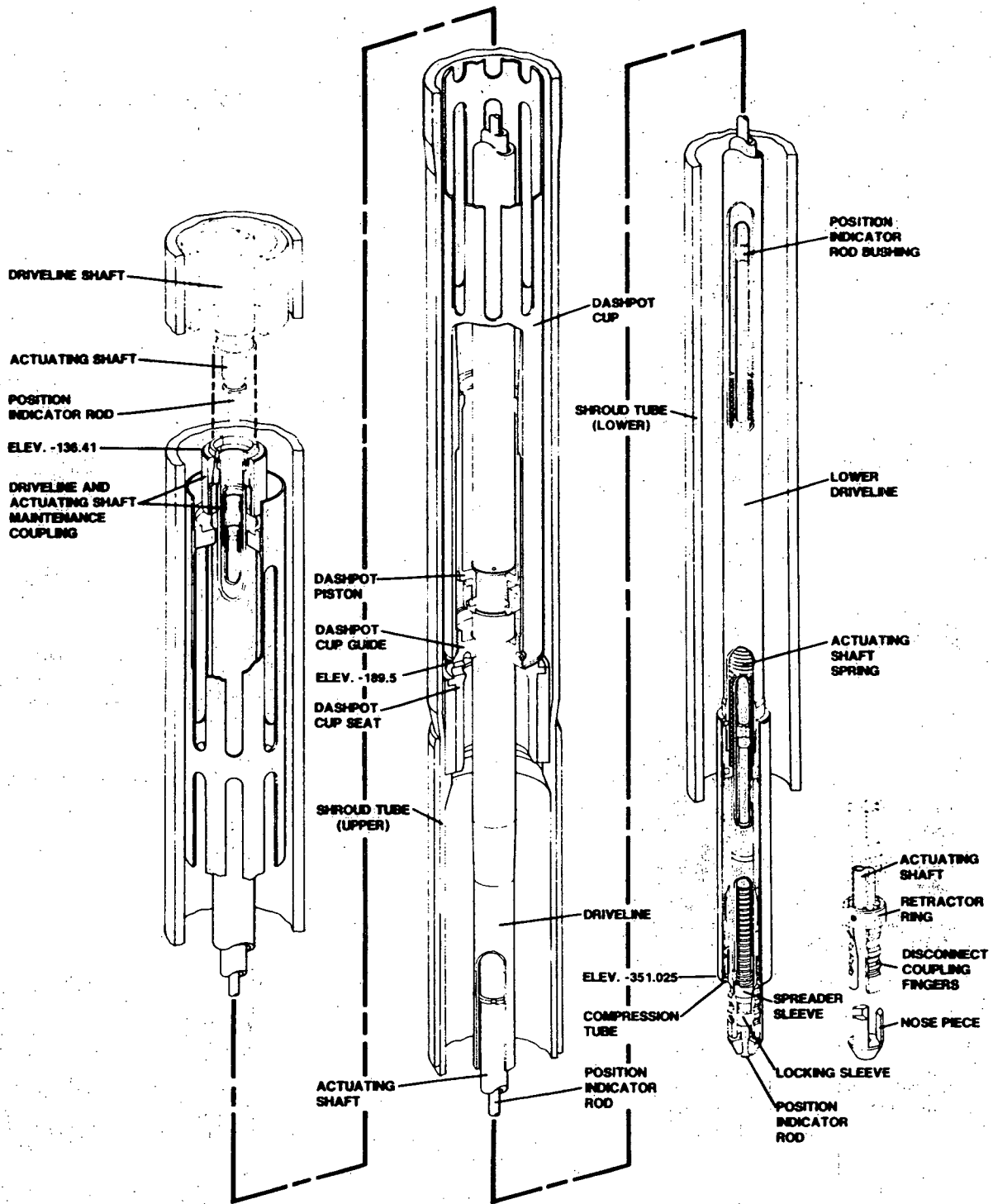


Figure 4.2-103 Lower CRD Assembly, Extension Nozzle and Lower Shroud Tube

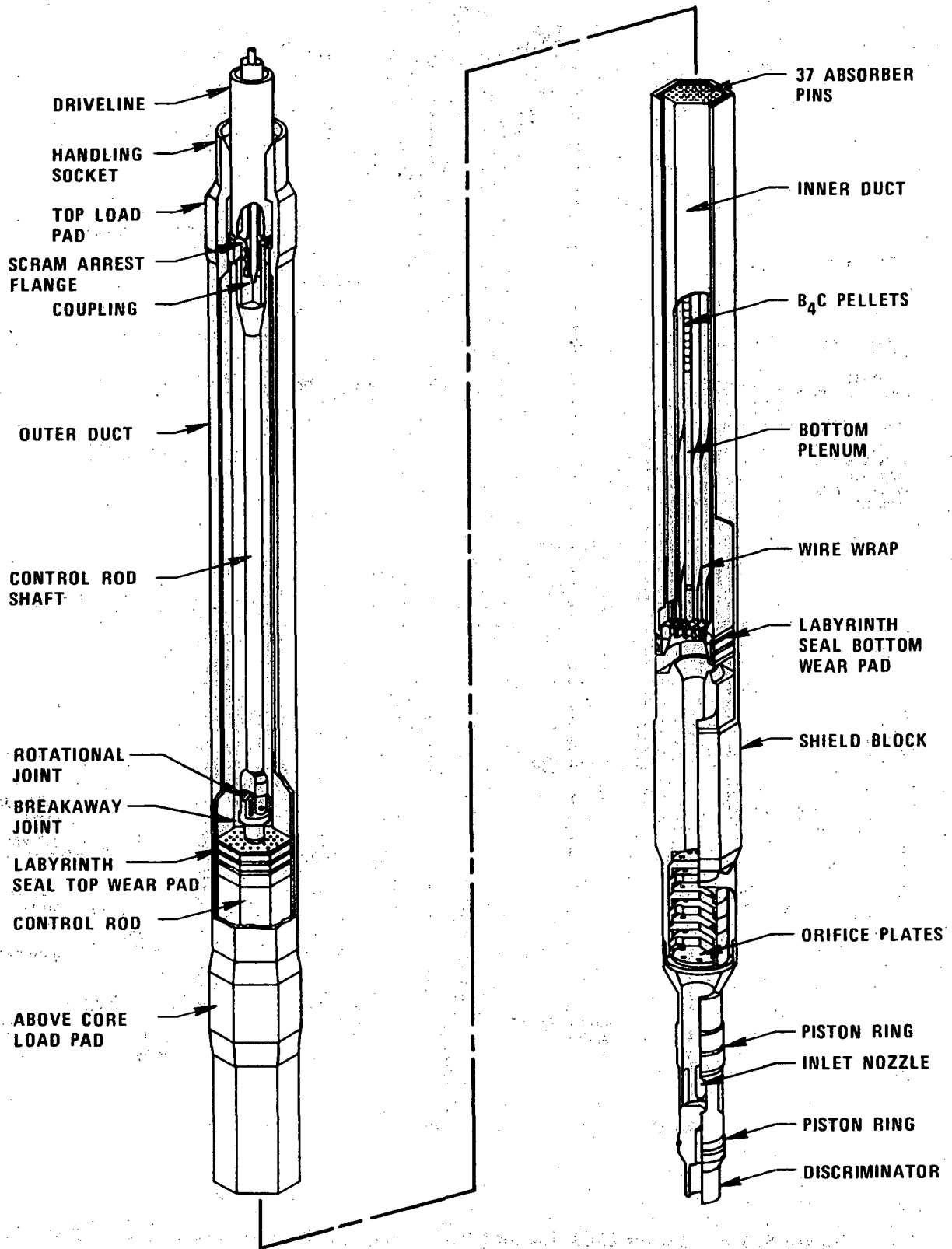
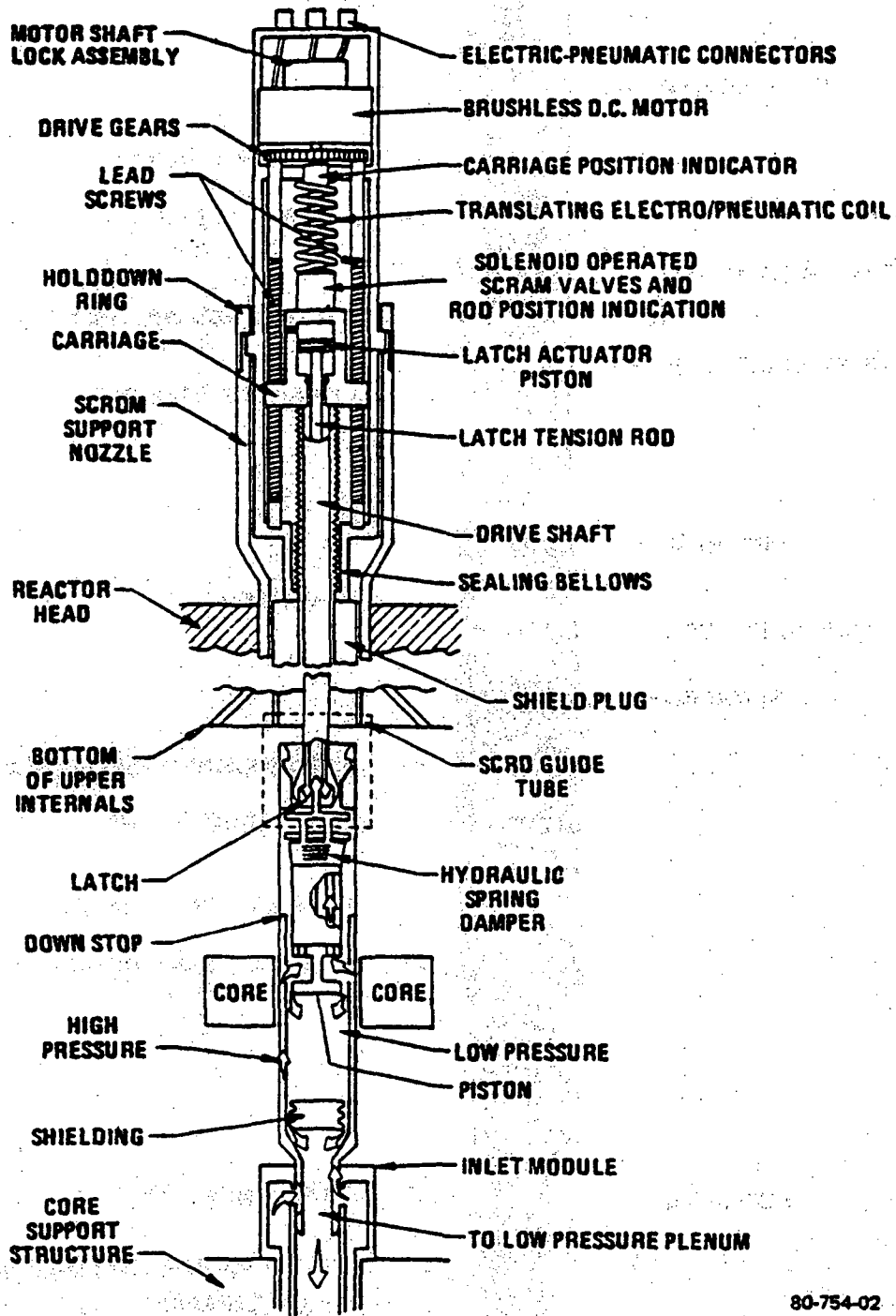


Figure 4.2-104 Primary Control Assembly (PCA)



80-754-02

Figure 4.2-105. SECONDARY CONTROL ROD SYSTEM SCHEMATIC

Amend. 59  
Dec. 1980

# SECONDARY CONTROL ASSEMBLY

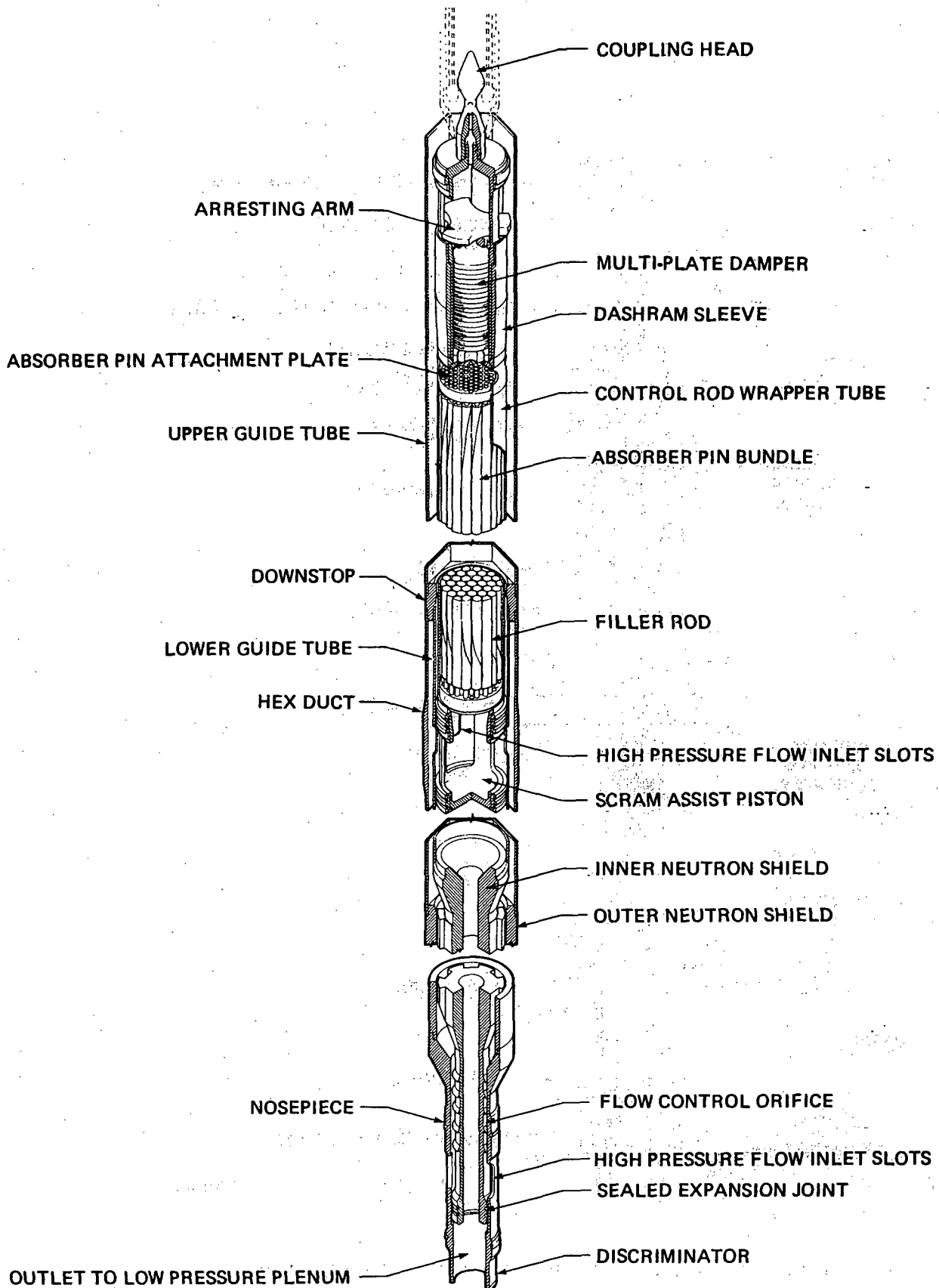


FIGURE 4.2-106. SECONDARY CONTROL ASSEMBLY

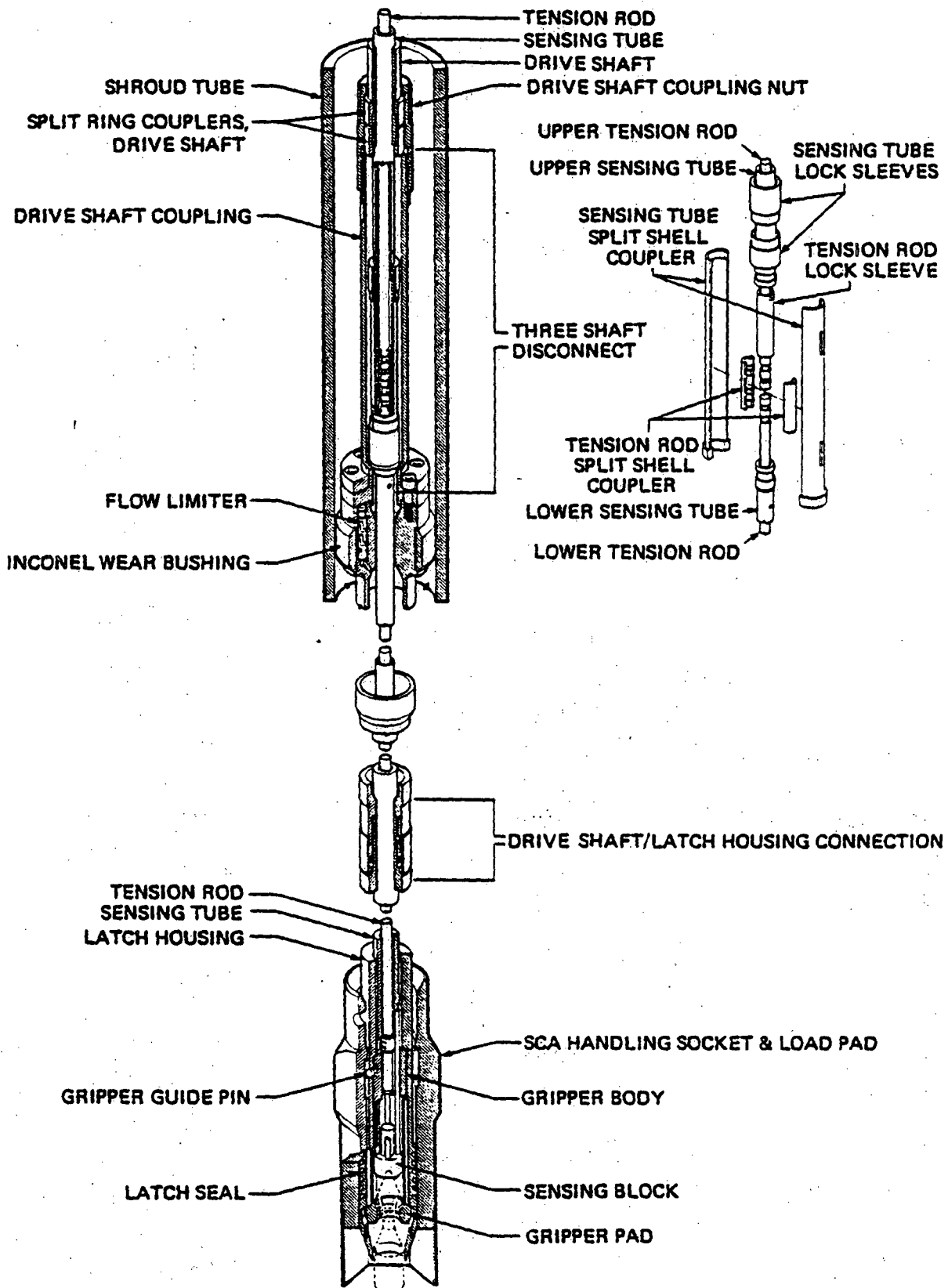
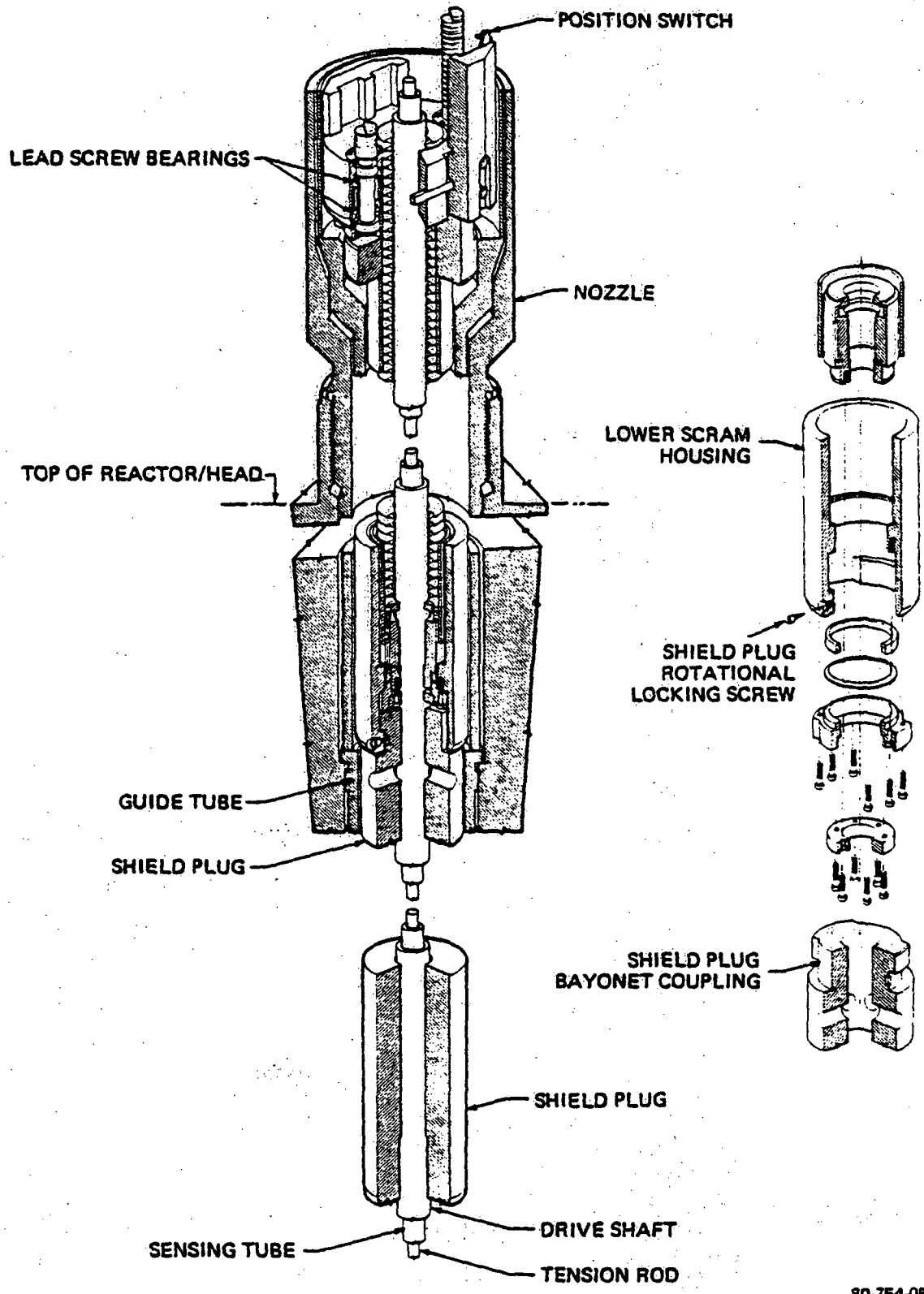


Figure 4.2-107A. SECONDARY CONTROL ROD DRIVE LINE

80-754-04

Amend. 59  
Dec. 1980



80-754-05

Figure 4.2-107B. SECONDARY CONTROL ROD DRIVE LINE  
 (IN REGION OF LOWER SCRDM, NOZZLE, HOUSING AND SHIELD)

Amend. 59  
 Dec. 1980

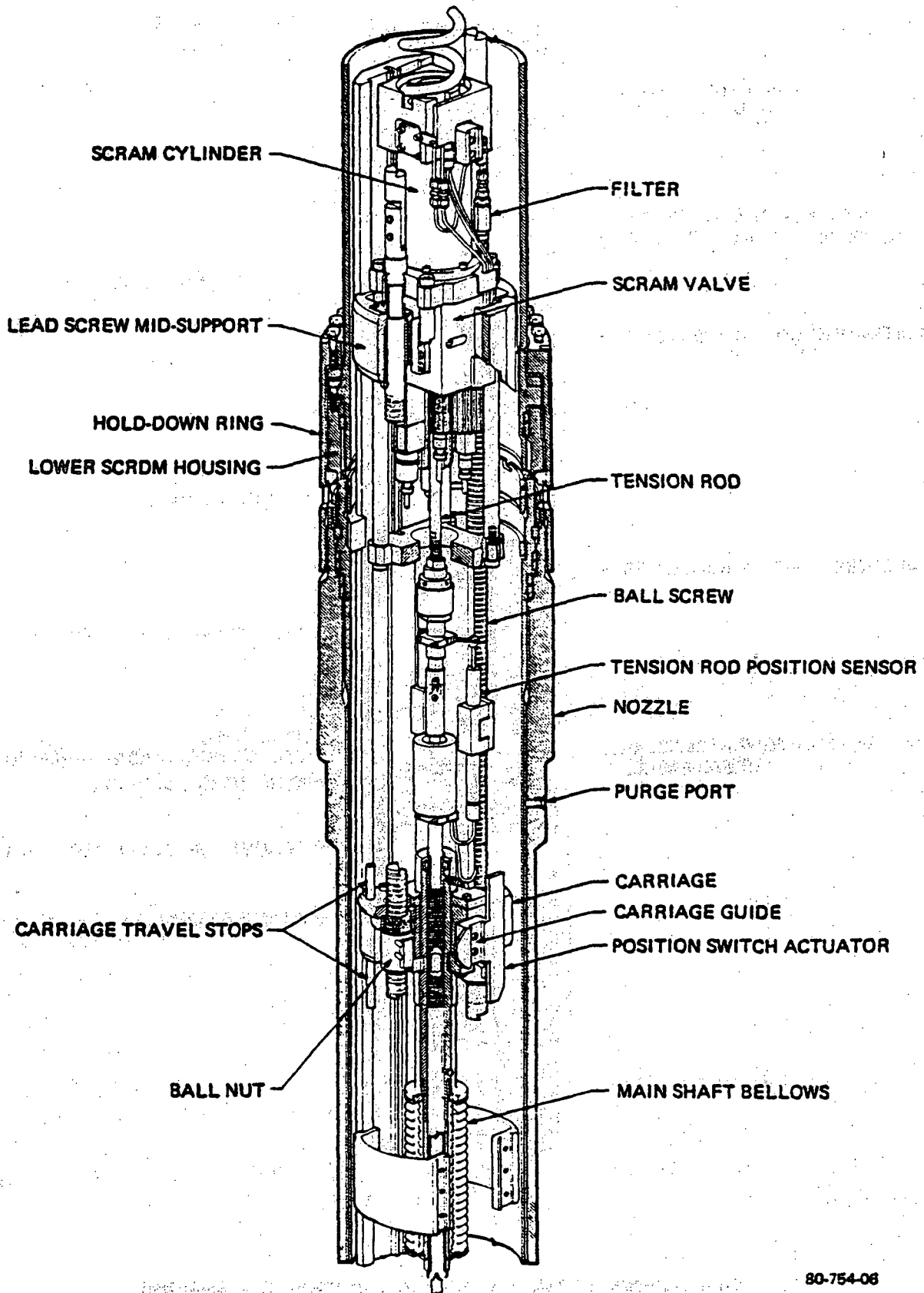
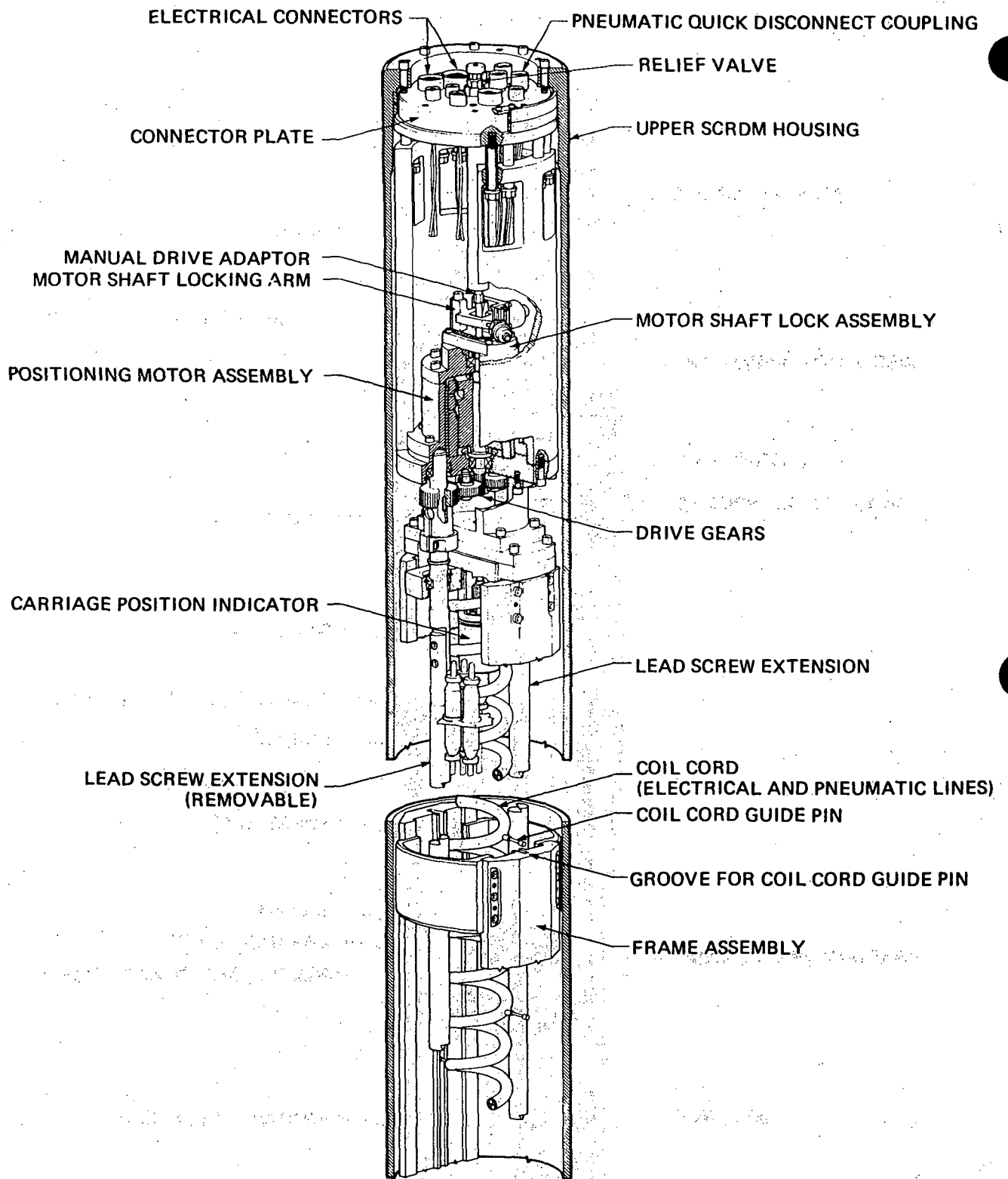


Figure 4.2-108A. SECONDARY CONTROL ROD DRIVE MECHANISM

80-754-06

Amend. 59  
Dec. 1980





82-402-03

Figure 4.2-108B SECONDARY CONTROL ROD DRIVE MECHANISM

1764-54

4.2-608

Amend. 53  
Jan. 1980

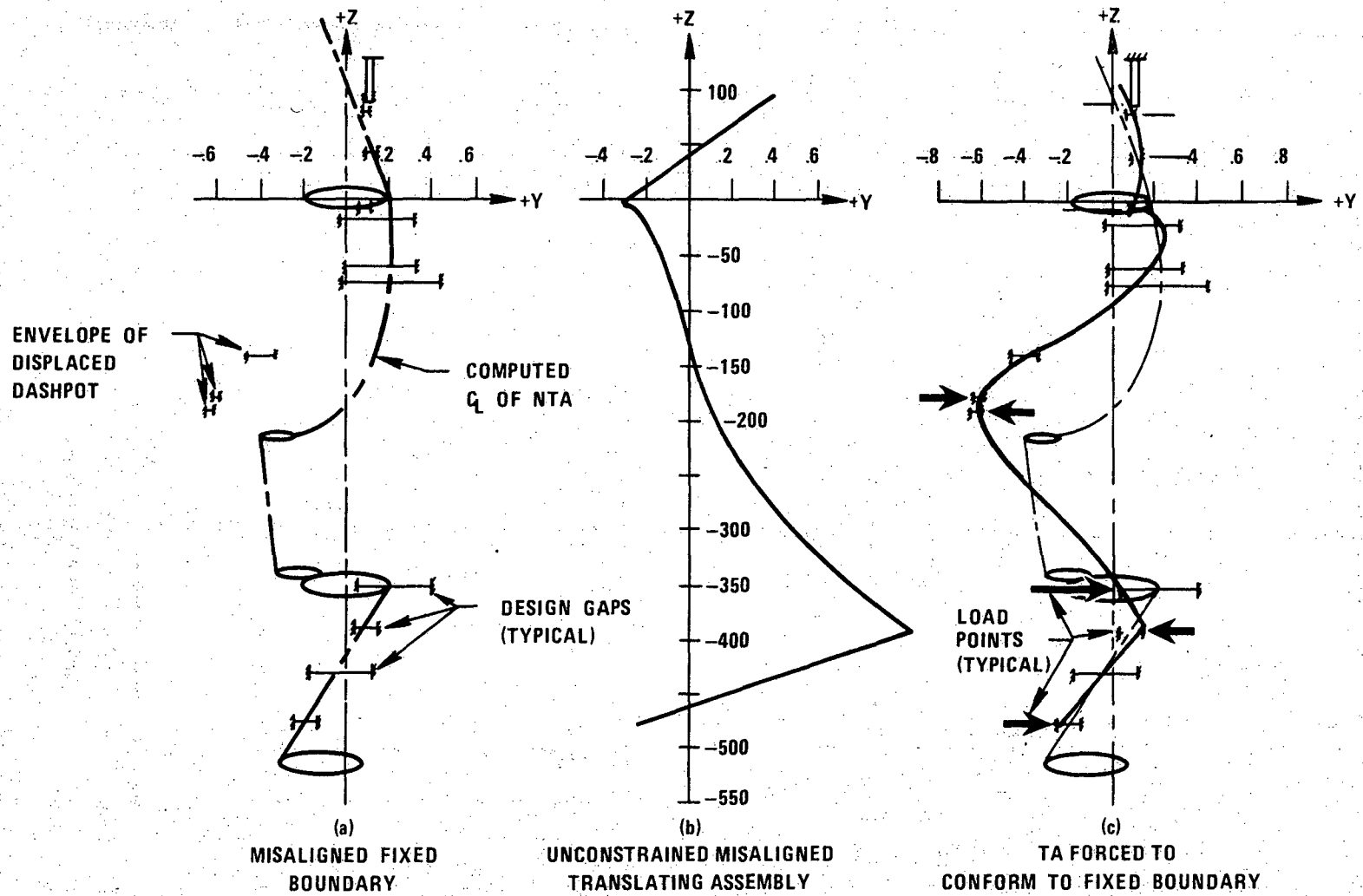


Figure 4.2-109 Lateral Misalignment Loads Model  
(All dimensions are in inches)

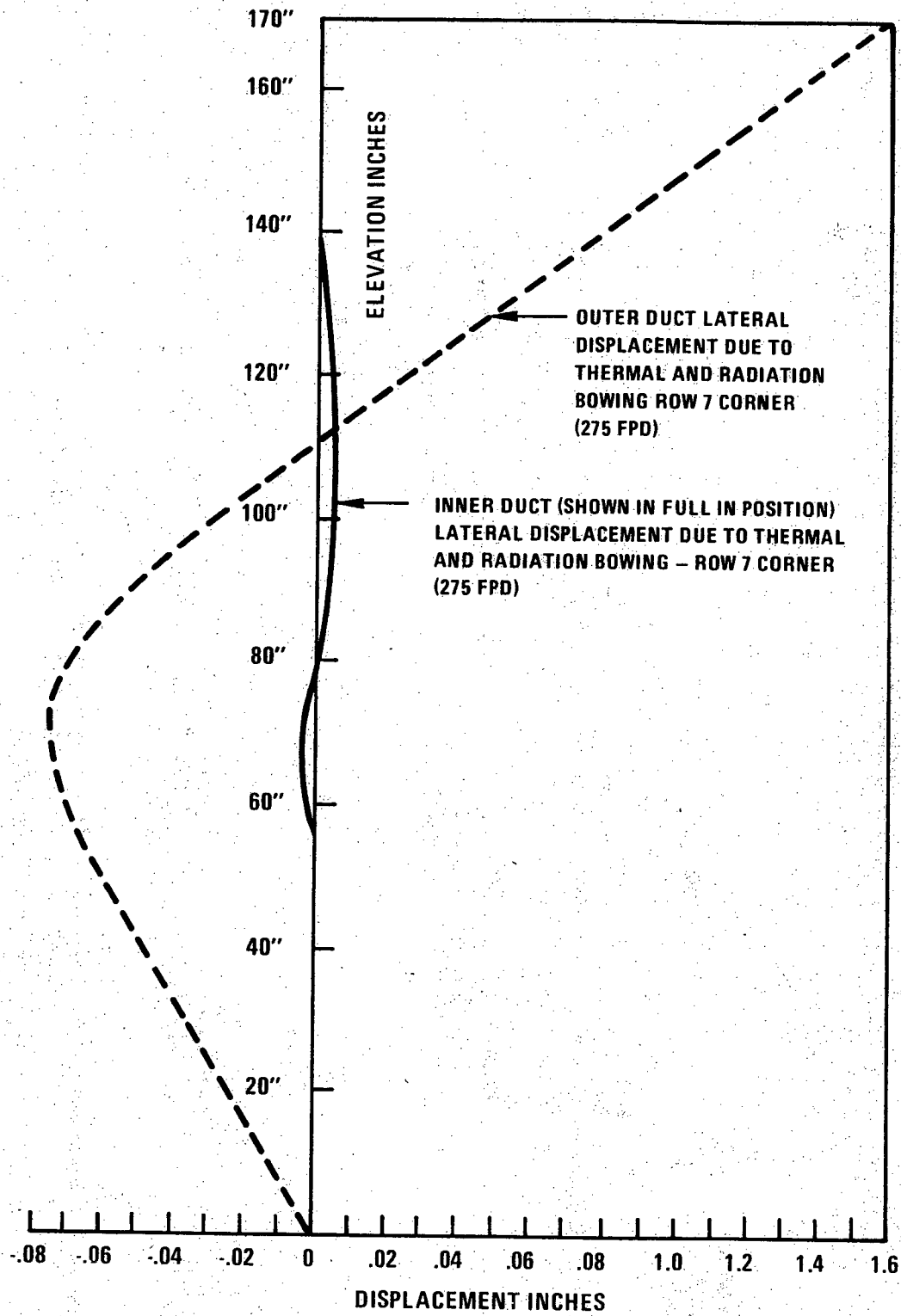


Figure 4.2-110. Predicted Inner/Outer Duct Bow – PCA

9649-2

4.2-610

Amend. 51  
Sept. 1979

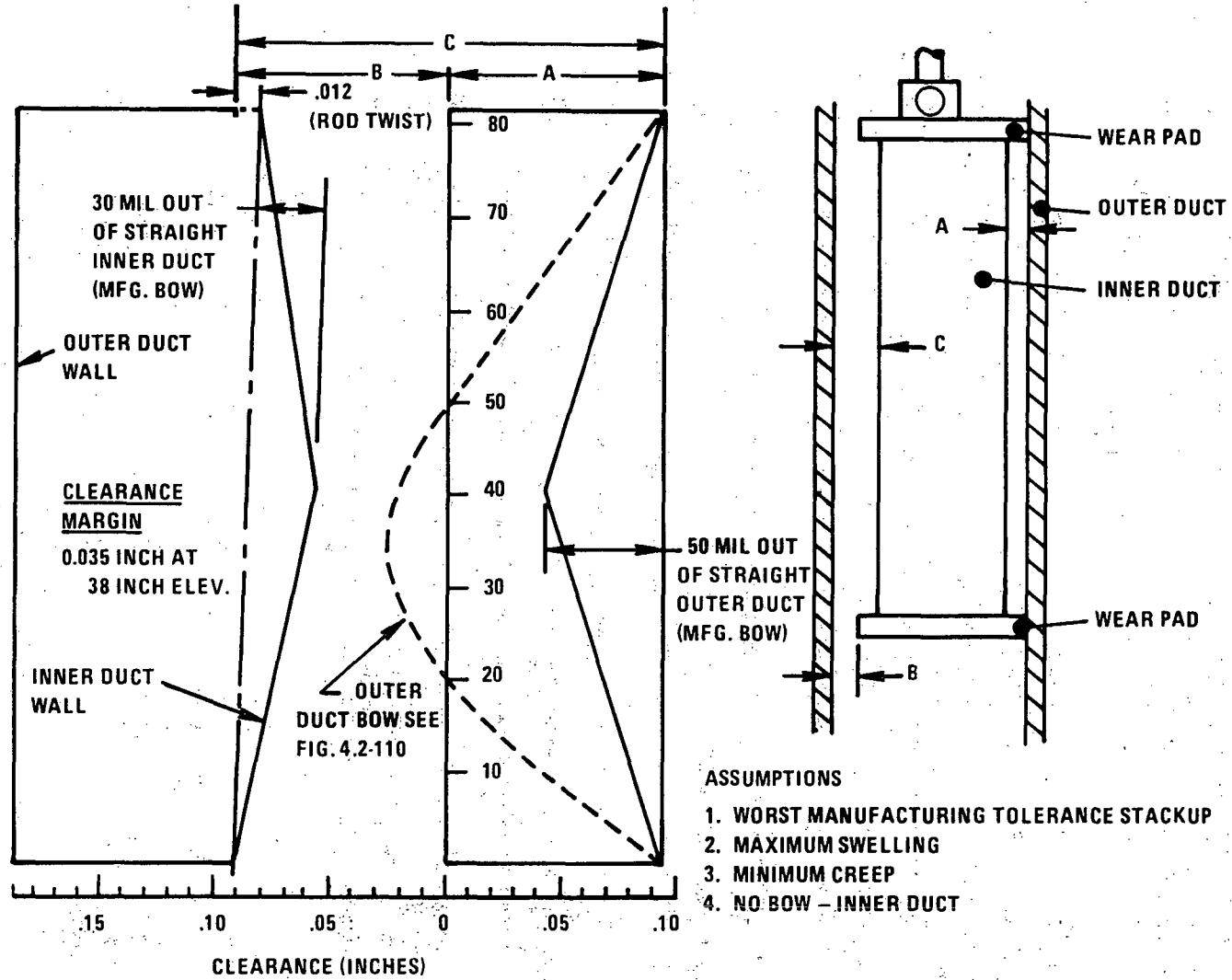


Figure 4.2-110A. PCA Clearance (Lateral Displacement Due To Thermal And Radiation Bowing Row 7 Corner For 1 Cycle)

9597-1

4.2-611

Amend. 51  
Sept. 1979

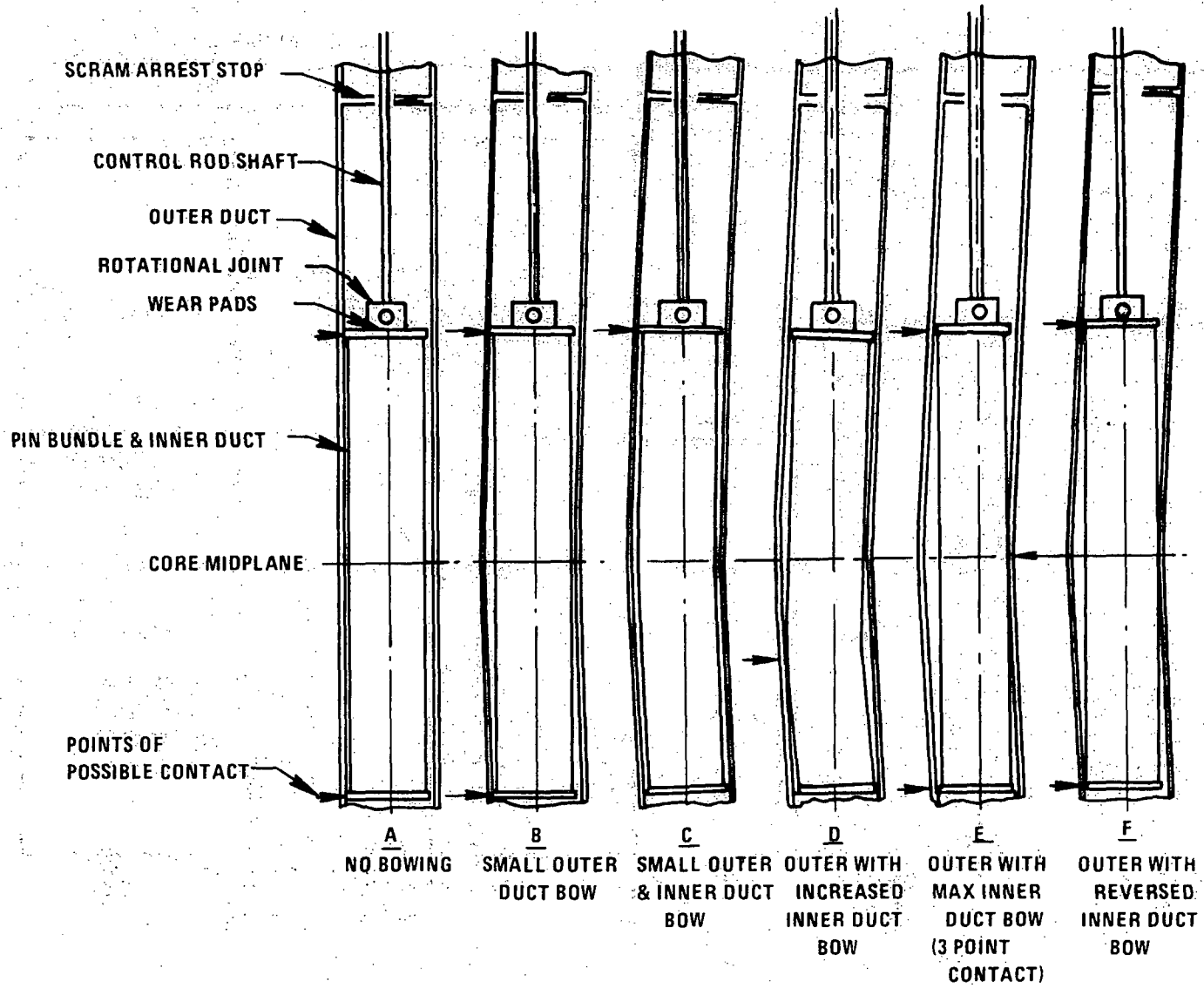


Figure 4.2-111. Primary Control Assembly Duct Bowing Configuration

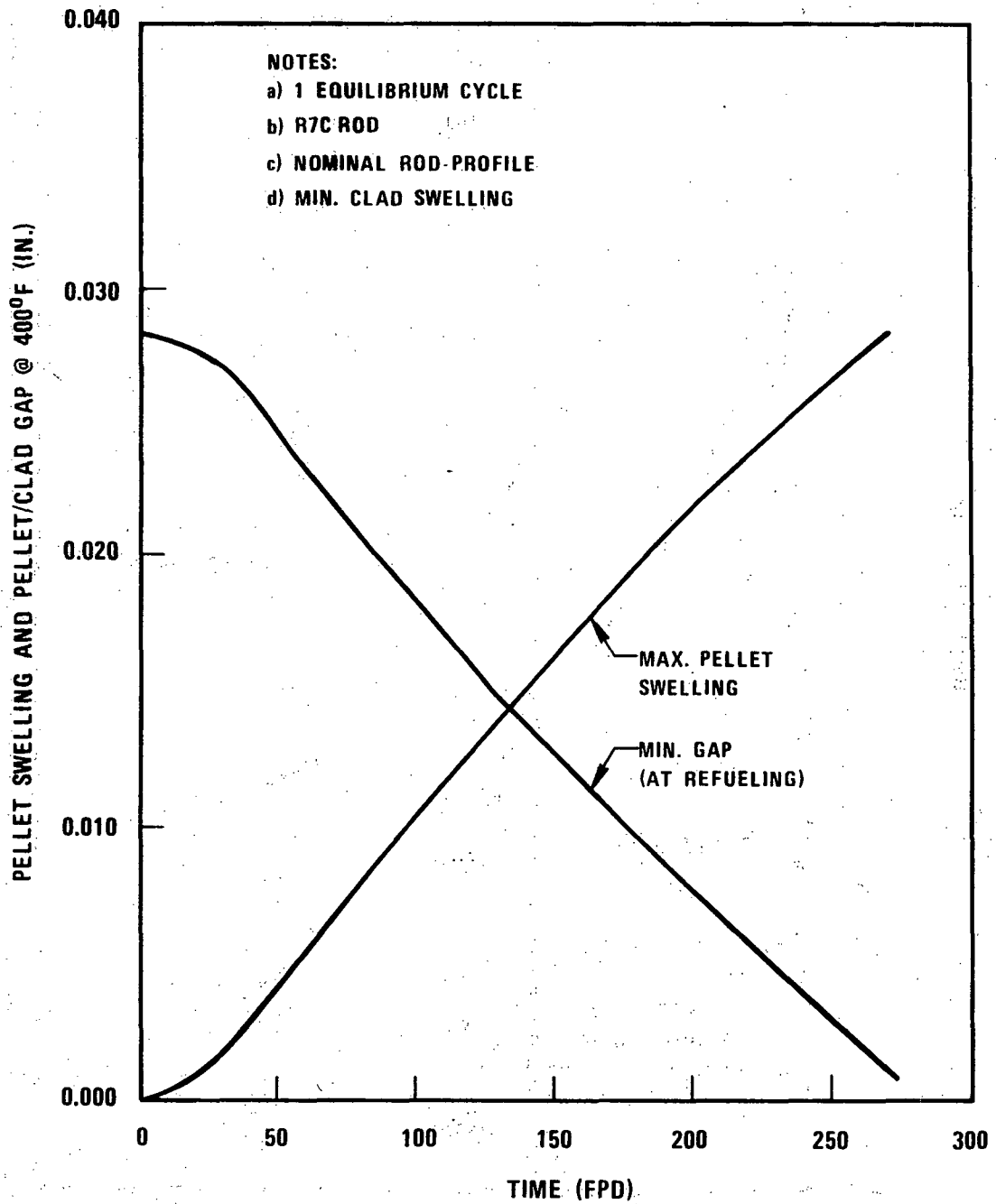


Figure 4.2-111a Pellet Swelling and Clad Gap

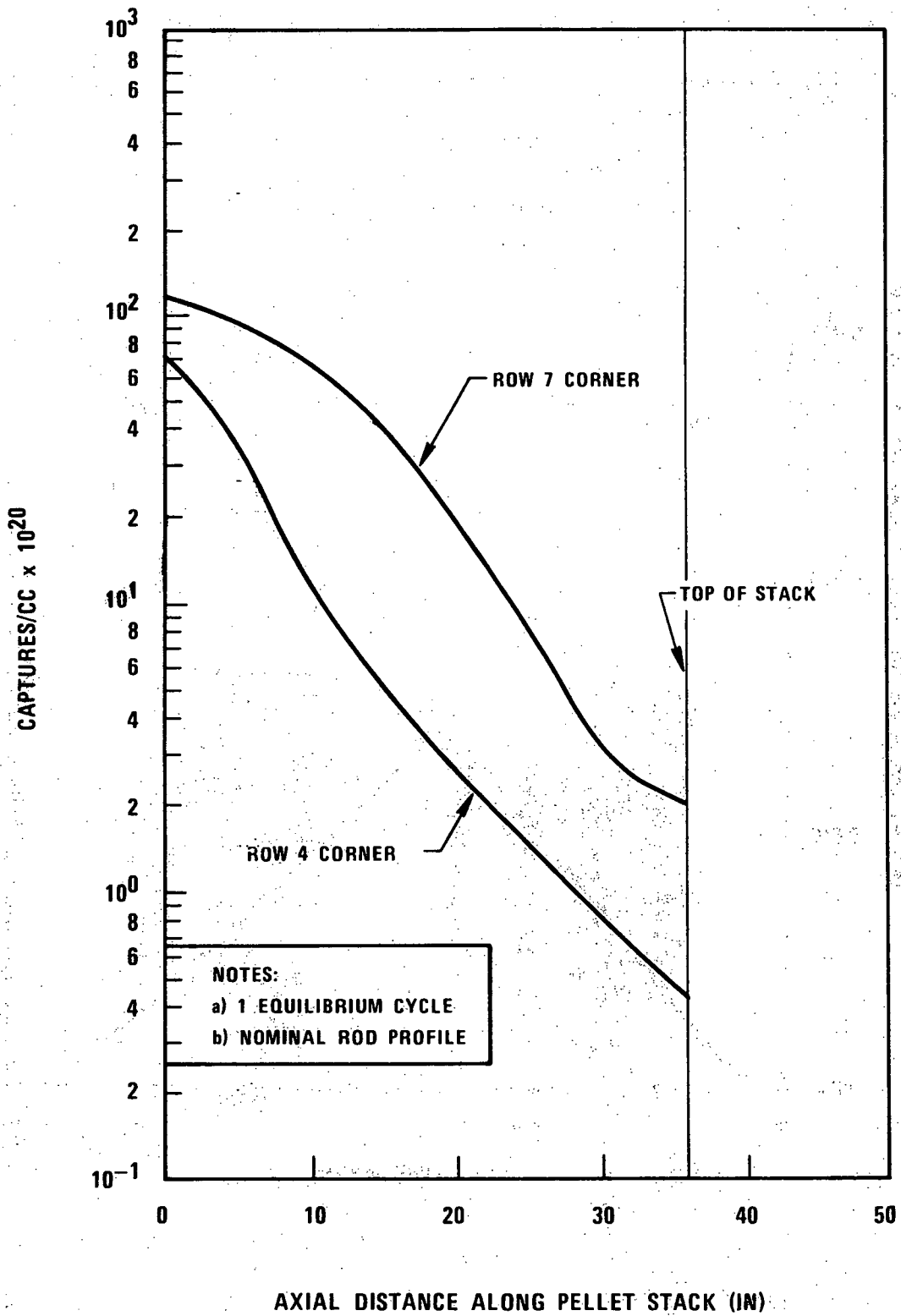


Figure 4.2-111b Primary Control Rod Axial Burnup Profile

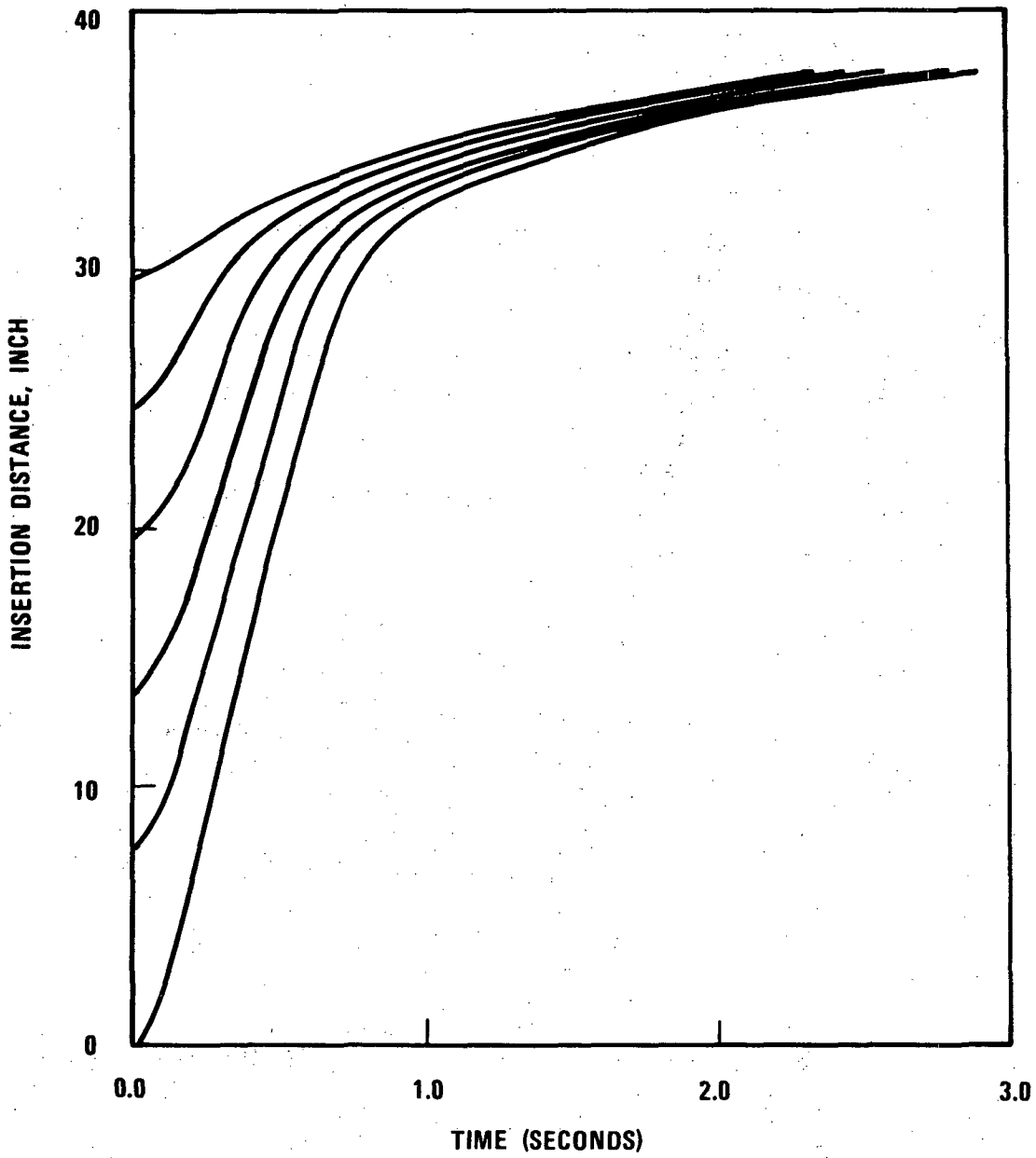


Figure 4.2-112. Primary Control Rod System Scram Insertion Distance vs Time

1764-57

4.2-614

Amend. 51  
Sept. 1979



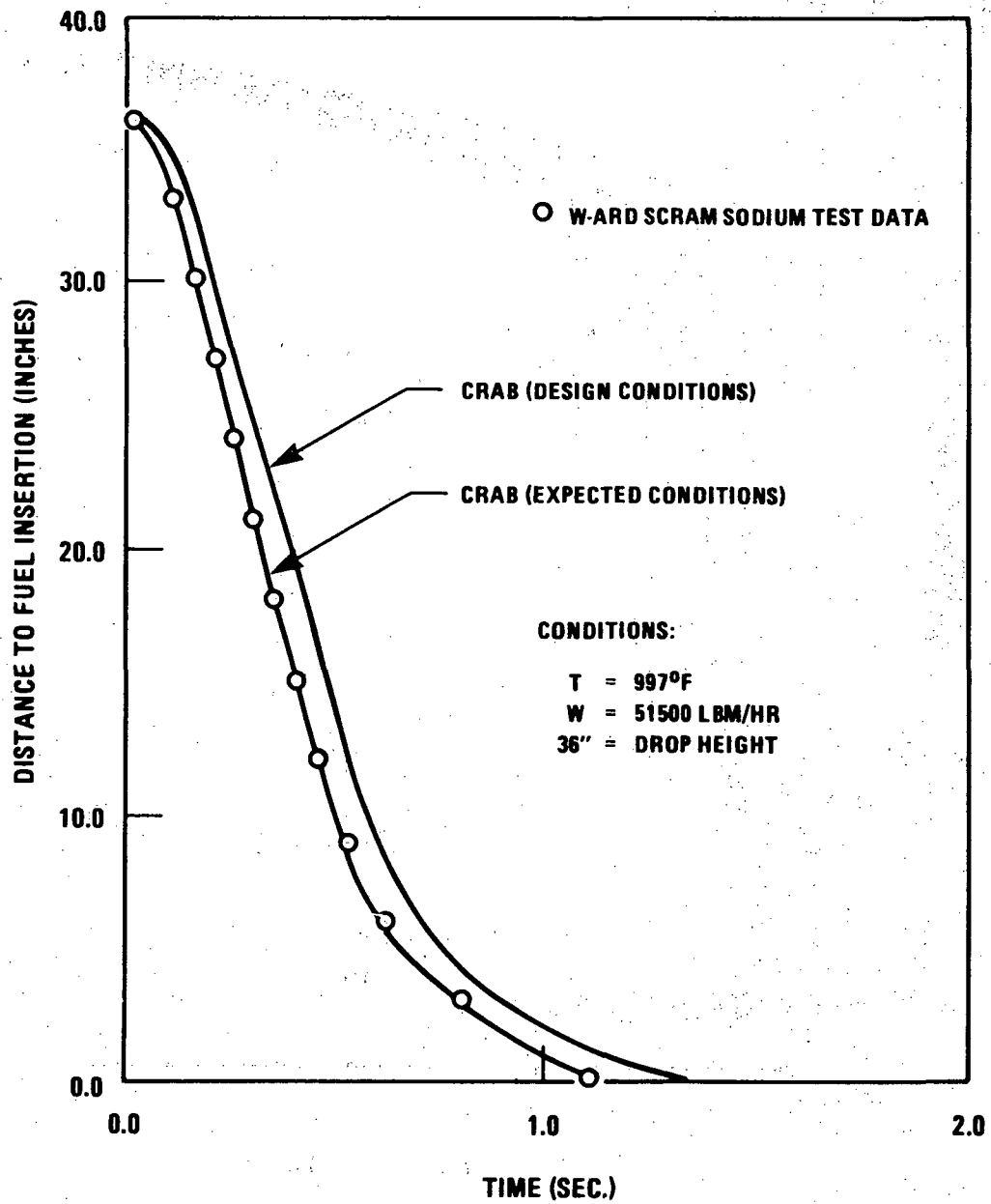
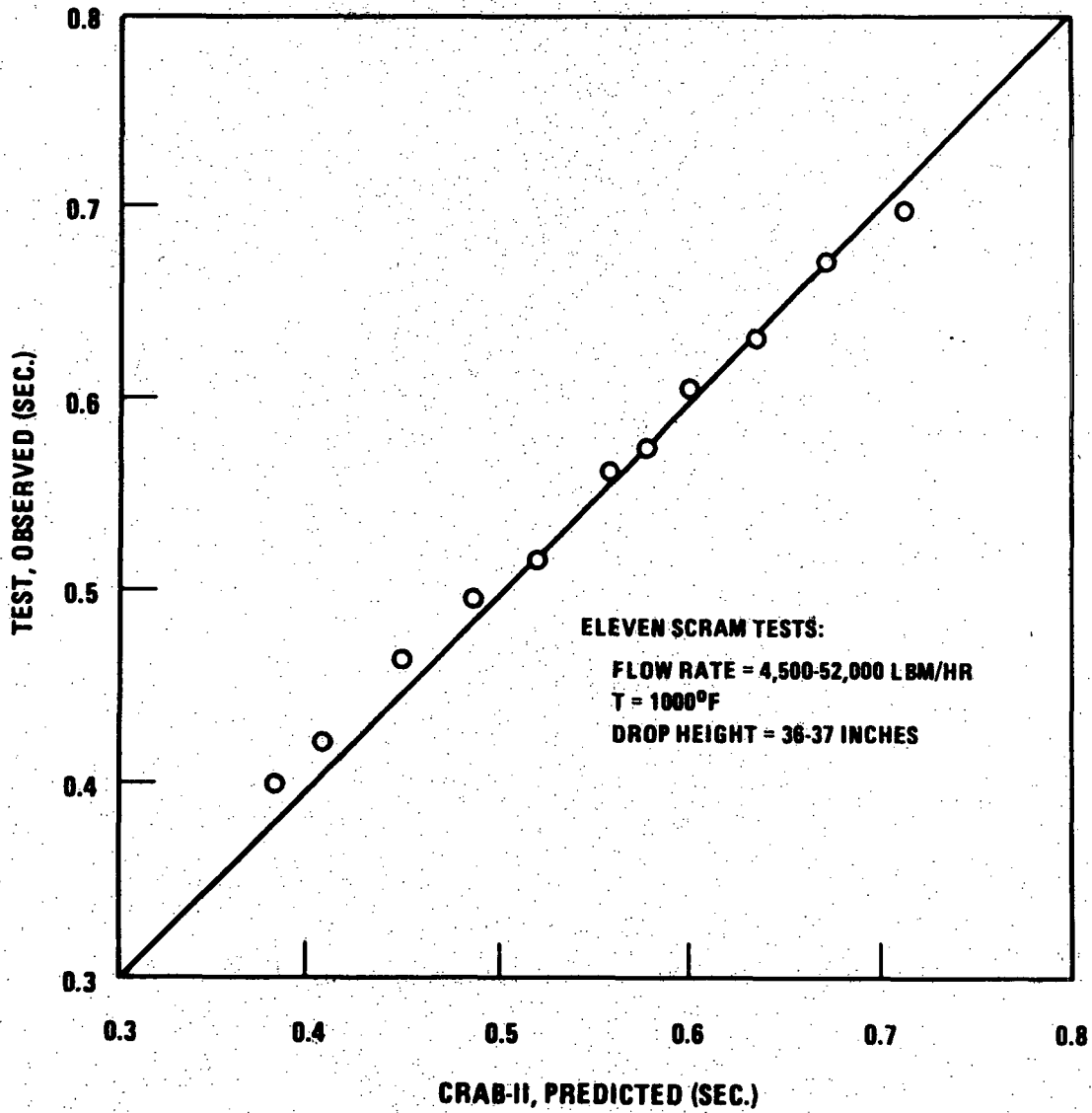


Figure 4.2-113. A Comparison Between Scram Predictions by CRAB-II and ARD Sodium Test Data



**Figure 4.2-113a. Summary Comparison of the CRAB-II Predicted Versus Test Observed Scram Time to Reach the Dashpot**

7081-2

4.2-615a

Amend. 72  
 Oct. 1982

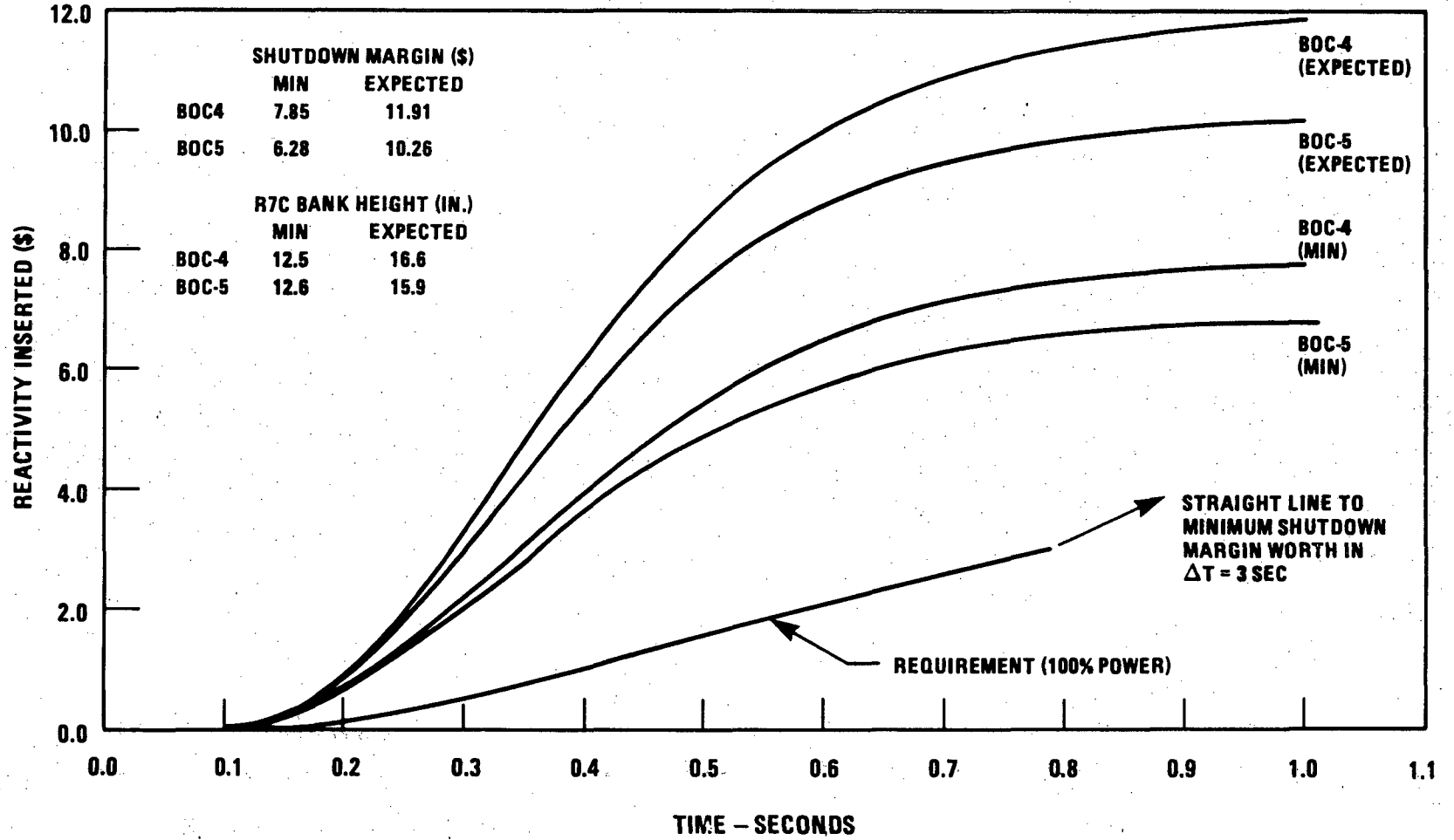


Figure 4.2-114. PCRS Scram Insertion Performance (Non-Seismic)

FIGURE 4.2-115 through 4.2-117 DELETED

4.2-617  
(next page is 4.2-620)

Amend. 53  
Jan. 1980

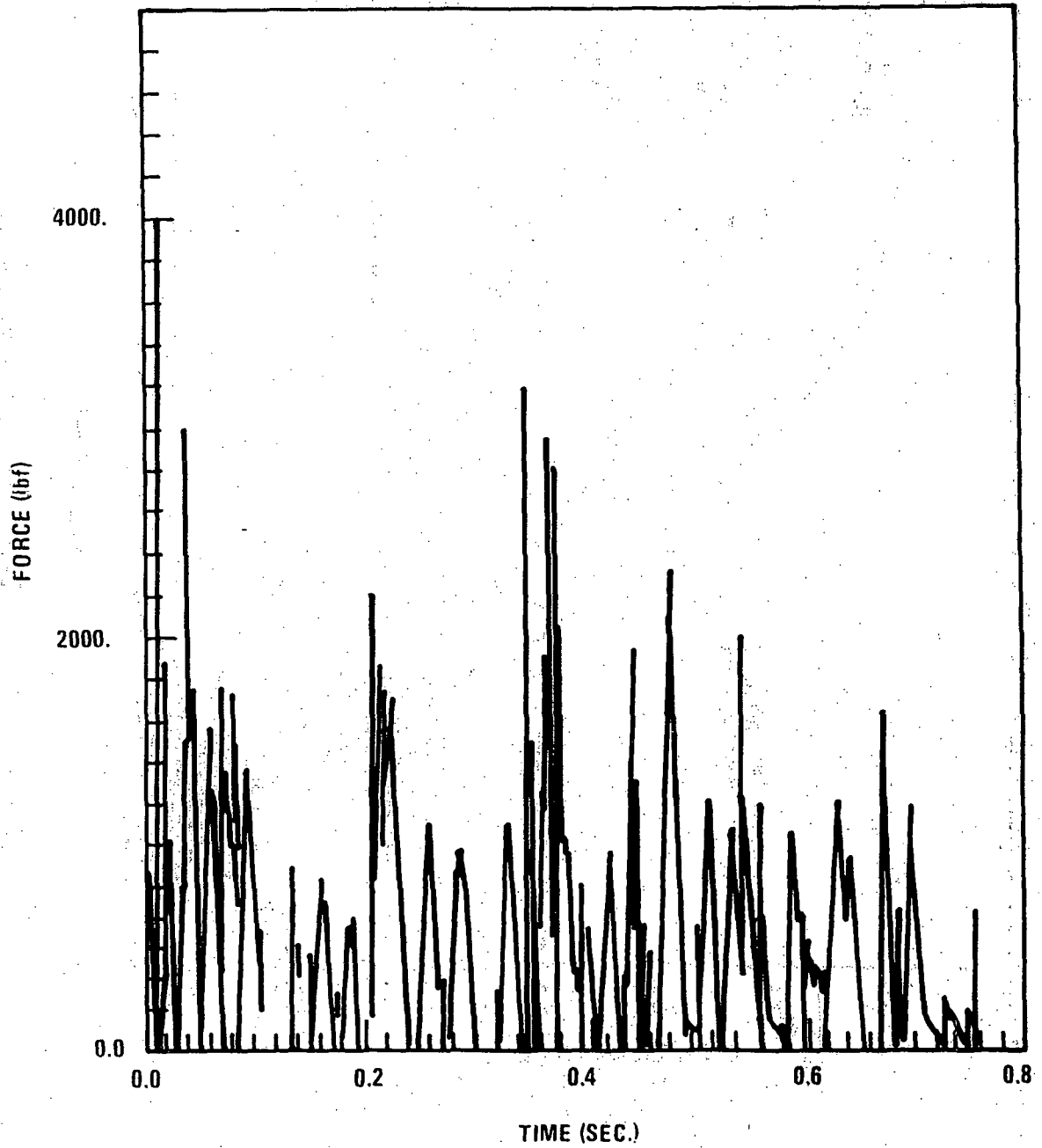


Figure 4.2-118. Typical PCRS Total Contact Force vs Time During SSE

9597-2

4.2-620

Amend. 51  
Sept. 1979

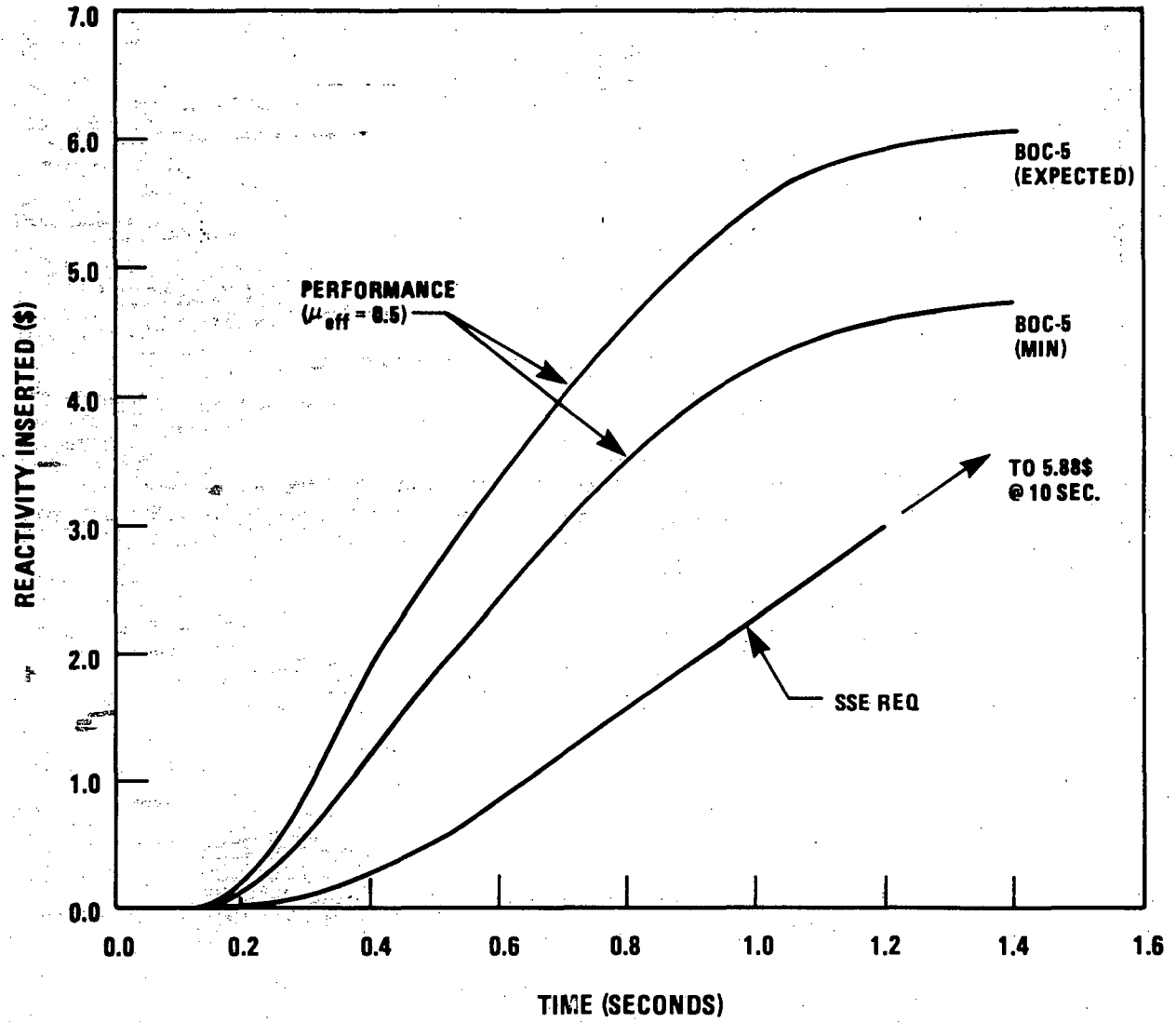


Figure 4.2-119. PCRS Seismic Scram Insertion Performance

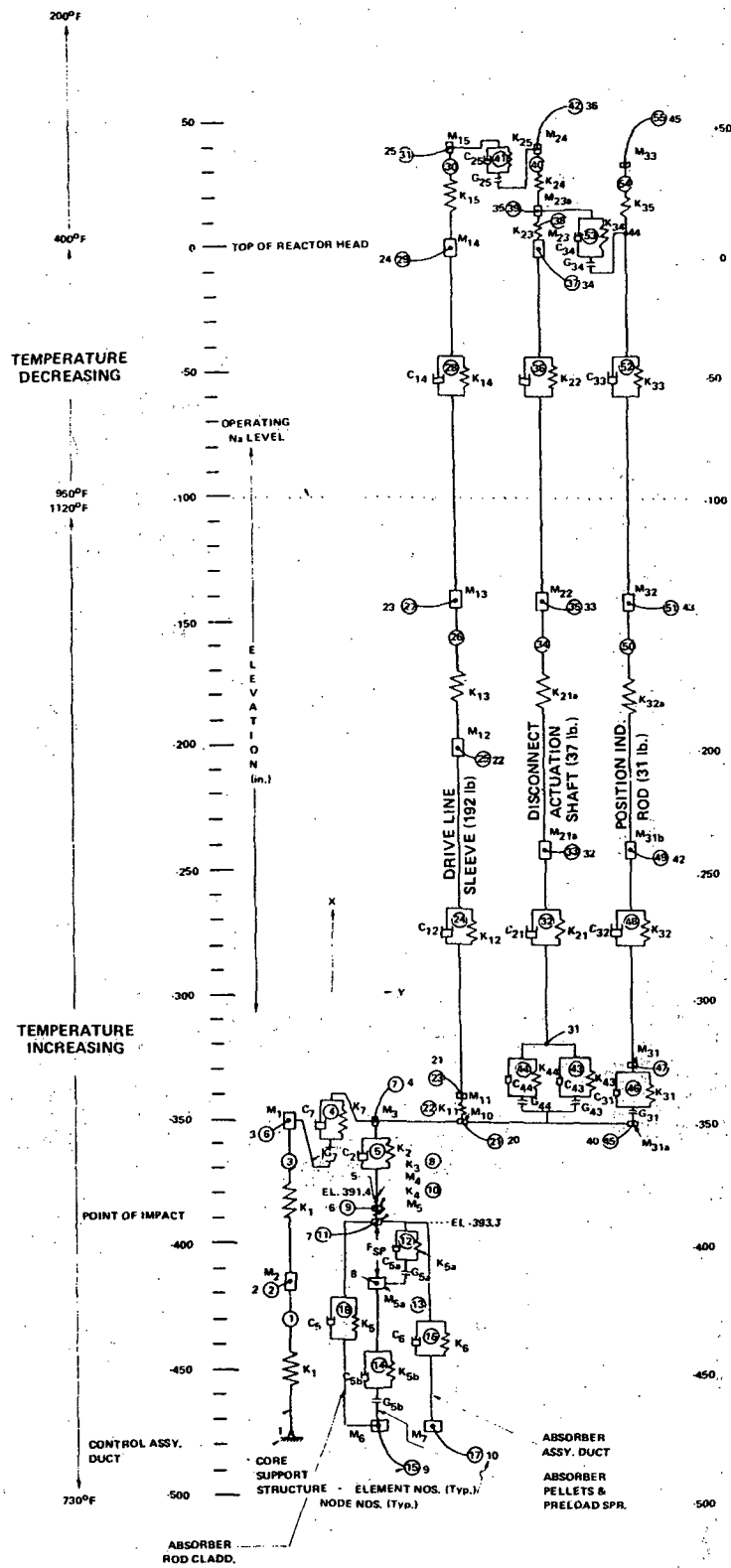


Figure 4.2-120. Absorber Assembly Scram Impact Dynamic Model

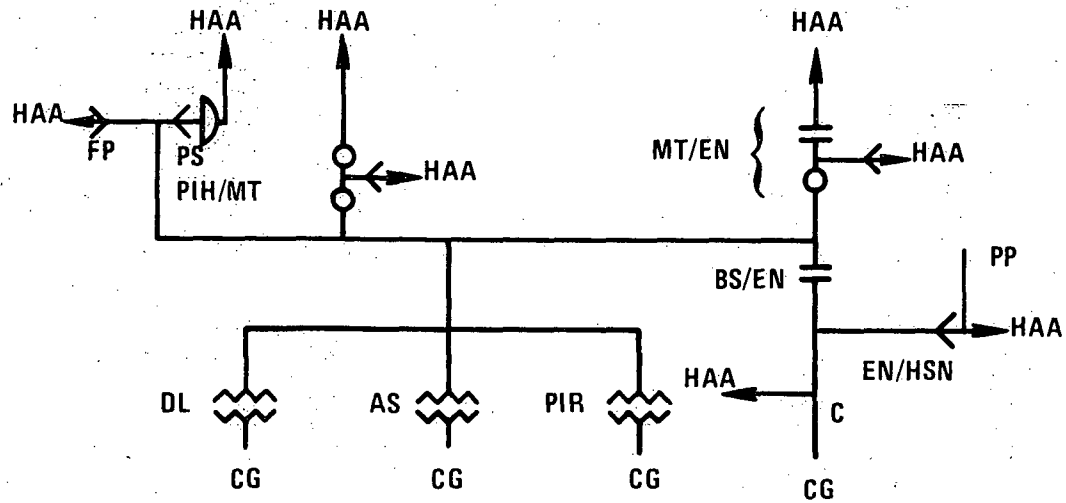
6664-148

4.2-622

Amend. 51  
Sept. 1979

9605-3

		<u>SYMBOLS</u>			
	CONOSEAL (METALLIC)	⌘	BELLOWS	FP	FILL PORT
○	ELASTOMER	HAA	HEAD ACCESS AREA	C	SEAL WELD
○	"O" RING	CG	COVER GAS	HSN	HEAD STUB NOZZLE
Y	VOISHAN METAL COMPRESSION SEAL	BS	BELLOWS SUPPORT	PP	PURGE PORT
		EN	EXTENSION NOZZLE	DL	DRIVELINE
		MT	MOTOR TUBE	AS	ACTUATOR SHAFT
		PS	PRESSURE SWITCH	PIH	POSITION INDICATOR HOUSING
		P	PIPING	PIR	POSITION INDICATOR ROD



4.2-623

Amend. 51  
Sept. 1979

Figure 4.2-120A. CRDM Primary Pressure Boundary Seals



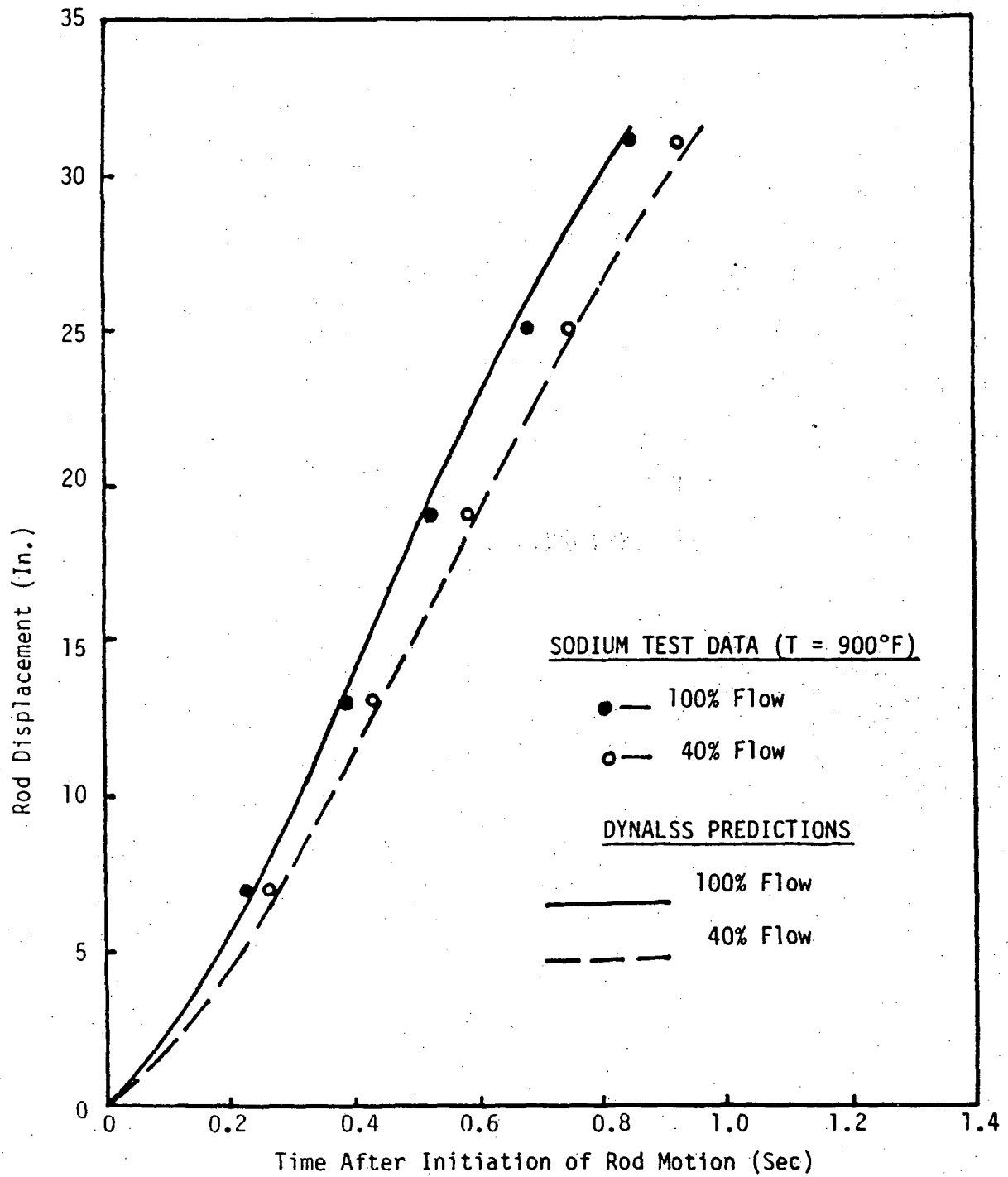


Figure 4.2-121 - SCRS ROD DISPLACEMENT VERSUS TIME

FIGURE 4.2-122  
HAS BEEN DELETED

4.2-625

Amend. 76  
March 1983

4.2-625a

Amend. 71  
Sept. 1982

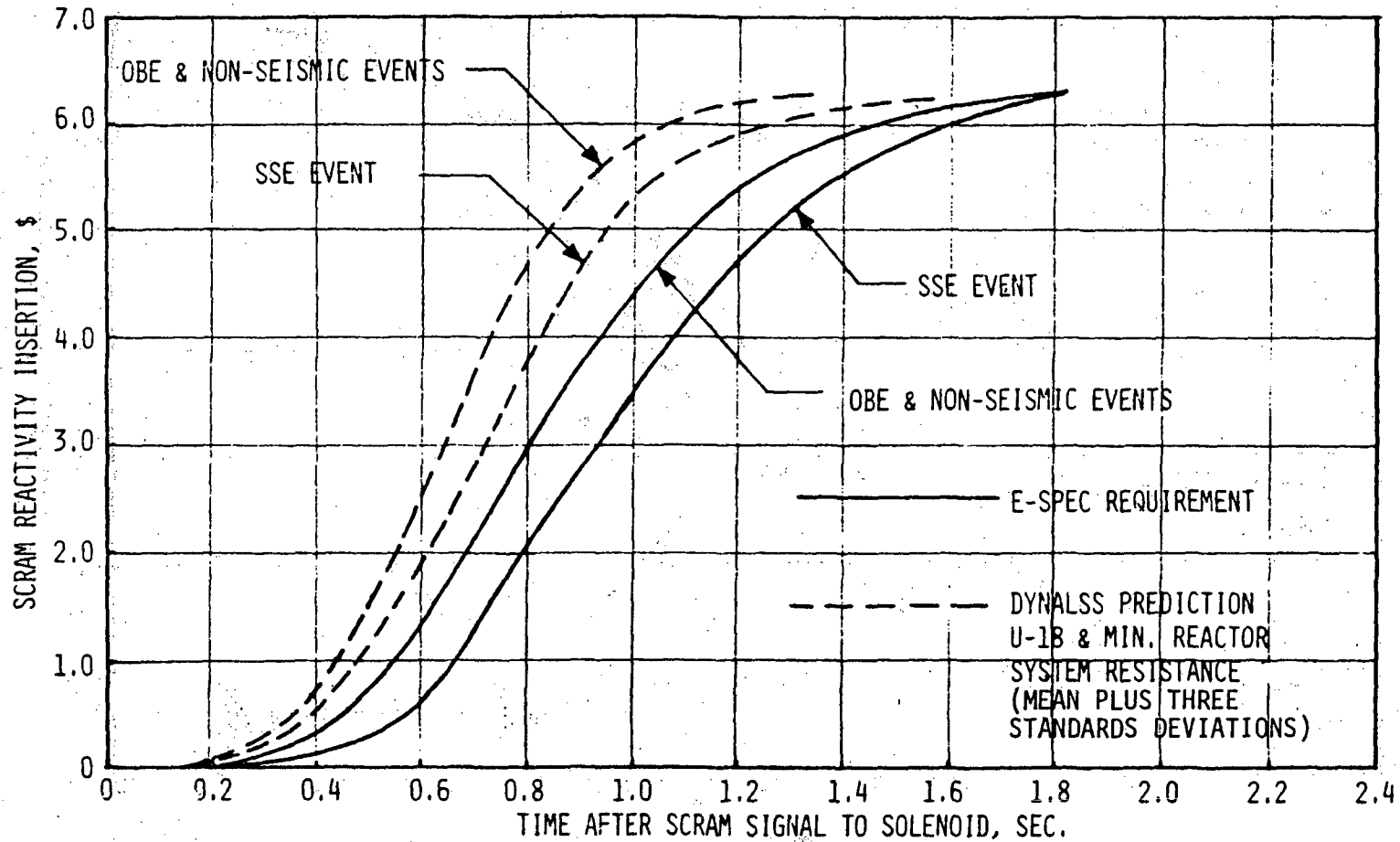


Figure 4.2-122a - SCRS SCRAM REACTIVITY INSERTION RATE AT 100% REACTOR FLOW

4.2-625b

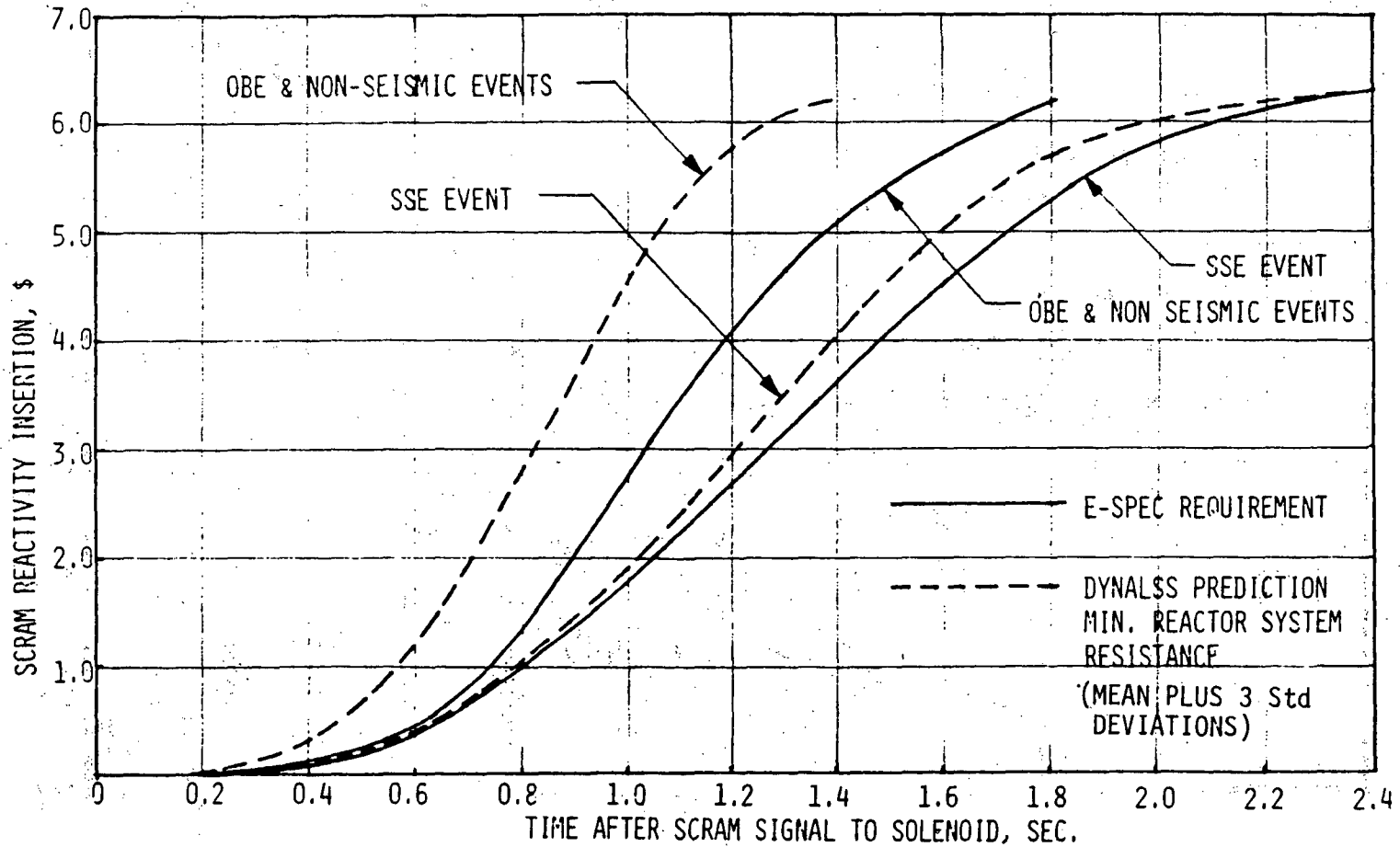
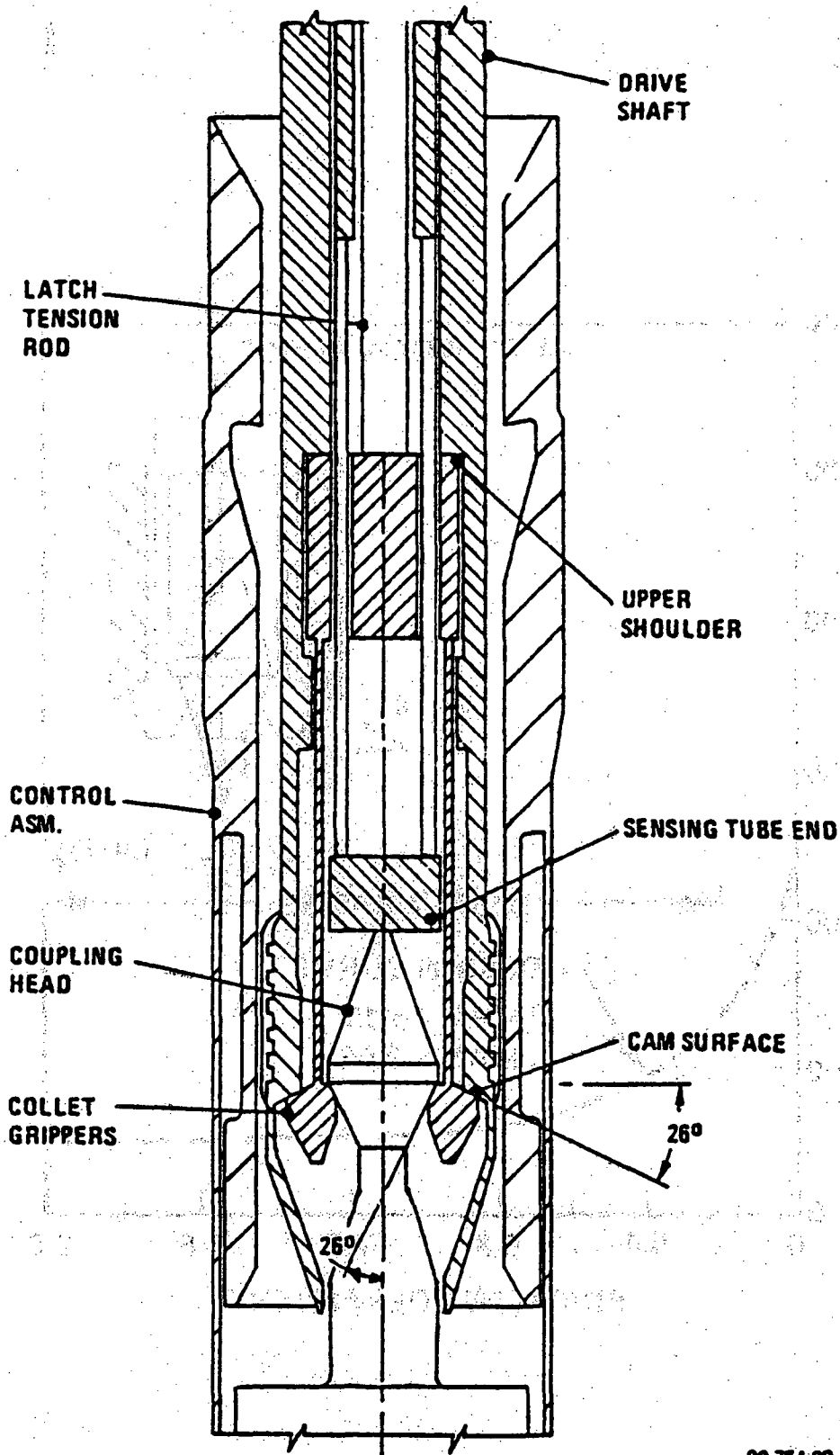


Figure 4.2-122b - SCRS SCRAM REACTIVITY INSERTION RATE AT 40% REACTOR FLOW

Amend. 71  
Sept. 1982

FIGURES 4.2-123 AND 4.2-124  
HAVE BEEN INTENTIONALLY DELETED



80-754-00

Figure 4.2-125. COLLET TYPE LATCH

Amend. 59  
Dec. 1980

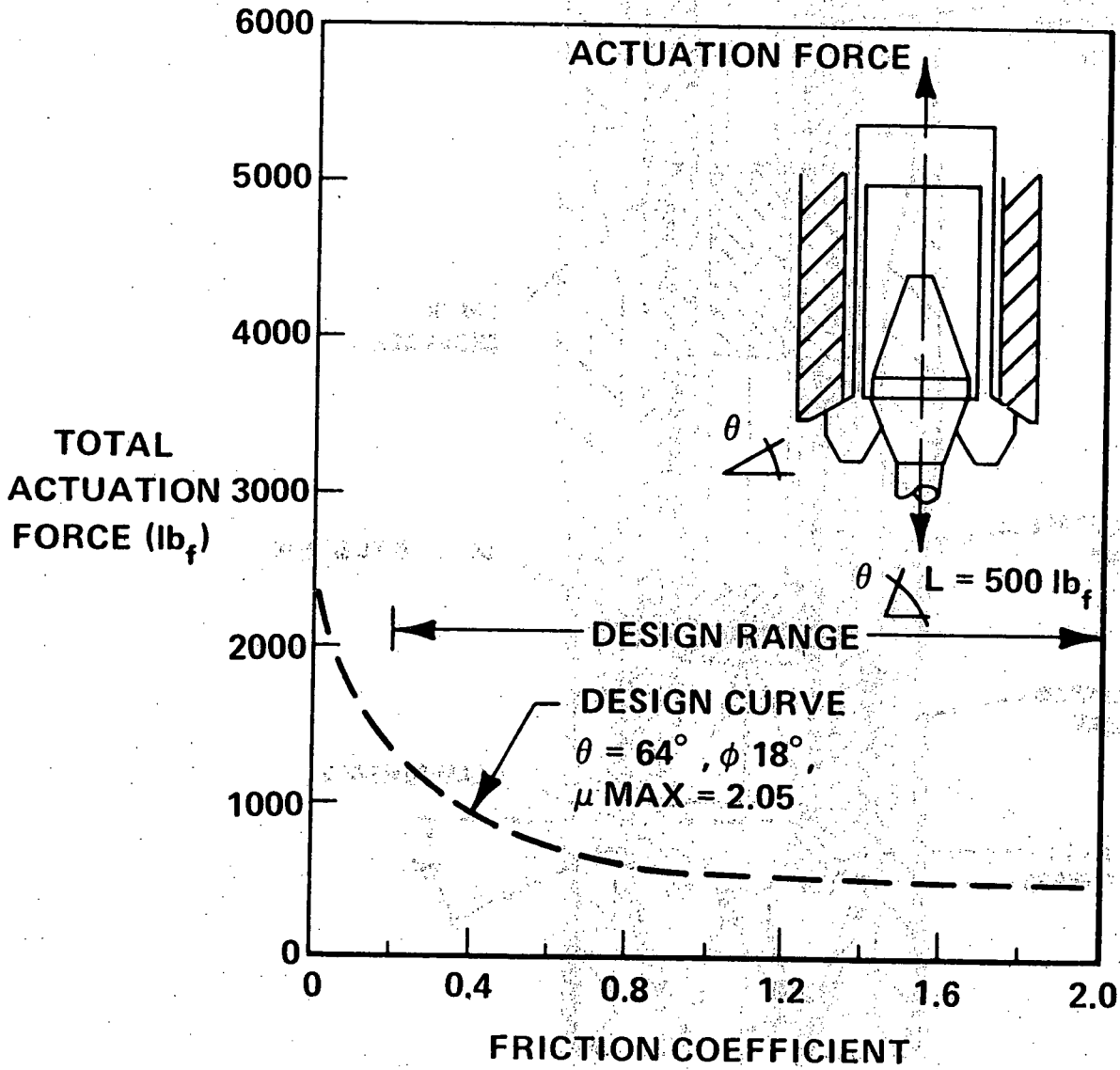


Figure 4.2-126. Total Actuation Force vs. Friction Coefficient with  $\mu_1 = \mu_2$

Figure 4.2-127 has been intentionally deleted.



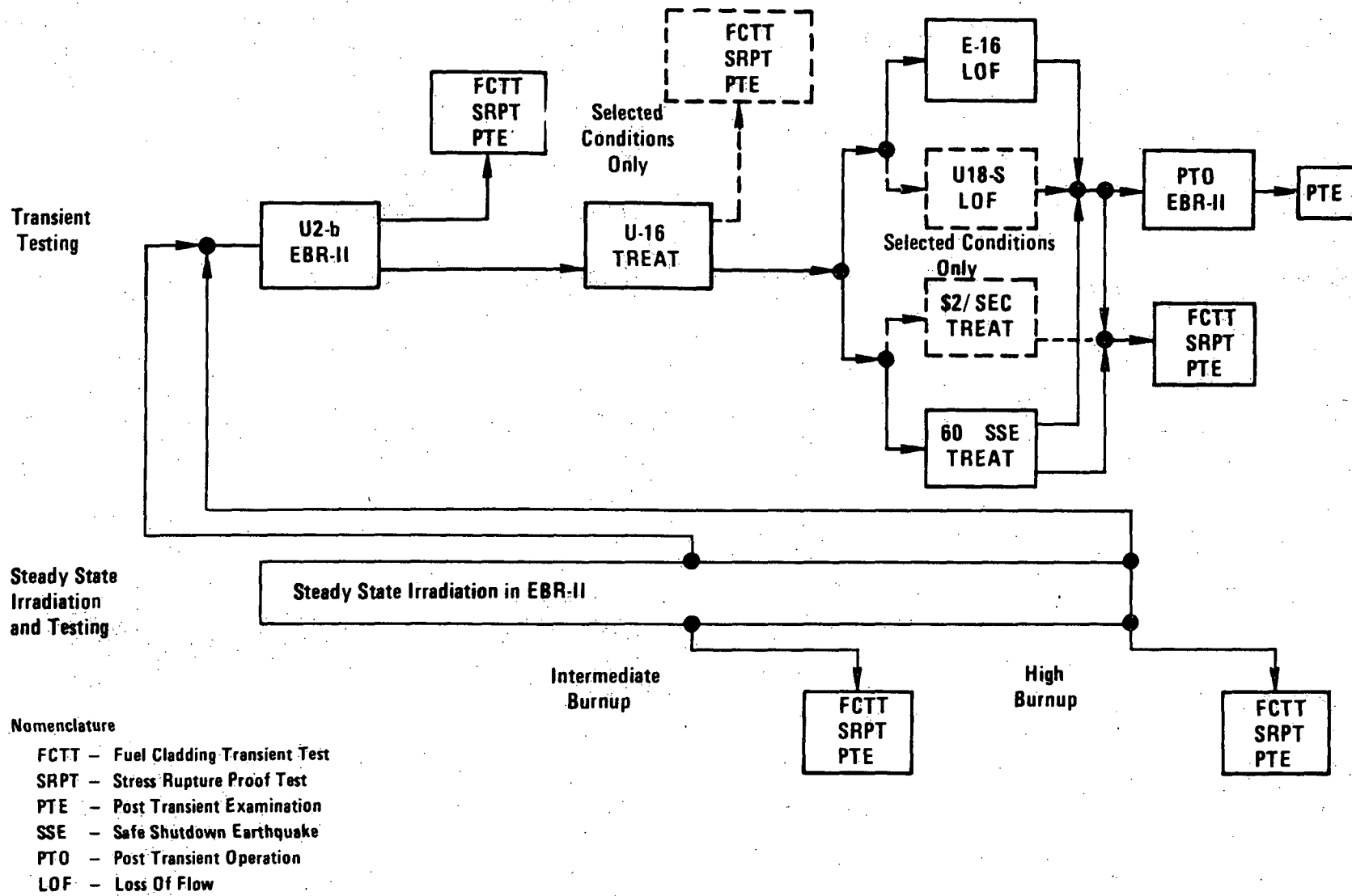


Figure 4.2-128 Typical Sequence for Reference Fuel Transient Testing

1764-61

4.2-632

Amend. 51  
Sept. 1979

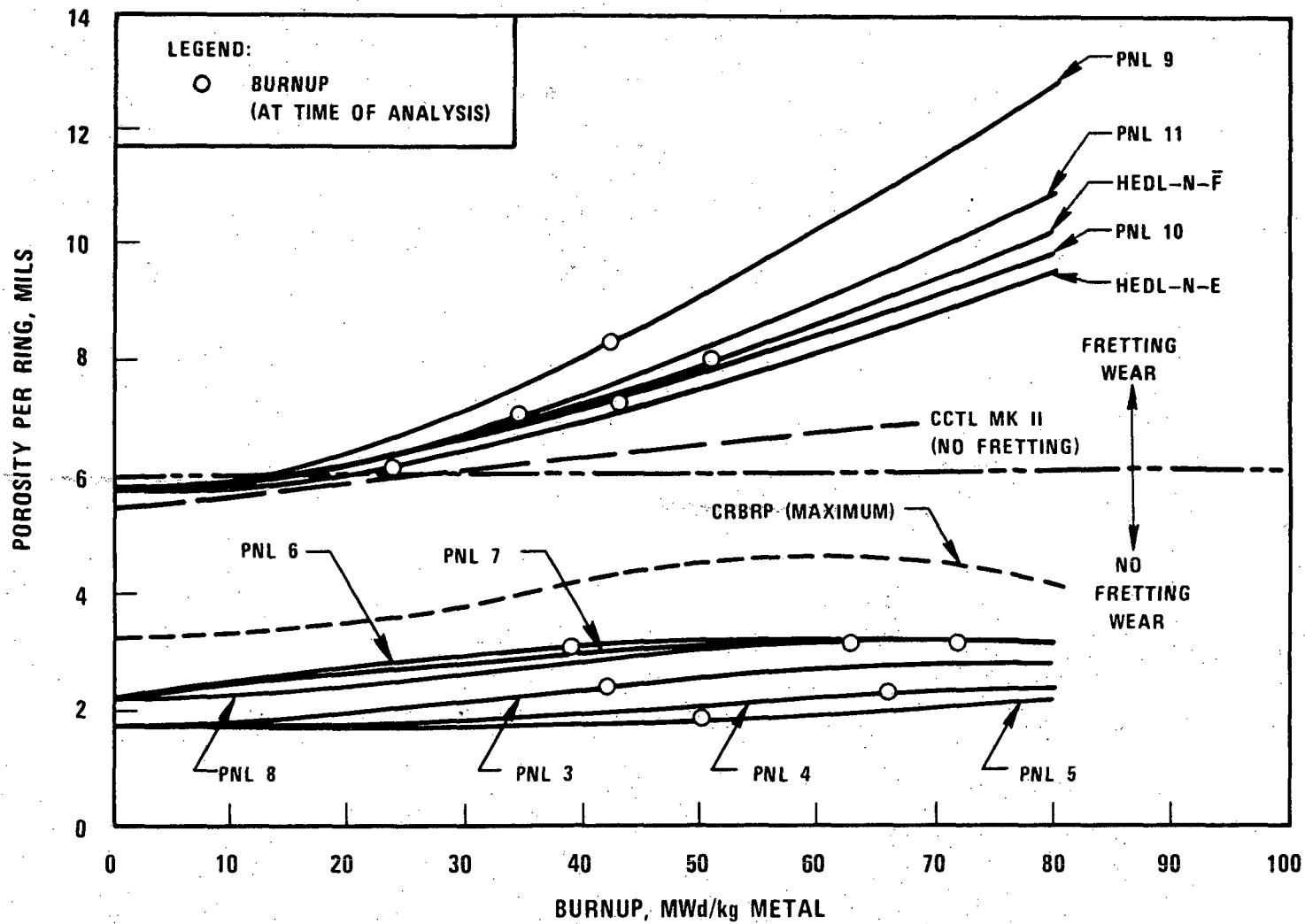


Figure 4.2-129 Porosity/Fuel Rod Ring Histories for Experimental and CRBR Fuel Assemblies

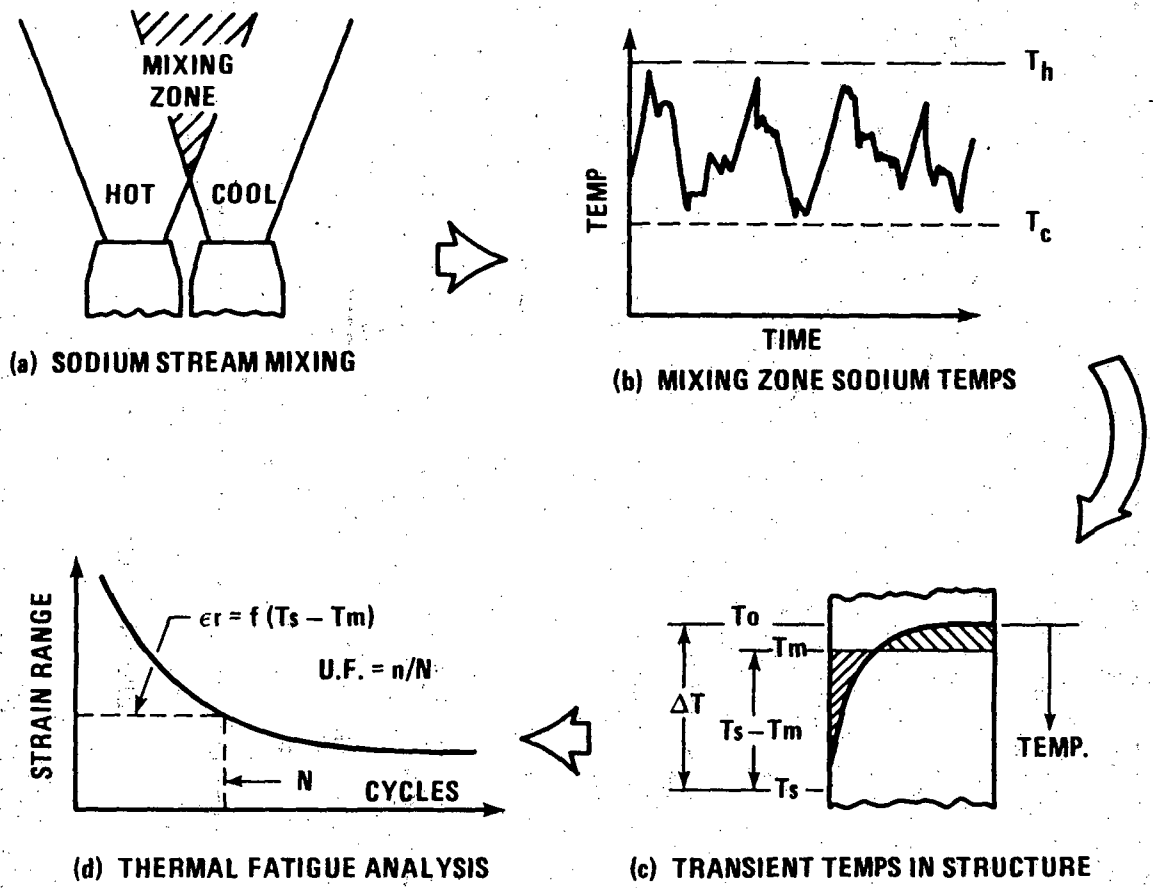


Figure 4.2-130. Thermal Stripping Evaluation Steps

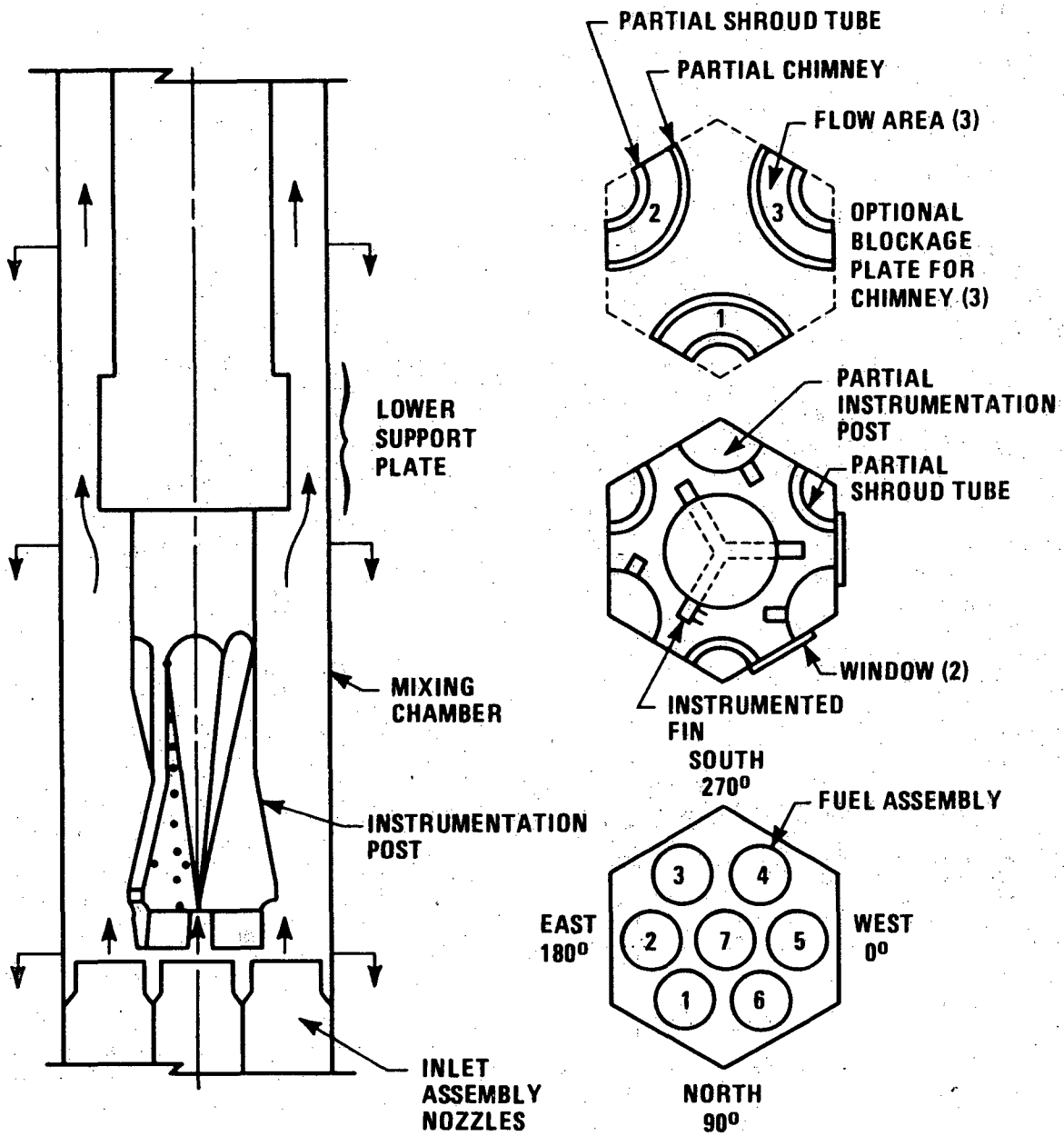


Figure 4.2-131. Instrumentation Post and Chimney Model

7044-2

4.2-634

Amend. 68  
May 1982

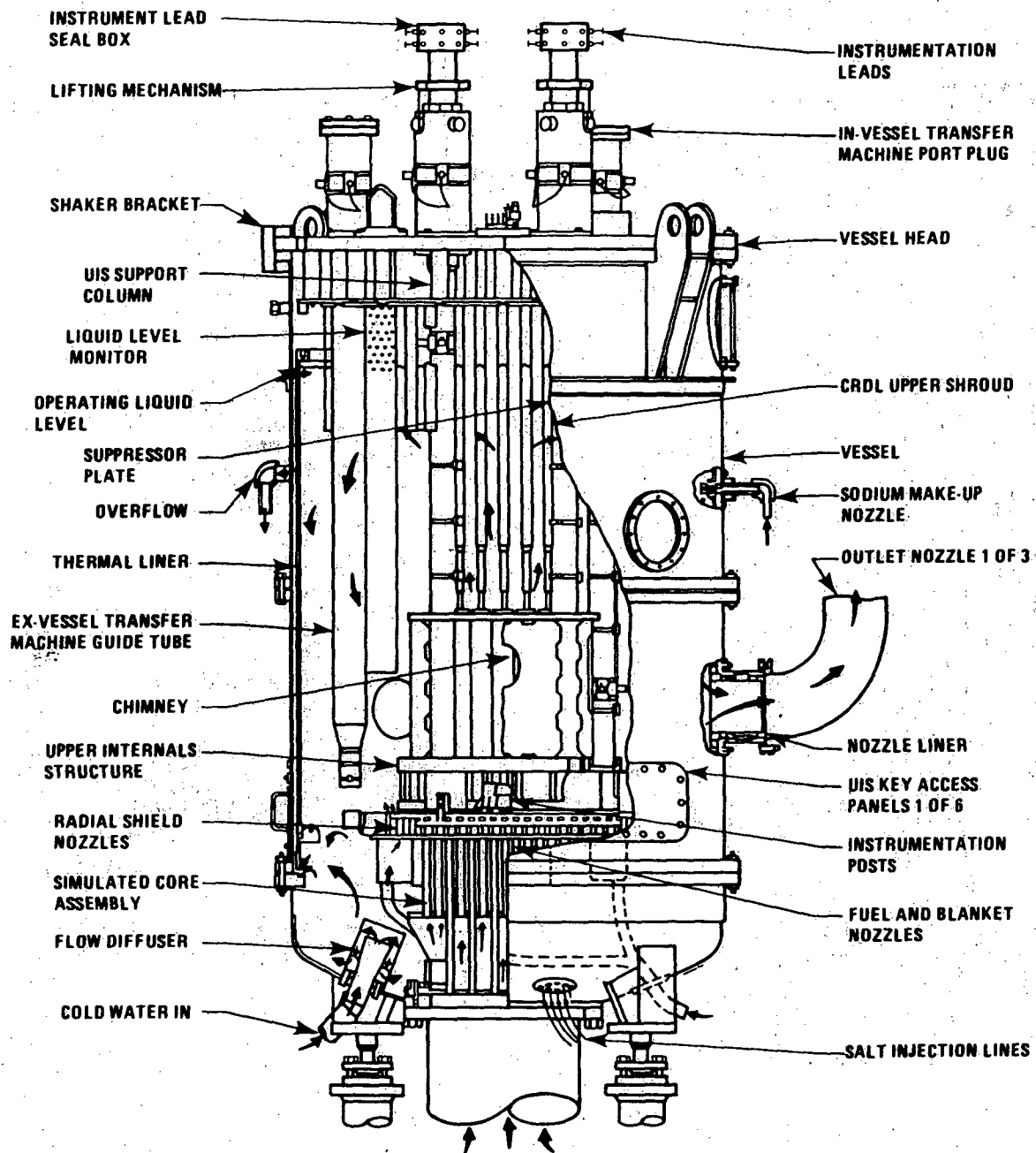


Figure 4.2-132. CRBRP Integral Reactor Flow Model

7044-3

4.2-635

Amend. 68  
May 1982

**RADIAL PROBE LOCATIONS**

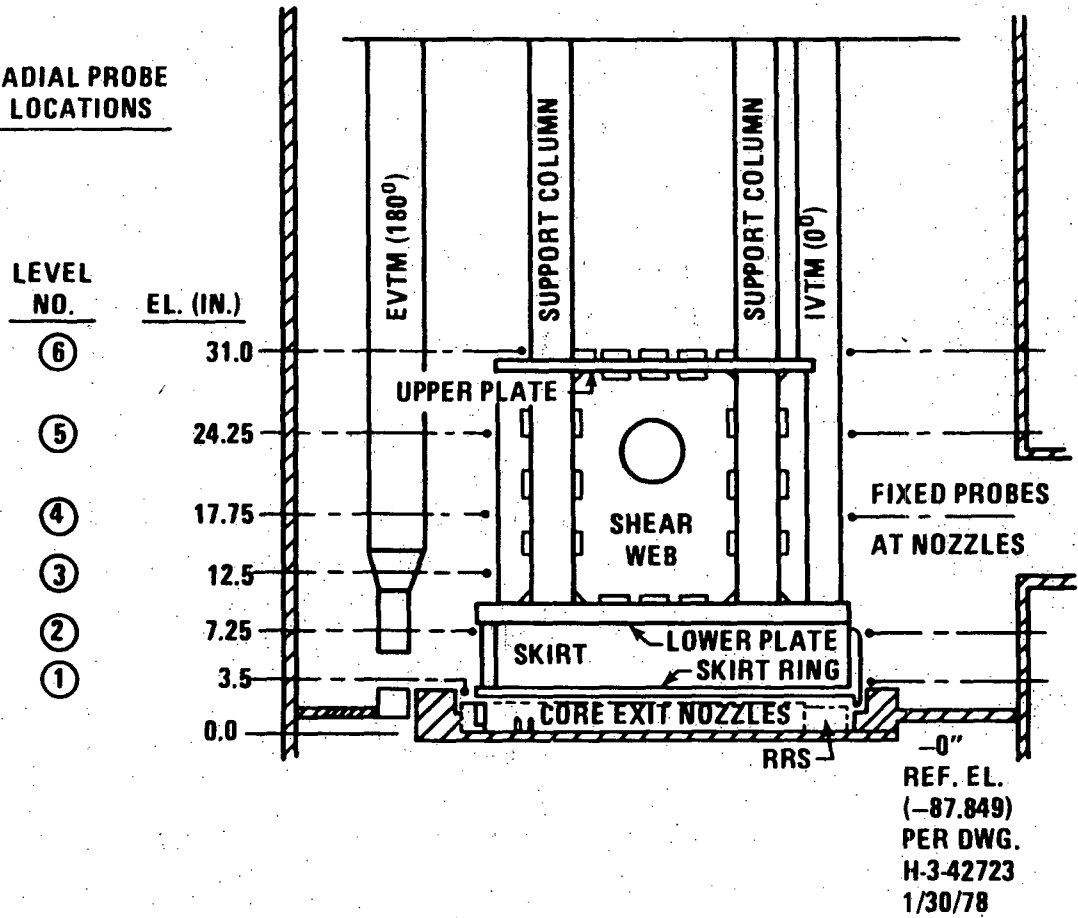


Figure 4.2-133. Radial Traversing Probes Axial Locations

7044-4

4.2-636

Amend. 68  
May 1982

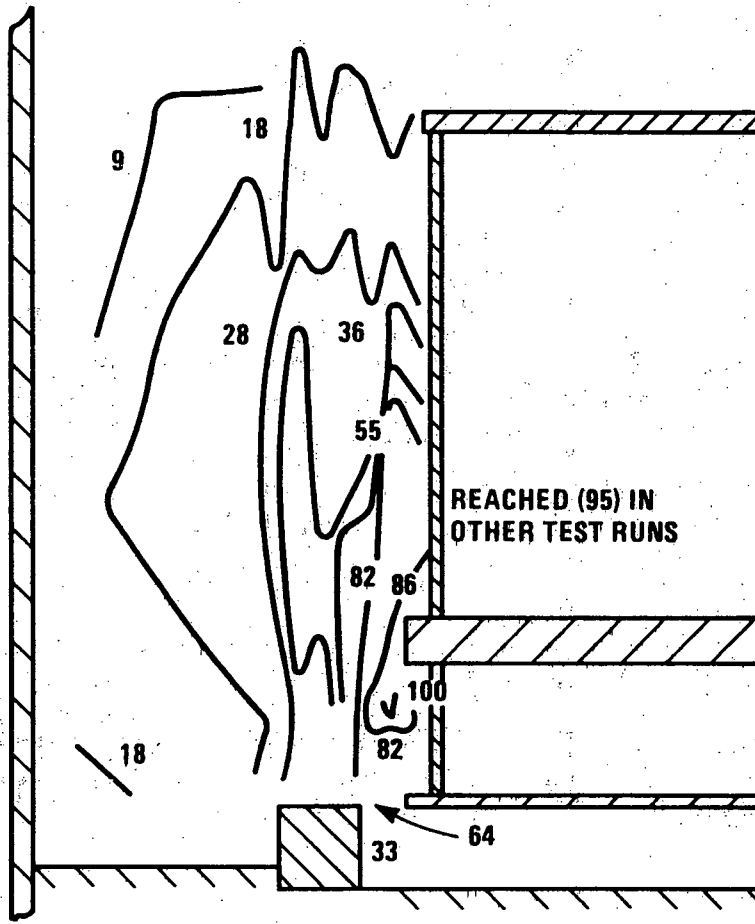


Figure 4.2-134. Striping Contours, °F, in the Outlet Plenum

7044-5

4.2-637

Amend. 68  
May 1982

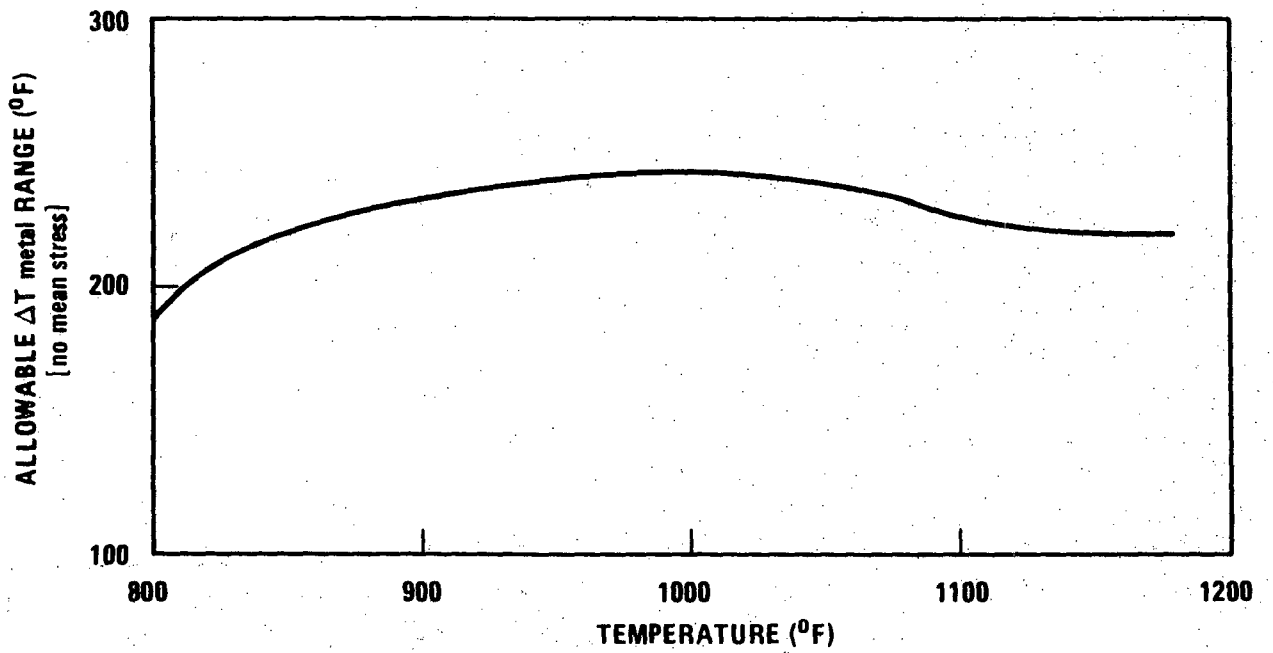


Figure 4.2-135. Allowable  $\Delta T$  metal Range for Alloy 718 for a Fully Constrained Biaxial Case (Grain Size 5 and Finer)

7044-7

4.2-638

Amend. 68  
May 1982



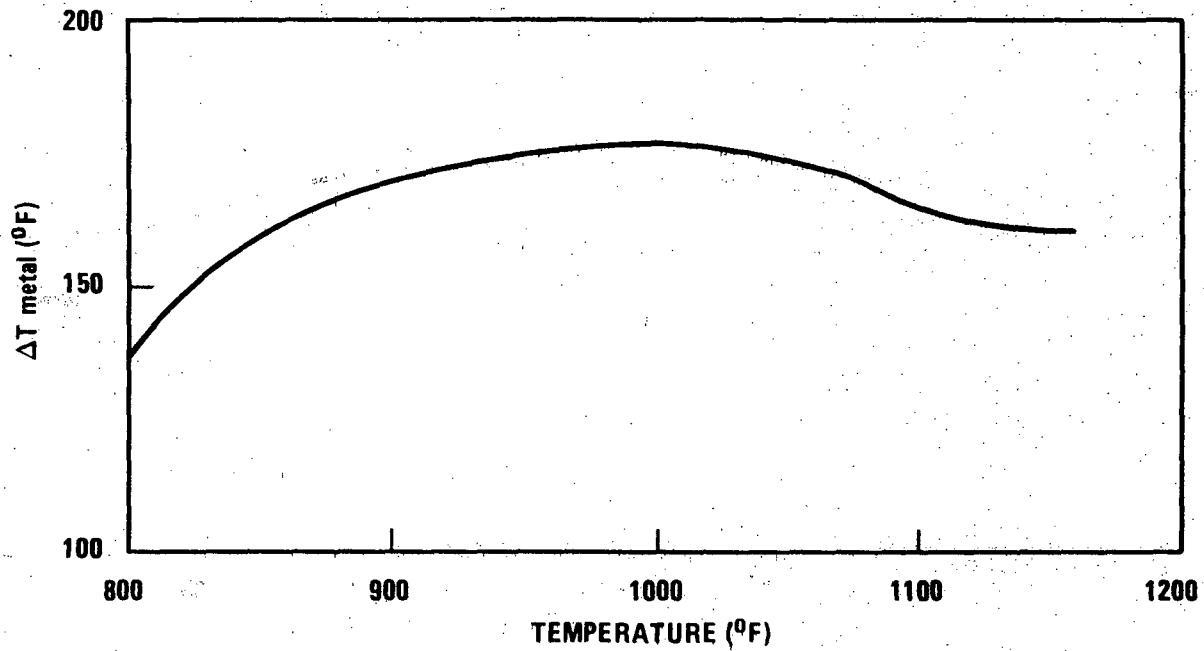


Figure 4.2-136. Allowable  $\Delta T$  metal Range Vs. Temperature for Alloy 718 (Grain Size of 2) for a Fully Constrained Biaxial Case

7044-8

4.2-639

Amend. 68  
May 1982

### 4.3 NUCLEAR DESIGN

#### 4.3.1 Design Bases

The overall nuclear system shall be designed such that safe operation is achieved through a controlled nuclear reaction. This controlled reaction will result in the generation of 975 MW of thermal power.

The full spectrum of plant conditions that are considered as design bases for the plant is divided into four categories in accordance with their anticipated frequency of occurrence (see Section 1.1). These four categories are:

- a. Normal Operation
- b. Anticipated Faults
- c. Unlikely Faults
- d. Extremely Unlikely Faults

The General Safety Design Criteria (GSDC) for CRBRP, as described in Section 3.1, have been considered in establishing the following design bases for the nuclear design of the reactor core.

##### 4.3.1.1 Core Design Lifetime and Fuel Burnup

The fuel rods are designed to remain in the core for two calendar years. The first-core fuel rods achieve a peak pellet burnup over the first two operating cycles (328 equivalent full power days) of 74,000 megawatt days per metric ton of heavy metal (MWd/T). Under equilibrium conditions (550 fpd), the peak pellet burnup increases to 110,000 MWd/T.

##### 4.3.1.2 Reactivity Control

Primary reactivity control shall be achieved through moveable control absorbers. Their design shall provide the required reactivity for full power operation, lifetime considerations, shutdown requirements and associated uncertainties. Inherent reactivity control shall be achieved through the negative feedback coefficients of the nuclear system. Their magnitude shall be confirmed experimentally in appropriate critical experiments such that controlled operation is assured through all operating conditions and is compatible with safety considerations.

51

#### 4.3.1.3 Power Oscillations

The reactor and associated coolant, control and protection systems shall be designed to assure that power oscillations which may result in conditions exceeding specified acceptable fuel design limits are not possible or can be reliably and readily detected and suppressed.

#### 4.3.1.4 Reactivity Coefficients

The reactor and associated coolant systems shall be designed so that in the normal operating range, including anticipated overpower transients, the net effect of the prompt inherent nuclear feedback characteristics mitigate the effects of a rapid increase in reactivity.

#### 4.3.1.5 Fuel Management and Power Distributions

The nuclear system specifies a fuel and blanket management scheme which will maximize the average discharge burnup and minimize the fuel cycle costs. The arrangement of fuel and blanket assemblies in the core shall be selected to minimize the power peaking factors. The resulting radial and axial power distributions shall be compatible with the maximum allowable linear power rating in the fuel and blanket assemblies.

#### 4.3.1.6 Excess Reactivity

The fissile fuel loading at the beginning of each operating cycle must provide sufficient excess reactivity for lifetime considerations and associated uncertainties.

#### 4.3.1.7 Fuel Buildup in Fertile Material

The reactor fuel and blanket assemblies will utilize the uranium-plutonium cycle to breed fissile fuel.

#### 4.3.1.8 Shim Control

Reactivity shimming in the CRBRP will be accomplished by movement of the primary control rods.

#### 4.3.1.9 Annual Refueling

An annual shutdown for refueling is planned for all operating cycles. The fuel management scheme described in Section 4.3.2.1.2 calls for the replacement of all fuel and inner blanket assemblies as a batch at two-year intervals. In alternating years, under equilibrium conditions, six inner blanket assemblies are exchanged for six fresh fuel assemblies. The mid-term refueling is designed to add sufficient excess reactivity to the system to

complete the two-year burnup interval. Radial blanket assemblies in the first and second rows are replaced as a batch at four and five-year intervals, respectively. The number, location, and type of core assemblies replaced at the end of each cycle must be compatible with excess reactivity, power peaking, and assembly lifetime requirements.

#### 4.3.1.10 Reactivity Insertion Rates

The maximum controlled reactivity insertion rate due to the withdrawal of one primary control rod at the design speed of 9 inches/minute is 4.1 cents/second. This rate of reactivity insertion maintains the peak clad temperature below the maximum allowable value at overpower conditions.

#### 4.3.2 Description

This section provides the detailed description of the nuclear characteristics of the CRBRP design using FFTF grade plutonium fuel (low Pu-240 content:  $\approx 12\%$ ) in all operating cycles. Light water reactor discharge grade plutonium fuel (high Pu-240 content:  $\approx 19\%$ ) may be employed in the CRBRP in later operating cycles. The Nuclear Design Description subsection presents nuclear characteristics not described in subsequent subsections. This is followed by subsections on Power Distribution, Reactivity Coefficients, Control, Criticality of Fuel Assemblies, Stability and Vessel Irradiation.

##### 4.3.2.1 Nuclear Design Description

The nuclear design is concerned with four major components: (1) the fuel assembly, (2) the blanket assembly (employed in both inner and radial blanket locations), (3) the primary control assembly, and (4) the secondary control assembly. These components are made up of hexagonal assemblies containing either fuel (mixed plutonium-uranium dioxide), blanket material (depleted uranium dioxide) or control material (enriched boron carbide). The pertinent characteristics of each of these assemblies are presented in Table 4.3-1. All dimensions and volume fractions are based on cold (room temperature) conditions.

##### 4.3.2.1.1 Fuel Enrichments and Loadings

The CRBRP core configuration is shown in Figure 4.3-1. The 156 core fuel assemblies contain a single fuel enrichment zone of mixed plutonium-uranium dioxide. The isotopic composition of the low-240 feed plutonium is given in Table 4.3-2. Eighty-two inner blanket assemblies (76 plus 6 alternate fuel/blanket assemblies) are dispersed heterogeneously throughout the central regions of the core. The core is surrounded by 126 radial blanket assemblies and 14-inch thick upper and lower axial blankets. Depleted uranium dioxide (0.2% U-235) is used throughout the fuel and blankets.

The fuel enrichment requirements in CRBRP are based upon guaranteeing hot-full power criticality at the end of each burnup cycle. The nominal excess reactivity requirement, which determines the required fuel enrichment, is

based on the cold-critical eigenvalue ( $k_{eff}$ ) plus the cold-to-hot temperature defect plus the fuel burnup reactivity deficit. The enrichments are further increased to include criticality calculation uncertainties, fuel burnup reactivity swing uncertainties, power (temperature) defect uncertainties, fissile loading and core geometry tolerances, modeling and refueling worth uncertainties. These uncertainties are statistically combined and added to the nominal excess reactivity requirement resulting in a one-sided probability distribution which gives an approximately 84% confidence that the fuel loadings will supply at least enough reactivity to meet the stated design fuel burnup (lifetime) requirements for that cycle.

Table 4.3-3 summarizes the excess reactivity requirements at the beginning of the first cycle. The CRBRP fuel management (Section 4.3.2.1.2) involves a batch refueling of the fuel and inner blankets at two-year intervals. The mid-term interchange of three fresh fuel assemblies (six assemblies under equilibrium conditions) for one-year burned inner blankets is designed to add sufficient excess reactivity for the second burnup cycle. The burnup reactivity swing values in the first and second cycles are 0.59 and 2.24%  $\Delta k$ , respectively. The end-of-cycle-one exchange of three fresh fuel assemblies for burned row-6 inner blankets adds 1.53%  $\Delta k$ . Since these three refueled assemblies do not supply a reactivity excess equal to or greater than the fuel burnup reactivity depletion in the second cycle (see Table 4.3-3), additional excess reactivity must be supplied in the beginning-of-cycle-one enrichments in order to maintain the system critical throughout the full 2-year cycle. The uncertainty in the burnup reactivity swing is composed of uncertainties in lumped fission product worth ( $\pm 25\%$ ) core conversion ratio uncertainties ( $\pm 7.5\%$ ), the maximum reactivity deficit at the end-of-life from the 2.3-day delay in the production of bred  $Pu^{239}$  from the decay of  $Np^{239}$ , and irradiation-induced fuel swelling. The sum of the aforementioned parts results in a maximum burnup reactivity swing uncertainty of  $\pm 20\%$  at the end-of-cycle-two. Insofar as this value is derived as a limit, the effective 1 burnup reactivity uncertainty is taken to be  $\pm 10\%$ .

The cold (room temperature) critical eigenvalue uncertainty is derived from the analysis of ZPPR-7 critical experiments (Section 4.3.3.9). Using CRBRP design methods (2D, coarse mesh, XY diffusion theory) and data (ENDF/B-III cross-sections in 9 energy groups) results in a systematic underprediction of the ZPPR-7 eigenvalue with an average calculation-to-experiment (C/E) ratio of  $0.9900 \pm 0.0019(1\sigma)$ . The inverse of the average C/E ratio (1.01) is applied directly as a bias in the calculation of the CRBRP critical eigenvalue ( $k_{eff}$ ) and the 1 variation is included as an uncertainty in the start-of-cycle excess reactivity requirement. An additional uncertainty of  $\pm 0.2\% \Delta k$  is

51

Included to account for potential systematic uncertainties in the extrapolation of the heterogeneous plate-geometry ZPPR-7  $K_{eff}$  bias to the nearly homogeneous pin-geometry of the CRBRP.

CRBRP criticality calculations are performed in hot-full-power geometry with cross-sections corrected for nominal Doppler reactivity feedback. The nominal hot-full-power temperature defect of about 1.7%  $\Delta k$  from Doppler and core expansion effects is therefore implicitly included in the criticality calculations. The  $1\sigma$  uncertainty in the Doppler and expansion feedback reactivity between room temperature and hot-full-power conditions results in a  $\pm 0.19\%$   $\Delta k$  uncertainty in the hot critical state of the reactor.

The tolerance on batch fissile content, arising from variations in plutonium isotopic composition, fuel enrichment, and pellet dimensional and density tolerances, results in an uncertainty in the reactor critical state of  $\pm 0.15\%$   $\Delta k$  ( $1\sigma$  equivalent). The manufacturing tolerance on the core pellet stack height and the relative position of each fuel rod with respect to the average core height results in a  $\pm 0.1\%$   $k$  uncertainty in core reactivity. Additionally, the worst combination of pellet and steel impurities results in a potential reactivity deficit of less than 0.1%  $\Delta k$ .

54 | The total excess reactivity requirement of 1.76%  $\Delta k$  at the beginning of cycle one in Table 4.3-3 is obtained from the difference between the two-cycle burnup reactivity swing and the mid-term refueling worth, plus the root-mean-square sum of the uncertainties. The fuel loading requirements for the first core in CRBRP are determined by searching the plutonium enrichment to an eigenvalue ( $k_{eff}$ ) equal to 1.0 plus  $k_{excess}$  less the ZPPR criticality bias. The resulting plutonium enrichment is 32.8 w/o  $\text{Pu}$  which corresponds to a fissile plutonium ( $\text{Pu}^{239+241}$ ) loading of 1498 kg. Due to the characteristics of the batch core refueling scheme, the equilibrium enrichments of 33 w/o  $\text{Pu}$  are only slightly higher than the first core values because of the longer  $\text{Pu}+\text{U}$  burnup interval. The heavy metal mass inventories at the beginning and end of the first five cycles are summarized in Table 4.3-4.

#### 4.3.2.1.2 Fuel and Blanket Management

Annual refueling is planned for all operating cycles. The first cycle is based on operation at 975 MWt for one calendar year (365 days) at 35% capacity (128 equivalent full power days). The capacity factor is increased to 55% (200 equivalent full power days) during the second cycle and further to 75% (275 equivalent full power days) during the third and subsequent cycles.

The CRBRP fuel management is a batch refueling scheme with a 2-year lifetime

for fuel and inner blanket assemblies. Under equilibrium conditions, the fresh fuel batch is burned for one cycle (275 fpd), at which time six inner blanket assemblies are replaced by six fresh fuel assemblies in order to add sufficient additional excess reactivity for the next 275 fpd burnup cycle. The six refueled assemblies are of the same enrichment as the preceding feed batch. The entire fuel and inner blanket batch is replaced at the end of the second cycle and the scheme is repeated in two-year intervals. The radial blanket assemblies reside in-place (that is, no shuffling or rotation) for four and five cycles, respectively, in the first and second "rows".

Table 4.3-5 summarizes the essential features of the CRBRP batch fuel management scheme throughout the first five cycles of operation. The initial core load (see Figure 4.3-1) contains 156 fuel assemblies, 82 inner blanket assemblies, and 126 radial blanket assemblies. At the end of the first cycle (128 fpd), three inner blanket assemblies in alternating row 6 corner positions ( $60^\circ$  removed from the row 4 control channels in Figure 4.3-1) are replaced with fresh fuel assemblies for the second burnup cycle (200 fpd). At the end of the second cycle, all the fuel and inner blanket assemblies are discharged and replaced with 156 fresh fuel assemblies and 82 fresh inner blanket assemblies. At the end of the third burnup cycle (275 fpd), six inner blanket assemblies in row 6 corner are replaced by six fresh fuel assemblies, and a fourth burnup cycle of 275 fpd follows. At the end of the fourth cycle, all the fuel and inner blanket assemblies are again discharged and replaced with a fresh load. The fuel and inner blanket management scheme for cycles 5-6, 7-8, and subsequent repeats that for cycles 3-4. The first row of radial blanket assemblies are discharged and replaced with fresh assemblies at the end of cycle four and every fourth cycle thereafter. The outer row of radial blanket assemblies are replaced at the end of cycle five and every fifth cycle thereafter.

#### 4.3.2.1.3 Delayed Neutron Fraction and Neutron Lifetime

Delayed neutron data are required for the evaluation of the reactor core transient (Chapter 15) and stability (Section 4.3.2.8) characteristics. The six delayed-neutron group parameters are calculated by weighting the isotope-dependent delayed neutron yields by the relative fission rates in CRBRP. Table 4.3-6 shows the resulting effective delayed neutron fraction and decay constants by precursor group.  $\beta_{\text{eff}}$  varies less than 1% over the first four cycles.

The prompt neutron lifetime,  $\ell^*$ , is the mean time from the birth of a neutron until it is absorbed or leaked out of the system.  $\ell^*$  ranges from  $0.34 \times 10^{-6}$  to  $0.41 \times 10^{-6}$  seconds for beginning-of-life and end-of-life conditions, respectively. The increase in  $\ell^*$  is due to a softening of the average core spectrum with burnup.

#### 4.3.2.1.4 Multi-Group Nuclear Cross Section Data

A complete description of the method used to generate the multi-group neutron cross sections is given in subsection 4.3.3.2.

#### 4.3.2.1.5 Source Range Flux Monitoring System

54 | The basic function of the source range flux monitor (SRFM) system is to follow the reactor low power neutron flux and to provide that information in a usable form so that a determination of the neutron flux status of the reactor from shutdown to low power (a few Kw) can be made during normal plant operation.

The following two operational requirements have been imposed on the SRFM system to achieve successful operation. First, the instrumentation must provide continuous flux monitoring during low power and normal shutdown operation. Second, during any subcritical operations, other than intentional approach to criticality, it must provide a warning to assure that the reactor does not approach criticality any closer than the worst single refueling error.

The SRFM instrumentation satisfies the first requirement by providing a means of following the reactor flux at both low power and shutdown conditions. This includes the capability for normally measuring the shutdown neutron flux level at all times while fuel is in the core as required for operational control and safe reactor operation. The design and operation of the SRFM will assure that significant changes in the reactor flux level can be detected. The SRFM will also accurately and reliably follow the reactor flux from full shutdown to low power operation. The SRFM provides an output signal that is proportional to the reactor power level from hot standby conditions (zero neutronic power) up to the top end of its sensitivity range.

54 | The second requirement specifies that during refueling, the SRFM must provide a warning to the operator and thereby assure that the reactor does not approach criticality any closer than that level from which criticality could be attained by a single refueling error, with adequate margin for the associated uncertainty. An alarm sounds in the control room if the minimum shutdown reactivity based on this criterion is exceeded.

51 | The source range flux monitoring system consists of three redundant channels that will monitor the flux level of the reactor core from shutdown power through low power. The measurements will be performed at the reactor midplane by three redundant  $\text{BF}_3$  neutron counters located in graphite blocks and spaced approximately 120 degrees apart in the reactor cavity external to the guard vessel.



The inherent neutron source in the core, due to spontaneous fission and ( $\alpha, n$ ) reactions, is multiplied within the core and is the source of neutrons at the ex-vessel SRFM locations during shutdown (source multiplication). The count rate at the SRFM is inversely proportional to the subcritical reactivity and directly related to the inherent neutron source strength in the fuel. Consideration will be given to the effect of control rod insertion to achieve shutdown and changes in the spatial source importance during refueling on the proportionality constant (calibration constant) when required. The derivation of the source multiplication equation is given later in this subsection. SRFM calibration measurements using the CRBR control system will be required for relating subcriticality and count rate. This calibration is performed with a control rod of known reactivity worth. The derivation of the inverse kinetics rod drop technique, which is used to establish the worth of the control rod, is also presented later in this subsection.

When fuel assemblies are present in the Fuel Transfer and Storage Assembly (FT&SA), no core component exchanges of any kind are anticipated. Under these conditions, the only requirement placed on the SRFM detectors is that they must provide continuous monitoring of the flux status of the reactor. The FT&SA and SRFM are being designed so that for FFTF grade fuel, the nominal background count rate from one maximum discharge and one fresh fuel assembly in the FT&SA will be one-fourth ( $1/4$ ) of the nominal foreground count rate from the core at the two SRFMs not adjacent to the FT&SA. For LWR recycle fuel, the nominal background count rate will be one-half ( $1/2$ ) of the nominal foreground count rate at the same two detectors with the same two assemblies in the FT&SA.

Five primary nuclear characteristics of the SRFM design were investigated to justify its use in the Clinch River Breeder Reactor. These characteristics are:

- a. The expected count rate at the ex-vessel location. This count rate is a function of the neutron flux spectrum and instrument sensitivity.
- b. The proportional relationship between reactor power and count rate at the instrument location. A principal function of the SRFM is the monitoring of reactor power through neutron flux detection. Non-linearities between neutron flux at the detector location and reactor power could be introduced by the presence of fuel assemblies in the Fuel Transfer and Storage Assembly or control rod movement.
- c. The ability to isolate the detectors from neutron flux which may arise from sources other than the reactor core.

During periods of reactor operation which required SRFM operability, the Flux Monitor System Mechanical Components (FMSMC) shall provide moderator and shielding to maintain the following neutron foreground-to-background ratios:

- o For reactor startup, with no core assembly of any kind resident in the FT&SA; or normal refueling with no core assembly of any kind in the FT&SA, and with any core assembly being exchanged within 64 inches of its fully inserted core lattice position, all three SRFM Detectors shall have nominal foreground-to-background ratios greater than:

"FFTF Grade" Fuel	10:1
"LWR Recycle" Fuel	7:1

- o In the fully shutdown condition, with a maximum of one spent and one fresh core assemblies resident in the FT&SA, and with no core assembly being exchanged two-out-of-three SRFM Detectors shall have nominal foreground-to-background ratios greater than:

"FFTF Grade" Fuel	4:1
"LWR Recycle" Fuel	2:1

These foreground-to-background ratios shall be calculated based on the following nominal conditions as applied to the last core assembly interchange during a particular refueling period:

- o The discharge fuel assembly with the highest neutron source strength is withdrawn from the central core matrix position 64 inches above its fully inserted position, and
- o All the other fuel and blanket positions in the core are loaded with fresh assemblies.

With all the nuclear and shielding uncertainties applied in the most conservative manner, foreground-to-background ratios at the SRFM Detectors as small as 1.4:1 for FFTF grade fuel and 1.0:1 for LWR recycle fuel (all three SRFM Detectors with no core assembly in the FT&SA); and 1.0:1 for FFTF grade fuel and 1.0:2 for LWR recycle fuel (two-out-of-three SRFM Detectors with a maximum of one spent and one fresh core assemblies in the FT&SA) may be possible. These lower ratios will not degrade the reactivity monitoring capability below minimum requirements nor cause spurious alarms for operations allowed under the above stated conditions. This requirement applies to the range of subcriticality below that level defined by the alarm setpoint.

59

- d. The gamma background at the detector location. The gamma background will be a primary factor in determining instrument sensitivity at a given location.
- e. The ability of the SRFM to accurately determine the reactivity worth of in-core control rods by means of the inverse kinetics rod drop technique. The application of this IKRD technique at the ex-vessel detector locations is required to properly calibrate the SRFM system for sub-criticality determination.

Extensive analyses at ARD and both analyses and experiments at Oak Ridge National Laboratory (Reference 1 and 2) have been performed in support of the ex-vessel SRFM system. Particular emphasis was placed on investigating the five nuclear characteristics listed above. The significant results of the analyses and experiments performed to date are summarized below.

Calculations were performed to assess the magnitude and spectrum of the neutron flux at the ex-vessel SRFM location during shutdown conditions. These calculations were performed for beginning-of-life conditions (all fresh fuel, FFTF-grade plutonium in the core). The minimum shutdown flux at the SRFM locations (beginning-of-life conditions) was calculated to be approximately 0.1 nV, which corresponds to about 4 counts per second at each  $\text{BF}_3$  proportional counter. The magnitude of this count rate which is smaller than during any subsequent refueling sequence, assures good counting statistics for monitoring subcriticality and refueling operations. Additional calculations have shown that the neutron flux is almost fully thermalized (85% below 0.1 eV) at the SRFM location, eight inches behind the front face of the graphite block. This enhancement of the thermal flux inside the graphite block has been confirmed by experiments performed by ORNL at the Tower Shield Facility near Oak Ridge, Tennessee (Reference 1).

To investigate the effect of core configuration on count rate, the homogeneous core configuration was modified by employing different banks of control rods to maintain a fixed reactor power level and  $K_{\text{eff}}$ . For these reactor configurations, the flux level at the SRFM varied by less than 10%. This result shows that the ex-vessel detectors are not sensitive to changes in the homogeneous core configuration during constant power operation. The detector response is proportional to the power level of the reactor. Similar calculations will be repeated for the present heterogeneous core layout and the results will be reported.

Regarding the possibility of the detector monitoring neutron flux from sources other than the core, analyses have shown that the flux monitoring requirements for the SRFM can be satisfied with the background associated with a maximum discharge fuel assembly withdrawn to a point 64 inches above its fully inserted position for any core location.

The count rate due to background is minimized by shielding in the form of boron carbide slabs which surrounds all sides of the graphite block except the front face. The shielding is used to reduce the count rate from neutrons which are scattered into the graphite block from the reactor cavity walls. Normal refueling procedures will require that no assembly of any type be in the FT&SA while any assembly is being inserted the last 64 inches into the core or withdrawn the first 64 inches from the core so that all three SRFM detectors will have an unhindered view of the core. For this case, the requirement of (c) above are imposed.

The gamma dose at the SRFM location immediately after shutdown has been analyzed in detail to assure that the sensitivity of the  $\text{BF}_3$  neutron counters is not adversely affected. The type of  $\text{BF}_3$  neutron detectors to be used in CRBR have a minimum sensitivity of 40 counts per second/thermal equivalent n $\nu$  for gamma dose rates less than 100 R/hr. When the gamma dose exceeds 100 R/hr the detector sensitivity falls off rapidly. Calculations have shown that the local gamma dose rate at the SRFM location is less than 100 R/hr with appropriate shielding in front of the graphite block and in the other locations as required.

A principal function of the SRFM is to determine the subcritical reactivity of the CRBRP based on proper calibration of the instrumentation near critical. The recommended method for calibrating the SRFM detectors is a two step procedure. First, a known value of negative reactivity must be established. This is accomplished by using the SRFM count rate trace that results from scrambling one or more control rods to determine the reactivity worth of the scrambled rods. This is known as the inverse kinetics rod drop (IKRD) technique. Second, the calibration constant, which relates the subcritical reactivity to the count rate, must be determined. This is accomplished by inserting the previously measured reactivity worth (the same control rods described above) and noting the corresponding count rate. This same calibration constant is then used to imply subcritical reactivity when all the control rods are inserted and the reactor is fully shutdown.

This procedure depends strongly on the accurate determination of the negative reactivity worth of the scrambled control rods by means of the IKRD technique. ORNL has performed numerous rod-drop experiments (Reference 2) in the Tower Shield Facility in addition to analytical calculations and both have supported the conclusion that reactivity interpretations, based on the change in count rate at the ex-vessel detectors, are consistent with in-core detectors. The experiments and analyses performed to date have not included the effect of neutron streaming in the reactor cavity. Future analyses will investigate these reactor cavity effects and the results will be included in the FSAR.

The neutron source multiplication technique is employed to monitor the subcritical reactivity state of the reactor during the loading to critical and all subsequent fuel reloadings. The relationship between the steady-state SRFM detector count rate and the subcritical reactivity is derived from the point kinetics equations:

$$\frac{dn(t)}{dt} = \frac{\rho(t) - \beta}{\Lambda} n(t) + \sum_{i=1}^M \lambda_i C_i(t) + S \quad (1)$$

and

$$\frac{dC_i(t)}{dt} = \frac{\beta_i}{\Lambda} n(t) - \lambda_i C_i(t) \quad (2)$$

where

- $n(t)$  = total neutron population
- $C_i(t)$  = delayed neutron precursor density for delayed group  $i$
- $\lambda_i$  = delayed neutron decay constant for delayed group  $i$
- $\beta_i$  = effective delayed neutron fraction for delayed group  $i$
- $\beta$  =  $\sum_{i=1}^M \beta_i$
- $\Lambda$  = neutron generation time
- $\rho(t)$  = reactivity
- $S$  = extraneous neutron source
- $M$  = number of delayed neutron groups

For steady-state conditions, in which the delayed neutron precursors are in equilibrium

$$\frac{dn(t)}{dt} = 0 \quad \text{and} \quad \frac{dC_i(t)}{dt} = 0$$

Equations (1) and (2) become

$$\frac{\rho - \beta}{\Lambda} n + \sum_{i=1}^M \lambda_i C_i + S = 0 \quad (3)$$

and

$$\frac{\beta_i}{\Lambda} n - \lambda_i C_i = 0 \quad (4)$$

Substituting (4) into (3)

$$\begin{aligned} \frac{n\rho}{\Lambda} &= -S \\ \rho &= \frac{-S\Lambda}{n} \end{aligned} \quad (5)$$

which is the source multiplication equation.

In practice, the detector count rate, CR, rather than the total neutron population,  $n$ , is measured and conversion of the measured count rate is required. This conversion, for a given neutron generation, is accomplished by determining the ratio of the detection efficiency,  $W$

$$W = \frac{\int_{\text{detector volume}} \int_E \Sigma_d(r,E) \phi(r,E) dr dE}{\int_{\text{core volume}} \int_E \Sigma_f(r,E) \phi(r,E) dr dE} \quad (6)$$

where

$\Sigma_f(r,E)$  = macroscopic fission cross section

$\Sigma_d(r,E)$  = macroscopic detection cross section

This ratio is essentially the number of neutrons counted in the detector per neutron produced by fission in the reactor. Therefore

$$W = \frac{(CR)\Lambda}{n/\nu} \quad \text{or} \quad n = \frac{\nu(CR)\Lambda}{W}$$

where

$\nu$  = average number of neutrons produced per fission.

Substituting this result into (5) we obtain

$$\rho = - \frac{W S}{\nu(CR)}$$

Rearranging this into the following form

$$CR = - \frac{W S}{\nu\rho} = \frac{W S}{\nu\beta(-\$\)} \quad (7)$$

relates the subcritical reactivity (in dollars) to the count rate in the flux detector.

Equation (7) can be rewritten as

$$CR = \frac{Q}{-\$}$$

where  $Q$  is the calibration constant and  $Q = WS/\nu\beta$ . This calibration constant is determined in the following manner: (1) the count rate,  $CR_1$ , is recorded which corresponds to the initial subcritical reactivity state  $\$_1$ , (hot standby), and (2) a control rod is dropped and the reactivity transient is allowed to decay completely. Analysis of the inverse kinetics rod drop (IKRD) algorithm will provide a reliable estimate of the initial subcritical reactivity state,  $\$_1$ . This data is substituted into the above equation and the following relationship results:

$$CR_1 = \frac{Q}{-\$_1}$$

This equation can then be solved for the unknown  $Q$  in terms of the known quantities  $CR_1$  and  $\beta_1$ . This value of  $Q$ , calculated at hot standby conditions, will be different from the value of the calibration constant at the full shutdown refueling conditions due to the change in detection efficiency associated with the insertion of all the control rods. A corrected value of  $Q$ , based on calculations and/or measurements at full shutdown, will be employed during refueling.

The derivation of the three-point IKRD technique is also based on the point kinetics equations (see Equations (1) and (2) above). Rewriting these equations in terms of count rate at the detector rather than neutron population gives:

$$\frac{v\Lambda}{W} \frac{d[CR(t)]}{dt} = \frac{\rho(t) - \beta}{W} vCR(t) + \sum_{i=1}^M \lambda_i C_i(t) + S \quad (8)$$

and

$$\frac{dC_i(t)}{dt} = \frac{v\beta_i}{W} CR(t) - \lambda_i C_i(t) \quad (9)$$

These two equations can be used to calculate the reactivity worth of a control rod based on the count rate trace which results from scrambling the rod. This procedure is explained below. Assume that the reactor is initially subcritical at  $\rho_0$ . A control rod is dropped at time  $t=0$  and stops moving at time  $t_s$ . The subcritical count rate approaches the final asymptotic value when time is much greater than  $t_s$ . Equations (8) and (9) may be combined and integrated over time greater than  $t_s$  until the reactivity equals  $\rho_f$ . The resulting equation has two unknowns,  $\rho_f$  and the source term. By integrating over two distinct time intervals in the range of the rod-drop transient, a system of two equations in two unknowns is generated. The solutions to these two equations can be written as

$$\rho_f = \left( \frac{A_1 \Delta t_2 - A_2 \Delta t_1}{B_1 \Delta t_2 - B_2 \Delta t_1} \right) \beta \quad (10)$$

and

$$S = \left( \frac{B_1 A_2 - B_2 A_1}{B_1 \Delta t_2 - B_2 \Delta t_1} \right) \left( \frac{v\beta}{W} \right) \quad (11)$$



where

$$A_1 = \frac{1}{\beta} \sum_{i=1}^M [C_i'(t_1) - C_i'(t_0)]$$

$$A_2 = \frac{1}{\beta} \sum_{i=1}^M [C_i'(t_2) - C_i'(t_1)]$$

$$B_1 = \int_{t_0}^{t_1} CR(t) dt$$

$$B_2 = \int_{t_1}^{t_2} CR(t) dt$$

$$\Delta t_1 = t_1 - t_0$$

$$\Delta t_2 = t_2 - t_1$$

$$C_i'(t) = \frac{W C_i(t)}{v}$$

$t_0$  = a time slightly greater than  $t_s$ ;  $t_0 - t_s \approx 0.5$  seconds.

$t_1$  = a time greater than  $t_0$  which occurs while the count rate transient is still decaying;  $t_1 - t_s \approx 25$  seconds.

$t_2$  = a time near the end of the transient when the reactor is approaching its final steady-state condition;  $t_2 - t_s \approx 240$  seconds.

The initial reactivity state  $\rho_0$  is calculated by solving Equations (8) and (9) at steady-state, or

$$\rho_0 = - \frac{WS}{v CR(0)} \quad (12)$$

Substituting Equation (11) into Equation (12) we have

$$\rho_0 = - \left( \frac{B_1 A_2 - B_2 A_1}{B_1 \Delta t_2 - B_2 \Delta t_1} \right) \left( \frac{\beta}{CR(0)} \right) \quad (13)$$

Equations (10) and (13) are evaluated for the final, and initial sub-critical reactivity states, respectively. The values for  $C_i'(t)$  are based on a recursive solution of Equation (9); see Reference 3 for details.

A study has been performed to assess the uncertainty in control rod worth as inferred from IKRD experiments due to the statistical uncertainty inherent in the observed count rate of the detector (Reference 4). The IKRD experiments were performed by ORNL personnel at the Southwest Experimental Fast Oxide Reactor. Two analytical methods were applied to the results from these experiments. First, a propagation of error analysis technique was applied to three-point IKRD subcritical measurements. The second verification method was an error analysis based on repeated rod-drops which were simulated from observed count rate vs. time data. In both cases, the assumption was made that the uncertainty in the reactivity estimate was due solely to the detection process itself. The reactivity uncertainties for various experimental rod-drop data sets were computed by both of these methods and the results were in good agreement. Both techniques yielded errors of approximately 0.6% in the initial and final reactivity states when control rods worth 1 to 2 dollars were inserted from a near critical state.

Additional analyses have been performed to determine the uncertainty in control rod worth as inferred from the IKRD technique which results from the uncertainty in the kinetics parameters  $\beta_i$  and  $\lambda_i$  (Reference 3). These analyses were based on rod-drop experiments performed on the Fast Flux Test Facility-Engineering Mockup Critical loaded into ZPR-9 at ANL. For this configuration, the uncertainty in the final reactivity measurement is 1.8% due to uncertainties in  $\beta_i$  and 0.6% due to uncertainties in  $\lambda_i$ . Similarly, the determination of the initial reactivity state is uncertain by as much as 3.0% due to uncertainties in  $\beta_i$  and as much as 2.0% due to uncertainties in  $\lambda_i$ . Adding together the  $\beta_i$  and  $\lambda_i$  related uncertainties and statistically combining the result with the 0.6% detector count rate uncertainty yields the following: the minimum uncertainty associated with the determination of the final reactivity state is 2.5%, and the minimum uncertainty associated with the determination of the initial reactivity state is 5.1% (minimum = theoretical, no systematic error included).

The precision of the IKRD technique depends to a large extent on systematic uncertainties, i.e., the ability to reproduce the same initial reactor conditions when a rod-drop experiment is to be repeated. Reference 4 discusses a particular rod-drop experiment that was repeated four times in SEFOR under nearly identical reactor conditions. The standard deviation (one  $\sigma$  error) for the control rod worth, which is based on the difference between  $\rho_f$  and  $\rho_0$ , is approximately 0.7%.

During refueling, the SRFM must provide a warning to the operator and thereby assure that the reactor does not approach criticality any closer than that level from which criticality could be attained by a single refueling error with adequate margin for the associated uncertainties. The uncertainties associated with the subcritical reactivity monitoring technique fall into three categories: (1) the uncertainty in the calculated reactivity worth of the single worst refueling error, (2) the

uncertainty in the application of the source multiplication equation technique and (3) the uncertainty in the count rate history during refueling from the SRFM detectors.

The highest reactivity worth refueling error is the inadvertent withdrawal of a control assembly near the end of a refueling sequence. An estimate of the calculational uncertainty in the refueling error is approximately 10% based on critical experiment analyses and the loading tolerance of B-10 in the boron carbide. The reactivity worth of the single worst refueling error plus the appropriate calculational uncertainty will be used to establish the count rate alarm set point during each refueling sequence.

The second uncertainty which must be considered is that associated with the use of the source multiplication equation to imply the subcritical reactivity state. This uncertainty is based on the calibration of Equation (7) with a control rod of known reactivity worth. As previously developed, the uncertainty in the worth of the control rod is in the range of 5 to 7%, based on the inverse kinetics rod drop (IKRD) technique described above. The uncertainty assigned to this item has been conservatively increased to 10% in order to account for additional uncertainties which might occur in the actual calibration procedure as performed in CRBRP.

The last category of uncertainties is specifically related to changes in the core configuration during refueling operations and how those changes are reflected in SRFM count rate uncertainty. First, is the uncertainty in count rate due to spatial flux distribution changes in the core during refueling. This uncertainty will be established by calculating the effect of typical refueling operation on the count rate at the three ex-vessel SRFM locations. Current estimates of this uncertainty are approximately 10%. Second, is the uncertainty due to changes in source strength during refueling. The count rate history during refueling is dependent on the decrease in the inherent neutron source strength which tends to decrease the count rate. The uncertainty in the change in inherent source is estimated to be approximately 25%. Third, the uncertainty associated with the counting rate statistics is assumed to be 5%. These uncertainties will be combined into an overall uncertainty factor applicable to the SRFM count rate.

Preliminary evaluations indicate that sufficient subcriticality exists to assure that the worst single refueling error will not result in inadvertent criticality during refueling using the above described subcritical reactivity monitoring technique. A complete description of this subcritical reactivity monitoring technique, including the treatment of all the appropriate uncertainties, will be included in the FSAR.

The operating characteristics of typical SRFM flux detectors will be experimentally determined in ZPPR critical experiments (using an expanded matrix) which will mock-up the actual CRBRP installation as close as practicable. Multidimensional transport theory calculations will be employed to account for the neutron streaming effects in the reactor cavity which cannot be mocked up in the ZPPR.

#### 4.3.2.2 Power Distribution

##### 4.3.2.2.1 Calculational Method

Figure 4.3-2 summarizes the CRBRP power distribution calculational sequence. ENDF/B-III neutron cross section data are resonance self-shielded, group collapsed, and gamma-coupled with ENDF/B-IV coefficients in XSRES/1DX (SPHINX) to result in a 9-neutron/13 gamma energy group, region, composition and temperature dependent CRBRP master cross section library. This cross-section library is used in two-dimensional diffusion and burnup calculations with the 2DB code in hexagonal-planar and RZ (cylindrical) geometry to determine the radial and axial power distributions, respectively, throughout the first 5 years of operation. The RZ calculations, employing an effective volume cylindrical model, result in axial blanket power contributions, normalized axial power shapes for the fuel and blankets, and axial leakage (buckling) factors for application to the hex calculations. The fuel and inner blanket rod power distributions are determined by two-dimensional least-squares fitting the 2DB power density by (triangular) mesh interval for each assembly with the POWPIN code. Due to the importance of the plutonium buildup distribution, the radial blanket power distributions are determined from PUMA calculations. The PUMA calculations utilize least-squares fitted fluxes, cross-sections, and gamma heating (from 2DB burnup calculations) to determine the power and burnup characteristics for each blanket rod. The product of normalized radial and axial power factors, the region power fraction, and the reactor thermal power determines the fuel and blanket power distribution throughout the core. Application of power bias factors (methods/modeling correction factors), overpower trip margin, and power uncertainty factors produces a conservative peak linear power envelope for the evaluation of limiting fuel and blanket capability.

##### 4.3.2.2.2 Core Layout

Figure 4.3-3 shows the heterogeneous core layout and fuel and blanket assembly numbering scheme. The initial core includes 156 fuel assemblies, 82 inner blanket assemblies and 126 radial blanket assemblies. Nine fully enriched (92% B-10) primary control assemblies are located in the six row 7 corner (6-R7C, positions 129 and 131 in Figure 4.3-3) and three row 4 (3-R4, position

130 in Figure 4.3-3) positions. Six fully enriched secondary control assemblies are located in the six row 7 flat (6-R7F, positions 7 and 35 in Figure 4.3-3) positions. The 6-R7C primary control rods, operated as a bank, serve to control the reactor throughout each cycle. The 3-R4 primary and 6-R7F secondary control rods are normally fully withdrawn for all power operations. The core contains a single fuel enrichment zone. The fuel, inner blanket, and radial blanket power distributions are reflectively symmetric in 60 degree sectors through the R7C positions. The fuel and blanket management is discussed in Section 4.3.2.1.2.

#### 4.3.2.2.3 Region Power Fractions

Table 4.3-7 shows the fuel and inner blanket power fractions over the central 36-inch high region at the beginning and end of the first six cycles of operation. This power split includes the distributions of both the isotopic fission rates and gamma heating in the system, determined with the 9-neutron/13-gamma group coupled cross section set and 2DB neutron gamma heating calculations. This capability makes possible an explicit representation of the gamma diffusion from the source zone in the fuel assemblies into the inner and radial blanket zones.

#### 4.3.2.2.4 Normalized Radial Power Shape

Figures 4.3-4 through 4.3-15 show the normalized radial power factors,  $*F_R^N$  for the peak and average-power-rods in each fuel and inner blanket assembly in a 120 degree sector of the core at the beginning and end of the first 6 cycles of operation. The location of the peak power rod in each assembly is indicated by a small circle in Figures 4.3-4 through 4.3-15 to highlight the radial/azimuthal power gradients throughout the core. The reflective core symmetry through the R7C control rods is evident in the radial power shapes. One can note the changes in the power gradients throughout life which are caused by the refueling in the R6C location and by the buildup of plutonium in the inner blankets, as well as by the effects of control rod withdrawal.

The just-critical R7C primary control rod bank withdrawal at the start and end of each cycle is also shown in Figures 4.3-4 through 4.3-15. The effects of criticality uncertainties, control rod worth uncertainties and control rod banking tolerances on the power distribution are included in the power uncertainty assessment.

---

\*Radial power factor is defined as the power in a particular fuel (inner blanket) rod divided by the power in the average fuel (inner blanket) rod in the whole core (inner blanket).

#### 4.3.2.2.5 Axial Blanket (Extension) Power

Table 4.3-8 lists the 64/36 inch\*\* power normalization factors for the fuel, inner blanket and radial blanket assemblies. These factors, when multiplied by the 36-inch core region power obtained from the power fractions in Table 4.3-7 and the radial power factors discussed above, produce full 64-inch rod or assembly powers including the contributions from the upper and lower axial blankets (UAB and LAB). Also listed in Table 4.3-8 are the normalization factors to include only the power contribution from the lower axial blankets for the determination of thermal conditions at the inlet region to the core.

#### 4.3.2.2.6 Radial Blanket Power History

Tables 4.3-9 and 4.3-10 are summaries of the radial blanket total assembly power and peak rod power histories, respectively, at the beginning and end of the first 5 cycles of operation for the 12 unique assembly locations identified in Figure 4.3-3. The powers in Tables 4.3-9 and 4.3-10 are total values over the full 64-inch blanket length (that is, the normalization factors in Table 4.3-8 have already been applied). The total radial blanket power is listed in the last column in Table 4.3-9. Table 4.3-11 shows the power and burnup history for the average and peak rod, as well as the peak kW/ft and peak pellet burnup history, for the highest power radial blanket assembly (assembly #1 in Figure 4.3-3) for both initial and "equilibrium" operation. The limiting equilibrium radial blanket reaches a (nominal) peak linear power of 46.6 kW/m (14.2kW/ft) and a peak (pellet) discharge burnup of 3.63 a/o after 4 full years of operation (1100 fpd).

#### 4.3.2.2.7 Normalized Axial Power Shape

The axial power factor (normalized axial power shape),  $F_N$ , defines the local axial power density distribution relative to the average power density in the same axial channel. Figures 4.3-16 and 4.3-17 show the normalized axial power distributions in the core fuel assemblies at the beginning and end of the first and second cycles. The decrease in axial peak-to-average power with burnup in the core is attributable to preferential fuel depletion near the flux peak at the core midplane. The local distortion in the axial power shapes from partial control rod insertion is clearly evident in Figure 4.3-17.

\*\*Actual hot-full-power core height dimensions are: central core region .9204 m (36.24 inches), lower axial blanket .3568 m (14.05 inches), upper axial blanket .3574 m (14.07 inches).

The distributions in Figure 4.3-17 labeled, "fuel zones with control rod influence" are applied to those fuel rods in the fuel assemblies directly adjacent to the R7C control rod only. The "clean fuel zone" distributions in Figure 4.3-16 apply to the remaining fuel rods in the core. A comparison of this technique with an explicit three-dimensional (VENTURE) benchmark calculation demonstrated agreement within a few percent in the power distribution around the inserted control rods as well as throughout the remainder of the core as discussed in relation to the modeling uncertainty in Section 4.3.2.2.9. The detailed three-dimensional power differences are enveloped in the power uncertainties. The differences in the primary control rod bank insertion in cycles other than 1 and 2, shown in Figure 4.3-17, result in additional perturbations to the axial power shapes which are also treated in the nuclear uncertainty assessment.

Figures 4.3-18 through 4.3-20 show the normalized axial power distributions in the inner and radial blankets, respectively, at the beginning and end-of-life. The blanket axial power shapes are normalized to 1.0 over the central 36-inch high region. The increase in the axial peak-to-average power with burnup in the blankets results from the peak in the axial distribution of the accumulated plutonium near the core midplane.

Figure 4.3-21 shows typical axial power distributions in the upper and lower axial blankets at the beginning and end-of-life. The steep axial power gradient is caused by a combination of the axial flux and neutron spectrum gradients. Plutonium accumulation tends to flatten the end-of-life axial power gradients since Pu-239 fission is less sensitive than U-238 fission to the fast-neutron component of the neutron spectrum.

Table 4.3-12 summarizes the axial peak-to-average power ratios for the fuel, inner, and radial blankets throughout the first four cycles of operation. The reduction in peak  $F_z^N$  in the core and the increase in peak  $F_z^N$  in the blankets with plutonium burnup/buildup, respectively, is evident in Table 4.3-12.

#### 4.3.2.2.8 Synthesis of Power Distribution Throughout the Core

The synthesis of the three-dimensional power distribution throughout the fuel and blankets is accomplished by the application of normalized radial and axial power peaking factors to the average fuel or blanket power generation as follows:

$$\text{Linear Power (kW/m)} = \frac{975,000 * \text{Power Fraction}}{\text{No. of Rods} * \text{Length of Rod}} * F_R^N * F_Z^N \quad (1)$$

Where "975,000" is the nominal reactor power level in kilowatts,

"Power fraction" is the fuel or inner blanket (36") power fraction from Table 4.3-7,

"No. of Rods" is the number of fuel (217) or blanket (61) rods per assembly times the number of fuel or inner blanket assemblies in the core (note that the number of fuel and inner blanket assemblies changes at the start of the even numbered cycles due to the refueling at the R6C locations),

"Length of Rod" is 0.9204 m over the central 36" region in all cases,

" $F_R^N$ " is the normalized nuclear radial power peaking factor for the fuel or inner blankets from Figures 4.3-4 through 4.3-15, and

" $F_Z^N$ " is the normalized nuclear axial power peaking factor from Figures 4.3-16 through 4.3-20.

The integrated (64") total rod power, on the other hand, is given by:

$$\text{Rod Power (kW)} = \frac{975,000 * \text{Power Fraction}}{\text{No. of Rods}} * 64/36 \text{ Power Factor} * F_R^N \quad (2)$$

Where, "64/36 Power Factor" is the ratio, given in Table 4.3-8, of the power in the full-length fuel or blanket rod (that is, including the power in the upper and lower axial blankets or axial extensions, respectively) to the power in the central 36" region (from Table 4.3-7).

The remaining terms are as defined in Equation 1.

#### 4.3.2.2.9 Power Uncertainty Evaluation

The total power or burnup uncertainty is composed of nuclear design methods uncertainties and/or biases (based on comparisons of calculations and measurements of isotopic fission and capture rates and gamma heating in ZPPR-7), CRBRP design uncertainties relating primarily to absolute power normalization and fissile content variations, and a general class of modeling uncertainties. In the fuel, the power uncertainty



is broken down into a statistical part which is combined in quadrature (root-mean-square) with other statistical uncertainties, and a nonstatistical bias and uncertainty which is applied directly to envelope the upper limits of the peak power density. Due to the limited scope of the available blanket data, only a nonstatistical uncertainty is developed. Uncertainties are provided for the fuel, inner blanket, and radial blanket assemblies. Where a basis exists for such, a spatial distribution of the uncertainty is provided (e.g., adjacent to, and removed from, the influence of inserted control rods, and by assembly-row in the radial blanket).

Experimental verification of the calculational methods and data used to predict the power distributions in CRBRP is provided by the measurements performed in the ZPPR critical facility. ZPPR is a zero power critical mockup of the CRBRP consisting of a matrix of rectangular drawers containing fuel, steel and sodium plates loaded to simulate the average compositions of the CRBRP core and blanket regions. CRBRP design methods are verified, and design bias factors and uncertainties are derived, by direct comparison of calculated and measured ZPPR parameters. These parameters include isotopic fission and capture rate and gamma heating distributions in support of power distribution predictions. The design (methods) bias factors and uncertainties are subsequently applied to the calculation of these parameters in CRBRP predicted with the same calculational tools and data.

The results presented herein are based primarily on the analysis of ZPPR-7 (phases A-E) measurements. ZPPR-7 modeled the basic characteristics of a heterogeneous CRBRP core with annular rings of inner blanket assemblies. The analysis of the ZPPR-7 experiments is presented in Section 4.3.3.9.

#### 4.3.2.2.9a Core Fuel Assembly Power Uncertainties

54 | Table 4.3-13 lists the statistical and nonstatistical uncertainties applicable to the predictions of both local and rod or assembly-integrated power density in the core fuel assemblies. The uncertainties are divided into those applicable to fuel regions directly adjacent to the partially inserted R7C control rods, and those applicable to all other core locations (designated "clean" fuel zones). The uncertainties grouped under the "Fuel Zones Adjacent to Inserted R7C Control Rods" heading are intended to be applied to all fuel assemblies surrounding the R7C control rod positions where the local power density is strongly influenced by the inserted poison. Where the power uncertainty is strongly space dependent, as in the modeling bias in the vicinity of the control rods, it is so indicated in Table 4.3-13. Uncertainty values are presented for the peak power density (near the core midplane), the power density at the top of the core (core/upper axial blanket interface), the rod-channel integrated power  
51 | and the assembly integrated power. As a general rule, the uncertainties in

Table 4.3-13 have been derived to best fit the high-power locations in the fuel. The uncertainty in the "power density at the top of the core" (core/UAB interface) in the vicinity of the R7C control rods is an end-of-cycle value with a substantial portion of the R7C control rods withdrawn.

The peak and integrated power densities in the fuel are well predicted with the standard 2D-synthesis nuclear design techniques. However, the "power density at the top of the core" is relatively poorly predicted due to difficulties in simultaneously modeling the behavior in this region while preserving the integral and peak (core midplane) power in two dimensions. In addition, the accuracy of few group diffusion theory is poorer in the presence of the steep flux gradient and in the region of the core/UAB material discontinuity. These factors are reflected in the larger "power density at top of core" uncertainty.

The statistical uncertainties consist of experimental uncertainties (fission rates and gamma heating) at the  $3\sigma$  level, criticality and control rod insertion uncertainties, and local fuel fissile content variations.

#### Experimental:

The experimental power uncertainty consists primarily of Pu-239 and U-238 fission rate and gamma heating uncertainties. The experimental (statistical) power uncertainty is derived from the  $\pm 2\%$  ( $1\sigma$ ) root-mean-square deviation between calculated and measured core fission rate (Pu-239, U-235) distributions in ZPPR-7, covering a variety of reactor critical configurations. There is an observed radial tilt in the calculation-to-experiment ratios for Pu-239 fission in Phases A and B of ZPPR-7 which tends to overestimate (by 3-5%) the Pu-239 fission rate in the area of the fuel "islands" in rows 7, 8, and 9 and, specifically, around the R7C control locations in the beginning-of-life configuration. This overprediction, coupled with the application of  $+3\sigma$  power uncertainties, would result in an overly high estimate of the peak power in these locations. Consequently, the beginning-of-life (BOC1, BOC3, and BOC5) power in the rows 7, 8, and 9 region of the core is biased downward in Table 4.3-13 (footnote f) by 1-3% to remove the basic tilted characteristics in the fission rate (power shape). This radial tilt was not observed in the Phase C, D, or E ZPPR-7 experiments with plutonium loaded in the inner blankets, so the aforementioned bias is not applied to the end-of-life power shape.

The analysis of the ZPPR-7 experimental U-238 fission rate distribution showed substantial fluctuations in the calculation-to-experiment ratios between fuel and inner blanket assemblies, possibly attributable to the infinite medium cross-section preparation scheme, coarse-mesh effects, transport effects, and the like. Based on these ZPPR-7 results, a one-sided  $+20\%$  U-238 fission uncertainty is indicated in the core fuel assemblies (although U-238 fission only accounts for about 6% of the total power in the fuel so that this uncertainty accounts for approximately 1% on the high side of the total power uncertainty).

Analysis of the preliminary ZPPR-7 gamma heating measurements show a scatter of  $\pm 10\%$  in the calculation-to-experiment (C/E) ratios in the core regions and a consistent 15-20% underprediction in the radial blanket. There was some evidence in the ZPPR-4 gamma heating measurements, however, that this underprediction behavior at the core/blanket interface is at least in part an anomaly caused by the comparison of homogeneous (cell-average) calculated heating rates with point-measured values in regions of substantial gamma fine structure. This uncertainty is therefore considered an upper bound. Gamma heating accounts for about 10% of the total fuel assembly power, so the  $\pm 10\%$  uncertainty accounts for approximately  $\pm 1\%$  of the total fuel assembly power uncertainty.

The direct combination of  $\pm 6\%$  ( $3\sigma$ ) plutonium fission rate uncertainty ( $\approx 85\%$  of the total core power),  $\pm 20\%$  U-238 fission rate uncertainty ( $\approx 6\%$  of the total core power), and  $\pm 10\%$  gamma heating uncertainty ( $\approx 10\%$  of the total core power) results in a  $\pm 7\%$  (approximately  $3\sigma$ ) total experimental power uncertainty in the fuel, in addition to the space-dependent beginning-of-life bias discussed earlier. This uncertainty applies equally to the local pellet, rod and fuel assembly power predictions.

#### Criticality Uncertainty:

541 The uncertainty in the prediction of the hot critical state of the reactor results in an uncertainty in the depth of primary control rod insertion which, in turn, affects the local power distribution (principally the radial and axial distributions in the immediate vicinity of the inserted control rods, and to a lesser extent throughout the remainder of the core). This uncertainty is derived from a bounding value of the criticality uncertainty of  $\pm 0.5\% \Delta k$  developed from the clean (unrodded) critical configurations in ZPPR-7. The resulting power uncertainty is derived parametrically by varying the control rod bank insertion by an amount corresponding to the  $0.5\% \Delta k$  to produce power perturbation maps. The criticality power uncertainty applies approximately equally to the beginning and end-of-cycle power distributions due to a partial cancellation between the lesser influence of the nearly-withdrawn primary control rods and the larger magnitude of the criticality uncertainty which includes burnup reactivity swing uncertainties near the end-of-cycle. This criticality (rod insertion) uncertainty results in a  $\pm 1\%$  power uncertainty throughout the core with the exception of those assemblies directly adjacent to the inserted control rods. The power distribution in the fuel assemblies directly adjacent to the inserted control rods is strongly influenced by the position (depth of insertion) of those rods so that the criticality uncertainty in these assemblies is both larger and space-dependent across the assemblies as indicated in Table 4.3-13.

#### Pellet Fissile Content Tolerance:

51 The fuel pellet fissile content (manufacturing) tolerance results in a local fission rate uncertainty of  $\pm 3\%$ . Because the pellets are fabricated in batches, this uncertainty is not reduced for groups of pellets comprising a single fuel rod or a single fuel assembly. Very large numbers of fuel assemblies are, however, subject to a smaller  $\pm 0.5\%$  fissile content tolerance.

## Modeling Uncertainties:

Specific model uncertainties in the CRBRP core power distribution predictions include parametric uncertainties arising from 3D effects, rod power interpolation and radial and axial burnup modeling. The aforementioned modeling uncertainties are derived parametrically, so no specific  $\sigma$  level can be assigned. The values quoted do, however, generally cover the range of variations noted. Modeling uncertainties are combined with other nonstatistical uncertainties directly rather than statistically.

CRBRP power, burnup and reaction rate distributions are predicted by a two-dimensional (2D) synthesis technique whereby "radial" shape factors,  $F_R$ , derived from hexagonal calculations, and axial shape factors,  $F_Z$ , derived from RZ calculations, are superimposed on average power conditions to result in the three-dimensional (3D) power distribution throughout the core and blankets. A benchmark calculation with consistent 3D and 2D-synthesis models has been used to infer the geometric modeling biases introduced by the 2D-synthesis technique at the beginning-of-life. In general, the agreement between the two models is good (with the exception of the regions strongly influenced by the partially inserted R7C control rods as noted in Table 4.3-13) with the peak power density predicted within the range of  $\pm 3\%$  and rod or assembly-integrated power predicted within  $\pm 1\%$  in the core. The polynomial fit to power-by-rod, performed with input from 24 mesh-per-assembly 2DB hexagonal calculations, introduces an additional uncertainty of  $\pm 1\%$  in the radial power shape within an assembly. Burnup modeling in the core generally introduces little error in the power distribution in high-power locations, although some uncertainty is necessarily introduced in the end-of-life axial power shapes due to smoothing. The axial peak-to-average power has been shown to be nominally overpredicted by 2% in ZPPR-4 and ZPPR-7. The net peak power density modeling uncertainty throughout the core (with the exception of assemblies directly influenced by inserted control rods) is therefore  $\pm 2\%$  ( $\pm 3\%$  3D effect plus  $\pm 1\%$  intra-assembly radial power shape uncertainty less  $\pm 2\%$  axial peak-to-average power overprediction). This value increases to  $\pm 10\%$  on the high-side for the "power density at the top of the core" with the inclusion of 5% fall-off in the prediction of the axial power shape indicated in the ZPPR-4 and ZPPR-7 experiments and with some additional uncertainty in the tail of the axial power shape. The  $\pm 2\%$  integrated rod power uncertainty is made up of  $\pm 1\%$  3D effect plus the  $\pm 1\%$  radial shape uncertainty, whereas the  $\pm 1\%$  total assembly power modeling uncertainty is entirely 3D effect.

The radial and axial power shapes in the vicinity of inserted control rods are particularly sensitive to control rod modeling. Partially inserted control rods in the CRBRP are modeled with an "effective" amount of control volume fraction which results in the same reactivity worth inserted in the 2D hexagonal calculations as would result from an explicit 3D representation. This technique results in a good representation

of the average power in the surrounding fuel assemblies but necessarily introduces some spatial bias in the radial power shape very close to the inserted control rods. In addition, the axial power shape is selected to best represent the assembly-average power so that the shape is somewhat more perturbed in the region of the fuel pins directly adjacent to the inserted control rod, and likewise, somewhat less perturbed on the side of the assembly farthest from the inserted rod. The combination of these radial and axial shape perturbations, derived primarily from the 3D-2D synthesis comparison, results in a space-dependent modeling bias, (uncertainty) which varies across the assembly as indicated in Table 4.3-13.

#### Control Rod Banking:

The maximum control rod out-of-bank tolerance of  $\pm 1.5$  inches introduces a power asymmetry in the core. The power uncertainty resulting from the control insertion asymmetry is estimated from full-core parametric calculations to be  $\pm 2\%$  except directly adjacent to the inserted rods where the uncertainty is increased to  $\pm 4\%$ .

#### Reactor Power:

The absolute reactor power normalization is required to be  $\pm 3\%$  including plant heat balance, control dead band, all measurements and any other uncertainties. It should be noted that for the evaluation of limiting linear power (temperature) at 15% overpower conditions, the 15% overpower margin is intended to include the 3% power normalization uncertainty.

#### 4.3.2.2.9b Inner Blanket Assembly Power Uncertainties

Table 4.3-14 lists the uncertainties applicable to the predictions of local and rod or assembly-integrated power uncertainties in the inner blanket assemblies. Blanket uncertainties are divided into beginning and end-of-life values primarily as a result of the large change in isotopic fission rates. Values are presented for the peak power density uncertainty (near the midplane at the location of the peak linear power), the power density uncertainty near the top of the 36-inch "core" (the approximate location of the peak clad temperature), the rod-channel integrated power uncertainty (for application to the total channel enthalpy rise and to the total rod burnup), and for the assembly-integrated power uncertainty (for the mixed mean coolant outlet temperature). The blanket uncertainties have been derived to best fit the respective high power locations.

#### Experimental:

Due to the somewhat limited scope of the measured blanket data in Phases A-E of ZPPR-7, it is recommended that the experimental fission and capture rate and gamma heating uncertainty component be combined

Amend. 54  
May 1980

directly (rather than in quadrature as with the purely statistical uncertainties) with the other uncertainties in the inner blanket assemblies which is a conservative approach. The experimental uncertainty component is defined to be three times the root-mean-square combination of the Pu-239 fission rate, U-238 fission rate, U-238 capture rate and gamma heating rate deviations weighted by their respective fractions of the total inner blanket power for any particular location and for any particular time-in-life.

The beginning-of-life blanket power experimental uncertainty is dominated by the  $\pm 10\%$  ( $\sim 3^*$ RMS) uncertainty in U-238 fission rate which contributes nearly 60% of the total fresh blanket power (compared to less than 30% of the end-of-life power in the burned blankets). The remaining uncertainty at the beginning-of-life results from the 15-20% uncertainty in the predicted blanket gamma heating which constitutes nearly 40% of the beginning-of-life blanket power and about 20% of the end-of-life blanket power. Pu-239 fission calculation-to-experiment ratios vary  $\pm 3\%$  to  $\pm 5\%$  ( $3^*$ RMS) at beginning and end-of-life, respectively, in the inner blankets. In addition, the U-238 capture rate (Pu-239 production rate) is substantially ( $9 \pm 4\%$ ) overpredicted, necessitating the application of an end-of-life fission rate bias of less than unity. Pu-239 fission comprises roughly 50% of the end-of-life inner blanket power. The 2% overprediction of axial peak-to-average power, as well as the  $\sim 5\%$  underprediction of power density at the extremities of the (36") "core", are biased out of the inner blanket experimental uncertainties in Table 4.3-14. Combining the aforementioned reaction rate and gamma heating uncertainties with their fractional contributions to the total blanket power results in the time dependent biases and uncertainties shown in Table 4.3-14. In particular, the peak power density uncertainty is  $\pm 10\%$  at beginning-of-life and  $-5 \pm 5\%$  at end-of-life.

#### Manufacturing Tolerances:

The  $\pm 1\%$  blanket heavy metal theoretical density tolerance gives rise to a similar  $\pm 1\%$  uncertainty in blanket power generation. The U-235 content tolerance in the depleted uranium blanket feed material results in a small ( $\pm 1\%$ ) uncertainty in the beginning-of-life blanket power and a negligible uncertainty in the end-of-life power where U-235 fission contributes only about 2% of the total blanket power.

#### Modeling Uncertainties:

Blanket modeling uncertainties consist of power-by-rod interpolation uncertainties, intra-assembly burnup uncertainties, axial power shape

and buildup uncertainties, and 3D geometric effects. The least-squares fit to power-by-rod in the inner blankets is performed with input from 24 mesh-per-assembly 2DB calculations. Pin-by-pin burnup does not substantially increase the peak end-of-life power in the highest power assemblies. The fitting uncertainty in the inner blankets is  $\pm 5\%$  at beginning of life (where the fresh blanket power is sensitive to both the total flux and neutron spectrum gradients), and  $\pm 1\%$  of the end-of-life (where the peak inner blanket power is relatively flat and less fast-spectrum sensitive). The axial peak-to-average power shape uncertainty, reduced from RZ burnup calculations, is  $\pm 1\%$  near the core midplane and  $\pm 5\%$  at the top of the 36 inch "core" region, primarily due to smoothing at the end-of-life. Additional three-dimensional effects do not contribute a substantial uncertainty in the inner blankets ( $\pm 1$  to  $2\%$ ).

#### Criticality and Control Rod Banking Uncertainties:

Criticality and control rod banking uncertainties primarily influence the inner blanket power distributions. In addition to the effect of criticality uncertainties on control rod insertion, and hence, on power distribution as discussed earlier, the uncertainty in fuel enrichment specification results in a flux level uncertainty which ultimately results in a  $\pm 1\%$  plutonium buildup and end-of-life blanket power uncertainty.

#### Reactor Power:

The absolute reactor power normalization uncertainty is  $\pm 3\%$ .

#### Non-Pellet Heating:

For purposes of evaluating the upper limits of the peak pellet power density (or peak linear power), the blanket power data is reduced by 5% and 2.5%-3% at beginning and end-of-life, respectively, to account for the fraction of power which is attributable to gamma heating in the non-pellet constituents of the blanket assembly (clad, sodium, and duct). This reduction is, of course, not used in the determination of total heat load in the assembly.

#### 4.3.2.2.9c Radial Blanket Assembly Power Uncertainty

Table 4.3-15 lists the uncertainties applicable to the predictions of local and rod or assembly-integrated power densities in the radial blanket assemblies.

#### Experimental:

The radial blanket calculation-to-experiment ratios of fission

541

and capture rate data in ZPPR-7 (Section 4.3.3.9) exhibit a characteristic space dependence, falling-off of the order of 10% in the radial direction from the core-blanket interface out to the blanket-reflector interface. Due to the limited number of radial blanket measurements and the space dependent nature of the data, the radial blanket experimental uncertainties are treated non-statistically for each blanket row. The radial blanket experimental power uncertainty is derived from the limits of the observed variations in the blanket fission and capture rates and gamma heating. The observed variation limits in the isotopic blanket fission and capture rates are doubled to result in approximately  $3\sigma$ -equivalent uncertainties. The total power uncertainty is obtained from the root mean square sum of the Pu-239 fission rate, U-238 fission rate, U-238 capture rate and gamma heating rate uncertainties weighted by their respective fractions of the total blanket power at any particular radial location and for any particular time-in-life.

The beginning-of-life row 1 radial blanket power experimental uncertainty is again dominated by the  $+6 \pm 8\%$  ( $\sim 3\sigma$ ) uncertainty in U-238 fission rate which constitutes approximately 60% of the fresh blanket power. In the second row, the beginning-of-life U-238 fission rate uncertainty is  $+23 \pm 20\%$  ( $3\sigma$ ) due to an apparent misprediction of the blanket spectral gradient. The remaining uncertainty results from the  $\pm 20\%$  uncertainty in the blanket gamma heating rate which constitutes about 40% of the fresh blanket power. The 2% overprediction of axial peak-to-average power, as well as the  $\sim 5\%$  underprediction of the power density at the extremities of the 36-inch "core", are biased out of the radial blanket experimental uncertainties. The net resultant beginning-of-life radial blanket peak power density experimental uncertainties are therefore  $+2 \pm 9\%$  (row 1) and  $+10 \pm 14\%$  (row 2).

51

At the end-of-life, the U-238 fission rate (15-25% of the total radial blanket power) uncertainty increases to  $+13 \pm 12\%$  (row 1) and  $+33 \pm 20\%$  (row 2). The U-238 capture rate (Pu-239 production rate) is again overpredicted ( $+10 \pm 8\%$  in the first row and  $+4 \pm 8\%$  in the second row). Additionally, the end-of-life Pu-239 fission rate uncertainty is  $+4\%$  (row 1) and  $+7 \pm 4\%$  (row 2). The U-238 capture rate (buildup) and Pu-239 fission rate uncertainties are both applied to the 60-70% of the end-of-life radial blanket power attributable to Pu-239 fission. Combining the Pu-239 fission rate, U-238 capture rate, U-238 fission rate, and gamma heating rate uncertainties with their fractional contributions to the total radial blanket power, and applying the aforementioned 2% axial peak to average bias, results in the time and space dependent experimental biases and uncertainties in Table 4.3-15. The resulting net end-of-life radial blanket peak power density experimental uncertainty is  $-4 \pm 7\%$  in the first row and  $+5 \pm 8\%$  in the second row.



## Modeling Uncertainties:

Radial blanket modeling uncertainties consist of power and burnup-by-rod (PUMA) uncertainties, axial power and buildup uncertainties, and 3D geometric effects. The rod-fitted flux, cross-sections, and gamma heating, and the resulting composite power and burnup (buildup) distribution uncertainties are taken to be  $\pm 5\%$  at the beginning-of-life and  $\pm 2$  to  $\pm 3\%$  at the end-of-life based on a comparison of PUMA calculations with fine-burnup-zone 2DB benchmark calculations. The axial power shape uncertainty in the radial blankets is  $\pm 1\%$  at the core midplane at the beginning-of-life,  $\pm 2\%$  at the core midplane at the end-of-life based on a chopped cosine approximation, and  $\pm 5\%$  at the top of the 36-inch "core" region due to smoothing of the burnup distribution at end-of-life. The 2D power synthesis is arranged to best predict the radial blanket power ( $\pm 1\%$ ) near the highest power locations on the sides of the assemblies closest to the core. The net blanket modeling uncertainty is  $\pm 7\%$ .

## Miscellaneous:

The manufacturing tolerances (blanket heavy metal and U-235 content), criticality and control rod banking uncertainties, reactor power normalization, and non-pellet heating biases are as discussed in the preceding sections.

### 4.3.2.2.10 Peak Linear Power

The peak fuel linear power is determined from Equation 1, using radial and axial power peaking factors from Figures 4.3-4 through 4.3-15 and Table 4.3-12. At the beginning-of-cycle one, the peak fuel linear power in the Row 8 fuel assemblies adjacent to the R7F secondary control rod channels is 40.6 kW/m (12.4 kW/ft). Application of the upper limit ( $3\sigma$ ) uncertainty of +10.7% from column 1 of Table 4.3-13, and 15% overpower conditions results in a maximum power of 51.6 kW/m (15.7 kW/ft). Figure 4.3-22 summarizes the peak linear power distribution ( $3\sigma$  + 15% overpower conditions) throughout the core in the fuel assemblies at BOC1 and in the inner blanket assemblies at EOC4. The peak linear power in the fuel assemblies surrounding the inserted R7C primary control rods, after application of  $3\sigma$  uncertainties, space-dependent modeling biases arising from the control rod influence and 15% overpower conditions, is only slightly lower than the 51.6 kW/m maximum around the secondary control rod channels. The highest calculated fuel linear power of 52.2 kW/m (15.9 kW/ft) occurs in the freshly refueled R6C assembly (#62 in Figure 4.3-3) at the beginning of the second cycle.

The peak end-of-life inner blanket linear power of 54.1 kW/m (16.5 kW/ft) occurs in the Row 6 assemblies adjacent to the freshly inserted fuel assemblies at the end-of-cycle four (550 fpd). Application of upper limit end-of-life uncertainties of + 8% from Table 4.3-14 and 15% overpower conditions and reducing the peak power density by

2.5% to account for non-pellet heating, results in a maximum inner blanket linear power of 65.6 kW/m (20.0 kW/ft). Similarly, the peak radial blanket linear power of 46.7 kW/m (14.2 kW/ft) occurs in blanket assembly #1 (see Figure 4.3-3) at the end-of-cycle 8. Application of the end-of-life Row 1 radial blanket peak power uncertainty of + 13% and 15% overpower conditions and reducing the peak power density by 3% to account for non-pellet heating, results in a maximum radial blanket linear power of 59.1 kW/m (18.0 kW/ft).

#### 4.3.2.2.11 Burnup

The fuel burnup is a function of the power history and accumulated full-power-days irradiation, the fuel management, and the heavy metal loading. The local burnup is obtained from the product of the accumulated core average burnup and time-averaged radial and axial power peaking factors as follows:

$$\text{BURNUP (Mwd/kg)} = \frac{975 \text{ MW}}{\text{HM/ass'y. (kg)}} \sum_i \left( \frac{\text{PF}_i * F_{Ri}^N * F_{Zi}^N * \text{fpd}_i}{2 * \text{No. Ass'ys.}_i} \right) \quad (3)$$

where the subscript "i" includes the beginning and end of consecutive cycles,

"HM/ass'y." is the total kg of heavy metal (uranium plus plutonium), per assembly (33.2 kg for fuel assemblies over the central 36-inch high core region and 100.9 kg for blanket assemblies over the full 64-inch height),

"PF<sub>i</sub>" is the fuel or inner blanket power fraction at the beginning or end-of-cycle (the power fraction for the 36 inch core height is given directly in Table 4.3-7 for the fuel, whereas PF<sub>i</sub> for the inner blankets is the 36-inch power fraction from Table 4.3-7 times the 64/36 power normalization factor from Table 4.3-8),

"F<sub>Ri</sub><sup>N</sup>" is the radial rod power factor for the fuel or blankets from Figures 4.3-4 through 4.3-15,

"F<sub>Zi</sub><sup>N</sup>" (included only in the calculation of peak pellet burnup) is the axial peak-to-average power factor from Table 4.3-12 or from Figures 4.3-16 through 4.3-20 (the F<sub>Z</sub><sup>N</sup> for the fuel are normalized over the central 36-inch core height in Table 4.3-12 and Figures 4.3-16 and 4.3-17; whereas F<sub>Z</sub><sup>N</sup> for the inner blankets must be multiplied by the 64/36 power factors in Table 4.3-8 and by 1.776, the ratio of 64/36 inches, to produce a renormalized peak-to-average axial power factor with respect to the power in the full 64-inch blanket rod),

"fpd<sub>i</sub>" is the full power days per cycle, and

"No. Ass'ys.<sub>i</sub>" is the number of fuel or inner blanket assemblies in the core in each cycle.

From equation 3, the core-average and peak (nominal) pellet discharge burnups in the fuel at the end of the 1-2, 3-4, and 5-6 cycles are 49.4 and 74.2 (fuel assembly #10), 76.9 and 110.2 (fuel assembly #37), and 78.2 and 113.8 (fuel assembly #37) MWd/kg, respectively. Similarly, the peak pellet (nominal) inner blanket discharge burnups at the end of these same cycles are 13.5 (blanket assembly #67), 23.0 (blanket assembly #67), and 24.1 (blanket assembly #103) MWd/kg, respectively. Burnup values in MWd/kg can be converted to atom percent fissioned (a/o) by multiplying by 0.106 in the fuel or by 0.090 in the inner blankets at the end-of-life.

Figures 4.3-23 through 4.3-25 show the distribution of peak-rod and assembly-average burnup\* (MWd/kg) at the end of the 1-2, 3-4, and 5-6 cycles, respectively. The location of the peak burnup rod in each assembly is indicated by the small circles in Figures 4.3-23 through 4.3-25. Radial blanket burnup was summarized for the peak and average rod in the highest-power blanket assembly in Table 4.3-11.

In-core instrumentation to determine and monitor the power density distributions (radial and axial peaking factors) associated with normal operation is not provided in the CRBRP. Both the radial and axial power distributions are relatively flat, symmetric and predictable during normal operation in a fast neutron spectrum reactor as indicated in the preceding paragraphs. Factors which contribute to the overall power flattening and symmetry in the CRBRP include: (1) the radial and azimuthal placement of fuel and inner blanket assemblies, (2) the selection of operational control rod banks to minimize perturbations in the radial power distribution, (3) operation of the control rods in the banked mode, and (4) in a fast spectrum, the absorber materials do not cause severe local flux depressions. Thermocouples located at the outlet of selected fuel and blanket assemblies are provided to monitor gross thermal power output and to detect gross asymmetric radial power distribution.

\* Burnup values in Figures 4.3-23 through 4.3-25 are total (36") rod values for the fuel and total (64") values for the inner blankets.

### 4.3.2.3 Reactivity Coefficients

Reactivity coefficients couple the response of the neutron multiplication process in the reactor to several parameters which are set by conditions external to the core such as plant conditions or operator adjustments during the steady state and transient modes of operation. The total reactivity feedback effect of these coefficients between refueling and operating conditions is termed the power defect. Since the reactivity coefficients change during the life of the core, a range of coefficients is employed in detailed simulations to determine the response of the overall plant throughout its life and to establish the design of the reactor control system and other parameters. The individual reactivity coefficients are discussed in the following sections. The analysis of accident conditions (presented in Chapter 15) uses conservative values of the appropriate reactivity feedback coefficients. In these calculations conservative assumptions are also made with regard to the modeling of the reactor conditions.

#### 4.3.2.3.1 Doppler Constants

The Doppler constant,  $T \frac{dk}{dT}$ , reflects the change in reactivity as a function of the fuel temperature. A rise in fuel temperature results in an increase in the effective resonance absorption cross sections. The predominant (strongly negative) reactivity effect is the Doppler broadening of the U-238 capture resonances, with a smaller (positive) effect attributable to the Pu-239 fission resonances. The Doppler effect is the most important negative reactivity feedback mechanism in the CRBRP. It is a prompt feedback mechanism and its large magnitude contributes significantly to the safety and stability of the CRBRP.

Figure 4.3-26 shows a flow chart for the calculation of Doppler constants in the CRBR. ENDF/B-III cross sections are collapsed from 30 energy groups to 21 in the local reactor spectrum using the XSRES and 1DX programs. These cross sections are then used in 2DB to generate flux and adjoint distributions for use in the perturbation theory program PERT-V. The integral reactivities from 2DB calculations and the integrals and distribution of Doppler reactivity from PERT-V are used to calculate the Doppler constants,  $T \frac{dk}{dT}$ , assuming a  $T^{-1}$  temperature dependence.

Table 4.3-16 shows the region-average Doppler constants ( $-T \frac{dk}{dT}$ ) for the fuel, inner blankets, radial blankets, and upper and lower axial blankets at the beginning and end of the first four cycles of operation. Cycles three and four are indicative of equilibrium conditions. The changes in region Doppler constants with burnup in Table 4.3-16 generally reflect a combination of 1) flux redistribution toward the center of the core resulting from inner blanket plutonium

buildup, 2) the mid-term row 6 refueling, and 3) control rod bank withdrawal effects. Equivalent Doppler constants at the beginning-of-cycle one and at the end-of-cycle four in a sodium-voided environment are shown in Table 4.3-17. The effect of the removal of sodium is to harden the neutron energy spectrum and substantially reduce the magnitude of the Doppler constants.

Table 4.3-18 presents a typical nodal-average Doppler distribution in the fuel, inner, and radial blankets at the beginning-of-cycle one. Each region contains a total of seven axial nodes; five equal-volume nodes in the 36-inch high "fuel" region and one node each in the upper and lower blankets (extension). The row 1 and row 2 radial blanket Doppler constants have been combined additively into a single region. This combination results in a slightly conservative (less negative) feedback reactivity due to temperature differences in the two rows of radial blankets.

Figures 4.3-27a and b show the distribution of Doppler constant by assembly in the 36-inch active fuel and inner blankets at the beginning of cycle one and the end of cycle four, respectively. The values in Figures 4.3-27a and b are condensed from three-dimensional (VENTURE) first-order perturbation theory calculations which were used to develop nodal feedback coefficient input to SAS analyses (see Chapter 15).

The temperature dependence of the Doppler constant is discussed in Reference 5. The Doppler contribution of the fissile material is a small positive effect, and generally follows a  $T^{-3/2}$  dependence. However, the U-238 contribution is strongly negative and overrides the small positive contribution from the fissile nuclides. Calculations of the temperature dependence for a series of U-238 resonances result in a Doppler temperature relationship of  $T^{-1}$ . Self-shielding effects will tend to decrease the absolute value of the temperature exponent, but for a fast reactor having a fertile/fissile content similar to CRBRP, the overall Doppler constant has approximately a  $T^{-1}$  variation.

The temperature dependence of the Doppler coefficient is in general characterized by the expression  $dk/dT = AT^{-n}$ , where the theoretical limits of  $n$  are 0.5 and 1.5 and the expected value for CRBRP and other LMFBR's is close to 1.0 (see Reference 6). Analysis of the SEFOR results (see Reference 7) indicates a value of  $n$  between 0.9 and 1.0; however, the temperature dependence of the SEFOR Doppler feedback in the range of the measurements is insensitive to the value of  $n$  for  $n$  between 0.8 and 1.2. For extrapolation to higher temperatures, calculations indicate a value for SEFOR of  $n = 1.0$ . Variations in  $n$  of 20% over the fuel temperature range of the SEFOR measurements lead to 10% variations in the Doppler feedback extrapolated from LMFBR operating conditions to HCDA conditions (see Figure 4.3-27a).

The one  $\sigma$  uncertainty in Doppler feedback reactivity due to the uncertainty in  $n$  was estimated (see Reference 7a) to be  $\sim 7\%$  for temperatures characteristic of an extreme (HCDA) accident. This uncertainty is independent of and uncorrelated with the uncertainty in the value of the Doppler reactivity constant. When estimating the total uncertainty in Doppler feedback reactivity, in accident conditions, these uncertainties should be combined statistically.

The  $\pm 7\%$  ( $1\sigma$ ) uncertainty in temperature dependence when statistically combined with the  $\pm 10\%$  ( $1\sigma$ ) uncertainty in Doppler constant (see next paragraph) yields a total uncertainty in Doppler feedback reactivity at elevated temperatures of  $\pm 12$  ( $1\sigma$ ). This additional component on the Doppler feedback uncertainty would only apply to the highly unlikely condition of an HCDA type of event. For static or operational and design transient evaluations, the Doppler feedback uncertainty is characterized by the  $\pm 10\%$  ( $1\sigma$ ) uncertainty in the CRBRP Doppler constant.

#### Doppler Uncertainty:

The uncertainty in the CRBRP Doppler Constant has been developed from the analysis of the SEFOR Core I and II experiments. The Southwest Experimental Fast Oxide Reactor (SEFOR) was constructed specifically to determine the LMFBR Core Doppler feedback through a series of power coefficient ( $\beta$ /MWth) and sub- and super-prompt transient energy coefficient ( $\beta$ /MWth.sec) measurements. SEFOR Core II had a material composition, resultant neutron energy spectrum and fuel temperature that was reasonably characteristic of that in CRBRP. The SEFOR experiments are described in, for example, Reference 8. The SEFOR Core II Doppler constant derived from these measurements ( $T dk/dT = -0.0060$ ) is in good agreement with the value of  $-0.0062$  calculated by GE in Reference 9. GE estimated the SEFOR Doppler constant uncertainty as  $\pm 9\%$  ( $1\sigma$  equivalent) in Reference 9. The principal contributions themselves, are estimated uncertainties in the fuel temperature-power relationships (fuel to coolant thermal conductance and fuel specific heat) required to extract the Doppler constant,  $-T dk/dT$ , from the measured power and energy coefficients ( $\beta$ /MWth and  $\beta$ /MWth.sec, respectively). Additional uncertainties in the extrapolation of the SEFOR power and energy coefficients to LMFBR power reactors are attributable to effects which are significantly different between the two reactors (uncertainties in fuel thermal properties, delayed neutron data, and the like are highly correlated between SEFOR and power reactors so that these uncertainties largely cancel in the normalization). The net extrapolated uncertainty in LMFBR power or energy coefficient was determined to be  $\pm 11\%$  ( $1\sigma$ ) in Reference 9. This extrapolation accounted for differences in the SEFOR and LMFBR core composition and spectrum, fuel thermal property differences, and spatial temperature and importance weighting uncertainties. The neglect of spatial temperature and importance weighting (that is, the use of region Doppler constants with average fuel temperatures) tends to (conservatively) underestimate the Doppler feedback in CRBRP. Reducing the

Reference 9 uncertainty for the already conservative neglect of global temperature-importance weighting results in an extrapolated Doppler uncertainty of less than  $\pm 10\%$  ( $1\sigma$ ) for CRBRP.

Further confirmation of the accuracy of LMFBR Doppler constant predictions is provided by the small-sample measurements in zero power critical mockups. Small, heated-sample Doppler constant measurements have been performed in the Zero Power Plutonium Reactor (ZPPR) critical assemblies simulating the CRBRP core configuration. The analysis of the Doppler constant experiments in ZPPR-2, 3, and 5 are reported in References 10, 11, and 12, respectively. Although these small-sample measurements do not represent a direct experimental determination of the total core Doppler constant, the good agreement between calculated and measured values does provide substantial confidence that the U-238 resonance parameters in the core spectrum are accurately predicted. From the total of 52 small-sample Doppler measurements throughout the core under a variety of reactor conditions (flooded, voided, control rods inserted and withdrawn, etc.), the mean calculation-to-experiment ratio is 0.98 (slightly conservative underprediction of Doppler) with an uncertainty of  $\pm 5.4\%$  ( $1\sigma$ ).

The CRBRP Doppler constant uncertainty, based principally on the aforementioned SEFOR evaluation, and supported by the small-sample measurements in ZPPR, is  $\pm 10\%$  ( $1\sigma$ ). This value is intended for use in operational and design transient evaluations within the reactor design duty cycle. The minimum Doppler feedback in anticipated design transients and the extremely unlikely class of events are based on Doppler constants with  $-2\sigma$  (80% of nominal Doppler) and  $-3\sigma$  (70% of nominal Doppler) uncertainties, respectively.

#### 4.3.2.3.2 Sodium Void Worth

The sodium void worth relates the change in neutron multiplication to the presence of voids in the sodium coolant. Small, distributed voids such as gases entrained in the coolant (see Section 4.4.4.1) are adequately treated by use of the sodium density coefficient (Section 4.3.2.3.3). The amount of entrained gas at equilibrium shall be limited to less than 1% volume to maintain reactivity changes below 5¢. (This limiting entrainment level is lower than the level that would impair reactor heat transfer to the extent that fuel lifetime would be shortened.) Large voids in a region of the reactor or complete voiding is an extremely unlikely situation. In the following discussion, the reactivity associated with this latter type of voiding is developed for use in accident analysis in Chapter 15.

Figure 4.3-28 is a flow chart showing the method for calculating the sodium voiding reactivity worth. Cross sections are processed both with sodium and without sodium to properly account for resonance self-shielding and the change in spectrum when sodium is removed.

Table 4.3-20 lists the regionwise sodium void worth at the beginning and end of the first four cycles. These data were developed from a 21 group, two-dimensional, RZ geometry core model using first order perturbation theory and serves primarily to illustrate the change in void worth distribution with burnup. The total sodium void worth is the sum of positive (moderation) and negative (leakage) components where the moderation component generally dominates in regions of little or no flux gradient (near the center of the core) and the leakage component dominates near the core periphery. The total fuel assembly void worth at the beginning of cycle one in Table 4.3-20 is nearly zero due to a near cancellation between these two terms. The maximum positive sodium void worth (sum of all positions which have a net positive worth) is also shown in Table 4.3-20. The increase in the maximum positive void worth in the fuel from \$1.51 at the beginning of cycle one to \$2.31 at the end of cycle four is attributable to the flux redistribution toward the center of the core due to plutonium accumulation in the inner blankets and due to the net fuel depletion.

Figures 4.3-29a and b show the sodium void worth distribution by assembly in the fuel and inner blankets at the beginning of cycle one and at the end of cycle four, respectively. The assembly void worth includes the 36-inch active fueled region plus the smaller contributions from the upper and lower axial blankets. These data were developed from explicit three-dimensional (VENTURE) calculations, again treating the sodium removal as a first-order perturbation. These spatial void worth distributions were developed as detailed nodal data (20 axial nodes per assembly in the fuel and inner blankets) for the third level design margin (SAS) analysis discussed in Chapter 15.

The uncertainty in sodium void worth is developed from the analysis of large-zone voiding experiments in ZPPR. This evaluation is discussed in Sections 4.3.3.5, 6, and 8.

#### 4.3.2.3.3 Sodium Density Reactivity Coefficient

The sodium density reactivity coefficient relates a change in reactivity to changes in sodium density brought about by bulk coolant temperature changes. The sodium density reactivity feedback is generally small when compared to the Doppler effect. The sodium density worth calculations were performed using 21-group, first order perturbation theory in RZ geometry. The change in sodium density with temperature was linearized over the range from 800 to 1000°F so that the sodium density reactivity feedback could be expressed in units of  $\beta/^\circ\text{F}$ . Table 4.3-21 shows the regionwise sodium density reactivity coefficient ( $\beta/^\circ\text{F}$  of bulk region coolant temperature change) at the beginning and end of the first four cycles. The distribution and



magnitude of the changes in sodium density reactivity with burnup are similar to those in the sodium void worth in Table 4.3-20. The uncertainty in the sodium density reactivity coefficient is taken to be the same as the sodium void worth uncertainty.

#### 4.3.2.3.4 Expansion and Bowing Reactivity Coefficients

Physical changes in the overall reactor configuration will result in corresponding reactivity perturbations. The reactivity coefficients discussed in this section are: (1) uniform axial fuel expansion (fuel surface temperature dependent), (2) uniform radial core expansion (inlet coolant temperature dependent), and (3) relative radial motion of fuel assemblies (bowing) resulting from a combination of temperature gradients and long-term swelling, the latter being highly dependent on irradiation history.

##### a. Uniform Axial Expansion Coefficient

The axial expansion coefficient defines the relationship between reactivity and changes in the length of the active core (fuel pellet stack height). It should be noted that the axial expansion is assumed to be dependent on the temperature at the radial surface (shoulder) of the dished fuel pellets. Implicit in this definition of the uniform axial expansion coefficient is the assumption of free movement of the fuel pellets within the clad tubes. This assumption tends to yield the largest (magnitude) coefficient insofar as degradation of the fuel pellets under irradiation will significantly reduce the magnitude of this coefficient. This effect was noted in the RAPSODIE reactor (Ref. 13).

The reactivity feedback due to core axial expansion or contraction consists of worth components from fuel and blanket expansion, stainless steel expansion, and another component for relative core/control rod motion. The fuel and steel expansion worths are determined from a perturbation technique whereby the axial expansion worth is taken to be the difference between the uniform material worth over the 36-inch active core and the material worth at the core/axial blanket boundaries. These material worth distributions are determined from a first-order perturbation theory calculation in RZ geometry. Table 4.3-22 shows the distribution of the pellet and steel components of the uniform axial expansion coefficient ( $\Delta/k$  of uniform expansion) in the fuel and blankets by radial "row" throughout the core at the beginning-of-cycle one and at the end-of-cycle four. Axial expansion of the fuel lowers the core density and removes reactivity from the system. The higher beginning of life fuel enrichment, and hence the relatively high fuel worth, results in a larger fuel expansion worth in the fresh core at the beginning-of-cycle

one than in the burned core at the end-of-cycle four. Expansion of the blankets removes absorber from the core and thereby slightly increases reactivity, except in the case of the radial blankets where the predominant effect is to lower the reflective (scattering) worth of the blanket material. Expansion of either the fuel or inner blanket steel again removes absorber from the core and increases reactivity. In addition to the direct core expansion reactivity, there is an added effect of net movement of the core with respect to the partly inserted control rods.

The axial expansion coefficients in Table 4.3-22 can be converted to  $\text{mils}/^\circ\text{F}$  using linearized material thermal expansion coefficients for fresh fuel pellet material (0.181 mils/ $^\circ\text{F}$ ) and for unirradiated stainless steel (0.425 mils/ $^\circ\text{F}$ ). However, these material expansion coefficients are expected to be a function of accumulated burnup and fluence. In the case of fuel pellet material, the mechanism of thermal expansion may vary substantially from the fresh unirradiated behavior due to pellet cracking. Consequently, the fuel expansion reactivity feedback can vary from a minimum of zero to the value calculated assuming free movement of the fuel column and thermal expansion driven by the pellet surface temperature. For this reason, fuel expansion negative reactivity feedback is generally not included in transient evaluations. At the other extreme, complete pellet-clad sticking could result in the fuel column growing axially according to the cladding temperature change. In this case, due to the higher thermal expansion coefficient for the steel cladding, the thermal growth of the fuel column in the startup transition from refueling temperature conditions to hot full power would increase approximately 20% (10% additional power defect) compared to the case of free-moving pellets. However, such global pellet-clad contact is unlikely to occur throughout the entire startup temperature transition, especially in fresh fuel where the axial expansion reactivity coefficients in Table 4.3-22 are highest. Therefore, pellet-clad sticking is not considered in the determination of the cold-to-hot temperature defect.

b. Uniform Radial Expansion Coefficient

The uniform radial expansion coefficient defines the relationship between reactivity and changes in the effective (equivalent circular) radius of the core (fuel/radial blanket boundary). The uniform radial expansion coefficient is dependent upon the change in dimensions of the lower core support structure which in turn depends on the inlet coolant temperature. This definition is convenient from a calculational standpoint since the detailed mechanical motion of the fuel and inner blanket assemblies need not be known (this detailed mechanical motion is subsequently

included in the bowing reactivity component). During the heat-up period between refueling and hot-standby temperature, the core is essentially isothermal and the uniform radial expansion coefficient is applicable.

Calculations of the uniform radial expansion coefficient for the CRBRP were performed in hexagonal geometry using the diffusion theory code 2DB with 9 energy groups. The pitch of all fuel, inner and radial blankets, primary and secondary control rods and removable radial shield assemblies is increased uniformly while at the same time the masses of structural and fuel materials are held constant. The mass of sodium necessarily increases in the expanded core. This calculational technique for the uniform radial expansion coefficient duplicates the results from three-dimensional calculations except for slight increases in axial leakage which accompany such expansions. The resulting values, expressed in terms of cents per mil of outward radial motion of the core/radial blanket boundary, are shown in Table 4.3-23 for various times-in-life. The beginning-of-cycle (hot standby startup conditions) are best characterized by the configuration with 6 Row 7 corner primary control rods inserted, whereas the end-of-cycle conditions are most nearly simulated by the all-control-rods-out configuration. The uniform radial expansion coefficients in Table 4.3-23 can be translated to units of  $\text{¢}/^{\circ}\text{F}$  change in coolant inlet temperature by multiplying by 0.415 mils/ $^{\circ}\text{F}$  which is derived from the linearized stainless steel (lower core support plate) thermal expansion coefficient. At the beginning-of-cycle-one, the reactivity change from uniform core radial expansion between refueling temperature ( $400^{\circ}\text{F}$ ) and hot-full-power conditions ( $730^{\circ}\text{F}$  inlet temperature) is  $-58.5\text{¢}$ .

c. Fuel Assembly Bowing Reactivity

In addition to structural reactivity changes associated with the uniform expansion of the fuel and blanket assemblies, additional reactivity contributions occur as a result of core assembly bowing during reactor startup and shutdown. Fuel and blanket assembly bowing is a complex function of both the local temperature and neutron flux irradiation. The temperature dependence is a function of the absolute temperature within and the temperature gradients across the assembly ducts and pins. The irradiation induced swelling and creep are complex functions of the flux magnitude and spectrum, temperature and assembly residence time.

Radial bowing reactivity coefficients are calculated for each row of fuel and blanket assemblies at various axial nodes. First-order perturbation theory calculations in RZ geometry are used to determine the material worth gradients for fuel, steel, and coolant throughout the core. The radial bowing reactivity worth coefficients, expressed in units of  $\beta$ /inch of node displacement, are determined from differences in fuel, structural and coolant edge worths simulating row-by-row radial displacements.

The radial-row model for CRBRP is shown in Figure 4.3-30. Radial bowing reactivity coefficients were generated for Rows 2 through 12; the central (Row 1) blanket assembly having a negligible reactivity contribution. Tables 4.3-24 and 4.3-25 give the radial bowing reactivity coefficients ( $\beta$ /inch of inward radial motion) for two core configurations. The beginning-of-cycle one results (Table 4.3-24) model hot-standby (initial startup) conditions and are characterized by a clean core and blankets and six Row 7 corner primary control rods partially inserted. The end-of-cycle two results (Table 4.3-25) were calculated with burned fuel assemblies, bred plutonium in the blankets, and with all 15 control rods fully withdrawn.

The predicted mechanical bowing displacements, discussed in Section 4.2.2.4.1.8.3, are superimposed on the reactivity worth coefficients in Tables 4.3-24 and 4.3-25 to determine the total reactivity feedback associated with various bowed configurations experienced by the core during the approach to power.

#### d. Uncertainty In Expansion Reactivity Worth Coefficients

Core expansion reactivity effects are difficult to simulate experimentally. However, an indirect verification of the core expansion reactivity worth calculational technique, using small-sample reactivity worth profiles in the homogeneous ZPPR-5 configuration, is discussed in Reference 14. Worth profiles from an RZ reactivity worth map, synthesized from small-sample reactivity worth traverses for major reactor materials in the fuel and blankets, are integrated to represent the reactivity worth changes due to uniform core axial and radial expansion, and thereby to deduce the "experimental" expansion coefficients. First-order perturbation theory calculations of these same expansion coefficients were compared with the experimental values in order to assess the calculational uncertainty. The experimental simulation of uniform expansion using measured small-sample worth distributions was validated by using this same small-sample worth data to predict the measured axial expansion reactivity worth of a shimmed oscillator fuel drawer in the inner and outer core zones.

Having accomplished the validation of the method for a measurable material rearrangement, the small sample traverses were used to determine an experimentally based (inferred) core expansion reactivity coefficient. First-order perturbation theory calculations of the reactor material worth distributions generally overestimated the magnitude of the worths themselves, consistent with the historically observed central worth discrepancy, but accurately predicted the shapes of the reactivity traverses upon which the expansion worth coefficients are based. The calculations of the measured expansion worth components resulted in calculation-to-prediction (C/P) ratios of 1.01 and 1.11 for axial and radial expansion, respectively. These differences are not only an indication of calculational uncertainty, but also an indication of the degree of accuracy in the measurement and integration techniques. In the expansion reactivity prediction from the small-sample traverses, two axial reactivity shapes were combined with the midplane radial worth measurements to create an RZ reactivity map from which the expansion coefficients were inferred by integration of the worth distributions over the fuel and blankets. The potential for systematic errors introduced by the approximations inherent in this technique was evaluated. The stainless steel contribution was found to be very sensitive to the location of the axial shape measurements and this was a substantial contributor to the estimated error in the radial expansion worth. In the case of the axial expansion worth coefficient, both positive and negative components were overestimated resulting in compensating errors so that the calculation and measurement agreed very well (C/P = 1.01).

Based on the ZPPR-5 measurements and analysis, the uncertainty in the calculated expansion coefficient was estimated to be  $\pm 15\%$  ( $1\sigma$ ) in Reference 14 for a clean, homogenous core configuration. This uncertainty has been increased to  $\pm 20\%$  ( $1\sigma$ ) for application to CRBRP expansion calculations to account for extrapolation effects.

#### 4.3.2.3.5 Power and Startup Coefficients and Temperature Defect

##### a. Power Coefficient

The power coefficient relates the change in reactor power level to a change in reactivity in the power operating range (40 to 100 percent of full power). The power coefficient consists mainly of Doppler reactivity feedback. The average power coefficient incorporates slower acting feedback mechanisms such as uniform radial expansion (Section 4.3.2.3.4-b) and coolant density changes (Section 4.3.2.3.3), as well as the fast-acting fuel and blanket Doppler (Section 4.3.2.3.1) and axial fuel expansion (Section 4.3.2.3.4.a). Between 40 percent

and 100% of full power, the average power coefficient is  $-0.18$   $\text{¢/Mwt}$  at the beginning-of-cycle one and  $-0.21$   $\text{¢/Mwt}$  at the end-of-cycle four. The increase in average power coefficient with fuel burnup is attributable primarily to the increase in Doppler feedback, particularly in the inner blankets.

The prompt power coefficient only incorporates the fast-acting feedback components: Doppler and axial fuel expansion. The Doppler reactivity feedback comes from both the fuel assemblies, where the fuel pellet temperature responds essentially instantaneously to changes in power and from the blanket assemblies where the feedback response is delayed due to the thermal inertia in the larger blanket rods. Fuel axial expansion, driven by the fuel pellet surface temperature, is considered as a fast-acting feedback response. The prompt power coefficient, averaged over the range of 40 to 100 percent of full power, is  $-0.15$   $\text{¢/Mwt}$  at the beginning-of-cycle one ( $-0.06$   $\text{¢/Mwt}$  when only fuel Doppler is considered) and  $-0.17$   $\text{¢/Mwt}$  at the end-of-cycle four ( $-0.05$   $\text{¢/Mwt}$  fuel Doppler only).

The hot-full-power prompt power coefficient provides the stabilizing, inherently negative, feedback mechanism in response to power level increases in the power operating range.

b. Startup Coefficient

The startup (shutdown) coefficient relates the change in power level to a change in reactivity in the startup and shutdown range from 0 to 40 percent of full reactor power. The startup coefficient includes the reactivity effect of fuel and blanket assembly bowing (Section 4.3.2.3.4-c) in addition to feedback from Doppler, uniform expansion, and coolant density changes as discussed in Item (a).

The startup profile (Appendix B) indicates that most of the core temperature gradients will be established during the interval when the reactor power is being incrementally increased from near zero to 40 percent at a constant coolant flow rate of 40 percent of full flow. Fuel and blanket assembly bowing occurs in response to the power-to-flow transitions as the core thermal gradients are established (Section 4.2.2.4.1.8.3). Above 40 percent power, the reactor power level and the coolant flow rate are increased simultaneously (power-to-flow ratio is maintained at a value of 1.0) so that no further assembly bowing occurs.

The reactor power ascent is initiated after the reactor coolant temperature has been raised isothermally from  $400^{\circ}\text{F}$  (refueling temperature) to  $600^{\circ}\text{F}$  (hot standby) using 100% primary flow (i.e. using pump work) and minimum or no reactor power. During

this initial heat-up, Doppler, uniform core expansion and sodium density changes provide a negative reactivity feedback of about -90¢ which is compensated by control rod withdrawal. Beyond hot-standby conditions, as the reactor power is increased from near zero to 40 percent (at 40% primary coolant flow), the reactor coolant inlet temperature increases from 600°F to 635°F and the 265°F core  $\Delta T$  is established. Table 4.3-26 summarizes the total feedback from Doppler, uniform radial and axial expansion, and sodium density changes between zero power (hot-standby conditions) and 40 percent power (40 percent flow). The largest negative feedback contribution in Table 4.3-26 is that from Doppler, ranging from -70.0¢ at the beginning-of-cycle one to -95.5¢ at the end-of-cycle four. The uncertainty in Doppler coefficient is  $\pm 10\%$  ( $1\sigma$ ). When the Doppler coefficient uncertainty is combined in quadrature with the temperature change uncertainties, the total uncertainty in Doppler feedback in the 0 to 40 percent power range is  $+12\%$  ( $1\sigma$ ). Uniform radial expansion only contributes about -6¢ ( $+20\%$   $1\sigma$ ) based on the coolant inlet temperature change from 600°F to 635°F. Uniform axial expansion of -17.2¢ at the beginning-of-cycle one and -8.1¢ at the end-of-cycle four includes both a negative component from fuel pellet expansion and smaller positive contributions from blanket and steel expansion. The uncertainty in axial expansion reactivity is  $+20\%$  from ZPPR -5 ( $+23\%$  when combined in quadrature with thermal uncertainties at the  $1\sigma$  level). Sodium coolant density changes contribute -1.4¢ ( $+30\%$ ) at the beginning of cycle one and +4.8¢ at the end of cycle four. The total negative feedback (excluding bowing) over the startup range from 0 to 40 percent power is therefore -94.8¢ (-76.0¢ minimum feedback with  $2\sigma$  uncertainties) at the beginning of cycle one and -105.3¢ (-81.7¢ minimum) at the end of cycle four.

56

The net bowing reactivity feedback is determined by superimposing the physical motion of the fuel and blanket assemblies (as described in Section 4.2.2.4.1.8.3) on the differential reactivity worth distributions (Section 4.3.2.3.4.c) throughout the core. The bowing reactivity response to the establishment of the core thermal gradients with increasing power-to-flow ratio (P/F) in the startup power range is characterized by an initial negative reactivity component as the assemblies bow outward and contact the TCLP (Top Core Load Pad). Further increases in P/F cause the fueled portion of the assemblies to be displaced inward toward the core centerline during which time reactivity is added to the system. The inward displacement continues until the assemblies again contact at the ACLP (Above Core Load Pad) in the upper axial blanket. From this point on, the assemblies assume an "S"-shape bowed configuration in which the fueled region of the core is again displaced radially outward and the reactivity contribution is again negative. When worst case data

57

uncertainties (maximum positive bowing reactivity coupled with minimum compensating negative Doppler feedback) are combined with conservative core compaction assumptions, the overall net startup reactivity feedback is predicted to be positive over a limited power range. The significance of this limited positive startup coefficient to reactor control and transient response is evaluated in Section 4.3.2.8 (Reactor Stability), 7.7.1.2 (Reactor Control System), and 15.1.4.5 (Reactor Assembly Bowing Reactivity Considerations). In the power operating range, from 40-100 percent of full power, no additional bowing takes place and the reactivity feedback is dominated by the strongly negative Doppler.

c. Temperature Defect

The net reactivity loss between zero-power, isothermal hot-standby or refueling temperature conditions and steady-state, hot-full-power thermal conditions is called the power or temperature defect. The temperature defect reflects the negative feedback reactivity contributions from Doppler, uniform radial and axial core expansion, sodium density changes and net negative bowing. Table 4.3-27 shows the temperature defect components in CRBRP at the beginning of the first cycle. Table 4.3-28 summarizes the net temperature defect at the beginning and end of the first four cycles of operation. The temperature defect, in part, determines the primary and secondary control rod worth (shutdown) requirements discussed in Section 4.3.2.4. The uncertainties in the temperature defect components in Table 4.3-27 reflect the statistical combination of both reactivity coefficient and temperature difference uncertainties.

4.3.2.4 Control Requirements

The reactivity control systems in CRBR are designed in accordance with the General Safety Design Criteria given in Section 3.1 and the appropriate design bases discussed in Section 4.3.1. These criteria assure that acceptable fuel design limits are not exceeded as a result of any anticipated operational occurrence or for any single malfunction of the reactivity control system.

Two independent reactivity control systems are utilized in the CRBRP. The primary system serves both a safety and an operational function. This system must have sufficient worth at any time in the reactor operating cycle, assuming the failure of any single active component (i.e. a stuck rod), to shutdown the reactor from any planned operating condition to the hot shutdown temperature of the coolant. Allowance must be made for the maximum reactivity fault associated with any anticipated occurrence. In addition, the primary



control system is designed to meet the fuel burnup requirements for each cycle as well as to compensate for criticality and refueling uncertainties. The other reactivity control system, which is identified as the secondary system, must have sufficient worth at any time in the reactor cycle, assuming the failure of any single active component (i.e., a stuck rod), to shut down the reactor from any planned operating condition and to maintain subcriticality over the full range of coolant temperatures expected during shutdown. Allowance must also be made for the maximum reactivity fault associated with any anticipated occurrence.

The primary and secondary control systems operate independently such that the capability of either system to fulfill its safety function is not dependent on the operation (or failure) of the other system. Design diversity and separation are provided to protect against common mode failures, as discussed in Section 4.2.3.

The aforementioned design criteria are interpreted to define the reactivity control requirements in terms of the minimum acceptable control capability under faulted conditions which will assure that the reactor power level can be brought down to zero at either the refueling temperature (in the case of the secondary system) or the hot shutdown temperature (in the case of the primary safety system). The faulted conditions are postulated to be the simultaneous failure of one system to scram, a stuck rod in the remaining system and a reactivity insertion resulting from the uncontrolled withdrawal of the highest worth control rod in the reactor.

The contributions to the control rod worth requirements are listed in Tables 4.3-29 and 30 for the primary and secondary systems, respectively, and are discussed in the paragraphs that follow.

a. Hot-to-Cold Temperature Defect

The temperature defect component of the control requirements compensates for the net positive reactivity insertion due to Doppler effect, radial and axial core contraction, bowing, and sodium density changes during reactor shutdown from hot-full-power to zero power isothermal temperature conditions as discussed in Section 4.3.2.3.5-c. The primary control system is designed to take the reactor temperature down from hot-full-power (including  $3\sigma$  temperature uncertainties and 15% overpower) to 550°F (the hot shutdown temperature, 600°F, less 50°F uncertainty). The secondary control system is designed to take the reactor temperature down from hot-full-power (including  $3\sigma$  temperature uncertainties and 15% overpower) to 375°F (the refueling temperature, 400°F, less 25°F

uncertainty). The largest contribution to the temperature defect comes from Doppler feedback. The uncertainties in the hot-to-cold reactivity swing, at the  $3\sigma$  level, are determined from the statistical combination of hot-full-power and shutdown temperature uncertainties with  $\pm 30\%$  Doppler coefficient,  $\pm 60\%$  for each of the radial and axial expansion feedbacks, and  $\pm 60\%$  for the sodium density feedback. Also included is a worst-case uncertainty for assembly bowing which would lead to an additional positive reactivity component (core compaction) during shutdown.

b. Excess Reactivity

The fuel enrichment requirements in CRBRP are based upon guaranteeing hot-full-power criticality at the end of each design burnup cycle as discussed in section 4.3.2.1.1 "Fuel Enrichments and Loadings." Consequently, at times-in-life other than the end of cycle, some excess reactivity is present in the reactor system. The primary control system is designed to suppress this reactivity. Fuel burnup over the cycle is the largest reactivity deficient which is included in the hot-full-power excess reactivity (fuel enrichment) requirements. Excess reactivity uncertainties include those in the burnup reactivity swing determination (primarily core conversion ratio and fission product worth uncertainties), criticality and ZPPR eigenvalue bias extrapolation uncertainties, fissile loading, core geometry and impurity concentration tolerances, and cold-to-hot temperature (power) defect uncertainties. These uncertainties are combined statistically and added to the nominal excess reactivity requirement resulting in an approximately 84% (nominal plus one sigma) confidence that the fuel loadings will supply at least enough reactivity to meet the design fuel burnup (lifetime) requirements.

The Primary control rod system is designed to suppress this planned excess reactivity plus that from uncertainties which could result in the reactor system excess reactivity being higher than planned. These uncertainties are developed at the  $3\sigma$  level and include the uncertainty in the determination of the ZPPR eigenvalue bias (section 4.3.3.3) as well as uncertainties in resonance heterogeneity, plate homogenization, streaming and ZPPR experimental eigenvalue which are treated as uncertainties in the extrapolation of the criticality bias to CRBRP. Other uncertainties include the CRBRP core fissile content tolerance and burnup reactivity swing and refueling worth uncertainties for times in life other than fresh-core, beginning of life conditions.

c. Maximum Reactivity Fault

The maximum reactivity insertion in any anticipated operational occurrence is postulated to occur upon the withdrawal of the highest worth inserted control rod from its furthest inserted to the full out position. Although mechanical and electrical systems are provided to preclude this event, the resulting positive reactivity insertion envelopes other postulated operational faults and is, therefore, imposed on the shutdown requirements of both the primary and secondary control systems.

The maximum depth of insertion of the row 7 corner primary control bank is determined by the inserted worth required to compensate for the planned excess reactivity (excess fuel loading) plus a combination of criticality

(excess reactivity) and temperature feedback uncertainties resulting in the highest (3 $\sigma$ ) anticipated excess reactivity in the system at any particular time-in-life. The maximum reactivity fault is postulated to occur upon the withdrawal of one of these row 7 corner control rods from the furthest bank insertion to the fully withdrawn position. It will be shown in Section 4.3.2.6 that the worth of a single control rod withdrawn from an inserted row 7 corner bank is substantially larger than the "average" worth of the rods in the bank due to asymmetric flux tilting effects. This fact has been verified against measurements in the CRBRP zero power, Engineering Mockup Critical (EMC) (Section 4.3.3.3). Consequently, the maximum reactivity fault is taken from the maximum excess reactivity divided equally among 6 row 7 corner inserted rods, multiplied by the rod interaction factor. Control rod interactions are further discussed in Section 4.3.2.6 and in Reference 33.

From Tables 4.3-29 and 30, the maximum control requirements for the primary and secondary control systems are determined from the direct sum of the hot-to-cold temperature defect, reactivity fault, and excess fuel loading (primary only) requirements plus the statistical sum (at the 3 $\sigma$  level) of the hot-to-cold uncertainty, criticality excess reactivity uncertainty (primary only) and the uncertainty in reactivity fault (which is correlated with the excess reactivity temperatures defect and control rod worth uncertainties). Therefore, the control rod requirements guarantee that at least enough reactivity worth will be present in each of the respective control systems at the worst time-in-life to perform their stated safety functions.

#### 4.3.2.5 Control Rod Patterns

The locations of the primary and secondary control rods are illustrated in Figure 4.3-1.

The primary control system consists of 9 control rods whose function, described in detail in Section 4.3.2.4, is to hold-down the start-of-cycle excess reactivity (plus uncertainties), to compensate for fuel burnup reactivity changes, and to provide a shutdown margin to hot shutdown temperature at any time-in-life. The principal components and design dimensions of the primary control system are grouped into banks according to their designated mode of operation. The 3 primary control rods in row 4 are designated as startup rods which are parked above the core during power operation. The six row 7 corner primary control rods constitute the burnup operating group which are partially inserted in the core throughout the cycle as dictated by excess reactivity requirements. The primary shutdown margin is provided by the three row 4 startup rods plus the remaining worth of the six, partly inserted, row 7 corner burnup rods.

The secondary control system consists of six control rods whose designated function is to provide backup shutdown capability. The principal components and design dimensions of the secondary control assemblies are described in Table 4.3-1. The secondary control rods, located in the row 7 flat positions, are fully withdrawn and parked above the core during all power operations.

Reactivity compensation is accomplished with the primary and secondary control rods by poisoning the core with neutron absorbing boron carbide ( $B_4C$ ) fully (92%) enriched in the B-10 isotope. The minimum B-10 loadings in the primary and secondary control rods are 5.08 Kg and 4.66 Kg, respectively for cycles 1-4.

Approach to power from refueling temperature, as described in the start-up power profile in Appendix B, will be accomplished by first withdrawing the six row 7 flat secondary rods to their parked positions. This is followed by

removing the three row 4 corner primary rods to their parked positions. The reactor will then be brought to critical by partially withdrawing the six primary row 7 corner operating bank rods. Subsequent power and burnup transitions are controlled by movement of this row 7 corner primary rod bank. Control rods operated in the banked-mode are ganged such that the bank, or group of rods, serves a single function. The rods in a designated bank are stepped-out successively in 0.025 inch increments in a staggered pattern such as to maintain a symmetric power distribution across the core. All the rods in a control bank are inserted within  $\pm 1.5$  inches of the nominal average bank height in the core over the full range of operating powers in order to avoid local power tilting variations in different sections of the core. The reference design lifetime for the primary and secondary control rods is 328 efpd (cycles 1 & 2). However, there is a goal to achieve a design lifetime of 550 efpd (2 equilibrium cycles). Consequently, in the control rod worth calculations in the following section,  $B^{10}$  depletion from the previous cycle is considered in the determination of the primary control system worth for cycle 4. This results in a small worth reduction (3% in R7C) compared with fresh, unburned control rods at BOC4. If fresh control rods are instead used in cycle 4, the reactivity worth of the primary control system will be somewhat higher than the values quoted.

At the beginning of the first cycle, the expected zero power (refueling temperature) critical row 7 corner control rod bank is withdrawn 15.0 inches from the bottom of the core (core/lower axial blanket interface). During the isothermal heatup from refueling temperature (400°F) to hot-standby conditions (600°F), the row 7 corner primary control rod bank is further withdrawn to 16.2 inches. In the startup power range from zero to 40% power (40% flow), the row 7 corner primary control rod bank is programmed to be withdrawn from 16.2 to 18.0 inches according to power demand and subject to the characteristics of the inherent reactivity feedbacks (including bowing) as described in Section 4.3.2.3.5-b. Above 40% power, the reactor power and primary coolant flow are increased concurrently so as to maintain a unity power-to-flow ratio. At hot-full-power, the row 7 corner primary control rod bank is withdrawn to an expected (nominal) 18.9 inches from the bottom of the core. Reactivity balance is maintained throughout each operating cycle by incrementally withdrawing the row 7 corner primary control rod bank whenever the lower limit on the control dead bank ( $\pm 2\%$  power) is reached. Primary control rod bank withdrawal histories for the first four cycles of operation are discussed in Section 4.3.2.6.

In a normal or planned shutdown, the reactor will be brought down to a low power level by inserting the row 7 corner operating control rod bank while simultaneously decreasing the coolant pump speed to 40% of full flow. Below 40% power, the coolant temperature rise across the reactor decreases until, at essentially zero-power critical, the control rods are tripped and the reactor is driven subcritical.

#### 4.3.2.6 Control Rod Worths

The locations of the primary and secondary control rod banks are shown in Figure 4.3-1. The principal components and dimensions of the control assemblies are summarized in Table 4.3-1.

##### 4.3.2.6.1 Calculational Method

The available control worths in the primary and secondary systems were calculated for a variety of control configurations as a function of time-in-life. The analytical technique used in these calculations is summarized in Figure 4.3-31. Microscopic cross sections for the primary and secondary control rods were generated from ENDF/B-4 data (Lib-4, reference 34) with the SPHINX code (Appendix A). The cross sections were self-shielded in a homogeneous control rod mixture, and collapsed to 9 energy groups in the appropriate row 4 or row 7 spectral zones of a 1D (radial) core model. Insofar as the control pin cluster in the CRBRP control rods is confined to the central portion of the assembly, the effective worth per absorber atom is lower than it would be in an equivalent system with the absorber atoms distributed uniformly over the assembly area. Homogenization of the absorber cross sections over the full hexagonal subassembly volume is therefore performed by flux and volume weighting and macroscopic cross sections in the pin bundle and surrounding duct and sodium regions using group-fluxes from a 1D transport (ANISN) calculation with a central control region surrounded by a mixture of fuel and blankets which reproduces the average CRBRP core spectrum. Homogenization preserves the isotopic reaction rates in the explicit and homogenized systems, but it does not totally preserve the control rod reactivity worth. For example, the difference between the calculated reactivity worth of a primary control rod with the absorber pin bundle envelope modeled explicitly and one with the materials simply volume homogenized is 6.1%. Transport flux weighting the cross sections reproduces 3.7% of the 6.1% worth reduction. Alternative homogenization techniques are available which improve the reactivity worth agreement between heterogeneous and homogeneous systems (including bilinear, flux-adjoint weighting), but we can have chosen to carry the residual worth difference (2.4% in the case of the primary control rods) as a bias applied to the calculated CRBRP control rod worths. Similarly, in the CRBRP secondary control rods with an even tighter absorber bundle, transport flux weighting the absorber cross sections reproduces 8.0% of the total 11.8% worth difference between explicit and volume-homogenized control rod models; the remaining 3.8% difference is applied as a bias.

The resulting macroscopic control rod cross sections are used in fine-mesh (24-mesh per hexagonal subassembly), two-dimensional diffusion eigenvalue difference calculations in hexagonal-planar geometry with the 2DB code (Appendix A) to determine the reactivity worth of the inserted control banks. The axial neutron leakage in these 2D calculations was modeled as an energy-dependent, region-dependent buckling obtained from an RZ model at each time in reactor life. At each time in life, the influence of local core burnup conditions on control rod bank worth was modeled as assembly-burnup-dependent spatial distributions of fuel and fission products. Absorber-atom depletion has only a small effect on control rod worth (on the order of 3% worth depletion per cycle) due to the strong self-shielding in the highly-enriched CRBRP control assemblies. The worth of the row 7 corner operating primary

control rod bank is determined from the eigenvalue difference between a clean core with all control rods removed (parked) and the R7C bank fully inserted. The worth of the row 4 primary bank is determined with the R7C bank inserted so that the total worth of the nine-rod primary control system (6 R7C + 3 R4) is preserved. The row 7 flat secondary control rod bank worth is determined for an initially-critical core configuration with the R7C primary operating bank partially inserted.

#### 4.3.2.6.2 Control Rod Worth Bias and Uncertainty

The nominal calculated control rod worths may contain errors attributable to methods and modeling approximations, cross section uncertainties, the use of few-group, two-dimensional diffusion theory, and others. Consequently, the control rod worth analysis methods and data are biased using calculations and measurements of control rod worths in the ZPPR critical experiments. The analysis of these experiments using CRBRP design methods and cross-section data is presented in Section 4.3.3.3, and summarized in the paragraphs that follow.

ZPPR-11 is the Engineering Mockup Critical for the CRBRP heterogeneous core. ZPPR-11B mocked up the CRBRP core at beginning of life with clean blankets. ZPPR-11C mocked up an end of life core with plutonium "depleted" from the fuel and built up in the inner and radial blankets. ZPPR-11, and the pre EMC ZPPR-7 series of critical experiments, (References 30, 31, 36), provide an extensive data base of control rod worth measurements (Reference 35) against which the accuracy of the CRBRP calculational methods and cross-section data are evaluated. Careful selection of the geometry and composition of the mockup results in a similitude between the neutronic sensitivities of the mockup and the CRBRP. Calculations of key neutron physics characteristics ( $k_{eff}$ , power distribution, control rod worth) of the mockup with CRBRP calculational methods and cross-section data result in calculation-to-experiment deviations which can reflect errors in modeling (2D versus 3D, mesh size, energy groups, ...), the use of diffusion theory, cross-section data uncertainties, reactivity scale, etc. Because of the similarities which have been established between the mockup and the power reactor, these integral parameter deviations are expected to be strongly correlated between the two reactor systems and the deviations can be extrapolated (as biases) to CRBRP physics characteristics calculated with the same methodology and cross-section data. Extrapolation uncertainties can arise from differences which still remain between the mockup and the power reactor (plate heterogeneity in the ZPPR mockup, for example, is significantly different than the more homogeneous pin fuel environment characteristic of the CRBRP).

Calculation of the ZPPR-11B control rod bank worths with two-dimensional (X-Y geometry) diffusion theory using 9-group ENDF/B-4 cross-sections (Section 4.3.3.3.7) results in calculation-to-experiment ratios (C/E) near unity in the inner (R4) control ring rod bank worths and approximately 4% greater than unity the outer ring (R7C and R7F) control rod bank worths. These values are adjusted parametrically to account for mesh-size differences in the CRBRP (24 mesh per assembly) and ZPPR (16 mesh per "assembly") control rod worth calculations. Corrections are further applied to account for the influence of direction-dependent neutron streaming (Reference 35) on the ZPPR control rod worth calculation to experiment ratios since this influence is not present to such a degree in the more homogeneous CRBRP pin environment. Control "rod" mockups in ZPPR consist of drawers filled entirely with natural enrichment  $B_{4}C$  to reproduce the reactivity worth of the CRBRP enriched  $B_{4}C$  pins. Measurements of equivalent worths of pin and plate control rod mockups in ZPPR indicate a tendency for the design methods to overpredict the worth of enriched-pin control rods relative to natural-enrichment plate mockups. The calculations of CRBRP enriched pin control rod worths are biased (reduced in worth by 1 to 5%) to cover this observed difference. The final bias multipliers applied to the CRBRP eigen-value difference control rod worth calculations are 0.912 for the row 4 (R4) bank, 0.920 for the row 7 flat (R7F SCA) bank and 0.951 for the row 7 corner (R7C) bank. The control rod worth uncertainty is developed from a statistical combination of  $\pm 2\%$  ( $1\sigma$ ) uncertainty in ZPPR control rod worth bias (Reference 35),  $\pm 3.5\%$  ( $1\sigma$ ) uncertainty in the capability of the CRBRP IKRD techniques with ex-core detectors to verify the as-built CRBRP control rod worth values (Section 4.3.2.1.5), and the  $\pm 5\%$   $B^{10}$  content tolerance. The total CRBRP control rod worth uncertainty is  $\pm 12.2\%$  ( $3\sigma$ ).

The final (biased) CRBRP primary and secondary control rod bank worths are shown in Tables 4.3-29 and 4.3-30, respectively.



#### 4.3.2.6.3 Control Rod Interactions

The control rod worths, reported in Tables 4.3-29 and 30, represent expected configurations with symmetric bank insertion patterns. Significant rod interaction effects exist between the rods within a given bank and between banks due to flux redistribution in the reactor in response to the insertion of the highly enriched poison (Reference 33). Table 4.3-31 summarizes various control rod interaction effects\* for several important asymmetric banks inserted with a stuck rod, determined from a series of parametric two-dimensional rod worth calculations with a full-core model. Of special significance is the higher worth of a single row 7 corner rod removed from an inserted bank (first-out effect) which increases the maximum worth available in a rod runout event. Figure 4.3-32 shows the variation in first-out row 7 corner rod interaction factor with depth of bank insertion. The worth of single rods inserted in a clean (or symmetrically poisoned) core are significantly lower than the average in the bank (first-in effect). The minimum worth of 5-out-of-6 secondary control rods is strongly influenced by whether the stuck secondary control rod is adjacent to the faulted primary rod which has been withdrawn (in which case the stuck secondary rod occurs in a local flux peak and is worth nearly twice as much as the average secondary rod) or opposite to the faulted primary rod (Reference 33).

Control rod interactions and flux tilting effects were investigated in ZPPR-7G (Section 4.3.3.3.6) and in ZPPR-11 (Section 4.3.3.3.7) where it was shown that control rod interaction factors (ratios of single first-in or first-out rod worths or asymmetric rod cluster worths to average rod worths in a symmetric bank) can be calculated with an accuracy better than the rod bank worths themselves. For a large number of measurements, the ratio of calculated to measured rod interaction factors was well within the stated control rod worth uncertainty.

#### 4.3.2.6.4 Stuck Rod

The control requirements specify that each of the primary and secondary control systems must perform their stated safety functions assuming the failure of a single active component. This is interpreted to be the failure of the highest worth single control rod in the system to respond to the trip signal (i.e., a stuck rod).

In the Primary Control System, for the evaluation in Table 4.3-29 of minimum control rod worth capability (with a single stuck rod) compared with maximum excess reactivity, the stuck rod must be taken to be the faulted (withdrawn) row 7 corner runout rod in order to realize the largest net reactivity deficit (fault plus stuck rod). This is not necessarily the case for design situations which do not consider a full rod runout fault (complete rod runout is not a design basis event). In the latter, the worth of one row 4 rod stuck in the parked position may be larger than the worth of a row 7 corner rod

\*Interaction defined as the ratio of the worth of a single rod, or group of rods, inserted in an asymmetric configuration relative to the "average" rod worth in a symmetric bank where, for example, the average rod worth in a 6-rod inserted bank is one-sixth of the total inserted bank worth.

stuck partly inserted. This case will be considered in the determination of minimum worth available for scram, later in this section.

In the case where the stuck rod is the faulted row 7 corner rod which has run out from some partially inserted position and sticks in the fully withdrawn position, one full row 7 corner rod is "missing" from the 9-rod primary shutdown reactivity (that is, 3 R4 and 5 R7C rods are fully inserted and 1 R7C is stuck fully withdrawn). The reactivity worth of the stuck rod/fault combination is then 1 R7C worth times a full row 7 corner interaction factor (from Table 4.3-31). The fault/stuck rod combination determined in this manner therefore effectively removes from the shutdown configuration, a reactivity equivalent to 2.3 high-worth row 7 corner rods. This is a very conservative approach for evaluating the shutdown capability of the Primary Control System. Since a fraction of this total reactivity deficit has already been accounted for in the rod runout fault, the remaining fraction associated with the stuck rod can be calculated from the following difference:

$$\text{stuck rod} = [\text{worth of average R7C rod} * \text{full first-out rod interaction factor}] - \text{rod runout fault,}$$

where the worth of the average row 7 corner rod is one-sixth of the total row 7 corner bank worth and the full first-out rod interaction factor, from Table 4.3-31, is 2.32 at beginning-of-cycle or 2.18 at end-of-cycle. This results in an entirely self-consistent definition of reactivity fault and the stuck rod worth. That is, for any smaller reactivity fault within the allowed criticality uncertainty band width, the stuck rod worth would be proportionately larger, thereby maintaining the relationship between the worth and requirement in Table 4.3-29 such that the capability will always exist for the Primary Control System to satisfy the stated design shutdown function.

For the evaluation of minimum secondary shutdown capability in Table 4.3-30, a similarly conservative approach is taken for the determination of the highest-worth stuck rod. Because of the strong asymmetry generated in the reactor flux shape by the withdrawal of one row 7 corner primary control rod from a partially inserted bank (rod runout fault), the minimum secondary shutdown capability in Table 4.3-30 is evaluated for the case where the stuck secondary control rod is adjacent to this fully withdrawn (faulted) primary control rod. The interaction factor for this configuration with two asymmetric control systems is 2.49 (Table 4.3-31); that is, effectively, the reactivity worth of 2.49 control rods are missing from the 5 R7F secondary shutdown capability due to the stuck R7F secondary rod adjacent to a primary fault. On the other hand, since the rod withdrawal fault is not a design basis event, the actual stuck rod worth interaction factor for 1 R7F, with 5 R7F fully inserted and the expected 6 R7C primary control rod bank partially inserted in a symmetric configuration, is 1.6. The latter value will be considered in Section 4.3.2.6.8 in the determination of minimum secondary control system worth available for scram.

#### 4.3.2.6.5 Minimum Shutdown Capability

The minimum primary or secondary control rod shutdown capability is determined from the difference between the control rod bank worths (less highest-worth stuck rod as determined above) and the shutdown reactivity requirements (hot-

to-cold temperature defect, reactivity fault, and system excess reactivity for the primary control rods), less  $3\sigma$  uncertainty. Consideration is given in the determination of  $3\sigma$  shutdown uncertainty for the correlation between the uncertainty in stuck rod/fault and the uncertainties in control rod bank worth, excess reactivity and temperature defect. From the data shown in Tables 4.3-29 and 30, the primary and secondary control rod worths meet or exceed the shutdown reactivity requirements, at all times in life (that is, the "balance" worth minus requirements minus  $3\sigma$  uncertainty is greater than or equal to zero), which satisfies the design criteria in Section 4.3.2.4. It should be noted that these shutdown requirements are satisfied even under the extremely pessimistic, postulated accident assumptions that: the highest worth burnup and load-follow rod is uncontrollably withdrawn, one of the two independent shutdown control systems fails to operate, and the highest worth control rod in the operating system remains stuck in the fully withdrawn position. In order to demonstrate the level of conservatism in the primary and secondary shutdown capabilities in Tables 4.3-29 and 30, the cold shutdown margin has been determined for each system, operating independently, each with a highest-worth stuck rod, but without the assumed rod runout reactivity fault. For the Primary Control System, the cold (600°F) minimum shutdown margin (nominal minus  $3\sigma$ ) at the beginning of equilibrium cycle (BOC3), where the excess reactivity is highest, is 1.7%Δk/k (approximately \$4.9) with 6 R7C + 2 R4 primary rods inserted and 1 R4 stuck full out. Similarly, for the Secondary Control System, the cold (400°F) minimum shutdown margin (nominal minus  $3\sigma$ ) for the same time in life is 1.6%Δk/k (\$4.6) with 5 R7F rods inserted in a symmetrically-shimmed core with 6 R7C primary control rods partially inserted. In both of these cases, the minimum shutdown margin substantially exceeds 1%Δk/k as an alternate shutdown criterion.

#### 4.3.2.6.6 Integral Worth Curve

The integral rod worth characteristic curve, fraction of worth inserted vs. rod bank distance inserted, over the operating range of fully inserted to fully withdrawn is presented in Figure 4.3-33. The integral rod worth is approximately a  $\sin^2$  function of rod bank height. The integral worth curve has been verified against measurements in the Engineering Mockup Critical, ZPPR-11 (Section 4.3.3.3.7).

#### 4.3.2.6.7 Primary Control Rod Withdrawal Histories

The primary control rods serve both as a burnup operational control system and as the primary shutdown system. The fraction of the total primary system reactivity worth which is available for shutdown increases over a cycle as the rod banks are withdrawn to compensate for fuel burnup. The lowest available hot-full-power primary shutdown reactivity worth occurs at the beginning of each burnup cycle when a relatively large fraction of the primary system control worth is inserted to suppress the start-of-cycle excess reactivity.

Figures 4.3-34 and 35 show the row 7 corner (hot-full-power) primary control rod bank withdrawal histories for the first core (Cycles 1 and 2) and the second core (Cycles 3 and 4). Control rod histories are shown for the following conditions:

- a. Expected control worths (nominal calculation) and nominal insertion requirements at the beginning and end-of-cycle (that is, nominal excess reactivity, hot-to-cold temperature defect, burnup reactivity swing, etc.). These conditions result in the best estimate of the "expected" hot-full-power critical rod insertion depths and rod withdrawal histories throughout each cycle.
- b. Minimum primary control rod worths and maximum insertion requirements (nominal excess reactivity plus the statistical sum of  $3\sigma$  criticality, rod worth, and other uncertainties which results in the highest excess reactivity at any time in the operating cycle). These hypothetical conditions would result in the maximum primary control rod bank insertion, and the minimum shutdown margin, at any time in life.

There is an additional  $\pm 1.5$  inch uncertainty on the position of any single R7C primary control rod with respect to the other rods in the bank.

#### 4.3.2.6.8 Minimum Worth Available for Scram

Table 4.3-32 lists the hot-full-power expected and  $3\sigma$  minimum shutdown worth (with a stuck rod), as determined above, for the primary and secondary control rod systems at the beginning of the first five cycles. Also shown in Table 4.3-32 are the expected and maximum hot-full-power row 7 corner primary control rod bank insertion depths. The row 4 and row 7 flat (secondary) control rods are fully withdrawn during each cycle as discussed in Section 4.3.2.5. The hot-full-power scram worths in Table 4.3-32 are developed for use in design transient analyses which do not assume a complete rod runout fault. As such, the primary stuck rod is 1R4 stuck full out or 1R7C stuck partly inserted. Furthermore, the stuck secondary rod does not see the enhanced interaction factor associated with a faulted primary rod which is fully withdrawn. Throughout a burnup cycle, the available primary shutdown capability increases as the row 7 corner primary control rod bank is withdrawn from the core to compensate for fuel burnup and fission product accumulation. This is demonstrated by the high EOC4 shutdown worth in Table 4.3-32. The row 4 and row 7 flat (secondary) shutdown capability also increases somewhat over the course of a burnup cycle in response to blanket plutonium buildup and flux redistribution effects. The smallest shutdown worth in Table 4.3-32 occurs in response to a combination of the highest excess reactivity requirement and the lowest control rod worths at the beginning of cycle three. This minimum shutdown worth is conservatively used to evaluate the capability for the control rod systems to meet limiting scram insertion requirements (Section 4.2.3) and for the evaluation of limiting thermal transient conditions (Chapter 15) with minimum control rod negative reactivity worth insertion.

#### 4.3.2.6.9 Minimum, Zero Power Subcriticality with 15 Control Rods Inserted

A minimum subcritical shutdown capability at zero power, refueling temperature conditions can be defined from the minimum primary and secondary control rod worths and the maximum excess reactivity (conditions similar to the minimum shutdown margin discussed above except that both the primary and secondary rod banks are inserted and no stuck rod worth is included). The resulting minimum subcritical shutdown, with all 15 control rods inserted at refueling

temperature (400°F), is  $K_{eff} = 0.937$  at the beginning of cycle one and  $K_{eff} = 0.947$  at the beginning of cycle three (equilibrium). The expected subcritical shutdown capability at times in life other than beginning of cycle is substantially higher than these minimum values (that is,  $K_{eff}$  is less than the quoted values).

#### 4.3.2.6.10 Maximum Ramp Reactivity

The highest worth single control rod in any hot critical state in CRBRP is a row 7 corner primary control rod. The control system operating mode is limited to the removal of only one control rod at a time. The nominal design rod withdrawal rate is 9 inches per minute, although a rod could be driven out of the core at a maximum rate of 73 inches per minute in the event of a controller failure. Control rod outmotion in the unlatched condition is not considered credible, as is discussed in Section 4.2.3, and in any event would be limited by the out-motion pawl. An uncontrolled withdrawal of the highest worth control rod (the nominal calculated rod worth with the high side 3 uncertainty and the maximum B-10 content) at ramp runout rates of 9 and 73 inches per minute ("anticipated" and "extremely unlikely" class accidents, respectively) would result in peak reactivity insertion rates of approximately 2.3 and 18.5  $\beta$ /sec, respectively, at the highest point on the differential worth curve near the core midplane.

#### 4.3.2.7 Criticality of Fuel Assemblies

Two aspects of the criticality of fuel assemblies are discussed in this section. First, the uncertainty in the prediction of the absolute eigenvalue for CRBRP is considered. This result has a direct impact on the calculation of the feed enrichments and the control shutdown margins for the first and equilibrium cycles. Second, the criticality of small bundles of fuel assemblies is discussed in detail. These results impact the safety-related aspects associated with the determination of the minimum number of fuel assemblies required for criticality.

##### 4.3.2.7.1 Reactor Eigenvalue Prediction

The uncertainty in the CRBRP eigenvalue prediction is obtained from analysis of zero power fast critical assemblies which mockup the composition and geometry of the CRBRP core. One major difference between the experimental configuration and the CRBRP core is the use of fuel plates in a square lattice in place of the cylindrical fuel pins in a hexagonal array. Another difference is the extrapolation of the room temperature reactivity, obtained in the critical assembly, to that expected in the hot-full-power reactor.

The accuracy of design eigenvalue calculations is evaluated by a comparison of calculated and measured criticality in ZPPR. Table 4.3-33 lists selected measured and calculated room temperature eigenvalues ( $k_{eff}$ ) for several ZPPR experiments modeling both homogeneous (ZPPR-4) and heterogeneous (ZPPR-7) core configurations. Using the CRBRP design method (coarse-mesh, XY diffusion theory in this case) and data (ENDF/B-III cross-sections in 9 energy groups)

results in a systematic underprediction of the reactor eigenvalue with an average C/E ratio of  $0.996 \pm 0.003$  in the homogeneous systems and  $0.990 \pm 0.002$  in the heterogeneous systems. The inverse of the average C/E ratio is applied as a bias in the calculation of CRBRP criticality (using the same calculational methods and data base) and the  $1\sigma$  variation is included as an uncertainty in the start-of-cycle excess reactivity requirement. In order to use such an eigenvalue bias, one must consider the sensitivity of the eigenvalue to particular ZPPR parameters (plate heterogeneity correction as discussed in Reference 16, streaming and the like) which are not present in the power reactor and which may therefore introduce errors in the extrapolation of the ZPPR-bias to the power reactor. Consequently, an additional uncertainty of  $0.2\% \Delta k$  is included to account for potential systematic uncertainties in the  $k_{eff}$  bias arising from extrapolation of the heterogeneous plate-geometry ZPPR  $k_{eff}$  bias to the nearly homogeneous pin-geometry power reactor.

In order to establish the criticality of the hot-full-power CRBRP, a cold-to-hot temperature defect correction is applied to the cold-critical eigenvalue. The temperature defect accounts for the net reactivity loss from Doppler feedback, radial and axial core thermal expansion, sodium density changes, etc., in the escalation to hot-full-power conditions. The calculation of the temperature defect is discussed in Section 4.3.2.3.5. The uncertainty in the components of the temperature defect are combined statistically with the cold criticality uncertainty to establish the overall uncertainty in the hot-full-power reactor eigenvalue.

#### 4.3.2.7.2 Minimum Critical Configuration

The highest expected fuel enrichment under equilibrium cycle conditions in CRBRP with low-240 grade plutonium fuel is 33.1 weight percent. Consideration of worst-case criticality uncertainties, highest fissile content tolerance, and simultaneous refueling of the entire core (including fuel, inner, and radial blankets) results in a 35.0 weight percent fuel enrichment envelope. A cluster of fresh fuel assemblies with the maximum fuel loading would contain a minimum number of assemblies required to achieve a critical configuration. Critical eigenvalue calculations were performed for various numbers of these maximum enrichment fuel assemblies in a regular hexagonal array spaced with a reactor pitch corresponding to refueling temperature. The assembly cluster was assumed to be immersed in a sodium pool with no control or blanket assemblies. One-dimensional  $S_4$ , Po, 21-group fundamental mode eigenvalue calculations were performed in ANISN to determine  $k_{eff}$  as a function of the number of fresh fuel assemblies in concentric annular rings. Axial leakage was modeled by buckling factors determined from two-dimensional, RZ geometry, diffusion theory calculations.

Figure 4.3-40 shows the variation in  $k_{eff}$  with cluster size (number of assemblies) with and without sodium in the system. The number of high enrichment fresh CRBRP fuel assemblies required to achieve criticality, interpolated between the 19 and 37-assembly calculations, is about 27. Removal of sodium inside and surrounding the fuel cluster increases the neutron leakage and significantly reduces the multiplication constant (by about 20% for the 27-assembly cluster in Figure 4.3-40).

#### 4.3.2.8 Reactor Stability

Linear system techniques are usually used to establish reactor stability. Stability predictions based on linearity assumptions are valid for small variations about operating points for a reactor model which includes non-linear reactivity feedback effects. Stability of the system for large variations about the operating point may be inferred if the linear analysis demonstrates that the system is stable at operating points throughout the operating range.

In a model containing a nonlinear reactivity feedback resulting from reactor assembly bowing, the assumptions of linearity may not be valid in predicting stability. In fact, a linear analysis of the system may predict a divergent condition at some localized operating points (where the bowing coefficient is positive); however, the system will actually be stable, since it exhibits self mitigating behavior.

A linear analysis of the reactor is presented in Section 4.3.2.8.1. The reactivity feedback due to reactor assembly bowing is ignored in this analysis. This is a valid (and conservative) assumption for small variations about a power to flow ratio (P/F) equal to one since the bowing feedback coefficient is negative for  $P/F > 0.7$ . In the power operating range (40 to 100% power) P/F is maintained at one by either the automatic control system or the operator.

In Section 4.3.2.8.2 a more general stability criterion (bounded input<sup>2</sup>-bounded output) is applied in a reactor stability analysis which includes the nonlinear effect of reactor assembly bowing. In this analysis the bounded input is a step reactivity perturbation which is applied to the reactor simulation. The reactor power, maximum fuel, maximum clad and coolant temperatures are the output variables which are found to be bounded within acceptable steady state levels.

Taken together, both the linear and general analyses

establish reactor stability over the normal operating range.

#### 4.3.2.8.1 Linear Stability Analysis

The CRBR is neutronically tightly coupled and is amenable to point-kinetic analysis for stability. The reactor is modeled by a set of coupled linearized first-order differential equations with constant coefficients describing the neutronics and temperature behavior of the system. The equations which describe the neutron kinetics are:

$$\frac{dn^*}{dt} = -\frac{\beta_T}{\ell} n^* + \sum_{i=1}^6 \lambda_i C_i + \frac{n^o}{\ell} \sum_{j=1}^{63} \alpha_j T_{j*} + \frac{n^o}{\ell} \delta k_e \quad (1)$$

$$\frac{dC_i}{dt} = \frac{\beta_i}{\ell} n^* - \lambda_i C_i \quad i = 1, 6 \quad (2)-(7)$$

The following notation is used:

$n^*$  Instantaneous neutron density (normalized power)

$\beta_T$  Total delayed neutron fraction,  $\beta_T = \sum_{i=1}^6 \beta_i$

$\ell$  Prompt neutron lifetime (sec.)

$C_i$  Concentration of precursors for the  $i^{\text{th}}$  delayed neutron group (normalized),  $i = 1, 6$

$\lambda_i$  Decay constant of precursors for the  $i^{\text{th}}$  delayed neutron group ( $\text{sec}^{-1}$ ),  $i = 1, 6$

$n^o$  Steady-state neutron density (normalized power)

$\alpha_j$  Temperature feedback coefficient ( $\Delta k/^{\circ}\text{F}$ ),  $j = 1, 63$

$T_{j*}$  Temperature ( $^{\circ}\text{F}$ ),  $j = 1, 63$

$j$  Number of temperature feedback coefficients used in the nodal model

$\delta k_e$  Externally applied reactivity perturbation



The equations describing the temperature dependence in the reactor are a simplified version of the ones in the computer code DEMO (Appendix A). All coefficients are assumed constant at nominal full-power conditions. The average channel in the core is modeled with seven axial nodes, one each for upper and lower axial blankets and five evenly spaced nodes in the fuel region. Radially, three nodes are used; one in the fuel, one in the clad, and one for the sodium coolant temperature at the node exit. Inner and radial blankets are modeled with seven evenly spaced axial nodes. Radially, three nodes are used; one in the fuel, one in the clad and one for the sodium coolant temperature at the node exit. The equations described thus treat only internal reactivity feedback mechanisms. Specifically, the effect of control system response, operator intervention and plant system operation resulting in variation in inlet coolant temperature and flow, are not included.

The above set of linear first-order differential neutronic and thermal equations is mathematically expressed as:

$$\dot{\underline{X}} = \underline{A} \underline{X} + \underline{b} \delta k_e \quad (8)$$

where  $A$  is a 70 x 70 matrix. The feedback network of this system is shown in Figure 4.3-41. The various reactivity coefficients used in the analysis are discussed in Section 4.3.2.3.

The criterion for absolute stability is based on Liapunov's "first method" (Ref. 17) which reduces the problem of determining the stability of the system to that of finding the eigenvalues of the matrix  $A$  of equation (8)\*. If the real part of all roots is negative, the system is stable. Conversely, if the real part of any root is positive, the system is unstable. The GASA program (Appendix A) is used to determine the eigenvalues of matrix  $A$  of equation (8).

The GASA program is also used to generate transfer functions for various combinations of reactivity feedback coefficients. The transfer functions at beginning and end of equilibrium cycle are shown in Figures 4.3-42 through 44. Normalization is at 100 Hz to zero decibels (DB) since at that frequency all feedback effects have negligible effect and the -20DB/decade roll-off due to the finite prompt neutron lifetime has not become apparent. The stability analysis was performed for an early version of the CRBRP heterogeneous core configuration in which the predominant negative Doppler feedback was slightly smaller than in the current design. The results of the stability

\* The eigenvalues of matrix  $A$  are identical to the roots of the characteristic equation of the system.

analysis presented herein are therefore somewhat conservative and the qualitative characteristics and the inherent reactor stability are valid. The interpretation of the transfer functions for the various reactivity feedback coefficient combinations is presented below.

a. Zero Power-Zero Feedback Transfer Function

The transfer function of the system at zero power with no feedback is shown in Figure 4.3-42, Curve A. The characteristic equation has one root equal to zero, which shows up in the -20DB/decade slope of the curve at low frequencies; i.e., the system acts as a pure integrator at low frequencies. Therefore, the system is unstable at zero frequency. This is expected since zero frequency corresponds to a constant reactivity insertion. In a system with no feedback, the power will increase indefinitely, thus invalidating the zero power transfer function. The utility of curve A is that it provides a basis to compare the stabilizing effect of feedback effects. A transfer function of lower magnitude than that of the zero power transfer function will be more stable and one of larger magnitude will be less stable at the particular frequencies where these differences occur.

b. Sodium Density Feedback

The transfer function of Figure 4.3-42, Curve B, results if credit is taken for the sodium density feedback only. The system is stable since all roots of the characteristic equation have negative real parts. This transfer function, which includes only the smallest negative feedback mechanism, already results in a noticeable improvement in stability as compared to the zero-power, zero-feedback transfer function.

c. Axial Expansion Feedback

Considering only the negative feedback due to axial expansion of the fuel (active core region only) results in the transfer function shown in Figure 4.3-42, Curve C. This feedback effect is noticeably stronger than the sodium expansion feedback.

d. Doppler Feedback

Curves D and E (Figure 4.3-42) depict transfer functions obtained when only the Doppler feedback is considered, with Curve D, representing the case where credit was taken for only half the nominal Doppler feedback, and Curve E, the case where the nominal Doppler feedback was used. It is apparent that the Doppler constant represents the strongest feedback mechanism, even taken at half its nominal value.

e. Nominal Doppler, Sodium Density, and Axial Expansion Feedback

The transfer function for all the nominal feedback coefficients is shown on Figure 4.3-42, Curve F, which shows excellent, stable frequency response characteristics. This is mainly due to the strong stabilizing effect of the Doppler constant as can be seen by comparing Curve F with Curve E. This case includes all the nominal feedback coefficients (Figure 4.3-41) and represents a high degree of stability.

f. Nominal Doppler Feedback

Figure 4.3-43 shows several transfer functions previously discussed along with the transfer function with Doppler feedback alone. The amplitude scale has been expanded by a factor of 10 to better show the effects of Doppler only, Curve A, compared to the case of Doppler and sodium expansion feedback, Curve B, and the case of all nominal feedbacks, Curve C. These curves clearly show the dominance of the Doppler effect.

g. Reactor Assembly Bowing Feedback

The reactivity feedback due to reactor assembly bowing is a function of power to flow ratio (P/F) as discussed in Section 4.2.2.4.1.8.3 and in Sections 4.3.2.3.4 and 5. From Figure 4.2-92B the slope of the reactivity curve, with worst-case uncertainties, is positive over a limited range, but again turns negative above P/F equal to about 0.7. This implies that the bowing reactivity feedback coefficient is negative above that point. The nominal P/F ratio is maintained at a value of 1.0 above 40% power so that no further bowing occurs. Neglecting the effect of this coefficient is conservative for variations in power of up to 30% or variations in flow up to 42% about nominal reactor operating power and flow levels. The stability predictions for the nominal power operating range are not affected by neglecting bowing feedback.

The results of Figure 4.3-44 are obtained with reactor neutronic parameters that exist at EOC4. The net feedback from sodium density in this case is slightly positive. The counteracting negative feedback components are from the Doppler effect and the axial expansion.

a. Doppler Feedback

The transfer function for Doppler feedback only is shown in Figure 4.3-44, Curve A, to provide a comparison with the other transfer functions.

b. Sodium Density (Twice Nominal) and Doppler Feedback (Half Nominal)

For the transfer function of Figure 4.3-44, Curve B, credit is taken for only half of the nominal negative Doppler, whereas the positive sodium density feedback is taken at double its nominal value. The system is stable and the transfer function has acceptable frequency response characteristics. Clearly, the effects of the Doppler feedback, even taken at a value well below the smallest value expected, is dominant.

c. Nominal Doppler, Sodium Density, and Axial Expansion Feedback

The transfer function for all the nominal EOC4 feedback coefficients is shown in Figure 4.3-44, Curve C, which shows excellent, stable frequency response characteristics.

Thus, for a wide range of variation of feedback coefficients, the CRBR is a stable, well-behaved system in the response of the reactor to reactivity perturbations. The main stabilizing feedback is due to Doppler, and even at half-nominal value, in any combination with the other feedback coefficients, a stable system results.

4.3.2.8.2 General Stability Analysis (Bounded Input-Bounded Output)

In the startup range ( $0^+$  to 40% power), P/F varies between 0 and 1.0. In this range, the bowing reactivity feedback is nonlinear, varying from positive to negative with increasing power/flow ratio as described in Sections 4.2.2.4.1.8.3, 4.3.2.3.4 and 4.3.2.3.5. Its change with power/flow ratio is sufficiently significant so that its impact on reactor stability must be established. The stability criterion which has been applied in this analysis is the following:

The system is stable if the system output is bounded for a given bounded input, the system is unstable if the system output is unbounded for a given bounded input (Ref. 18). The system is stable in the practical sense if the system output is bounded within acceptable parameter levels (Ref. 19).

Figure 4.2-92C illustrates bowing reactivity responses which were predicted using nominal data and with maximum analytical uncertainties applied. The maximum positive bowing reactivity feedback effect is obtained when a positive reactivity perturbation is introduced at an operating point corresponding to the low end of the positive slope portion of the bowing reactivity vs. power-to-flow ratio curve. To this end, bowing reactivity functions which closely approximated the results in Figures 4.2-92B and 4.2-92C were input into the FORE-2M reactor kinetics and feedback model.

Figures 4.3-46 through 49 illustrate key reactor responses during an inherent response transient (no control or PPS action) initiated at a reactor startup operating point (9% power; 40% flow) at which the reactivity insertion due to bowing would be maximum. The transient was initiated by a +2% step reactivity perturbation.

The responses illustrate that all parameters rise initially due to the dominance of positive bowing reactivity at low power-to-flow ratios. However, when the bowing reactivity coefficient becomes negative at higher power-to-flow ratios, all parameter responses change slowly and approach a new stable equilibrium state. The final values of the parameters are shown in Table 4.3-34 together with acceptability limits.

It is concluded that if the limits for acceptability (Table 4.3-34) are selected so as to remain below reactor parameter severity levels associated with a major incident (Table 15.1.2-1), and parameter responses remain below acceptability limits, the reactor is stable in the practical sense and inherent reactor protection shall have been demonstrated.

Additional reactor stability (inherent response) transients have been evaluated which were initiated at other operating states (i.e., reactor flow, reactor power, etc.). All of these indicate the response characteristics typically exhibited in Figures 4.3-46 through 4.3-49 and were bounded by the acceptability levels of Table 4.3-34.

As a result of these studies, it is concluded that the reactor is stable given the bowing reactivity characteristics exhibited in Figure 4.2-92a since all transient responses are bounded for a bounded input perturbation. Furthermore, the reactor is stable in the practical sense since the maximum values of key reactor variables are below levels which are considered acceptable for the reactor when responding to its inherent feedbacks. Therefore, reactor inherent protection is demonstrated and Criterion 9 is satisfied.

#### 4.3.2.9 Vessel Irradiation

The spatial and energy dependent neutron flux distributions are utilized in obtaining the irradiated characteristics of the reactor structural materials and components. One application of this flux data is in determining the total and fast fluence received by both replaceable and non-replaceable reactor components. The neutron fluence must be limited so that the end-of-life ductility for structural materials exceeds the specified minimum requirements.

Assembly-by-assembly radial neutron flux distributions (assembly-average in the central 36-inch active core height) are given in Figures 4.3-50 and 51 for core conditions reflecting the beginning of cycle one with the six row 7 corner primary control rods partly inserted and with fresh fuel and clean blankets, and for the end of cycle four conditions with all control rods fully withdrawn and with plutonium burned out of the fuel and built up in the blankets. Values are shown in Figures 4.3-50 and 51 for both the total neutron flux and for the fraction of the flux with an energy greater than 0.11 MeV. The latter reflects the relative spectral behavior throughout the core. The shift in the critical flux shape toward the center of the core with increasing burnup, and the spectral hardening in the blankets, is evident by comparing the fluxes in Figure 4.3-50 at the beginning-of-life with the end-of-life fluxes in Figure 4.3-51. Figures 4.3-52 and 53 show typical axial distributions of the total flux and the fast flux fraction in the core. These axial distributions are normalized to 1.0 over the central 36-inch active core height such that the product of the axial shape factors in Figures 4.3-52 and 53 with the fluxes in Figures 4.3-50 and 51 results in the three-dimensional flux distribution throughout the central core and blankets. The total flux in Figure 4.3-52 exhibits the typical bell-shaped axial distribution. Figure 4.3-53 indicates that the neutron energy spectrum (as measured by the fraction of the flux with an energy greater than 0.11 MeV) is relatively flat throughout the central core and degrades rapidly through the axial blankets. These radial and axial flux and spectrum distributions were obtained from two-dimensional, 21-group diffusion calculations in hexagonal-planar and RZ geometry, respectively.

The peak total and fast ( $E > 0.11$  MeV) fluxes in CRBRP ( $5.5 \times 10^{15}$  n/cm<sup>2</sup> sec and  $3.4 \times 10^{15}$  n/cm<sup>2</sup> sec, respectively) occur in the rows 7 and 8 fuel cluster around the row 7 corner primary control rods.

The peak total (fast) fluences in the fuel and inner blanket assemblies have been determined for cycles one and two (first core) and for the subsequent equilibrium cycles. The first-core peak total (fast) fluences for the fuel and inner blanket assemblies are  $1.47 \times 10^{23}$  ( $9.20 \times 10^{22}$ ) neutrons/cm<sup>2</sup> and  $1.46 \times 10^{23}$  ( $8.66 \times 10^{22}$ ) neutrons/cm<sup>2</sup>, respectively. For the equilibrium core, the peak total (fast) fluences of the fuel and inner blanket assemblies are  $2.38 \times 10^{23}$  ( $1.45 \times 10^{23}$ ) neutrons/cm<sup>2</sup> and  $2.29 \times 10^{23}$  ( $1.35 \times 10^{23}$ ) neutrons/cm<sup>2</sup>, respectively. The most conservative estimate of the neutron flux at the reactor vessel boundary is obtained at the beginning of equilibrium cycle. Later in life, the flux has shifted toward the center of the core and away from the core periphery in response to the inner blanket plutonium buildup, and therefore, the corresponding vessel fluxes would be somewhat lower. Table 4.3-35 summarizes the flux and spectrum data for the core, core and shield boundaries, core barrel, and the reactor vessel wall at the beginning of equilibrium cycle.

#### 4.3.3 Analytical Methods

Each preceding section described briefly the neutron data and computer codes used in the analysis. In most cases, calculational flow diagrams were presented for the particular analysis. This section describes the overall analytical techniques used in analysis of CRBRP and the supporting critical experiments performed in the ZPPR assemblies.

##### 4.3.3.1 Analytical Approach

The CRBRP analytical methodology is summarized in Figure 4.3-54. Specific details about the development of particular nuclear characteristics were discussed in the preceding subsections. The core mockup experiments in ZPPR are analyzed with the same CRBRP design methods and cross-section data as described in Figure 4.3-55.

The multigroup cross-section libraries for CRBRP (or for ZPPR) are developed using the Bondarenko formalism (Reference 20). A generalized cross-section file, consisting of infinitely dilute fine-group cross sections, inelastic scatter transfer matrices, and temperature dependent self-shielding factors as a function of  $\sigma_0$  (the total cross-section per atom), is obtained from the ENDF/B-III data file by way of the MINX\* or ETOX\* code. Using atom densities

\* Appendix A contains computer code abstracts.

and cell models from the reactor or critical assembly, resonance self-shielding factors are calculated in the SPHINX\* (XSRES) resonance module for each isotope as a function of temperature and non-resonant total cross-section ( $\sigma_0$ ) using an iterative scheme whereby the self-shielding factors are used to calculate  $\sigma_0$  for the mixture and  $\sigma_0$  and temperature are then used to interpolate new self-shielding factors. A Dancoff correction is applied to the cross-sections using Sauer's approximation for a cylindrical fuel pin in a hexagonal lattice (reactor design calculations) or Bell's approximation for plate lattices (critical assembly calculations). The resulting cross-sections are corrected for elastic removal and collapsed (condensed) to the desired few-group structure (9 or 21 neutron energy groups are generally used in CRBRP nuclear design calculations) in the SPHINX\* (IDX) diffusion module. Both the elastic removal correction and group condensation are performed over the local reactor spectrum obtained from a one-dimensional (cylindrical or slab) diffusion calculation. Due to the size of the fuel plates in the ZPPR criticals, these cross-sections are further corrected for the in-cell fine structure in the flux by applying spatial flux-weighted cell homogenization factors obtained from one dimensional SPHINX\* (ANISN) transport calculations with  $P_0$  scattering and  $S_{16}$  quadrature.

The resulting 9 and 21-group master cross-section libraries are employed in the W-2DB\* code in both hexagonal-planar and cylindrical (RZ) geometry to determine critical reactor eigenvalue ( $k_{eff}$ ), radial and axial power and flux distributions, and control rod worth parameters and to perform burnup (depletion) calculations. Reactor depletion and power distribution calculations are performed in two-dimensional hexagonal geometry with each of the fuel, inner and radial blanket assemblies modeled as a separate burnup zone in order to accurately model the spatial dependence of the fuel depletion, and blanket plutonium accumulation. Axial leakage in the hexagonal calculations is modeled as a  $DB^2$ -type absorption cross section with a region-dependent, group-independent buckling determined from an equivalent RZ geometry calculation at the beginning and end of each cycle. Using these depletion models, control rod worth parameters are determined using 2DB eigenvalue difference calculations for a variety of reactor configurations as a function of time in life. Reactivity feedback coefficients, such as Doppler constants and sodium void worth, are calculated using first-order perturbation theory (PERT-V)\* and forward and adjoint flux distributions from RZ 2DB calculations.

\* Appendix A contains computer code abstracts.



There are particular areas in the nuclear design process where the two-dimensional synthesis methods are known to be lacking due to spatial inseparability. One of these areas is the prediction of the local power distribution in the vicinity of partly inserted control rods as described in Section 4.3.2.2. Another area is the determination of the sodium void worth distribution throughout the core for input to design-limiting (margin) safety analyses (Section 4.3.2.3.2). In these particular areas, three-dimensional methods with the VENTURE\* code (Reference 21) have been employed for the analysis of benchmark design problems.

#### 4.3.3.2 Neutron Cross Section Data

The cross section data used in the CRBRP nuclear design calculations is obtained from the ENDF/B-III data file. A description of the Evaluated Nuclear Data File/B Version III is given in Ref. 15. The ENDF/B-III pointwise data and resonance parameters were processed by the ETCX code (Appendix A) at HEDL and supplied as punched-card output in the Bondarenko format for final processing as described in the preceding section. The 30 neutron energy group structure consists of basically 0.5 lethargy width groups with some subdivisions to handle the principal resonance structure of the diluents Na, Fe and O. Details of this group structure and that of the condensed 9- and 21-group sets are shown in Table 4.3-36.

The inclusion of axial and radial blankets is a primary design feature of LMFBR's. Therefore, the prediction of in-core gamma heating has become an important post-FFTF LMFBR design problem. LMFBR gamma heating is calculated for CRBRP by the neutron-gamma coupled diffusion method in which the coupling between neutron and gamma groups, which occurs due to gamma production by way of neutron interactions, is mathematically represented in the cross sections in the scattering matrix. The scattering matrix contains gamma energy yield data from fission, capture and inelastic scattering sources. The gamma energy yield cross-section matrix is developed and coupled with a neutron cross-section data set, producing an N plus G group master cross section library in a module of SPHINX\*. The SPHINX neutron-gamma coupling libraries currently contain data from three basic sources: (1) Westinghouse's local coupling library designed for use in the APPROPOS\* code, (2) ENDF/B-IV coupling data processed through AMPX by ORNL, and (3) particle energy release data (MeV/fission) from M. F. James (Reference 22).

\* Appendix A contains computer code abstracts.

#### 4.3.3.3 Critical Experiments in Support of CRBRP

The LMFBR design methods and cross section data are verified by direct comparison of calculated parameters with integral measurements in critical mockup experiments. In the following sections, we will discuss the historical application of these integral experiments as benchmarks against which the accuracy of the design methods and data are evaluated and design bias factors and uncertainties are developed for application to the CRBRP (Reference 23).

#### 4.3.3.4 ZPPR Assembly 2 and ZPR-6 Assembly 7

ZPPR Assembly 2 was the first demonstration plant benchmark critical assembly. It was designed in accordance with the general LMFBR design features envisioned by the major LMFBR contractors, including Atomics International, General Electric and Westinghouse Electric Corporation. The experimental program was developed by the Argonne National Laboratory for pin versus plate measurements in order to assess the influence of the critical assembly plate environment, which generates local heterogeneities that are significantly different than those found in the nearly homogeneous pin environment in power reactors. Special emphasis was placed on reactivity, reaction rate ratios, Doppler effects and sodium voiding. The ZPPR-2 program on pin versus plate experiments and analyses was essential to the verification of the general applicability of the plate critical experiments to the design analyses of pin geometry power reactors. Prior to the ZPPR-2 pin measurements, the only experimental data for testing heterogeneity estimates involved plate bunching experiments wherein reactivity effects of varying plate drawer arrangements were made. The pin replacement experiments provided a more direct test of heterogeneity effects even though the experimental pin cells are somewhat more heterogeneous than an LMFBR fuel assembly. Similar measurements were performed in ZPR-6-7 which is a large single-zone assembly with a cell structure and composition nearly identical to the inner core zone in ZPPR-2.

The pin versus plate measurements in ZPPR-2 and ZPR-6-7 were performed by replacing small regions of the normal plate core with pin calandria containing 16 fuel rods (0.410 and 0.348 inch cladding and mixed oxide fuel pellet diameters, respectively) within each approximately 2x2 inch drawer. Figure 4.3-56 shows a cross section view of the ZPPR-2 assembly which outlines the central pin region (69 matrix drawers) and the radial pin sector. Initial pin versus plate measurements were performed in the central 69 drawers and the pin calandria were then rearranged into the radial pin sector for later measurements. Figure 4.3-56 also shows cross sections of the ZPPR-2 inner core zone plate arrangement and of the pin calandria.

In ZPR-6-7, the pin sector was comprised of 25 drawers. Axially, the ZPPR-2 pin region included the full 36 inch core height and extended 6-inches into the axial blankets, while the ZPR-6-7 pin region included only the central 24 inches of the 60 inch core height.

56 | The evaluation and analysis of the pin versus plate ZPPR-2 measurements have been reported elsewhere (Ref. 16, 24, & 25). This data is summarized in Table 4.3-37. With the exception of the pin versus plate interchange reactivity effects, calculations at both ANL and ARD accurately reproduced the measured values for pin/plate ratios including sodium void, Doppler effect, reaction rate ratios and central Pu<sup>239</sup> worth measurements (Ref. 16). These results gave considerable confidence that biases and uncertainties derived for these quantities from the plate-critical integral experiments could be applied to the power reactor. However, there was a substantial discrepancy in the capability to calculate the pin versus plate interchange reactivity effect in ZPPR-2 compared to ZPR-6-7 (C/E ratio of 1.64 in ZPPR-2 compared to 1.07 in ZPR-6-7). The axially longer region of pin versus plate replacement in ZPPR-2 (48 inches) compared with ZPR-6-7 (24 inches) was pointed out (Ref. 24) as a possible cause for the significant effects in ZPPR-2 due to rod/plate streaming differences. A difference of about 5-6% in diffusion coefficients between pin and plate environments was shown to be sufficient to explain the inconsistency between ZPPR-2 and ZPR-6-7 pin versus plate reactivity effects (Ref. 16 & 24). The direction-dependent streaming in the conventional pin versus plate reactivity analysis in ZPPR-2 has been confirmed by Zoltar, etc. (Ref. 26). Application of Benoist's streaming corrections (Ref. 27) to the analyses of ZPPR-2 and ZPR-6-7 put the two comparisons in reasonable consistency. The ratio of calculation to experiment for the pin versus plate fuel replacement reactivity is about 1.2 for ZPPR-2 and 1.07 for ZPR-6-7.

#### 4.3.3.5 ZPPR Assembly 3

ZPPR-3 was a two enrichment zone assembly with each zone containing approximately 50% of the core volume. Axial and radial blankets surround the core. The drawer fuel loading pattern remained the same as ZPPR-2. The major difference between ZPPR-2 and ZPPR-3 was the simulation of a control system in ZPPR-3.

51 | A series of critical experiments were performed in ZPPR Assembly 3 to investigate the effects of the control system on core nuclear characteristics as a part of the Demonstration Plant Benchmark Critical Program. The experimental configuration of ZPPR-3 (shown in Figure 4.3-57) was separated into 3 phases corresponding to the end-of-cycle (Phase 1B), middle-of-cycle (Phase 2), and beginning-of-cycle (Phase 3) reactor control conditions. The principal reactor parameters experimentally studied in ZPPR-3 were power distri-

distribution, control worth and sodium void reactivity effects. ZPPR-3 was used primarily to provide a preliminary estimate of the Demonstration Plant power and control rod worth uncertainties.

#### 4.3.3.6 ZPPR-3 Modified Phase 3 Sodium Void Benchmark

The Modified Phase 3 configuration of ZPPR-3 was designed to more closely mockup the homogeneous core design of the CRBRP with seven inserted control rods. An extensive series of sodium void measurements were performed in ZPPR-3. The primary purpose of these experiments was to measure the reactivity effect of large sodium void zones with a number of control rods inserted. One of the measurement configurations, the 632 drawer reference void in the Modified Phase 3 configuration as shown in Figure 4.3-58, has been chosen to be the basis for the sodium void benchmark.

This series of experiments provided considerable insight into the ability of the design methodology and cross section data to predict the maximum positive sodium void reactivity worth in a CRBRP-size LMFBR. Sodium voiding was accomplished in ZPPR-3 by replacing a number of steel-clad sodium plates with empty steel cans such that only a change in sodium content occurred. The axial height of the voided zone was  $\pm 12$  inches about the core midplane which is approximately the void height which is predicted to result in the maximum positive reactivity effect. The sodium void reactivity worth was determined for void zones extending from the core centerline out to a total of 632 matrix drawers (approximately 80% of the core cross sectional area).

Figure 4.3-59 shows the two-dimensional RZ calculational model which was used for the analysis of the ZPPR-3 Modified sodium void worth experiments. First-order perturbation calculations were performed using 21-group ENDF/B-III cross section data. The results of this analysis are shown in Figure 4.3-60 for 228, 466, 510, and 632-drawer voided zones. Experimentally, the maximum positive void worth occurs at approximately 510 drawers voided where the ratio of the calculated void reactivity worth to the measured value is about 1.33. All of the calculated void worths lie within  $\pm 50$  percent of the measured values up to and including the point of maximum positive void worth, and in fact, the RZ calculation conservatively overpredicts the positive void reactivity worth. The experimental voiding patterns did not lend themselves particularly well to the cylindrical modeling in two dimensional RZ geometry. This was particularly evident in Figure 4.3-60 where the calculation-to-experiment ratios were somewhat divergent in the vicinity of the smeared row seven control ring. Consequently, a series of three-dimensional (VENTURE) perturbation calculations were performed for the sodium voiding experiments in both ZPPR-3 Phase 3 and Phase 3 Modified configurations. The results of these

51

calculations are shown in Figures 4.3-61 and 62, respectively. The three-dimensional calculations produced void reactivity worth results which were within  $\pm 10$  percent of the measured values for the Phase 3 experiments and  $\pm 4$  percent of the measured values for the Phase 3 Modified experiments. This overall good agreement suggests that the design method and data can indeed accurately predict the worth of large-scale sodium voiding so long as the void zone is confined to the strongly moderation-driven positive void worth regions of the core.

#### 4.3.3.7 ZPPR-4 (Pre-Engineering Mockup Critical for Homogeneous CRBRP)

The primary objectives of the ZPPR-4 program were to verify the homogeneous CRBRP core nuclear characteristics including power margins for the first and equilibrium cycles, control rod worth characteristics and the effect of control insertion patterns on the core power distribution, and radial and axial blanket effects. The reference ZPPR-4 configuration is shown in Figure 4.3-63. The drawer fuel loadings and core layout of ZPPR-4 closely simulated the CRBRP first-core configuration.

The detailed results of the analysis of the ZPPR-4 experiments are presented in References 28 and 29. Table 4.3-38 summarizes the measured and calculated eigenvalues for the four phases of ZPPR-4. The calculations systematically underpredict the critical eigenvalue resulting in a  $k_{\text{eff}}$  bias of 1.0036 and an uncertainty of  $\pm 0.0031$  (1).

Foil activation measurements of  $\text{Pu}^{239}$  (n,f),  $\text{U}^{235}$  (n,f),  $\text{U}^{238}$  (n,f), and  $\text{U}^{238}$  (n, ) (for the prediction of blanket plutonium buildup and core conversion ratio) reaction rates and TLD measurements of gamma heating rate support the determination of the power distribution uncertainty throughout the core and blankets. Foil and thermoluminescent dosimeter (TLD) irradiations are performed at a large number of locations throughout a symmetric core sector at both the core midplane and for axial distributions in selected fuel and blanket drawers. Special emphasis is placed on enrichment-zone, blanket and reflector interfaces, as well as regions surrounding inserted control rods. The pointwise foil data are corrected for cell fine-structure through a combination of cell calculations and drawer-averaging measurements, making the measured reaction rate data compatible with homogenized-drawer calculations. In order to avoid a first-order uncertainty in the normalization to ZPPR power level, the calculated reaction rates are normalized such that the total calculated  $\text{Pu}^{239}$  fission rate in the fuel is equal to the total measured  $\text{Pu}^{239}$  fission rate. This is nearly equivalent to a power level normalization since  $\text{Pu}^{239}$  fission accounts for 80-90% of the total reactor power. The remaining

reaction rates are then compared based on this same power (flux level) normalization. Complete details of the analysis of the ZPPR-4 reaction rate measurements are given in References 28 and 29. Table 4.3-39 summarizes this analysis in terms of a mean or average calculation-to-experiment (C/E) ratio and a 1 variation about this mean, with each calculated distribution being power (flux) normalized to the measured  $\text{Pu}^{239}$  fission rate as described above. The normalization factors indicate that  $\text{U}^{235}$  fission is overpredicted by about 2% relative to  $\text{Pu}^{239}$  fission, and  $\text{U}^{238}$  fission is underpredicted by nearly 7%, suggesting an underprediction of the high-energy fluxes in the few-group diffusion calculation.  $\text{U}^{238}$  capture is overpredicted by nearly 6% relative to  $\text{Pu}^{239}$  fission, indicating an overprediction of the end-of-life blanket plutonium content. Several general trends are noted in the data. Most importantly, it appears that the standard power reactor design calculational method does a good job of predicting the power distributions throughout a great majority of the core. The RMS variation in the C/E ratio for the important  $\text{Pu}^{239}$  fission rate is less than  $\pm 2\%$ . There does tend to be some degree of misprediction of the C/E ratios across the inner core/outer core boundary and the core/blanket interface. The largest differences show up in the radial blanket where the C/E ratios consistently fall off approximately 10 to 15% in the vicinity of the blanket/reflector interface which is generally a low power region. The normalized axial reaction rate distributions indicate a 2-3% overprediction of the midplane values with respect to the core-average, resulting in an overprediction of the axial peak-to-average ratio. Correspondingly, these same C/E ratios are low by about 5% in the vicinity of the core/axial blanket interface.

The ability to accurately and reliably predict the minimum available control rod worth in a variety of reactor configurations is clearly important in the design of reactors. Consequently, a substantial amount of effort has been expended in the recent ZPPR program, commencing with ZPPR-3 and 4, toward confirmation of control rod worth calculational methods and the establishment of calculational bias factors and uncertainties. The analysis of the ZPPR-4 control rod worth measurements is contained in References 28 and 29. Table 4.3-40 summarizes the results of ZPPR-4 control rod bank worth calculations using the standard power reactor coarse mesh, two-dimensional diffusion theory methods with 9-group ENDF/B-III data. Overall, the control rod bank worths were well predicted, confirming the adequacy of the design calculational method, with calculation-to-experiment ratios ranging from 0.95 to 1.04. There is a very slight tendency to underpredict the worth of the central and inner ring (row 4) rods. The average control rod worth bias (inverse of the calculation-to-experiment ratio), based on 27 control rod worth measurements in all four phases of ZPPR-4 is  $1.01 \pm 0.02$  (1). In addition to the determination of the control rod worth bias and uncertainty, a number of

51

special experiments were performed to investigate particular design problems. Among these special experiments were the determination of the worth as a function of B-10 enrichment ( $B_{10}$  loading), the measurement of several data points on the integral worth curve for partly inserted rod banks (ZPPR-6), and the confirmation of the worth reduction associated with a tightly clustered control absorber bundle (ZPPR-4).

#### 4.3.3.8 ZPPR-5 (HCDA Engineering Mockup Critical for Homogeneous CRBR)

Upon completion of the ZPPR-4 program, an Engineering Mockup Critical program for CRBRP was initiated. The program was to consist of measurements and analysis of two distinct configurations. The first, ZPPR-5, was designed to provide HCDA related measurements, and the second, ZPPR-6, was to provide measurements of basic design related parameters such as power distributions and control rod worths. Due to the implementation of the ZPPR-7 program for the heterogeneous core (Section 4.3.3.9), only the ZPPR-5 results are considered herein.

ZPPR-5 investigated such HCDA related parameters as sodium voiding, steel slumping, fuel slumping and Doppler feedback. The sodium voiding experiments encompassed portions of the core and the upper axial blanket in a sequence representative of a hypothetical power reactor voiding pattern. Two-dimensional RZ analysis indicated a non-statistical uncertainty of  $\pm 20\%$  in regions of large positive voiding worths (central core regions). The error is much larger in the axial blankets due to the inability of the method to accurately predict neutron streaming in the plates. Three-dimensional (XYZ) perturbation theory analysis has been performed in the voiding sequence in ZPPR-5 but has indicated no significant improvement in the uncertainty. It should be noted that the voiding was not confined axially to  $\pm 12$  inches as was the case in the ZPPR-3 experiments but extended into the axial blankets in order to model a representative sodium voiding sequence. Voiding was performed in the axial blankets prior to the fuel height region. Consequently, the uncertainty in these predictions are larger than ZPPR-3 due to the enhanced neutron streaming. The neutron streaming effect due to plate heterogeneity in the criticals will not be so predominant in power reactors because of their more homogeneous material distribution.

56 |

#### 4.3.3.9 ZPPR-7 (Pre-Engineering Mockup Critical for CRBRP Heterogeneous Core)

The purpose of the ZPPR-7 program was to provide pre-EMC design support for the heterogeneous CRBRP core arrangement. Information obtained from this program was used to validate and provide preliminary design bias factors and

uncertainties for the CRBRP heterogeneous core physics characteristics, and to affect the selection of the CRBRP core layout and fuel management scheme. The experimental program was divided into a number of phases, highlighted by a clean benchmark configuration with annular blanket rings and no control rod or control channel heterogeneities; simulations of both a clean, beginning-of-life, core with fresh blankets and a burned, end-of-life, core with depleted fuel and plutonium buildup in the internal blankets; and various simulations of control pattern effects on core characteristics. The initial ZPPR-7 configurations modeled an early version of the CRBRP heterogeneous core layout. These measurements were followed by a brief series of experiments which validated the earlier results in a mockup of the final CRBRP heterogeneous core configuration in Figure 4.3-1. The analysis and description of the ZPPR-7 measurements is contained in References 30 and 31. Figure 4.3-64 shows the core layouts for the principal ZPPR-7 configurations.

ZPPR-7A was a benchmark configuration with clean (no plutonium) annular blanket rings inside a single enrichment core with no control rods or control rod channels which was intended to isolate the characteristics of the heterogeneous core geometry. The principal experiments investigated criticality, key isotopic neutron reaction rate distributions and sodium void worth.

The Phase B core was rearranged to provide a better simulation of a CRBRP fresh core with 12 control rod channels (6 in row 4 and 6 in row 7 corner) and inner blanket islands in the outer fuel zones. The objectives of this configuration included an examination of criticality, control rod bank worths and fuel/blanket interchange worths, and isotopic fission and capture rate distributions in the fuel and blankets.

Many of the Phase B measurements were repeated in the Phase C configuration which simulated end-of-life core conditions with depleted fuel and plutonium loaded in the inner blankets. This series of experiments provided information on the flux and power shift associated with blanket plutonium buildup and its effect on criticality, reaction rate distributions, and control rod worth.

The Phase D configuration more closely simulated the CRBRP control pattern with a total of 15 control rods (6 row seven corner rods, 6 row seven flat rods, and 3 row 4 rods) in the end-of-life mockup. The Phase E configuration examined the effects of the inserted row seven corner control rod bank on the core power distribution.

After the completion of the ZPPR matrix expansion to 14 feet by 14 feet to accommodate larger core configurations, the ZPPR-7B configuration was reassembled as a normalization to the earlier measurements (designated Phase F).



Extensive control rod worth measurements were performed in Phase G. The Phase G core configuration was the same as that of Phase D with 15 control rods except that no plutonium was loaded in the blankets in order to simulate beginning-of-life clean core conditions. Control rod interactions and flux tilting effects were investigated through a series of symmetric and asymmetric rod-cluster and individual rod insertion measurements.

56 |

In Phase H, the row seven corner control rod bank was half inserted and extensive foil irradiations were performed in order to simulate the three-dimensional power perturbations encountered in a clean, beginning-of-life core with partial control rod insertion.

Following a series of non-CRBRP thorium-zone measurements in ZPPR-8, the Phase 8F configuration was assembled to simulate the final CRBRP heterogeneous core configuration at the beginning-of-life with fuel islands surrounding both the row seven corner and the row seven flat control rod banks (Figure 4.3-1). The experimental program was structured to verify the power shape and control rod worth biases and uncertainties which were determined in the earlier ZPPR-7 experiments. In addition, the power tilt associated with an out-of-bank control rod was measured as was the control rod/fuel assembly interchange worth in the shutdown configuration.

The ZPPR-7 Critical experiments provide a valuable integral data base against which the accuracy of the CRBRP design methods and cross section data can be evaluated for application to the heterogeneous core configuration. Because of differences in geometry, composition, size, and temperature between the zero power critical experiments and the CRBRP, the measured integral parameters obtained from the critical are not applied directly to the reactor design. Rather, the accuracy of the design calculational methods and cross section data are evaluated by comparing calculated and measured critical parameters. The resulting biases and/or uncertainties from this comparison are then applied to the calculation of these same parameters in the reactor design using the same calculational methods and data. In the paragraphs that follow, the development of the preliminary design bias factors and uncertainties from the ZPPR-7 and 8 data base will be summarized for application to the heterogeneous core configuration in the principal design areas of reactor eigenvalue prediction, power distribution accuracy, control rod worth uncertainty and sodium void worth. Complete details of the ZPPR-7 and 8 analysis are included in References 30 and 31.

57 |

Amend. 56  
Aug. 1980

#### ZPPR-7 and 8 Eigenvalue Prediction:

Table 4.3-41 summarizes the measured and calculated critical eigenvalues ( $k_{eff}$ ) for ZPPR-7 and 8. In order to avoid mixing the control rod worth biases in with the development of the reactor eigenvalue bias, only the clean (unrodded) phases of ZPPR-7 and 8 are included in Table 4.3-41. The calculations systematically underpredict the critical eigenvalue, resulting in a  $k_{eff}$  bias of 1.0101 and an uncertainty of + 0.19%  $\Delta k$  ( $1\sigma$ ). Within the stated standard deviation in the calculation-to-experiment ratios in Table 4.3-41, there is no statistical difference between the eigenvalue bias in the beginning-of-life and end-of-life phases of ZPPR-7 and 8. The ZPPR-7 and 8 eigenvalue bias is included directly in the determination of the CRBRP critical loading and the  $1\sigma$  variation is included as an uncertainty in the excess reactivity requirements for both the critical fuel loading and control rod worth requirements determinations.

#### Power Distribution:

The integral data from the ZPPR experiments supporting the power distribution analysis consists of foil activation measurements of  $Pu^{239}$  (n,f),  $U^{235}$ (n,f),  $U^{238}$ (n,f), and  $U^{238}$ (n, $\gamma$ ) (for the prediction of blanket plutonium buildup and core conversion ratio), and TLD measurements of gamma heating rate. Foil and TLD irradiations are performed simultaneously in a large number of locations throughout a symmetric core sector at the core midplane and axial distributions in selected fuel and blanket drawers. Special emphasis is placed on blanket and reflector interfaces as well as regions surrounding inserted control rods. The pointwise foil data are corrected for cell fine structure through a combination of cell calculations and drawer-averaging measurements, making the measured reaction rate data compatible with homogenized-drawer calculations. In order to avoid a first-order uncertainty in the normalization to ZPPR power level, the calculated reaction rates are normalized such that the average calculated  $Pu^{239}$  fission rate in the fuel is set equal to the average measured value. This is nearly equivalent to a power normalization since  $Pu^{239}$  fission accounts for between 80 and 90% of the total reactor power generation. The remaining reaction rates are then compared based on this same power (flux level) normalization.

Table 4.3-42 summarizes the analysis of the ZPPR-7 reaction rates in terms of an average calculation-to-experiment (C/E) ratio and a  $1\sigma$  variation, with each calculated distribution being power (flux level) normalized to the measured  $Pu^{239}$  fission rate in the fuel as described above. The normalization factors indicate that  $U^{235}$  fission is overpredicted by about 4% relative to  $Pu^{239}$  fission in the heterogeneous critical assemblies.  $U^{238}$  fission is underpredicted by nearly 20% in the fuel and about 6% in the inner blankets, indica-

ting both a general underprediction of the high energy fluxes and substantial errors in predicting the spectral gradients between the fuel and blanket assemblies with the coarse-mesh, few-group diffusion calculations.  $U^{238}$  capture is overpredicted by nearly 10% relative to  $Pu^{239}$  fission, indicating a general overprediction of the end-of-life blanket plutonium buildup, and hence, the end-of-life blanket power generation. The important  $Pu^{239}$  fission rate is, however, well predicted with the standard reactor design methods, with an RMS deviation of less than  $\pm 2\%$  in the C/E ratios throughout the core and blankets.

Figures 4.3-65 and 66 show the normalized distributions of the midplane  $Pu^{239}$  fission rate calculation-to-experiment ratios representing the general radial distribution trends at the beginning-(Phase B) and end-of-life (Phase C). In the beginning-of-life core (Phase B in Figure 4.3-65) with no plutonium in the blankets, the C/E ratios tend to be low in the central core regions and tilted toward 3-5% higher values around the outer ring fuel clusters especially around the row-seven corner control channels. The impact of refinements in the power distribution calculation methods, and the sensitivity of this tilted characteristic to cross section data variations is discussed in Reference 32. The CRBRP power predictions in comparable regions are biased downward 1-3% as described in Section 4.3.2.2.9 to compensate for this inherent overprediction. This tilt is not observed in the end-of-life (Phase C in Figure 4.3-66) simulation with a more homogeneous distribution of plutonium throughout the core.\* The largest differences in both phases occur in the radial blanket where the C/E ratios consistently fall off 10-15% or more in the vicinity of the blanket/reflector interface (which is generally a low power region). This fall-off, which is similar to that observed in the homogeneous ZPPR-4 experiments, is included in the blanket uncertainty assessment in Section 4.3.2.2.9. The normalized axial reaction rate distributions indicate a 2% overprediction of the midplane reaction rates with respect to the channel-average and a corresponding 5% underprediction of the reaction rates at the core extremities in the vicinity of the core/axial blanket interface.

The power-normalized reaction rate biases and uncertainties (at the  $3\sigma$  level) are applied in the reactor design, with appropriate weighting for the time and space dependent fraction of power attributable to each reaction type, in order to determine the limits of the power distribution in Section 4.3.2.2.10 for design margin and safety analyses.

\* The Phase C configuration has plutonium loaded in the inner blankets and removed from selected fuel locations to simulate an end-of-life burned core.

## Control Rod Worth:

A substantial amount of effort was expended in the ZPPR-7 and 8 program toward confirmation of the control rod worth calculational methods and the development of calculation bias factors and uncertainties supporting the minimum shutdown margin. Table 4.3-43 lists the results of control rod worth calculations in the heterogeneous ZPPR-7 mockup for both the beginning-of-life with a clean core and blankets and for an end-of-life simulation with plutonium loaded in the inner blankets. In contrast to the generally well predicted ZPPR-4 results in Section 4.3.3.7, the heterogeneous ZPPR-7 control rod worth calculation-to-experiment ratios exhibit a strong spatial bias in the beginning-of-life core (Phase B), varying between 0.91 in the inner ring (row 4) rod worths and 0.99 in the outer ring (row 7 corner) rod worths. The end-of-life worths (Phase C) are consistently underpredicted by nearly 10%. It would seem that the close prediction of the beginning-of-life row 7 corner rod worths is an anomaly associated with the calculated reaction rate tilt (overprediction) in this same region. Transport and mesh effects no longer compensate in the highly-loaded ZPPR-7 control rods as noted by the much closer overall agreement obtained with a finer mesh diffusion calculation in Table 4.3-43. The coarse-mesh (1 mesh per ZPPR drawer corresponding to 4 meshes per control assembly) control rod bias is therefore not directly applicable to the power reactor control rod worths, calculated with 6 triangular meshes per control assembly, without adjustment for mesh sensitivity. Although the consistent underprediction of control rod worths in ZPPR-7 may not be fully understood at this time, the experiments do seem to indicate that the unbiased power reactor calculated rod worths are probably conservatively low (that is, final resolution of a set of heterogeneous ZPPR-7 control rod worth biases will tend to raise the calculated power reactor rod worths).

Due to the importance of the control rod withdrawal event (reactivity fault) in the design of the heterogeneous CRBRP where flux shifting and control rod interactions have been found to be substantial, a series of experiments (ZPPR-7G) were performed in which a large number of asymmetric control rod insertion patterns were studied. These patterns included single and small clusters of rods inserted asymmetrically in the core, five-out-of-six rods inserted in a bank (simulating the stuck rod condition), and five-out-of-six secondary control rods inserted in a core containing five-out-of-six inserted primary rods (simulating the limiting condition where the stuck secondary control rod is adjacent to a faulted-withdrawn-primary control rod). The patterns produced substantial flux shifts in the reactor, resulting in control rod interaction factors\* exceeding a factor of two. Pre-

\* Control rod interaction factor is defined as the ratio of the rod worth in a particular asymmetric pattern to the average worth in a symmetric bank.

liminary analysis of these experiments in Reference 30 indicates that the grossly asymmetric patterns (or control rod interactions) are predicted with approximately the same accuracy as the symmetric bank worths in Table 4.3-43 using the standard power reactor design method and a full-core two-dimensional calculation model, thereby confirming the adequacy of the maximum reactivity fault values used in the development of the heterogeneous power reactor control requirements.

#### Sodium Void Worth:

A series of sodium void worth measurements were performed in the clean benchmark ZPPR-7A configuration. The voiding was more confined to the central core regions than the HCDA simulation in ZPPR-5 (Section 4.3.3.8). The voided region extended stepwise from the central blanket out through the second fuel ring (see Figure 4.3-64) at a radius of about 50 cm, and the axial void included parts of the axial blanket (+ 60 cm from the core midplane) in the central blanket and first fuel ring, and only the central core regions (+30.5 cm) in the first blanket ring and the second fuel ring in Figure 4.3-64. Two-dimensional (RZ) first order perturbation theory calculations indicated that the positive (moderation) component of the void worth is reduced compared to the homogeneous ZPPR core values, confirming the lower positive sodium void worth characteristic of the heterogeneous core, and the calculation-to-experiment ratios for the positive void worth regions were somewhat lower than the comparable ZPPR-3 and 5 values.

#### 4.3.3.10 Computer Code Abstracts

56 | Nine computer codes were used to support the nuclear analysis described in the previous sections. They are: ANISN-W, W-2DB, PERT-V, ETOX, XSRES-WIDX, PUMA, SPHINX, VENTURE, and POWPIN. A brief abstract of each of these codes is found in Appendix A.

#### 4.3.4 Changes

51 | The design features of the Clinch River Breeder Reactor can be compared with at least four different sodium cooled, fast reactors built or currently under construction in the United States. These include: (1) the Experimental Breeder Reactor (EBR)-II, (2) the Enrico Fermi Atomic Power Plant, (3) the Southwest Experimental Fast Oxide Reactor (SEFOR), and (4) the Fast Flux Test Facility (FFTF). These four reactors were all designed to test and verify specific features and components of fast breeder reactors.

The EBR-II was originally designed as a demonstration of the feasibility of operating an LMFBR power plant with integral closed fuel cycle provided by an on-site fuel reprocessing and refabrication plant. Although not specifically designed for the purpose, it was designated as the nation's principal fast flux irradiation facility. Samples are irradiated in high temperature sodium and high fast neutron flux environment. The reactor core employs metallic uranium fuel surrounded by radial and axial blankets and produces 62.5 MWt and 20 MWe.

The Fermi reactor was designed and built to serve as the first full-scale mockup of a large, sodium cooled, fast breeder reactor. More specifically, its objectives included the testing of such components as the steam generator, sodium pump and fuel handling equipment and to demonstrate the economic feasibility of the LMFBR to produce power on an electric utility grid. The Fermi reactor also employed metallic uranium fuel, radial and axial blanket assemblies. The rated power of the first core loading was 200 MWt.

56 | SEFOR was a ceramic fueled, sodium cooled fast flux reactor intended to provide data in support of a test program to demonstrate that fast power reactors could be designed with desirable operating and safety characteristics. In particular, it was designed for the systematic determination of the Doppler coefficient of reactivity at temperatures up to the vicinity of fuel melting. SEFOR employed a mixed uranium-plutonium oxide fueled core with a nickel reflector and was rated at 20 MWt.

56 | The FFTF, currently under construction, was designed to provide a fast neutron, sodium cooled environment typical of a large LMFBR. This reactor will act as a full size test bed for both current and advanced fast reactor fuel, absorber and structural materials. These samples will be irradiated in both open and closed test loop locations within the reactor core. The FFTF employs (U-Pu)<sub>2</sub>O<sub>7</sub> fuel in two enrichment zones surrounded by a nickel reflector and has a nominal power rating of 400 MWt.

51 | The CRBRP has particular design objectives which set it apart from previous fast reactors built in the United States. Principal among these is the requirement that CRBRP must breed fissile plutonium with a breeding ratio in excess of 1.2 to demonstrate the potential for large scale commercial LMFBR operation. A second distinctive feature is the nominal power capability of 975 MWt which is more than twice as large as any of the four reactors described above. In addition, CRBRP is the first sodium-cooled LMFBR in the United States to incorporate the heterogeneous core configuration.

Amend. 56  
Aug. 1980

These requirements imply that the fuel and blanket regions of the CRBR must be designed to maximize both the breeding of fissile material and the thermal power output. But at the same time the reactor must be maintained and operated in a safe and reliable manner throughout its thirty year design life. In the following discussion a detailed comparison will be made between the CRBRP and the FFTF designs with particular emphasis on safety related features and components.

Pertinent nuclear design features of the two reactors are compared in Table 4.3-44. It should be noted that the dimensions included in Table 4.3-44 are based on cold (room temperature) conditions.

For the initial core loading, the CRBRP fuel pin and fuel assembly designs take the maximum advantage of the FFTF fuel experience. Essentially, the same design has been employed with a slightly larger assembly pitch. Because of the increased power capability, the CRBRP fuel volume was increased by approximately 2.3 times compared to FFTF. Since the demonstration of breeding was not an FFTF design objective, axial and radial blankets were not employed.

The fuel enrichments, compositions and loadings are also compared in Table 4.3-44. In the early operating cycles the CRBRP fuel assemblies employ the same type of low-240 plutonium fuel as the FFTF. In later cycles the CRBRP may employ light water reactor discharge grade plutonium which has a fractionally lower relative amount of Pu-239 and larger concentrations of the higher plutonium isotopes. More than twice as much fissile plutonium is employed in the first core loading of the CRBRP as in FFTF.

The designs of the control rod systems for these two reactors are summarized in Table 4.3-44. Both the primary and secondary control systems in CRBRP and FFTF employ boron carbide as the neutron absorber. All CRBRP control assemblies are fully enriched in B-10 to meet the control requirements (see subsection 4.3.2.6 for details).

The operating conditions, including burnup limits, refueling, power distributions and peak flux for these two reactors are also listed in Table 4.3-44. The overall radial power peaking factors for the CRBRP are smaller than those quoted for FFTF. This is due to the larger core radius, different control rod patterns and the heterogeneous fuel and blanket arrangement.

The reactivity coefficients for the CRBRP are discussed in detail in subsection 4.3.2.3. Table 4.3-45 compares the different reactivity coefficients of CRBRP and FFTF.

The Doppler effect in fast reactors with a large U-238 content provides a reliable, prompt negative reactivity feedback to mitigate the effects of reactivity transients which can lead to rapid power increases. Consequently, the magnitude of the Doppler coefficient has special significance in the safety analysis of fast reactors. The Doppler coefficients in Table 4.3-45 are listed by reactor zone for four different times in the life of the plant.

In all four cases the CRBRP Doppler coefficient summed over all core zones is at least 60% larger (more negative) than the FFTF value. The fuel and inner blanket Doppler constant is nearly 40% larger than the FFTF value. The fast-acting fuel Doppler contribution alone is about half the comparable FFTF value.

The remaining reactivity coefficients compared for these two reactors are all associated with mechanical motion due to temperature changes in the fuel, coolant and structure. The average sodium density coefficients for the CRBRP and FFTF during the first cycle are given in Table 4.3-45. These results are based on changing the density of the coolant in all fueled zones, including the inner and radial blankets in the CRBR. The sodium density coefficient is significantly smaller (less negative) in the CRBRP because of the positive contribution from the fuel zone.

The uniform radial expansion coefficients for the two reactors during the first cycle are also shown in Table 4.3-45. These values are based on the expansion of the lower core support structure, which changes the average assembly pitch with changes in the coolant inlet temperature. The uniform radial expansion coefficient for CRBRP is smaller than the FFTF value because of the heterogeneous fuel and blanket arrangement in the CRBRP core. Radial bowing effects, including those imposed by the core restraint mechanism, are discussed in Section 4.3.2.3.4.

Finally, the uniform axial expansion coefficients for the two reactors at beginning-of-life are listed in Table 4.3-45. These results are based on the expansion of the fuel pellet stack with changes in the average surface temperature of the dished fuel pellets. It is assumed that the pellets move freely within the cladding tubes and that the axial motion is governed solely by the linear expansion coefficient of the mixed uranium-plutonium oxide. This assumption tends to yield the largest (magnitude) coefficients; fuel pellet sticking to the clad or degradation of the fuel pellets under irradiation will significantly reduce the magnitude of this coefficient.

Additional safety related features and components of the CRBRP are compared with selected foreign built LMFBRs in Section 1.3.



### REFERENCES FOR SECTION 4.3

1. R. L. Childs, F. R. Mynatt, L. S. Abbott, "Analyses of the TSF First-Fission Stored-Fuel and Ex-Vessel Low-Level Flux Monitor Experiments for the Clinch River Breeder Reactor", ORNL-TM-5057, March 1976 (Chapters 3, 4 and 5).
2. J. B. Bullock, M. V. Mathis, J. T. Michalczko, "Inverse Kinetics Rod Drop Measurements With a Mockup of the Clinch River Breeder Reactor Shields", ORNL-TM-4828, March 1976 (Chapters 5 and 6).
3. J. W. Allen, "Development and Application of a Three-Point Inverse Kinetics Rod Drop Technique for Subcriticality Determination", ORNL-TM-4758, November 1975.
4. J. W. Allen, J. C. Robinson and N. J. Ackerman, Jr., "Statistical Errors in Subcritical Reactivity Inferred from Inverse Kinetics Rod-Drop Measurements Using the Three-Point Method", ORNL-TM-4101, July 1973.
5. Harry H. Hummel and David Okrent, "Reactivity Coefficients in Large Fast Power Reactors", Monograph Series on Nuclear Science and Technology, American Nuclear Society, 1970.
6. P. Greebler, B. A. Hutchins, and J. R. Sueoke, Calculation of Doppler Coefficient and Other Safety Parameters for a Large Fast Oxide Reactor, GEAP-3636, General Electric Company, 1961.
7. D. D. Freeman et al., "SEFOR: Verification of the Doppler Transient Shutdown Capability in LMFBR's", Proc. ANS National Topical Meeting on New Developments in Reactor Physics and Shielding, Conf.-720901, Book 2, Kiamesha Lake, NY, 1972.
- 7a. P. Greebler, et al., "Status of Reactivity Feedback and Stability", Fast Breeder Reactor - Status of Safety Technology Development, DOE/TIC-11209, Department of Energy, Reactor Research and Technology, August 1980.
8. L. D. Noble, G. Kussmaul and S. L. Derby, "Experimental Program Results in SEFOR Core II", GEAP-13838, June 1972.
9. D. D. Freeman, "SEFOR Experimental Results and Application to LMFBRs", GEAP-13929, January 1973.
10. R. E. Kaiser and J. M. Gasidlo, "On the Effect of Core Configuration on <sup>U238</sup> Doppler Measurements in ZPPR Assembly 2", New Developments in Reactor Physics and Shielding, Conf.-720901, September 12-15, 1972, p. 1006.

11. "Reactor Development Program Progress Report, October 1973", RDP-21. Argonne National Laboratory.
12. S.L. Stewart, J. T. Hitchcock, and C. L. Cowan, "Critical Experiments and Analysis - Task 5 Quarterly", GEAP-13771-21, October-December 1976, p. A-39.

- 56 |
13. Proceedings of the International Symposium on Physics of Fast Reactors, October 16-23, 1973, Tokyo, Japan, Vol. 1, p. 19, Power Reactor and Nuclear Fuel Development Corp., Tokyo, Japan.
  14. B. W. Lee, R. E. Kaiser, J. T. Hitchcock and C. S. Russell, "Thermal Expansion Worths for a Liquid Metal Fast Breeder Reactor Inferred from Small-Sample Reactivity Measurements", Nuclear Science Engineering, 65, pg. 429, 1978.
  15. T. A. Pitterle, N. C. Paik, and C. Durston, "Evaluation and Integral Testing of Modifications to ENDF/B Version II Data", WARD-4210T4-1, December 1971.
  16. N. C. Paik and T. A. Pitterle, "Analysis of ZPPR-2 Measurements Topical Report", WARD-3045T4B-5, February 1973. (Availability: USDOE Technical Information Center).
  17. A. M. Letov, Stability in Nonlinear Control Systems, Princeton University Press, Princeton, N.J. 1961.
  18. "Modern Control Principles and Applications", Hsu and Meyer, McGraw Hill, New York, 1968, p. 131.
  19. "Stability by Liapunov's Direct Method with Applications", LaSalle and Lefschetz, Academic Press, New York, 1961, p. 122.
  20. I. Bondarenko, Group Constants for Nuclear Reactor Calculations, Consultants Bureau, New York, N. Y. 1964.
  21. D. R. Vondy, T. B. Fowler and G. W. Cunningham, "VENTURE: A Code Block for Solving Multigroup Neutronics Problems Applying the Finite-Difference Diffusion-Theory Approximation to Neutron Transport", ORNL-5062, October 1975.
  22. M. F. James, "Energy Released in Fission", J. Nuclear Energy, 23, p. 517, 1969.
  23. R. A. Doncals, J. A. Lake, and N. C. Paik, "Use of Integral Data in the Development of Design Methods for Fast Reactors", from the Proceedings of the American Nuclear Society Topical Meeting on Advances in Reactor Physics, Gatlinburg, Tennessee, April 1978 (CONF-780401).
  24. T. Pitterle and N. C. Paik, "Summary of Analyses of Plate vs. Pin Measurements Emphasizing Reactivity and Sodium Void Effects", presented at the National Topical Meeting on New Developments in Reactor Physics and Shielding, September 12-15, 1972, Kiamesha Lake, New York.
- 51 |

25. W. G. Davey, et. al., "Rod and Plate Heterogeneity Studies in ZPPR-2", ANL-7961, March 1974.
26. B. A. Zolotar, G. Grassesechi, and P. H. Kier, "Analysis of Plate-Rod Heterogeneity Measurements in Demonstration Reactor Benchmark Assemblies Including the Effect of Streaming", Trans. Amer. Nucl. Soc. 18, pp. 309-310 (1974).
27. P. Benoit, "Streaming Effects and Collision Probabilities in Lattices", Nucl. Sci. Eng. 34, pp. 285-307 (1968).
28. J. T. Hitchcock and A. K. Hartman, "Analysis of the ZPPR-4 Critical Experiments - Phases 1 and 2", GEAP-14077, February 1976. See also A. K. Hartman and J. T. Hitchcock, "Analysis of the ZPPR-4 Critical Experiments - Phases 3 and 4", GEFR-00108, August 1977. (Availability: USDOE Technical Information Center)
29. R. W. Rupnik, "ZPPR-4 Cooperative Analysis Program - Critical Experiments", CRBRP-ARD-0155, January 1979.
30. R. V. Rittenberger and J. A. Lake, "ZPPR-7 and 8F Cooperative Analysis Program: Critical Experiments", CRBRP-ARD-0237, March 1979.
31. A. K. Hartman and J. T. Hitchcock, "Analysis of the ZPPR-7 Experiments", CRBRP-GEFR-00025, July 1977 (Availability: USDOE Technical Information Center).
32. P. J. Collins, et. al., "A Comparison Between Physics Parameters in Conventional and Heterogeneous LMFBRs using Results from ZPPR", from the Proceedings of the American Nuclear Society Topical Meeting on Advances in Reactor Physics, Gatlinburg, Tennessee, April 1978 (Conf. 780401).
33. J. A. Lake, R. V. Rittenberger and R. W. Rathburn, "Influence of Control Rod Worth Interactions on LMFBR Control Systems Design," Trans. Amer. Nucl. Soc. 34, pp. 778-80 (1980).
34. R. B. Kidman and R. E. McFarlane, "LIB-IV, A Library of Group Constants for Nuclear Reactor Calculations," LA-6260-MS, March 1976.
35. H. F. McFarlane and P. J. Collins, "Control Rods in LMFBRs: A Physics Assessment," ANL-82-13, April 1982.
36. M. J. Lineberry, et al., "Physics Studies of a Heterogeneous Liquid Metal Fast Breeder Reactor," Nuclear Technology 44, pp. 21-43 (1979).

TABLE 4.3-1  
REACTOR DESCRIPTION

<u>FUEL ASSEMBLIES</u>	<u>UNITS</u>	<u>DESCRIPTION</u>
Fuel Height	M	0.9144
Geometry		Hexagonal
Number in Core (BOC1)		156
Rod Array		Triangular
Rods per Assembly		217
Rod Pitch (Fully Compacted)	MM	7.264
Overall Assembly Dimensions:		
Flat to Flat Distance Outside Edges of Hexagonal Duct (away from load pads)	M	0.1162
Flat to Flat Distance Inside Edges Hexagonal Duct	M	0.1101
Pitch	M	0.1209
Volume Fractions in Fuel Assembly (Drawing Dimensions)		
Fuel		0.325
Sodium		0.419
Gap		0.022
Structure		0.234
Total Heavy Metal (Plutonium and Uranium) Weight in Fuel (BOC1)	Kg	5189.

4.3-90

Amend. 51  
Sept. 1979

TABLE 4.3-1 (Continued)

<u>FUEL RODS</u>	<u>UNITS</u>	<u>DESCRIPTION</u>
Number in Plant (BOCI)		33852
Clad Outside Diameter	MM	5.842
Diametral Gap	MM	0.165
Clad Material		20 Percent CW-Type 316 SS
Clad Thickness	MM	0.381
Pitch/Diameter Ratio		1.24
Smear Density	%theoretical	85.5
<u>FUEL PELLETS</u>		
Material		Plutonium Oxide and Uranium Oxide
Density (Percent of Theoretical)	%	91.3
Plutonium Weight Fraction (First Core)		0.328
Plutonium Weight Fraction (Typical Equilibrium Core)		0.330
Pellet Diameter	MM	4.915
Pellet Length	MM	6.096
Isotopic Composition of Feed Plutonium (Low - 240 Grade)		
Pu-238	% by weight	0.06
Pu-239	% by weight	86.04
Pu-240	% by weight	11.70

4.3-91

Amend. 51  
Sept. 1979  
51

TABLE 4.3-1 (Continued)

<u>FUEL PELLETS (Cont)</u>	<u>UNITS</u>	<u>DESCRIPTION</u>
Pu-241	% by weight	2.00
Pu-242	% by weight	0.20
Isotopic Composition of Depleted Uranium		
U-235	% by weight	0.2
U-238	% by weight	99.8
<u>BLANKET THICKNESS AND COMPOSITION</u>		
Top Axial (Fuel Assemblies)	M	Sodium, Stainless Steel Plus Depleted Uranium Oxide (0.356)
Bottom Axial (Fuel Assemblies)	M	Sodium, Stainless Steel Plus Depleted Uranium Oxide (0.356)
Radial	M	Sodium, Stainless Steel Plus Depleted Uranium Oxide (~0.28)
<u>TOP AND BOTTOM AXIAL BLANKETS</u>		
Geometry		Same as Fuel
Blanket Pellets		Depleted Uranium Oxide
Material		Depleted Uranium Oxide
Density (Percent of Theoretical)	%	96.0
Diameter	MM	4.826
Length	MM	10.016
Total Heavy Metal (Uranium) Weight in Blanket (Upper and Lower)	Kg	4225

4.3-92

Amend. 51  
Sept. 1979

TABLE 4.3-1 (Continued)

<u>INNER/RADIAL BLANKET ASSEMBLIES</u>	<u>UNITS</u>	<u>DESCRIPTION</u>
Geometry		Hexagonal
Number In Plant, Inner/Radial (BOC1)		82/126
Rods Per Assembly		61
Rod Pitch	MM	13.778
Assembly Drawing Dimensions		
Flat to Flat Distance Outside Edges of Hexagonal Duct	M	0.1162
Flat to Flat Distance Inside Edges of Hexagonal Duct	M	0.1101
Volume Fractions in Blanket (Drawing Dimensions)		
Fuel		0.539
Gap		0.014
Sodium		0.278
Structure		0.169
Total Heavy Metal (Uranium) Weight In Blanket, Inner/Radial (BOC1)	Kg	8270/12707
<u>INNER/RADIAL BLANKET RODS</u>		
Number In Plant, Inner/Radial (BOC1)		5002/7686
Clad Outside Diameter	MM	12.852
Diametral Gap	MM	0.152

4.3-93

Amend. 64  
Jan. 1982



TABLE 4.3-1 (Continued)

	<u>UNITS</u>	<u>DESCRIPTION</u>
<u>INNER/RADIAL BLANKET RODS (Cont)</u>		
Clad Material		20 Percent CW-Type 316 SS
Clad Thickness	MM	0.381
Pitch/Diameter Ratio		1.072
<u>INNER/RADIAL BLANKET PELLETS</u>		
Material		Depleted Uranium Oxide
Pellet Density (Percent of Theoretical)	%	95.6
56   Pellet Diameter	MM	11.938
Pellet Stack Height	M	1.626
<u>CONTROL ROD ASSEMBLIES</u>		
Geometry		Hexagonal
Number in Plant		15
Primary Rods (Startup, Burnup and Load Follow)		9
Secondary Rods (Safety)		6
Neutron Absorber		Enriched Boron Carbide
Fraction of Theoretical Density	%	92.0
B-10 Enrichment in Boron Carbide:		
1) Primary Rods (all cycles)	atom percent	92.0
2) Secondary Rods	atom percent	92.0

4.3-94

Amend. 56  
Aug. 1980

TABLE 4.3-1 (Continued)

<u>CONTROL ROD ASSEMBLIES (Cont)</u>	<u>UNITS</u>	<u>DESCRIPTION</u>
Rods Per Assembly		
Primary System		37
Secondary System		31
Clad Material		20 Percent CW-Type 316 SS
Clad Outside Diameter		
Primary System	MM	15.291
Secondary System	MM	14.036
Clad Thickness		
Primary System	MM	1.270
Secondary System	MM	0.699
Pellet Diameter		
Primary System	MM	11.659
Secondary System	MM	11.951
Pellet Stack Height	M	0.9144

4.3-95

51

Amend. 51  
Sept. 1979

TABLE 4.3-2

## FUEL ISOTOPIC COMPOSITION

Isotope	Weight Fraction
Pu238	.0006
Pu239	.8604
Pu240	.1170
Pu241	.0200
Pu242	.0020
Depleted Uranium	
U235	.002
U238	.998

51

TABLE 4.3-3

## START-OF-CYCLE EXCESS REACTIVITY REQUIREMENT

## FIRST-CORE FUEL

	% $\Delta k$ $\pm 1\sigma$
$\Delta k_{\text{Burnup}}$ , Cycle 1 (128 fpd)	0.594 $\pm$ .059
Net Refueling Interchange Worth	-1.526 $\pm$ .061
$\Delta k_{\text{Burnup}}$ , Cycle 2 (200 fpd)	2.240 $\pm$ .224
Room Temperature Criticality Uncertainty	$\pm$ .19
Uncertainty in ZPPR Bias	$\pm$ .2
Room Temperature to Hot-Full-Power Uncertainty	$\pm$ .19
Fissile Loading Tolerance	$\pm$ .14
Pellet Stack Height Uncertainty	$\pm$ .1
Impurities	$\pm$ .1
	1.304 $\pm$ .457
Total Requirement	1.761 % $\Delta k$

TABLE 4.3-4

## HEAVY METAL\* MASS (KG) INVENTORY IN THE CRBRP.

	<u>Fuel</u>	<u>Inner Blanket (a)</u>	<u>Radial Blanket (a)</u>	<u>Lower Axial Blanket</u>	<u>Upper Axial Blanket</u>
Beginning-of-First-Cycle					
Pu-239	1468.	---	---	---	---
Pu-240	199.7	---	---	---	---
Pu-241	34.0	---	---	---	---
Pu-242	3.4	---	---	---	---
U-235	7.6	16.7	25.7	4.3	4.3
U-238	3476.	8253.	12681.	2108.	2108.
Fission Products	---	---	---	---	---
Total Heavy Metal	5188.7	8269.7	12706.7	2112.3	2112.3
End-of-First-Cycle					
Pu-239	1384.	60.5	48.5	8.6	5.0
Pu-240	217.7	0.6	0.3	0.1	---
Pu-241	32.9	---	---	---	---
Pu-242	3.9	---	---	---	---
U-235	6.9	15.6	24.8	4.1	4.2
U-238	3432.	8184.	12629.	2099.	2102.
Fission Products	108.5	9.1	4.4	0.6	0.4
Total Heavy Metal	5185.9	8269.8	12707.0	2112.4	2111.6

\*Heavy metal excludes oxygen.  
(a) Including axial extensions.

4.3-98

Amend. 64  
Jan. 1982

TABLE 4.3-4 (Cont.)  
HEAVY METAL\* MASS (KG) INVENTORY IN THE CRBRP

	<u>Fuel</u>	<u>Inner Blanket(a)</u>	<u>Radial Blanket(a)</u>	<u>Lower Axial Blanket</u>	<u>Upper Axial Blanket</u>
Beginning-of-Second-Cycle					
Pu-239	1412.	58.2	48.5	8.6	5.0
Pu-240	221.5	0.5	0.3	0.1	---
Pu-241	33.6	---	---	---	---
Pu-242	3.9	---	---	---	---
U-235	7.0	15.0	24.8	4.2	4.3
U-238	3498.	7885.	12629.	2139.	2143.
Fission Products	108.5	8.8	4.4	0.6	0.4
Total Heavy Metal	5284.5	7967.5	12707.0	2152.5	2152.7
End-of-Second-Cycle					
Pu-239	1291.	141.4	116.7	21.7	12.9
Pu-240	246.7	3.5	1.8	0.4	0.1
Pu-241	32.5	---	---	---	---
Pu-242	4.5	---	---	---	---
U-235	6.1	13.5	23.5	3.9	4.1
U-238	3432.	7779.	12551.	2124.	2134.
Fission Products	266.2	29.7	13.8	2.2	1.2
Total Heavy Metal	5279.0	7967.1	12706.8	2152.2	2152.3

\*Heavy metal excludes oxygen.

(a) Including axial extensions.

4.3-99

Amend. 64  
Jan. 1982

TABLE 4.3-4 (Cont.)

## HEAVY METAL\* MASS (KG) INVENTORY IN THE CRBRP

	Fuel	Inner Blanket(a)	Radial Blanket(a)	Lower Axial Blanket	Upper Axial Blanket
<b>Beginning-of-Third-Cycle</b>					
Pu-239	1477.	---	116.7	---	---
Pu-240	200.9	---	1.8	---	---
Pu-241	34.2	---	---	---	---
Pu-242	3.5	---	---	---	---
U-235	7.5	16.7	23.5	4.3	4.3
U-238	3465.	8253.	12551.	2108.	2108.
Fission Products	---	---	13.8	---	---
Total Heavy Metal	5188.1	8269.7	12706.8	2112.3	2112.3
<b>End-of-Third-Cycle</b>					
Pu-239	1308.	118.1	208.5	17.6	10.6
Pu-240	236.1	2.2	5.9	0.2	0.1
Pu-241	32.2	---	---	---	---
Pu-242	4.3	---	---	---	---
U-235	6.2	14.5	21.8	3.9	4.1
U-238	3377.	8113.	12438.	2088.	2096.
Fission Products	218.2	22.2	33.0	1.6	1.0
Total Heavy Metal	5182.	8270.0	12707.2	2111.3	2111.8

\*Heavy metal excludes oxygen.

(a) Including axial extensions.

4.3-100

Amend. 64  
Jan. 1982

TABLE 4.3-4 (Cont.)  
HEAVY METAL\* MASS (KG) INVENTORY IN THE CRBRP

	<u>Fuel</u>	<u>Inner Blanket</u> (a)	<u>Radial Blanket</u> (a)	<u>Lower Axial Blanket</u>	<u>Upper Axial Blanket</u>
<b>Beginning-of-Fourth-Cycle</b>					
Pu-239	1365.	109.4	208.5	17.6	10.6
Pu-240	243.9	2.1	5.9	0.2	0.1
Pu-241	33.5	---	---	---	---
Pu-242	4.4	---	---	---	---
U-235	6.5	13.4	21.8	4.1	4.2
U-238	3509.	7519.	12438.	2169.	2177.
Fission Products	218.2	20.6	33.0	1.6	1.0
<b>Total Heavy Metal</b>	<b>5380.5</b>	<b>7664.5</b>	<b>12707.2</b>	<b>2192.5</b>	<b>2192.9</b>
<b>End-of-Fourth-Cycle</b>					
Pu-239	1216.	206.8	285.6	34.9	21.2
Pu-240	273.5	8.0	11.3	0.9	0.3
Pu-241	32.7	---	---	---	---
Pu-242	5.2	---	---	---	---
U-235	5.4	11.6	20.3	3.8	4.0
U-238	3421.	7381.	12334.	2149.	2165.
Fission Products	414.2	55.2	55.7	4.4	2.4
<b>Total Heavy Metal</b>	<b>5368.0</b>	<b>7662.6</b>	<b>12706.9</b>	<b>2193.0</b>	<b>2192.9</b>

\*Heavy metal excludes oxygen.

(a) Including axial extensions.

4.3-101

Amend. 64  
Jan. 1982



TABLE 4.3-4 (Cont.)  
HEAVY METAL\* MASS (KG) INVENTORY IN THE CRBRP

	<u>Fuel</u>	<u>Inner Blanket(a)</u>	<u>Radial Blanket(a)</u>	<u>Lower Axial Blanket</u>	<u>Upper Axial Blanket</u>
<b>Beginning-of-Fifth-Cycle</b>					
Pu-239	1471.	---	130.1	---	---
Pu-240	200.0	---	4.9	---	---
Pu-241	34.1	---	---	---	---
Pu-242	3.5	---	---	---	---
U-235	7.6	16.7	23.1	4.3	4.3
U-238	3474.	8253.	12531.	2108.	2108.
Fission Products	---	---	18.1	---	---
<b>Total Heavy Metal</b>	<b>5190.2</b>	<b>8269.7</b>	<b>12706.9</b>	<b>2112.3</b>	<b>2112.3</b>
<b>End-of-Fifth-Cycle</b>					
Pu-239	1301.	119.7	224.7	17.6	10.6
Pu-240	235.8	2.3	8.7	0.2	0.1
Pu-241	32.1	---	---	---	---
Pu-242	4.3	---	---	---	---
U-235	6.2	14.5	21.4	3.9	4.1
U-238	3382.	8111.	12416.	2088.	2096.
Fission Products	219.	22.6	36.1	1.6	1.0
<b>Total Heavy Metal</b>	<b>5180.4</b>	<b>8270.1</b>	<b>12706.9</b>	<b>2111.3</b>	<b>2111.8</b>

\*Heavy metal excludes oxygen.

(a) Including axial extensions.

4.3-102

Amend. 64  
Jan. 1982

TABLE 4.3-4 (Cont.)  
HEAVY METAL\* MASS (KG) INVENTORY IN THE CRBRP

	<u>Fuel</u>	<u>Inner Blanket(a)</u>	<u>Radial Blanket(a)</u>	<u>Lower Axial Blanket</u>	<u>Upper Axial Blanket</u>
<b>Beginning-of-Sixth-Cycle</b>					
Pu-239	1358.	110.7	56.8	17.6	10.6
Pu-240	243.5	2.1	0.7	0.2	0.1
Pu-241	33.4	---	---	---	---
Pu-242	4.4	---	---	---	---
U-235	6.5	13.4	24.6	4.1	4.2
U-238	3518.	7518.	12617.	2169.	2177.
Fission Products	219.0	20.9	8.1	1.6	1.0
Total Heavy Metal	5382.8	7665.1	12707.2	2192.5	2192.9
<b>End-of-Sixth-Cycle</b>					
Pu-239	1205.	211.5	145.4	34.9	21.2
Pu-240	274.4	8.5	3.0	0.9	0.3
Pu-241	32.7	---	---	---	---
Pu-242	5.2	---	---	---	---
U-235	5.4	11.6	23.0	3.8	4.0
U-238	3424.	7374.	12514.	2149.	2165.
Fission Products	421.1	57.6	21.5	4.4	2.4
Total Heavy Metal	5367.8	8773.2	12706.9	2193.0	2192.9

\*Heavy metal excludes oxygen.

(a) Including axial extensions.

4.3-103

Amend. 64  
Jan. 1982

TABLE 4.3-5  
CRBRP FUEL MANAGEMENT SCHEME

SØC1:	Charge 156 fresh fuel assemblies, 82 fresh inner blanket assemblies and 126 fresh radial blanket assemblies.
EØC1 (128 fpd)	Discharge 3-Row Six Corner (3-R6C) inner blankets. Charge 3 fresh fuel assemblies in R6C.
EØC2 (200 fpd)	Discharge entire core (159 fuel assemblies) and inner blanket (79 blanket assemblies). Charge 156 fresh fuel assemblies and 82 fresh inner blanket assemblies.
EØC3 (275 fpd)	Discharge 6-R6C inner blankets. Charge 6 fresh fuel assemblies in R6C.
EØC4 (275 fpd)	Discharge entire core (162 fuel assemblies), inner blanket (76 blanket assemblies) and first row radial blanket (60 blanket assemblies). Charge 156 fresh fuel assemblies, 82 fresh inner blanket assemblies and 60 fresh row 1 radial blanket assemblies.
EØC5 (275 fpd)	Discharge 6-R6C inner blankets and outer row radial blanket (66 radial blanket assemblies). Charge 6 fresh fuel assemblies in R6C and 66 fresh row 2 radial blanket assemblies.

TABLE 4.3-6

## DELAYED NEUTRON CONSTANTS FOR CRBRP

Delayed Neutron Precursor Group (i)	Effective Delayed Neutron Fraction ( $\beta_i$ )	Decay Constant ( $\lambda_i$ ) sec.
1	$0.836 \times 10^{-4}$	0.0130
2	$0.718 \times 10^{-3}$	0.0314
3	$0.632 \times 10^{-3}$	0.1350
4	$0.123 \times 10^{-2}$	0.3450
5	$0.556 \times 10^{-3}$	1.3700
6	$0.183 \times 10^{-3}$	3.7650
Total $\beta_{eff}$	$0.340 \times 10^{-2}$	

51

TABLE 4.3-7

## FUEL AND INNER BLANKET POWER FRACTION SUMMARY\*

<u>Time-In-Life</u>	<u>Fuel</u>	<u>INNER Blanket (36")</u>
BOC1	.8603	.0720
EØC1	.8174	.0989
BOC2	.8208	.0967
EØC2	.7618	.1330
BOC3	.8308	.0683
EØC3	.7526	.1190
BOC4	.7623	.1129
EØC4	.6973	.1536
BOC5	.8351	.0690
EØC5	.7541	.1214
BOC6	.7895	.1195
EØC6	.7172	.1639

51 \* fraction of full operating power in central 36 inch high region.

Amend. 51  
Sept. 1979

TABLE 4.3-8

AXIAL BLANKET, AXIAL EXTENSION POWER NORMALIZATION FACTORS

TIME IN LIFE	$\frac{\text{POWER IN CORE + LAB + UAB}}{\text{POWER IN CORE}}$		$\frac{\text{POWER IN CORE + LAB}}{\text{POWER IN CORE}}$		
	Fuel Assemblies	Inner Blankets		Radial Blankets	
		Rows 2,4	Rows 6,8	RB1	RB2
BOC1	1.0137:1.0079	1.13:1.07	1.11:1.07	1.11:1.06	1.17:1.09
EOC1	1.0176:1.0102	1.12:1.07	1.11:1.07	1.11:1.06	1.15:1.08
BOC2	1.0177:1.0105	1.12:1.07	1.11:1.07	1.11:1.06	1.15:1.08
EOC2	1.0247:1.0140	1.12:1.07	1.11:1.07	1.11:1.06	1.14:1.07
BOC3	1.0140:1.0081	1.13:1.07	1.11:1.07	1.11:1.06	1.13:1.07
EOC3	1.0224:1.0132	1.12:1.07	1.11:1.07	1.11:1.06	1.13:1.07
BOC4	1.0229:1.0143	1.12:1.07	1.11:1.07	1.11:1.06	1.13:1.07
EOC4	1.0329:1.0192	1.12:1.07	1.11:1.07	1.11:1.06	1.13:1.07
	(a)	(b)		(c)	(d)

(a) Cycles 5-6 and subsequent repeat cycles 3-4 for the fuel.

(b) Cycles 5-6 and subsequent repeat cycles 3-4 for the inner blankets.

(c) Cycles 5-8 and subsequent repeat cycles 1-4.

(d) Assume cycle 5 = 1.12:1.07. Cycles 6-10 and subsequent repeat cycles 1-5.

TABLE 4.3-9  
 RADIAL BLANKET ASSEMBLY POWER\* SUMMARY  
 (MW)

Cycle	Assembly Position												Total Blanket Power
	1	2	3	4	5	6	7	8	10	11	12	13	
BOC1	.658	.389	.502	.492	.466	.347	.222	.142	.206	.197	.171	.132	40.9
EOC1	.805	.498	.626	.612	.574	.438	.298	.192	.284	.268	.230	.178	52.1
BOC2	.815	.505	.614	.609	.577	.443	.302	.194	.279	.267	.231	.180	52.3
EOC2	1.017	.657	.765	.760	.718	.568	.410	.267	.378	.361	.312	.246	67.3
BOC3	1.096	.706	.878	.859	.800	.623	.439	.284	.426	.400	.341	.266	74.2
EOC3	1.309	.880	1.064	1.041	.966	.772	.573	.379	.560	.524	.446	.353	92.4
BOC4	1.222	.821	1.021	.995	.916	.726	.537	.354	.535	.499	.422	.332	87.4
EOC4	1.383	.956	1.143	1.118	1.035	.838	.641	.430	.629	.589	.502	.401	100.8
BOC5	.664	.411	.521	.511	.484	.370	.668	.445	.663	.619	.524	.416	67.3
EOC5	.955	.630	.770	.753	.702	.556	.764	.516	.752	.704	.600	.480	86.7

\* Total 64-inch blanket power per assembly (assembly positions from Figure 4.3-3).

4.3-108

Amend. 64  
 Jan. 1982

TABLE 4.3-10  
 RADIAL BLANKET PEAK ROD POWER\* SUMMARY  
 (kw)

Cycle	Assembly Position											
	1	2	3	4	5	6	7	8	10	11	12	13
BOC1	16.6	11.1	15.0	14.6	14.3	10.2	5.3	3.2	5.0	4.8	4.2	3.0
EOC1	19.6	13.4	17.5	17.1	16.5	12.1	7.1	4.3	6.7	6.4	5.6	4.0
BOC2	19.8	13.6	17.1	17.0	16.6	12.3	7.2	4.4	6.6	6.4	5.6	4.0
EOC2	24.0	16.8	19.9	19.9	19.4	15.0	9.7	6.0	8.8	8.5	7.5	5.4
BOC3	25.7	18.1	23.1	22.6	21.8	16.5	10.3	6.3	9.9	9.5	8.2	5.9
EOC3	29.7	21.4	26.3	25.9	24.7	19.4	13.3	8.3	12.8	12.1	10.5	7.7
BOC4	27.6	19.9	25.3	24.7	23.4	18.2	12.4	7.8	12.2	11.6	9.9	7.2
EOC4	30.6	22.6	27.2	26.7	25.5	20.4	14.7	9.3	14.2	13.4	11.6	8.6
BOC5							15.4	9.6	14.9	14.1	12.1	8.9
EOC5							17.4	11.0	16.7	15.8	13.7	10.3

\* Total 64-inch peak blanket rod power (assembly positions from Figure 4.3-3).

4.3-109

Amend. 64  
 Jan. 1982



TABLE 4.3-11

RADIAL BLANKET POWER AND BURNUP HISTORY  
HIGHEST POWER ASSEMBLY (#1)

	Average Rod		Peak Rod		Peak Power	Peak Burnup
	Power(kw) <sup>+</sup>	Burnup(a/o) <sup>+</sup>	Power(kw) <sup>+</sup>	Burnup(a/o) <sup>+</sup>	(kw/ft)	(a/o)
<b>Initial:</b>						
SOC1	10.78	0.0	16.55	0.0	6.37	0.0
EOC1 (128 fpd)	13.19	0.075	19.59	0.114	7.83	0.241
SOC2	13.37	0.075	19.86	0.114	7.94	0.241
EOC2 (200 fpd)	16.67	0.235	24.00	0.347	9.92	0.749
SOC3	17.96	0.235	25.68	0.347	10.58	0.749
EOC3 (275 fpd)	21.46	0.536	29.68	0.770	12.53	1.695
SOC4	20.03	0.536	27.62	0.770	11.66	1.695
EOC4 (275 fpd)	22.67	0.871	30.65	1.227	13.11	2.737
<b>"Equilibrium":</b>						
SOC5	10.89	0.0	16.44	0.0	6.33	0.0
EOC5 (275 fpd)	15.65	0.187	22.27	0.272	9.13	0.580
SOC6	14.45	0.187	20.89	0.272	8.57	0.580
EOC6 (275 fpd)	17.84	0.430	25.10	0.618	10.56	1.352
SOC7	20.97	0.430	29.60	0.618	12.43	1.352
EOC7 (275 fpd)	23.91	0.783	32.80	1.108	13.99	2.465
SOC8	22.31	0.783	30.50	1.108	13.01	2.465
EOC8 (275 fpd)	24.59	1.159	33.03	1.616	14.23	3.634

+ total power and burnup in full 64" blanket rod.

4.3-110

Amend. 55  
Aug. 1980

TABLE 4.3-12

AXIAL PEAK-TO-AVERAGE POWER FACTORS,  $F_Z^N$ 

(Normalized to 1.0 Over 36-inch Active Core Height)

Time-in-Life	Peak $F_Z^N$					
	Clean Fuel <sup>(a)</sup>	Fuel With CR Influence <sup>(b)</sup>	Row 2, 4 Inner Blanket	Row 6, 8 Inner Blanket	Radial Blanket Row 1	Radial Blanket Row 2
BOC1	1.282	1.381	1.280	1.325	1.290	1.273
EOC1	1.255	1.309	1.340	1.377	1.331	1.331
BOC2	1.262	1.347	1.342	1.395	1.334	1.332
EOC2	1.210	1.210	1.371	1.370	1.344	1.353
EOC3	1.271	1.381	1.276	1.306	1.373	1.373
EOC3	1.230	1.269	1.365	1.377	1.376	1.387
BOC4	1.242	1.356	1.369	1.426	1.383	1.391
EOC4	1.186 (c)	1.193 (c)	1.375 (c)	1.360 (c)	1.359	1.378

- (a) applicable to all core fuel assemblies excluding those directly adjacent to R7C control rods.
- (b) applicable to those fuel assemblies directly adjacent to R7C control rods. Note, first year of life (i.e. cycles 1, 3,...) values should be applied to freshly refueled R6C fuel assemblies.
- (c) cycles 5-6, and subsequent, assumed to repeat cycles 3-4 for the fuel and inner blankets.

4.3-111

Amend. 51  
Sept. 1979

TABLE 4.3-13

CRBRP POWER DISTRIBUTION UNCERTAINTY (%)  
FUEL ASSEMBLIES

	CLEAN FUEL ZONES				FUEL ZONES ADJACENT TO INSERTED R7C CR			
	Peak Power Density	Power Density At Top Of Core	Rod Power	Assembly Power	Peak Power Density (near/far) <sup>a</sup>	Power Density at Top of Core (near/far) <sup>a</sup>	Rod Power (near/far) <sup>a</sup>	Assembly Power
<b>STATISTICAL<sup>b</sup></b>								
Experimental (3σ)	+7	+7	+7	+7	+7	+7	+7	+7
Criticality	+1	+1	+1	+1	+4/+1	+0/+3	+4/+1	+2
Fissile Content (tolerance)	+3	+3	+3	+3	+3	+3	+3	+3
SUBTOTAL (RHS)	+7.7	+7.7	+7.7	+7.7	+8.6/+7.7	+7.6/+8.2	+8.6/+7.7	+7.9
<b>NON-STATISTICAL (DIRECT)<sup>c</sup></b>								
Modeling	+2	+10	+2	+1	+3/-5 <sup>g</sup>	+15 <sup>e</sup>	+4/+1 <sup>g</sup>	+2 <sup>g</sup>
Control Rod Banking	+2	+2	+2	+2	+4/+2 <sup>g</sup>	+1	+4/+2 <sup>g</sup>	+3 <sup>g</sup>
Power Level/Dead Band <sup>d</sup>	+3	+3	+3	+3	+3	+3	+3	+3
ZPPR-7 Tilt (BØL)	f	f	f	f	f	f	f	f

<sup>a</sup> near refers to side of F/A directly adjacent to inserted R7C CR; far refers to far side of F/A adjacent to R7C CR.

<sup>b</sup> statistical uncertainties combine by quadrature.

<sup>c</sup> non-statistical uncertainties combine directly.

<sup>d</sup> not applied simultaneously with 15% overpower.

<sup>e</sup> EØL value with substantial portion of R7C control rods withdrawn. BØL apply +25+5 on far side of F/A adjacent to R7C CR.

<sup>f</sup> direct bias power down 3% in F/A #s 9, 10, 13-17, 23, 25, 37, 38, 41-45, 51 and 53; bias power down 1% in F/A #s 8, 11, 19, 36, 39, 47, 65, 68, 101 and 104 (BØC1, BØC3, BØC5,.... only); bias power down 1% in F/A #62 at BØC2 and F/A #'s 62 and 98 at BØC4, BØC6,.....

<sup>g</sup> for EØC, use corresponding clean fuel zone uncertainty.

4.3-112

Amend. 51  
Sept. 1979

TABLE 4.3-14

## CRBRP INNER BLANKET POWER DISTRIBUTION UNCERTAINTY (%)

	Beginning-Of-Life				End-Of-Life			
	Peak-Power Density	Power Density At Top Of Core (36")	Rod Power	Assy. Power	Peak-Power Density	Power Density At Top Of Core (36")	Rod Power	Assy. Power
56   NONSTATISTICAL (Direct) <sup>(a)</sup>								
Experimental	$\pm 10$	$+7 \pm 10$	$+2 \pm 10$	$+2 \pm 10$	$-5 \pm 5$	$+2 \pm 5$	$-2 \pm 5$	$-2 \pm 5$
Heavy Metal Content	$\pm 1$	$\pm 1$	$\pm 1$	$\pm 1$	$\pm 1$	$\pm 1$	$\pm 1$	$\pm 1$
U-235 Content	$\pm 1$	$\pm 1$	$\pm 1$	$\pm 1$	-	-	-	-
Modeling	$\pm 7$	$\pm 11$	$\pm 6$	$\pm 1$	$\pm 4$	$\pm 12$	$\pm 2$	$\pm 1$
Criticality	$\pm 2$	$\pm 2$	$\pm 2$	$\pm 2$	$\pm 1$	$\pm 1$	$\pm 1$	$\pm 1$
Control Rod Banking	$\pm 2$	$\pm 2$	$\pm 2$	$\pm 2$	$\pm 2$	$\pm 2$	$\pm 2$	$\pm 2$
Reactor Power <sup>(b)</sup>	$\pm 3$	$\pm 3$	$\pm 3$	$\pm 3$	$\pm 3$	$\pm 3$	$\pm 3$	$\pm 3$
Non-Pellet Heating <sup>(c)</sup>	-5	-5	-5		-2.5	-2.5	-2.5	
TOTAL	$-5 \pm 26$	$+2 \pm 30$	$-3 \pm 25$	$+2 \pm 20$	$-7.5 \pm 16$	$-0.5 \pm 24$	$-4.5 \pm 14$	$-2 \pm 13$

(a) Nonstatistical uncertainties combine directly.

(b) Not applied simultaneous with 15% overpower.

(c) Gamma heating in clad, Na and duct. Apply only to calculation of pellet (stack) power density.

56 |

56 |

4.3-113

Amend. 56  
Aug. 1980

51

TABLE 4.3-15

## CRBRP RADIAL BLANKET POWER DISTRIBUTION UNCERTAINTY (%)

	Beginning-Of-Life				End-Of-Life			
	Peak-Power Density	Power Density At Top Of Core (36")	Rod Power	Assy. Power	Peak-Power Density	Power Density At Top Of Core (36")	Rod Power	Assy. Power
<b>NONSTATISTICAL (Direct)<sup>(a)</sup></b>								
<b>Row 1:</b>								
Experimental	+2+9	+9+9	+4+9	+4+9	-4+7	+3+7	-2+7	-2+7
Heavy Metal Content	+1	+1	+1	+1	+1	+1	+1	+1
U-235 Content	+1	+1	+1	+1	-	-	-	-
Modeling	+7	-3+5	-2+5	+2	+7	-3+8	-2+3	+2
Control Rod Banking	+2	+2	+2	+2	+2	+2	+2	+2
Reactor Power <sup>(b)</sup>	+3	+3	+3	+3	+3	+3	+3	+3
Non-Pellet Heating <sup>(c)</sup>	-5	-5	-5	-	-3	-3	-3	-
<b>TOTAL</b>	<b>-3+23</b>	<b>+1+21</b>	<b>-3+21</b>	<b>+4+18</b>	<b>-7+20</b>	<b>-3+21</b>	<b>-7+16</b>	<b>-2+15</b>
<b>Row 2:</b>								
Experimental	+10+14	+18+14	+13+14	+13+14	+5+8	+13+8	+7+8	+7+8
Heavy Metal Content	+1	+1	+1	+1	+1	+1	+1	+1
U-235 Content	+1	+1	+1	+1	-	-	-	-
Modeling	+7	-6+5	-2+5	+2	+7	-6+8	-2+3	+2
Control Rod Banking	+2	+2	+2	+2	+2	+2	+2	+2
Reactor Power <sup>(b)</sup>	+3	+3	+3	+3	+3	+3	+3	+3
Non-Pellet Heating <sup>(c)</sup>	-5	-5	-5	-	-3	-3	-3	-
<b>TOTAL</b>	<b>+5+28</b>	<b>+7+26</b>	<b>+6+26</b>	<b>+13+23</b>	<b>+2+21</b>	<b>+4+22</b>	<b>+2+17</b>	<b>+7+16</b>

a) Nonstatistical uncertainties combine directly.

b) Not applied simultaneous with 15% overpower.

c) Gamma heating in clad, Na and duct. Apply only to calculation of pellet (stack) power density.

56

4.3-114

Amend. 56  
Aug. 1980

51

TABLE 4.3-16

CRBRP DOPPLER CONSTANTS  
 (-T dk/dT \* 10<sup>4</sup>)

	Fuel	Inner <sup>(a)</sup> Blankets	Radial <sup>(a)</sup> Blankets	Lower Axial Blanket	Upper Axial Blanket
BOC1	25.8	44.0	11.8	1.90	0.68
EOC1	25.8	47.6	12.4	2.10	0.74
BOC2	25.3	45.9	11.7	2.26	0.69
EOC2	25.8	49.3	12.0	2.38	0.88
BOC3	24.3	40.6	15.3	1.99	0.68
EOC3	24.6	47.7	14.9	2.32	0.83
BOC4	23.6	44.6	13.1	2.68	1.00
EOC4	24.2	45.9	12.8	2.56	1.16

(a) Includes axial extensions

TABLE 4.3-17

CRBRP VOIDED DOPPLER CONSTANTS

(-T dk/dT \* 10<sup>4</sup>)

	Fuel	Inner <sup>(a)</sup> Blankets	Radial <sup>(a)</sup> Blankets	Lower Axial Blanket	Upper Axial Blanket
BOC1	16.6	35.4	9.9	1.6	0.6
EOC4	15.8	35.1	10.8	2.1	0.9

51

(a) Includes axial extensions

Amend. 51  
Sept. 1979

TABLE 4.3-18  
 NODAL DOPPLER CONSTANTS  
 BOC1  
 (T DK/DT)

UPPER EXTENSION -.5110E-04	UPPER AXIAL BLANKET -.6780E-04	UPPER EXTENSION -.2359E-04
INNER BLANKET -.4284E-03 -.7519E-03 -.1272E-02 -.1139E-02 -.6084E-03	Fuel -.2471E-03 -.4391E-03 -.7865E-03 -.7098E-03 -.3942E-03	RADIAL BLANKET -.1373E-03 -.2168E-03 -.3340E-03 -.2899E-03 -.1471E-03
LOWER EXTENSION -.1459E-03	LOWER AXIAL BLANKET -.1904E-03	LOWER EXTENSION -.3213E-04

56 |

51



TABLE 4.3-19

(INTENTIONALLY DELETED)

TABLE 4.3-20

## CRBRP REGIONWISE SODIUM VOID REACTIVITY

(\$)<sup>(a)</sup>

	Fuel	Inner <sup>(b)</sup> Blankets	Radial <sup>(b)</sup> Blankets	Lower Axial Blanket	Upper Axial Blanket	Maximum Positive Void Worth		
						Fuel	Inner Blankets	Total
BOC1	+0.02	+1.38	-0.79	-0.27	-0.15	1.51	1.40	2.91
EOC1	+0.28	+1.43	-0.72	-0.25	-0.16	1.60	1.46	3.06
BOC2	+0.51	+1.45	-0.67	-0.27	-0.15	1.76	1.48	3.24
EOC2	+0.82	+1.51	-0.58	-0.23	-0.17	1.89	1.55	3.44
BOC3	+0.28	+1.36	-0.81	-0.28	-0.15	1.60	1.36	2.96
EOC3	+0.79	+1.47	-0.63	-0.25	-0.16	1.77	1.49	3.26
BOC4	+1.20	+1.48	-0.56	-0.27	-0.15	2.10	1.50	3.60
EOC4	+1.56	+1.61	-0.46	-0.22	-0.20	2.31	1.64	3.95

(a)  $\beta_{eff} = 0.0034$ 

(b) Includes axial extensions

TABLE 4.3-21

## CRBRP SODIUM DENSITY REACTIVITY COEFFICIENT

 $(\text{¢}/^{\circ}\text{F} * 10^3)$  (a)

	Fuel	Inner <sup>(b)</sup> Blankets	Radial <sup>(b)</sup> Blankets	Lower Axial Blanket	Upper Axial Blanket
BOC1	-4.3	+18.2	-13.1	-4.3	-2.4
EOC1	-0.3	+18.7	-12.1	-4.1	-2.6
BOC2	+3.4	+18.6	-11.3	-4.3	-2.4
EOC2	+8.0	+19.3	-9.9	-3.8	-2.7
BOC3	-0.1	+17.6	-13.7	-4.5	-2.4
EOC3	+7.5	+19.1	-11.0	-4.0	-2.5
BOC4	+13.7	+19.3	-9.7	-4.5	-2.4
EOC4	+19.1	+21.2	-8.2	-3.6	-3.2

(a) Cents per degree Fahrenheit of bulk region sodium temperature,  $\beta_{eff} = 0.0034$ . Correlation of  $0.157 \times 10^{-3} \Delta \text{ density}/\Delta^{\circ}\text{F}$  used.

(b) Includes axial extensions

TABLE 4.3-22  
 CRBRP AXIAL EXPANSION COEFFICIENT BY ASSEMBLY ROW  
 (¢/mil)

	<u>PELLET</u>		<u>STEEL</u>	
	BOC1	EOC4	BOC1	EOC4
Central Blanket	+.00390	+.00266	+.00060	+.00106
Row 3 Fuel	-.01496	-.01644	+.00221	+.00320
Row 4 Blanket	+.01144	+.00676	+.00189	+.00273
Row 5 Fuel	-.02508	-.02566	+.00373	+.00504
Row 5 Blanket	+.02657	+.01316	+.00427	+.00584
Refueling Positions	+.00530	-.01029	+.00088	+.00181
Row 7 Fuel	-.04110	-.02923	+.00552	+.00609
Row 8 Blanket	+.02486	+.00896	+.00450	+.00387
Rows 9, 10, 11 Fuel	-.17626	-.10136	+.01336	+.01214
Radial Blanket 1	-.00208	-.00532	-.00285	-.00093
Radial Blanket 2	+.00015	-.00095	-.00062	-.00037
<b>Total Fuel</b>	- .25740	-.18298	+.02482	+.02828
<b>Total Inner Blanket</b>	+.072207	+.03154	+ 01214	+.01350
<b>Total Radial Blanket</b>	-.00193	-.00627	-.00347	-.00130
<b>Control Rod</b>	-.049*	-.035*	*	*

\*movement of the core (pellets and steel) with respect to inserted control rods.

TABLE 4.3-23

CRBRP UNIFORM RADIAL EXPANSION COEFFICIENTS

	Cents per Mil of Outward Radial Motion			
	BOC-1	EOC-2	BOC-3	EOC-4
All Control Rods Out	-0.461	-0.441 <sup>(1)</sup>	-0.459	-0.448 <sup>(1)</sup>
6 Row 7 Corner Rods In	-0.427 <sup>(2)</sup>	-----	-0.426 <sup>(2)</sup>	-----
All 15 Control Rods In	-0.422 <sup>(3)</sup>	-----	-----	-0.390 <sup>(3)</sup>

(1) Recommended values for end-of-cycle conditions.

(2) Recommended values for beginning-of-cycle conditions.

(3) Refueling conditions.

TABLE 4.3-24

RADIAL MOTION REACTIVITY COEFFICIENTS  
(BEGINNING OF CYCLE ONE -- HOT STANDBY)

AXIAL LOCATION (Inches above bottom of fuel assembly)		CENTS PER INCH OF INWARD RADIAL MOTION														
		Row 2	Row 3	Row 4	Row 5	Row 6A	Row 6B	Row 7	Row 8A	Row 8B	Row 8C	Row 9	Row 10	Row 11	Row 12	
		Blkt.	Fuel	Blkt.	Fuel	Blkt.	Refuel*	Fuel	Fuel	Fuel	Blkt.	Fuel	Fuel	Radial Blkt.	Radial Blkt.	
Upper Axial Blanket	107.0	0.0	0.0	0.0	0.0	0.0	0.0	0.0	0.0	0.0	0.0	0.0	0.0	+0.01	0.0	
	103.0	0.0	0.0	0.0	0.0	0.0	0.0	-0.01	0.0	+0.01	0.0	+0.01	+0.1	+0.11	0.0	
	97.0	+0.01	-0.01	0.0	-0.01	-0.01	0.0	-0.07	0.0	+0.05	0.0	+0.08	+0.7	+1.10	+0.29	
Core Zone	93.0	+0.08	-0.18	-0.03	-0.39	-0.12	-0.07	-1.44	-0.08	+1.08	+0.19	+1.45	+10.5	+5.30	+1.13	
	87.0	+0.43	-0.59	-0.16	-1.34	-0.67	-0.47	-4.99	-0.29	+3.71	+1.51	+4.88	+36.0	+11.44	+2.56	
	81.0	+0.91	-1.02	-0.35	-2.35	-1.48	-1.07	-9.27	-0.53	+6.79	+3.53	+8.68	+64.5	+15.27	+2.80	
	75.0	+0.97	-1.03	-0.38	-2.43	-1.67	-1.21	-10.29	-0.58	+7.40	+4.03	+9.14	+67.6	+15.06	+3.42	
	69.0	+1.02	-1.13	-0.40	-2.72	-1.87	-1.36	-11.88	-0.67	+8.52	+4.45	+10.34	+76.0	+19.14	+3.75	
	63.0	+0.55	-0.73	-0.22	-1.79	-1.06	-0.75	-7.95	-0.45	+5.69	+2.34	+6.80	+49.1	+16.56	+3.78	
	57.0	+0.14	-0.23	-0.06	-0.56	-0.31	-0.21	-2.50	-0.14	+1.85	+0.46	+2.24	+16.0	+8.76	+1.90	
	Lower Axial Blanket	50.0	+0.01	0.0	-0.01	0.0	-0.04	-0.02	0.0	0.0	+0.03	+0.03	+0.05	+0.5	+0.76	+0.19
		43.0	0.0	0.0	0.0	0.0	0.0	0.0	0.0	0.0	0.0	0.0	0.0	0.0	+0.02	0.0
Row Total		+4.12	-4.92	-1.61	-11.59	-7.23	-5.16	-48.40	-2.74	+5.13	+16.54	+43.67	+321.0	+93.53	+19.82	

\*Six refueling locations contain blanket assemblies in cycle one.

4.3-123

Amend. 56  
Aug. 1980

TABLE 4.3-25

RADIAL MOTION REACTIVITY COEFFICIENTS  
(END OF CYCLE TWO -- ALL RODS OUT)

AXIAL LOCATION (Inches above bottom of fuel assembly)		CENTS PER INCH OF INWARD RADIAL MOTION													
		Row 2	Row 3	Row 4	Row 5	Row 6A	Row 6B	Row 7	Row 8A	Row 8B	Row 8C	Row 9	Row 10	Row 11	Row 12
		Blkt.	Fuel	Blkt.	Fuel	Blkt.	Refuel*	Fuel	Fuel	Fuel	Blkt.	Fuel	Fuel	Radial Blkt.	Radial Blkt.
↑ Upper Axial Blanket	107.0	0.0	0.0	0.0	0.0	0.0	0.0	0.0	0.0	0.0	0.0	0.0	0.0	+0.01	-0.01
	103.0	0.0	0.0	0.0	0.0	0.0	0.0	-0.01	+0.01	+0.01	0.0	+0.03	+0.1	+0.12	+0.01
	97.0	0.0	-0.01	0.0	-0.02	-0.01	+0.03	-0.07	+0.06	+0.08	-0.04	+0.19	+0.8	+1.22	+0.34
Core Zone	93.0	+0.03	-0.17	-0.05	-0.30	-0.11	+0.35	-0.92	+0.77	+1.20	+0.24	+2.78	+10.4	+5.93	+1.35
	87.0	+0.17	-0.55	-0.40	-0.95	-0.79	+0.82	-2.73	+2.31	+3.69	+3.33	+8.58	+32.9	+12.85	+3.02
	81.0	+0.33	-0.85	-0.79	-1.46	-1.52	+1.12	-4.06	+3.42	+5.51	+6.69	+13.08	+51.0	+17.31	+3.33
	75.0	+0.32	-0.80	-0.74	-1.37	-1.40	+1.05	-3.69	+3.12	+5.02	+5.98	+12.12	+47.5	+16.88	+4.06
	69.0	+0.34	-0.87	-0.81	-1.50	-1.52	+1.16	-4.06	+3.42	+5.50	+6.37	+13.22	+51.5	+18.05	+4.45
	63.0	+0.19	-0.58	-0.45	-1.01	-0.84	+0.86	-2.74	+2.31	+3.71	+3.24	+8.79	+33.7	+13.58	+4.50
	57.0	+0.05	-0.19	-0.12	-0.32	-0.23	+0.29	-0.89	+0.77	+1.25	+0.41	+2.97	+11.3	+6.92	+2.25
↓ Lower Axial Blanket	50.0	+0.01	0.0	-0.02	0.0	-0.03	-0.01	-0.01	+0.02	+0.04	+0.02	+0.10	+0.4	+0.65	+0.23
	43.0	0.0	0.0	0.0	0.0	0.0	0.0	0.0	0.0	0.0	0.0	0.0	0.0	+0.01	-0.01
Row Total		+1.44	-4.02	-3.38	-6.93	-6.45	+5.67	-19.18	+16.21	+26.01	+26.24	+61.80	+239.6	+93.53	+23.52

\*Six refueling locations contain three fuel and three blanket assemblies in cycle two.

4.3-124

Amend. 56  
Aug. 1980

TABLE 4.3-26

CRBRP INHERENT FEEDBACK REACTIVITY (\$)
   
STARTUP FROM HOT-STANDBY CONDITIONS\* TO 40% POWER/40% FLOW<sup>+</sup>

	Feedback (\$)	
	BOC1	EOC4
Doppler		
Fuel	-0.385	-0.295
Axial Blankets	-0.008	-0.013
Inner Blankets	-0.259	-0.547
Radial Blankets	<u>-0.048</u>	<u>-0.100</u>
Total	-0.700 ± 0.084	-0.955 ± 0.115
Uniform Radial Expansion	-0.062 ± 0.012	-0.065 ± 0.013
Uniform Axial Expansion		
Fuel	-0.219	-0.126
Structure (FA)	+0.023	+0.021
Blankets	+0.020	+0.015
Structure (BA)	<u>+0.004</u>	<u>+0.009</u>
Total	-0.172 ± 0.040	-0.081 ± 0.019
Sodium Density	-0.014 ± 0.004	+0.048 ± 0.014
Total ± 1σ**	-0.948 ± 0.094	-1.053 ± 0.118

\* 600°F isothermal

+ 635°F inlet temperature

\*\*Uncertainty in net feedback includes both nuclear uncertainty in reactivity coefficient and thermal uncertainty.



TABLE 4.3-27  
 CRBRP TEMPERATURE DEFECT COMPONENTS  
 Beginning of Cycle One

	Temperature Defect (\$)	
	Refueling Temp. to Hot Full Power	Hot Standby Temp. to Hot Full Power
<b>Doppler</b>		
Fuel	-0.879	-0.719
Axial Blankets	-0.032	-0.016
Inner Blankets	-0.837	-0.564
Radial Blankets	-0.177	-0.104
<b>Total</b>	<u>-1.925 ± 0.258</u>	<u>-1.403 ± 0.243</u>
<b>Uniform Radial Expansion</b>	-0.584 ± 0.117	-0.230 ± 0.046
<b>Uniform Axial Expansion</b>		
Fuel	-0.504	-0.407
Structure	+0.054	+0.033
Blankets	+0.069	+0.042
Structure	+0.015	+0.007
<b>Total</b>	<u>-0.366 ± 0.099</u>	<u>-0.325 ± 0.095</u>
<b>Sodium Density</b>		
Fuel	-0.022	-0.013
Axial Blankets	-0.030	-0.017
Inner Blankets	+0.072	+0.036
Radial Blankets	-0.051	-0.025
<b>Total</b>	<u>-0.031 ± 0.010</u>	<u>-0.019 ± 0.006</u>
<b>Bowing</b>	± 0.300	± 0.300
<b>Total ± 1σ*</b>	-2.907 ± 0.425	-1.977 ± 0.400

\* Net feedback uncertainty includes both nuclear uncertainty in reactivity coefficient and thermal uncertainties.

TABLE 4.3-28  
CRBRP TEMPERATURE DEFECT SUMMARY

	Temperature Defect (\$)	
	Refueling Temp. to Hot Full Power	Hot Standby Temp. to Hot Full Power
BOC1	-2.907 ± 0.425*	-1.977 ± 0.400*
EOC1	-3.112 ± 0.447	-2.145 ± 0.423
BOC2	-3.046 ± 0.402	-2.097 ± 0.395
EOC2	-3.234 ± 0.471	-2.298 ± 0.445
BOC3	-2.869 ± 0.423	-1.939 ± 0.399
EOC3	-3.144 ± 0.465	-2.204 ± 0.440
BOC4	-2.955 ± 0.450	-2.063 ± 0.426
EOC4	-3.106 ± 0.468	-2.223 ± 0.441

\*Uncertainties (at approximately the 1σ level) include both nuclear uncertainty in feedback coefficients and thermal uncertainties.

TABLE 4.3-29

CRBRP PRIMARY CONTROL SYSTEM REACTIVITY REQUIREMENTS AND  
CONTROL ROD WORTHS ( $\Delta K/K$ )

<u>REQUIREMENTS</u>	BOC1	EOC1	BOC2	EOC2
Hot-To-Cold Temperature Defect	0.74 $\pm$ .33	0.67 $\pm$ .33	0.66 $\pm$ .32	0.77 $\pm$ .35
Excess Reactivity	2.95 $\pm$ .63	1.59 $\pm$ .66	3.17 $\pm$ .70	1.04 $\pm$ .85
Reactivity "Fault"	0.72 $\pm$ .25*	.33 $\pm$ .19*	0.79 $\pm$ .28*	0.20 $\pm$ .22*
<u>PRIMARY CONTROL SYSTEM WORTH</u>				
6R7C	6.27 $\pm$ .77	6.04 $\pm$ .74	6.35 $\pm$ .78	5.94 $\pm$ .73
3R4	1.63 $\pm$ .20	1.95 $\pm$ .24	1.94 $\pm$ .24	2.42 $\pm$ .30
Stuck Rod	-1.68 $\pm$ .41*	-1.99 $\pm$ .35*	-1.64 $\pm$ .43*	-2.08 $\pm$ .36*
<u>BALANCE</u>				
(Worth-Requirements $\pm 3\sigma$ Uncertainty)	1.81 $\pm$ .98 (3 $\sigma$ )	3.41 $\pm$ 1.01 (3 $\sigma$ )	2.03 $\pm$ 1.06 (3 $\sigma$ )	4.27 $\pm$ 1.60 (3 $\sigma$ )

\*Uncertainties in reactivity fault and stuck rod are partly correlated with uncertainties in temperature defect, excess reactivity, and control rod worth. Therefore, the magnitude of these uncertainties are reduced when they are combined with the uncertainties in temperature defect, excess reactivity and control rod worth to determine the net uncertainty in worth-minus-requirement.

4.3-128

Amend. 76  
March 1983

TABLE 4.3-29 (Continued)

CRBRP PRIMARY CONTROL SYSTEM REACTIVITY REQUIREMENTS AND CONTROL ROD WORTHS ( $\Delta K/K$ )

	BOC3	EOC3	BOC4	EOC4	BOC5
<b>REQUIREMENTS</b>					
Hot-to-Cold Temperature Defect	0.70 $\pm$ .32	0.74 $\pm$ .34	0.70 $\pm$ .32	0.81 $\pm$ .34	0.70 $\pm$ .32
Excess Reactivity	3.57 $\pm$ .63	0.85 $\pm$ .77	3.61 $\pm$ .87	1.00 $\pm$ 1.15	3.73 $\pm$ .63
Reactivity "Fault"	0.95 $\pm$ .30*	0.16 $\pm$ .19*	0.95 $\pm$ .37*	0.18 $\pm$ .28*	1.00 $\pm$ .29*
<b>PRIMARY CONTROL SYSTEM WORTH</b>					
6R7C	6.13 $\pm$ .75	5.75 $\pm$ .71	6.29 $\pm$ .77	5.72 $\pm$ .70	6.25 $\pm$ .77
3R4	1.44 $\pm$ .18	2.06 $\pm$ .25	2.16 $\pm$ .26	2.72 $\pm$ .33	1.55 $\pm$ .19
Stuck Rod	-1.40 $\pm$ .45*	-2.04 $\pm$ .33*	-1.46 $\pm$ .50*	-1.92 $\pm$ .39*	-1.40 $\pm$ .45*
<b>BALANCE</b>					
(Worth-Requirement $\pm 3\sigma$ Uncertainty)	0.95 $\pm$ .95 (3 $\sigma$ )	4.02 $\pm$ 1.09 (3 $\sigma$ )	1.73 $\pm$ 1.19 (3 $\sigma$ )	4.53 $\pm$ 1.43 (3 $\sigma$ )	0.97 $\pm$ 0.97 (3 $\sigma$ )

\*Uncertainties in reactivity fault and stuck rod are partly correlated with uncertainties in temperature defect, excess reactivity, and control rod worth. Therefore, the magnitude of these uncertainties are reduced when they are combined with the uncertainties in temperature defect, excess reactivity and control rod worth to determine the net uncertainty in worth-minus-requirements.

TABLE 4.3-30

CRBRP SECONDARY CONTROL SYSTEM REACTIVITY REQUIREMENTS AND CONTROL ROD WORTHS ( $\Delta K/K$ )

	BOC1	EOC1	BOC2	EOC2
<b>REQUIREMENTS</b>				
Hot-To-Cold Temperature Defect				
Reactivity "Fault"	1.05 $\pm$ .37	0.99 $\pm$ .37	0.97 $\pm$ .36	1.08 $\pm$ .39
	0.72 $\pm$ .25*	0.33 $\pm$ .19*	0.79 $\pm$ .28*	0.20 $\pm$ .22*
<b>SECONDARY CONTROL SYSTEM WORTH</b>				
6R7F	4.49 $\pm$ .55	4.62 $\pm$ .56	4.68 $\pm$ .57	4.78 $\pm$ .58
Stuck Rod	-1.87 $\pm$ .23**	-1.93 $\pm$ .23**	-1.95 $\pm$ .24**	-1.99 $\pm$ .24**
<b>BALANCE</b>				
(Worth-Requirement $\pm$ 3 $\sigma$ Uncertainty)	0.85 $\pm$ .46 (3 $\sigma$ )	1.37 $\pm$ .47 (3 $\sigma$ )	0.97 $\pm$ .49 (3 $\sigma$ )	1.51 $\pm$ .51 (3 $\sigma$ )

\*Uncertainty in reactivity fault partly correlated with uncertainty in temperature defect.  
 \*\*Stuck rod uncertainty directly correlated with rod bank worth uncertainty.

4.3-130

Amend. 76  
 March 1983

TABLE 4.3-30  
(Continued)

CRBRP SECONDARY CONTROL SYSTEM REACTIVITY REQUIREMENTS AND CONTROL ROD WORTHS ( $\Delta K/K$ )

	BOC3	EOC3	BOC4	EOC4	BOC5
<b>REQUIREMENTS</b>					
Hot-to-Cold Temperature Defect	$1.02 \pm .36$	$1.06 \pm .38$	$1.00 \pm .37$	$1.11 \pm .39$	$1.02 \pm .36$
Reactivity "Fault"	$0.95 \pm .30^*$	$.16 \pm .19^*$	$0.95 \pm .37^*$	$0.18 \pm .28^*$	$1.00 \pm .29^*$
<b>SECONDARY CONTROL SYSTEM WORTH</b>					
6R7F Stuck Rod	$4.27 \pm .52$ $-1.78 \mp .22^{**}$	$4.56 \pm .55$ $-1.90 \mp .23^{**}$	$4.63 \pm .56$ $-1.77 \mp .22^{**}$	$4.72 \pm .57$ $-1.34 \mp .16^{**}$	$4.37 \pm .53$ $-1.82 \mp .22^{**}$
<b>BALANCE</b>					
(Worth-Requirements $\pm 3\sigma$ Uncertainty)	$0.52 \pm .46 (3\sigma)$	$1.44 \pm .48 (3\sigma)$	$0.91 \pm .55 (3\sigma)$	$2.09 \pm .51 (3\sigma)$	$0.53 \pm .47 (3\sigma)$

\*Uncertainty in reactivity fault partly correlated with uncertainty in temperature defect.

\*\*Stuck rod uncertainty directly correlated with rod bank worth uncertainty.

4.3-131

TABLE 4.3-31

CRBRP SUMMARY OF CONTROL ROD INTERACTION EFFECTS

Interaction factor defined as the ratio of the worth of a single rod, or group of rods, inserted in an asymmetric configuration relative to the average worth of these same rods when inserted in a symmetric, banked configuration.

ROW-7-CORNER (R7C) PRIMARY CONTROL ROD BANK:

- o single R7C (faulted) rod removed from a fully inserted\* 6 R7C bank.

fresh core 2.11

burned core 1.82

- o single R7C (faulted) rod removed from a fully inserted 6 R7C bank with 3 R4 fully inserted.

fresh 2.32

burned core 2.18

ROW-7-FLAT (R7F) SECONDARY CONTROL ROD BANK:

- o single (stuck) R7F rod removed from a fully inserted 6 R7F bank with a faulted (withdrawn) R7C in an adjacent PCA channel.

fresh core 2.49

burned core 1.71

- o single (stuck) R7F rod removed from a fully inserted 6 R7F bank with an expected, symmetric 6 R7C PCA bank insertion.

fresh core 1.63

ROW-4 (R4) PRIMARY CONTROL ROD BANK:

- o single (stuck) R4 rod removed from a fully inserted 3 R4 bank

fresh core 1.10

\*Interaction factor for 1 R7C removed from a partly inserted 6 R7C bank see Figure 4.3-32.

TABLE 4.3-32

CRBRP PRIMARY AND SECONDARY SCRAM SHUTDOWN WORTH FROM HOT-FULL-POWER  
EXPECTED (NOMINAL) CORE CONDITIONS (% $\Delta$ K/K)

Time In Life	PRIMARY CONTROL SYSTEM			SECONDARY CONTROL SYSTEM	
	Stuck Rod	R7C Bank Insertion (Inches) (1)	R7C Shutdown Worth (% $\Delta$ K/K)	R4 Shutdown Worth (% $\Delta$ K/K)	R7F Shutdown Worth (% $\Delta$ K/K) With 1 Rod Stuck Full Out
BOC1	1 R4, full out	17.3	3.32	1.03	3.27
	1 R7C, partly in		2.47	1.63	
BOC2	1 R4, full out	18.1	3.18	1.23	3.41
	1 R7C, partly in		2.38	1.94	
BOC3	1 R4, full out	20.0	2.53	.91	3.11
	1 R7C, partly in		1.94	1.44	
BOC4	1 R4, full out	19.6	2.68	1.37	3.37
	1 R7C, partly in		2.04	2.16	
EOC4	1 R4, full out	9.3	4.72	1.72	3.44
	1 R7C, partly in		3.21	2.72	
BOC5	1 R4, full out	20.3	2.51	.98	3.18
	1 R7C, partly in		1.93	1.55	

(1) Core height = 36.2 inches (hot)



TABLE 4.3-32 (Continued)

CRBRP PRIMARY AND SECONDARY SCRAM SHUTDOWN WORTH FROM HOT-FULL-POWER  
EXPECTED (NOMINAL) CORE CONDITIONS (%ΔK/K)

(3σ Maximum Excess Reactivity and Minimum Control Rod Worth)

Time In Life	PRIMARY CONTROL SYSTEM			SECONDARY CONTROL SYSTEM	
	Stuck Rod	R7C Bank Insertion (Inches) <sup>(1)</sup>	R7C Shutdown Worth (%ΔK/K)	R4 Shutdown Worth (%ΔK/K)	R7F Shutdown Worth (%ΔK/K) With 1 Rod Stuck Full Out
BOC1	1 R4, full out	20.2	2.27	.90	2.87
	1 R7C, partly In		1.75	1.43	
BOC2	1 R4, full out	21.1	2.08	1.08	2.99
	1 R7C, partly In		1.62	1.70	
BOC3	1 R4, full out	23.3	1.50	.80	2.73
	1 R7C, partly In		1.19	1.26	
BOC4	1 R4, full out	23.7	1.47	1.21	2.96
	1 R7C, partly In		1.17	1.90	
EOC4	1 R4, full out	15.1	3.33	1.51	3.02
	1 R7C, partly In		2.41	2.39	
BOC5	1 R4, full out	23.6	1.46	.86	2.79
	1 R7C, partly In		1.17	1.36	

(1) Core height = 36.2 inches (hot)

TABLE 4.3-33

ZPPR CRITICAL EIGENVALUE ( $k_{eff}$ ) PREDICTED BY CRBRP DESIGN METHOD AND DATA

	Homogeneous: ZPPR4			Heterogeneous: ZPPR 7 & 8			
	Measured	Calculated	C/E	Measured	Calculated	C/E	
ZPPR-4/1	1.00080	0.99527	0.9945	ZPPR-7A	1.00028	0.99019	0.9899
ZPPR-4/2	1.00065	1.00049	0.9998	ZPPR-7B	1.00064	0.98924	0.9886
ZPPR-4/3	1.00088	0.99916	0.9983	ZPPR-7C	1.00002	0.99089	0.9909
ZPPR-4/4	1.00083	0.99390	0.9931	ZPPR-7D	1.00001	0.99348	0.9935
		Mean C/E = 0.9964		ZPPR-7E	1.00058	0.98873	0.9882
		$1\sigma = \pm 0.0031$		ZPPR-7F	1.00053	0.98858	0.9881
				ZPPR-7G	1.00053	0.98858	0.9881
				ZPPR-8F	1.00062	0.99156	0.9901
						Mean C/E = 0.9900	
						$1\sigma = \pm 0.0019$	

4.3-134

Amend. 51  
Sept. 1979

TABLE 4.3-34

MAXIMUM PARAMETER VALUES DURING A REACTOR INHERENT RESPONSE  
 TRANSIENT AT A REACTOR STARTUP OPERATING POINT (9% POWER,  
 40% FLOW)

<u>Parameter</u>	<u>Maximum Value</u>	<u>Acceptability Limits</u>
Reactor Power	39%	
Maximum Fuel Temperature	1597 <sup>0</sup> F	Less than fuel melting temperature
Maximum Cladding Temperature	984 <sup>0</sup> F	Less than cladding melting temperature
Maximum Coolant Temperature	984 <sup>0</sup> F	Less than sodium boiling temperature

Amend. 59  
 Dec. 1980

TABLE 4.3-35  
EX-CORE NEUTRON FLUX AT BEGINNING OF CYCLE THREE

Core Midplane Location	Total Neutron Flux (n/cm <sup>2</sup> sec)	Fraction of Neutron Flux with Energy Greater than 0.1 MeV
Radial Blanket/Removable Shield Interface	$8.5 \times 10^{14}$	0.37
Fixed Radial Shield Surface*	$4.1 \times 10^{13}$	0.24
Core Barrel Surface*	$6.1 \times 10^{12}$	0.20
Reactor Vessel Surface*	$< 6 \times 10^{11}$	$< 0.1$

\* Design lifetime of non-replaceable components is 30 calendar years (22.5 equivalent full power years).

TABLE 4.3-36

GROUP STRUCTURE OF 30, 21, AND 9 NEUTRON ENERGY GROUP SETS

Group			Lethargy Width	Lower Energy Limit
30	21	9		
1	1	1	0.5	6.065 MeV*
2			0.5	3.679
3			0.5	2.231
4	3	2	0.5	1.353
5	4		0.5	820.8 KeV
6	5	3	0.5	497.9
7	6		0.25	387.7
8			0.25	302.0
9	7		0.5	183.2
10	8	4	0.5	111.1
11	9		0.5	67.38
12	10		0.5	40.87
13	11	5	0.47	25.54
14			0.25	19.89
15	12		0.28	15.03
16			0.5	9.119
17			13	0.5
18	14		0.5	3.355
19	15	6	0.1667	2.840
20			0.1667	2.404
21			0.1667	2.035
22	16	7	0.5	1.234
23	17		0.5	748.5 eV
24	18		0.5	454.0
25	19	8	0.5	275.4
26	20		0.75	130.1
27			0.75	61.44
28		1.5	13.71	
29			3.0	0.6826
30	21	9	1.0	0.2511

51

\*Upper energy 10 MeV

Amend. 51  
Sept. 1979

TABLE 4.3-37

COMPARISONS OF W-ARD CALCULATIONS WITH PIN AND PLATE MEASUREMENTS  
(Reactivity Units are Inhours)

<u>Measurement</u>	<u>Experiment</u>		<u>Calculation</u>	
<u>Plate vs. Pin, (ih)</u>	<u>Plate Minus Pin</u>		<u>Ratio of C to E<sup>a</sup></u>	
ZPPR-2	75.8 ± 7.2		1.64 (1.2) <sup>c</sup>	
ZPR-6-7	52.3 ± 3.4		1.07	
<u>Sodium Voiding (ih/kg)</u>	<u>Plate</u>	<u>Ratio of Pin to Plate</u>	<u>Ratio of Plate C to E<sup>a</sup></u>	<u>Ratio of Pin to Plate<sup>b</sup></u>
69 matrices (ZPPR-2)	3.23 ± 0.02	1.05 ± 0.01	0.94	1.05
9 matrices (ZPR-6-7)	6.94 ± 0.6	0.92 ± 0.11	0.97	-
<u><sup>238</sup>U Doppler (ih/kg)</u>				
300°K to 1100°K (ZPPR-2)	-0.621 ± 0.009	0.89 ± 0.03	0.96	0.91

a Calculation to Experiment

b Calculated

c The value in parenthesis results when anisotropic diffusion coefficients for plate geometry were used.

Amend. 51  
Sept. 1979

TABLE 4.3-38

ZPPR-4 CRITICAL EIGENVALUE PREDICTED WITH CRBRP DESIGN METHOD AND DATA\*

	Measured $k_{eff}$	Calculated $k_{eff}$	C/E
ZPPR-4 Phase 1	1.00080	0.99527	0.9945
ZPPR-4 Phase 2	1.00065	1.00049	0.9998
ZPPR-4 Phase 3	1.00088	0.99916	0.9983
ZPPR-4 Phase 4	1.00083	0.99390	0.9931
			Mean = 0.9964
			$1\sigma \pm 0.0031$

\* Two-dimensional (hexagonal-planar geometry) diffusion calculations with 9-group ENDF/B-III cross section data.

51

Amend. 51  
Sept. 1979

TABLE 4.3-39  
ZPPR-4 REACTION RATE SUMMARY

	Number of Data Points	Power Normalization*	Mean C/E	RMS Deviation
Pu <sup>239</sup> (n, fission)	245	1.000	0.997	± 1.9%
U <sup>235</sup> (n, fission)	234	1.022	0.989	± 2.1%
U <sup>238</sup> (n, fission)	289	0.938	0.997	± 5.5%
U <sup>238</sup> (n, capture)	291	1.057	1.001	± 1.9%
Gamma Heating in Steel	32	---	---	± 10% <sup>+</sup>

\* Power normalization normalizes all reactions to the Pu<sup>239</sup> fission rate in the core.

+ Uncertainty in gamma heating estimated from scatter in preliminary data. No statistical significance implied.



TABLE 4.3-40  
ZPPR-4 CONTROL ROD WORTHS

Control Rod Bank	C/E
Central Rod	0.973
Row 4	0.977
Row 7 Flat (or C+R7F)	0.981
Row 7 Corner (or C+R7C)	0.995

51

Amend. 51  
Sept. 1979

4.3-141

TABLE 4.3-41

ZPPR-7 &amp; 8 CRITICAL EIGENVALUE PREDICTED WITH CRBRP DESIGN METHOD AND DATA\*

	Measured $k_{eff}$	Calculated $k_{eff}$	C/E
ZPPR-7A	1.00028	0.99019	0.9899
ZPPR-7B	1.00064	0.98924	0.9886
ZPPR-7C	1.00002	0.99089	0.9909
ZPPR-7D	1.00001	0.99347	0.9935
ZPPR-7F	1.00058	0.98873	0.9882
ZPPR-7G	1.00053	0.98858	0.9881
ZPPR-8F	1.00062	0.99156	0.9909
			Mean = 0.9900
			$1\sigma = \pm 0.0019$

\* Two-dimensional (hexagonal-planar geometry) diffusion calculations with 9-group, ENDF/B-III cross section data.

4.3-142

Amend. 51  
Sept. 1979

TABLE 4.3-42

## ZPPR-7 REACTION RATE SUMMARY

	Core Region	Number of Data Points	Power Normalization*	Mean C/E	RMS Deviation
Pu <sup>239</sup> (n, fission)	Fuel	106	1.000	1.000	+ 1.8%
	Inner Blankets	66	1.000	1.012	+ 1.3%
U <sup>235</sup> (n, fission)	Fuel	173	1.040	1.000	+ 1.6%
	Inner Blankets	93	1.040	1.001	+ 1.7%
U <sup>238</sup> (n, fission)	Fuel	148	0.832	1.002	+ 4.1%
	Inner Blankets	92	0.832	1.131	+ 4.9%
U <sup>238</sup> (n, capture)	Fuel	148	1.097	1.002	+ 2.6%
	Inner Blankets	92	1.097	0.994	+ 1.8%
Gamma Heating in Steel	All	18	Un-normalized		+ 10% <sup>†</sup>

\* Power normalization normalizes all reactions to Pu<sup>239</sup> fission in fuel.

† Uncertainty in gamma heating estimated from scatter in preliminary data. No statistical significance implied.

TABLE 4.3-43

## ZPPR-7 CONTROL ROD WORTH CALCULATION-TO-EXPERIMENT RATIOS\*

	<u>Beginning-of-Life Phase B</u>	<u>End-of-Life Phase C</u>
Row 4	0.916 (0.963)	0.906 (0.973)
Row 7 - Flat	0.898 (0.987)	0.887 (0.952)
Row 7 - Corner	0.992 (1.074)	0.905 (0.986)

\* Calculated with standard two-dimensional (hexagonal planar geometry) coarse-mesh direct eigenvalue difference diffusion theory methods using 9-group ENDF/B-III data. Values in ( ) from four-mesh per ZPPR drawer diffusion calculations.

51

Amend. 51  
Sept. 1979

TABLE 4.3-44

## COMPARISON OF NUCLEAR PARAMETERS FOR CRBRP AND FFTF

	CRBRP	FFTF
<b>LAYOUT</b>		
Number of Fuel Assemblies	156	73
Inner Enrichment Zone		28
Outer Enrichment Zone		45
Number of Test Loop Locations	-	9
Number of In-Core Control Rods	15	9
Number of Inner Blanket Assemblies	82	-
Number of Radial Blanket Assemblies	126	-
Number of Radial Reflector Assemblies	-	108 <sup>(1)</sup>
Number of Removable Radial Shields	312	-
<b>DIMENSIONS</b>		
Assembly Pitch (meters)	0.1209	0.1198
Core <sup>(2)</sup> Equivalent Diameter (meters)	2.019	1.200
Core <sup>(2)</sup> Cross-Sectional Area (meters)	3.203	1.131
Active Fuel Height (meters)	0.9144	0.9144
Height-to-Diameter Ratio	0.453	0.762
Axial Blkt. Height, Upper/Lower (meters)	0.3556/0.3556	-
Inner and Radial Blanket Height (meters)	1.6256	-
<b>INITIAL CORE ENRICHMENTS AND FUEL MASSES</b>		
Enrichments (Pu/U+Pu)		
Inner Enrichment Zone	0.328	0.224
Outer Enrichment Zone		0.274
Enrichment Ratio (Outer/Inner)	N/A	1.22
Isotopic Composition of Feed Plutonium		
Pu-238	0.0006	-
Pu-239	0.8604	0.864
Pu-240	0.1170	0.117
Pu-241	0.0200	0.017
Pu-242	0.0020	0.002

<sup>(1)</sup> Includes positions for as many as fifteen peripheral shim rods.

<sup>(2)</sup> "Core" includes fuel, inner blankets and in-core control rods.

TABLE 4.3-44 (Continued)

	<u>CRBRP</u>	<u>FFTF</u>
Fuel Masses, BOL (kg)		
U-235	7.6	13.1
U-238	3476.0	1862.
Pu-239	1468.0	552.6
Pu-240	199.7	74.7
Pu-241	34.0	10.7
Pu-242	3.4	1.12
Fissile Plutonium <sup>(3)</sup>	1502.0	563.3
Radial, Inner & Axial Blanket Fuel Masses, BOL, (kg)		
U-235	51.0	-
U-238	25150.0	-
CONTROL SYSTEM DESIGN		
Number of In-Core Control Rods	15	9
Primary (Burnup, Startup, Shutdown)	9	6
Secondary (Shutdown)	6	3
Neutron Absorber Material	B <sub>4</sub> C	B <sub>4</sub> C
Absorber Pellet Height (meters)	0.9144	0.9144
Primary System		
Rods per Assembly	37	61
B-10 Enrichment		
First Cycle (atom percent)	92	Natural
Equilibrium Cycle (atom percent)	92	Natural
Secondary System		
Rods per Assembly	31	61
B-10 Enrichment		
First Cycle (atom percent)	92	Natural
Equilibrium Cycle (atom percent)	92	Natural

<sup>(3)</sup> Fissile Plutonium = Pu-239 + Pu-241

TABLE 4.3-44 (Continued)

	<u>CRBRP</u>	<u>FFTE</u>
<b>OPERATING CONDITIONS</b>		
Total Reactor Power (MWt)	975	400
Cycle Length (full power days)		
First cycle	128	100
Second cycle	200	100
Equilibrium cycle	275	100
Peak Pellet Burnup (MWd/T)		
First Core	74,200	80,000
Equilibrium Core	110,200	80,000
Residence Time for Equilibrium Conditions (Cycles)		
Fuel and Inner Blanket Assemblies	2	3 and 4
Radial Blanket Assemblies	4 or 5	-
Number of Assemblies Replaced per Equilibrium Cycle (Average)		
Fuel Assemblies	81	22 or 23
Inner Blanket Assemblies	41	-
Radial Blanket Assemblies	28	-
Power Peaking Factors (Fuel Assemblies not adjacent to inserted control rods)		
First Core		
Radial, BOC1	1.18	1.36
Radial, EOC1	1.15	1.28
Axial, BOC1	1.28	1.24
Axial, EOC1	1.26	1.23
Equilibrium Core		
Radial, BOL	1.18	1.41
Radial, EOL	1.24	1.32
Axial, BOL	1.27	1.23
Axial, EOL	1.19	1.23

TABLE 4.3-44 (Continued)

	<u>CRBRP</u>	<u>FFTF</u>
Peak Neutron Flux <sup>(4)</sup> (neutrons/cm <sup>2</sup> sec) Fuel and Inner Blanket Zone		
Total Flux	5.5 x 10 <sup>15</sup>	8 x 10 <sup>15</sup>
Fast Flux (energy ≥ 0.1 MeV)	3.4 x 10 <sup>15</sup>	5 x 10 <sup>15</sup>
Radial Blanket Zone		
Total Flux	3.9 x 10 <sup>15</sup>	-
Fast Flux (energy ≥ 0.1 MeV)	2.4 x 10 <sup>15</sup>	-

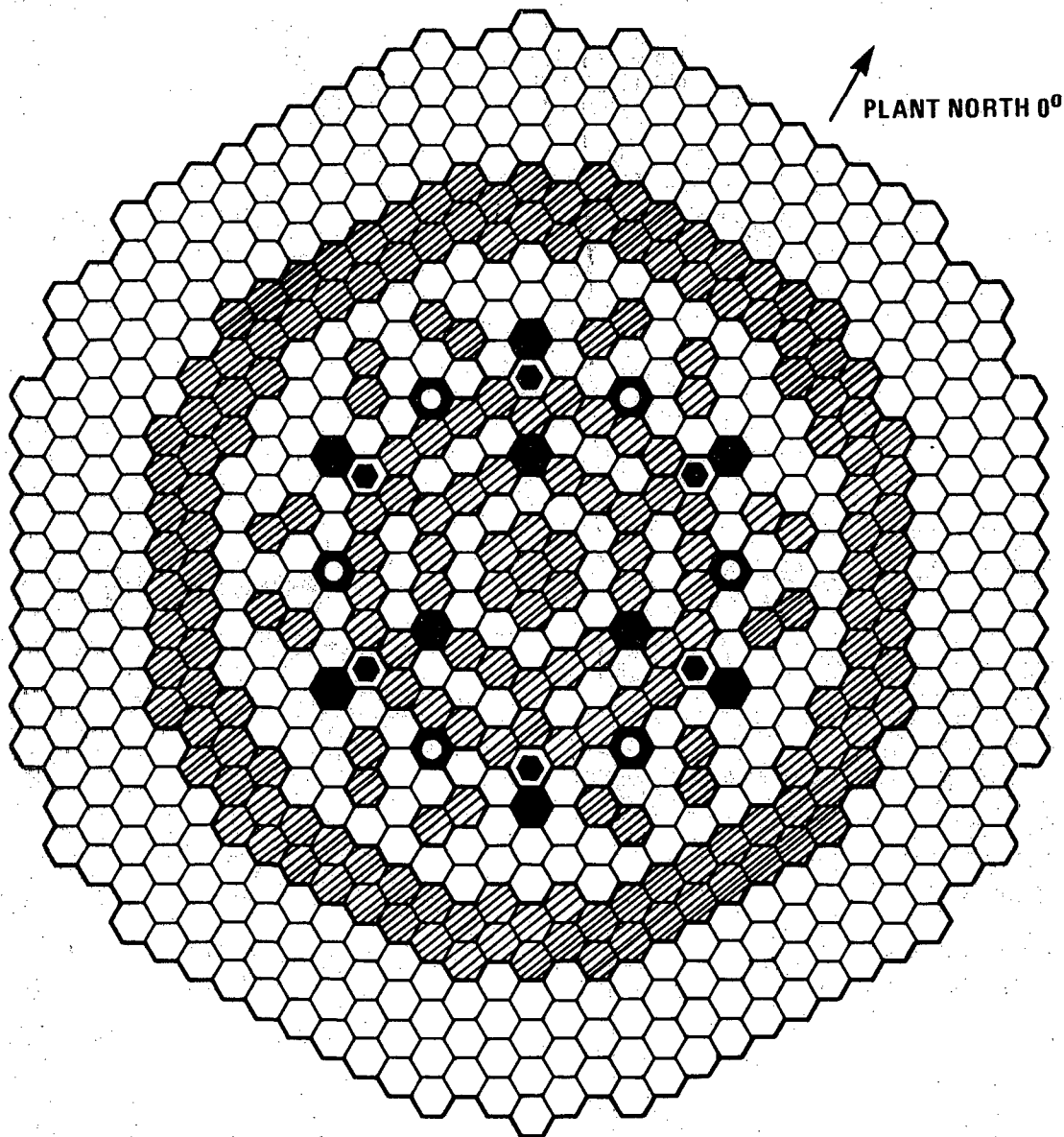
<sup>(4)</sup> Maximum value attained at any time in life and at any point in the zone.



TABLE 4.3-45

## COMPARISON OF REACTIVITY COEFFICIENTS FOR CRBRP AND FFTF

		<u>CRBRP</u>	<u>FFTF</u>
<u>Doppler Constant</u> ( $-T \frac{dk}{dT}$ )			
Initial Core, BOC1	Fuel	0.0026	0.0050
	Inner Blanket	0.0044	-
	Radial Blanket	0.0012	-
	Axial Blankets	0.0003	-
Initial Core, EOC2	Fuel	0.0026	0.0055
	Inner Blanket	0.0049	-
	Radial Blanket	0.0012	-
	Axial Blankets	0.0003	-
Equilibrium Core, BOL	Fuel	0.0024	0.0050
	Inner Blanket	0.0041	-
	Radial Blanket	0.0015	-
	Axial Blankets	0.0003	-
Equilibrium Core, EOL	Fuel	0.0024	0.0055
	Inner Blanket	0.0046	-
	Radial Blanket	0.0013	-
	Axial Blankets	0.0004	-
<u>Core-Average Sodium Density Coefficients</u> (cents/ $^{\circ}$ F)			
	First Cycle	-0.006	-0.049
<u>Uniform Radial Expansion Coefficient</u> (cents/ $^{\circ}$ F)			
	First Cycle	-0.177	-0.21
<u>Uniform Axial Expansion Coefficient</u> (cents/ $^{\circ}$ F)			
	First Cycle	-0.038	-0.038









- |                                                                                     |                               |                                                                                     |                                     |
|-------------------------------------------------------------------------------------|-------------------------------|-------------------------------------------------------------------------------------|-------------------------------------|
|  | 156 FUEL ASSEMBLIES           |  | 6 ALTERNATE FUEL BLANKET ASSEMBLIES |
|  | 76 INNER BLANKET ASSEMBLIES   |  | 6 SECONDARY CONTROL ASSEMBLIES      |
|  | 126 RADIAL BLANKET ASSEMBLIES |  | 9 PRIMARY CONTROL ASSEMBLIES        |
|                                                                                     |                               |                                                                                     | 312 RADIAL SHIELD ASSEMBLIES        |

FIGURE 4.3-1. Clinch River Breeder Reactor Core Layout

5894-22

4.3-150

Amend. 64  
Jan. 1982

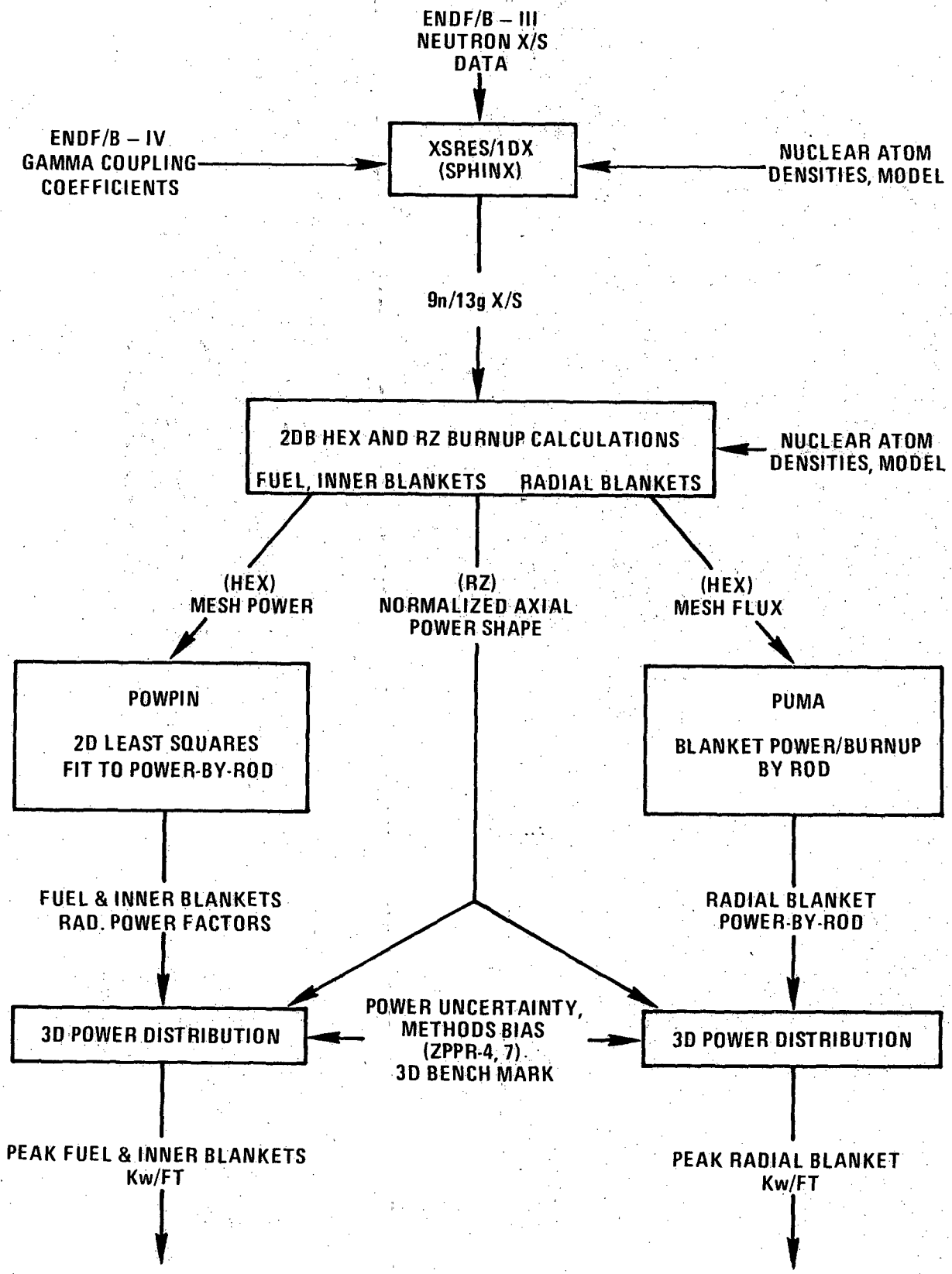


Figure 4.3-2. Power Distribution Calculational Method

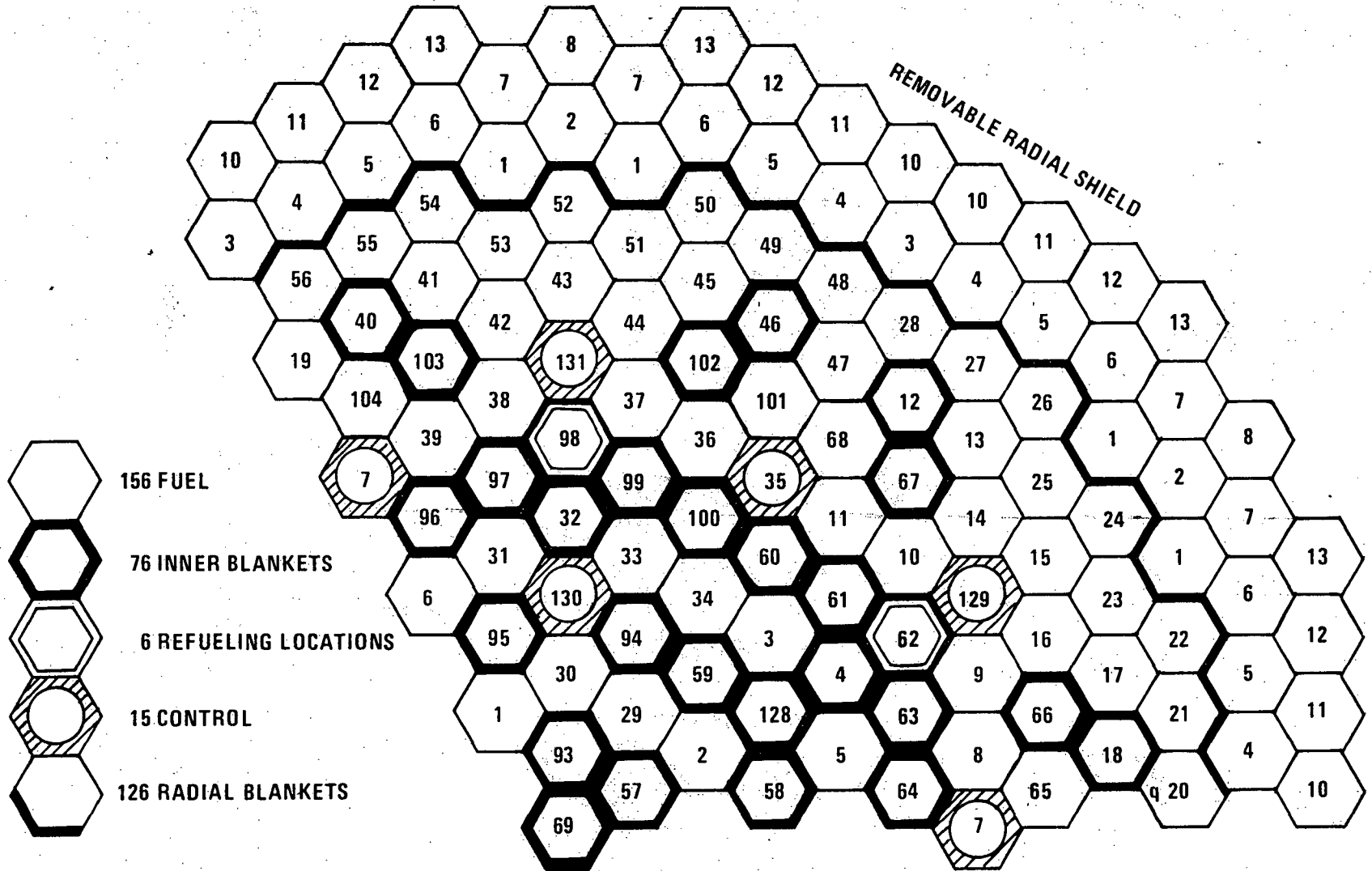
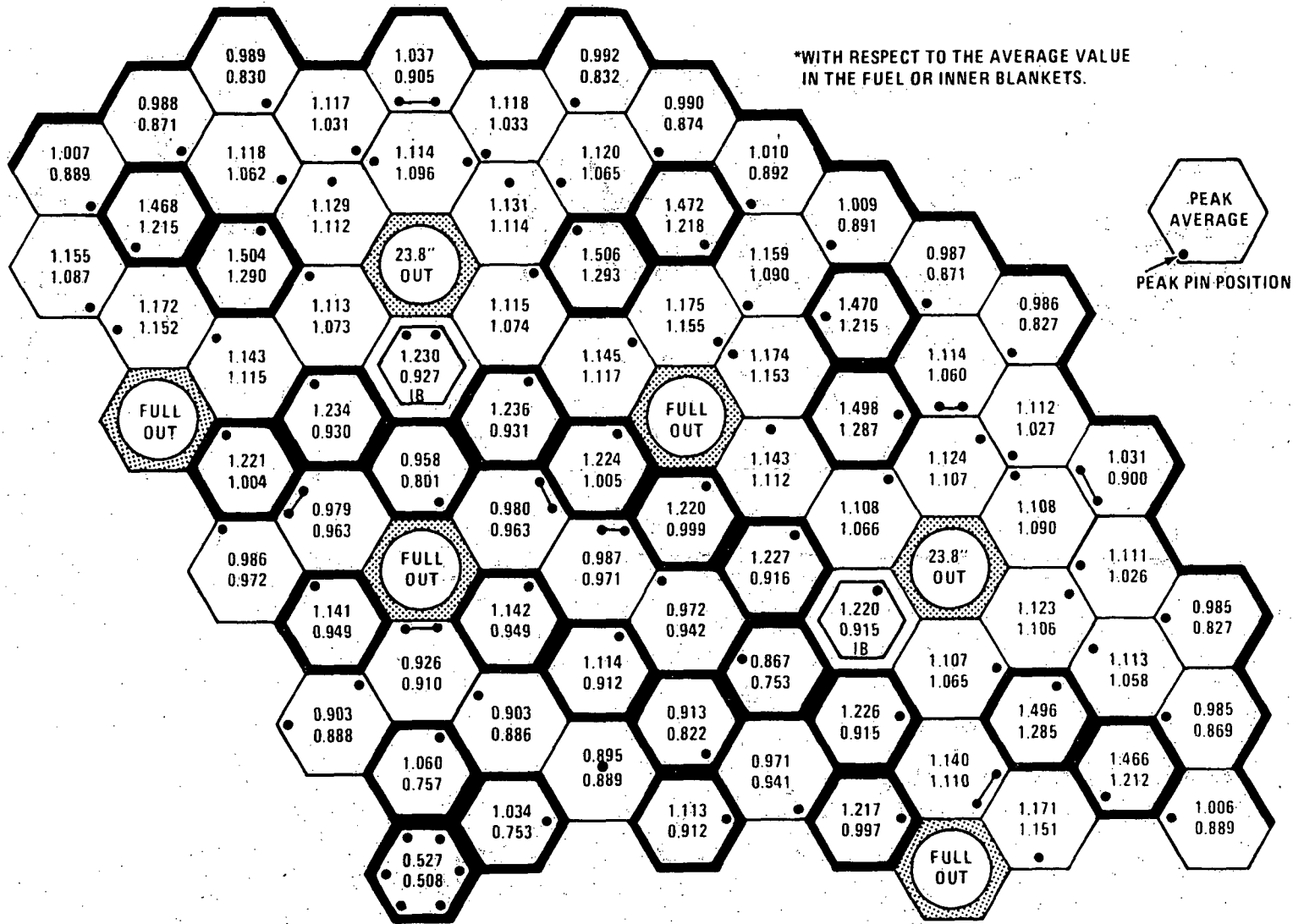


FIGURE 4.3-3. CRBRP Assembly Numbering Scheme

15444

\*WITH RESPECT TO THE AVERAGE VALUE  
IN THE FUEL OR INNER BLANKETS.



4.3-153

Amend. 51  
Sept. 1979

Figure 4.3-4. Peak and Average Radial Power Factors\* BOC1

1544-5

4.3-154

Amend. 51  
Sept. 1979

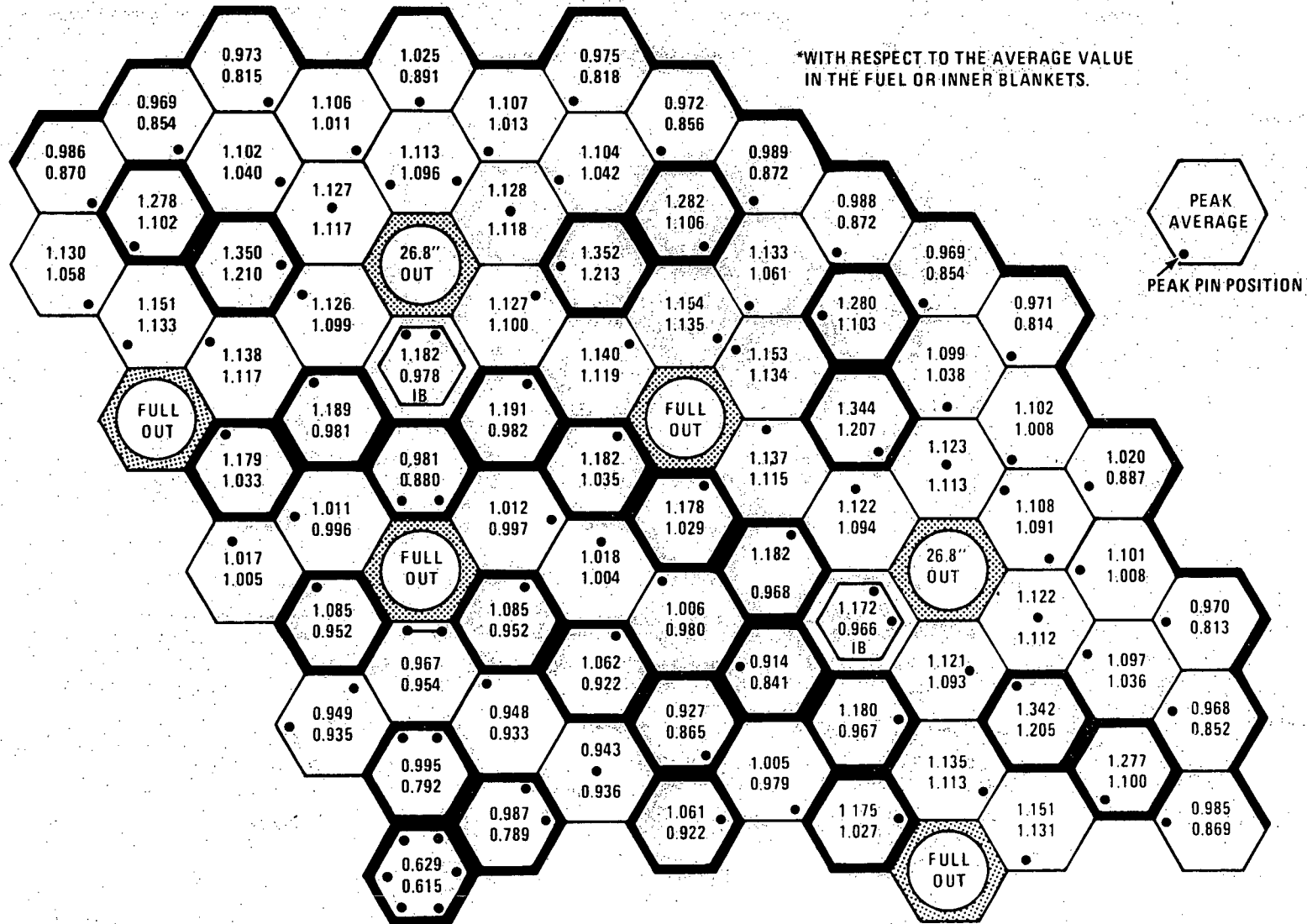
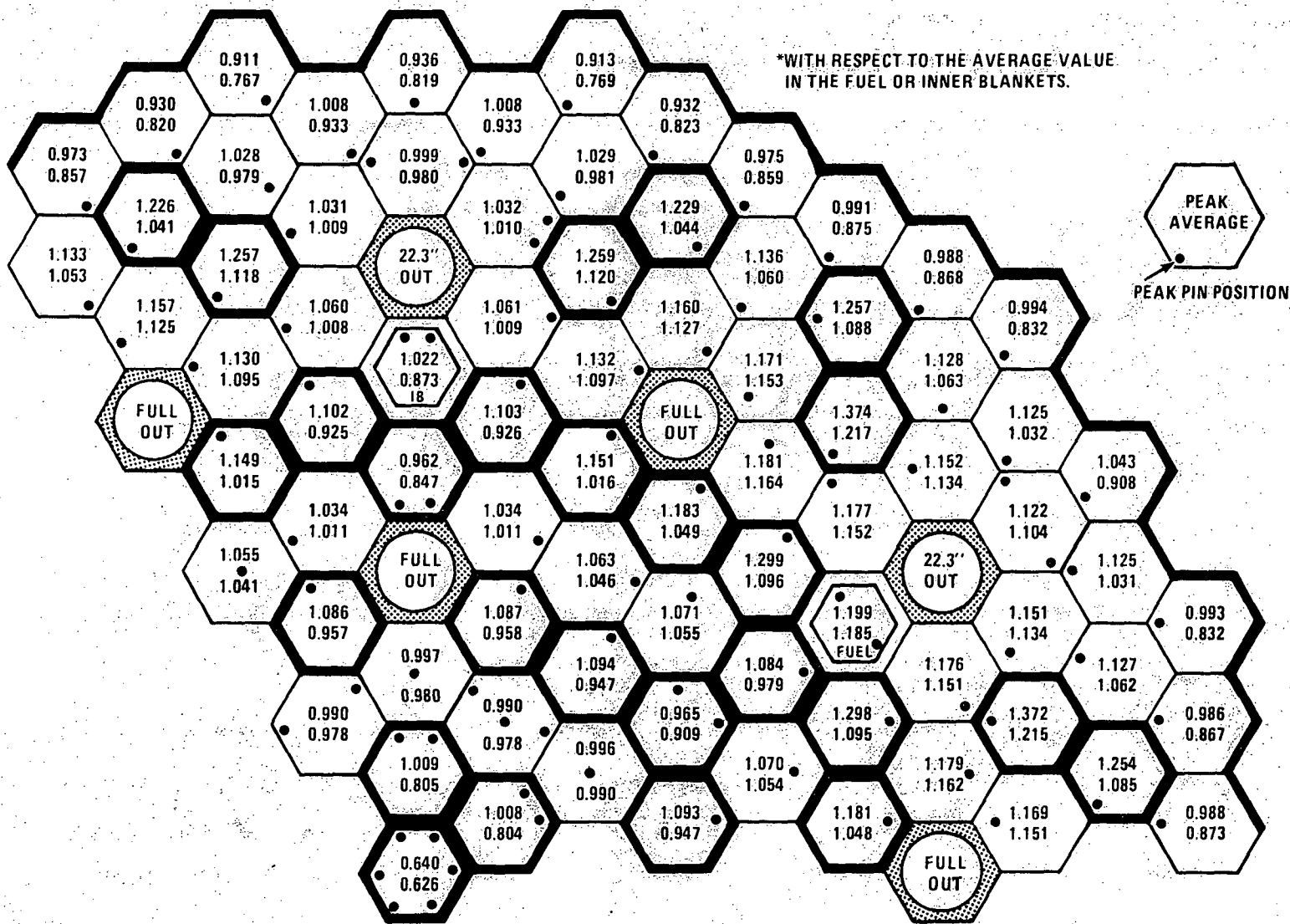


Figure 4.3-5. Peak and Average Radial Power Factors\* EOC1

1544-6

\*WITH RESPECT TO THE AVERAGE VALUE  
IN THE FUEL OR INNER BLANKETS.



4.3-155

Amend. 51  
Sept. 1979

Figure 4.3-6. Peak and Average Radial Power Factors\* BOC2

1544-7

4.3-156

Amend. 51  
Sept. 1979

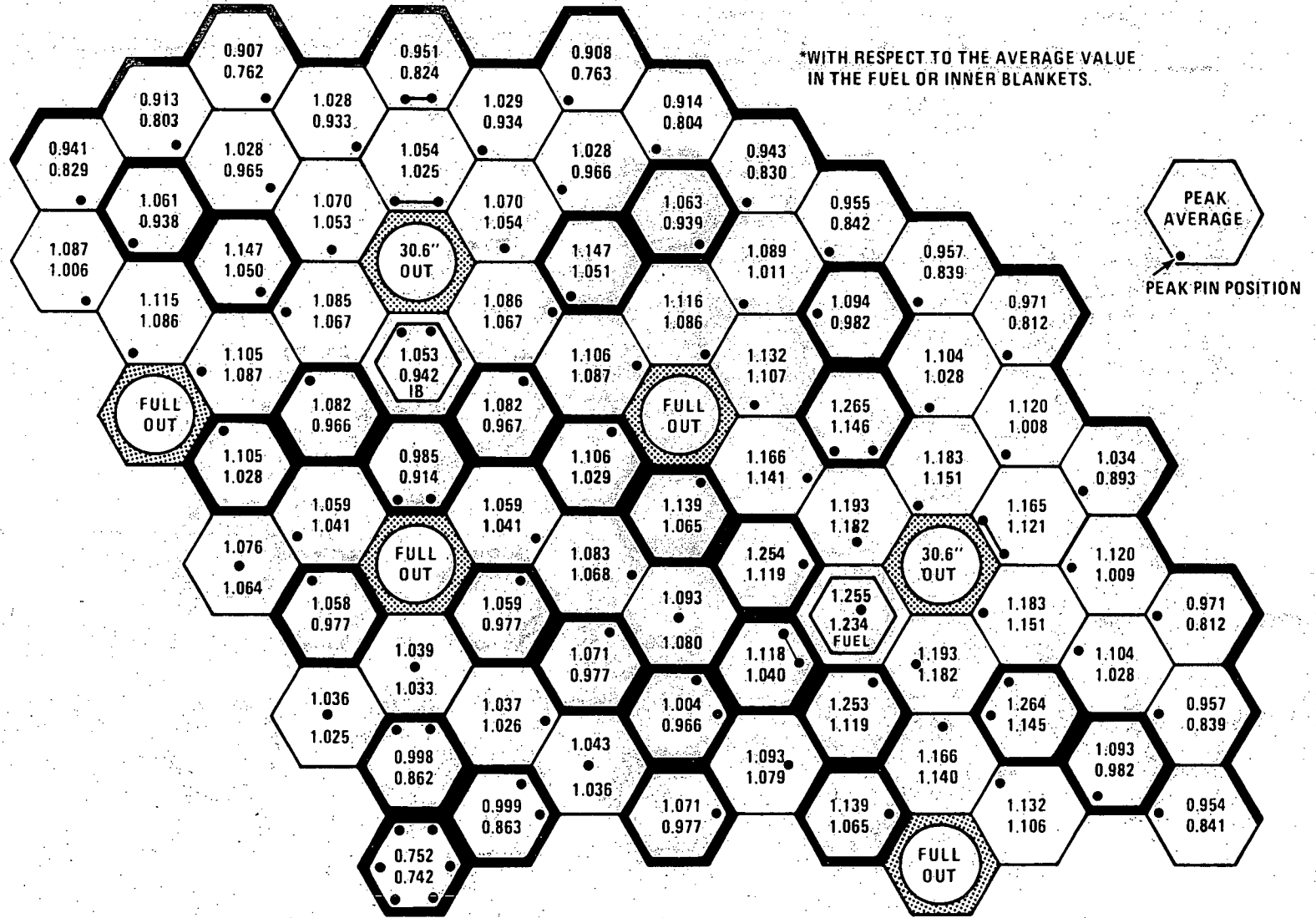
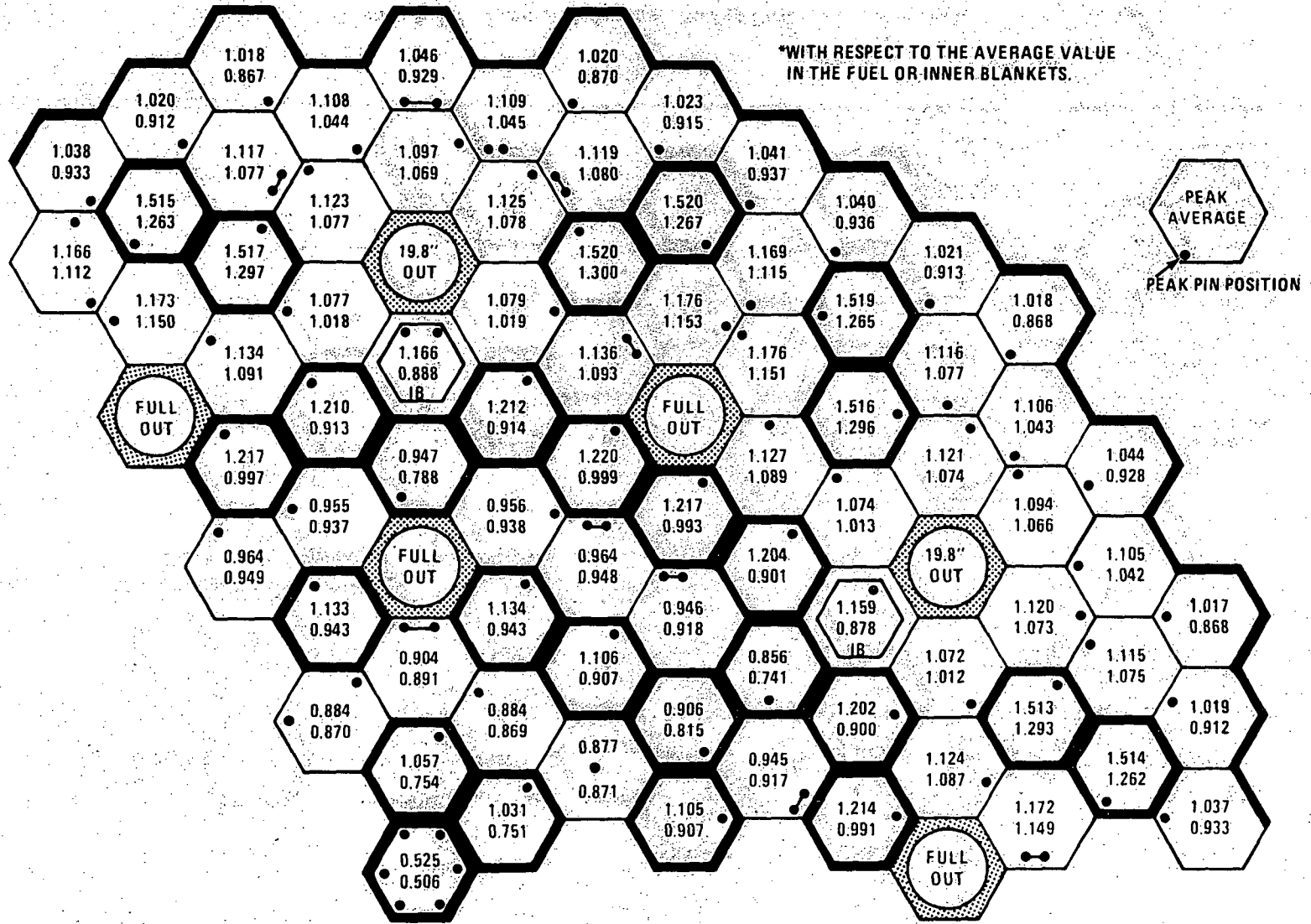


Figure 4.3-7. Peak and Average Radial Power Factors\* EOC2



1544-8



4.3-157

Amend. 51  
Sept. 1979

Figure 4.3-8. Peak and Average Radial Power Factors\* BOC3

1544-9

4.3-158

Amend. 51  
Sept. 1979

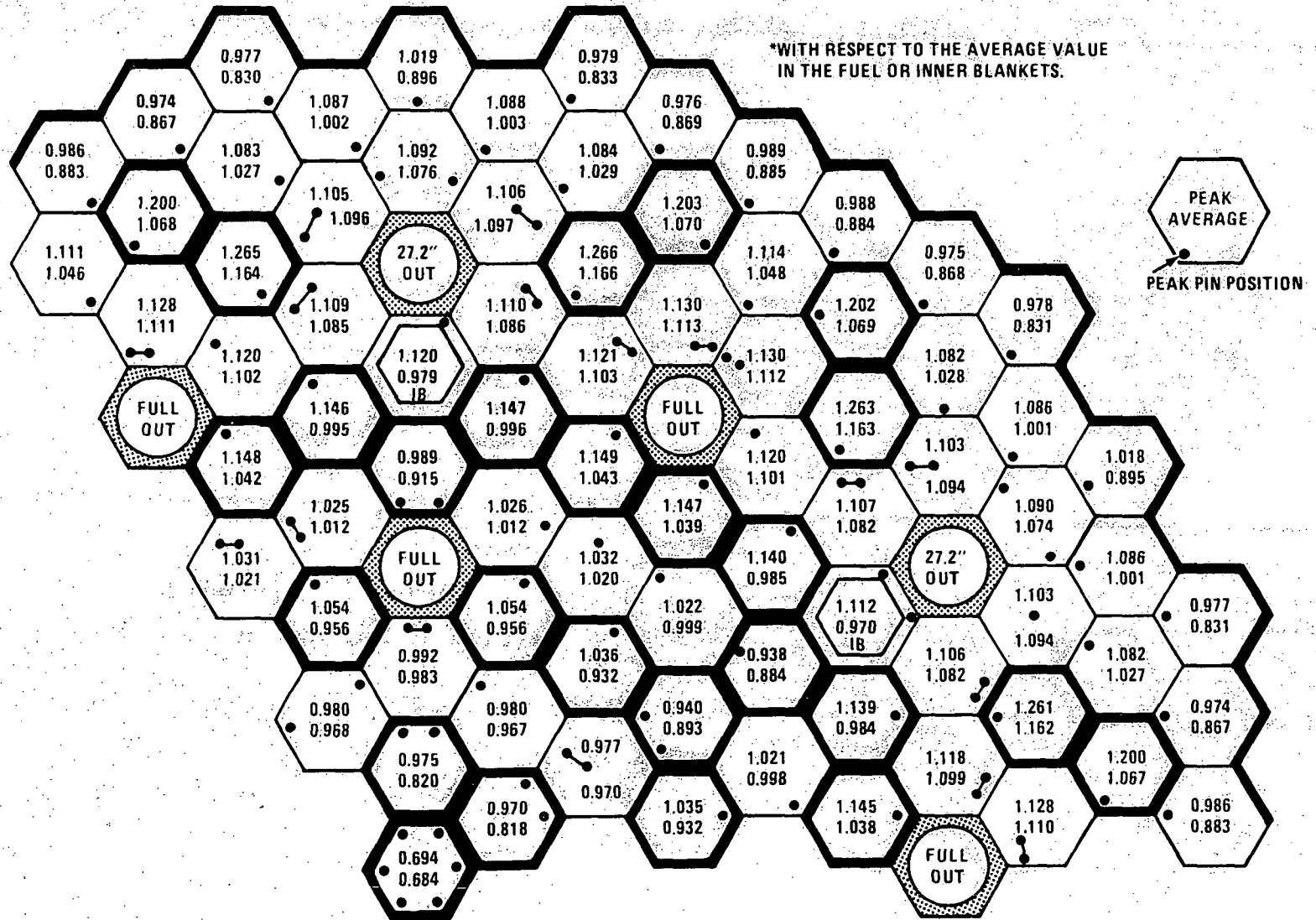
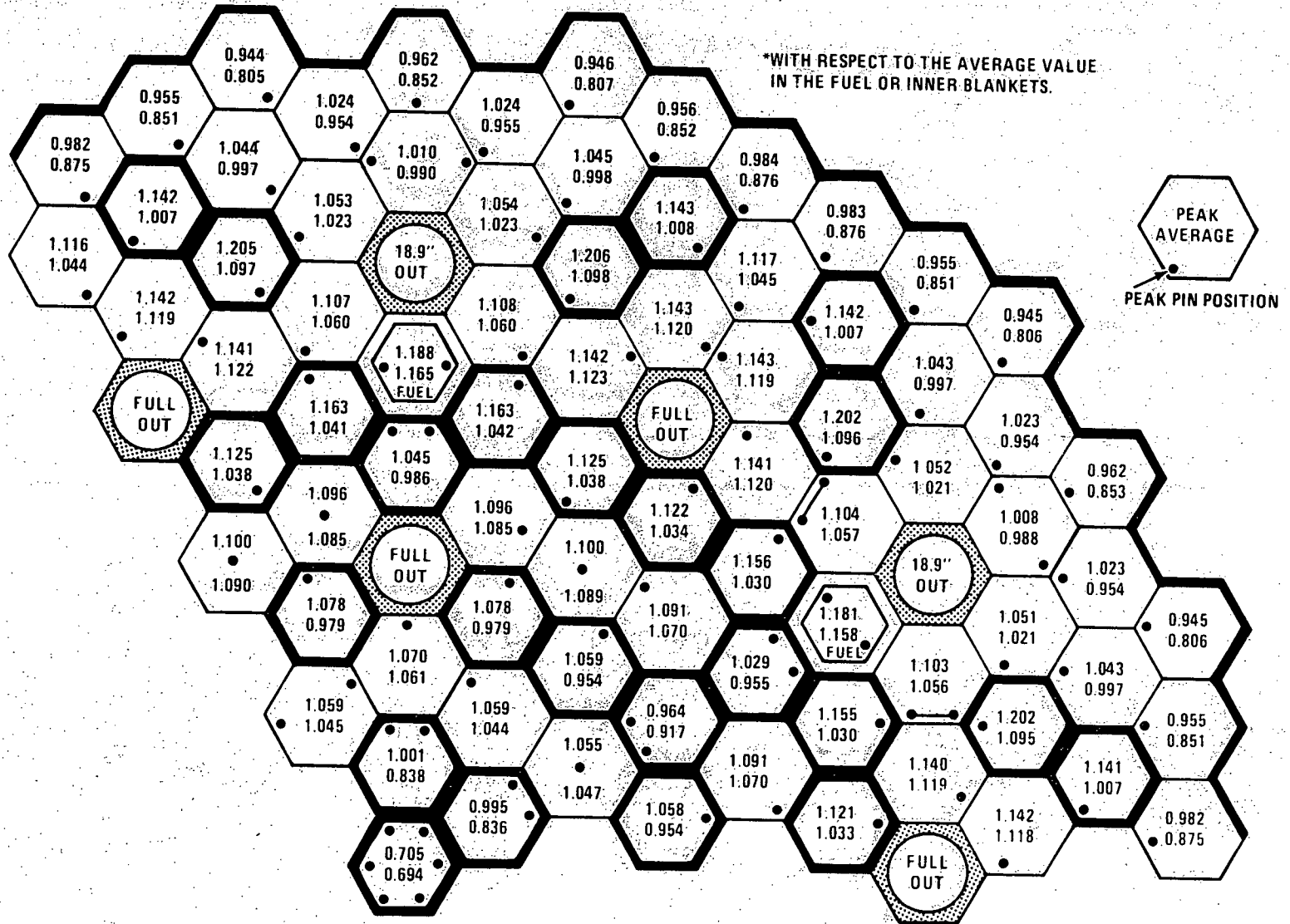


Figure 4.3-9. Peak and Average Radial Power Factors\* EOC3

1544-10



4.3-159

Amend. 51  
Sept. 1979

Figure 4.3-10. Peak and Average Radial Power Factors\* BOC4

1544-11

4.3-160

Amend. 51  
Sept. 1979

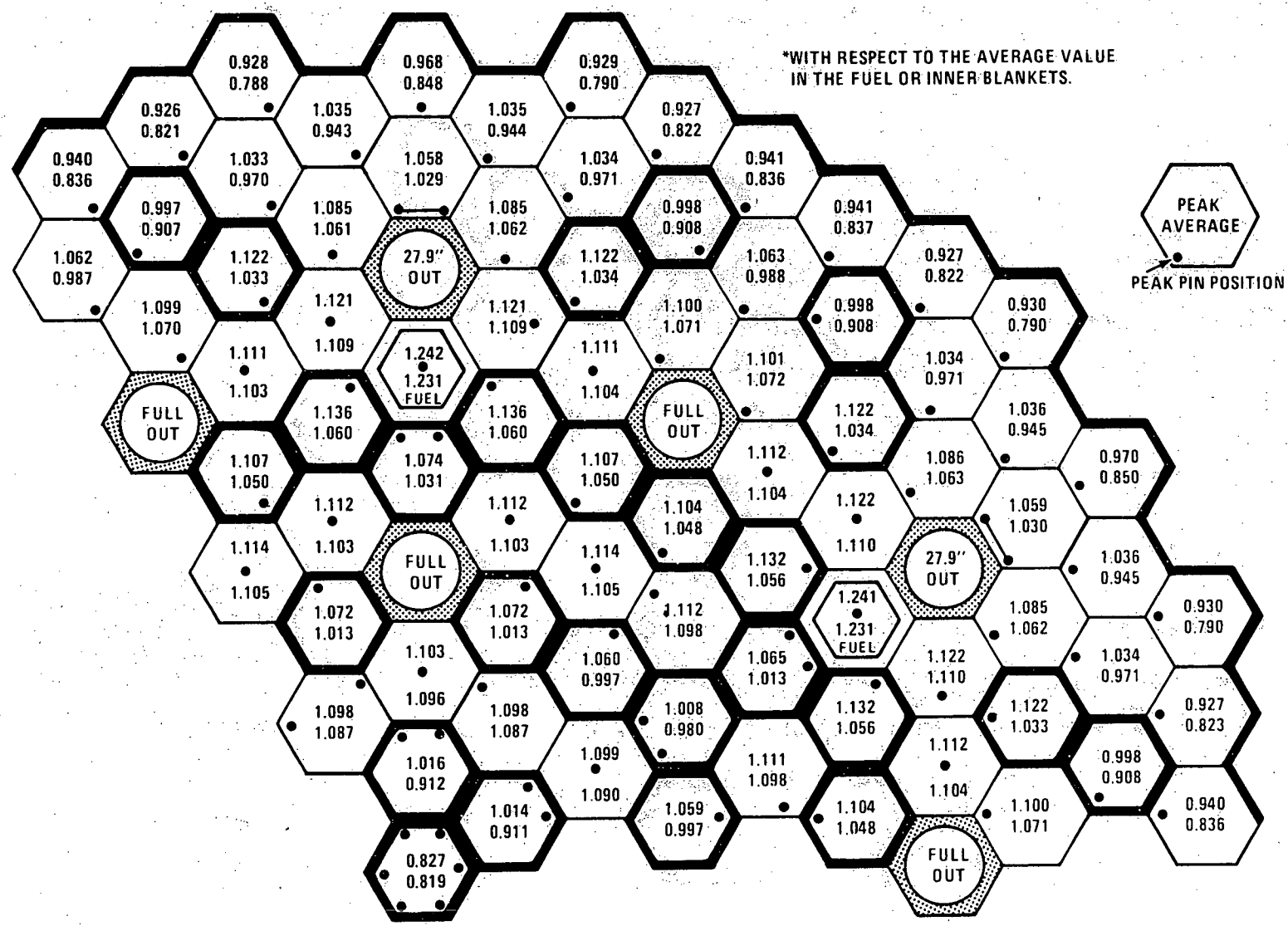


Figure 4.3-11. Peak and Average Radial Power Factors\* EOC4

1544-12

4.3-161

Amend. 51  
Sept. 1979

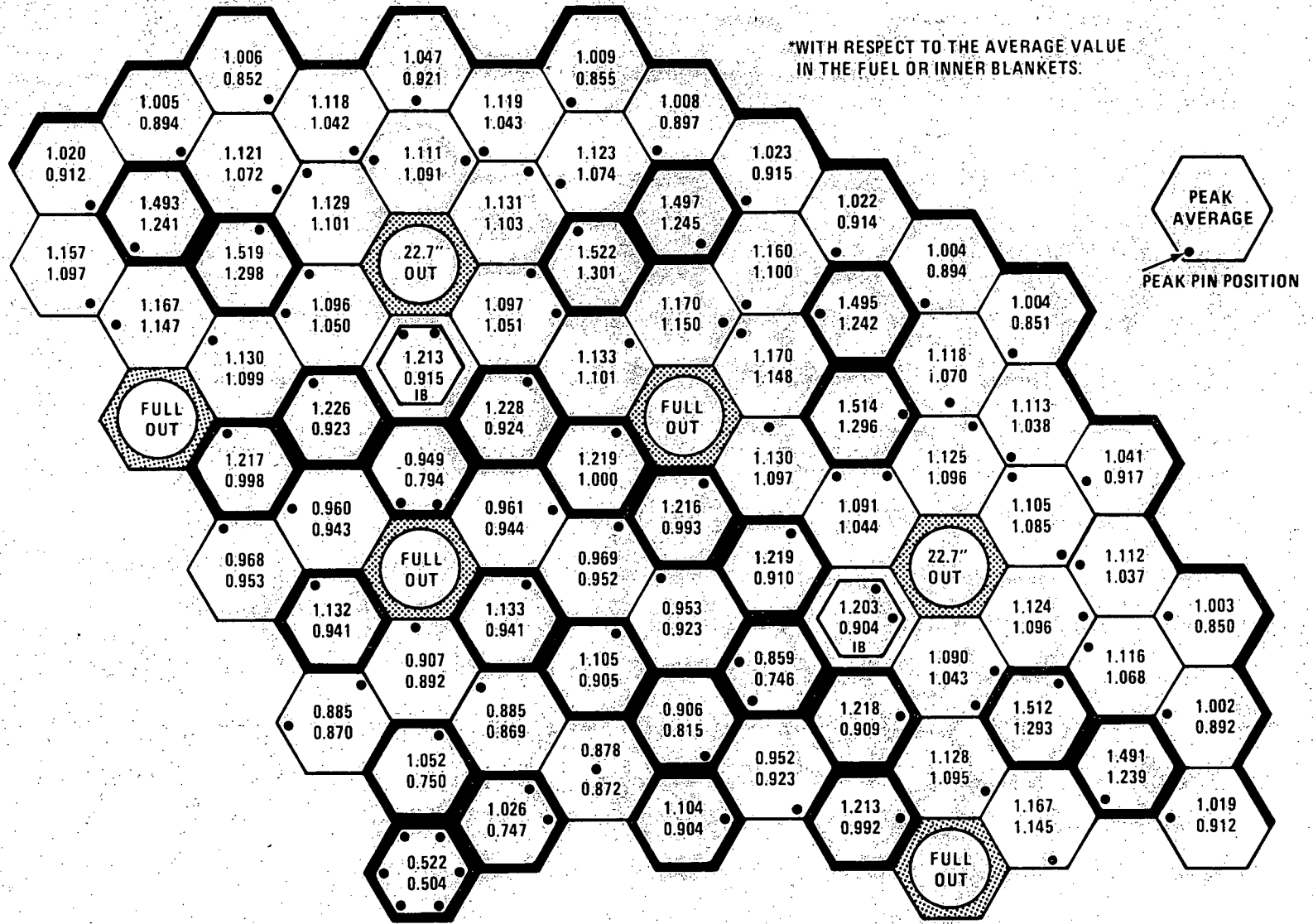


Figure 4.3-12. Peak and Average Radial Power Factors\* BOC5

1544-13

4.3-162

Amend. 51  
Sept. 1979

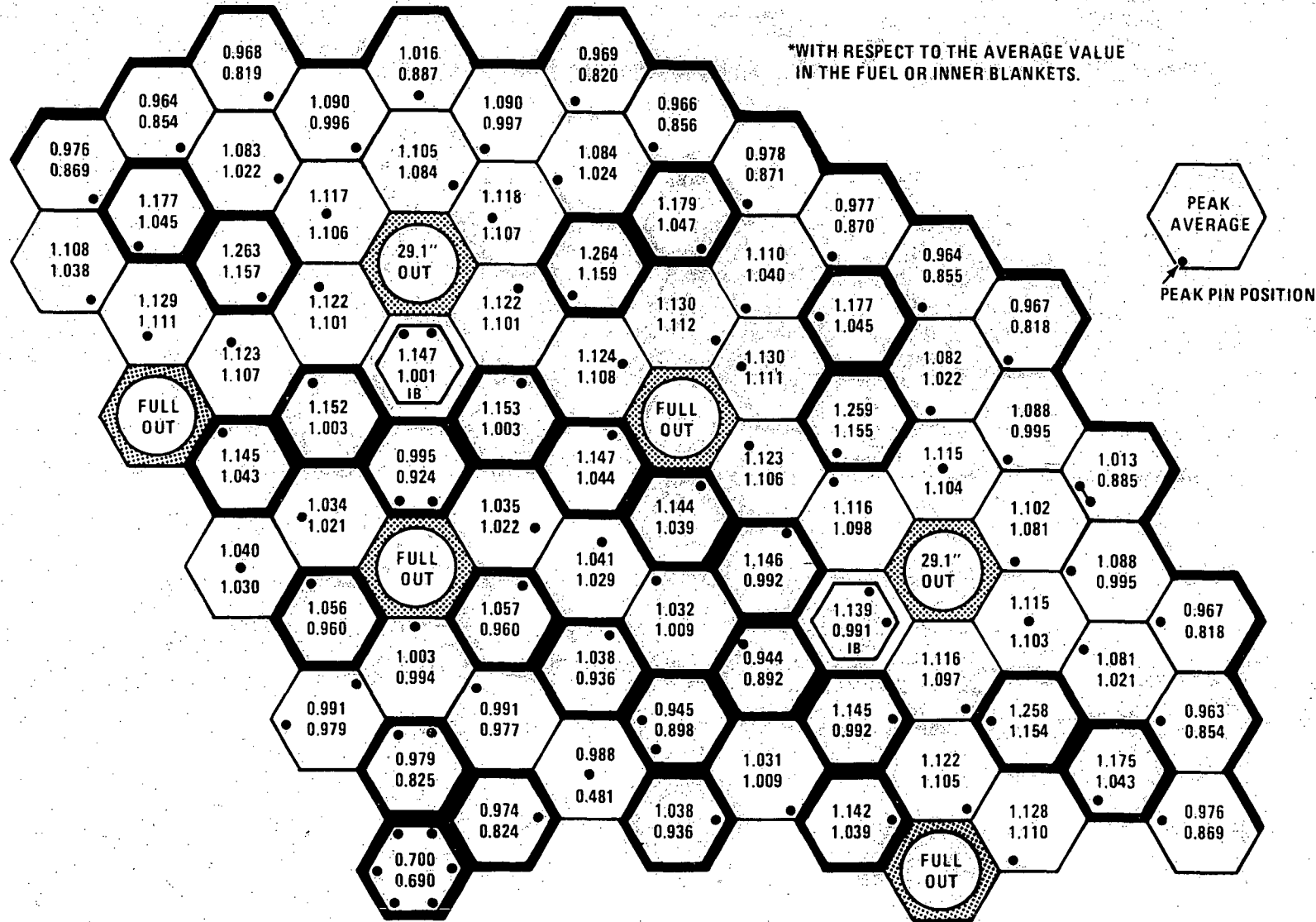


Figure 4.3-13. Peak and Average Radial Power Factors\* EOC5

1544-14

4.3-163

Amend. 51  
Sept. 1979

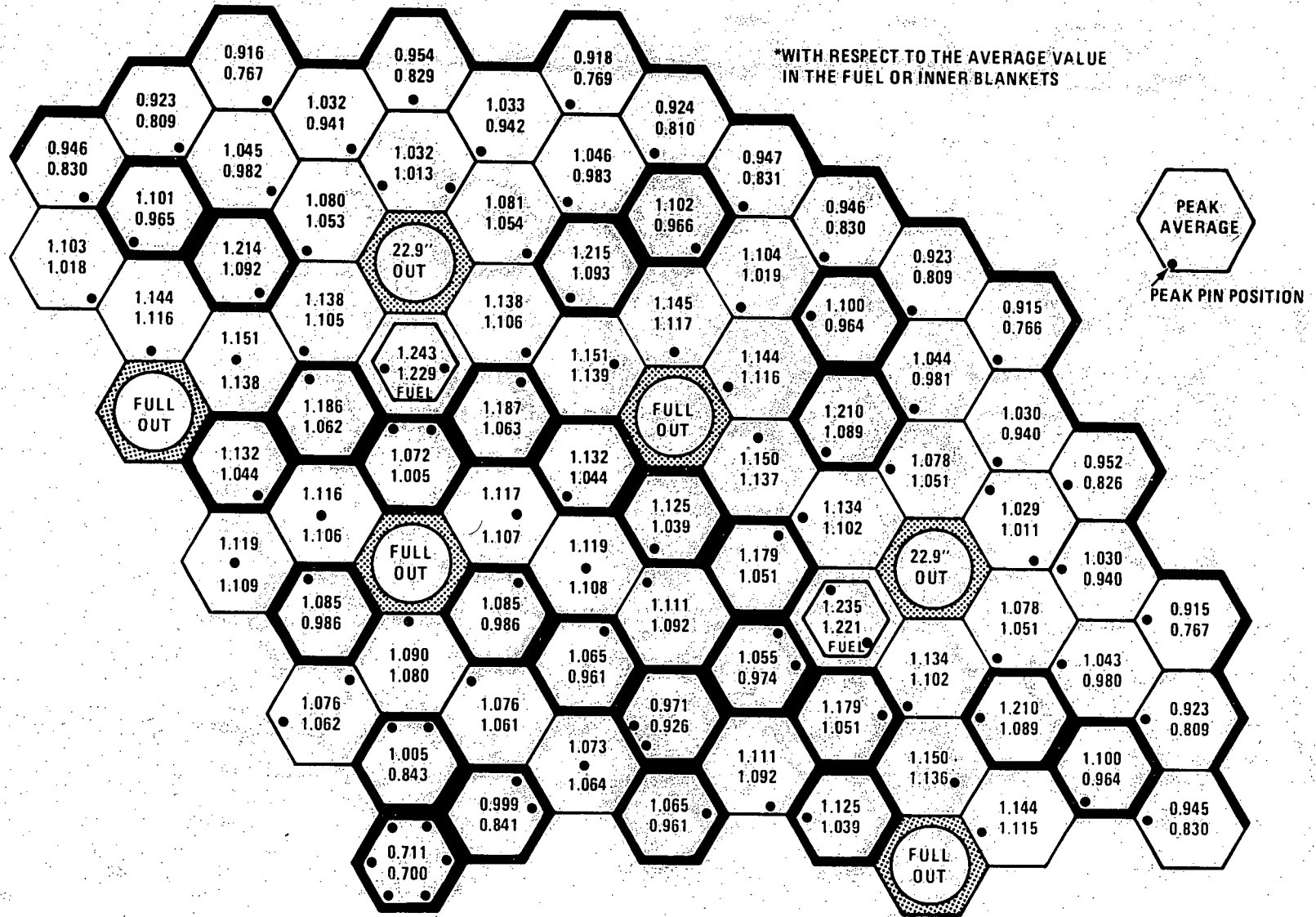


Figure 4.3-14. Peak and Average Radial Power Factors\* BOC6

1544-15

4.3-164

Amend. 51  
Sept. 1979

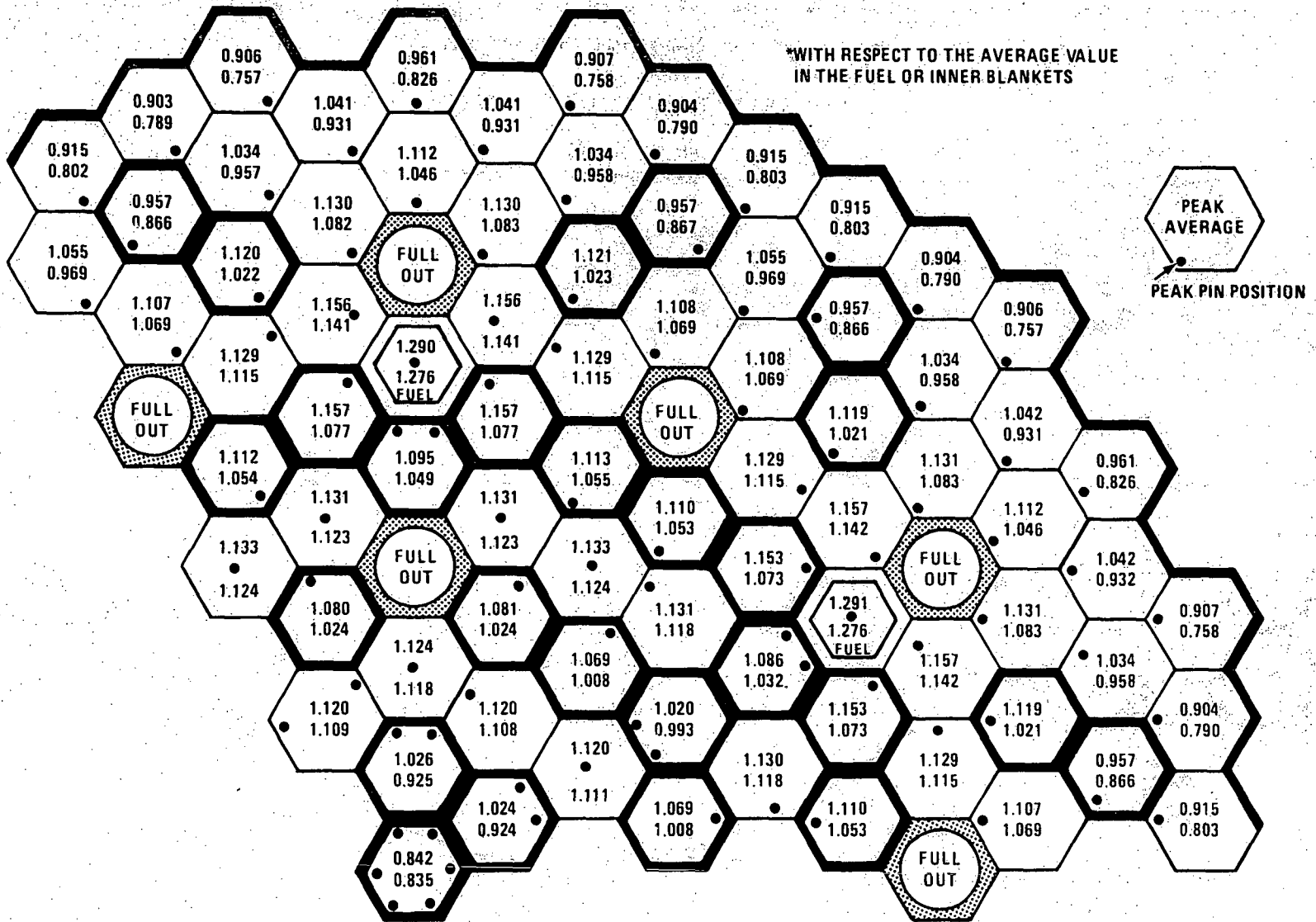


Figure 4.3-15. Peak and Average Radial Power Factors\* EOC6



1544-16

4.3-165

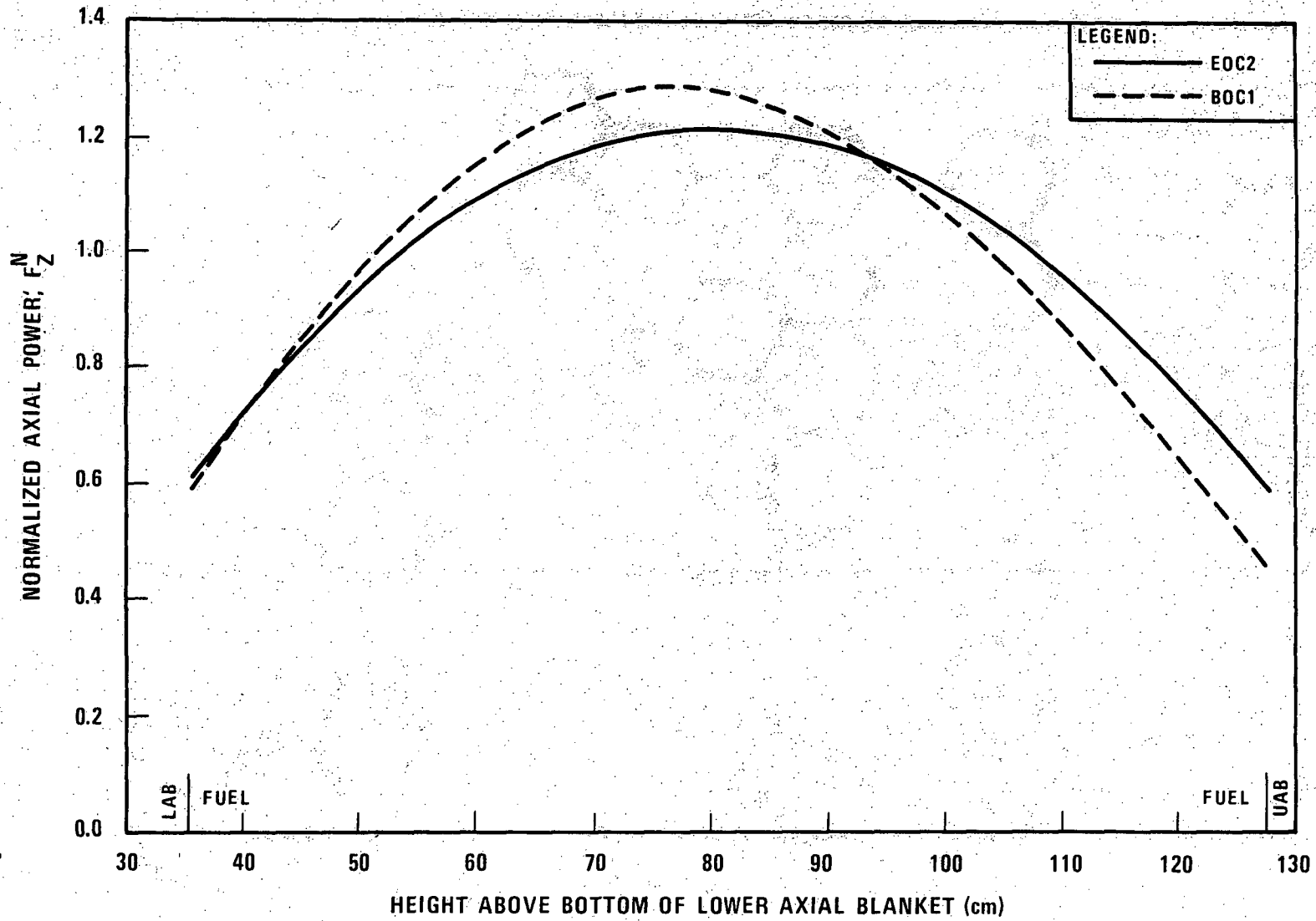


Figure 4.3-16 Normalized Axial Power Distribution Clean Fuel Zones (Power Normalized to 1.0 Over 92.04 cm Core Height)

Amend. 51  
Sept. 1979

1544-17

4.3-166

Amend. 51  
Sept. 1979

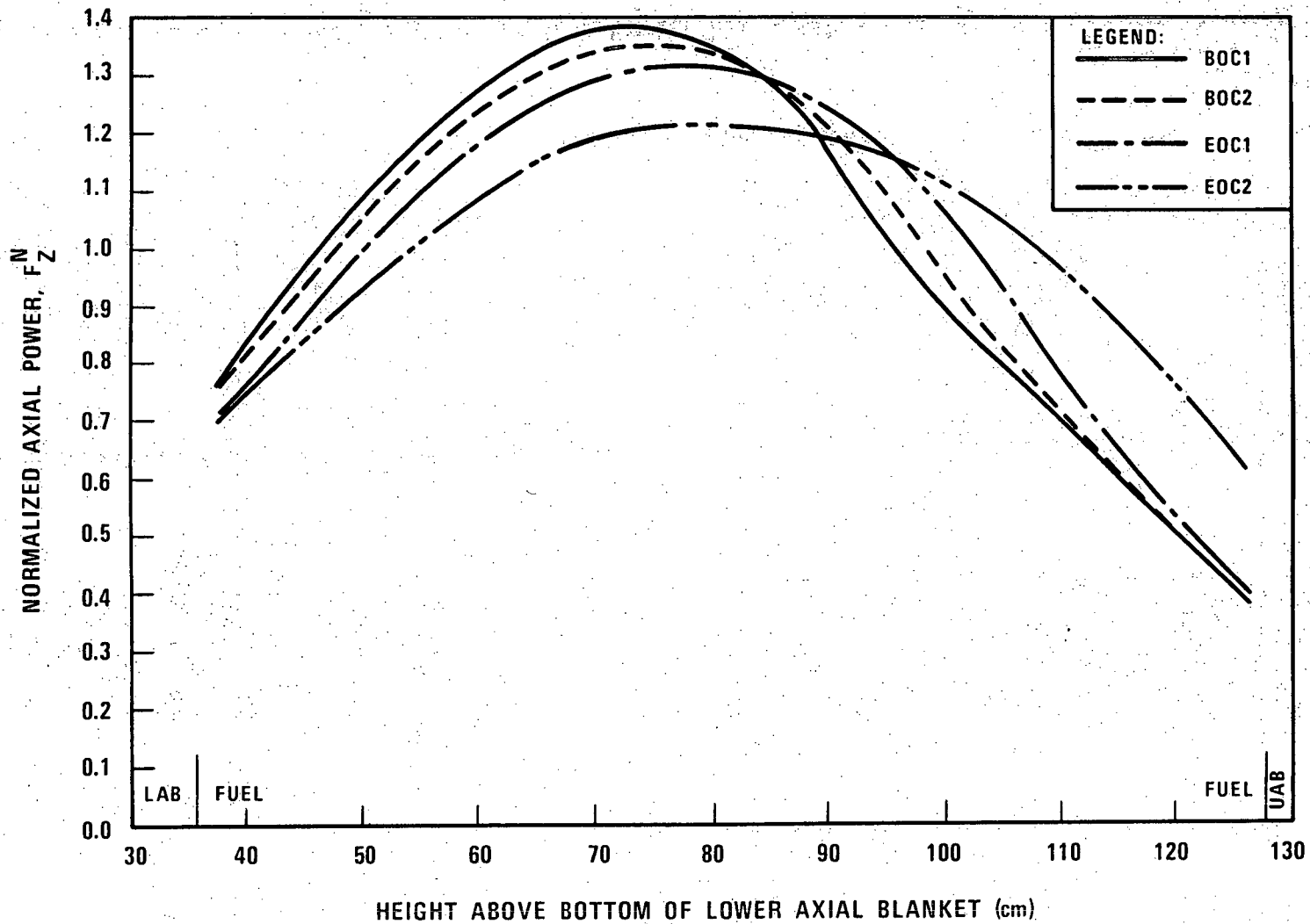


Figure 4.3-17 Normalized Axial Power Distribution Fuel Zones with Control Rod Influence (Power Normalized to 1.0 Over 92.04 cm Fuel Height)

1544-18

4.3-167

Amend. 51  
Sept. 1979

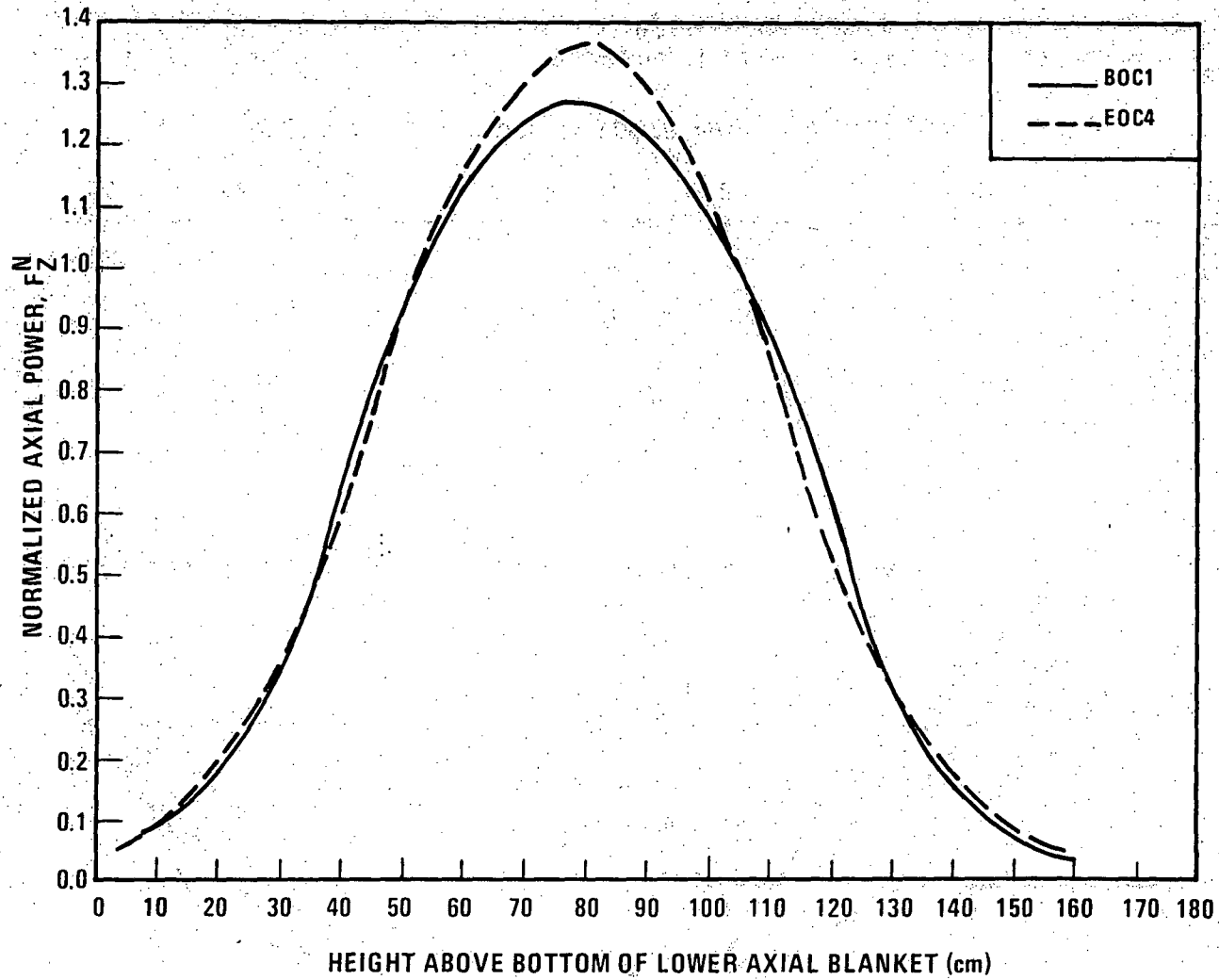


Figure 4.3-18. Normalized Axial Power Distribution Inner Blanket Rows 2, 4 (Power Normalized to 1.0 Over 92.04 cm Central Region)



1544-19

4.3-168

Amend. 51  
Sept. 1979

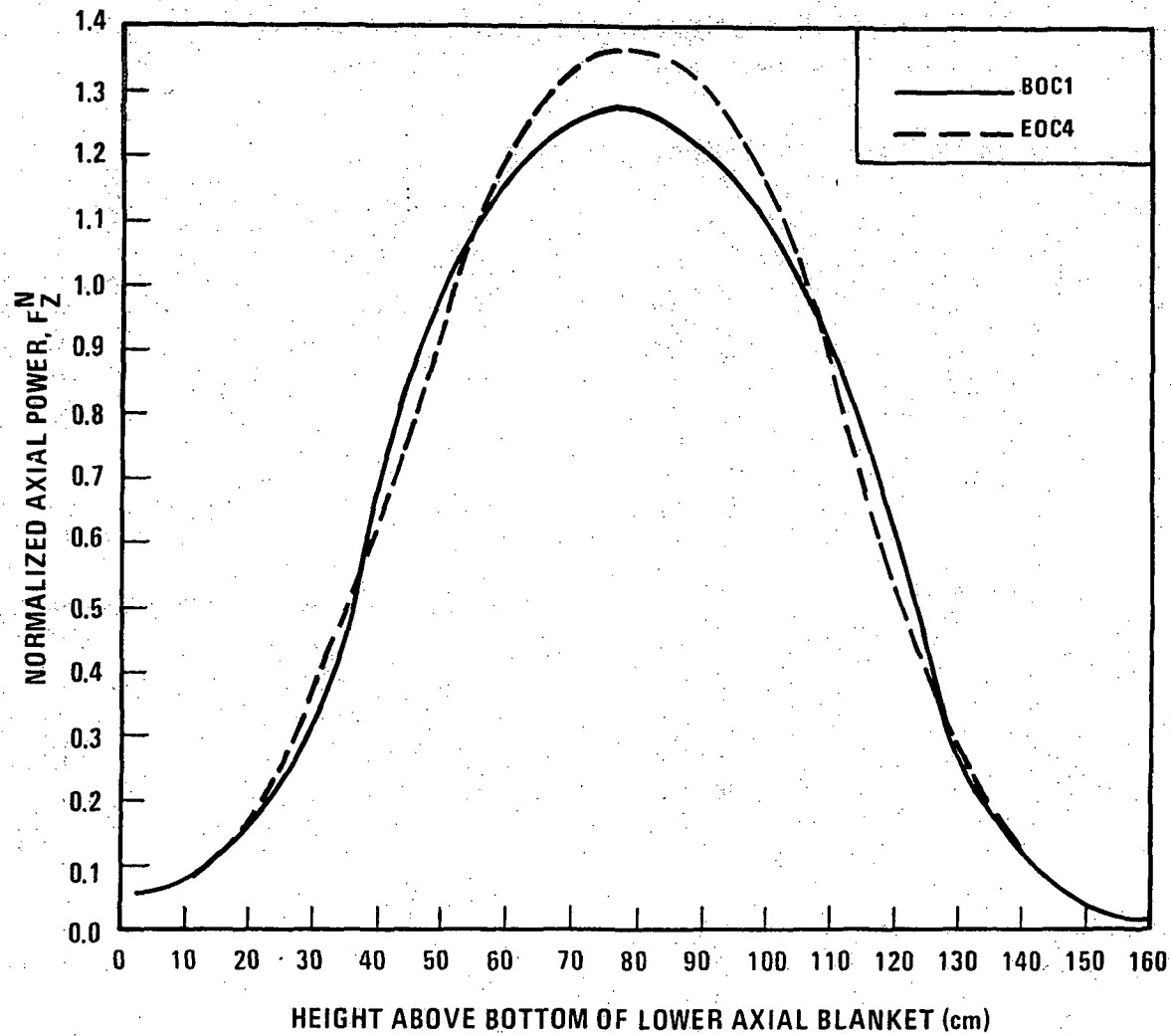


Figure 4.3-19. Normalized Axial Power Distribution Inner Blanket Rows 6, 8 (Power Normalized to 1.0 Over 92.04 cm Central Region)

1544-20

4.3-169

Amend. 51  
Sept. 1979

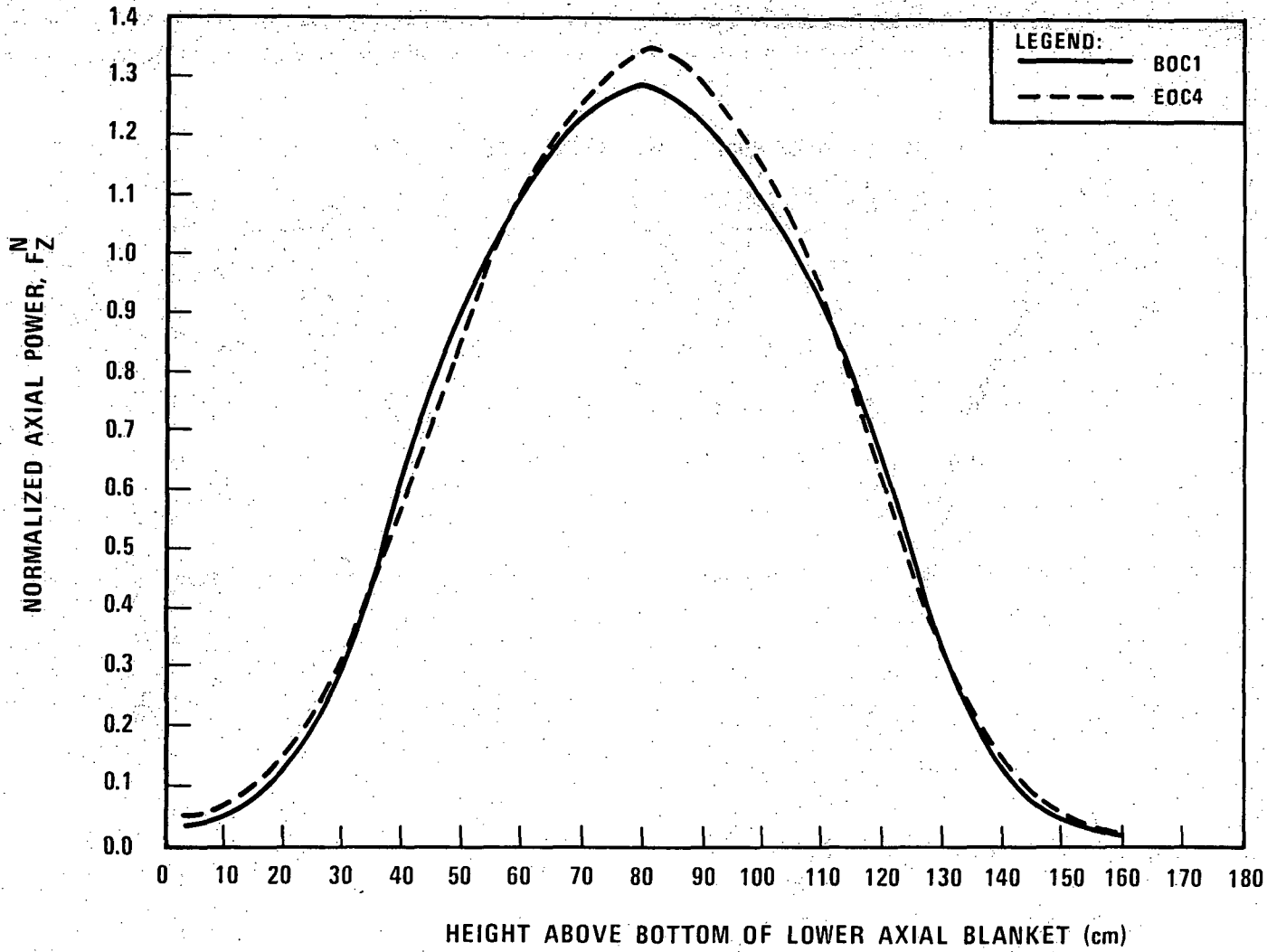


Figure 4.3-20 Normalized Axial Power Distribution Radial Blanket (Power Normalized to 1.0 Over 92.04 cm Central Region).

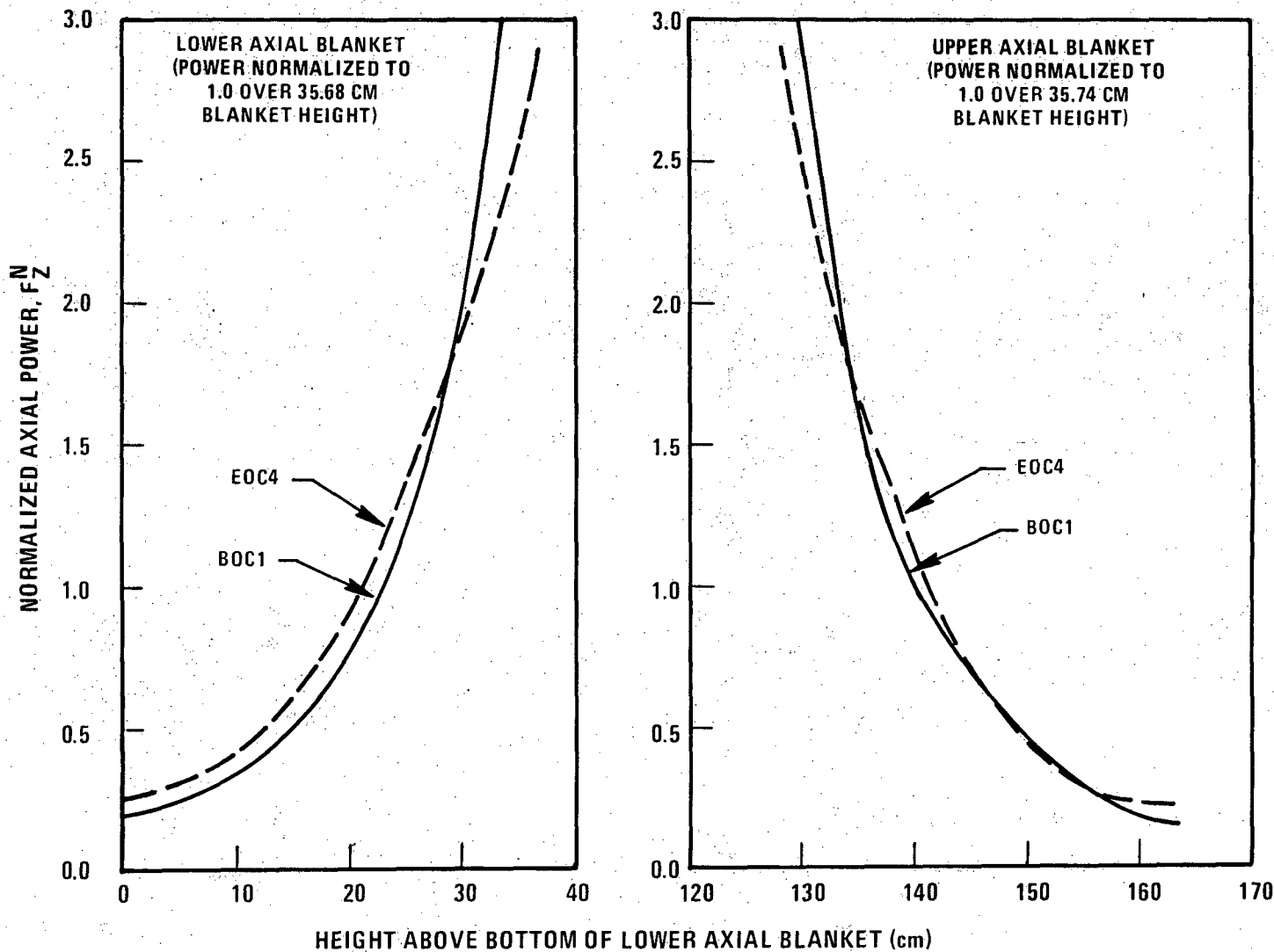


Figure 4.3-21. Normalized Axial Power Distribution, Axial Blankets (Typical)

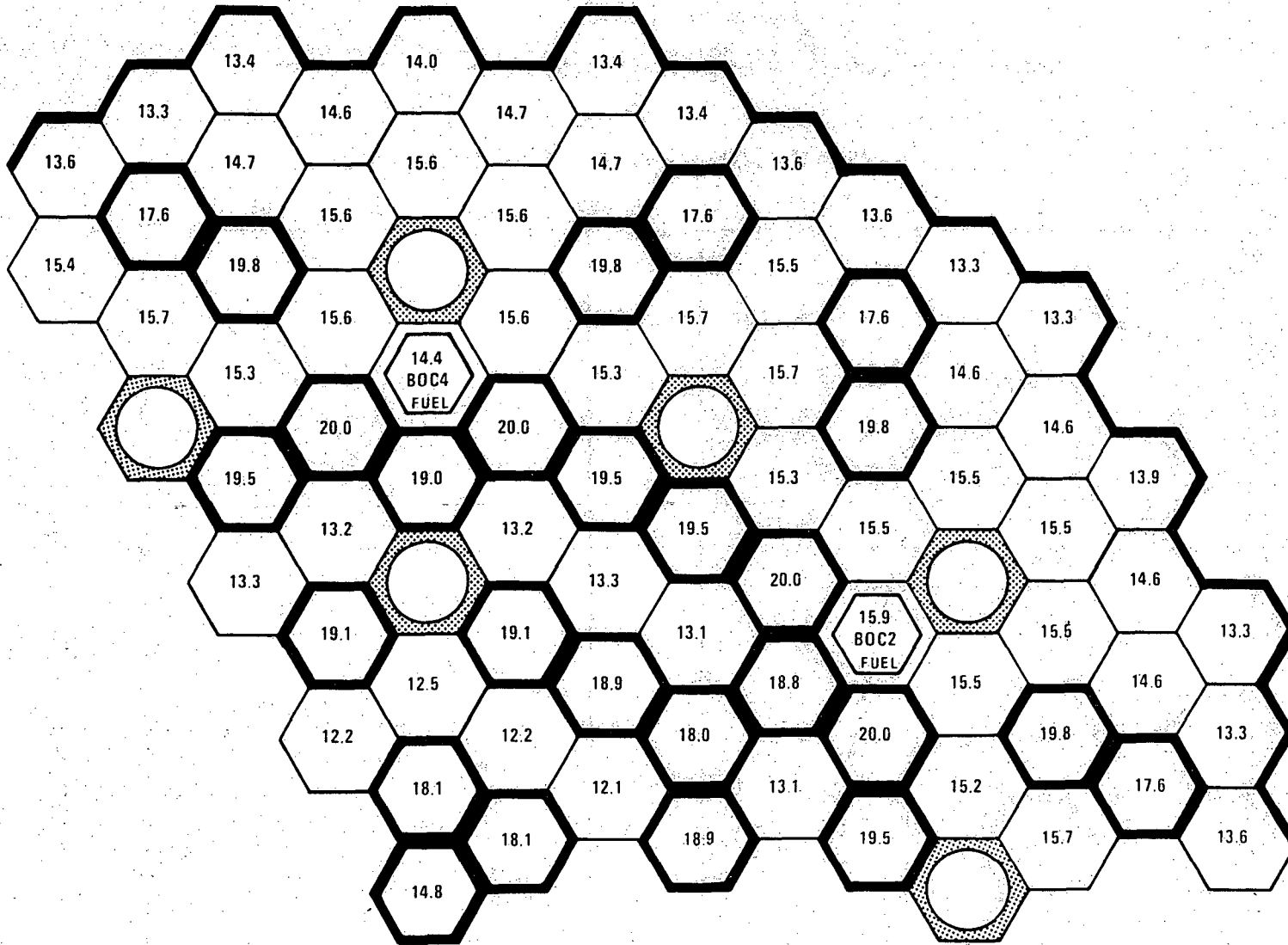


Figure 4.3-22. Peak Linear Power Distribution (KW/FT) ( $3\sigma + 15\%$  Overpower Conditions) Fuel at BOC1 (except refuel channels) Inner Blankets at EOC4 (Note: These Values do not Occur Simultaneously).

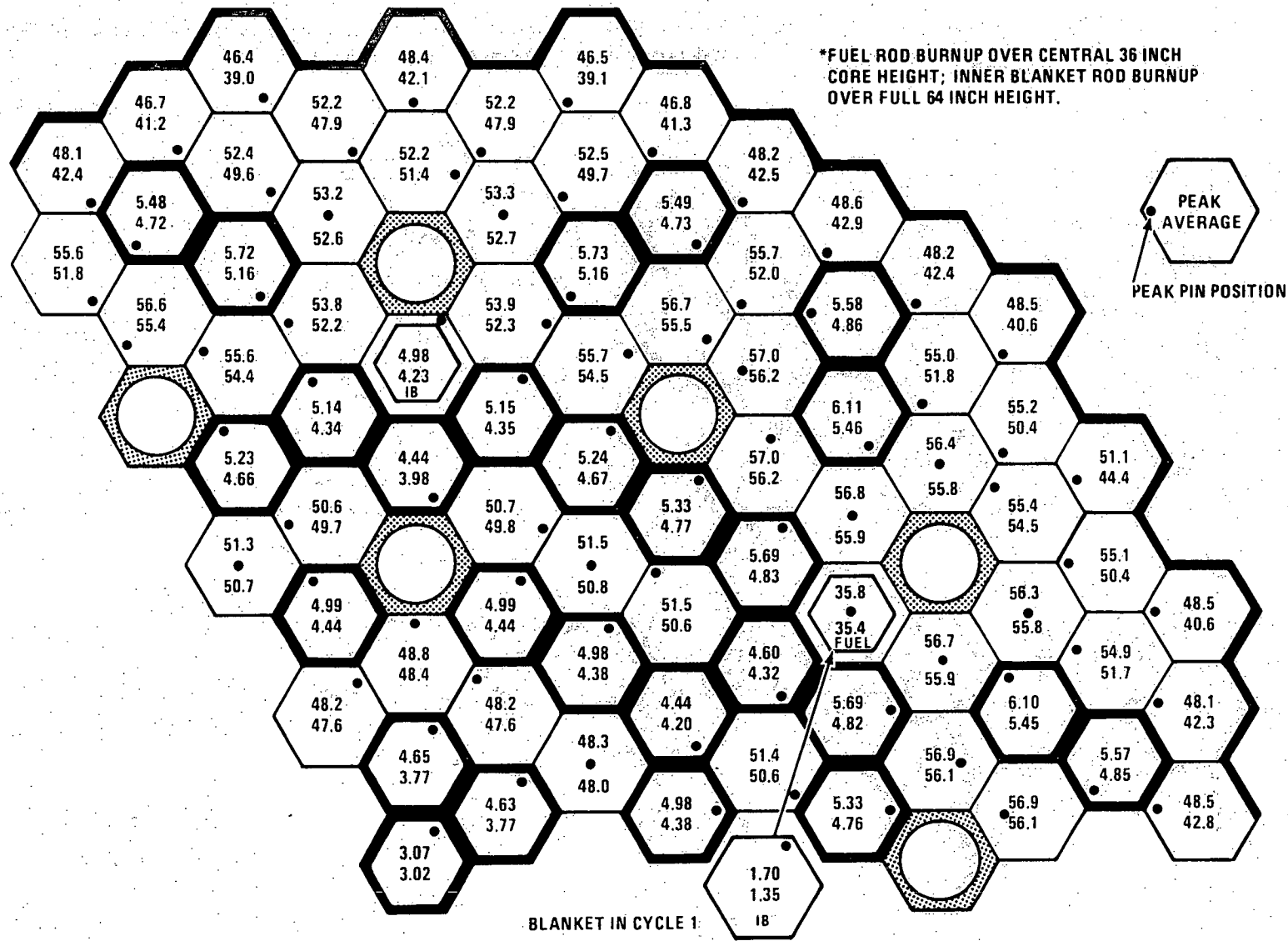
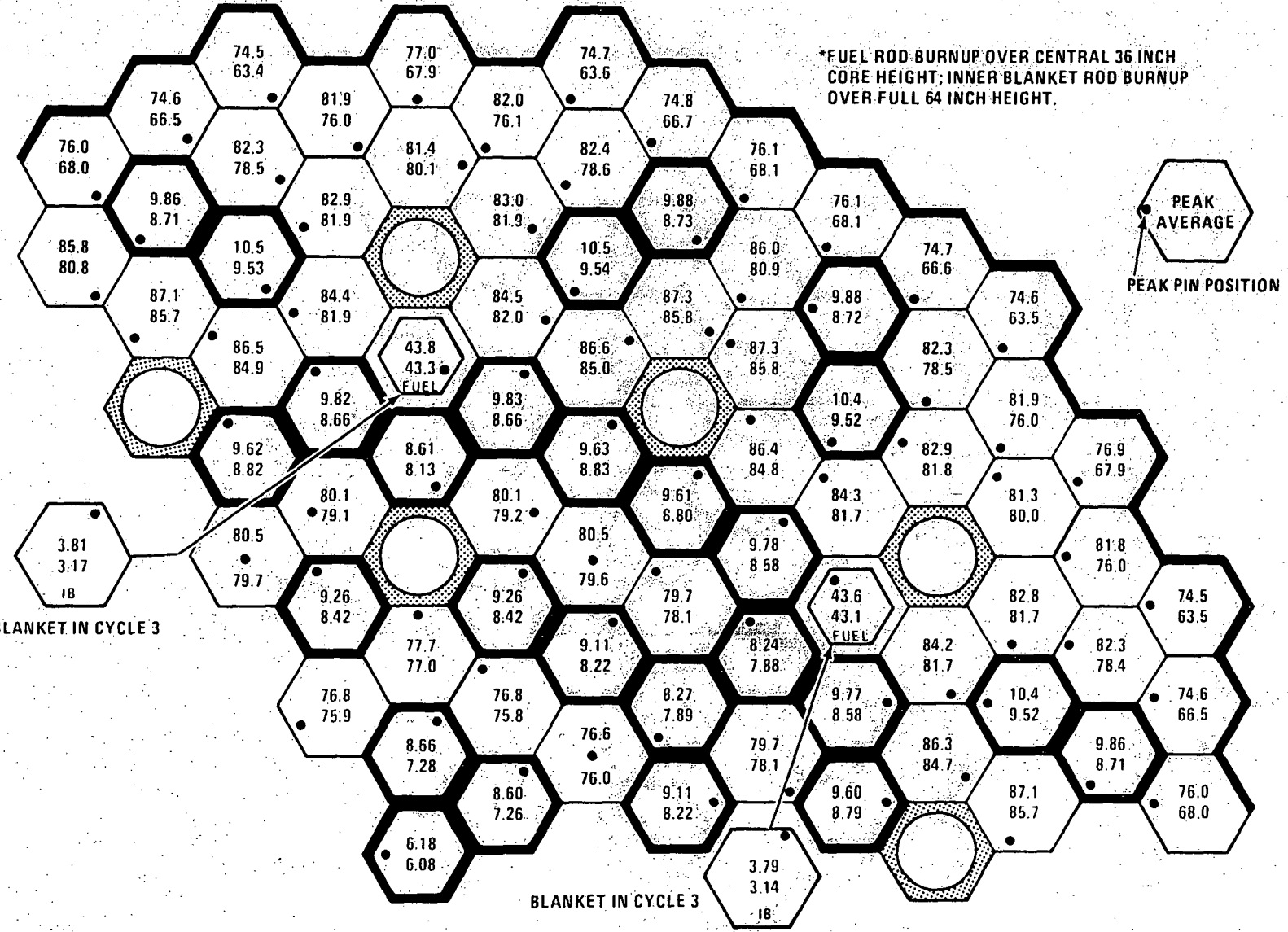


Figure 4.3-23. Peak and Average Rod Burnup\* (MWD/KG) Cycles 1-2



1544-24

\*FUEL ROD BURNUP OVER CENTRAL 36 INCH CORE HEIGHT; INNER BLANKET ROD BURNUP OVER FULL 64 INCH HEIGHT.



4.3-173

Amend. 51  
Sept. 1979

Figure 4.3-24. Peak and Average Rod Burnup\* (MWD/KG) Cycles 3-4

1544-25

4.3-174

Amend. 51  
Sept. 1979

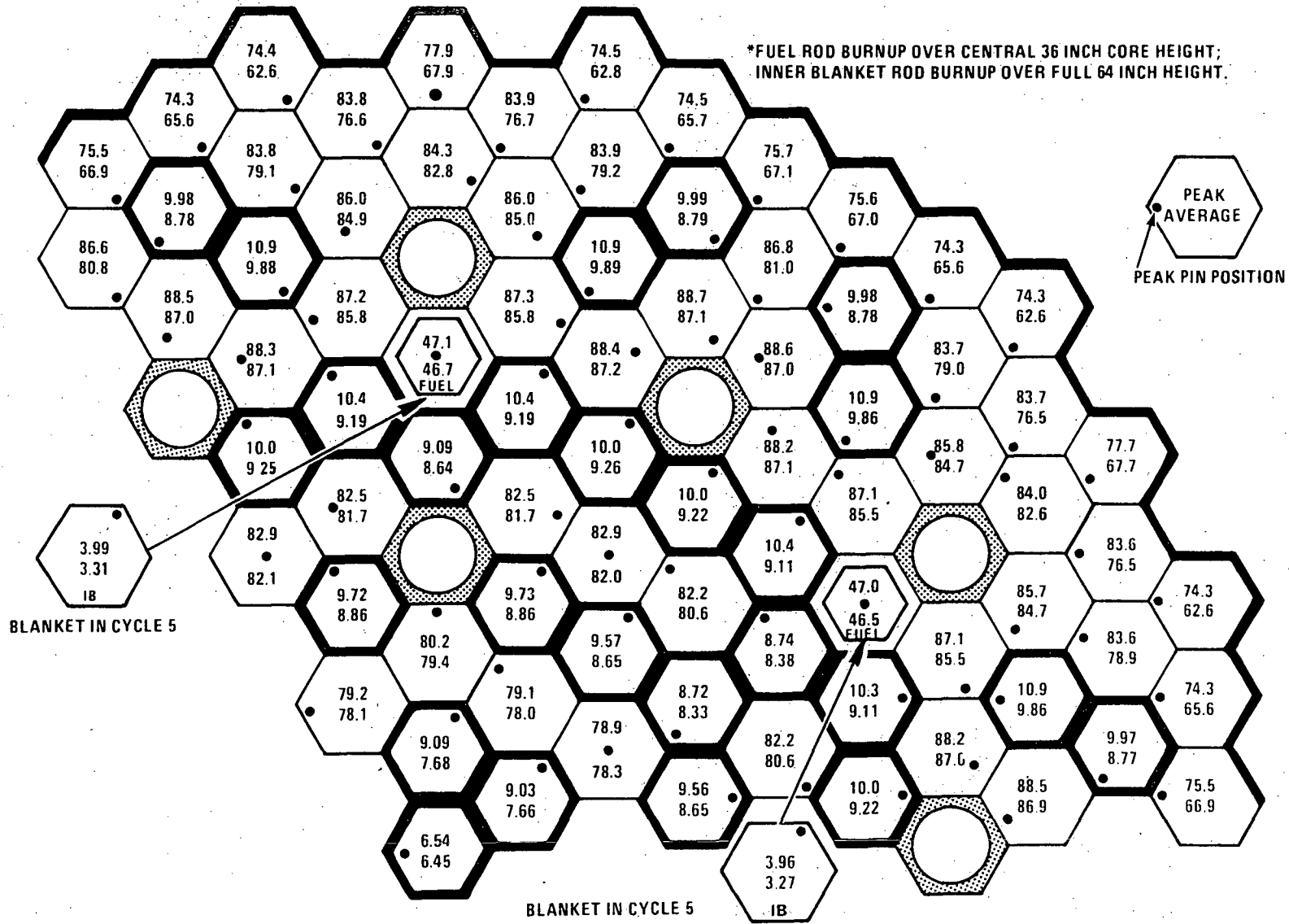
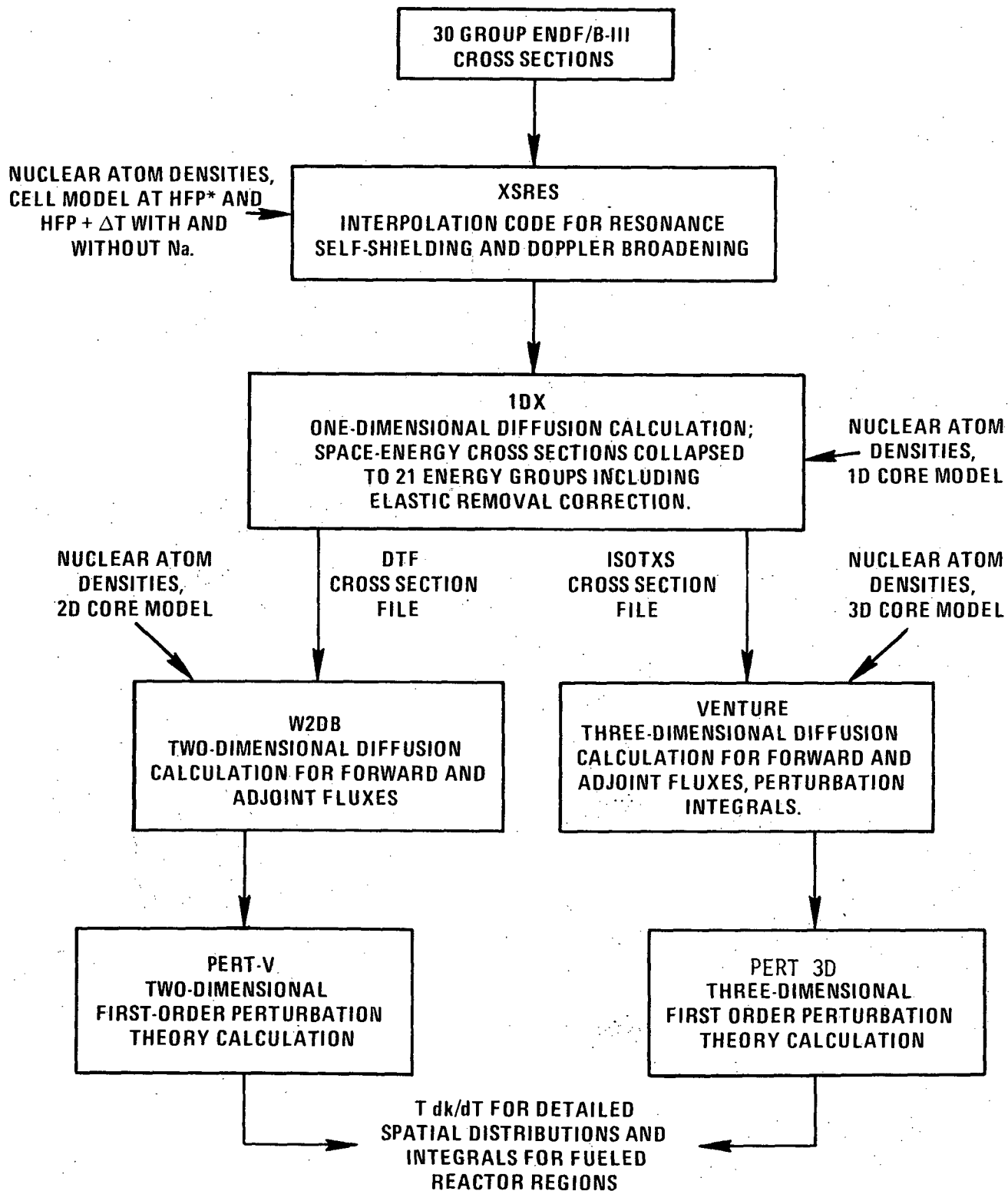
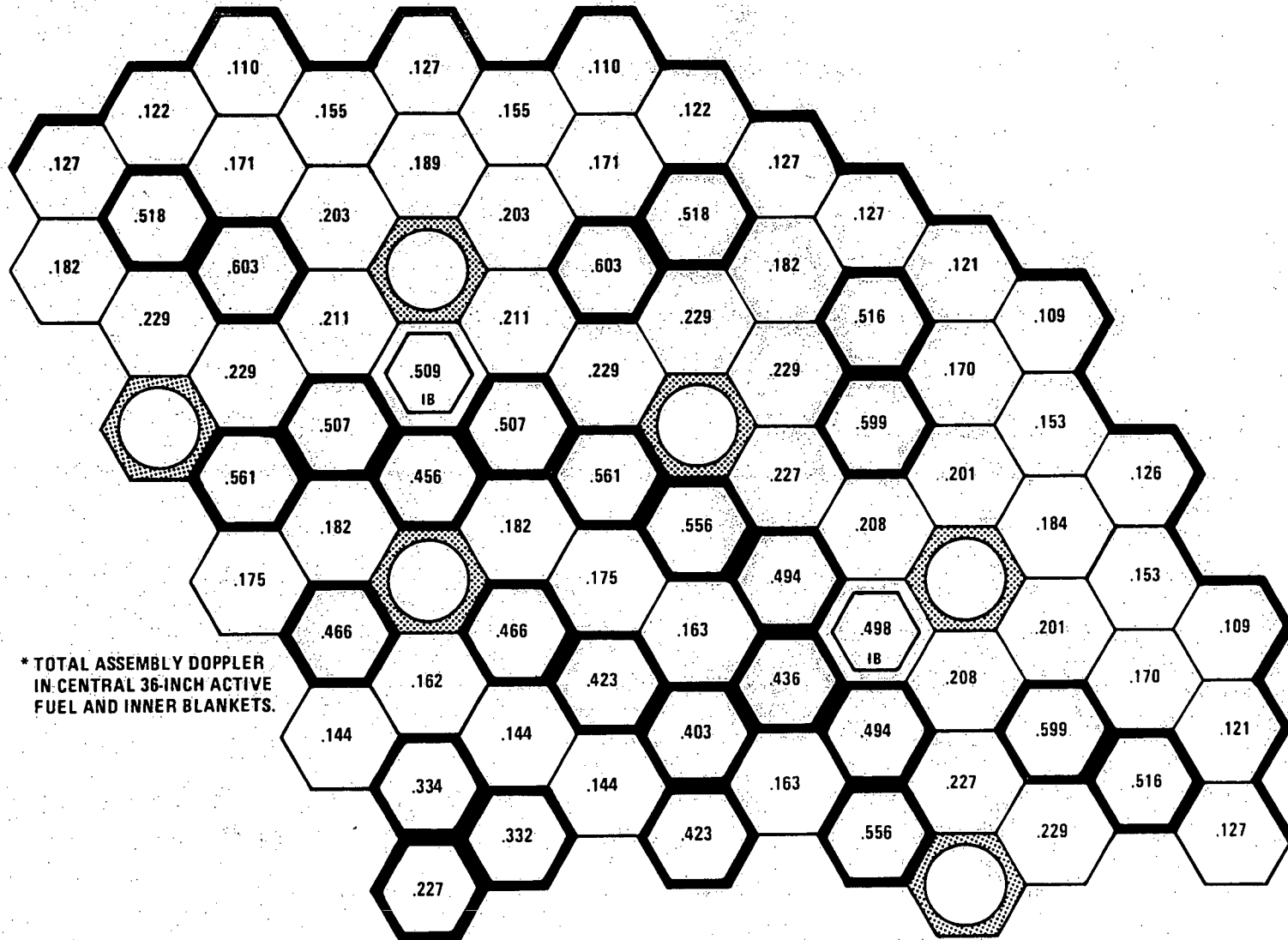


Figure 4.3-25. Peak and Average Rod Burnup\* (MWD/KG) Cycles 5-6



\*HFP = HOT FULL POWER TEMPERATURE CONDITIONS

Figure 4.3-26. Flow Chart for Doppler Calculations



\* TOTAL ASSEMBLY DOPPLER  
IN CENTRAL 36-INCH ACTIVE  
FUEL AND INNER BLANKETS.

Figure 4.3-27a. CRBRP Doppler Constant by Assembly\* Beginning of Cycle One ( $-T \frac{dk}{dT} \times 10^4$ )

1544-28

4.3-177

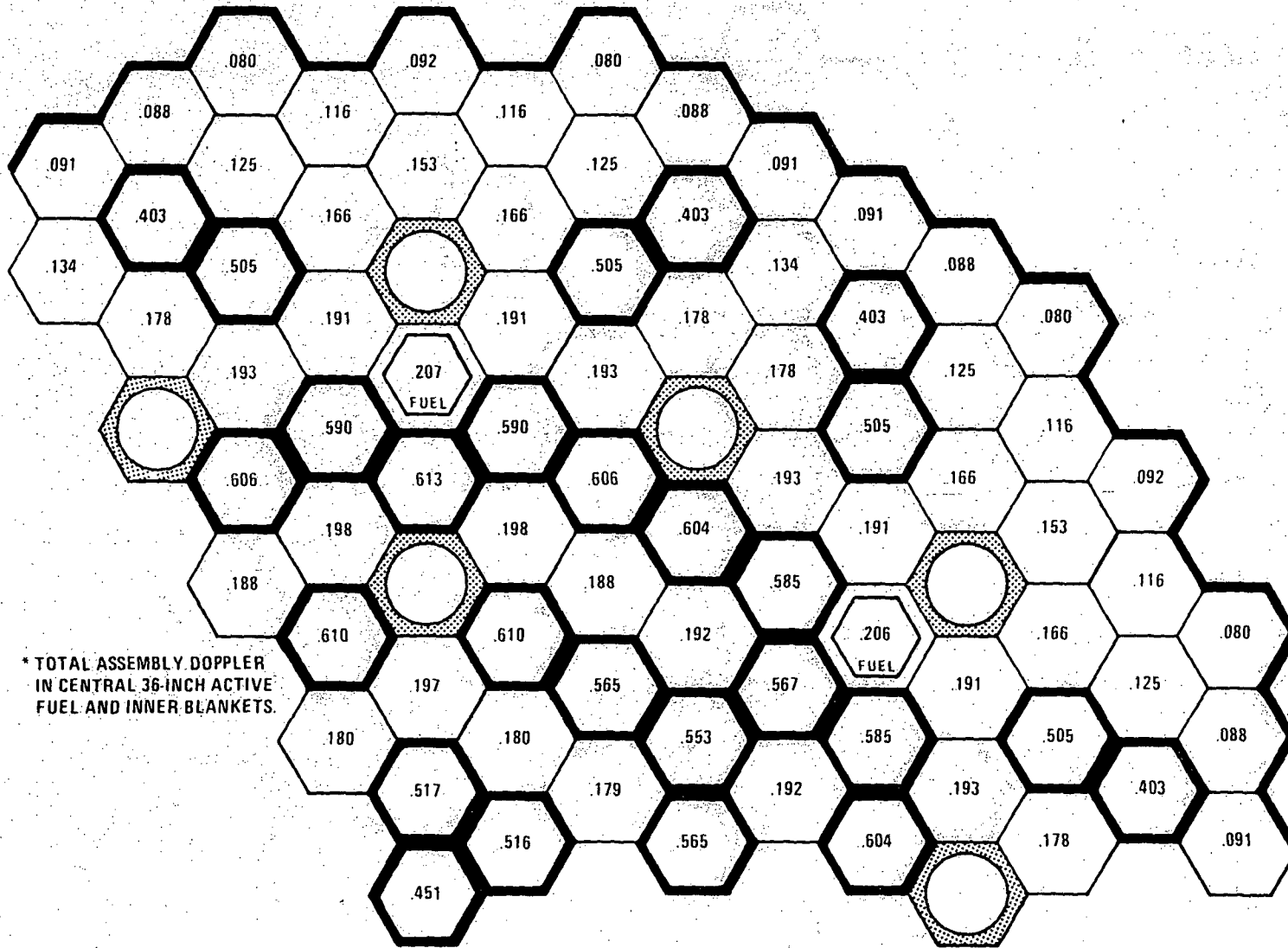


Figure 4.3-27b. CRBRP Doppler Constant by Assembly\* End of Cycle Four ( $-T dk/dT \times 10^4$ )

Amend. 51  
Sept. 1979

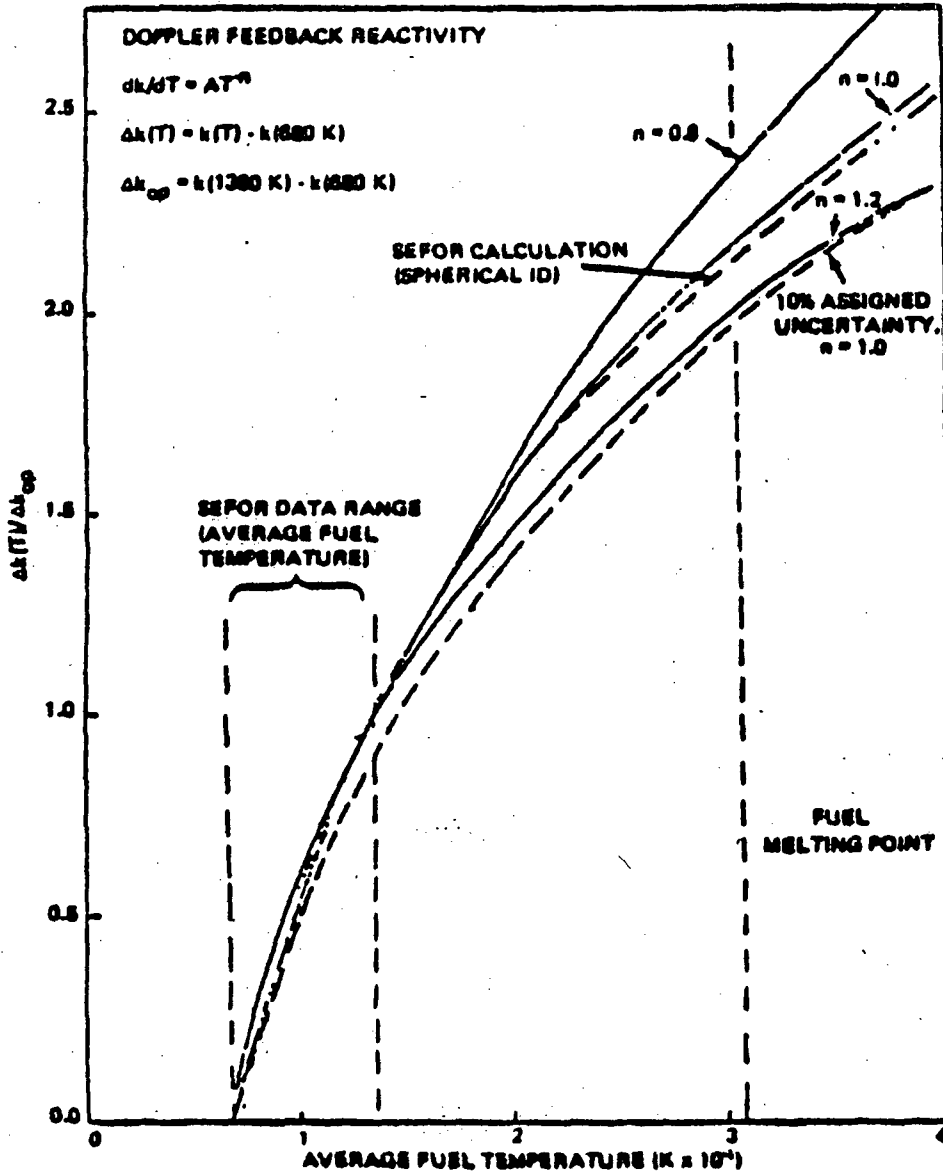


Figure 4.3- 27c Extrapolation of Doppler Feedback to Elevated Temperatures

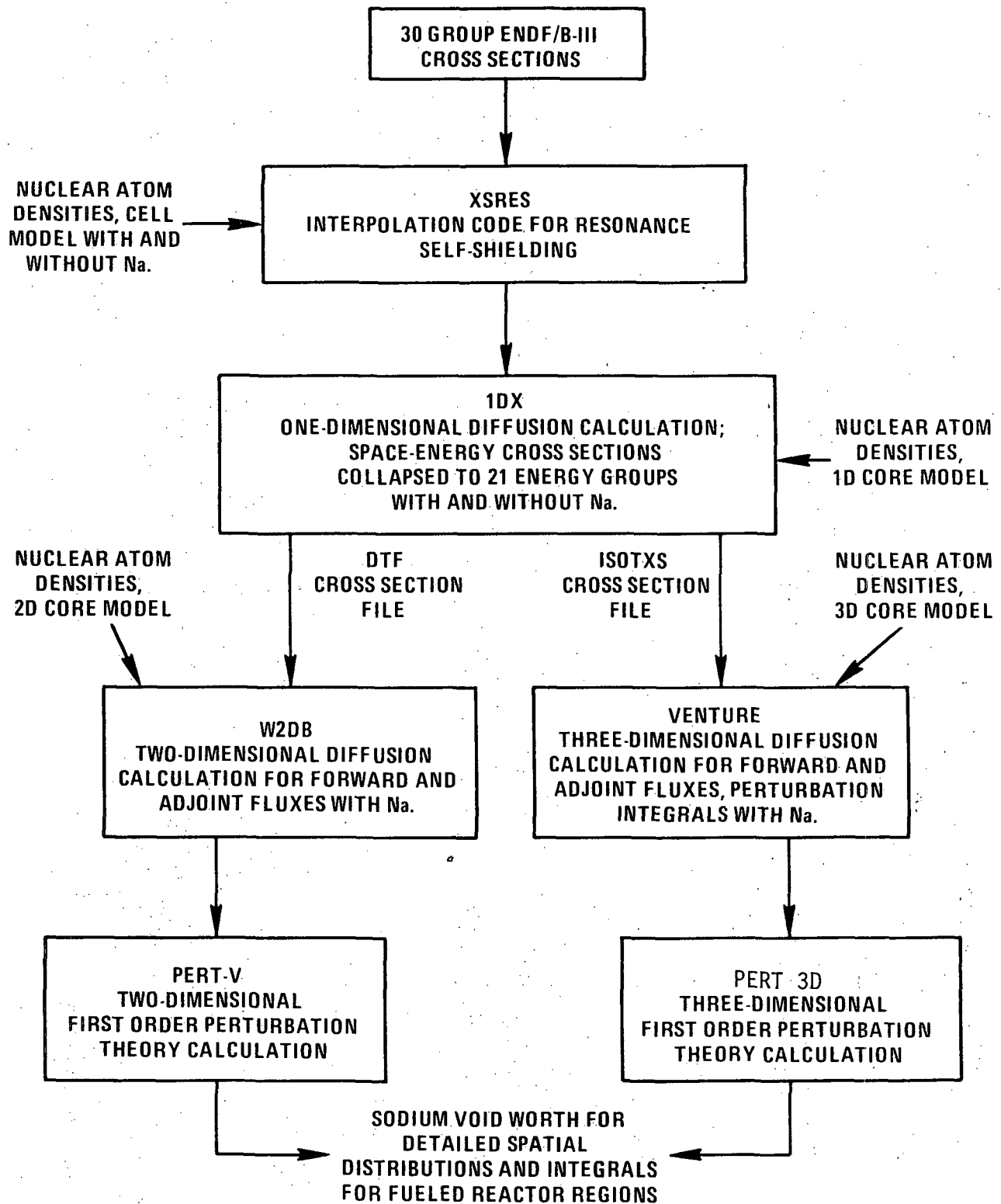
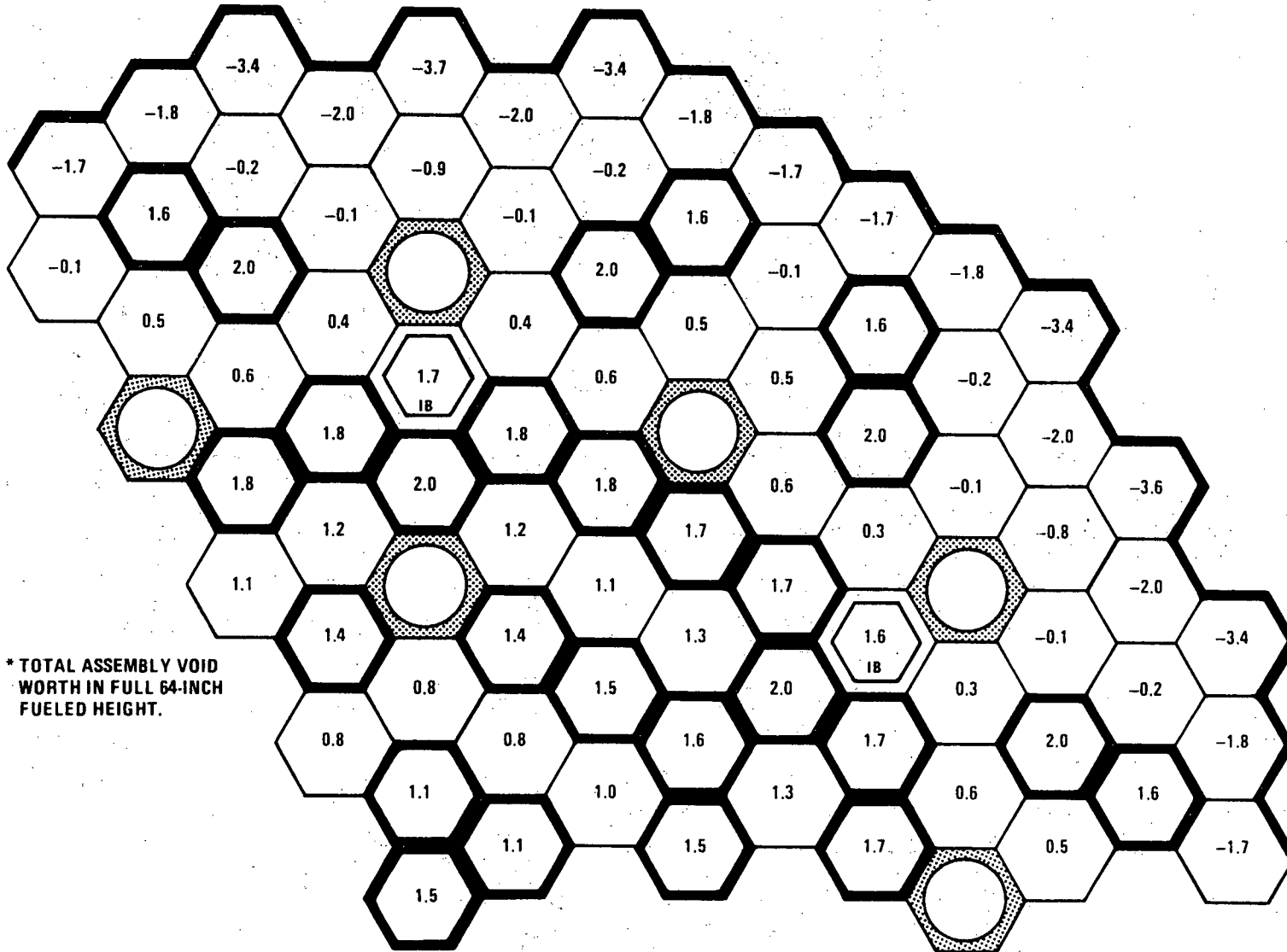


Figure 4.3-28. Flow Chart for Sodium Voiding Reactivity Worth Calculations



\* TOTAL ASSEMBLY VOID WORTH IN FULL 64-INCH FUELED HEIGHT.

Figure 4.3-29a. CRBRP Sodium Void Worth By Assembly Beginning of Cycle One\* ( $\phi$ )



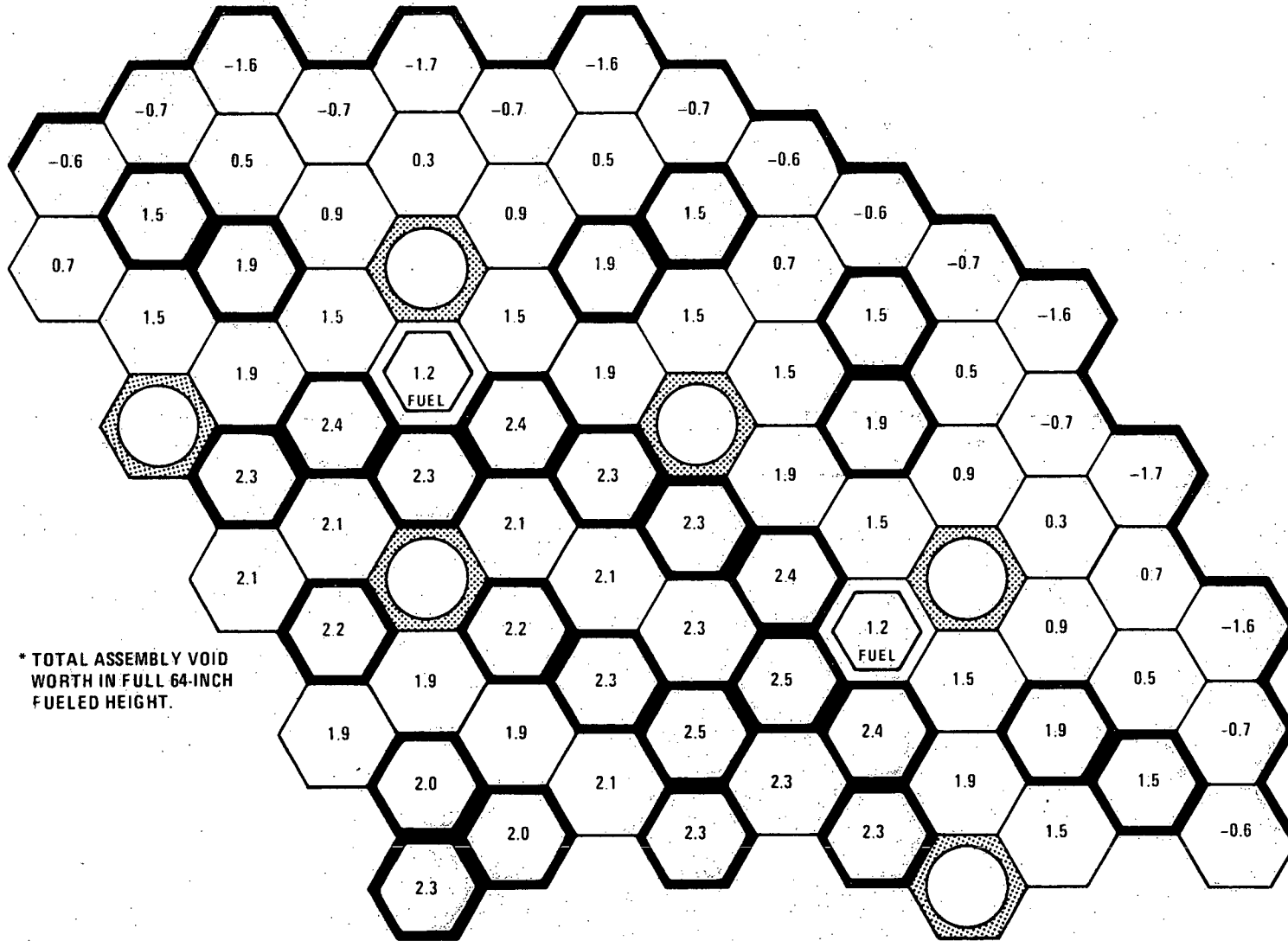


Figure 4.3-29b. CRBRP Sodium Void Worth by Assembly End of Cycle Four\* ( $\phi$ )

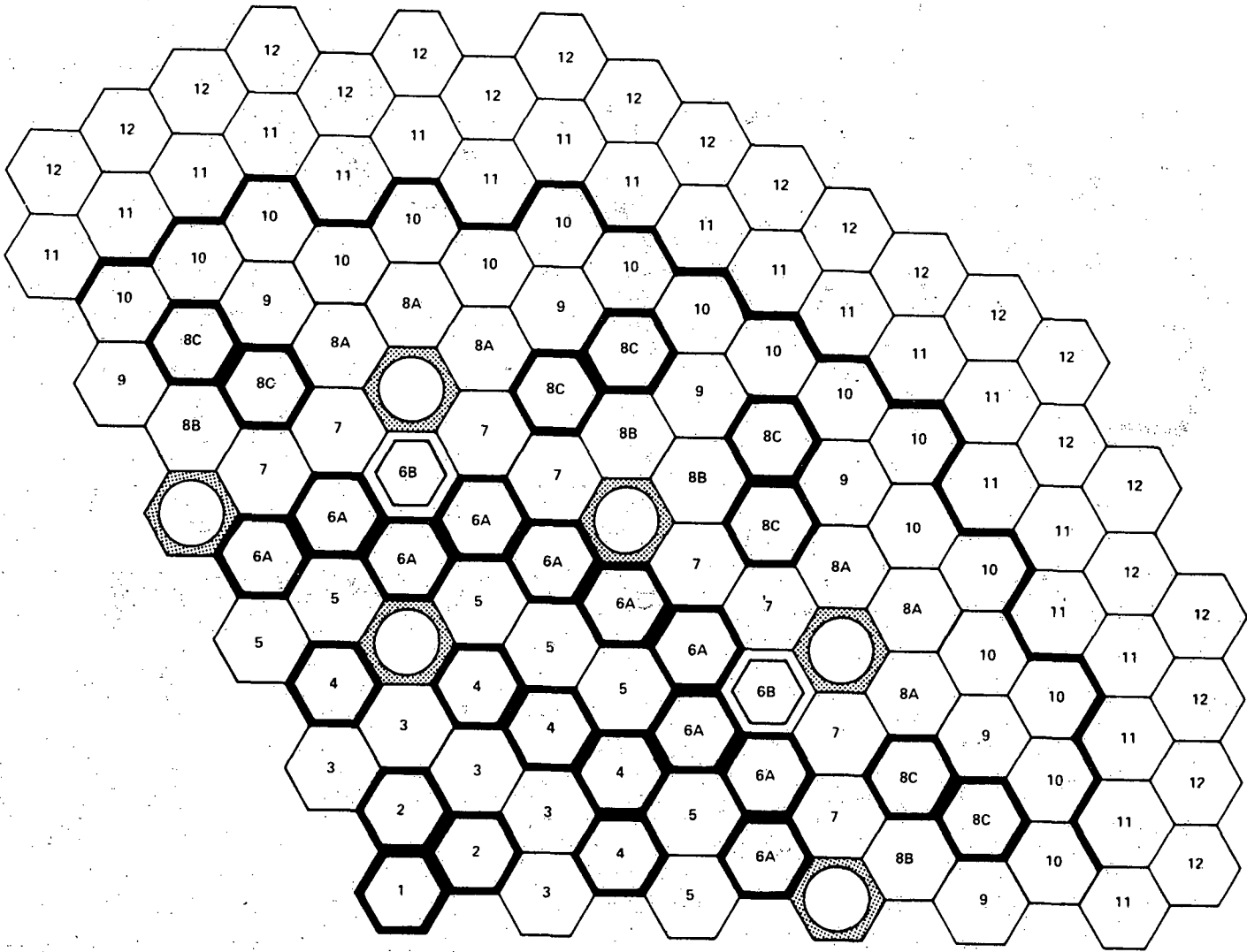


FIGURE 4.3-30. Radial Row Numbering Scheme for CRBRP Bowing Model

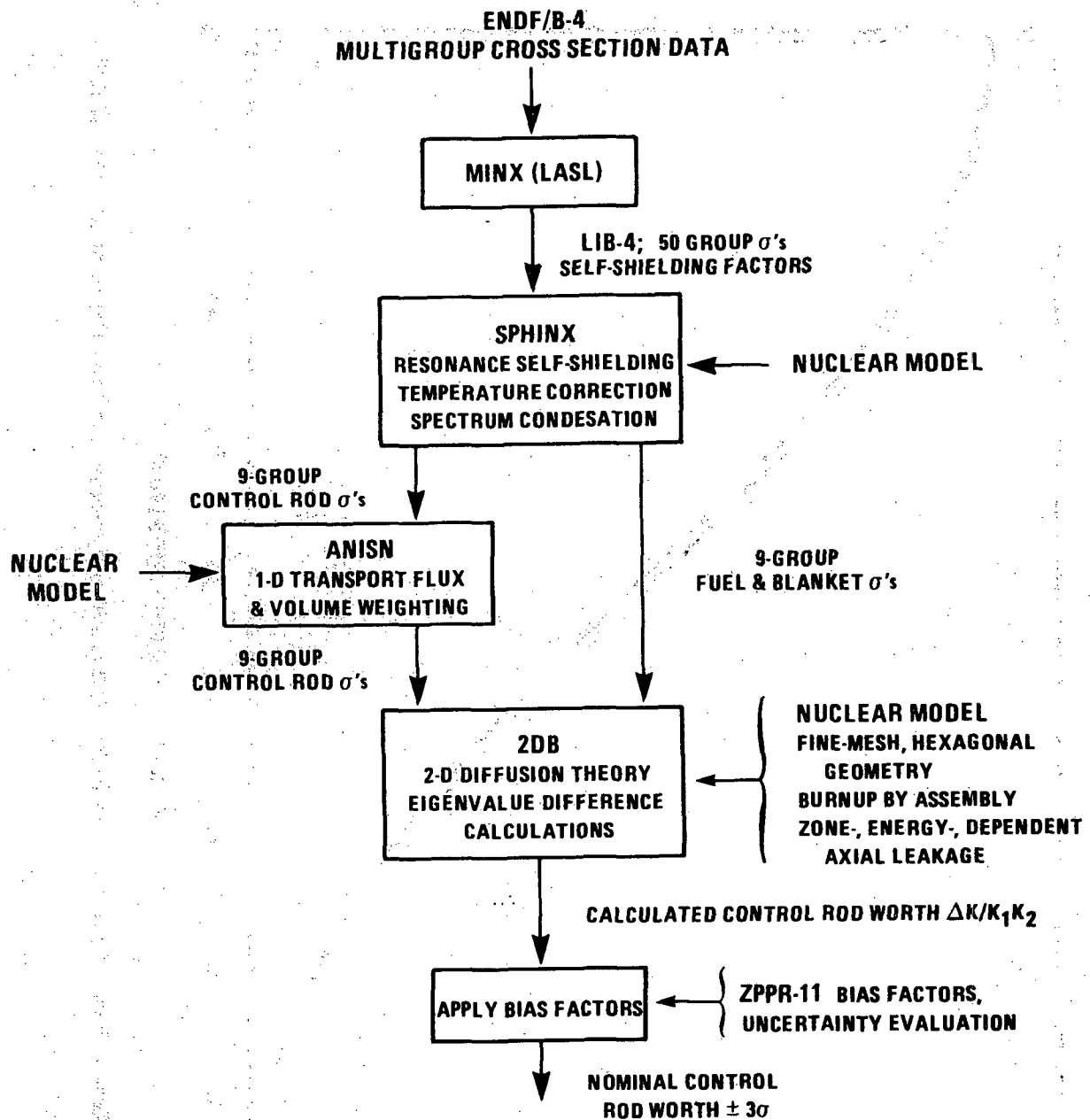


Figure 4.3-31. Control Rod Worth Calculational Sequence

7484-2

4.3-183

Amend. 76  
March 1983

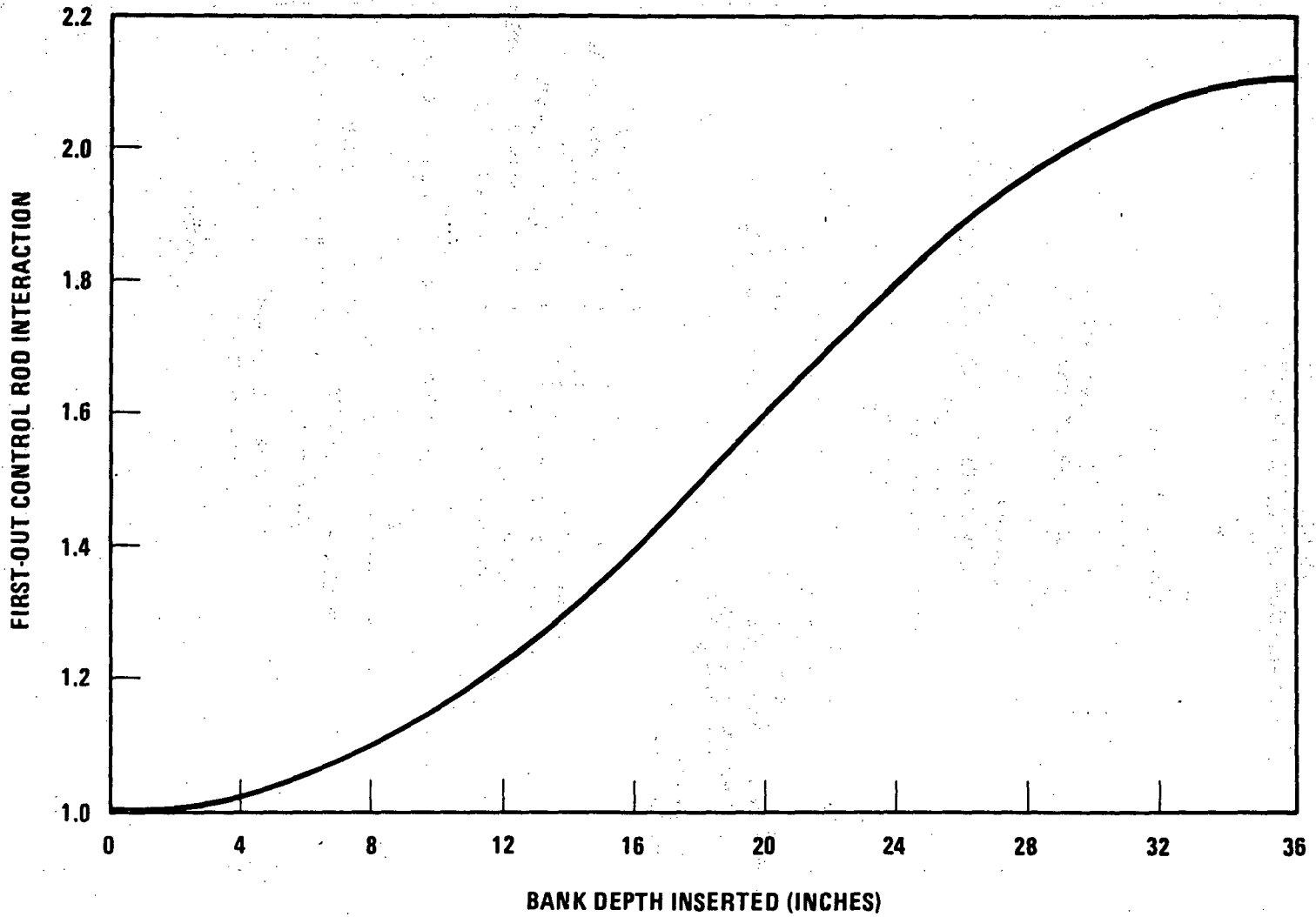


Figure 4.3-32. Row 7 Corner First-Out Control Rod Interaction as a Function of Bank Depth of Insertion BOC3

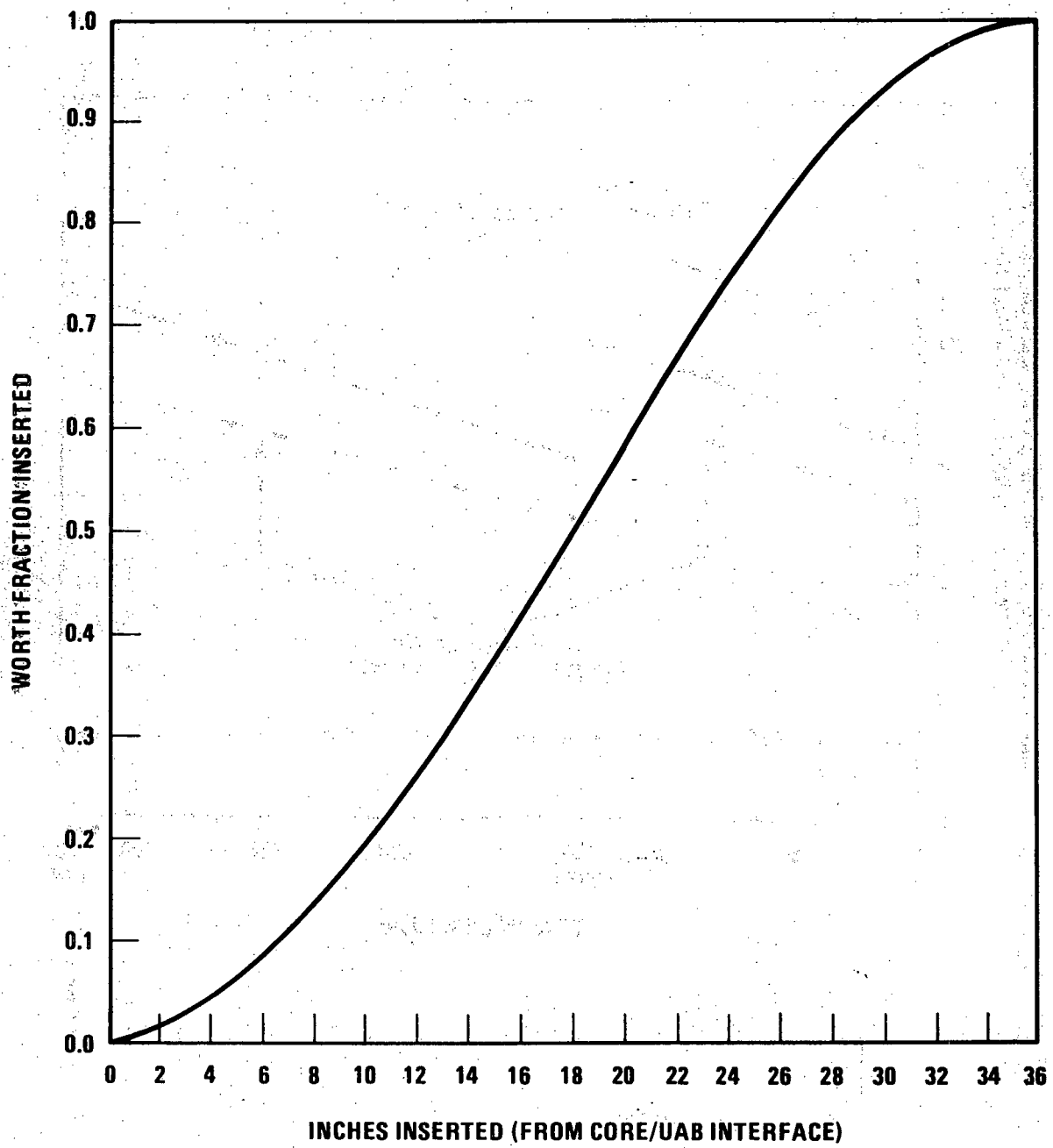


Figure 4.3-33. Control Rod Integral Worth Curve

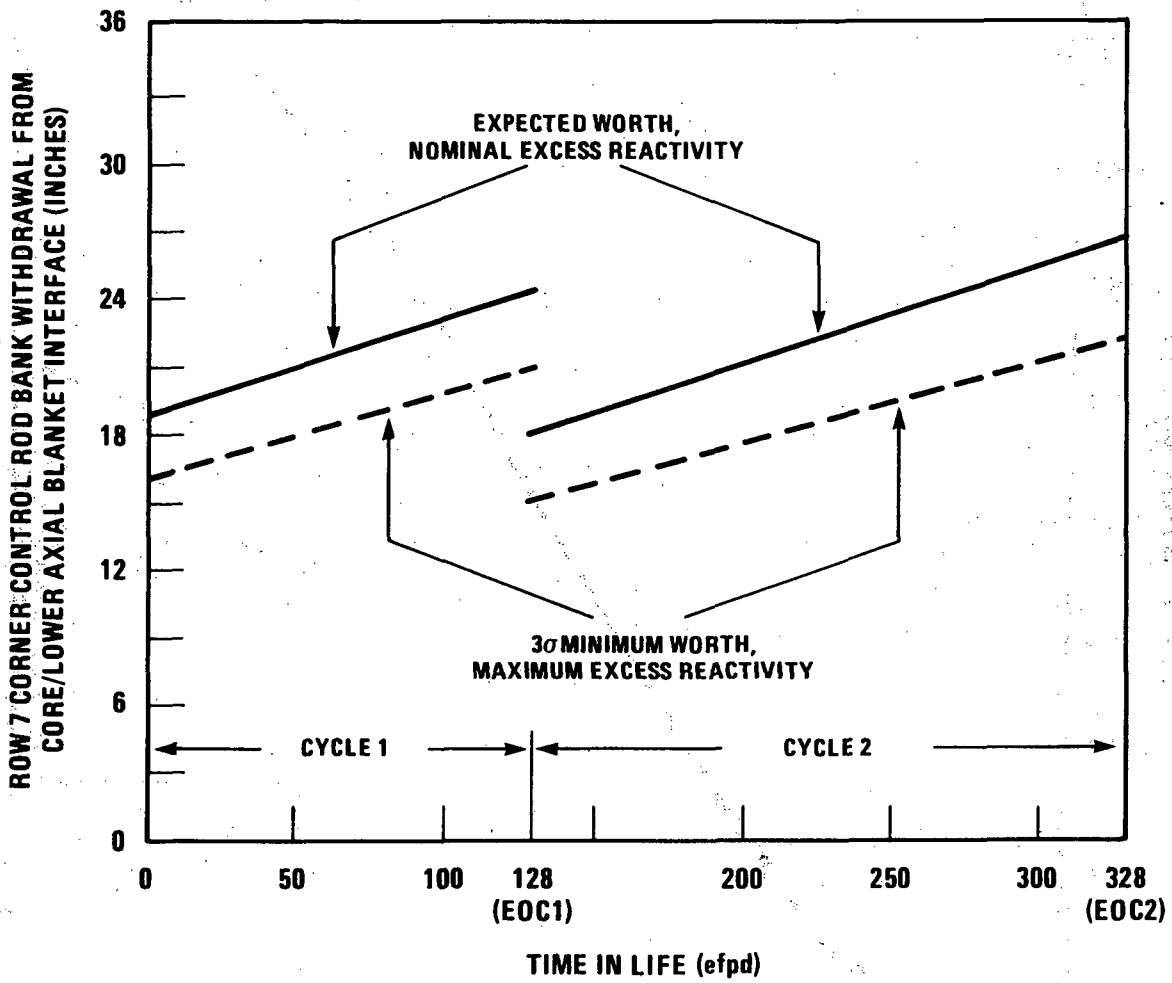


Figure 4.3-34. CRBRP Row 7 — Corner Control Rod Bank Withdrawal History Core One (Cycles 1 & 2)

7484-4

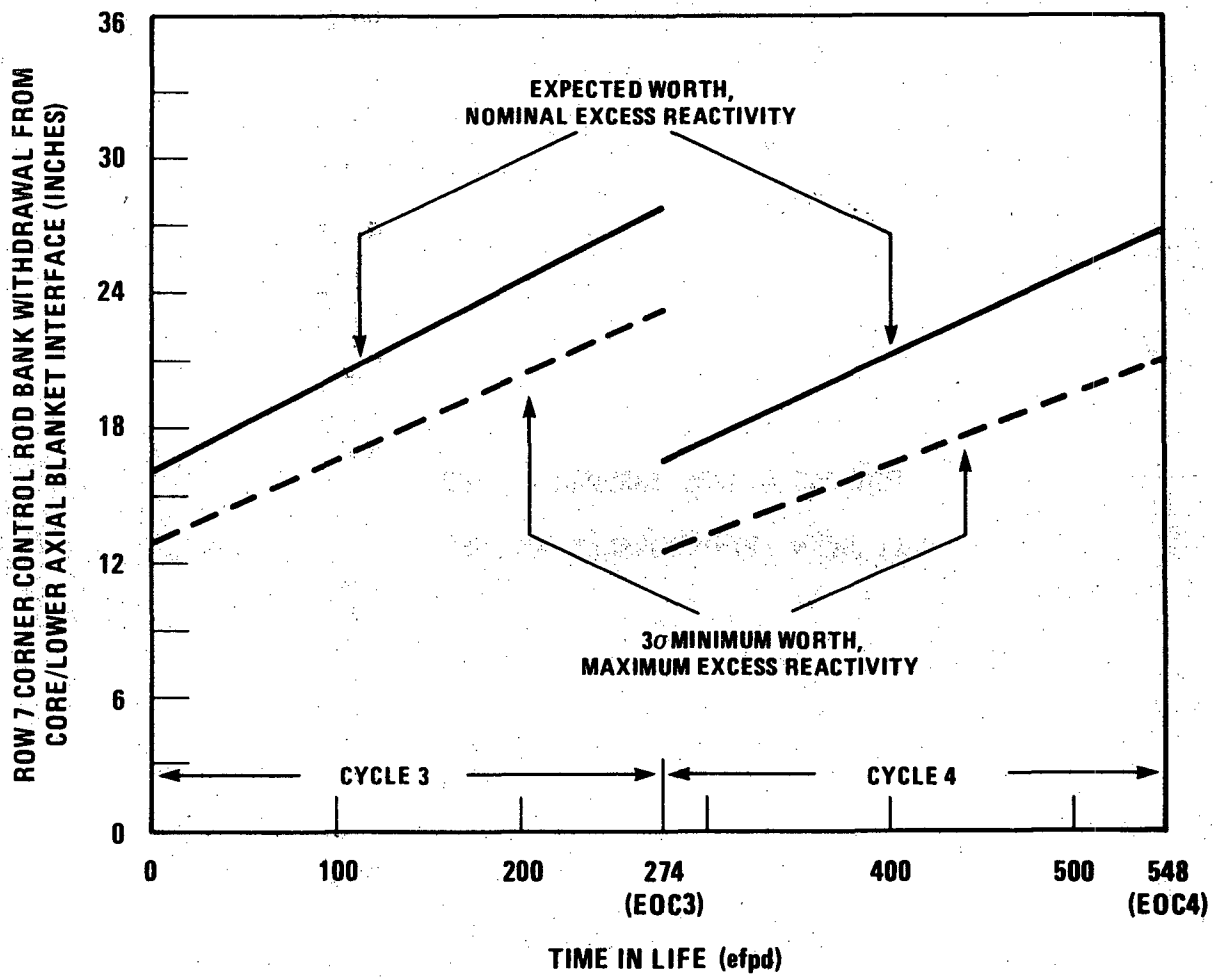


Figure 4.3-35. CRBRP Row 7 – Corner Control Rod Bank Withdrawal History Core Two (Cycles 3 & 4)

FIGURES 4.3-36 THROUGH 4.3-39  
HAVE BEEN INTENTIONALLY DELETED.



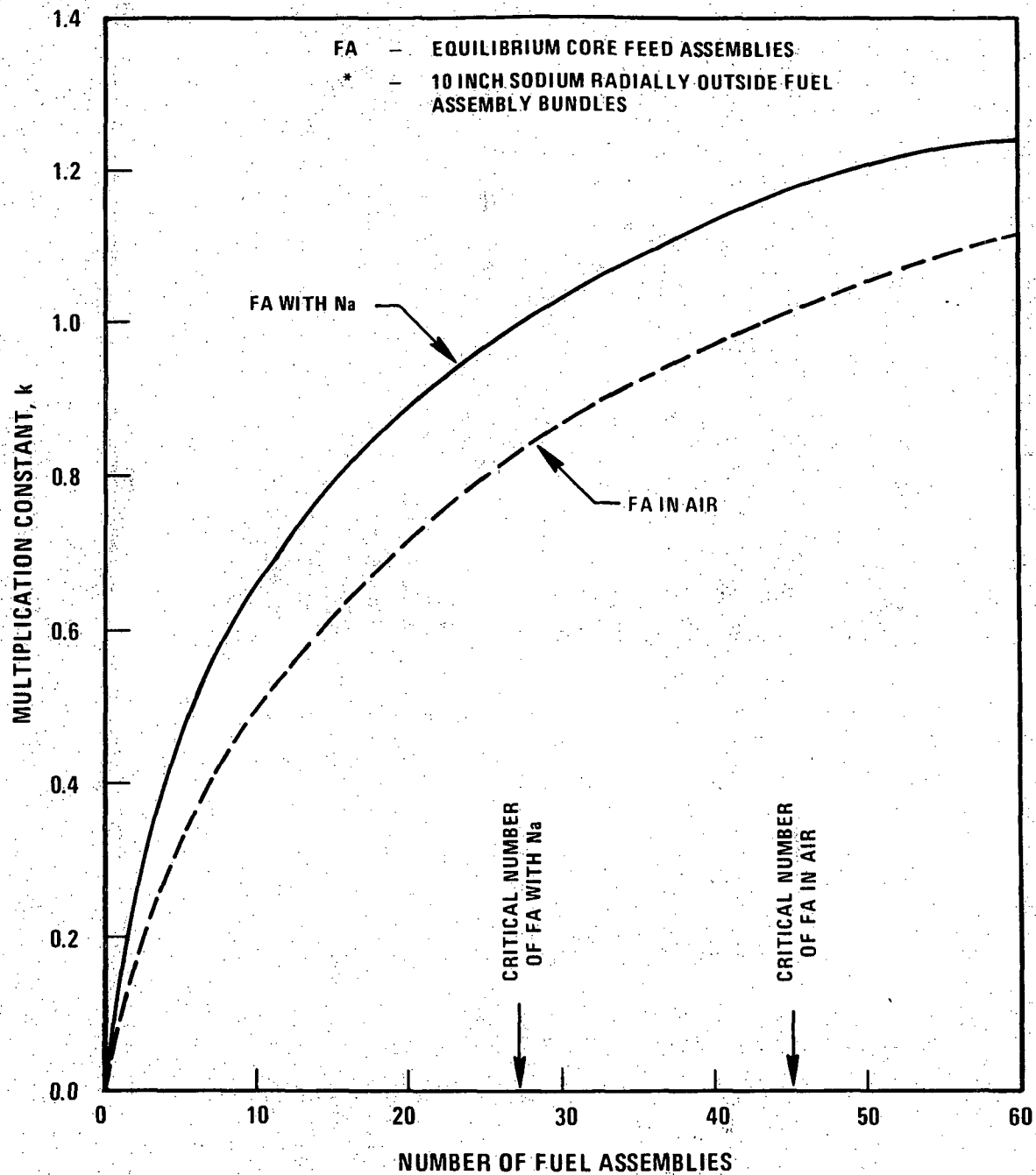


Figure 4.3-40. Criticality of Fuel Assemblies (Immersed in Sodium\* and in Air)

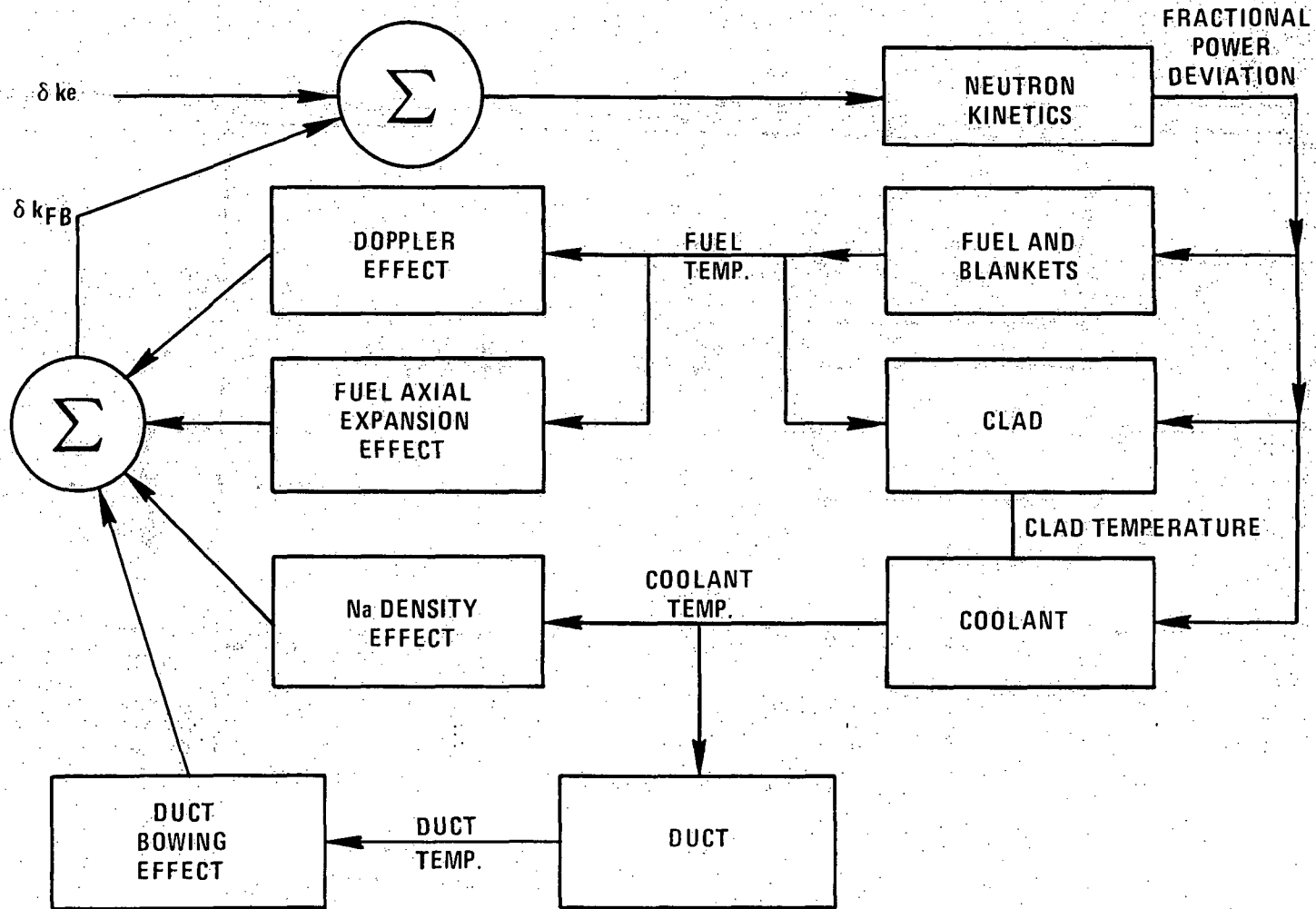


Figure 4.3-41. Schematic of Feedback Effects.

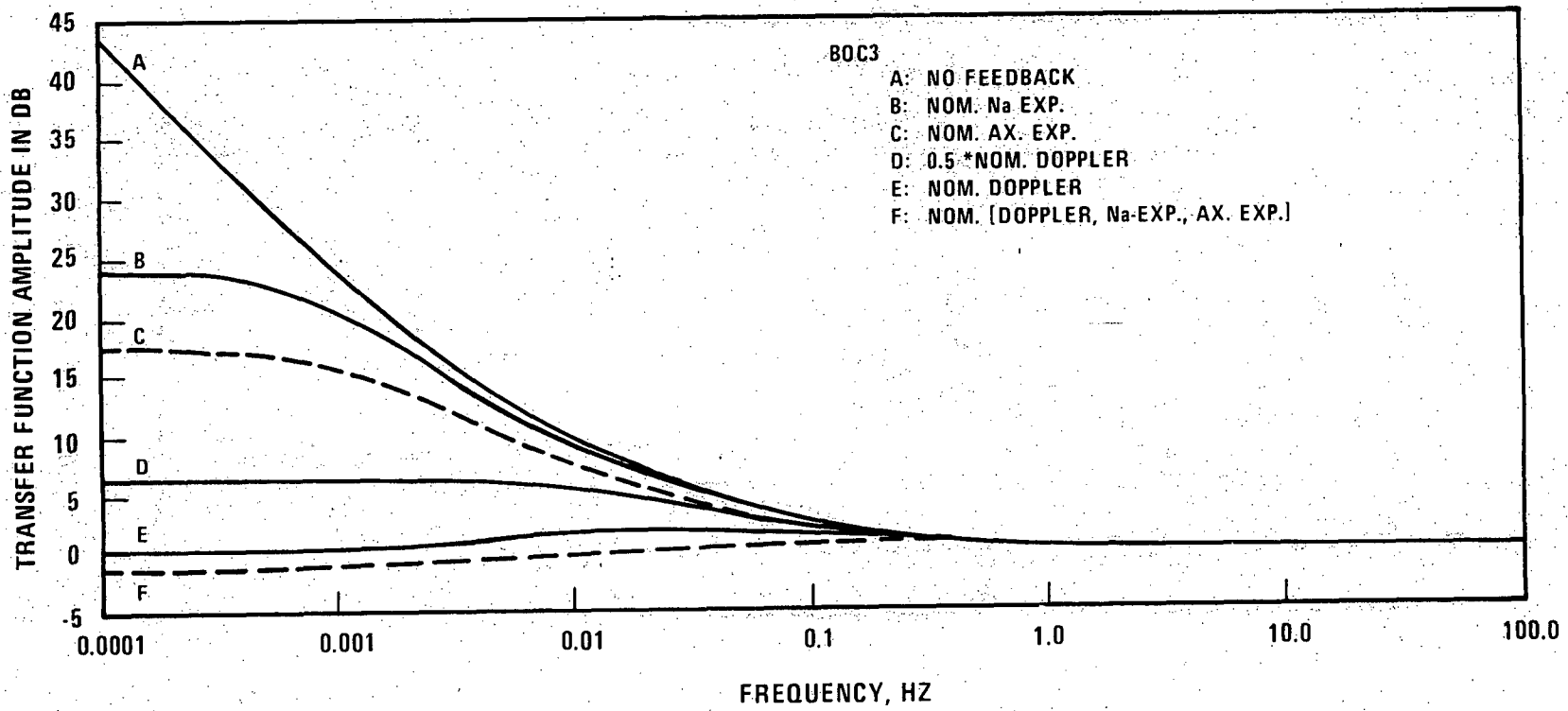


Figure 4.3-42. Transfer Functions for Various Feedback Reactivities

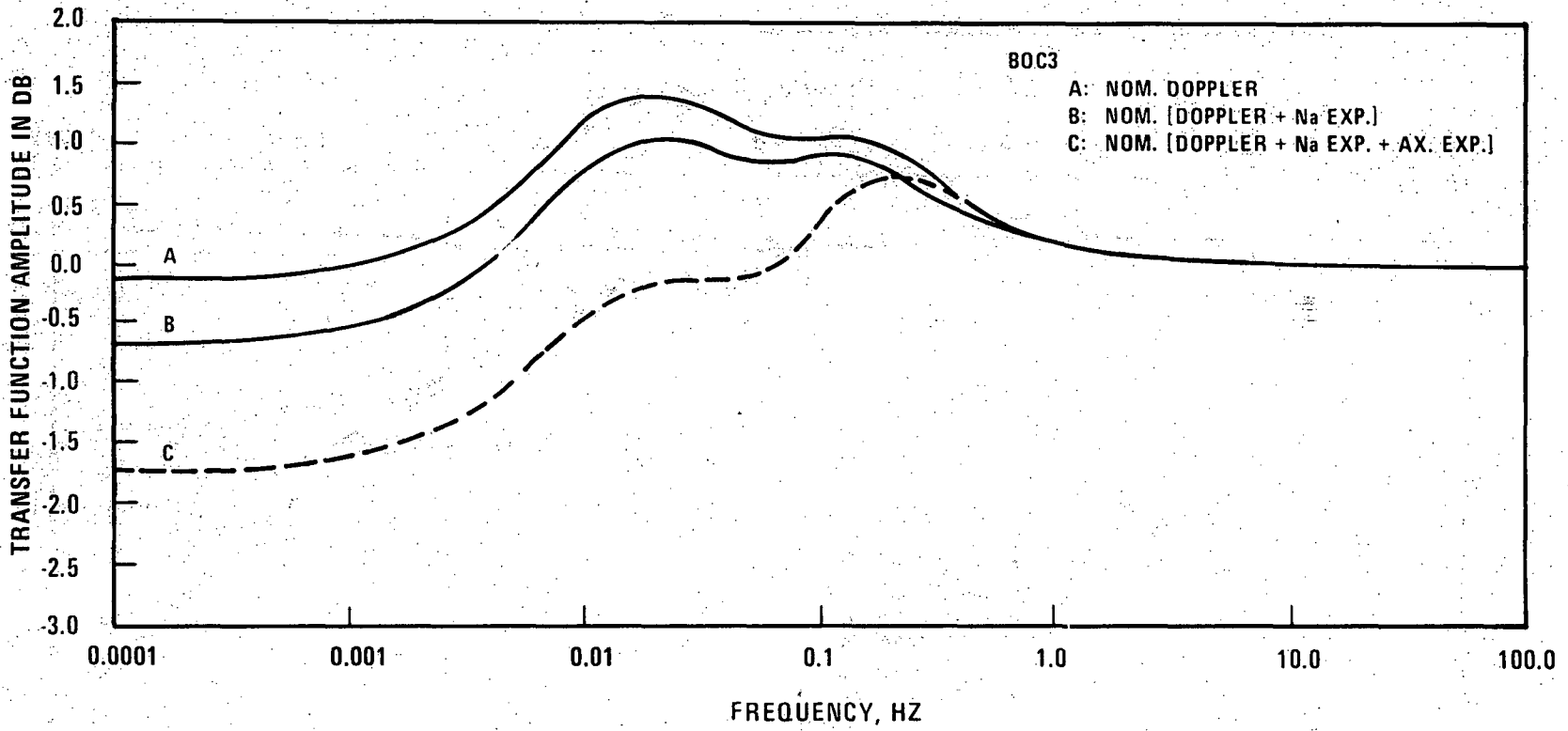


Figure 4.3-43. Transfer Functions for Various Feedback Reactivities (Note Expanded Scale).

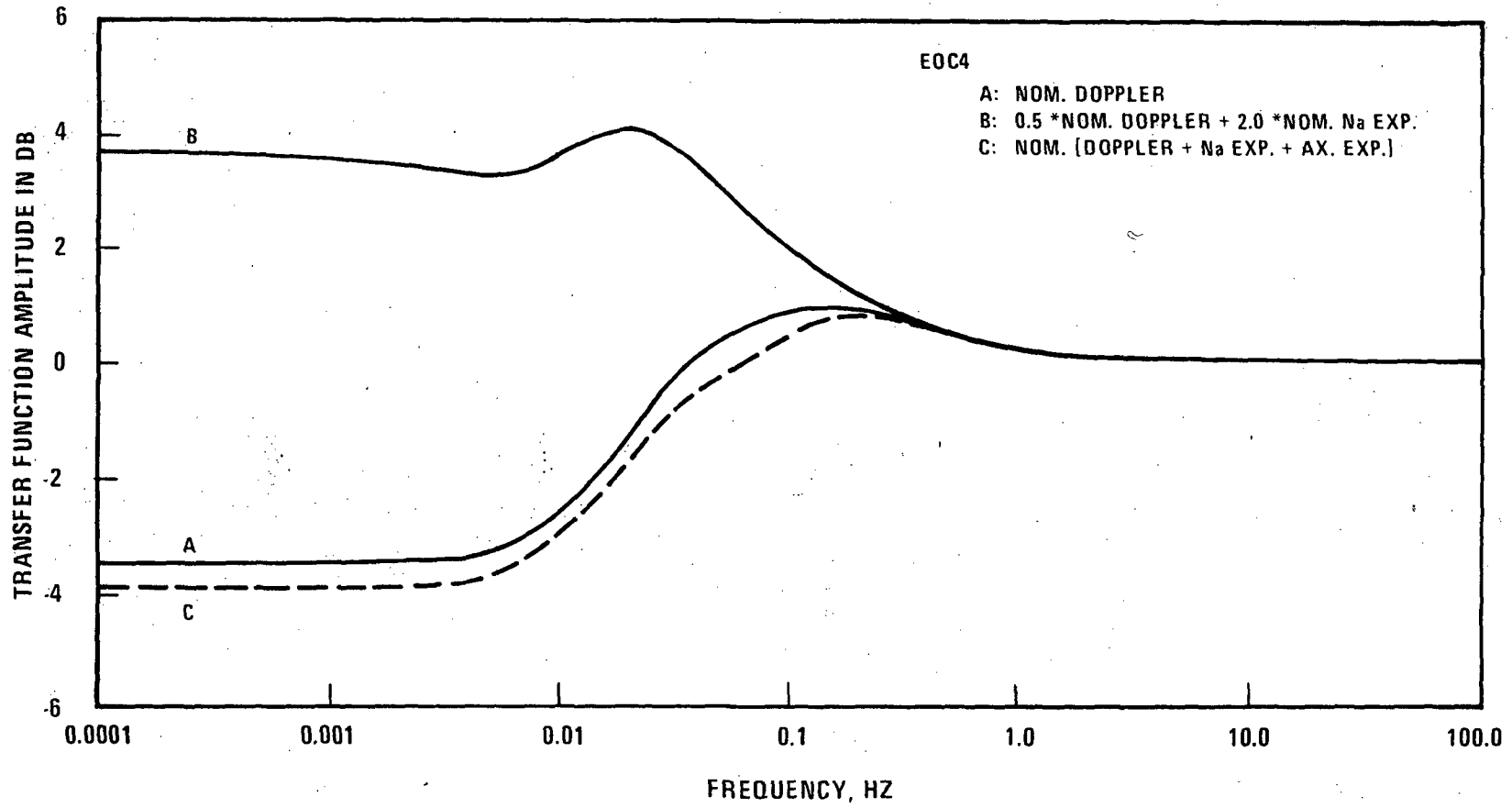


Figure 4.3-44. Transfer Functions for Various Feedback Reactivities (Note Expanded Scale)

59 |

THIS PAGE INTENTIONALLY BLANK

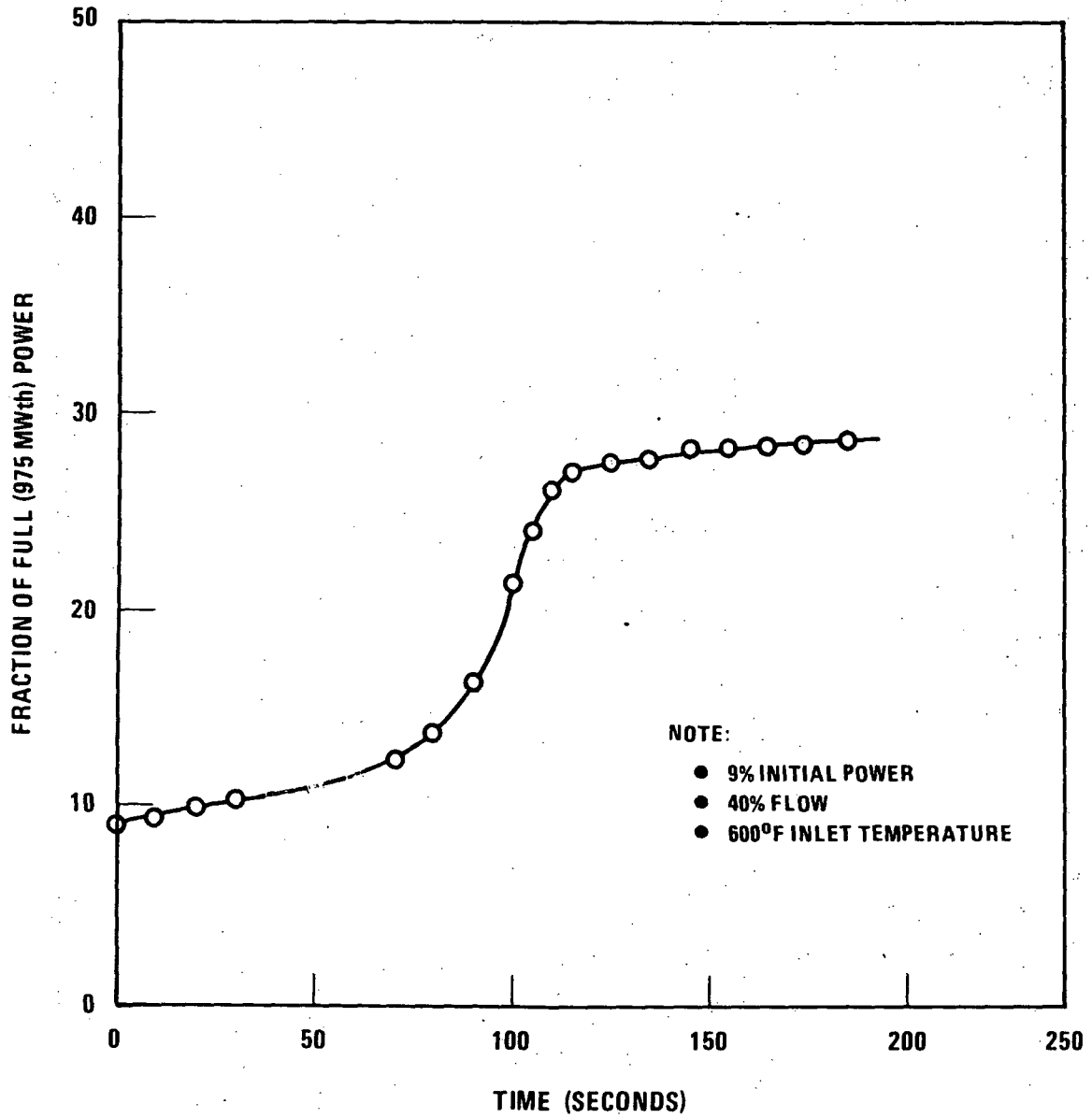


Figure 4.3.46. Reactor Power Response to Inherent Reactivity Feedback Following a 2¢ Step Insertion

4655-8

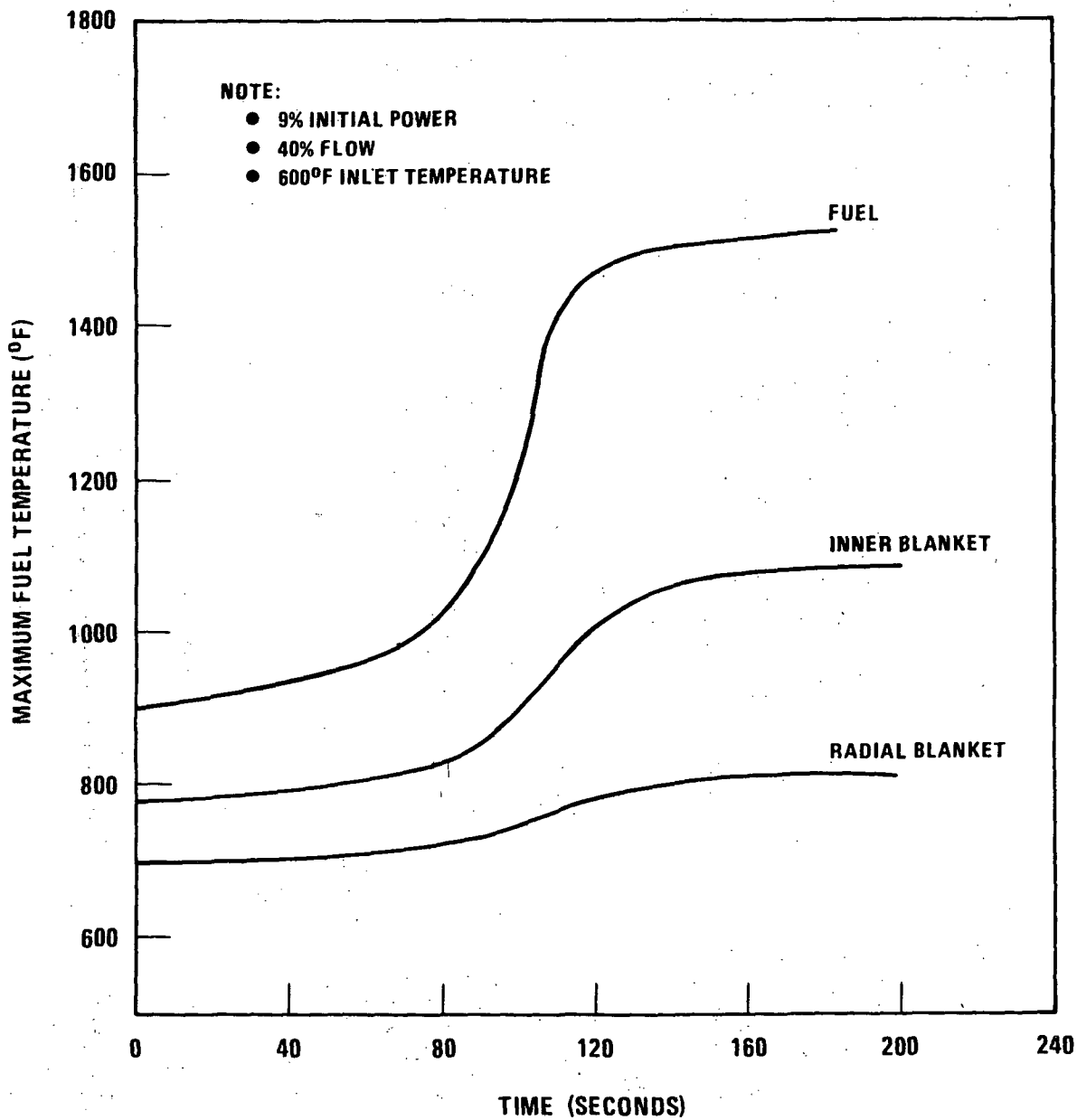


Figure 4.3-47. Base Case Maximum Fuel Temperature Response to Inherent Reactivity Feedbacks Following a 2% Step Insertion

4655-7

4.3-195

Amend. 59  
Dec. 1980



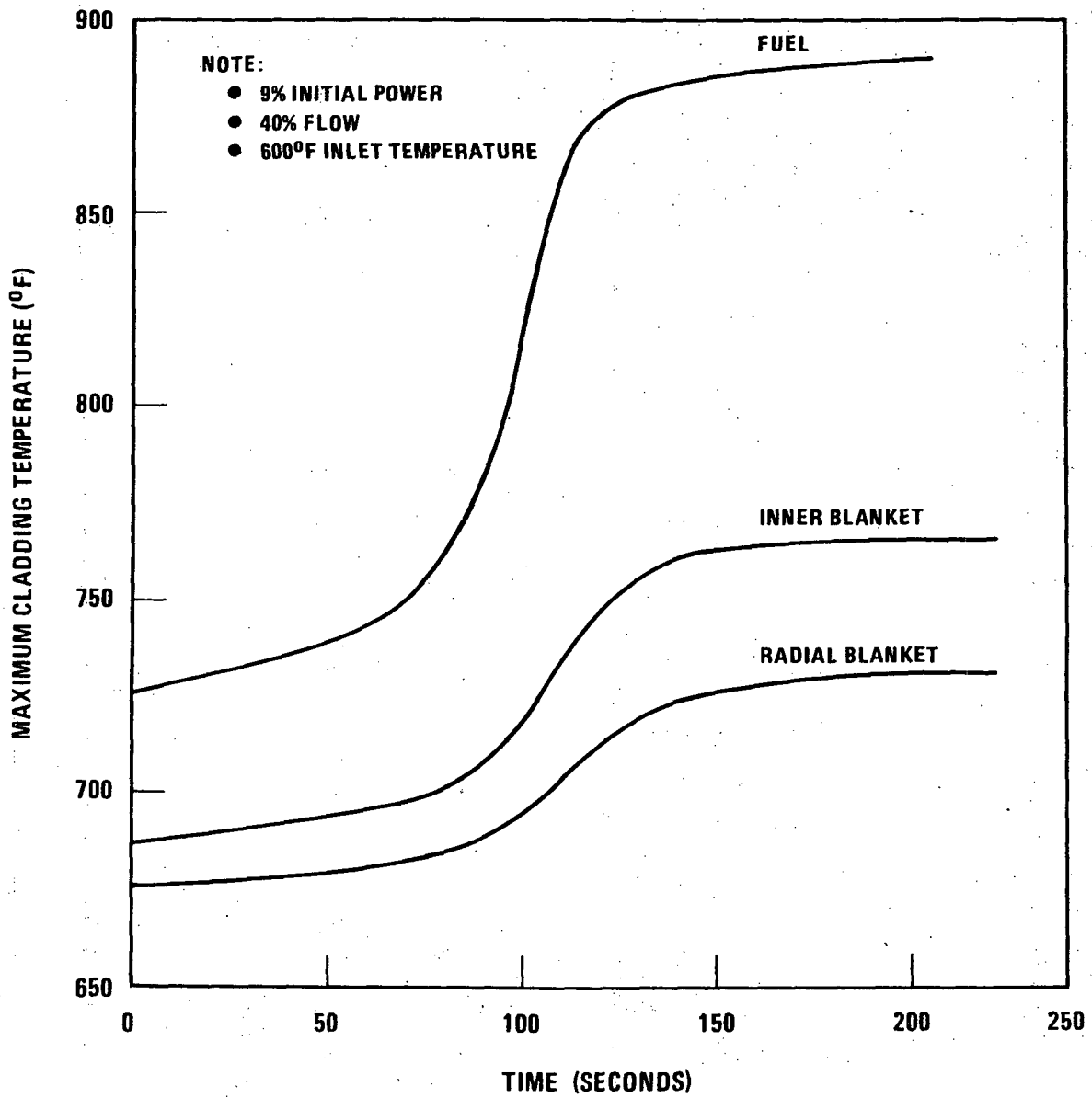


Figure 4.3-48. Base Case Maximum Cladding Temperature Response to Inherent Reactivity Feedbacks Following a  $2\phi$  Step Insertion

4655-6

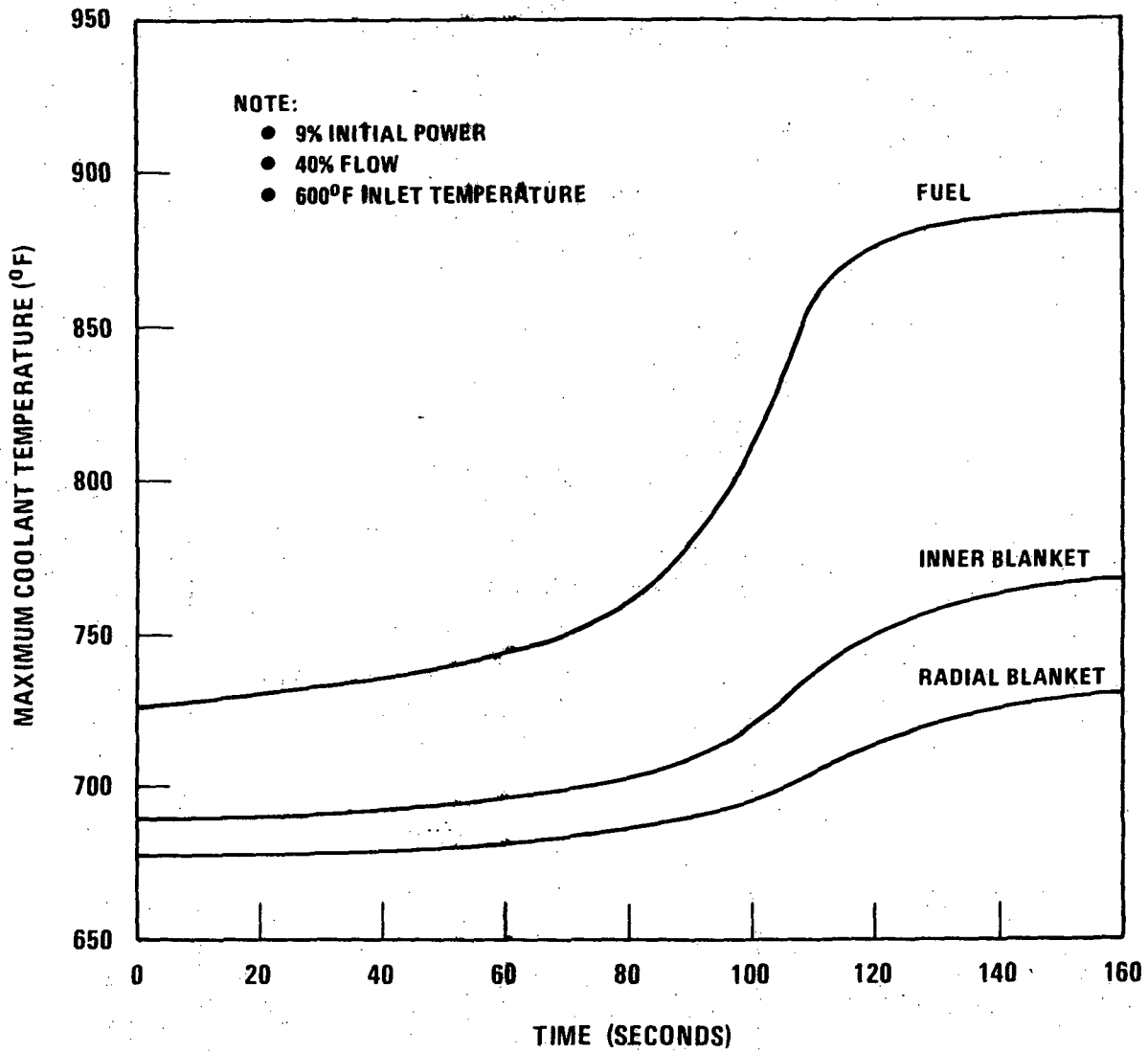


Figure 4.3-49. Base Case Maximum Coolant Temperature Response to Inherent Reactivity Feedbacks Following a 2¢ Step Insertion

4655-5

4.3-197

Amend. 59  
Dec. 1980

154449a

4.3-198

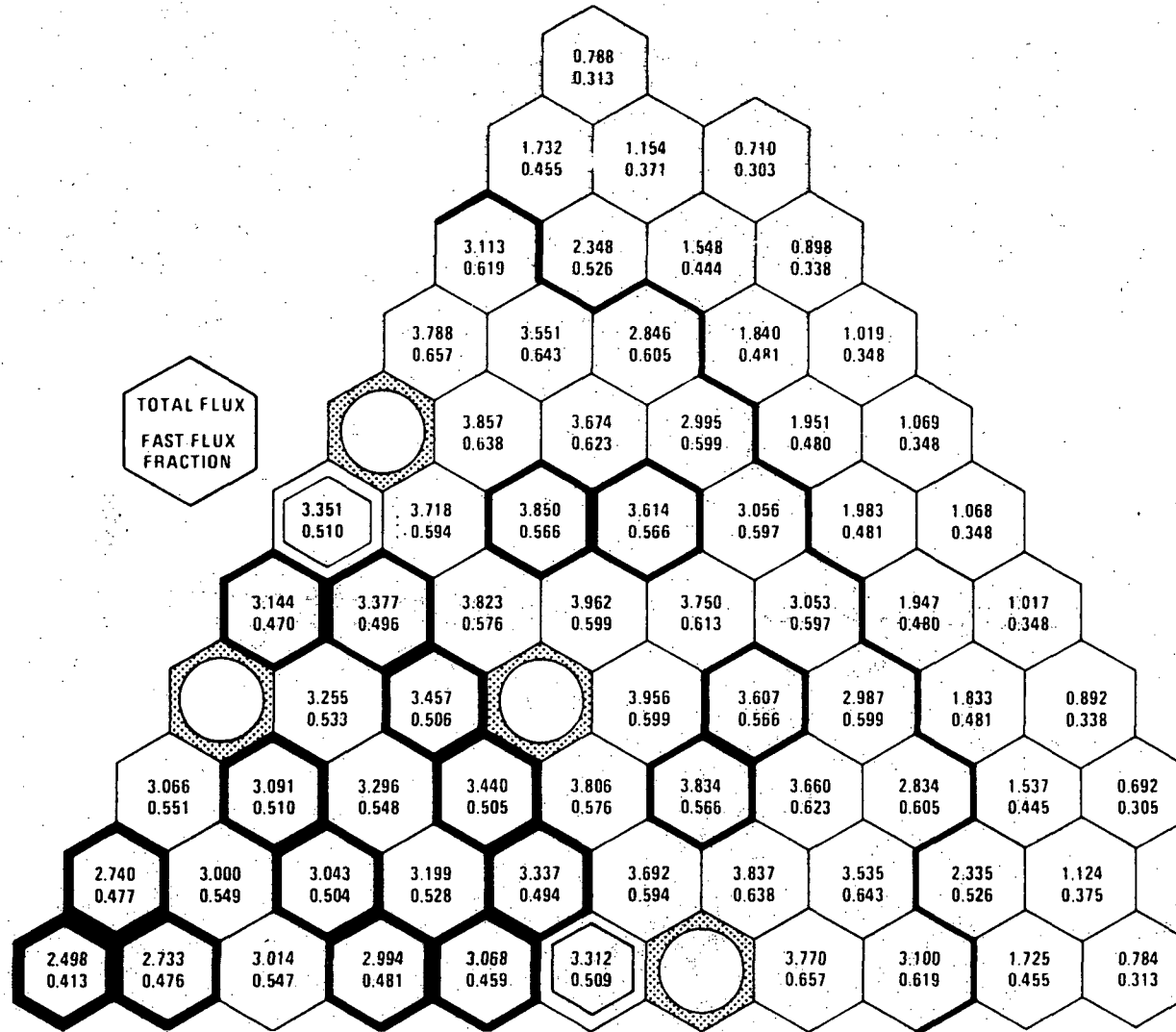


FIGURE 4.3-50. Assembly Average (36 inch) Total Flux ( $10^{15}n/cm^2 \cdot sec$ ) and Fast Flux Fraction at the Beginning of Cycle One

Amend. 64  
Jan. 1982

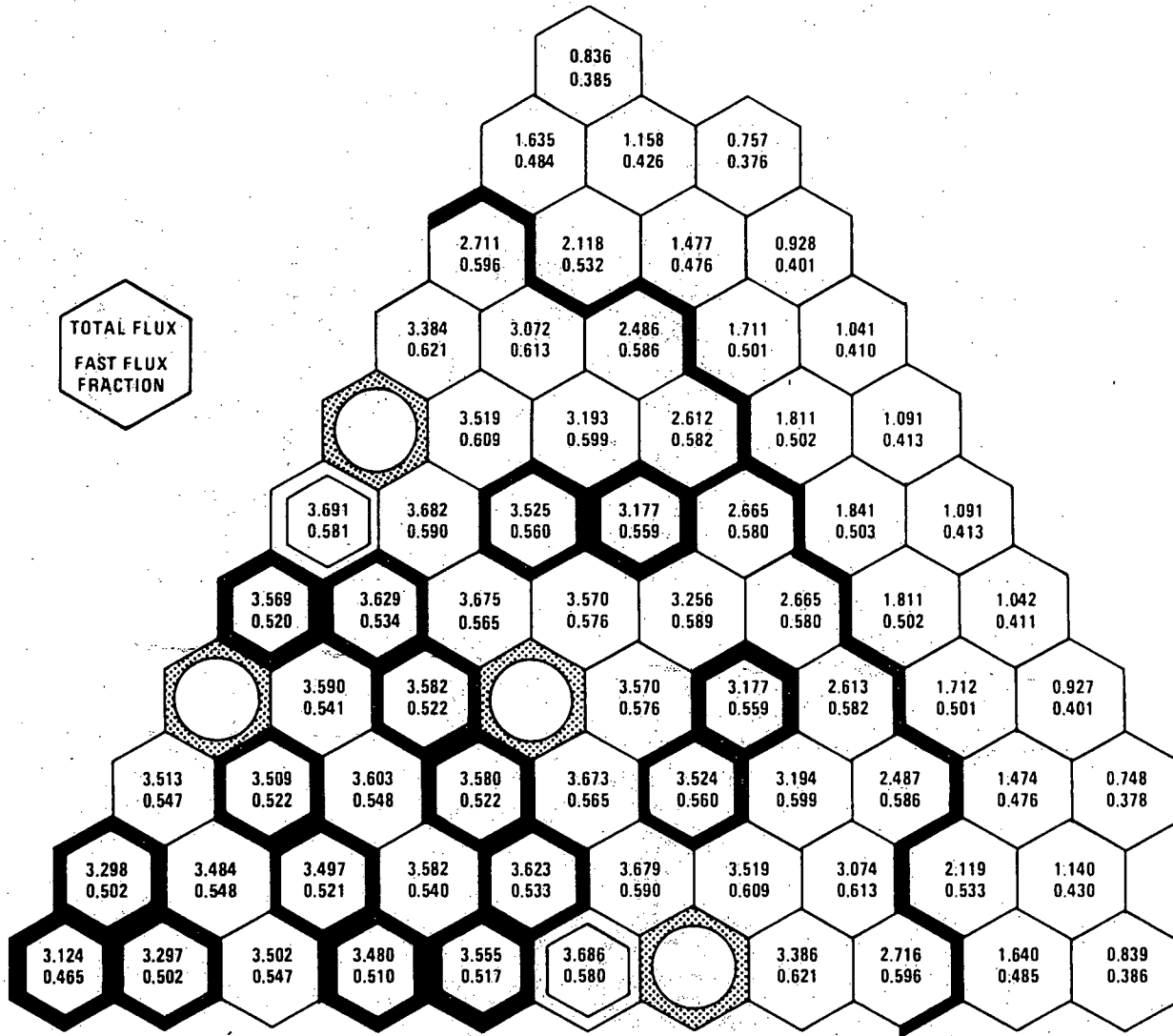


FIGURE 4.3-51. Assembly Average (36 inch) Total Flux ( $10^{15}n/cm^2sec$ ) and Fast Flux Fraction at the End of Cycle Four

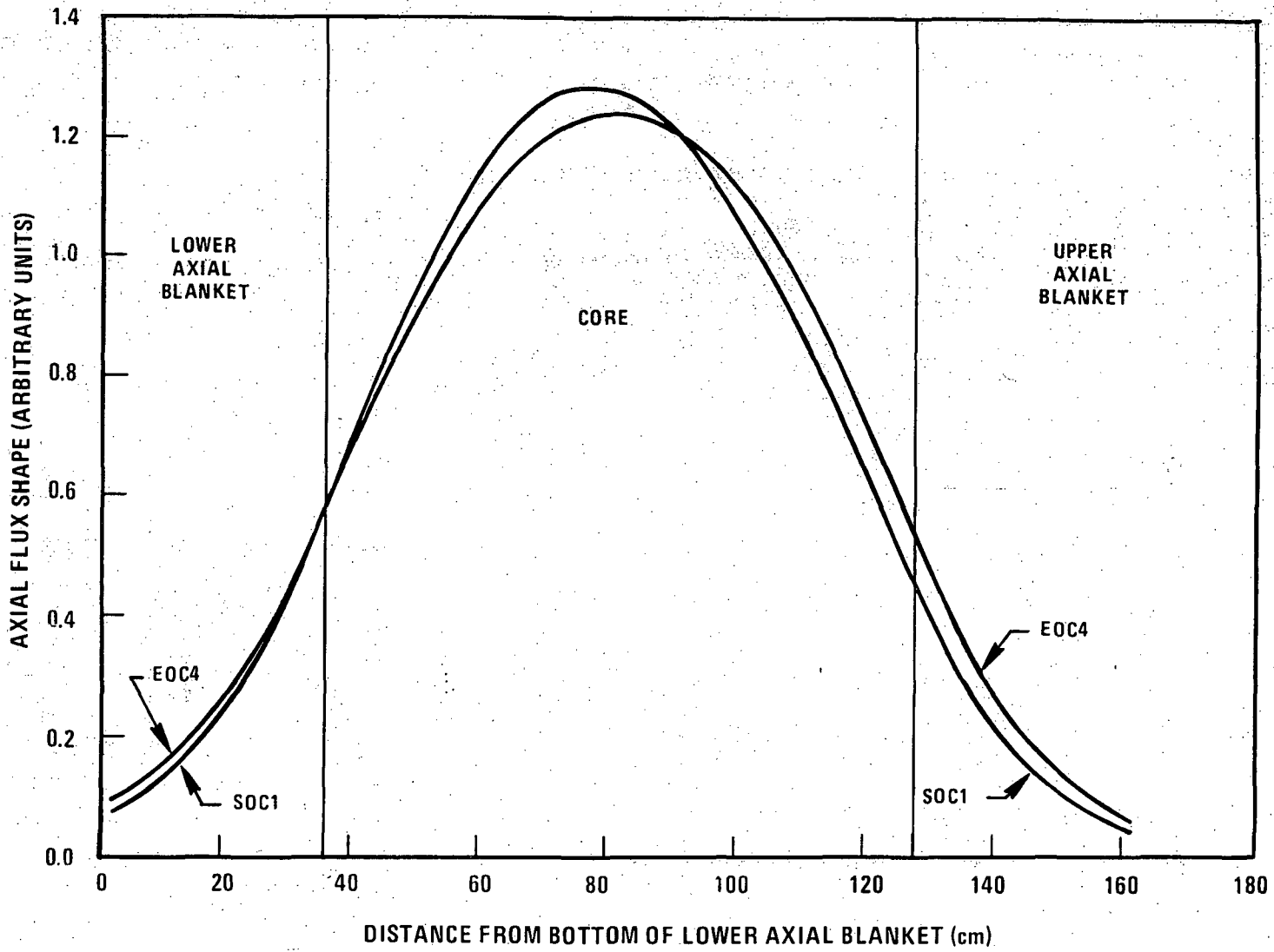


Figure 4.3-52. Axial Distribution of the Total Flux in Clean Fuel at the SOC1 and EOC4

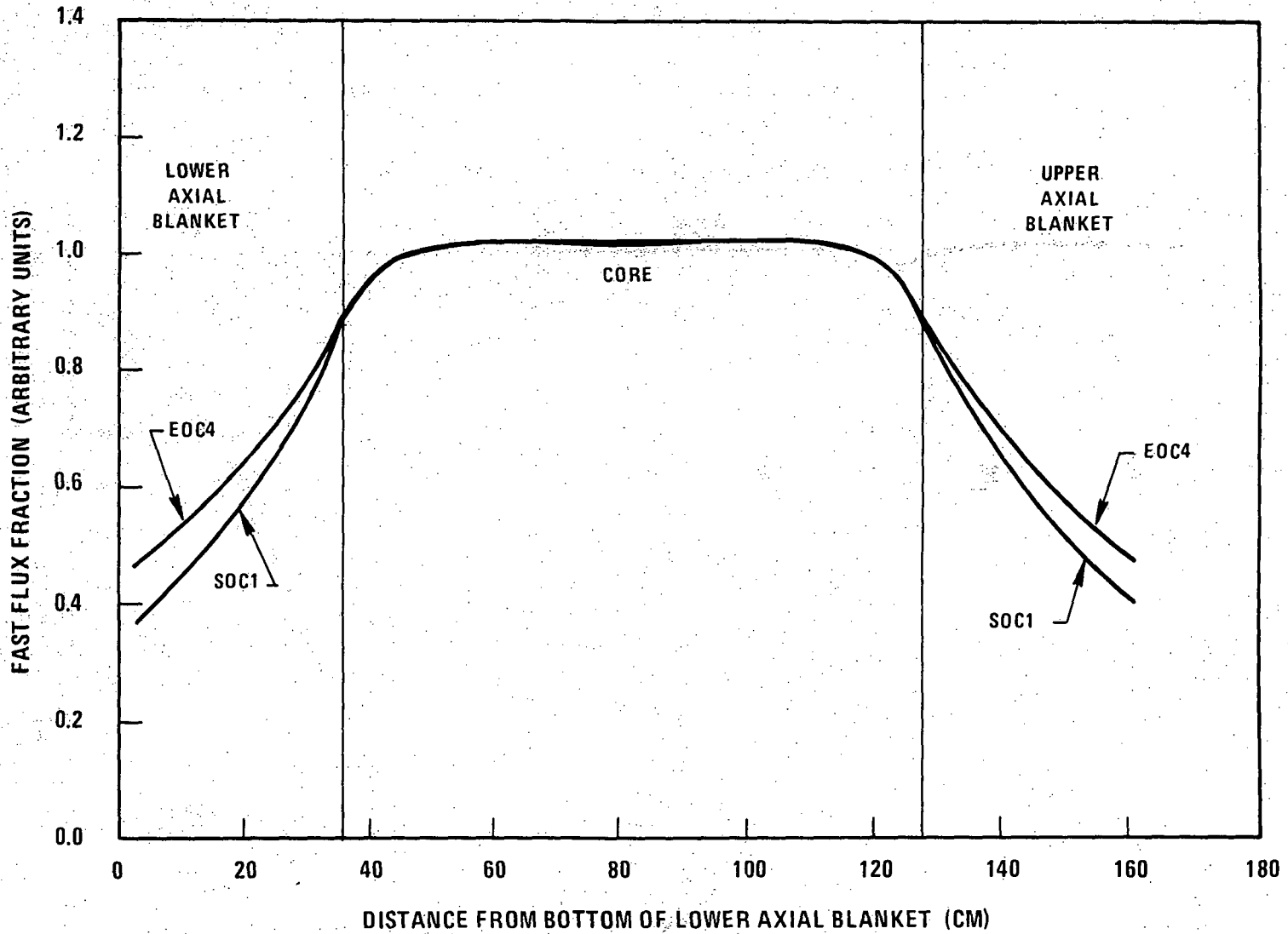


Figure 4.3-53. Axial Distribution of the Fast Flux Fraction in Clean Fuel at the SOC1 and EOC4

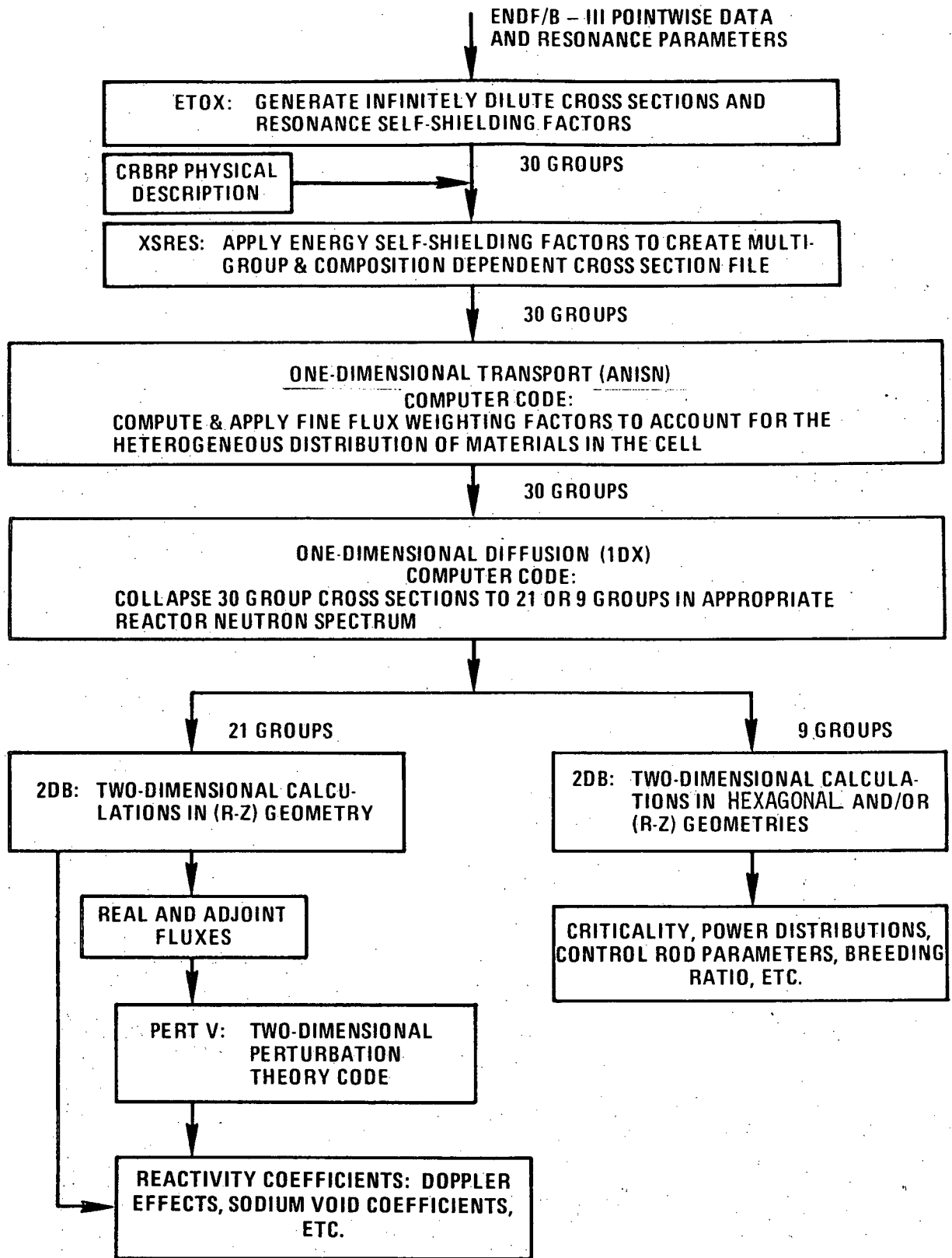


Figure 4.3-54. Calculational Scheme for Analysis of CRBRP

1544-53

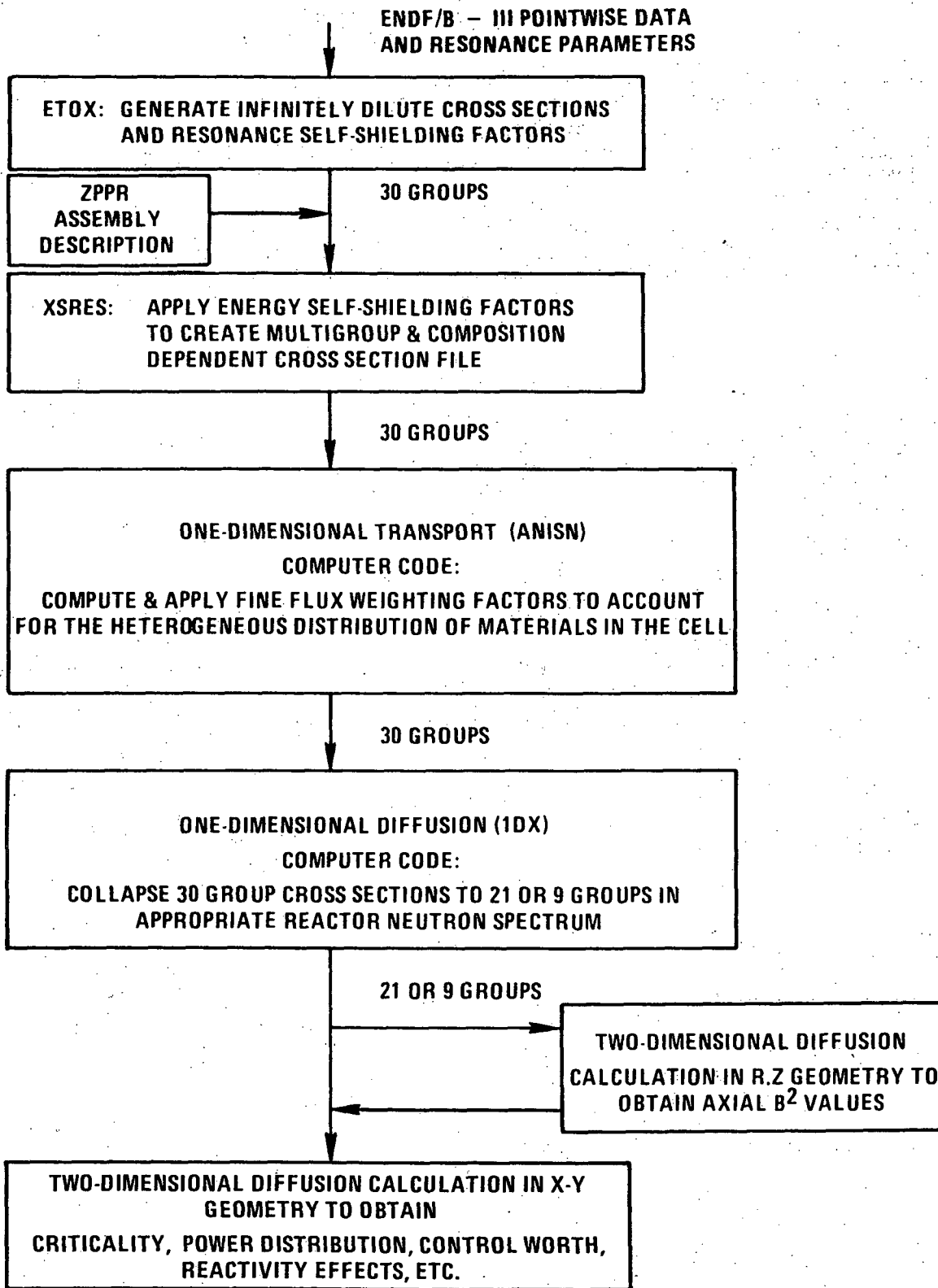


Figure 4.3-55. Calculational Scheme for Evaluation of ZPPR Critical Experiments

1544-54

Amend. 51  
Sept. 1979



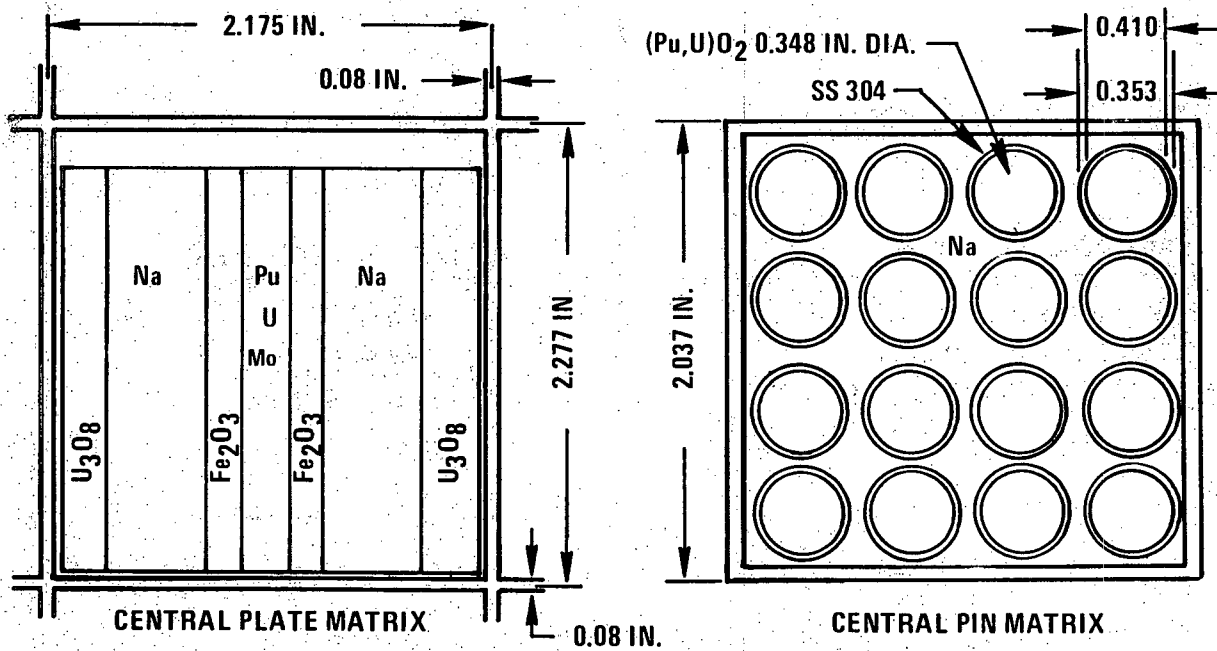
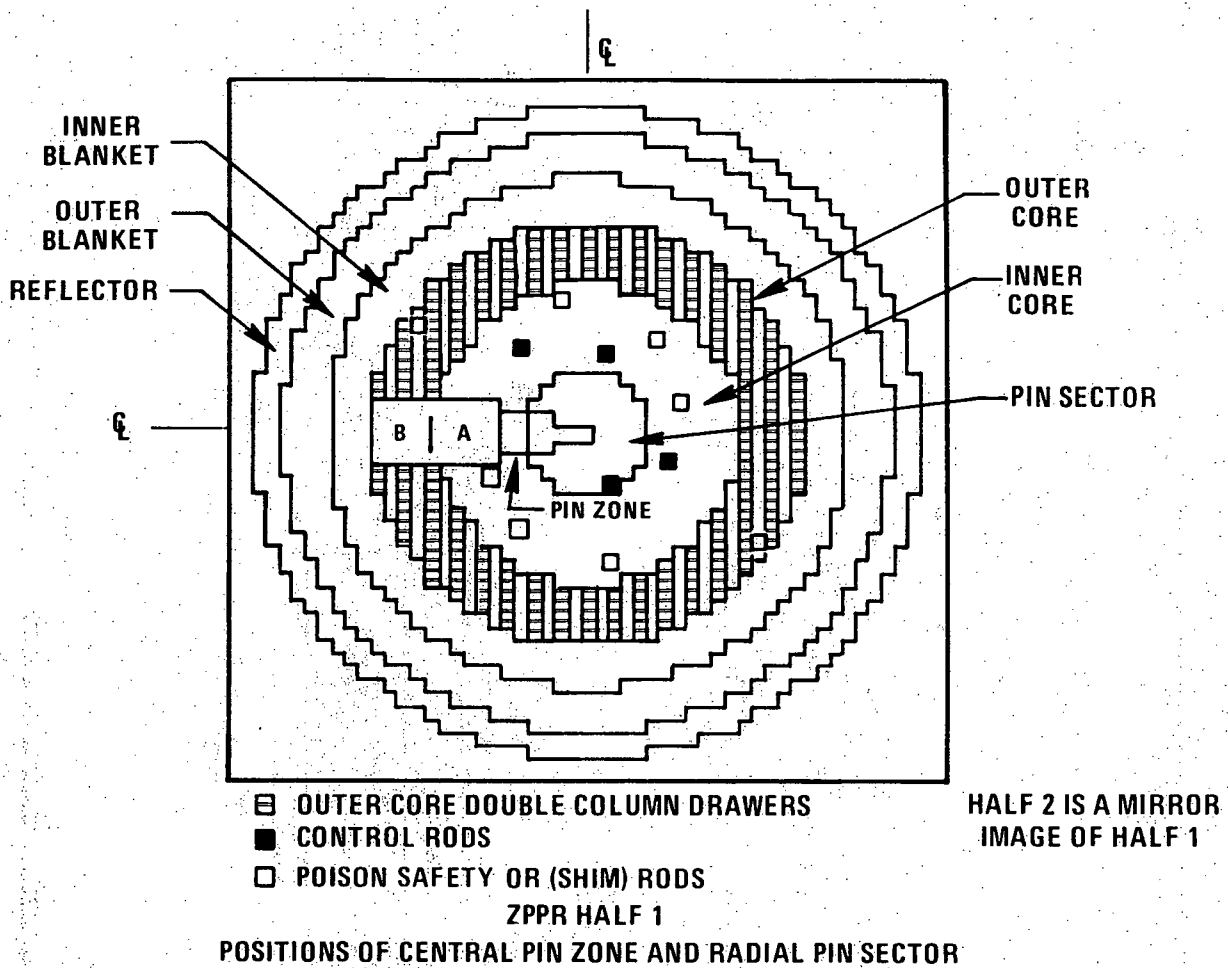
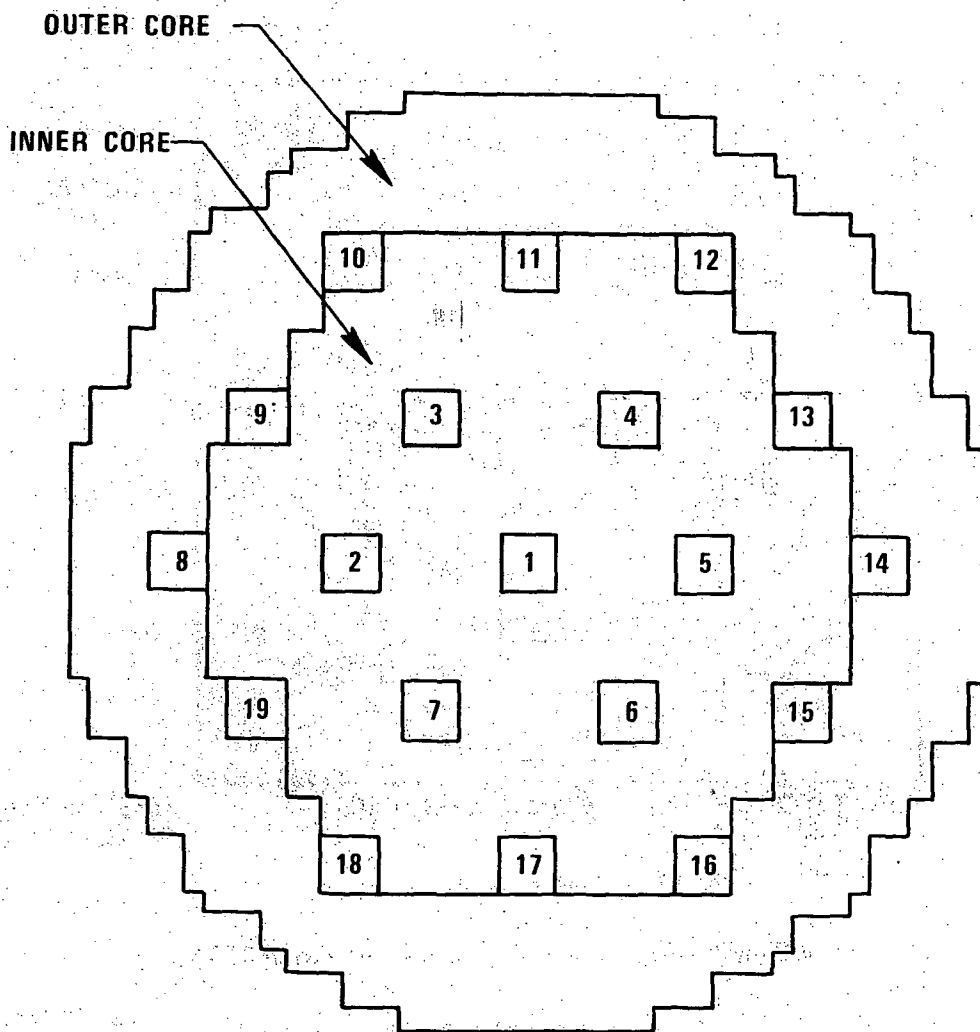


Figure 4.3-56. Pin Zones and Central Plate and Pin Cells for ZPPR-2



CONTROL ROD CHANNEL

CORE CONFIGURATION	CONTROL RODS INSERTED
PHASE 1B (END-OF-CYCLE)	NONE
PHASE 2 (MIDDLE-OF-CYCLE)	2,4,6,10,14,18
PHASE 3 (BEGINNING-OF-CYCLE)	2,4,6,8,10,12,14,16,18

Figure 4.3-57 Core Layout for ZPPR-3, Phases 1B, 2, and 3

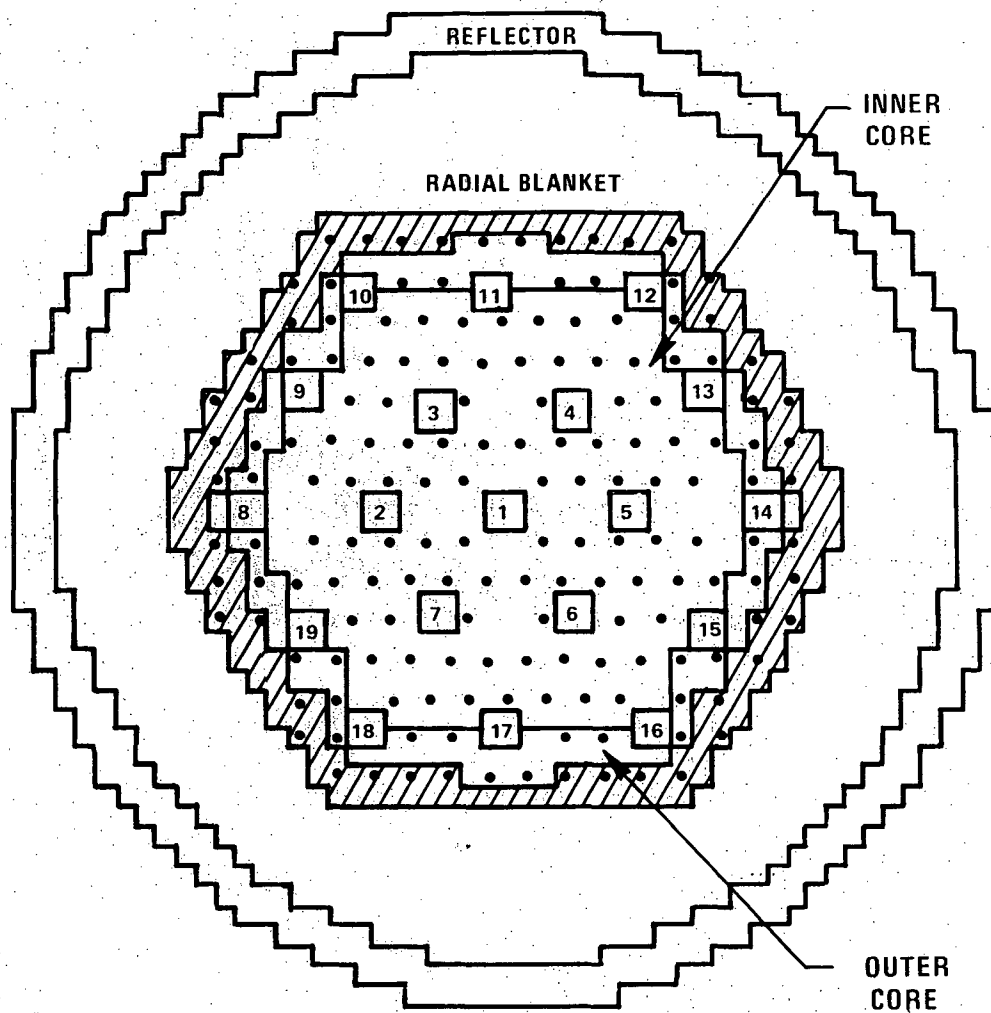


Figure 4.3-58. Reference 632 Drawer Sodium Void Configuration for the Modified Phase 3 Core of ZPPR Assembly 3

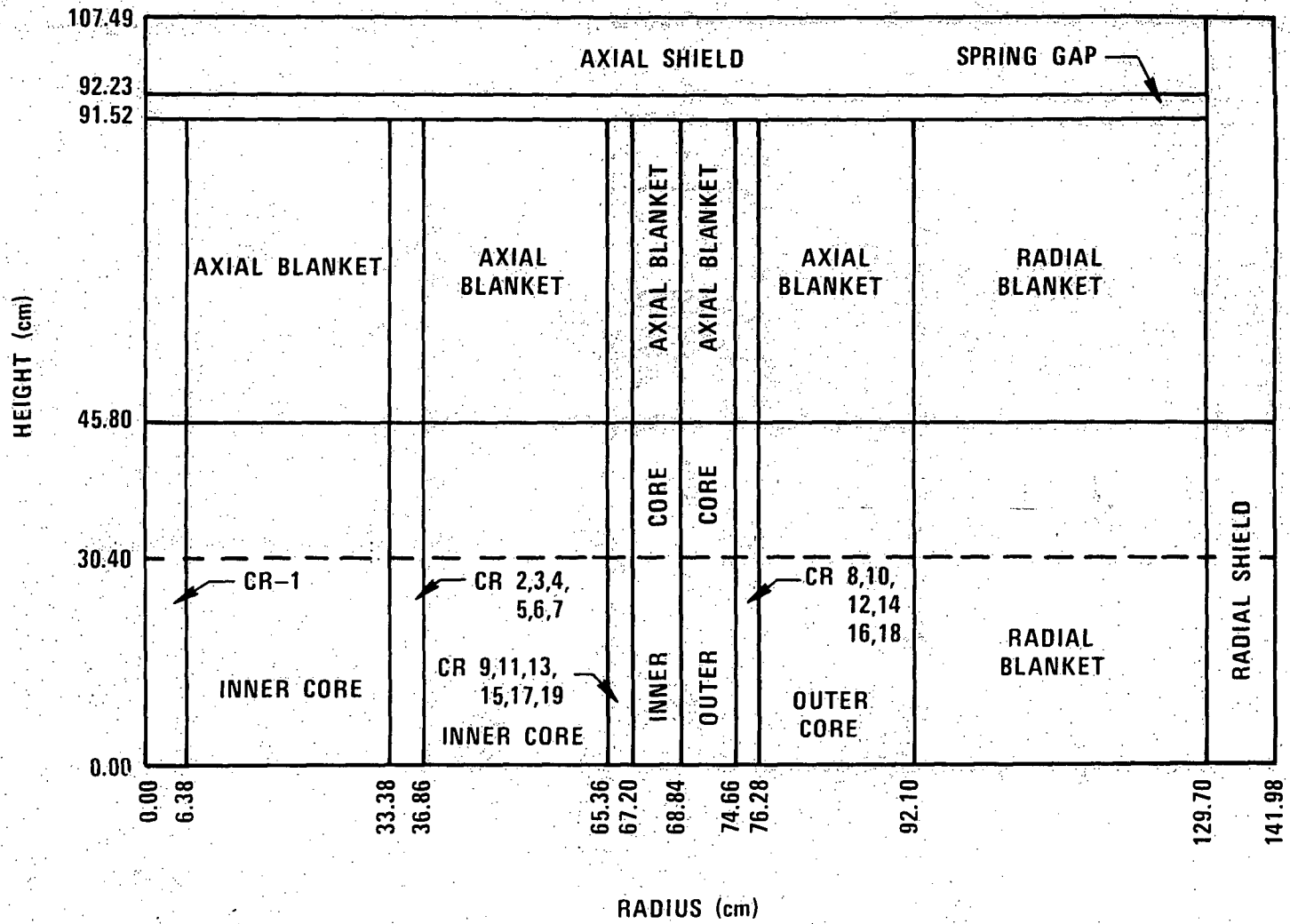


Figure 4.3-59 ZPPR-3, Modified Core, Two-Dimensional (R, Z) Calculation Model

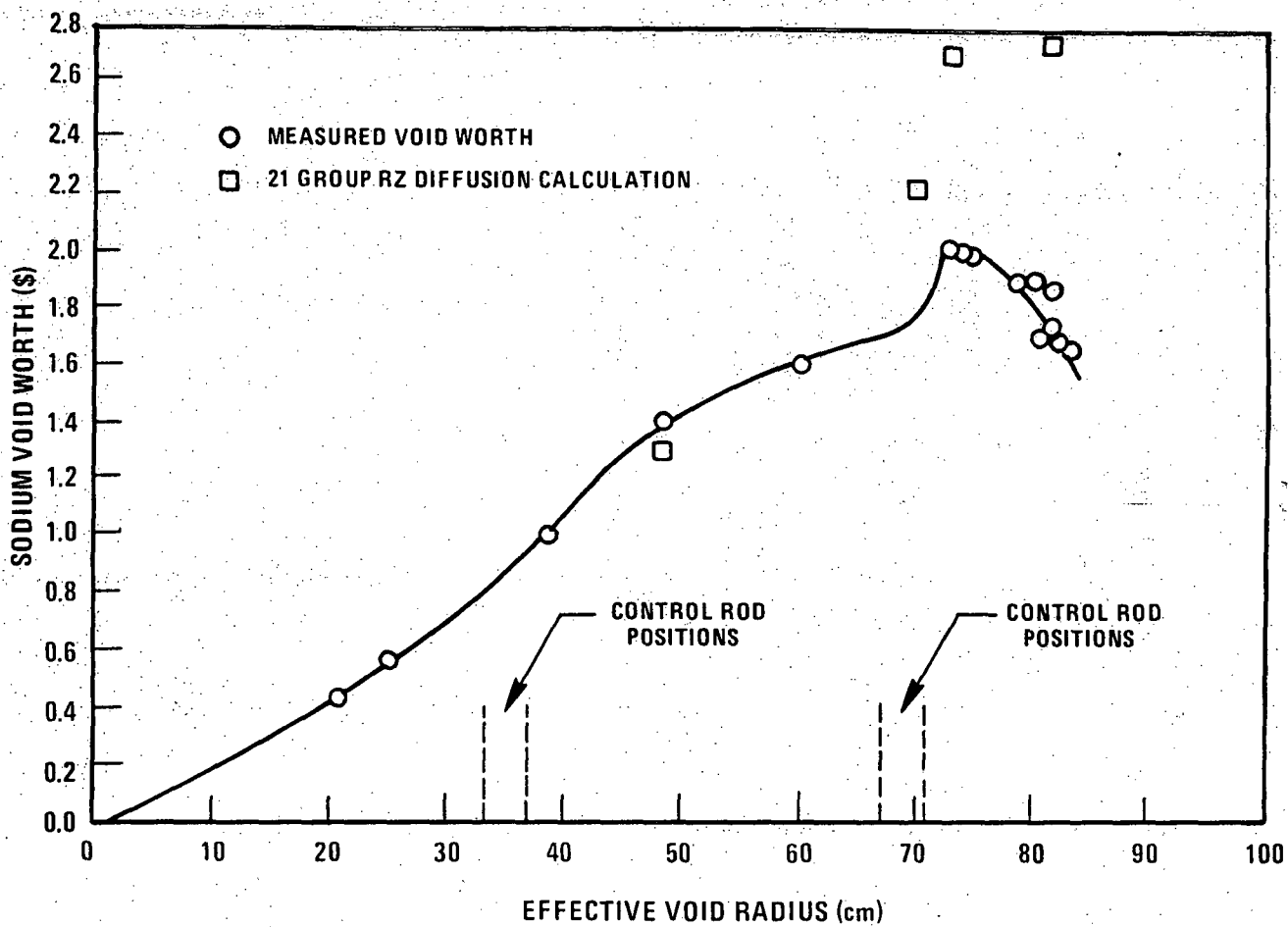


Figure 4.3-60. Measured Sodium Void Reactivity Effect in ZPPR-3 Modified Phase 3 as a Function of the Void Radius

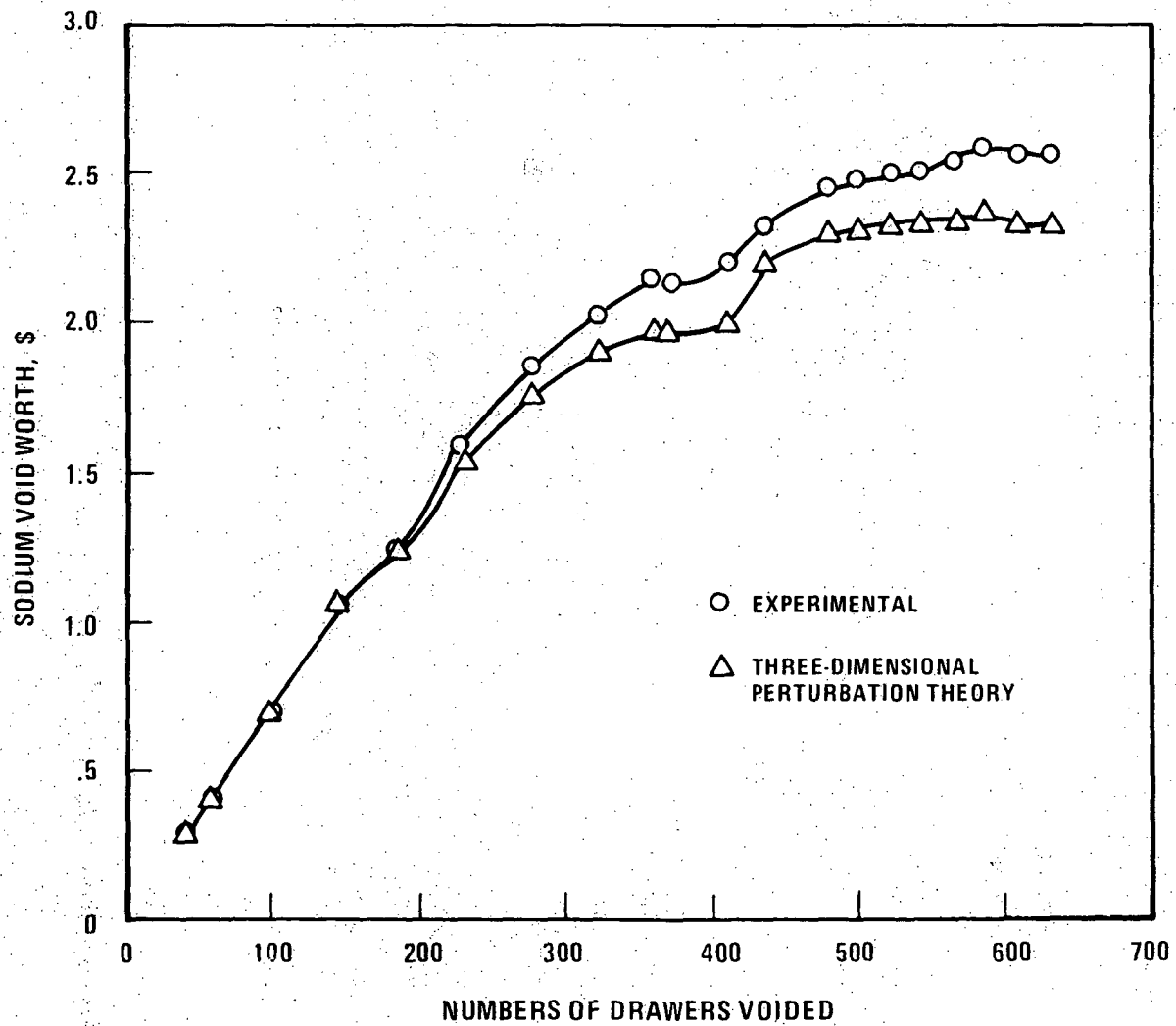


Figure 4.3-61. Sodium Void Worths in ZPPR-3, Phase 3

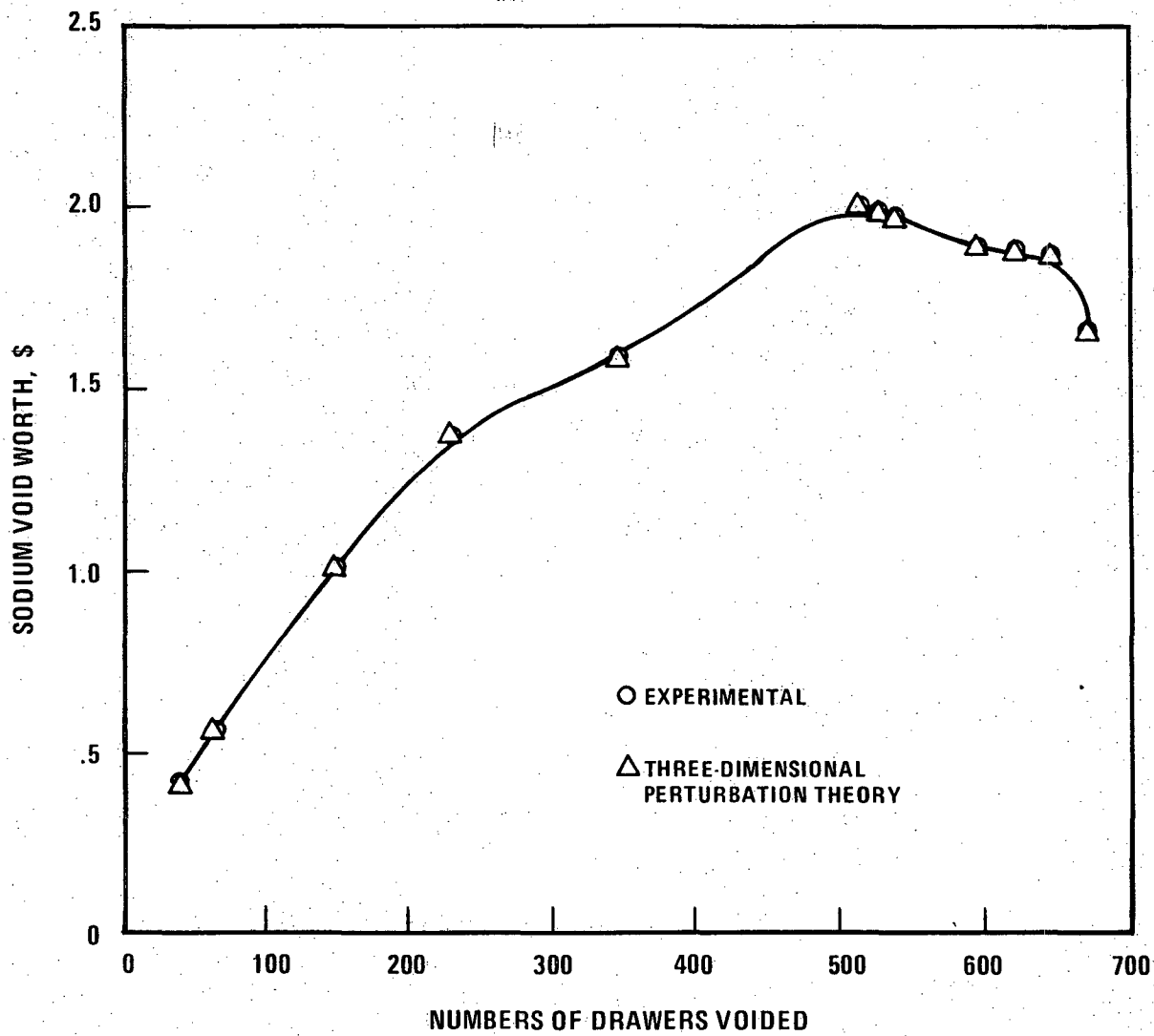


Figure 4.3-62. Sodium Void Worths in ZPPR-3, Phase 3 Modified Core

1544-61

Amend. 51  
Sept. 1979

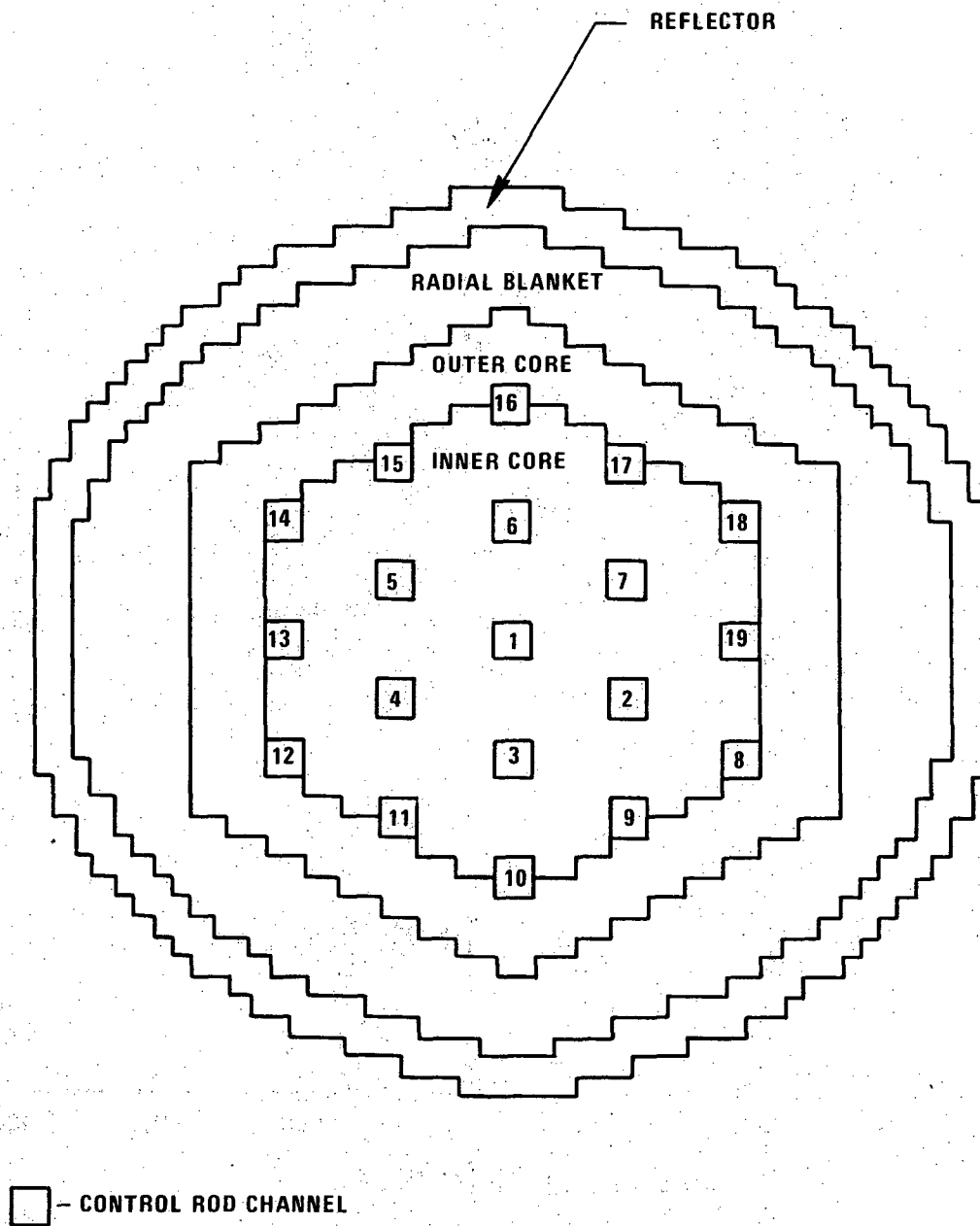


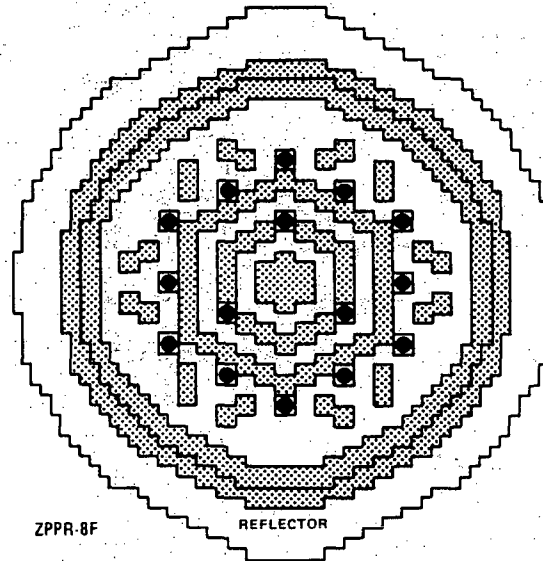
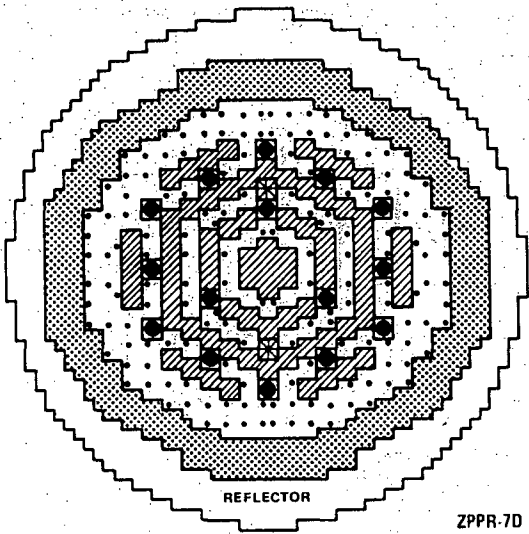
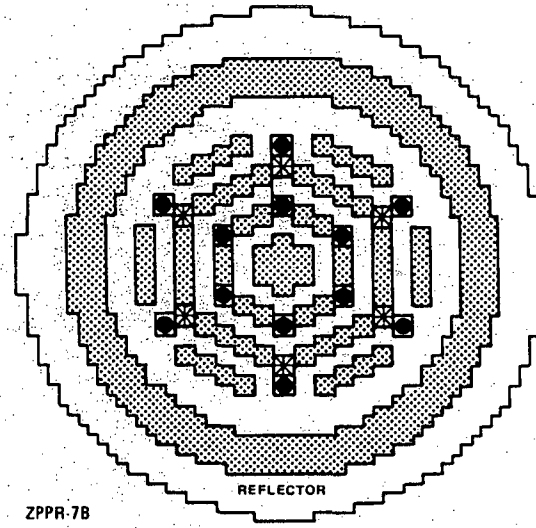
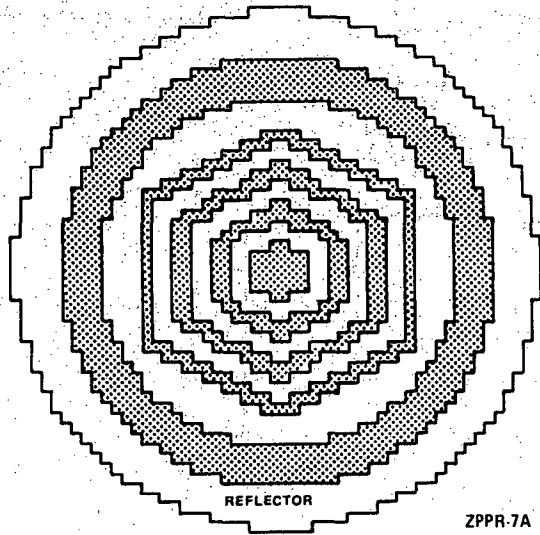
Figure 4.3-63 ZPPR Assembly 4 Phase 1 Reference Configuration



1544-63

4.3-212

Amend. 51  
Sept. 1979









-  CLEAN BLANKET
-  CONTROL ROD POSITION
-  DEPLETED CORE FUEL
-  SPIKED BLANKET DRAWER
-  NORMAL CORE FUEL
-  FUEL/BLANKET INTERCHANGE

Figure 4.3-64. ZPPR-7,8 Heterogeneous Core Layout

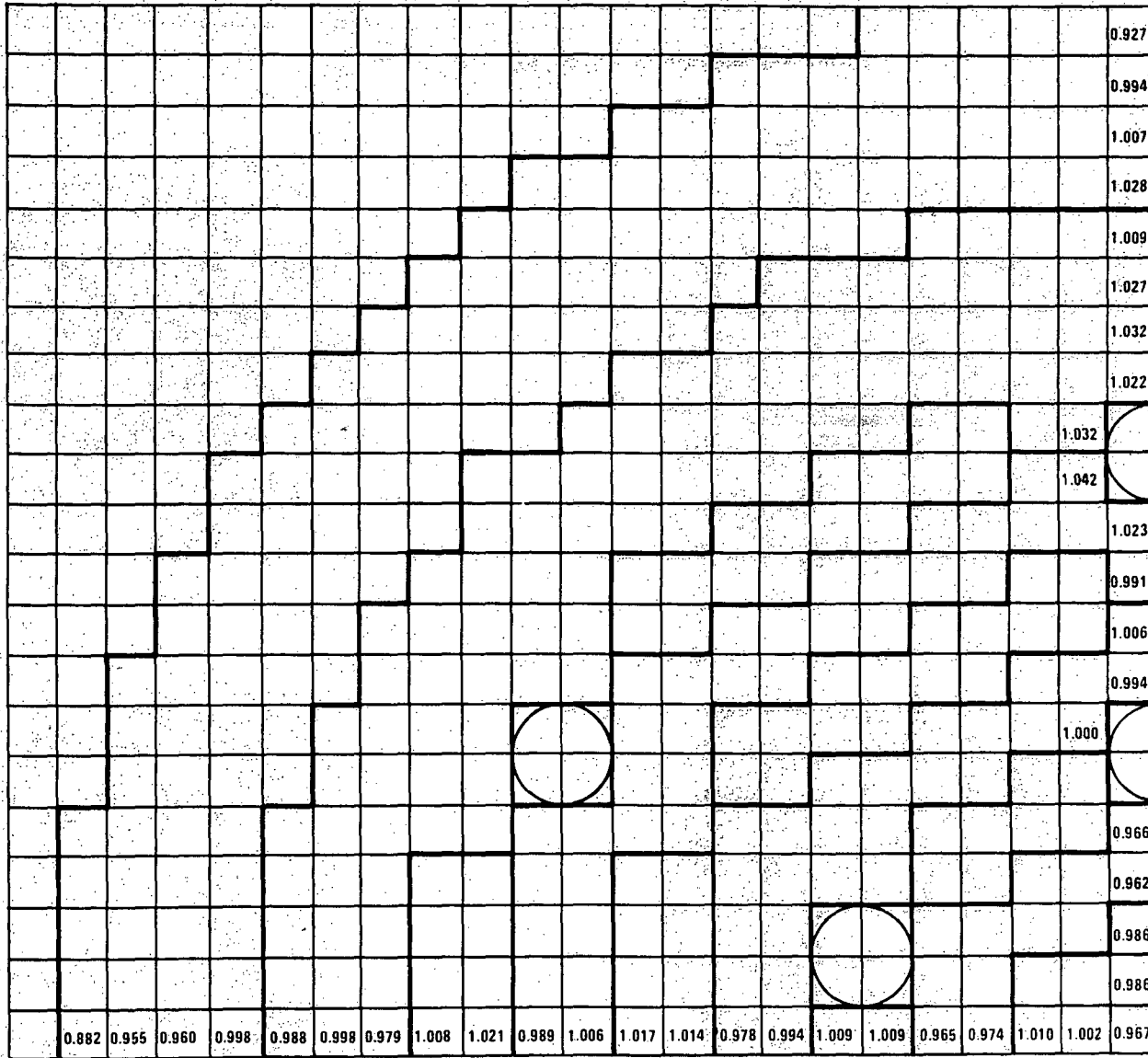


Figure 4.3-65. ZPPR-7 Phase B Midplane Calculated-to-Experimental Ratios for 239 PU (n,f)

1544-65

4.3-214

Amend. 51  
Sept. 1979

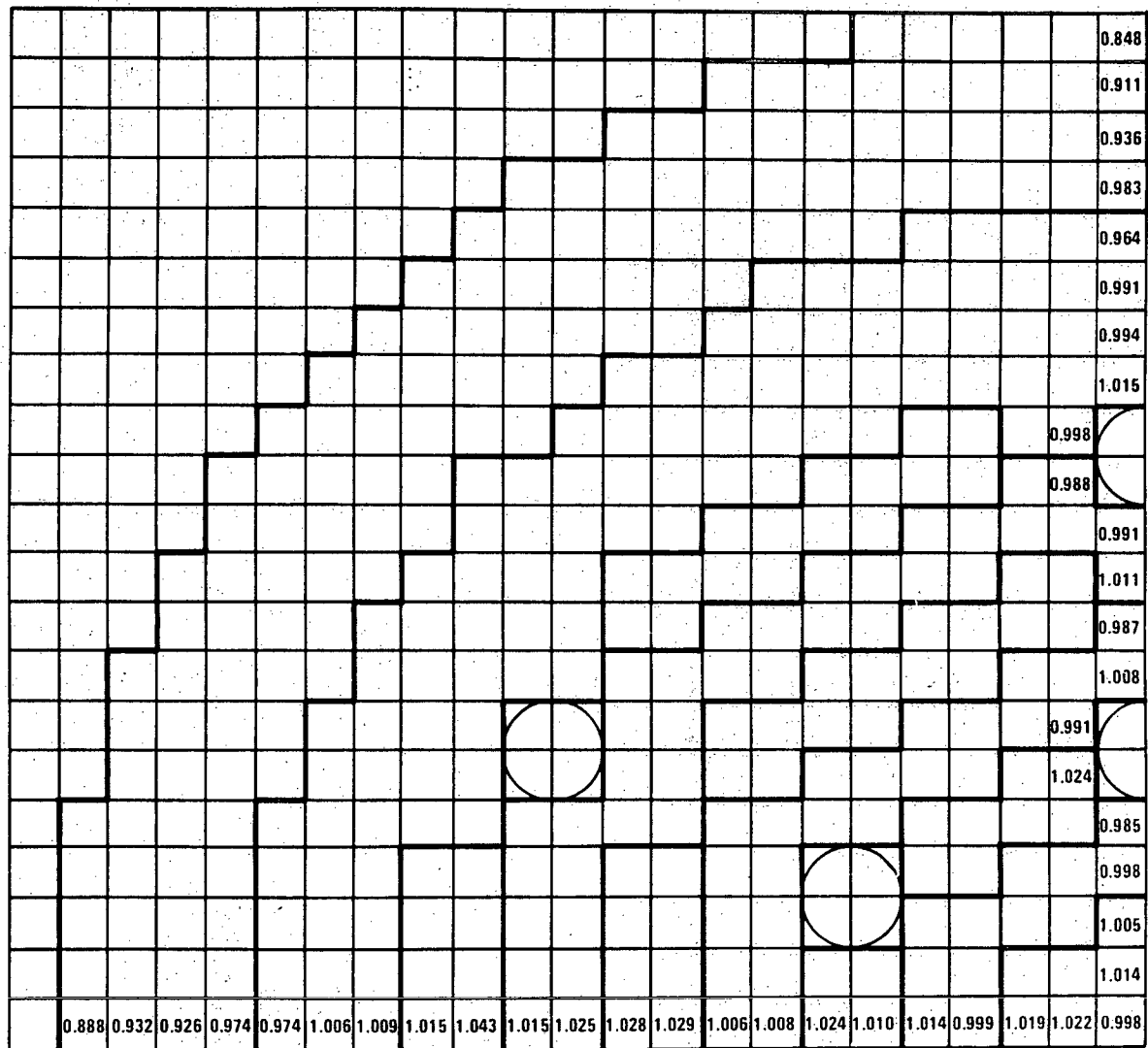


Figure 4.3-66. ZPPR-7 Phase C Midplane Calculated-to-Experimental Ratios for 239-PU (n,f)

## 4.4 THERMAL AND HYDRAULIC DESIGN

### 4.4.1 Design Bases

54

The thermal-hydraulic steady state design of the reactor is consistent with and limited by the following design bases. The design bases and limits for plant transient conditions (e.g., prevention of sodium boiling and cladding melting, and cumulative cladding damage within the permissible limits corresponding to the transient class considered) are discussed in Section 15.1.2.

1. The maximum fuel assembly hot spot cladding temperature for steady long term power conditions will be consistent with burnup objectives and the fuel integrity limits (Sections 4.2.1 and 4.4.2.5.1). The hot spot long-term power cladding temperature is calculated for plant expected operating conditions (see Section 4.4.3.3.1) applying design uncertainties (see Section 4.4.3.2) at the 2 $\sigma$  confidence level. The cladding temperature/pressure history during the entire assembly lifetime (see Section 4.4.3.3.4) is factored into the structural analysis to determine the cumulative cladding damage, hence, the maximum burnup attainable in the assembly.
2. The maximum hot spot cladding temperature in the blanket(\*) for steady state long term power conditions will be consistent with lifetime objectives. The hot spot long-term power cladding temperature is calculated as described above for the fuel assembly. The cladding temperature/pressure history during the entire assembly lifetime is factored into the structural analysis to determine the cumulative cladding damage, hence the maximum assembly lifetime.
3. The maximum hot spot cladding temperature in the control assemblies for steady state long term power conditions will be consistent with lifetime objectives. The cladding temperature is also calculated as described for the fuel assemblies.

(\*)

In Chapter 4.4, "blanket" refers to both inner and outer (or radial) blanket assemblies; if a statement explicitly applies to either inner or outer blanket, it will be specified.

51

4. No fuel melting is allowed in the fuel assemblies at 115% overpower conditions(\*), including design and experimental uncertainties at  $3\sigma$  confidence level. Consequently, the linear power rating will not exceed the limiting power-to-melt under the aforementioned conditions.
5. No fuel melting is allowed in the blanket assemblies at 115% overpower conditions(\*), including design and experimental uncertainties at  $3\sigma$  confidence level. The blanket management scheme will therefore be arranged not to exceed the limiting power-to-melt under the aforementioned conditions.
6. No absorber melting is allowed in the control assemblies at 115% overpower conditions(\*), including design and experimental uncertainties at  $3\sigma$  confidence level.
7. The sodium temperature exiting the core assemblies will be consistent with the limitations reported in Section 4.2.2.1.3.2 to assure the structural integrity of the upper internals structure during its prescribed lifetime.
8. Mixing in the inlet and outlet plena will mitigate the effects of thermal transients on the internal structures, such that the components structural requirements are met.
9. Adequate cooling shall be provided to the shielding, core barrel and core former components to yield a thermal environment capable of assuring their structural integrity as specified in Section 4.2.2.1.3. Sufficient flow shall be provided to the reactor vessel thermal liner to limit the vessel wall temperature below 900°F during normal operation. Adequate cooling shall be provided for the Fuel Transfer and Storage Assembly to preserve the structural integrity of stored fuel assemblies.
10. Adequate heat removal by forced and free convection from heat producing reactor components shall be assured for all operating conditions.
11. During operating conditions, fuel, blanket and control assemblies total pressure drop along with the rest of the primary system pressure drop will be within the primary pump head capability at the corresponding flow.
12. Coolant velocities shall be less (unless test data support higher acceptable velocities) than the following limits dictated by cavitation and/or corrosion/erosion considerations: 30 ft/sec for non-replaceable components; 40 ft/sec for replaceable components in the high coolant temperature region (exit); 50 ft/sec for replaceable components in the low coolant temperature region (inlet).

---

(\* ) This definition means a power equal to 115% of rated power conditions.

13. The control assemblies flow rate will be such as to assure adequate margin against flotation in case the driveline becomes accidentally disconnected (see Section 4.2.3.1.3).
14. Assemblies orificing will be designed to be consistent with the requirement that the lower shield in the fuel, blanket and control assemblies will have sufficient solid volume fraction to limit radiation damage to the core support structure and to assure its prescribed lifetime.
15. The thermal-hydraulic design of the control assemblies will be such as to satisfy the scram insertion requirements during the reactor lifetime (see Section 4.2.3.1.3).
16. The sodium temperature shall be less than its boiling point during normal operation and anticipated and unlikely transient conditions.
17. The reactor will meet the aforementioned design bases operating over a range of power and flow rates, including power ranges and flow variations, from 0 to 100% of nominal conditions.
18. Adequate design margins (see Section 4.4.3.2) will be provided to account for design, fabrication, operational uncertainties and tolerances to ensure meeting the aforementioned limitations. The semi-statistical hot channel factors approach will be adopted in combining individual fuel, blanket and control assembly uncertainties.
19. As explained in Section 4.4.3.3.1, plant T&H design conditions are considered in performance evaluations of permanent plant components ( ), e.g., vessel, internals, heat exchangers. Therefore, these conditions shall be considered in evaluation of Items 7 through 10, 16 through 18. On the other hand, plant expected operating conditions are adopted in steady state performance and design evaluations of replaceable components such as the reactor assemblies. Therefore, plant expected operating conditions shall be considered in evaluation of Items 1 through 6, 11 through 15, 17 and 18.
20. The design shall prevent gas entrainment sufficient to cause significant heat transfer or reactivity changes in the core.
21. The design shall provide features to minimize the potential for flow blockage of Incore assemblies.

#### 4.4.2 Description

##### 4.4.2.1 Summary Comparison

This section presents a comparison of general and core assemblies design parameters for the CRBRP and FFTF reactors.

#### 1. CRBRP AND FFTF GENERAL PARAMETER COMPARISON

	<u>Units</u>	<u>CRBRP**</u>	<u>FFTF*</u>
Design Life	Yrs.	30	20
Reactor Power (Thermal)	MWt	975	400
Primary Coolant	-	Sodium	Sodium
Primary Coolant Design Flow Rate	10 <sup>6</sup> lbm/hr	41.45	17.28
Coolant Temperature:			
Reactor Vessel Inlet	OF	730	600
Reactor Vessel Outlet	OF	995	858
Reactor Vessel Temperature Rise	OF	265	258
Pressure Drop:			
Reactor Inlet Nozzle-to-Outlet Nozzle ( $\phi$ )	psi	123	110
Lower Inlet Module to Assembly Outlet Nozzle	psi	116	101
Primary Pump Design (static)	psi	160.3	182.5
Number of Primary Loops	-	3	3
Suppressor Plate	-	Yes	Yes
Cover Gas	-	Argon	Argon
Cover Gas Pressure (nominal)	psig	0.36	0.36
Allowable Overpower	percent	15	15

(+) Permanent plant components are those components which: 1) will be designed for 30-year life; and 2) cannot be easily replaced.

\*FFTF Initial Condition

\*\*CRBRP T&H Design Values

CRBRP value includes uncertainties; FFTF value is nominal.

	<u>Units</u>	<u>CRBRP</u>	<u>FFTF</u>
Maximum Allowable Coolant Velocity:			
Replaceable Component (exit/inlet)	ft/sec	40/50	***
Non-Replaceable Component	ft/sec	30	30
Heat Transfer Areas:			
Fuel region/assembly	ft <sup>2</sup>	39.2	39.2
Axial Blanket region/assembly	ft <sup>2</sup>	30.5	-
Blanket assembly	ft <sup>2</sup>	43.1	-
Control Assemblies	ft <sup>2</sup>	17.5	22.7
Flow Areas:			
Fuel assembly	in <sup>2</sup>	6.72	6.72
Blanket assembly	in <sup>2</sup>	3.96	-
Control Assembly Rod Bundle	in <sup>2</sup>	2.95	3.03
Control Assembly Bypass	in <sup>2</sup>	2.15	1.82

#### 4.4.2.2 Fuel Rod Temperature

Fuel (blanket or absorber) rod temperature distributions have been calculated for fuel, blanket and primary control assemblies.

Analytical methods and tools employed in the calculations are discussed in Section 4.4.3.4; uncertainty factors adopted in evaluation of "hot" rod temperatures are summarized in Section 4.4.3.2; physical properties, data and correlations used in the calculations are listed in Section 4.4.2.8. A complete core-wide mapping of fuel, inner and outer blanket relevant thermal-hydraulic parameters along with preliminary control assemblies performance predictions are reported in Sections 4.4.2.5 and 4.4.3.3.

Rod temperatures calculations in the fuel and blanket assemblies are performed employing the Westinghouse Proprietary code NICER (see Appendix A). The same procedure is basically followed in calculating absorber temperatures, the only differences being that the CRSSA instead of the NICER code is used and ad hoc gap conductance (Section 4.4.2.8.6) and absorber conductivity (Section 4.4.2.8.8) correlations are employed.

The coolant temperature distribution across the assembly is calculated through subchannel analysis codes utilizing a detailed pin-by-pin power distribution. The coolant channel under consideration is identified (this may be the one with the highest temperature, or the one next to the rod with highest power or any other specified) and the axial temper-

\*\*\*No requirement.



ature profile is used as the coolant temperature boundary condition for all subsequent calculations. Rod temperatures are then calculated(\*) through one-dimensional Fourier equations, progressively moving across the coolant film, cladding, fuel/cladding gap and fuel pellet to the fuel centerline. Uncertainties associated with each temperature drop are properly accounted for as discussed in Section 4.4.3.2.

Fuel temperatures can be calculated in NICER utilizing empirical models of the complex fuel/gap behavior. Whenever these models have been calibrated against experimental data, as is the case for beginning-of-life behavior calibrated against the P-19 data (Ref. 37), NICER calculated pellet temperatures are quite accurate. However, in actual design calculations, especially in power-to-melt analyses (see Section 4.4.3.3.6) integral calculations performed with the LIFE-III code are adopted, using the cladding ID temperature calculated by NICER as boundary conditions, along with the detailed NICER rod power profile.

In fact, the fuel/gap behavior is a function of the type of rod (fuel or blanket) and of the time in life; therefore, to accurately calculate fuel temperatures by NICER for the entire CRBRP core throughout life would require calibration of a large number of empirical fuel/gap models. Since detailed phenomenological models are already available in LIFE, and since fuel temperature calculations are actually needed in core design only for a few critical conditions when the probability of incipient melting is greatest, it was decided that direct LIFE calculations were the appropriate technical choice, as the one providing the most accurate evaluation with the minimum design effort. In fact, the LIFE code is continuously updated and calibrated against experimental data as they become available, under an ongoing national effort.

Figure 4.4-1 shows an example of the axial temperature profile in a fuel rod calculated by NICER. Specifically, it refers to the hot rod (i.e., the rod having the maximum cladding temperature) in fuel assembly #101 at beginning of the third cycle. Plant expected operating conditions and hot channel factors at the 2 $\sigma$  level of confidence were utilized. The midwall cladding temperature shown in Figure 4.4-1 is a circumferentially averaged value and is not the local (maximum) value located under the wire wrap which is generally reported in Section 4.4.3.3.

#### 4.4.2.3 Flux Tilt Considerations

Flux tilt due to burnup effects is taken into consideration in the design, as discussed in Sections 4.4.3.2 and 4.4.3.3. Effect of control rod position is discussed in Section 4.3.2.5 and is directly accounted for in the detailed spatial heating rates utilized. The uncertainties are accounted for through appropriate hot channel factors, as outlined in Section 4.4.3.2.

(\*)NOTE: Calculations are performed at each axial level (30 positions over the fuel and axial blanket sections are evaluated) using the proper coolant boundary condition.

51

55

Amend. 55

June 1980

#### 4.4.2.4 Reactor Coolant Flow Distributions

The core fuel management requires that, at six locations within the reactor core, blanket and fuel assemblies be interchanged from fuel cycle-to-cycle (see Table 4.4-1). The interchanging of blanket and fuel assemblies results in a cycle-to-cycle change in the flow splits through the core assemblies. Flow splits associated with components other than core assemblies are not significantly affected by the blanket-fuel interchanging.

For illustrative purposes, the flow distribution throughout the reactor at cycle 4 is presented in Figure 4.4-2. A detailed discussion of the coolant flow through the reactor components follows.

##### 4.4.2.4.1 Reactor Component Flow Path Description

###### Inlet Plenum

Coolant enters the reactor vessel inlet plenum through three 24-inch inlet nozzles spaced  $120^\circ$  apart. The inlet nozzle outlets are directed approximately  $60^\circ$  towards the bottom of the vessel to enhance mixing of flow from the three loops. Experimental data, obtained at HEDL, in the Inlet Plenum Feature Model (Section 4.4.4.1), demonstrated the degree of mixing in the inlet plenum: i.e., the maximum  $2\sigma$  core inlet temperature uncertainty to any fuel, blanket or control assembly is  $4.6^\circ\text{F}$  based on a long-term steady state primary loop temperature imbalance of  $+17^\circ\text{F}$ . The core inlet temperature uncertainty was based on a Monte Carlo analysis which made use of the HEDL experimental data and the loop temperature imbalance analysis. This steady state temperature variation has no significant effect on the structural adequacy of inlet plenum components. It has a minor effect on fuel assembly lifetime (see Sections 4.4.3.2 and 4.4.3.3).

The mixing during a transient in the inlet plenum affects the thermal stresses of structures located in this region. Mixing during transients is sufficient to ensure that the thermal stresses in the core support structure, lower inlet modules and reactor vessel, when combined with the other pressure and mechanical load stresses, satisfies the primary, secondary and peak stress criteria of Section III and applicable code cases of the ASME Code.

## Core Support Structure

From the inlet plenum, the flow enters the 61 lower inlet modules located in the core support structure. The flow maldistribution to the modules will not exceed 2 percent of the specified flow rate, based on inlet plenum flow testing. As shown in Figure 4.4-3, a module may contain all blanket assemblies, fuel and blanket assemblies, fuel assemblies and a control assembly, fuel and blanket assemblies and a control assembly, or blanket and removable radial shield assemblies. There are 306 removable radial shield assemblies located outside the outer blanket assemblies. Forty-two of the removable radial shield assemblies are located in the peripheral modules containing blanket assemblies. As shown in Figures 4.4-4 and 4.4-5, flow passes through holes and slots in the module liners and enters the module through 1/4-inch diameter strainer holes. Inside the module (see Figure 4.4-5) the coolant flows vertically upward into the module receptacle region. From the receptacle region the flow passes through slots or holes in the fuel, blanket, control and those radial shield assemblies located in the modules. The core support structure contains a low pressure manifold to distribute both the LIM leakage and orificed bypass flow to the reactor vessel/core barrel annulus (see Figure 4.4-6). In addition, there are six separate low pressure flow passages in the CSS which direct flow to six bypass flow modules from six peripheral LIM modules.

## Fuel, Blanket and Control Assemblies

Figure 4.4-5 shows the layout of a module with blanket orificing. The distribution of fuel and blanket assemblies results in a variety of different types of modules as shown in Figure 4.4-3. The flow through each type is different and orificing is required to provide the correct flow to all core assemblies. For the fuel, control, inner blanket and radial blanket zone 9 assemblies, the orifices are located within the assembly. Because of the requirement that radial blanket assemblies be capable of being shuffled between zones, the radial blanket assemblies must be hydraulically identical which precludes locating the differential orifices in the assembly. For this reason, the orifices for the radial blanket assembly flow zones 10 through 12 are located in the inlet modules. Orificing for those radial shield assemblies that are located in the peripheral modules are similar to the radial blanket assembly orificing. The control system consists of the primary and secondary assemblies with flows controlled to assure that the maximum cladding temperature is compatible with the prescribed assembly lifetime.

51

### Bypass Flow

Figure 4.4-7 shows the bypass orificing which regulates the bypass flow that is used for radial shield and vessel thermal liner cooling. This bypass orificing is located in the 24 peripheral inlet modules. In 18 of the modules, the bypass orificing feeds a controlled portion of the flow downward into the low pressure plenum below the module where it reverses direction and flows upward and is then directed radially outward through the core support structure low pressure manifold to the reactor vessel/core barrel annulus. In the other 6 modules, the flow is directed upward to the bypass flow module where it is distributed to those radial shield assemblies (264) outside the inlet module region of the core.

### Radial Shielding

The radial shielding is made up of fixed shielding attached to the core barrel and removable shielding supported by the core support structure as described in Section 4.2. The removable shielding is cooled by external flow through the inter-assembly gaps as well as internal flow through the assemblies. The orifices in the assembly are sized to provide adequate cooling to meet assembly lifetime requirements. External cooling alone was found to be adequate for the fixed shielding.

### Vessel Cooling Flow

The flow from the annulus between the reactor vessel and the core barrel passes upward into an annulus formed by the reactor vessel and the vessel thermal liner. A horizontal baffle is installed between the liner and the core barrel; it minimizes leakage from the liner-barrel annulus into the outlet plenum. From the vessel-liner annulus the coolant discharges into the outlet plenum region above the suppressor plate. Two percent of total flow enters the vessel-liner annulus; a fraction of this flow appears as leakage at the outlet nozzle and the makeup nozzle penetrations in the thermal liner.

57

### Leakage

Seals between the core support structure and core inlet module liner, and other mechanical interfacing locations are sources of leakage. This leakage is estimated to be 1.05% of total flow and is assumed to pass upward through the core interstitial and peripheral region without contributing to the cooling of any reactor component.

51

## Outlet Plenum

All fuel, blanket, control, and a portion of the radial shield assembly flow discharges into the upper internals structure. The coolant first enters a mixing chamber before entering the chimneys (Figure 4.4-8). The chimneys duct the flow vertically upward and discharge the flow into the upper region of the vessel outlet plenum. The flow is directed into the upper region of the plenum to minimize flow stratification in this region during a reactor trip transient.

The flow from some of the removable radial shields which are located outside of the peripheral skirt of the upper internal structure discharge directly into the outlet plenum. Also, 14% of total reactor flow from the fuel, blanket, control and radial shield assemblies bypasses the chimneys through the gap between the top of the core assemblies and the skirt of the upper internals structure and discharges directly into the outlet plenum.

The coolant leaves the reactor vessel outlet plenum through three 36-inch diameter outlet nozzles.

### 4.4.2.5 Fuel and Blanket Assemblies Orificing

#### 4.4.2.5.1 Orificing Philosophy, Approach and Constraints

Core orificing, i.e., flow allocation to the various fuel and blanket assemblies is an important step in the core thermal-hydraulic design. Since the assembly temperatures are directly dependent on the amount of flow and since the flow allocation is the only thermal-hydraulic design parameter which can be varied, within certain limits, by the designer, it logically follows that the core T&H design and performance is only as "good" as the core orificing. Therefore, much attention in the CRBRP core T&H design has been placed on core orificing.

Orificing analyses do not provide the final design results. Following the orificing, T&H performance parameters of the core assemblies are predicted. Using these predicted performance parameters, actual design calculations are conducted to assess the adequacy of the design. If all the design constraints were already factored in the orificing, no further iteration would be necessary. Although exact prognostication and correct representation of all the constraints is not always possible, a priori consideration of the design constraints as orificing guidelines nevertheless serves as a useful means in enhancing the efficiency of the analysis process. This was the approach adopted in CRBRP core T&H analyses where a systematic orificing analysis was developed, which accounted for lifetime/burnup, transient, upper internals temperature constraints. This new approach represented a change in philosophy and a significant improvement over the previous maximum temperature equalization method. Characteristic features of this approach are determination of the limiting temperatures (see Section 4.4.2.5.2) for all types of assemblies and simultaneous orificing of the fuel and blanket assemblies. Finally, both first and second core conditions were investigated in determining the orificing constraints and the most restrictive in either core was used in deriving the orificing configuration. This guaranteed, a priori, that the thermal-hydraulic performance would satisfy the constraints considered in both cores.

The following orificing constraints (Reference 1) are satisfied in selecting the flow orificing for the CRBRP fuel, inner blanket and radial blanket assemblies:

- o Maximum cladding temperature must be compatible with lifetime and burnup objectives, which can be expressed in terms of maximum allowable inelastic cladding strain and cladding cumulative damage function (CDF);
- o Maximum coolant temperature conditions must be such as to assure, with adequate margin, that no boiling occurs during the worst emergency transient (e.g., the three-loop natural circulation event), accounting for uncertainties at the 3 level confidence;
- o Maximum assemblies mixed mean outlet temperature and radial temperature gradient at the assemblies exit must be compatible with upper internals structure (UIS) limitations;
- o Maximum of eight discrimination zones (fuel plus inner blanket) are allowed;
- o Flow allocation to fuel, inner blanket and radial blanket assemblies must not exceed 94.0% of the total reactor flow to account for cooling requirements of other reactor components.

Since the heterogeneous core contains a single fuel enrichment zone and because the number of required discriminators depends on the unique combinations of flow orificing and fuel enrichment zones, the maximum number of fuel plus inner blanket assembly orificing zones is equal to the total allowable number of discriminators (i.e., 8). Inner blanket and fuel assemblies employ identical inlet nozzles. Therefore, both must be considered in determining the total number of discriminator zones. The outer blanket assemblies employ a unique inlet nozzle and, therefore, are not considered in determining the total number of discriminators. The two 6 corner positions(\*) which alternate between inner blanket and fuel assemblies during successive cycles, form a separate discriminator zone which is included among the eight.

To put the lifetime/burnup and transient temperature constraints on the same basis and to provide quantitative, comparable orificing guidelines, the concept of equivalent limiting temperature is employed. The equivalent limiting temperature is defined as that cladding temperature at a specified radial position (cladding ID in these analyses) and time in life (end-of-life) which must not be exceeded in order to satisfy the considered constraint.

---

(\*) A map of the 60° core symmetry sector analyzed in the thermal-hydraulic studies and assemblies numbering scheme are shown in Figure 4.4-9.

Three equivalent limiting temperatures were defined to represent the lifetime/burnup and transient constraints, i.e., SELT, DELT and TELT. They are defined as the end-of-life maximum cladding ID temperatures for Plant Expected Operating conditions (see Section 4.4.3.3.1), considering uncertainty factors at the 2 level of confidence, such that accounting for the assembly temperature/pressure lifetime history, the limiting value of the inelastic cladding strain (SELT), or cumulative damage function (DELTA), or worst time-in-life transient coolant temperature (TELT) is not exceeded. As it appears from the above definition, the equivalent limiting temperatures are calculated for each assembly. In fact, all the various assemblies have individually different lifetime histories of cladding temperature and fission gas pressure, and therefore, the limiting equivalent temperatures are necessarily different from assembly to assembly to stay within a constraint common to all assemblies. Calculations are performed for plant expected operating conditions, which are the conditions where the CRBRP is expected to operate on a probabilistic basis and the conditions used in the design of replaceable components such as the core assemblies (see Section 4.4.3.3.1).

As previously mentioned, both first and second core conditions have been considered in defining the core orificing, therefore, the SELT, DELT and TELT have been calculated for both cores. In the case of the radial blanket assemblies, where the lifetime spans both cores, obviously only one set of limiting temperatures was calculated. Using the OCTOPUS code, the assemblies minimum flow in the first and second core necessary to satisfy the most restrictive of the limiting conditions was calculated for each assembly. Subsequently, the various assemblies were grouped in zones and the orificing arrangement was selected such that the flow allocated to each assembly was at least equal to the larger of the flow requirements in first and second core. This assured meeting all constraints for both cores. Finally, the excess flow, if any, is allocated among the fuel assemblies to minimize and equalize the assemblies exit temperature and temperature gradients.

#### 4.4.2.5.2 Calculation of Equivalent Limiting Temperatures

Assemblies lifetime/burnup goals are achieved when both the cladding inelastic strain and cladding CDF are within the established limits during steady-state operation. The ductility strain guideline was set at 0.2% and the CDF guideline for orificing analyses was set at 0.7 in the fuel assemblies and 0.5 in the blanket assemblies. Since the CDF limit for steady-state plus transient operation is by definition 1.0, the margin for CDF transient accumulation was 0.3 in the fuel assemblies and 0.5 in the blanket. Both cumulative cladding strain and CDF depend on the rod cladding temperature/pressure history. Thus, using a preliminary estimate of the assembly flow (but using the proper physics data), the hot rod (\*) in each assembly at end-of-life was identified

using the subchannel analysis code CØTEC. Subsequently, the hot rod was followed throughout lifetime and the lifetime temperature/pressure history was calculated with the NICER code. Uncertainty factors (see Section 4.4.3.2) at the 2 $\sigma$  level of confidence were used in the cladding temperature/pressure calculations. Based on the above lifetime histories, a strain equivalent limiting temperature (SELT) was calculated for each assembly. The SELT serves as an analytical expression of an orificing guideline. It represents the end-of-life temperature which, if maintained constant throughout lifetime, would cause an end-of-life cumulative strain of 0.2% for the particular assembly relative behavior of cladding temperature and pressure through lifetime. Accordingly, the SELT does not depend on any guessed value of assembly flow, but rather on the relative behavior through lifetime, which is only a function of the power generation changes during life.

Since the DELT is the equivalent end-of-life temperature corresponding to a CDF of 0.7 or 0.5, the method employed in its determination was to extract it from a curve correlating the cladding ID temperature at EOL with the corresponding CDF. Thus, at least three (in some instances more were necessary) lifetime temperature/pressure histories were generated for each assembly by varying the flow and the corresponding CDF was calculated. Typical curves are reported in Figures 4.4-10 through 4.4-14 for the fuel and inner blanket assemblies (first and second cores) and radial blanket assemblies. By interpolation, the DELT corresponding to the CDF constraint was then determined.

Regarding the transient constraint, the design guideline is to provide adequate margin-to-sodium boiling throughout the assembly lifetime during the worst transient. This was quantitatively translated into an orificing guideline of 1550°F which was conservatively defined as the maximum coolant temperature allowable during a natural circulation transient in any assembly at any time in life accounting for uncertainty factors at the 3 level of confidence. This guideline also assumes plant THDV conditions and a 750°F reactor inlet temperature.

---

(\*) Each assembly is characterized by its hot rod at end-of-life, which is obviously the one with the highest strain and CDF.



From previous transient calculations performed for the heterogeneous core using the FØRE-2M code, the maximum coolant transient temperature at the worst time in life and the corresponding steady state coolant temperature were obtained for the worst fuel, inner blanket and radial blanket assembly. As previously mentioned, the transient considered was the natural circulation event which had proved to be the most severe. Then the temperature  $T_M$  was calculated, which is defined as the maximum steady state coolant temperature at plant expected operating conditions and  $2\sigma$  hot channel factors corresponding to a  $1550^\circ\text{F}$  transient maximum coolant temperature at plant THDV conditions,  $3\sigma$  hot channel factors and  $750^\circ\text{F}$  inlet. Calculation of  $T_M$  was quite straightforward from ratioing the transient temperature rise calculated by FØRE-2M, fixing the maximum transient temperature at  $1550^\circ\text{F}$  for all three types of assemblies and accounting for the differences in plant conditions and hot channel factors. Table 4.4-3 summarizes the FØRE-2M and  $T_M$  temperatures.

Rigorously speaking, the  $T_M$ s thus calculated are only valid for the three assemblies whose transient behavior was actually investigated; it was conservatively assumed that they apply to all other assemblies of the same type. Since: a) the value of  $T_M$  essentially depends on the magnitude of the temperature swing from steady state to transient; b) higher swing implies higher  $T_M$ ; and c) other assemblies will have lower steady state transient swings than the worst representatives investigated through FØRE-2M; it follows that adoption of the values of  $T_M$  from Table 4.4-3 in calculation of the TELT's for assemblies of the same type is conservative.

Finally, using the lifetime temperature profile for each individual assembly, the TELT in each core assembly is calculated by the equation:

$$\text{TELT} = T_{in} + \frac{(T_M - T_{in})}{(T_{cool} - T_{in})} t', x' + \frac{(T_{cool} - T_{in})}{(T_{ID} - T_{cool})} t'', x'' \quad (4.4.2.5-1)$$

where  $T_{in}$  = reactor inlet temperature in first or second core;

$T_{cool}$  = hot subchannel coolant temperature;

51

$T_{ID}$  = hot spot cladding ID temperature;

$t'$  = time in life when maximum transient temperature occurs;

$t''$  = EOL (i.e., EOC2, EOC4 or EOC5);

$x'$  = axial position where maximum transient coolant temperature occurs;

$x''$  = axial position where maximum  $T_{ID}$  occurs at EOL.

Again, it should be noted that since the TELT's depend on temperature differences rather than absolute values, lifetime temperature profiles corresponding to first estimates of assembly flows are perfectly adequate for an accurate evaluation of the TELT's.

The SELT, DELT and TELT thus calculated for each assembly are reported in Figure 4.4-15 (first core) and Figure 4.4-16 (second core). Since the radial blanket assemblies are refueled only once, their values are reported only in Figure 4.4-16. No SELT's are reported for the blanket assemblies; nor for the fuel assemblies in the first core since very little cladding strain occurs, and therefore, their SELT was very high, thus being not limiting at all. Actually, an inspection of Figure 4.4-16 shows that even in the second core, no fuel assembly is strain limited. The limiting constraint in each assembly is given by the ELT with the minimum value. Fuel assemblies are generally CDF limited with the exception of the ones farther from the core center which are transient limited; inner blanket assemblies are transient limited; radial blanket assemblies are CDF limited if flanked by at least two fuel assemblies, otherwise, they are transient limited.

#### 4.4.2.5.3 Results

The ØCTØPUS code was used to calculate the flow rate needed in each assembly to produce an end-of-life cladding ID temperature equal to the most limiting of the ELT's, as discussed in the previous section. Figure 4.4-17 reports such flow rates for the first and second cores (cycles 2 and 4, respectively). Obviously, the minimum flow in each assembly necessary to satisfy all considered constraints in both cores is equal to the most restrictive of the two flow requirements. The higher of the two values reported in Figure 4.4-17 is not necessarily the most restrictive. In fact, due to the alternating of fuel and inner blanket assemblies in the six row 6 positions, the total core flow varies slightly from cycle-to-cycle. The replacement of three inner blanket assemblies by fuel assemblies at the beginning-of-cycle 2 results in ~0.8% flow reduction in each of the remaining assemblies. At the beginning-of-cycle 4, six inner blanket assemblies are replaced by six fuel assemblies with an ~1.6% resultant flow reduction in the remaining assemblies. Thus, when comparing the flow requirements for

the first and second cores, minimum flows must be put on the same basis. Cycle 4 was chosen as the standard basis since it will require the higher core flow fraction (fuel assemblies are in alternating row 6 positions). When flow requirements for cycle 2 are translated to cycle 4 equivalent values, second core requirements are found to be slightly more restrictive in some outer fuel assemblies, as shown in Figure 4.4-17. Cycle 5 flows are reported for the transient limited second row radial blanket assemblies, since their TELT's are maximum at EOL.

Using the required minimum flows as guidelines, the OCTOPUS code selected, for a given number of orificing zones, that combination of assemblies grouping into orificing zones which among all the various possible combinations, yielded the minimum value of total core flow and was therefore the most effective. As mentioned in Section 4.4.2.5.1, a maximum number of eight discriminators (and orificing zones) is allowed for the fuel and inner blanket assemblies. Four orificing zones in the radial blanket assemblies were chosen, thus, the total number of core orificing zones resulted equal to 12. The selected arrangement is reported in Figure 4.4-18, where the starred assemblies are the ones which determine the amount of flow allocated to the orificing zones (they are called zone driver assemblies, or drivers). Also indicated are the limiting assemblies in each orifice zone for first and second core; obviously the driver is the one with the more restrictive flow requirement (compare with Figure 4.4-17).

As shown in Figure 4.4-18, the orificing arrangement does not have a 30° symmetry because the control rod location and insertion pattern, hence the power generation, does not have a 30° symmetry. For example, considering the assemblies around the row 7 corner control assemblies (see Figure 4.4-16), first core conditions are limiting for the fuel assemblies around the control assembly at the right of the figure, while second core conditions are prevalently limiting for the fuel assemblies surrounding the control assembly at the left.

The minimum amount of core flow necessary to satisfy the various constraints and the grouping of the core assemblies into 12 orificing zones was equal to 93.07% of the total reactor flow of cycle 4 conditions. Since 94% of the total reactor flow is allocated to the fuel and blanket assemblies and since 93.07% is the minimum required to meet the conservatively selected constraints, it follows that slightly less than 1% of the total reactor flow is available to be allocated as deemed desirable by the designer. Usually, if a significant amount of excess flow is available, this is distributed among the fuel assemblies to minimize/equalize the assemblies mixed mean temperature and temperature gradient. This was not, however, the procedure adopted in these studies since the amount of available excess flow is not enough to significantly influence the value of the outlet temperatures. Additionally, the relative assemblies power generation and the sophisticated orificing, which

are characteristics of this heterogeneous design, yielded maximum differences in exit temperature (see Sections 4.4.3.3.3 and 4.4.3.3.5) between two adjacent assemblies (which generally occur at the fuel/inner blanket interface in rows 6 through 8) within the UIS capability. Therefore, the excess flow was distributed roughly evenly among the various core orificing zones. The final core flow allocation is reported in Table 4.4-4, which shows the cycle-by-cycle variation of flow in the various orificing zones. Both thermal-hydraulic design value (THDV) and plant expected operating condition (PEOC) flows are reported in Table 4.4-4.

Subsequent performance predictions and design calculations reported in Sections 4.4.3.3 and 4.2.1 demonstrated that the core orificing so determined was adequate and that design constraints and objectives were met.

#### 4.4.2.6 Reactor Coolant Flow Distribution at Low Reactor Flows

The normal mode of CRBRP core heat removal upon reactor shutdown is by forced circulation from AC powered pony motors (which have emergency backup power from diesel generators) driving the primary pumps. However, the CRBRP has been designed to have the added capability of adequate cooling by means of natural circulation. This inherent emergency coolant flow is provided by the thermal driving head developed by the thermal center of the IHX being elevated above that of the core (plus the respective elevation differences in the intermediate loops and steam generator system).

At the ~10% pony motor flow level after shutdown, insignificant flow redistribution occurs between the parallel flow core assemblies. However, for the core natural convection cooling mode, the effect of dynamically approaching low flow with worst case decay heat loads results in a power-to-flow ratio greater than one. Consequently, core temperatures increase and natural convection phenomena such as inter- and intra-assembly flow redistribution due to different thermal heads and hydraulic characteristics of the core assemblies become important. In general, the core thermal head becomes significant relative to the form and friction loss across the core below 5% of full flow. Coupled with the flow redistribution, significant heat redistribution on an inter- and intra-assembly basis occurs throughout the core due to large temperature differentials and an increased heat transport time (low power assemblies can have a transport time of over 20 seconds). These effects (i.e., natural convection flow and heat redistribution) are found to significantly reduce maximum core temperatures. This has been demonstrated in the EBR-II and FFTF natural circulation experiments (Ref. 68 and 79).

In addition to the in-pile data, a large out-of-pile data base exists to characterize the flow behavior of the various components over a wide range of operation, including low flow conditions. A listing of the experimental data references for flow distribution calculations is provided in Table 4.4-36.

Independent studies outside the CRBRP Project have been published which show a significant decrease in predicted maximum core temperatures due to reactor flow redistribution during natural circulation conditions. For example, Brookhaven National Laboratory (Agrawal, et al., in Ref. 69), using the SSC-L code, predicted localized flow increases as large as 20% in the hot fuel assembly and 40% in hot blanket assembly for the CRBRP during natural convection cooling. Corresponding reductions in the predicted maximum

transient coolant temperature on the order of 16 and 22% (130°F and 210°F) were shown for the hot fuel and blanket assemblies, respectively, relative to the maximum temperatures predicted without flow redistribution. Similar results were found in Reference 70 using the CURL-L code. For these studies, inter-assembly heat transfer as well as intra-assembly flow redistribution and heat conduction effects were neglected. Inclusion of these effects would further reduce the maximum core temperatures.

Preliminary studies with CORINTH have been performed to demonstrate the effect of inter-assembly flow redistribution for the heterogeneous core design. The effects of inter-assembly heat transfer and intra-assembly flow and heat redistribution which were neglected are discussed later. Figure 4.4-66 shows the results of these analyses for the peak fuel, peak inner blanket and peak radial blanket assemblies. Figure 4.4-67 shows results for a typical orificing zone for the fuel, inner blanket and radial blanket assemblies. Consistent with other natural circulation studies, the flow increase to the hotter core regions is apparent. This effect, along with the other natural convection phenomena, will significantly decrease the maximum hot rod temperatures in the core.

To assess the effect of all natural convective cooling phenomena (i.e., inter- and intra-assembly flow redistribution and heat transfer) on the maximum transient coolant temperatures in the CRBRP core, the following system of three computer codes is used:

- 1) DEMO - predicts the overall plant-wide, dynamic natural circulation performance and defines the core boundary conditions;
- 2) COBRA-WC - predicts the detailed dynamic, core-wide performance including all inter- and intra-assembly flow and heat redistribution effects;
- 3) FØRE-2M - predicts the localized hot rod dynamic temperatures including effects of localized rod phenomena and uncertainties in nuclear/thermal-hydraulic/mechanical data.

A linkage between the COBRA-WC and FØRE-2M codes has been developed to incorporate the inter- and intra-assembly phenomena into the localized hot rod transient analyses by using the expression for the heat transported to the coolant for each axial node of the hot element modeled in FØRE-2M. Coupled with this, the axial mass flow rate for each axial node is also input from COBRA-WC analyses. The heat and axial mass flow rate for each axial node are based on nominal conditions in the COBRA-WC code. This is a conservative approach because these values are lower than those calculated for the hot channel temperature conditions and thus, result in a conservatively higher predicted hot channel temperature.

Typical results illustrating the effects of inter- and intra-assembly flow and heat redistribution are shown in Figure 4.4-68 for a high temperature fuel rod. These results are presented as normalized temperature differences relative to the steady state temperature difference in Case 1, i.e.,

$$\phi = \frac{[T_c(\tau) - T_{in}(\tau)]_i}{[T_c(o) - T_{in}(o)]_1} \quad i = \text{Case 1, 2, 3 or 4}$$

where

$T_c(\tau)$  = maximum hot channel coolant temperature;

$T_{in}(\tau)$  = inlet temperature.

As can be noted by comparing Cases 2, 3 and 4, accounting for inter- and intra-assembly flow and heat redistribution effects significantly decreases the predicted transient coolant temperatures in the hot channel. It can also be seen that the uncertainty factors cause a significant increase in the predicted expected hot channel coolant temperatures (i.e., Case 1 versus Case 2).

In summary, natural convection cooling of the core represents one of the few CRBRP core design transients where low power/high temperature conditions exist. Due to the long coolant transport time and low pressure drop for the core while descending into and operating in this mode, core inter-assembly and intra-assembly flow/heat redistribution: a) becomes significant with regard to accurately predicting temperatures; and b) significantly decreases the maximum hot rod temperatures in all core regions.

54

#### 4.4.2.7 Reactor Pressure Drops and Hydraulic Loads

##### 4.4.2.7.1 Introduction

The area of pressure drop calculations has gone through many improvements and re-evaluations throughout the CRBRP core design, such as:

- o More experimental data from prototypic hydraulic experiments of various reactor and assembly components have become available, thus replacing analytical/engineering estimates with experimentally derived correlations.

51

- - Uncertainties on predicted pressure drops of several components have changed from engineering estimates (a typical example being a 20% uncertainty on form losses) adopted in previous analyses to actual calculations based on regression analysis of experimental data.
- - Several modifications have been factored into the lower inlet modules (LIM) design. The requirement of a constant pressure drop across the various LIMs, and consequent orificing, has been removed. Thus, assemblies belonging to the same orificing zone but to different LIMs will have slightly different flows, depending on the total pressure drop across the respective LIMs. To retain the capability for future radial blanket assemblies shuffling, all the blanket assemblies are identical and the radial blanket orificing is apportioned between the assembly and the LIM. Thus, in zone 9 (highest flow orificing zone in the radial blanket) all the orificing is in the assembly, while in zones 10, 11 and 12, a progressively increasing pressure drop is incorporated in the LIM orificing to balance the decrease in assembly pressure drop going to lower flow orificing zones. The amount of orificing in the LIMs is thus designed to permit shuffling of zone 9 assemblies in 10, 11 and 12, zone 10 assemblies in zones 11 and 12 and zone 11 assemblies in zone 12.

A complete discussion of pressure drop calculations during CRBRP normal operation is reported in Section 6 of Reference 3, along with a description of the CATHISH code, used in these analyses.

#### 4.4.2.7.2 Core Assemblies Pressure Drop Correlations

Preliminary hydraulic characteristics of the CRBRP fuel, blanket and control assemblies are reported here. Since several test programs are still in progress, the best available information has been included in this analysis which will be reviewed as new test data are obtained.

Correlations reported here are valid over the entire range of operation, either turbulent, transition or laminar. However, in this study, only full flow conditions are of interest, therefore, the flow in all components is in the turbulent regime. This distinction is important when considering the uncertainties associated with the proposed correlations, as discussed later.

The data included in the characterizations developed herein are from tests of FFTF assemblies and components (Refs. 4 through 6), and tests of CRBR components (Refs. 7 through 9). Form losses have been correlated with the Reynolds number by a function of the type  $CR\epsilon^{-n}$ .

Linear regression analyses were performed on the fuel assembly component pressure drop data. The coefficients of the regression functions were calculated for the fuel assembly components and are presented in Table 4.4-5 along with the relevant statistical parameters. Rigorous statistical analyses will be performed for the blanket assemblies, when more complete data is available.

The data in Table 4.4-5 may be used to calculate the confidence band on the form loss coefficient K at any values of the independent variables from the equation (Ref. 10)

$$\Delta Y = t_{\sigma_y} \left( 1 + 1/N + \sum_{i=1}^M (\bar{X}_i - X_i)^2 / N \sigma_{X_i}^2 \right)^{1/2} \quad (4.4.2.7-1)$$

55 |

55 |

where  $\Delta Y$  is the one-sided confidence band;

$t$  is Student's T statistic;

$\sigma_y$  is the "standard error of estimate" from Table 4.4-5;

$N$  is the number of data points;

$M$  is the number of independent variables;

$\bar{X}_i$  is the experimental mean of the  $i$ th independent variable from Table 4.4-5;

$X_i$  is the value of  $i$ th independent variable at which is calculated; and

$\sigma_{X_i}$  is the standard deviation about  $\bar{X}_i$  from Table 4.4-5

55 |

Note that  $t$  is evaluated at some desired confidence level and hence, the resulting value of  $Y$  has associated the same confidence limit.

Since only full turbulent flow is of interest in these studies, the uncertainties on the pressure drop correlation at 100% flow is lower than over the entire flow range, as indicated in Table 4.4-5. In fact, the data scatter in three separate flow tests (Refs. 4 through 6) was greater in the transition region than at higher Reynolds numbers.

The recommended hydraulic correlations for fuel assembly components are presented in Table 4.4-6. All fuel assemblies are hydraulically identical except for the orifice stack which is unique to each flow orificing zone. Selection of the proper orifice design from the five orifice correlations requires selection of both the number of plates and the hole diameter to achieve the zone flow rate. Selection should be done to minimize the number of orifice plates while still having adequate margin to cavitation/erosion. While final selection must await the results of final cavitation tests, in the

51 |



present analyses a design criterion(\*) of 40 ft/sec maximum coolant velocity in the orifice holes was selected as a first approximation and the maximum achievable pressure drop for each orifice configuration was determined and is presented in Figure 4.4-25 as a function of assembly flow rate. Given an assembly flow rate, the pressure drop resulting from all components except the inlet nozzle/orifice/shield can be determined from the correlations in Table 4.4-6. This result subtracted from the total assembly pressure drop is the required inlet nozzle/orifice/shield pressure drop. The number of orifice plates for this pressure drop and flow rate can be determined from Figure 4.4-25 and the corresponding Reynolds number-dependent hydraulic correlation determined by solving for the orifice hole diameter.

The correlation presented for the rod bundle outlet results from a calculation of expansion form losses (Ref. 11), since no relevant data are available. Because the associated pressure drop is of the order of 1 psi or less, the inherently large uncertainty of such a calculation is acceptable for preliminary calculations. Data from the CRBR fuel assembly flow and vibration test will be used.

Similarly, the correlation presented for the rod bundle inlet results from a calculation of expansion and contraction form losses (Ref. 11), since experimental data obtained for this component's pressure drop (Ref. 6), were ambiguous, as discussed in Section 6 of Reference 3.

The recommended hydraulic correlations for the blanket assemblies components are presented in Table 4.4-7. The inner blanket assemblies utilize a fuel assembly type inlet nozzle, radial blanket type shield, rod bundle and outlet nozzle, and a unique orifice stack within the assembly. The inlet nozzle geometry and hydraulic correlation are identical to the fuel assembly. The inlet nozzle/orifice/shield has not been tested, so the weak Reynolds number dependence shown on Table 4.4-7 is recommended, based on the Reynolds number dependence of the four and five plate fuel assembly orifices (Ref. 7) and the dependence of sample cases of the radial blanket inlet module orificing (Ref. 8). The parameter C represents the geometry of the orifices satisfying the desired pressure drop/flow relationship and is uniquely defined once the orifice stack characteristics are selected. The shield, rod bundle inlet and rod bundle outlet form losses were estimated based on Reference 11. The rod

---

(\*)Figure 4.4-24 shows typical results being obtained in the cavitation tests of CRBRP fuel assembly orifice stacks. Following completion of the cavitation tests, an experimentally verified maximum allowable cavitation number limit will be used with the maximum velocity limit specified in Section 4.4.1 (whichever is more stringent) as the design criterion in sizing the orifices. It should be noted, however, that the amount of pressure drop allocated in the orificing is independent of the particular design criterion selected, which will only determine the geometry necessary to satisfy such a limit. Therefore, all the data reported in Section 4.4.2.7.4 for the various component pressure drops will vary only marginally following redefinition of the no-cavitation criterion.

bundle friction was measured (Ref. 9) over a sufficiently wide range of flow rates to cover the full range of blanket flow rates. The blanket assembly and fuel assembly outlet nozzles are sufficiently similar to permit application of the fuel assembly outlet nozzle test data (Ref. 7) with the smaller blanket assembly reference area in determining the blanket assembly outlet nozzle form loss.

Except for the inlet nozzle and rod friction, no data are available on the blanket assembly component pressure drops. However, because there is no a priori reason to anticipate worse uncertainties on blanket assembly components than were found on fuel assembly components once tests are completed, the same uncertainties as for the corresponding fuel assembly components(\*) (Table 4.4-5) are applied. In the case of the blanket rod friction, where data exist (Ref. 9), the standard error on the recommended correlation is 5% over the entire flow range and 3.3% over the full flow design range.

The radial blanket assemblies have low rod bundle pressure drops and are dominated by orificing located both within the assembly and in the lower inlet module. The orificing located in the lower inlet module was characterized (Ref. 8) over a range of flow rates near design conditions. A preliminary examination of the test data shows the losses can be modeled proportional to  $Re^{-0.05}$  as was typically found for the four and five plate fuel assembly orifices (Ref. 7).

Final characterization of all inner and radial blanket assembly components over the necessary range of Reynolds numbers will result from the CRBRP blanket assembly flow and vibration test.

In the control assemblies case, approximately 90% of the total pressure drop occurs in the orifice stack. The remaining 10% is divided about evenly between rod bundle friction and the combined inlet nozzle, shield and outlet nozzles form losses. Preliminary pressure drop correlations for the various control assembly components are reported in Reference 13; since the contribution from components other than the orifice is quite modest, these correlations are still being used at present. For the orifice stack, the same correlation as experimentally determined for the inner blanket assemblies is adopted in the interim until ad hoc data are available. Similarly, the same uncertainties as for the fuel assemblies are used until pertinent information is available. Final characterization of the control assembly components over the necessary range of Reynolds numbers will result from CRBRP control assembly flow tests.

(\*)It should also be kept in mind that the limiting pressure drop is represented by orificing zone 1, thus, the blanket orificing can be easily adjusted to accommodate possible discrepancies between predictions and actual test data.

#### 4.4.2.7.3 Reactor Internals Pressure Drops

The pressure drops for the reactor internals, along with their bases are presented in Table 4.4-8, which gives the nominal losses for the plant thermal and hydraulic design condition. The pressure drops are based on testing from the Inlet Plenum Feature Model test and the Integral Reactor Flow Model test and on analysis. The uncertainty in the individual pressure losses are reported in Table 4.4-8.

#### 4.4.2.7.4 Results

Pressure drops were calculated for all reactor components by the CATFISH code. CATFISH has the capability of accounting for the effect of uncertainties associated with prediction of the various resistances. In addition to the hydraulic resistance, an uncertainty also exists on the pump head/flow characteristics, i.e. a 5% spread between minimum and maximum pump head capability for the given flow.

Various calculations are discussed in Section 6 of Reference 3. Reported here is the case investigating plant THDV conditions, where the flow is specified ( $41.446 \times 10^6$  lb/hr). Since these are the worst possible conditions from the thermal performance standpoint, i.e., minimum reactor flow, it is consistent to assume positive uncertainties for the various hydraulic resistances and the minimum pump head curve. As the most conservative assumption, uncertainties on all resistances were taken at their maximum value, either  $3\sigma$  where a statistical basis exists, or at their bounding value (generally 1.2) where only an engineering estimate was available. It is rather obvious that assuming that all the resistances in all components are simultaneously at their maximum value, is extremely pessimistic, in fact, it is extremely improbable. Calculations were, however, performed for this set of conditions to provide an absolute minimum, worst case and the results are reported in Table 4.4-9. All pressure drops are reported for cycle 4 conditions, which were the ones used in determining the orificing (see Section 4.4.2.5). The only obvious exception is zone 6 inner blanket, since only fuel assemblies are in zone 6 during cycle 4. Flow and pressure drops for zone 6 IB are at cycle 2, conditions adopted for orificing of assembly #98, the only inner blanket remaining for two years in zone 6. The distinction between zones 10C and 10P is due to the fact that zone 10 assemblies are the only assemblies which belong to the same orificing zone, but to two different types of modules. The modules at the core periphery (see Figure 4.4-26) have a different geometry from the other modules (called central) and therefore, a different resistance and pressure drop. Assemblies 10C are the zone 10 assemblies located in the central modules, while assemblies 10P are located in the peripheral modules. The lower inlet modules have been orificed for zones 10,11 and 12 to provide the capability of shuffling radial blanket assemblies if required at a later time. Thus, the pressure drop reported under "LIM upper portion and

51

orifice" for zones 1 through 9 is due to the hardware of the upper portion of the LIM, i.e., the region where the orificing plates are inserted for zones 10 through 12; the plates pressure drops are added for zones 10, 11 and 12. Whether or not orificing plates are physically in the LIM is quite obvious from the relative magnitude of the reported pressure drops. The "LIM, lower portion"  $\Delta P$  is attributable to the resistance in the remainder of the LIM.

The average zone flows thus calculated for THDV conditions by CATFISH and reported in Table 4.4-9 exactly agree (within 0.05%) with the flows reported in Table 4.4-4, which is quite a strong indication of the soundness of the CATFISH model. The vessel nozzle-to-nozzle pressure drop was calculated at 126.4 psi, which is actually consistent with the 123 psi value reported in Section 5 when one considers that 126.4 psi is the vessel nozzle-to-nozzle irreversible pressure loss, while 123 psi is the vessel nozzle-to-nozzle static pressure difference minus the nozzle-to-nozzle elevation head. The difference of 3.4 psi is therefore the difference in velocity head between the reactor vessel inlet nozzle and outlet nozzle. Similarly, the reported value of the pump head, 163.5 psi reported in Table 4.4-9, is the total developed head, while the value 160.3 psi reported in Section 4.4.2.1 is the static pump head.

#### 4.4.2.7.5 Hydraulic Loads and Hydraulic Balance

The maximum hydraulic loads on the core components, considering steady state, transient and test operations, are shown in Figure 4.4-2. The reactor component which is subjected to the highest hydraulic load is the core support structure (CSS). During operation with the core in place, the maximum hydraulic load on the CSS occurs during steady state and is  $7.37 \times 10^6$  pounds. This corresponds to a conservatively estimated maximum core pressure drop of 160 psi. This maximum core pressure drop is based on assumptions that the pump head-flow characteristic is at the maximum and all non-core pressure losses are at their minimum values. For all other components, during upset, emergency, faulted and test events, the hydraulic loads are also less than the steady state values.

Hydraulic Balance - The function of the hydraulic balance system is to equalize (balance) the pressure forces on the fuel, blanket and control assemblies so that there is little or no force tending to lift the assembly so that the resultant net force due to gravity is downward and equal to approximately the buoyant weight of the assembly. This is accomplished by exposing a significant portion of the bottom of the assembly to the low pressure of the outlet plenum.

It is unlikely that loss of hydraulic balance will occur, as discussed in Chapter 15.2.2.1.

#### 4.4.2.8 Correlations and Physical Properties

The physical properties and correlations employed in the steady state thermofluids design of the CRBRP fuel, inner and outer blanket and control assemblies are listed and discussed below.

##### 4.4.2.8.1 Sodium Properties

All sodium properties used in the design studies are according to Reference 15.

##### 4.4.2.8.2 Film Heat Transfer Coefficient

The following correlations, (Reference 16) based on theoretical analyses and best fit of available experimental data for sodium flowing through rod bundles with pitch-to-diameter ratios between 1.05 and 1.30, are used:

For Fuel Assemblies:

$$Nu = 4.0 + 0.33 (P/D)^{3.8} (Pe/100)^{0.86} + 0.16 (P/D)^{5.0} \quad (4.4.2.8-1)$$

range of validity:  $1.2 \leq P/D \leq 1.3$ ;  $20 \leq Pe \leq 1000$

lower bound of uncertainty for the above ranges:

-12% at  $3\sigma$  level of confidence.

For Blanket and Control Assemblies:

$$Nu = [-16.15 + 24.96 (P/D) - 8.55 (P/D)^2] Pe^{0.3} \quad (4.4.2.8-2)$$

for  $1.05 \leq P/D \leq 1.15$ ;  $150 < Pe \leq 300$

$$Nu = 4.496 [-16.15 + 24.96 (P/D) - 8.55 (P/D)^2] \quad (4.4.2.8-3)$$

for  $1.05 \leq P/D \leq 1.15$ ;  $4 \leq Pe \leq 150$

lower bound of uncertainty for the above ranges of validity:

-21% at  $3\sigma$  level of confidence.

In the above equations, the following nomenclature applies:

Nu = Nusselt number

Pe = Peclet number

P = rod pitch

D = rod outer diameter

#### 4.4.2.8.3 Cladding Thermal Conductivity

The following correlation (Reference 17) was adopted for the cladding thermal conductivity, K:

$$K = 7.645 + 4.187 \times 10^{-3}T \quad (4.4.2.8-4)$$

where K is in Btu/Hr-Ft<sup>2</sup>F and T in °F.

The correlation for the thermal conductivity of 316 SS was based on unirradiated data which are reported in Reference 18.

It should be noted that the correlation equation adopted yields results which are 5% lower than the data given in Reference 18. In addition, a 10% uncertainty (3 $\sigma$  level) is applied to account for irradiation effects, which is very conservative as discussed in Reference 19. It is important to note that the temperature drop across the cladding wall is relatively small (of the order of 60° F or less), so that uncertainties in the thermal conductivity of the cladding due to in-reactor effects have only a small effect on temperature. The thin layers of cladding affected by sodium-corrosion and fuel-corrosion have very small temperature drops so that reductions in thermal conductivity have only very minor influence on cladding temperatures. Thus, the effects of these thin layers were included in the overall 10% uncertainty applied to the cladding conductivity as opposed to being handled separately. It should also be noticed that the effect of cladding thickness tolerances (maximum  $\pm$  1 mil) has been accounted for, and statistically combined with the in-reactor effects to yield a total uncertainty factor on cladding thickness and conductivity of 12% (3 $\sigma$  level).

#### 4.4.2.8.4 Cladding Linear Thermal Expansion Coefficient

The following correlation (Ref. 17) was adopted for the cladding linear thermal expansion coefficient,  $\alpha$ :

$$\alpha = 8.33 \times 10^{-6} + 1.67 \times 10^{-9}T \quad (4.4.2.8-5)$$

where  $\alpha$  is in °F<sup>-1</sup> and T in °F.

An uncertainty of 10% (at 3 $\sigma$  level of confidence) applies to the above correlation, accounting mainly for irradiation effects.

#### 4.4.2.8.5 Fuel and Blanket Assemblies Fuel-Cladding Gap Conductance

The fuel-cladding gap conductance varies during the lifetime of the assembly, depending on the type of fuel, burnup, power and temperature level in the assembly. The gap conductance is also correlated with the fuel thermal conductivity, and fuel restructuring parameters;

in other words, gap conductance, fuel conductivity and restructuring parameters are the three components of a unique, self-consistent set which is determined through irradiation experimental data as they become available. The LIFE-III code provides analytical modeling of the components of this set. Specifically, LIFE-III models used in fuel behavior evaluation are:

- A gap conductance model based on heat transfer and molecular theory fundamentals;
- A pore migration model which is not tied to any fixed restructuring boundaries (threshold temperature, density), but is based on migration of the as-fabricated fuel porosity into the central hole and consequent growth of the central hole;
- A gap closure model which correlates the gap size with burnup, accounting for operational conditions of the fuel, effect of thermal expansion, cracking and swelling of the fuel;
- A model to calculate the fuel-cladding contact pressure;
- Updated fission gas release model.

All the above models are explicitly dependent on fuel rod burn-up, power and operating conditions history.

Regarding the transient behavior of gap characteristics, a national effort is currently being pursued to develop detailed transient analysis codes in the same manner as the LIFE code has been developed for steady state analyses. For the time being, until the detailed transient code is developed and its prediction calibrated against experimental data, steady state gap characteristics are adopted during the transients which are discussed in Chapter 15. A qualitative evaluation of the cladding/fuel gap behavior is briefly discussed in the following.

During transients characterized by a power increase, the rise in fuel temperature will cause thermal expansion of the fuel and a concomitant reduction in the fuel-cladding gap. The resultant effect of the transient will be to increase the gap conductance over its steady state value; therefore, adoption of the former during the transient will represent a conservative estimate, since the predicted fuel temperature will be greater than the actual. In this respect, it should be noted that the fuel temperature is the most important parameter sought after in a power-increase transient.

The situation is not quite as obvious for the case of an under-cooling transient. These transients consist of two phases, an initial

one before the reactor scram when the coolant flow decreases while the power remains constant, and a second after scram when both flow and power rapidly decrease. During the first phase, the cladding temperature will increase more rapidly than the fuel temperature, therefore, the fuel-cladding gap will increase due to the differential thermal expansion. In the second phase, the fuel temperature will quickly decrease with subsequent pellet contraction and further enlarging of the gap. Therefore, the gap conductance will decrease with respect to its steady state value and the actual transient fuel temperature will be somewhat higher than predicted. However, the fuel temperature is of secondary importance in a loss of flow transient, the critical parameters being the cladding and coolant temperatures. In this respect, adoption of steady state gap conductance is conservative; in fact, the actual cladding and coolant temperatures will be less than predicted, since owing to the lower gap conductance, a smaller amount of heat will be transferred from the fuel into the cladding and coolant at the time the first peak temperature occurs. The effects discussed above occur in a relatively short time when compared with the coolant coastdown period; as the coastdown continues, equilibrium conditions between fuel, cladding and coolant temperatures are reached. The opening and/or enlargement of the gap, therefore, has the effect of delaying the attainment of the thermal equilibrium conditions. In addition, heat fluxes are small in this period and this results in an insensitivity to gap conductance variations.

#### 4.4.2.8.6 Control Rod Gap Conductance

The hot gap ( $g$ ) is defined as the difference between the pin cladding inside radius ( $R_i$ ) and the  $B_4C$  absorber pellet outside radius ( $R_p$ ), at operating conditions, i.e.,

$$g = R_i - R_p \quad (4.4.2.8-6)$$

Accounting for thermal expansion, the hot cladding inside radius is calculated by,

$$R_i = (R_i)_{cold} [1 + \alpha_{cl} (T_{cl,m} - 70)] \quad (4.4.2.8-7)$$

where  $(R_i)_{cold}$  is the cold cladding inside radius;

51

Amend. 51  
Sept. 1979



$\alpha_{cl}$  is the cladding thermal expansion coefficient reported in Section 4.4.2.8.4; and

$T_{cl,m}$  is the cladding midwall temperature(\*).

The hot absorber pellet outside radius is calculated by,

$$R_p = (R_p)_{cold} [1 + \alpha_{abs} (T_{abs, avg} - 70)] \quad (4.4.2.8-9)$$

where  $(R_p)_{cold}$  is the cold absorber pellet outside radius;

$\alpha_{abs}$  is the  $B_4C$  thermal expansion coefficient (see Section 4.4.2.8.9);

$T_{abs, avg}$  is the average absorber temperature (see discussion below).

Of the two radii, the hot cladding inside radius ( $R_i$ ) is simply evaluated by Equation (4.4.2.8-7) upon the calculation of the cladding midwall temperature.

To calculate the hot pellet radius, an iterative procedure is followed until the average absorber temperature, and consequently, the hot absorber pellet outside radius ( $R_p$ ) calculated in two successive iterations converge within prefixed limits.

The average absorber temperature can be defined as the arithmetic mean between the absorber pellet centerline and the surface temperatures, i.e.,

$$T_{abs, avg} = \frac{T_{abs, c} + T_{abs, s}}{2} \quad (4.4.2.8-10)$$

(\* The cladding midwall temperature,  $T_{cl,m}$  as well as the ID temperature  $T_{cl,i}$  are calculated based on the general equation representing the heat conduction through the cladding at a radius  $r$  for a height  $\Delta Z$ , considering separate heat production in the cladding, i.e.,

$$Q_{abs} + Q_{cl} \frac{(r^2 - R_i^2)}{R_o^2 - R_i^2} = -K_{cl} 2\pi r \Delta Z \frac{dT}{dr} \quad (4.4.2.8-8)$$

where  $Q_{abs}$  and  $Q_{cl}$  are heat generations in the absorber and cladding, respectively;

$K_{cl}$  is the cladding thermal conductivity (Equation 4.4.2.8-4)

$R_o$  and  $R_i$  are the cladding outer and inner radius, respectively.

Since the absorber pellet centerline temperature ( $T_{abs,c}$ )(\*), is dependent on the absorber pellet surface temperature ( $T_{abs,s}$ ) as a boundary condition, the iterative process on  $T_{abs,avg}$  actually involves  $T_{abs,s}$ . Based on the heat transfer across the absorber pellet-to-cladding gap, considering the bond (helium) thermal conductivity and the (hot) gap size, the surface temperature can be expressed (under nominal rod operating conditions), as the following:

$$T_{abs,s} = T_{cl,i} + \frac{Q_{abs}}{2\pi K_{gap} \Delta Z} \ln \left( \frac{R_i}{R_p} \right) \quad (4.4.2.8-11)$$

where  $T_{cl,i}$  is the cladding inside temperature;

$Q_{abs}$  is the absorber heat generation within a length  $\Delta Z$ ;

$R_i$  is the hot cladding inside radius based on Equation (4.4.2.8-7);

$R_p$  as indicated by Equations (4.4.2.8-9) and (4.4.2.8-10), is a function of  $T_{abs,s}$ ;

$K_{gap}$  is the gap (helium) thermal conductivity (see following Equation 4.4.2.8-14).

The gap thermal conductivity is again dependent on the absorber pellet surface temperature  $T_{abs,s}$ , since it is a function of the average gap temperature which can be defined as,

$$T_{gap, avg} = \frac{T_{abs,s} + T_{cl,i}}{2} \quad (4.4.2.8-13)$$

\*The absorber centerline temperature,  $T_{abs,c}$ , is calculated based on the general differential equation representing the heat transfer through the absorber pellet,

$$K_{abs} \frac{d^2T}{dr^2} + \frac{K_{abs}}{r} \frac{dT}{dr} + q'''_{abs} = 0 \quad (4.4.2.8-12)$$

where  $K_{abs}$  is the absorber ( $B_4C$ ) thermal conductivity reported in Section 4.4.2.8.8; and

$q'''_{abs}$  is the volumetric heat generation rate in the pellet.

The iterative procedure on the hot pellet radius ( $R_p$ ) is initiated by the first guesstimate of  $T_{abs,s}$  from Equation (4.4.2.8-11), assuming  $R_p = (R_p)_{cold}$  and  $T_{gap,avg} = T_{cl,i}$ . This first guesstimate value is used next to estimate values of  $R_p$  by Equations (4.4.2.8-9) and (4.4.2.8-10), and  $T_{gap,avg}$  by Equation (4.4.2.8-13). As mentioned previously, this process is repeated until the value  $R_p$  calculated in two successive iterations converges within a prefixed limit; with the established values of  $R_p$  and  $R_i$  (see Equation 4.4.2.8-7), the hot gap is obtained by Equation (4.4.2.8-6).

Experimental values of the control rods gap conductance have been determined (Reference 20) to be consistent with the method used.

The helium thermal conductivity is given by (Ref. 21).

$$K = 0.097 + 7 \times 10^{-5}T \quad (4.4.2.8-14)$$

where  $K$  is in Btu/hr-ft- $^{\circ}$ F and  $T$  in  $^{\circ}$ F.

The above equation is valid for  $T > 700$   $^{\circ}$ F.

#### 4.4.2.8.7 Fuel Thermal Conductivity

The following equation (Ref. 18) is used in evaluating the fuel thermal conductivity in the fuel assemblies:

$$K = FP \left[ \frac{1}{A+BT} + CT^3 \right] \quad (4.4.2.8-15)$$

where  $K$  = thermal conductivity, W/m $^{\circ}$ K;

$T$  = temperature,  $^{\circ}$ K;

$$FP = \frac{1.079(1-P)}{(1.0+0.5P+4.62P^2)}$$

$P$  = fractional porosity (1-fraction of theoretical density);

$$A = -6.0656 \times 10^{-4}$$

$$B = 3.04212 \times 10^{-4}$$

$$C = 0.75137 \times 10^{-10}$$

A review of the effects of plutonium weight percent on conductivity revealed that for the range  $0.12 \leq Pu \leq 0.3$ , such effect was within the range of experimental uncertainties, and therefore, the thermal conductivity could be considered independent of plutonium content. No experimental conductivity data exist for a plutonium content corresponding

to the CRBRP heterogeneous core value (33%). However, based on existing data, it is believed that such a slight extrapolation outside the range is not significant enough to change the above conclusion. Moreover, effects of plutonium content extrapolation on power-to-melt, which is the parameter of ultimate importance, are properly accounted for as discussed in Section 4.4.3.2.2.

Equation (4.4.2.8-15) has been adopted also for the radial blanket assemblies; this is conservative for BOL conditions since the conductivity of single-phase uranium oxide is higher than for mixed oxides.

The thermal conductivity of mixed oxide fuel is dependent on the porosity fraction, pore conductivity, and pore shape, size and distribution. These variables are normally accounted for in terms of a porosity correction factor in an equation relating the actual conductivity to that of the 100% dense material.

The effect of porosity and pore morphology have been the subject of extensive investigation, with many theoretical and empirical relationships being proposed to explain and correlate these effects (References 22 through 25). Most of the available relationships for porosity corrections have been reviewed in the technical literature.

The experimental studies on this subject (Ref. 24) have shown that fuel pellets with open, interconnected porosity and microcracks had thermal conductivities from 14 to 33% less than pellets at the same density, but containing uniformly distributed isometric pores. The fuel fabrication procedure for the low thermal conductivity pellets involved high pressure preslugging of this powder prior to final compaction of the pellets. The results showed that the thermal conductivities decreased with an increase in open porosity, laminar pores and/or microcracks with the major axis normal to the heat flow direction.

However, results from an in-reactor experiment (Reference 26) showed that the effects of pore morphology on heat rating-to-melting was small. The heat rating-to-melting of fuels with laminar porosity and microcracks was only 3-6% lower than the fuels with isometric porosity. The small difference in the heat rating-to-melting, despite the significant differences in the preirradiation thermal conductivity, is attributed to fuel restructuring and possibly radial oxygen redistribution effects (Reference 26). The restructuring of the fuel in the inner hot region of the fuel increases the fuel density due to formation of columnar grains and lenticular porosity oriented in the radial direction, thus effectively reducing the thermal resistance to radial heat flow.

51 | The results from the HEDL P-20 experiment (Reference 27) also indicate that the effect of fuel microstructure (primarily pore morph-

ology) on heat rating-to-melting is relatively small. A difference of approximately 6% was observed between isometric and laminar type porosity fuels.

In summary, theoretical expressions for understanding pore morphology effects and correlating data are available. Experimental data show that differences in pore morphology brought about by differences in fabrication procedures can cause significant differences in out-of-reactor thermal conductivities. However, in-reactor effects, such as restructuring, substantially reduce these differences.

#### 4.4.2.8.8 B<sub>4</sub>C Thermal Conductivity

The thermal conductivity of the B<sub>4</sub>C absorber in the control assemblies is given by (Ref. 20):

$$K = \left( \frac{1}{6.87 + 0.0095(T+460)} \right) \left( \frac{1 - \phi}{1 + 2.2\phi} \right) (0.102\theta - 14.492) \quad (4.4.2.8-16)$$

where

K = B<sub>4</sub>C thermal conductivity, Btu/hr-ft-°F

T = B<sub>4</sub>C absorber temperature, °F

φ = Porosity

θ = irradiation temperature, °F; for steady state θ=T, for transient analyses the irradiation temperature is equal to the initial steady state temperature.

The above equation is valid for:

B-10 captures > 5 x 10<sup>20</sup> captures/cc  
440 < T < 1800 °F

The maximum uncertainty was reported in Reference 20 to be in the range of 6 to 9%. To conservatively accommodate this possible variation, a 3σ uncertainty value of 10% has been incorporated in the thermal and structural analyses of the absorber pin. Also, the use of an expression based on burnup levels greater than 5 x 10<sup>20</sup> captures/cc provided further conservatism, since for lower burnup, the B<sub>4</sub>C thermal conductivity is much higher than that expressed by the equation.

Since the average PCA absorber temperature is of the order of 2500 °F, some extrapolation of the above equation is necessary.

51

Amend. 51  
Sept. 1979

#### 4.4.2.8.9 B<sub>4</sub>C Linear Thermal Expansion Coefficient

The following equation (Ref. 20) is used:

$$\alpha = 2.253 \times 10^{-6} - \frac{0.434}{T} \times 10^{-3} + 0.592 \times 10^{-9} T - 0.525 \times 10^{-13} T^2 \quad (4.4.2.8-17)$$

where  $\alpha$  is in (in/in-°F) and T in (°F)

The temperature range of validity is from 20°C to 2500°C.

#### 4.4.2.8.10 B<sub>4</sub>C Density

The theoretical density (Ref. 20) of natural (19.78 a/o B<sup>10</sup>) B<sub>4</sub>C is 2.512 g/cm<sup>3</sup>; fully enriched (92 a/o B<sup>10</sup>) B<sub>4</sub>C has a theoretical density of 2.381 g/cm<sup>3</sup>. A linear variation between those two extremes can be assumed to calculate B<sub>4</sub>C density for intermediate values of enrichment.

#### 4.4.2.8.11 Fuel Theoretical Density

The fuel theoretical density is given by:

$$\rho = \frac{NM}{AV} \quad (4.4.2.8-18)$$

where

$\rho$  is in g/cc

M is the molecular weight in grams

A is the Avogadro's number

N = 4 is the number of molecules per unit cell

V is the unit cell volume in cm<sup>3</sup> and depends on the stoichiometric ratio and percentage of plutonium. Values of V are reported in Reference 28.

#### 4.4.2.8.12 Fuel Melting Temperature

The unirradiated mixed oxide fuel melting (solidus) temperature (Ref. 28) is 2760°C (5000°F). The observed decrease in melting temperature with burnup (range: 15,000 to 200,000 Mwd/Mt) is approximated by the following correlation, according to Reference 29:

$$\Delta T = -0.20645 \times 10^{-3} B - 58.887 \quad (4.4.2.8-19)$$

where  $\Delta T$  is the change in the solidus temperature in °C  
B is the burnup in Mwd/Mt

55| The melting temperature of radial blanket fuel is (Ref. 30) 2850°C (5162°F) for unirradiated conditions and 2760°C (5000°F) for irradiated conditions at ~2 a/o burnup.

Since the mixed oxide fuel is a solid solution, melting occurs over a range of temperatures. For fuel pin analysis, however, the solidus temperature, i.e., the temperature at which melting starts, is used as the melting temperature of the fuel. The melting temperature of the mixed oxide fuel is a function of composition, i.e., U and Pu content and the oxygen-to-metal (O/M) ratio. In addition, with burnup, some of the fission products form solid solutions with the fuel matrix, which decrease the melting temperature.

For unirradiated fuel, the melting temperatures used in the fuel pin analysis were obtained from the work of Aitken and Evans (Reference 31). These data are shown in Table 4.4-10 and Figure 4.4-27. These data were obtained by a thermal arrest technique and the accuracy is  $\pm 25^{\circ}\text{C}$ . These data show the melting temperature to be independent of the O/M ratio in the range of 1.96 to 2.00 within the accuracy of the experiment.

55| For irradiated fuel, the melting temperatures were obtained from the work of Krankota and Craig (Reference 32). These data were obtained by the tungsten "V" filament technique for both thermal and fast flux irradiated mixed oxide fuel. An exact interpretation of these data, however, is difficult because: a) distinguishing between solidus and liquidus by this technique is prone to experimental error; b) decomposition of the specimens near the melting temperature cannot be controlled and c) samples taken from different radial positions could have different compositions due to non-homogeneous distributions of fission products.

To minimize the uncertainties, the change in melting point with burnup was utilized rather than absolute temperature values and were correlated with burnup statistically using a least squares technique. The results are shown in Table 4.4-11 and Figure 4.4-28. These data are used with the unirradiated melting temperatures to determine the melting temperature as a function of burnup.

The solidus temperature of mixed oxide fuel is a function of composition, oxygen-to-metal ratio and burnup. Since the redistribution of actinides changes the local composition of the fuel, the solidus temperature will correspondingly change. Hence, a change in solidus temperature will depend on the actinide concentration profiles across the fuel pellet. A detailed description of the actinide redistribution phenomena is, therefore, a prerequisite for determining the changes in solidus temperature.

51| Migration of uranium and plutonium occur primarily by a vapor transport mechanism. Since the vapor phase composition, i.e., Pu/U ratio in the

vapor phase, in equilibrium over the fuel is different from that in the solid fuel, segregation from an originally homogeneous mixture occurs. For a nearly stoichiometric mixed oxide fuel, the vapor phase would be rich in uranium relative to the solid. Therefore, as the vapor condenses in the cooler regions of the fuel, plutonium enrichment occurs near the fuel centerline. As the oxygen-to-metal ratio is reduced, the vapor phase becomes plutonium rich. Thus, in fuels with a low initial O/M ratio, uranium enrichment near the fuel centerline will occur. These conclusions are in excellent agreement with observations from irradiated fuel pins (References 33-35). Experimental studies (Ref. 36) suggest that the quasi-congruently vaporizing composition is between 1.96 and 1.97. These experiments have also indicated that at lower O/M ratios, the rate of transport is reduced and, therefore, the total amount of vapor transported down the temperature gradient is diminished. The net result is diminished actinide segregation. The amount of porosity in the fuel and the temperature gradients play an important role in determining the actinide segregation. In fuels with low initial density, slightly enhanced segregation is expected because of the large amount of the porosity available for vapor transport.

From the above discussion, the actinide redistribution and its effects on solidus temperature can be summarized as follows:

1. For fuels with an initial O/M > 1.97, plutonium enrichment will occur near the fuel centerline resulting in decrease in solidus temperature (or melting point).
2. For fuels with an initial O/M < 1.96, uranium enrichment will occur near the fuel centerline resulting in an increase in solidus temperature (or melting point).
3. For fuels with an initial O/M in the range of 1.96 to 1.97, little change in actinide distribution is expected.

Statistically, the fuel is expected to be in an O/M ratio range where either no significant segregation occurs, or uranium enrichment will occur at the fuel center resulting in an increase in the solidus temperature. Moreover, at beginning-of-life conditions, which is the worst time for incipient melting, no significant actinide redistribution would occur because of the very short irradiation times involved. This of course, applies also to the P-19 tests, conducted on prototypic CRBRP fuel for practically unirradiated conditions.

#### 4.4.2.8.13 B<sub>4</sub>C Melting Temperature

51 The generally recommended B<sub>4</sub>C melting temperature is 2450°C (4442°F) (Reference 20).



At the present time, there are insufficient data to correlate the  $B_4C$  melting temperature with irradiation and burnup effects. However, it must be considered that operating  $B_4C$  maximum centerline temperatures are of the order of  $2500^{\circ}F$ , which is about one-half of the unirradiated melting temperature.

#### 4.4.2.8.14 Fuel Linear Power-to-Melt

Results from the HEDL P-19 experiments (Ref. 37) indicate the following correlation for the linear power rating causing incipient melting in the fuel assemblies rods:

$$\left. \begin{aligned} Q'_m &\sim 19.5 \text{ Kw/ft. for diametral gap} \leq 5 \text{ mils} \\ Q'_m &= 13.52 + \frac{14.95}{G - 2.77} \text{ for diametral gap} > 5 \text{ mils} \end{aligned} \right\} (4.4.2.8-20)$$

where

$Q'_m$  is the power-to-melt in kw/ft;

$G$  is the diametral cold gap in mils.

The above correlation is valid for FFTF conditions (0.230" diameter pins and  $1060^{\circ}F$  cladding I.D. temperature). Approximately a 0.1 kw/ft decrease (increase) in power-to-melt corresponds to a  $20^{\circ}F$  increase (decrease) in cladding I.D. temperature.

A regression analysis of the HEDL P-19 power-to-melt data (adjusted to FFTF conditions, i.e.,  $1060^{\circ}F$  I.D. cladding temperature and 0.23" pin) performed at ARD yielded the following cubic polynomial as best fit of the data:

$$Q'_m = 8.44 + 6.828 G - 1.259 G^2 + 0.06549 G^3 \quad (4.4.2.8-21)$$

where

$Q'_m$  = linear power-to-melt (kw/ft)

$G$  = diametral cold gap (mils).

The standard deviation of the data about the correlated curve was 0.31 kw/ft or a  $3\sigma$  value of  $\pm 0.92$  kw/ft.

In parallel with ARD analysis, three analytical fits were proposed by HEDL: an arc-tangent, a cubic and a hyperbolic relationship. The cubic fit correlation:

$$Q'_m = 9.99 + 5.9 G - 1.09 G^2 + 0.056 G^3 \quad (4.4.2.8-22)$$

was in good agreement with ARD correlation. The root mean square deviation of the HEDL cubic fit was 0.2643. The arc-tangent curve had a much larger spread (0.418), while the hyperbolic relationship:

$$\begin{aligned} Q'_m &= 19.5 & G \leq 5 \text{ mils} \\ Q'_m &= 13.60 + \frac{12.96}{G-3.11} & G > 5 \text{ mils} \end{aligned} \quad (4.4.2.8-23)$$

had a root mean square deviation of 0.2953, i.e., comparable to the cubic fit. Finally the HEDL data were officially published (Reference 37), where the hyperbolic correlation (Equation 4.4.2.8-20) was selected as the most accurate fit while the numerical constants were slightly readjusted.

Figure 4.4-29 shows Equation 4.4.2.8-20 and the experimental data. The  $\pm 0.92$  kw/ft band earlier determined for the cubic polynomial fit is superimposed. As evident from the figure, the uncertainty band is definitely overestimated when the optimum hyperbolic fit is adopted.

Subsequent to the P-19 test, additional power-to-melt data on very low burnup irradiated pins (P-20 test, Reference 38) indicated an improvement of about 20% in the value of the power-to-melt for pre-irradiated pins to 0.3% burnup, which can be achieved by initial operation at reduced power. Based on this experimental evidence, several programmed startups (combinations of reduced power and holding time) can be utilized to satisfy the no-melting criterion in the high power CRBRP fuel rods. A detailed power-to-melt analysis and preliminary suggestions for a startup procedure are reported in Section 5 of Reference 3. An optimum programmed startup will be selected following final analyses.

#### 4.4.2.8.15 Fuel Restructuring Parameters

The LIFE-III code features a continuous pore migration model which supercedes the previous finite restructuring zones approach, and therefore no longer requires the definition of threshold restructuring temperatures or restructured zone densities.

56

#### 4.4.2.8.16 Fission Gas Release and Fission Gas Yield

The model employed to predict fission gas release from the fuel pellets is basically an updating and refinement of the HEDL model (Reference 39).

The correlation for fission gas release from non-restructured fuel as determined in Reference 39 is:

51

$$F_N = 1 - \frac{1 - \exp(-A_1 B)}{A_1 A_2 B \exp(A_3 Q)} \quad (4.4.2.8-2.4)$$

where

$F_N$  = fractional gas release from non-restructured fuel

$B$  = local burnup (a/o)

$Q$  = local linear heat generation rate (kw/ft)

$A_1 A_2 A_3$  = empirical constants.

The experimental data considered covered the following range of parameters (see Table 4.4-12):

Peak Burnup	0.87 - 5.8 a/o
Peak Linear Power	8.9 - 16 kw/ft
Fuel Density	0.895 - 0.956 theoretical pellet density
Beginning of Life Peak Cladding ID Temperature	837 - 1070°F
Diametral Gap Thickness	0.0022 - 0.008 inch (cold dimensions)

By fitting the correlation to experimental data, the values of the empirical constants were determined as follows:

$$\begin{aligned} A_1 &= 0.5748 \\ A_2 &= 0.3745 \\ A_3 &= 0.0911 \end{aligned}$$

Subsequently, the model predictions of total gas release were compared with two sets of experimental data not used in the calibration and equation fitting, thus providing an independent check.

The first set (Reference 40) of data referred to high burnup (up to 12.7 a/o) fuel, the second set (Reference 41) to high cladding temperature (1160-1170°F) rods.

Tables 4.4-13 and 4.4-14 list the additional data for high burn-up and high cladding temperature conditions, respectively, which were used to verify the validity of the previously determined constants.

Figure 4.4-30 provides an overall summary of this study by showing the correlation between predicted and observed fission gas release for each experimental pin examined. As shown in the Figure, a good agreement was found between the calibration and verification pins, thus substantiating the soundness of the model.

The  $2\sigma$  and  $3\sigma$  lines are also identified in Figure 4.4-30. It should be noted that the  $+2\sigma$  calculated release, which was used in CRBRP fission gas pressure calculations, envelops all the experimental data.

The overall standard deviation was equal to 8.62%, the maximum deviation 17.6% (which is the point near the  $-2\sigma$  line in Figure 4.4-30) and a correlation coefficient of 0.9554 was calculated.

The local linear power rating and burnup are calculated from physics input, adopting the appropriate radial and axial power (and burnup) profiles. The local gas release from non-restructured fuel is calculated through the above equation; subsequently, the total gas released from non-restructured fuel is evaluated by integration over the entire pin length. Finally, the total gas release from the fuel is obtained by summing up the above release (at a conservative  $2\sigma$  level of confidence) from non-restructured fuel to the release (100% is assumed) from restructured fuel.

The fission gas plenum pressure is then calculated from the ideal gas law equation

$$pV = nRT \quad (4.4.2.8-25)$$

where  $n$  is related to the total gas release previously calculated.

Table 4.4-15 (from Reference 18) gives the ENDF/B-IV(\*) fission yields for gaseous Xe and Kr in a fast fission spectrum. The CRBRP neutron energy spectrum is somewhat softer than the fission energy spectrum on which the data in Table 4.4-15 is based. However, the general tendency in the data is for the fission yields to decrease slightly with decreasing energy. Therefore, use of these fission energy yields in predicting CRBRP fission gas pressures is slightly conservative.

The ENDF/B-IV reference data files do not contain fission yield data for the higher plutonium isotopes, Pu-240, Pu-241 or Pu-242. However, based on published Pu-241 thermal fission yields (Reference 42) compared with the equivalent Pu-239 thermal fission yields, the Pu-241 fast fission yield is expected to be slightly lower than those for Pu-239. Therefore, for calculation purposes, the Pu-241 fission yields have been assumed equivalent to those for Pu-239.

(\*) Evaluated Nuclear Data Files (ENDF/B)

Based on a 90%/10% Pu (239 + 241)/U-238 fission rate split, the weighted average fission gas yield value may be calculated directly from the data presented in Table 4.4-15. The value of the Xe + Kr fission yield in fuel rods resulted equal to 0.249.

For the blanket case, the fuel isotopic composition, and hence, the isotopic fission rate, changes significantly with burnup (plutonium accumulation). For a fresh assembly in either the inner or outer blanket, about 90% of the fissions occur in U-238, and the remaining 10% occur in U-235. Therefore, the beginning-of-life fission gas yield is equal to 0.240.

At end-of-life, just prior to discharge, the breakdown of fissions is as follows: In U-238, 33% for inner and 16% for outer blanket; in U-235, 2% for both inner and outer blankets; in Pu-239, 65% for inner and 82% for outer blanket. Thus, the fission gas yield calculated from data in Table 4.4-15 is 0.247 in inner blanket assemblies at EOL and 0.249 in outer blanket assemblies at EOL.

Conservatively, a nominal fission yield of 0.249 constant throughout life for both fuel and blanket assemblies was adopted.

The isotopic uncertainty in the ENDF/B-IV fission yields results in a  $\pm 3.5\%$  ( $1\sigma$ ) uncertainty in the rare gas (Xe+Kr) yield from U-235, U-238 and Pu-239 fissions. Therefore, the  $2\sigma$  fission yield adopted in plenum pressure calculations was equal to 0.266.

The substantial conservatism in calculating plenum pressures is discussed in Section 4.4.3.2.4, together with a quantitative evaluation of the over-estimation of plenum pressure for two typical blanket rods.

#### 4.4.2.9 Thermal Effects of Operational Transients

Current design practice is that LMFBR components must meet the required conditions of ASME Code Section III (Ref. 43) and RDT Standard C-16-1T (Ref. 44). Transient reactor design events are divided into categories of normal, upset, emergency and faulted according to their likelihood of occurrence. Table 4.4-16 gives: a) the definitions for the various incidents; and b) the allowable severity with respect to structural consequences. Note that the RDT Standard respective terminology for the events are: normal operation, anticipated fault, unlikely fault and extremely unlikely fault.

Table 4.4-17 presents a summary of preliminary design criteria (Limits and Guidelines) for emergency and faulted events to assure that the core operates safely over its design lifetime and meets the requirements of the ASME Code and RDT Standard. The frequency of occurrence and classification of events is established by the designer based on industrial and nuclear experience and also the special characteristics and differences in LMFBR design (as compared with an LWR for example).

Under normal steady state operating conditions, the cladding is loaded due to the internal gas pressure. Fission gases are released from the fuel with burnup, and thus, the internal pressure continually increases over the rod's

lifetime. This pressure produces very slow and small creep deformation of the cladding. In addition to this long term creep effect associated with steady state operations, there are two basic types of transients that could cause dynamic loading of the cladding. All the upset, emergency and faulted events which result in a cladding temperature increase could be categorized into one or the other of these types.

The first type transient results from undercooling or slow overpower events. This type of transient can cause an increase in the cladding temperature. The fill gas (helium) and fission gas in the plenum of the rod may have time to heat up if the transient is of sufficient duration. The resultant gas expansion increases the internal rod pressure, and subsequently, increases the cladding loading. Simultaneously, with the load buildup, the cladding becomes weaker due to its increased temperature. The cladding deformation due to these effects must be factored into structural evaluations of the cladding.

The second type of transient involves fast overpower events. Worst case transients of this type are extremely rapid such that the fuel temperature increases at a much faster rate than the cladding and coolant temperatures. This can cause differential thermal expansion between fuel and cladding which may result in increased fuel/cladding contact pressures. The fission gas in the rod plenum does not have time to heat up and expand as with the first type.

The evaluation of fuel rod damage due to the various design transients over the rod lifetime comes from in-depth structural evaluation of the temperature and other effects such as cladding wastage, irradiation effects and chemical effects between the fuel and cladding. The sequence and/or combination of occurrence of the transients are also considered in the analysis.

A discussion of temperatures that result for several of the most significant anticipated faults is given in the following sections of chapter 15.0:

- o Section 15.1: Accident Analyses.
- o Section 15.2: Reactivity Insertion Design Events and Protective Action;
- o Section 15.3: Undercooling Design Events and Protective Action.

As can be seen, they fall into the two dynamic loading mechanism categories described previously. The ability of the core to meet the design requirements for anticipated faults is discussed in Section 4.2.1.3.

#### 4.4.2.10 Plant Configuration Data

Each core flow path and the total coolant flow within the flow path is presented in Figure 4.4-2. Primary and intermediate loop flows are presented in Table 5.1-1 with the number of loop flow paths designated in Tables 5.1-2 and 5.1-3.

The volume and elevation description of each major plant component is summarized in Table 5.1-2 and 5.1-3, and in Figure 5.1-3 for both the primary and intermediate heat transport systems. For all nominal operations, the flow is single phase (liquid) and turbulent. Equivalent flow path lengths for major plant components are not explicitly summarized; however, the values can be derived from the volumes presented in Table 5.1-2 and 5.1-3, and the flow areas obtained from the component dimensions presented in Sections 5.1.2 and 5.1.3 and Figure 5.1-2. The reactor core flow path lengths are presented in Table 4.2-4. See Section 5.1.8 for physical arrangement.

With the exception of the reactor vessel and primary coolant pumps, the sodium within each component of the primary heat transport system completely occupies the volume of the component during normal operation. In the reactor vessel, the free surface sodium level is nominally maintained at an elevation of 794.75 ft. with a minimum safe operating level of 781.9 ft. These sodium level elevations provide a clearance to the bottom of the reactor vessel head which corresponds to 5.43 ft. and 18.28 ft., respectively, and is occupied by an argon cover gas. The primary sodium pumps are also free surface and are more fully described in Section 5.3.2.3.1. and Figure 5.3-14.

The location, capacity and sizes of all safety related equipment are presented in Section 6.2 for the Reactor Containment, Section 6.2.4 and 7.3.1 for the Reactor Containment Isolation System, Section 6.3 for the Habitability Systems, Section 5.2 for the Reactor Guard Vessel, Section 5.3 for the Guard Vessels of the Primary Heat Transport System major components, Sections 5.6, 7.4.1 and 7.6.3 for the Residual Heat Removal System, and Sections 5.6 and 9.3 and Figure 5.1-7 for the Auxiliary Liquid Metal System. Reactor guard vessel characteristics not explicitly defined elsewhere include a volume of 2800 ft<sup>3</sup>, minimum-maximum elevations of 741.08 ft. and 788 ft., respectively, and a vessel I.D. of 263.5 in.

The steady state full power-full flow pressure and temperature distribution throughout the primary and intermediate systems is presented in Table 5.1-1 and Figure 5.1-1 for the thermal and hydraulic design operating conditions, and in Table 5.3-3 for operating conditions used in structural component evaluations.

The primary pump head flow characteristics and reference operating points are presented in Section 5.3.2.3.1 and 5.3.3.3 and Figures 5.3-19, 5.3-20 and 5.3-21. The primary pump flow coastdown is presented in Figure 5.3-22. The intermediate pumps are identical to the primary pumps with the exceptions noted in Section 5.4.2.3.1 with operating characteristics shown in Figure 5.4-3.

#### 4.4.3 Evaluation

##### 4.4.3.1 Reactor Hydraulics

The total reactor flow rate is one of the primary parameters that affect the thermal performance of the CRBRP. The hydraulic analyses include the effects of uncertainties such as: instrumentation errors, correlation uncertainties, experimental accuracy, manufacturing tolerances and primary loop temperature and flow uncertainties.

The method used to perform the steady-state hydraulic analysis consists essentially of identifying all possible flow paths in the reactor, establishing a hydraulic network and solving the network by use of such codes as CATFISH, HAFMAT and COBRA-WC. Solution of the network will provide reactor flow rate and flow distribution within the reactor for certain specified plant operating conditions, which in the case of the CATFISH code are the pump head/flow characteristics curve. The CATFISH code includes pressure drop analytical correlations obtained from the results of the out of file tests reported in Tables 4.4-36.

The coolant flow distribution is determined by the geometry of the regions through which sodium flows. Their hydraulic resistance establishes the reactor pressure drop and pressure distribution. These paths include inlet and outlet nozzles, inlet and outlet plena, core support structure modules, annulus between radial shielding and core barrel, annulus between vessel and core barrel, annulus between vessel and vessel liner and the core assemblies upper internal structures region. Because of their importance, the resistance and hydraulic characteristics of the main flow paths are determined by scale model tests. The tests conducted for CRBRP are discussed in Section 4.4.4, Testing and Verification. The results from similar tests in the FFTF Development Program are used where applicable. Also see Section 4.4.2.7 for a discussion on hydraulic resistance correlations.

In addition to the main flow path, leakage flow paths exist in the CRBRP; these are taken into account in the flow distribution studies, but no credit is taken for leakage flow when satisfying cooling requirements. Seals between the core support structure and the core inlet module liner, between various parts of the hydraulic balance system, etc., form flow paths for leakage. The design objective of the seals is to minimize leakage. Where possible, the piston ring type seal developed in FFTF will be used and others of different design will be evaluated experimentally with the intent to minimize leakage.



#### 4.4.3.2 Uncertainties Analysis (\*)

##### 4.4.3.2.1 Introduction

The impact of theoretical and experimental analyses uncertainties, instrumentation accuracy, manufacturing tolerances, physical properties and correlations uncertainties must be considered in predicting the reactor thermal-hydraulic performance to ensure the safe and reliable operation of the CRBRP core and to guarantee that proper margins are provided so as not to exceed the design limits and requirements.

Hot channel/spot factors for all core assemblies have been determined to account quantitatively for the above uncertainties. Consistent with previous studies, the semi-statistical hot spot analysis method is used for the CRBRP core assemblies; i.e., random variables are combined statistically and together with the direct bias uncertainties they characterize a hot channel/spot as the one affected by the simultaneous occurrence of all uncertainties. Predicted hot channel/spot temperatures are the ones to be compared with the required limits.

The preliminary uncertainties analysis made certain simplifying assumptions, such as the overall temperature difference is a linear function of individual variables, statistical uncertainties are normally distributed, and a large number of samples are implicit in the data base. The effect of these assumptions have been investigated in a detailed study (Ref. 19) which showed that the overall uncertainty analysis approach adopted in these analyses is conservative. A full evaluation of the adopted uncertainties, of the confidence levels of the hot channel factors and of the effects of non-linear application of the hot channel factors, will be performed for the FSAR.

Use of the semi-statistical method requires the separation of the variables which cause the hot spot temperatures into two principal groups, one of statistical origin and the other non-statistical. The two categories are defined below.

A non-statistical (or direct) uncertainty is defined as a variable, the exact value of which cannot be predicted in advance, but which

---

(\*) The information specified in the Standard Format and Content for Section 4.4.3.2 "Influence of Power Distribution", is included in Section 4.4.3.3 to enable the inclusion of this major area of T&H analysis as Section 4.4.3.2.

is not subject to random occurrence. Computationally, the non-statistical factors represent multipliers applied to the nominal magnitudes of the variables to provide the worst possible values which can be assumed. A variable which has a frequency distribution of occurrence due to its random character is treated statistically. For example, experimental data (such as materials properties) are treated statistically since their evaluation includes some statistical error.

The following briefly illustrates the method of combining hot spot factors (see Figure 4.4-31 for a graphical representation).

The nominal temperature difference  $\Delta T_{j,nom}$  of component  $j$  is increased by the nuclear radial and axial peaking factors to the peak temperature difference  $\Delta T_{j,peak}$  and successively by the direct or non-statistical uncertainties to the temperature difference  $\Delta T_{j,dir}$ . Correspondingly, the nominal temperature  $T_{j,nom}$  will increase to  $T_{j,peak}$  and to  $T_{j,dir}$ , which represents the mean value for the statistical temperature distribution by the variables of random origin; in other words,  $T_{j,dir}$  or  $T_{j,0\sigma}$  will be synonymous.

Finally,  $T_{j,2\sigma}$  or  $T_{j,3\sigma}$  will be determined according to the desired level of confidence.

To avoid any ambiguity in terminology, following is the definition of the terms "average, nominal, peak and hot" as used in the CRBRP core thermofluids analyses.

Average - The average rod is the one with a power generation equal to the total assembly power divided by the number of rods in the assembly. Thus, it may be a fictitious rod, not exactly corresponding to any of the rods in the considered assembly. Temperatures in the average rod are calculated without accounting for any nuclear or engineering hot spot factors.

Nominal - Nominal temperatures are the actual values calculated for the considered rod, without accounting for any nuclear or engineering uncertainty factor. The difference between nominal and average is that the nominal refers to the particular rod investigated, average to a representative fictitious rod.

Peak - The peak rod is the one in the assembly with the highest power generation, i.e., the highest nuclear radial peaking factor. No hot channel/hot spot factors are considered in evaluating peak temperatures.

Hot - The hot (or maximum) rod is the one in the assembly with the maximum cladding midwall temperature; due to the flow distribution in a wire wrapped assembly, generally it does not coincide with

the peak rod. Hot channel/hot spot factors are added to the nuclear peaking factors characteristic of the hot rod. Hot rod temperatures at  $0\sigma$ ,  $2\sigma$ , or  $3\sigma$  are generally quoted, depending on the selected degree of confidence.

Separate groups of hot channel/hot spot factors have been established for calculation of:

- a. Fuel rod temperatures (coolant, cladding, fuel or absorber);
- b. Coolant mixed mean temperature (assembly exit and upper mixing chamber-chimney-exit);
- c. Rod fission gas plenum pressure (plenum temperature, burnup).

The uncertainty factors adopted for the thermal-hydraulic performance predictions of the CRBRP core are presented in Tables 4.4-18 through 4.4-27. For convenience, the factors have been tabulated by assembly type (fuel, inner/radial blanket, control(\*)), intended application (rod temperatures, mixed mean temperatures, plenum pressure calculations), and type (engineering - table numbers with the "A" suffix; nuclear - table numbers with the "B" suffix). Note that  $3\sigma$  statistical values are presented which are the basis for transient and safety analyses. Uncertainties at  $2\sigma$  level are used in calculation of steady state thermal-hydraulic parameters, such as cladding temperature and pressure, which are input to replaceable core assembly lifetime analyses. These factors represent an adaptation to the heterogeneous core configuration of the hot channel factors previously used in the thermal-hydraulic design of the homogeneous core. Thus, primary emphasis was directed to evaluate the nuclear uncertainty factors for the power and burnup histories reported in Section 4.3.2.2.9. The significant features in the application of the nuclear uncertainty factors to the thermal-hydraulic analyses are reported in Section 4.4.3.2.3.

In parallel with the studies reported here, a thorough re-evaluation of uncertainties analyses, their numerical values and methodology of application was performed. This re-evaluation led to a revised set (Ref. 19), which was approved by the CRBRP Project Office in December, 1978. It must, therefore, be emphasized that the performance predictions herein contained are not consistent with the

(\*)Values reported in Tables 4.4-24 through 4.4-27 are the same as used in the analyses of the homogeneous configuration. However, the overall uncertainty factors for the control assemblies in the heterogeneous configuration are not expected to be changed such that existing criteria would be exceeded, due to the similarity of the two designs.

51

uncertainty factors documented in Reference 19, but are actually more conservative. In fact, temperatures calculated using the factors and method of Reference 19 are lower(\*\*) than the values reported in Section 4.4.3.3 which were predicted utilizing the hot channel factors from Tables 4.4-18 through 4.4-23.

The hot channel/spot factors presented here differ from those presented in Reference 19 as follows(\*):

- pellet-cladding eccentricity hot channel factor. Both a direct and statistical component were evaluated in Reference 19 as well as a lifetime dependency, while only a statistical component unchanged throughout life was considered here. Note that the latter is conservative when calculating end-of-life temperatures, which are the ones of utmost importance in steady state analyses, since Reference 19 recommends to consider no end-of-life uncertainty factor, neither direct nor statistical due to pellet-cladding eccentricity:
- inlet flow maldistribution factor. Detailed analyses conducted in Reference 19 recommended a split of this factor into a direct and a statistical component, in lieu of the entirely direct factor adopted here; and again, the latter approach is more conservative;
- subchannel flow area. A re-evaluation of the analyses performed to establish this factor led to a reduction in its value;
- cladding circumferential temperature variation. Recent modifications to the FATHOM-360 code allowed calculation in Reference 19 of individual hot spot factors representing separately the effect of the wire wrap on the film and cladding temperature drop. Previous practice was to consider only one factor to be applied to the temperature difference between the bulk coolant and the radial cladding position considered. Of the two factors reported in Reference 19, the cladding hot spot is less than unity, as it physically should be, since it represents the beneficial effect of circumferential heat transfer through the cladding. The film hot spot, on the other hand,

(\*\*) Calculations for typical fuel, inner blanket and radial blanket assembly hot rods  $2\sigma$ , plant expected conditions at end-of-life showed the present analysis yielding maximum cladding ID temperatures approximately  $54^{\circ}\text{F}$ ,  $25^{\circ}\text{F}$  and  $8^{\circ}\text{F}$ , respectively higher than obtained using Reference 19 uncertainty factors and analytical procedure.

(\*) Comparison between hot spot factors used here and recommended in Ref. 19 are limited to the fuel and blanket assemblies (Table 4.4-18 through 4.4-23).

accounts for the presence of the wire wrap in the channel. The approach recommended in Reference 19 is therefore more adherent to reality than used here, however, the two methods yield the same overall effect on cladding temperature. In fact, the film hot spot factor in Reference 19 is higher than the overall factor reported in Tables 4.4-18.A and 4.4-21.A, which compensates for the less than unity cladding hot spot factor;

- cladding thickness and conductivity. A critical re-evaluation conducted in Reference 19 of the correlation adopted in design, its deviation from experimental data and the effect of irradiation led to the conclusion that the 5% under-estimation directly built in the correlation is more than adequate to account for the irradiation swelling and cladding thickness effects on temperatures and therefore, no hot channel factor is recommended in Reference 19. Again, the present analysis conservatively adopts a 1.12 hot spot factor;
- fissile fuel maldistribution. The value recommended in Reference 19 (1.052) is higher than the value used here (1.03), by a factor of  $\sqrt{3}$ ; this is due to the use of rectangular distribution, rather than normal as adopted in the preliminary hot channel factors assessment;
- reactor  $\Delta T$  and inlet temperature variation. A statistical analysis performed in Reference 19 showed that the value assigned here to the uncertainty factor on  $\Delta T$  is actually inclusive of the inlet temperature variation effect as well. The result of this more refined analysis was not surprising since it was realized that the analysis leading to the values used here was conservative, as discussed in Section 4.4.3.3.1. The loop-to-loop imbalance uncertainty recommended in Reference 19 is 7.4°F, higher than the 4.6°F used here, but this is more than offset by the fact that an inlet temperature uncertainty of 33°F (first core) or 36°F (second core) is adopted here (see Table 4.4-29), while in Reference 19, the inlet temperature uncertainty is included in the  $\Delta T$  factor (1.14), as mentioned above;
- flow distribution calculational uncertainty. There are several differences between the values adopted in this study and those recommended in Reference 19. In the fuel and inner blanket assemblies case, the values used for rod temperature calculations are similar, while the values for plenum temperature calculation adopted in these studies were conservatively assumed to be higher. In the radial blanket case, the values both for rod and plenum temperature calculations, adopted in these studies are lower than recommended in Reference 19.

These discrepancies are attributable to the fact that comparison/calibration/verification of the CØTEC code is an ongoing task as more data become available. For example, since issuance of Reference 19, data have been obtained from the ARD full scale 61-rod blanket heat transfer test in sodium for flow and skewed power conditions prototypic of the radial blanket assemblies. Comparison of experimental data with CØTEC predictions indicated that CØTEC consistently predicts higher temperatures, both at the hot rod maximum cladding temperature axial position and in the unheated plenum region, than obtained in the tests. Preliminary evaluation of this data justify reducing the mal-distribution calculation uncertainty factor for the radial blankets from 1.2 to 1.1, at this time. A similarly conservative approach was taken for the inner blanket; since experimental data for flatter power distributions typical of inner blanket assemblies were not yet available, the higher uncertainty factors were retained in this study, even though every indication exists that they can be significantly reduced.

58 Neither in Reference 19 nor here have results been incorporated from the recently obtained fuel bundle test data from the MIT 61-rod salt-injection in water (Ref. 45), the KFK 61-rod heating in sodium (Ref. 46) and the JOYO 91-rod heating in sodium (Ref. 47). Additionally, the 5:1 air flow tests on a blanket assembly conducted at the Westinghouse Research Laboratory have just been completed, the ARD 61-rod bundle blanket heat transfer test is in progress and the ORNL 61-rod fuel assembly bundle sodium heat transfer test is planned in CY 1979 (see Section 4.4.4.2). As these additional test data are factored into the code calibration, the basis for the statistical component of the flow distribution calculational uncertainty will be improved and, the direct component (simulation bias) will be reduced or eliminated altogether, since the forthcoming data are from larger bundle, more prototypic heated rod experiments in sodium.

In conclusion, as previously mentioned, the overall effect of using the hot channel factors in Tables 4.4-18 through 4.4-23 rather than those recommended in Reference 19 is a more conservative evaluation of the core steady state thermal performance reported in Section 4.4.3.3.

51 Finally, gap and fuel uncertainty factors for fuel temperature calculations are not reported in Reference 19 since steady state fuel temperatures in fuel/blanket rods are no longer calculated through the NICER code (see Section 4.4.2.2) where individual uncertainties on the temperature drop through the gap and fuel are required. They are, however, retained here in Tables 4.4-18.A and 4.4-21.A since they are used as input to safety and transient analyses. Uncertainties on the fuel/gap behavior adopted in power-to-melt analyses, which are consistent with the values recommended in Reference 19, are briefly summarized in Section 4.4.3.2.2; for a quanti-

tative and more detailed discussion see Reference 19 and Section 5 of Reference 3.

A discussion of uncertainties considered in fission gas plenum pressure calculations and how they are conservatively accounted for is reported in Section 4.4.3.2.4.

#### 4.4.3.2.2 Power-to-Melt Uncertainties

The LIFE-III code is used to assure that the no-melting criterion at 115% rated power conditions and  $3\sigma$  level of confidence is actually satisfied. This essentially translates in verifying that the limiting power-to-melt calculated by LIFE-III (which has been calibrated against experimental data such as P-19 (Ref. 37) and P-20 (Ref. 38)) is equal to or greater than the maximum fuel (or blanket) pin linear power rating at  $3\sigma$ , 115% power conditions. Of course, uncertainties must be properly considered in such analysis. The first group are uncertainties in LIFE-III predictions of the power-to-melt arising from data scatter and the overall accuracy of measurements in the EBR-II reactor. They are:

- Uncertainty on overall power level due to variations in EBR-II instrumentation and the uncertainty in the neutronics calculation for a given core loading. This uncertainty causes random fluctuations in quoted power level that vary with time.
- Uncertainty due to a difference between actual and quoted overall EBR-II power that doesn't change with time. It is known that a systematic shift in EBR-II power level exists and a correction is made by experimenters. An estimate is thus required of the uncertainty on this correction. This uncertainty does not show up as scatter in the data, but it is rather a systematic uncertainty which would show up in the scatter of data comparing different reactors (i.e., EBR-II versus CRBRP).
- Uncertainties in the spatial dependence of neutronics calculations and local inhomogeneities in the EBR-II core.
- Uncertainty due to variation in fuel pin fabrication parameters from their nominal values.
- Uncertainty in post-irradiation examination measurements.

A second group of uncertainties covers the extrapolation from the EBR-II data used for LIFE-III calibration to CRBRP conditions. They are:

- Extrapolation from P-19/P-20 to CRBRP conditions.
- Use of fuel in CRBRP with different Pu enrichment (33%) from the 25% enrichment in the experiments used for LIFE-III calibration, specifically change in melting point with Pu content.

Finally, the uncertainties directly dependent on CRBRP operating conditions must be considered; they are:

- Uncertainties due to tolerances and fabrication parameters, i.e., fuel pellet diameter, cladding ID, fuel pellet density.
- Uncertainties on actual rod linear power rating, due to reactor power level, instrumentation and nuclear uncertainties reported in Tables 4.4-18.A and .B, 4.4-21.A and .B.
- All the thermal-hydraulic engineering uncertainties (not already accounted for in power uncertainties) which affect the cladding ID temperature and reported in Tables 4.4-18.A and 4.4-21.A.

As previously mentioned, a detailed quantitative discussion of all the above uncertainties can be found in Reference 19 and in Section 5 of Reference 3, where their application to power-to-melt analyses is also reported.

#### 4.4.3.2.3 Nuclear Uncertainties

The total power or burnup uncertainty is composed of nuclear design methods uncertainties and/or biases (based on comparisons of calculations and measurements of isotopic fission and capture rates and gamma-heating in ZPPR criticals), plus CRBR design uncertainties relating primarily to absolute power normalization and fissile content variations, and a general class of modeling uncertainties. In the fuel, the power uncertainty is broken down into a statistical part which can be combined in quadrature (root-mean square) with other statistical uncertainties, and a non-statistical bias and uncertainty which is applied directly to envelope the upper limits of the peak power density. Due to the limited scope of the available blanket data, only a non-statistical uncertainty is developed. Uncertainties are provided for the fuel, inner and radial blanket assemblies. Where a basis exists, a spatial distribution of the uncertainty is provided (e.g., adjacent to, and removed from the influence of inserted control rods, and by assembly-row in the outer blanket). Otherwise, the uncertainty is developed for the peak power locations and should be assumed to be applicable throughout the region for the stated time-in-life. For a detailed discussion, and definition of all the nuclear power uncertainties and individual factors, see Section 4.3.2.2.9.

Of particular interest to the thermal-hydraulic design is the spatial dependence of the uncertainties. Essentially, they are:

- a. Radial (i.e., adjacent to, and removed from the influence of an inserted control rod; locally dependent bias due to ZPPR-7 flux tilt; and by assembly-row in the outer blanket).



- b. Axial (i.e., at the peak power density near the core mid-plane, and at the core/upper axial blanket interface).

In the case of the radially distributed uncertainties, how and where the uncertainties are to be applied is shown in Tables 4.4-18 through 4.4-23 with the B suffix. The axial uncertainties are a result of the nuclear design calculations and modeling techniques. In particular, the peak and integrated power densities in the fuel are well predicted with the standard two-dimensional synthesis nuclear design techniques, while the "power density at the top of the core" is relatively poorly predicted due to difficulties in simultaneously modeling the behavior in the region while preserving the integral and peak (core midplane) power in two dimensions. In addition, the accuracy of few group diffusion theory is poorer in the presence of the steep flux gradient and in the region of the fuel/upper axial blanket material discontinuity. These factors are reflected in the larger "power density at top of core" uncertainty.

The temperature distribution along the entire fuel rod is necessary for the evaluation of relevant thermal-hydraulic parameters (i.e., fuel temperature, cladding temperature, fission gas generation and release, etc.). As noted above, only two values of the spatially-dependent (in the axial direction) factors are provided. Therefore, it was necessary to make several assumptions and approximations. First, it was assumed that the value of uncertainties at the fuel/upper axial blanket (UAB) interface also apply at the fuel/lower axial blanket (LAB) interface. The actual shape of the axial variation of the heat flux uncertainty from the peak power position to the fuel/UAB and fuel/LAB interfaces is generally not a very critical item since: a) it does not affect the channel enthalpy rise (an uncertainty integrated over the rod length is provided); b) the heat flux is specified at those positions of most interest (i.e., top of the core for cladding temperature calculations, peak power position for fuel temperatures). Thus, the most immediate assumption, i.e., a linear variation in both directions, was assumed. This was also a conservative assumption for plenum pressure calculations, as discussed in Section 4.4.3.2.7. In power-to-melt calculations, however, it was discovered that due to the effect of cladding swelling, which is extremely sensitive to the cladding temperature value, the fuel could be closest to melting not at a location corresponding to the peak power position. A more realistic definition of the heat flux uncertainty axial shape was therefore necessary. An inverted chopped cosine curve fitting the heat flux uncertainties at the peak power and interfaces positions was therefore adopted in predicting the axial profiles of rod temperature necessary as input to power-to-melt evaluations. For both assumed distributions, linear and inverted chopped cosine, the local values of the heat flux factor are routinely calculated by NICER.

Finally, the uncertainties at the fuel/UAB and fuel/LAB interfaces were assumed constant over the respective axial blankets. This assumption, adopted for simplicity in the absence of an uncertainty analysis of the axial blankets, is not seen to be critical, since the power generated in the axial blankets is between 1% and 3% of the total rod power depending on the considered time in life.

#### 4.4.3.2.4 Plenum Pressure Uncertainties

The fission gas plenum pressure in CRBR fuel and blanket rods is calculated from the perfect gas law:

$$p = \frac{nRT}{V} \quad (4.4.3.2-1)$$

The physical parameters affecting the pressure value are, therefore(\*):

- Fission gas generation, which depends on the rod burnup;
- Fission gas yield, which depends on the type of atom fissioned;
- Fission gas release to the plenum, which depends on the rod burnup, linear power rating and temperature;
- Plenum temperature; and
- Plenum volume.

Uncertainties on the above parameters are accounted for as follows:

- Uncertainties on burnup (see Tables 4.4-20 and 4.4-23;  $2\sigma$  level of confidence is adopted for performance calculations reported in Section 4.4.3.3.4);
- The adopted value for the fission gas yield, regardless of the fissioned atom, is 0.266. Recommended (Ref. 18) values are: 0.255 for U-235, 0.238 for U-238 and 0.250 for Pu-239 (see Table 4.4-15);
- A comparison between fission gas release predictions and experimental data from EBR-II irradiation experiments was performed for the fuel assemblies and the  $+2\sigma$  release correlation was adopted in the analyses as discussed in Section 4.4.2.8.16. In the blanket case, since no pertinent experimental data are available, nominal fission gas release predictions from the fuel assemblies calibrated model were increased by 15%;

(\*) Discussed here is only the component due to fission gases, which is by far overwhelming, especially at EOL. The pressure component due to initial gases is computed separately and added to the fission gas component to yield the total plenum pressure.

- Uncertainties on plenum temperature ( $2\sigma$  level of confidence is adopted - see Tables 4.4-20 and 4.4-23); and
- Minimum plenum volume was adopted in the calculations.

It is evident from the above that while the resulting fission gas pressure is labeled as " $2\sigma$ ", in reality, the level of confidence is much higher. In fact,  $2\sigma$  uncertainties on the various parameters are superimposed on each other; the uncertainty on the plenum volume is a bounding value rather than a  $2\sigma$ ; and, the adopted uncertainty on fission gas yield is much higher for U-238 and Pu-239 than for U-235 (which is only a small fraction of the fuel, even more so at EOL when the plenum pressure value is most important). Predictions of fission gas plenum pressure have additional conservatism in the blanket assemblies case since: a) the same release model as for the fuel assemblies is assumed, which is by preliminary indications conservative; b) the release so calculated is multiplied by a 1.15 factor, thus very closely approaching 100% release. Assumption of a linear, rather than inverted chopped cosine heat flux uncertainty distribution (which affects the fuel temperature, hence the gas release) as discussed in Section 4.4.3.2.3 is also conservative, since it tends to increase the fuel temperature and gas release in the central region of the rod where most of the gases are released.

A more proper and realistic way of calculating the  $2\sigma$  plenum pressure would be to individually vary each of the affecting parameters by the corresponding  $2\sigma$  level of uncertainty and calculate the induced change in plenum pressure. Adding the root-mean square of the various changes in plenum pressure to the  $0\sigma$  value will yield the true  $2\sigma$  value of the fission gas pressure. This calculation was performed for the hot pin in inner blanket assembly #99 and radial blanket assembly #201 at end-of-life (EOC4) to quantify the margin of conservatism implicit in the current evaluation of plenum pressure. Factored in this analysis were also the very recently obtained fission gas release data from WBA-20 (the first fission gas release data for blanket assemblies) which indicated a very substantial over-estimation of fission gas release by the present high burnup fuel calibrated LIFE-III code model. It was found that for the inner blanket rod using the r.m.s. method, the calculated  $2\sigma$  total plenum pressure was 175 psi, while the value used in design by accounting simultaneously for all uncertainties was 249 psi. For the radial blanket pin, the calculated  $2\sigma$  pressure was 188 psi versus a design adopted value of 273 psi. For comparison, the total plenum pressure assuming 100% fission gas release and simultaneously accounting for all the other uncertainties was 264 psi for the inner blanket and 310 psi for the radial blanket. Thus, the design adopted value is quite comparable with the 100% release value, a direct consequence of the over-prediction of the fission gas release model and the additional 15% increase. The above examples therefore show quite clearly the large amount of conservatism implicit in the plenum pressure values used throughout these analyses.

#### 4.4.3.3 Steady-State Performance Predictions

Reported in this section are the analyses performed to characterize the steady-state thermal behavior of the CRBRP core together with highlights of the results. For a much more detailed report of the results, see Sections 4 and 5 of Reference 3.

##### 4.4.3.3.1 Plant Conditions

Two sets of plant conditions are used in the thermal-hydraulic design, i.e., plant thermal-hydraulic design value (THDV) conditions and plant expected operating conditions (PEOC). The THDV conditions (730°F inlet/995°F outlet temperature; total reactor flow  $41.446 \times 10^6$  lb/hr) are the Clinch River rated plant conditions and are used in: a) analyzing permanent components which have the same 30-year lifetime as the plant; b) transient and safety analyses, since they are more conservative than the plant expected conditions and represent the "worst bound" of plant conditions. The plant expected operating conditions represent the plant conditions at which the CRBR is expected to operate accounting for the operating conditions of the heat transport systems, such as pump characteristics, reactor and primary loop pressure drop uncertainties, fouling and plugging of heat exchangers, etc. During actual reactor operation, the long-term damage accumulated by the fuel and blanket assembly components is expected to correspond to the damage which would be calculated using time averaged nominal temperatures. However, in assessing the effects of steady-state operation and anticipated faults (normal and upset conditions), fuel and blanket assembly component temperatures are based on maximum expected plant operating conditions (PEOC) and upper  $2\sigma$  levels. At this level, there is a 97.5% probability that the corresponding temperatures are not exceeded. This is conservative since the calculated damage accumulation generally increases with temperature. For the unlikely and extremely unlikely events (emergency and faulted conditions) an upper limit on plant conditions (Thermal Hydraulic Design Values - THDV) and the upper  $3\sigma$  uncertainty level is used, simply to add additional conservatism for the safety analyses. At this level, the probability of exceeding the calculated temperature is  $\sim 0.1\%$ .

The above designated use of plant conditions and uncertainties derives from the premise that stochastic failures are not a safety issue and the plant is capable of operation with limited fuel rod cladding failures. To support safe operation with failed fuel, all the safety analyses described in Chapter 15 of this PSAR are based on continued and extended plant operation with 1% failed fuel.

The primary heat transport system principal parameters (inlet, outlet temperature and  $\Delta T$ ) are evaluated, together with the associated uncertainties. The results of this study for the heterogeneous core, which comprised a Monte Carlo type analysis, are reported in Table 4.4-28. Some significant features are: 1) the consideration of the progressive fouling of the heat exchangers during the plant 30-year lifetime, which affects the predicted values of the plant operating conditions (rather than conservatively assuming end-of-life fouling, i.e., after thirty years operation); and 2) a comprehensive accounting of all uncertainties affecting plant operation. Plant expected operating conditions are adopted in core thermofluids analyses of replaceable components, such as the core assemblies, chiefly in determining the fuel rod parameters (cladding temperature, fission gas pressure) which are the basis for

evaluating the structural behavior and for assessing whether lifetime/burnup objectives are actually met.

Plant expected operating conditions and associated uncertainties adopted in the thermal performance analyses are reported in Table 4.4-29. Following is a brief discussion of the rationale in determining the values reported in Table 4.4-29 from the ones in Table 4.4-28.

First, the mean values of Table 4.4-28 are chosen as the nominal values of Table 4.4-29, thus, conservatively including the bias factor directly into the nominal values. Since the most critical time for core

assemblies is at the end-of-life, when cladding strain and damage function are maximum, second core values have been selected as corresponding to four-year fouling conditions. Due to the fact that four-year fouling conditions were not evaluated, it was assumed that the same difference in plant parameters between year two and year zero repeats between year four and year two. Again, the selected approach is conservative for two reasons: 1) plant conditions have been considered constant over the two-year span and equal to the worst end-of-span conditions, thus neglecting the more favorable conditions which exist throughout the core lifetime; and 2) the effect of fouling is not linear with time, but it is rather pronounced at the beginning and then tapers off during the plant lifetime, as can be seen by comparing plant parameters in Table 4.4-28 for 0, 2, and 30 years. Thus, the assumption that the same degradation of plant conditions which occurs in the first two years (first core) also occurs during the third and fourth year (second core) is conservative.

While the mean values of plant parameters are consistent (i.e., outlet temperature equals inlet temperature plus  $\Delta T$ ), the same is not true when uncertainties are included. In fact, uncertainties quoted in Table 4.4-28 are for each parameter independently; thus if the inlet temperature and the  $\Delta T$  at the 97.7 confidence level (e.g., for the two year fouling) are added, the outlet temperature is equal to 999°F, significantly higher than the 976°F reported. Actually, 976°F represents the  $2\sigma$  outlet temperature, while 999°F is, roughly, a  $4\sigma$  value.

Because the inlet temperature and  $\Delta T$  are defined, while the outlet temperature is derived, the following procedure is used:

- The uncertainty in the  $\Delta T$  is calculated as a dimensionless factor and is combined statistically with other engineering and nuclear uncertainties.
- The uncertainty on the inlet temperature (which is due to all effects related to plant operating conditions) is combined statistically with the loop-to-loop imbalance effect and the combined uncertainty is directly added to the nominal value. The loop-to-loop imbalance effect was evaluated from experimental data obtained in the CRBR inlet plenum feature test conducted at HEDL where different values were obtained for each inlet module ranging from practically zero near the reactor center to a maximum value of 4.6°F at the core periphery (see Section 4.4.2.4.1). Because such variation was minimal, compared with the much greater plant uncertainty with which the imbalance effect is combined, for simplicity the maximum value is conservatively used for all assemblies.

This approach is still conservative, since the loop-to-loop imbalance effect is much smaller than the inlet temperature uncertainty. Therefore, if there were no other uncertainties, the outlet temperature would be at approximately the  $4\sigma$  level, as previously mentioned. However, other uncertainties, engineering and nuclear, do affect the reactor  $\Delta T$ , and therefore, when combined statistically with the plant conditions uncertainty on  $\Delta T$ , will actually decrease its effective value.

Finally with regard to the uncertainties on plant operation conditions reported in Table 4.4-29, it must be noted that the power level measurement/control dead band uncertainty (which is used for THDV conditions) is not considered as a separate hot channel factor, since it is already included in the Monte Carlo evaluation of plant operating conditions uncertainties.

#### 4.4.3.3.2 Linear Power

55 | Linear power ratings over a  $60^\circ$  core sector (fuel, inner and outer blanket assemblies) have been calculated at beginning and end of each of the initial five years of operation. Complete results are reported in Section 4 of Reference 3. As an example, core-wide linear power mappings at beginning-of-cycle 1 (when the maximum fuel linear power is attained - 15.8 kw/ft in assemblies 101 and 68) and at end-of-cycle 4 (maximum value in inner blanket-20.6 kw/ft in assembly 99) are reported in Figures 4.4-32 and 4.4-33, respectively.

Average, peak,  $3\sigma$  and  $3\sigma$  plus overpower linear ratings are reported. To clarify the adopted nomenclature, "average" represents an arithmetic average over the 217 (61) rods of the fuel (inner/outer blanket) assembly. Therefore, it generally represents a fictitious rod not exactly corresponding to any physical rod in the assembly. "Peak" refers to the rod in the assembly having the highest power; i.e., no uncertainty factors are applied in the evaluation of the peak power rating. " $3\sigma$ " power rating refers to the value resulting from applying to the peak rod both the uncertainties on the nuclear peaking factors (radial and axial) and the engineering uncertainty factors, both at the  $3\sigma$  level of confidence. The " $3\sigma$  plus overpower" values are derived from the  $3\sigma$  linear power ratings by applying an additional 15% over the CRBR rated nominal full (975Mwt) power.

#### 4.4.3.3.3 Assemblies Mixed Mean Temperatures

51 | Assemblies mixed mean temperatures were calculated for beginning and end of each of the first four (five for second row radial blanket assemblies) cycles. Typical examples are reported in Figure 4.4-34 (beginning-of-cycle 1) and 4.4-35 (end-of-cycle 4). Plant THDV condi-

tions were adopted since calculated values of the mixed mean temperatures, specifically maximum temperatures and temperature gradients between adjacent assemblies, are an important input to the upper internals structure design.

Nominal (no uncertainty factors applied),  $0\sigma$  (only direct uncertainty factors are applied),  $2\sigma$  and  $3\sigma$  (direct plus statistical uncertainty factors at the  $2\sigma$  and  $3\sigma$  level of confidence are applied) are reported in Figures 4.4-34 and 4.4-35.

First core conditions are the worst for the UIS from the point-of-view of both maximum temperatures and temperature gradients. The maximum temperature(\*) is  $1123^{\circ}\text{F}$  in assembly 45 at BOC1, with a maximum gradient ( $273^{\circ}\text{F}$ ) between assembly 52 and 302. Mixed mean temperatures follow the same lifetime pattern as the power generation, thus, inner blanket assemblies which start very cold at beginning-of-life ( $\sim 850^{\circ}\text{F}$  at BOC1) attain temperatures comparable with those of the fuel assemblies at EOC2. The same pattern repeats in the second core, cycles 3 and 4. The radial blanket assemblies start at approximately the same temperature as the inner blanket at BOC1, but it is not until cycle 4 or 5, which is the end of their life, that their temperatures are comparable with those of other assemblies. The maximum mixed mean temperature for the second core occurs at BOC3 in assembly 45 ( $1115^{\circ}\text{F}$ ). While first and second cores are quite similar in terms of maximum mixed mean temperature, they show a markedly different behavior as far as maximum gradients are concerned. During the first core, the maximum temperature difference between adjacent assemblies occurs at the fuel/radial blanket interface: in cycle 1 between assemblies 52 and 302 ( $273^{\circ}\text{F}$  at BOC1,  $225^{\circ}\text{F}$  at EOC1), in cycle 2 between assemblies 24 and 202 ( $227^{\circ}\text{F}$  at BOC2,  $163^{\circ}\text{F}$  at EOC2). In the second core, the maximum gradient position moves to the fuel/inner blanket interface: between assemblies 37 and 99 at BOC3 ( $239^{\circ}\text{F}$ ), assemblies 2 and 128 at EOC3 ( $136^{\circ}\text{F}$ ), assemblies 4 and 62 at BOC4 ( $149^{\circ}\text{F}$ ). At end-of-cycle 4, the mixed mean temperatures of fuel and inner blanket assemblies are quite close, so that the maximum gradient occurs between two radial blanket assemblies, i.e., assemblies 206 and 213 ( $96^{\circ}\text{F}$ ).

Mixed mean temperatures reported in this section are calculated assuming adiabatic boundaries at the assemblies interface. Thus, the beneficial effect of inter-assembly heat transfer in flattening the high temperature gradients is not taken into account.

Mixed mean temperatures accounting for inter-assembly heat transfer are calculated by TRITON. Core-wide TRITON calculations were performed for BOC1 and EOC4, as reported in Section 4.4.3.3.5. A comparison of mixed mean temperatures under adiabatic conditions and more realistically accounting for inter-assembly heat transfer (Figures 4.4-51 and 4.4-52) is discussed in that section.

(\*) All temperature values reported in this discussion are nominal.



#### 4.4.3.3.4 Rod Lifetime Cladding Temperature/Pressure Histories

All fuel, inner blanket and outer blanket assemblies in a 60° core symmetry sector were followed during their lifetime (i.e., first and second cores for fuel and inner blanket assemblies; row 1 outer blanket assemblies over cycles 1 through 4 and row 2 radial blanket assemblies over cycles 1 through 5). The maximum cladding temperature and fission gas pressure in the hot rod at the 2σ level of confidence for plant expected operating conditions were predicted for each assembly. Lifetime profiles for all the limiting assemblies are reported in Section 4 of Reference 3. Typical examples are shown here in Figures 4.4-36 through 4.4-44. The following combinations are possible in orificing zone 6, where fuel and inner blanket assemblies are alternating: inner blanket assembly remaining in the same location in the first two cycles (e.g., #98, Figure 4.4-40), inner blanket assembly in the odd cycle followed by a fuel assembly in the even cycle (e.g., #62, cycles 3 and 4, Figure 4.4-41). As a general trend, fuel assemblies in the inner region of the core (see, e.g., Figure 4.4-38), experience a cladding temperature jump from the odd to the even cycle, while the fuel assemblies in the outer region (see, e.g., Figure 4.4-39), experience a drop. The fuel cladding temperature generally decreases during a given cycle. The cladding temperature, however, increases during the even cycle (see, e.g., Figure 4.4-36) in those fuel assemblies adjacent to the Row 7 corner control assemblies. Blanket assemblies obviously have a continuously increasing temperature during their lifetime, a direct consequence of the increase in power. The lifetime behavior of a given assembly during the first and second cores is quite similar, both qualitatively and quantitatively. The only major difference is that a higher fission gas pressure is attained in the second core, due to the longer residence time and burnup.

As an overall summary, the highest cladding ID temperature attained in each assembly in the first and second core is reported in Figures 4.4-45 and 4.4-46, respectively, together with the time of occurrence. As shown in the figures, the maximum cladding temperature varies significantly from assembly to assembly, a direct consequence of the orificing philosophy, where assemblies were orificed to satisfy burnup/lifetime goals and transient limitations, rather than equalizing cladding temperature. It can be noted for example that fuel assemblies in the inner core region, which are CDF limited, require lower temperatures than assemblies in the outer region, which are transient limited. Blanket assemblies, when starting from the same steady state temperature, attain a higher transient temperature than fuel assemblies. Thus, the steady state maximum cladding temperature in blanket assemblies is lower than for the transient limited fuel assemblies, a direct reflection of the adoption of the same transient limit for all core assemblies.

Structural analyses performed utilizing the core assemblies thermal performance data reported here verified that indeed the burnup/lifetime goals are satisfied in all assemblies during the first and

second cores.

Similarly, transient analyses were performed for the worst assemblies, starting from the steady state conditions reported here, and the transient limitations are met.

#### 4.4.3.3.5 Core Assemblies Duct Temperatures

Detailed three-dimensional duct temperature distributions (axially, radially and circumferentially) were predicted in support of the core restraint design and related (duct bowing, dilation, reactivity coefficient) analyses. A 60° core symmetry sector was analyzed at plant THDV conditions at BOC1 and EOC4, thus bracketing the entire lifetime considered.

The current version of the TRITON code which models a cluster of seven adjacent assemblies was used. The outer boundaries of the cluster are assumed to be adiabatic, while heat is transferred across the internal interfaces (i.e., ducts and interstitial sodium flow gap). The CRBRP core 60° symmetry sector, plus one row of assemblies at each of the boundaries to provide the necessary boundary conditions to the assemblies within the sector, was analyzed in groups of seven assemblies at one time and changing each time to a different central assembly, which is "dumped" to output. The TRITON model, based on the subchannel analysis code COTEC, explicitly solves the thermal-hydraulics of wire wrapped assemblies (by considering turbulent mixing, sweeping, pumping and swirl flow). In addition, it accounts for the exchange of heat between adjacent assemblies. The code is able to model all types of core assemblies, including the radial shield, which were analyzed to provide the proper boundary to the second row radial blanket assemblies.

55 | Gamma-heating in the ducts is considered in TRITON by including it in the total assembly power. For the control assemblies case, the gamma-heating is split between the absorber bundle and the bypass. Therefore gamma-heating is accounted for in a global fashion when calculating duct temperatures, rather than as a localized effect.

51 | Typical results of duct temperatures calculated by TRITON under nominal conditions are reported in Figures 4.4-47 through 4.4-50. Much more comprehensive results can be found in Section 4 of Reference 3. Midwall duct temperatures reported for each face are the average over the face of the detailed temperature profile calculated by TRITON (TRITON calculates local duct temperatures circumferentially along the face at each peripheral subchannel). In addition, the direction (with arrow) and magnitude of the maximum cross-duct (midwall) temperature gradient in each assembly is shown. Generally, the largest gradients occur at the fuel/radial blanket interface, which is therefore a very critical region for the core restraint design. The typical mappings shown here

are for two axial elevations; i.e., 60" (approximately the above-core load-pad location) and 112" (top of the rod bundle). TRITON calculates core-wide duct temperatures at 0.5" intervals and all these data were transmitted, via computer tapes, to the core restraint designers.

Calculations of assemblies mixed mean temperatures have also been performed by TRITON; the results are reported in Figures 4.4-51 and 4.4-52 for BOC1 and EOC4, respectively, which compare TRITON calculated temperatures with the corresponding temperatures obtained for adiabatic conditions in Section 4.4.3.3.3 (and reported in Figures 4.4-34 and 4.4-35), thus showing the effect of inter-assembly heat transfer. As expected at BOC1 where the fuel assemblies have the maximum power in life and the blanket assemblies the minimum, heat is transferred from the fuel to the blanket assemblies and mixed mean temperatures are higher in the blanket and lower in the fuel than otherwise calculated under adiabatic conditions. The maximum temperature difference between adjacent assemblies, which occurred between assemblies 52 and 302 was 273°F under adiabatic conditions and is reduced to 261°F when considering inter-assembly heat transfer, a reduction of ~4%. Reductions in adjacent assemblies gradients are greatest at the core center (where the power production in the fuel is maximum); for example, between assemblies 34 and 59, the gradient of 227°F calculated under adiabatic conditions, is reduced by ~10% to 205°F when accounting for inter-assembly heat transfer. It should also be pointed out that the coolant does not exit from the assembly with a uniform temperature equal to the mixed mean, but a radial temperature gradient exists within the assembly exit. TRITON divides the assembly exit area into 6 sectors and calculates the local temperature in each of these sectors; thus, this detailed information is available to the structural designers for refined analyses.

#### 4.4.3.3.6 Power-to-Melt Analyses

Analyses for the worst fuel and blanket assemblies were performed to assure that the criterion of no-incipient melting at 115% rated power and accounting for uncertainties at the 3 $\sigma$  level of confidence is actually met. These are reported in Section 5 of Reference 3, while the principal results are summarized here. Fuel assemblies 101 and 14 were investigated using the LIFE-III code. Assembly 101 was selected as the one with the maximum power rating at 3 $\sigma$  overpower condition, while assembly 14 has the highest peak power pin (see Figure 4.4-32). The programmed startup used in these studies is shown in Figure 4.4-53. Since BOL is the time when the power is maximum, and since the power decreases with life due to the depletion effects, power-to-melt analyses for the fuel assemblies were not conducted beyond the programmed startup.

51 The LIFE-III code used in this study has been calibrated and verified primarily against the HEDL P-19 (Ref. 37) and P-20 (Ref. 38)

tests, in addition to a number of intermediate and high burnup pins. In fact, P-19 and P-20 conditions are most representative of actual CRBRP fuel operating conditions at beginning-of-life. Table 4.4-30 shows the very good agreement of LIFE-III predictions with P-19 and P-20 data.

The results of these power-to-melt analyses are summarized in Table 4.4-31. Satisfaction of the no-melting criterion requires that, throughout life, the fuel linear power rating is at least three standard deviations below melting power, when the reactor power is 15% above nominal conditions, i.e.:

$$K * REPOW(t) \leq \overline{REPOW_M}(t) - 3\sigma_{REPOW_M}(t) \quad (4.4.3.3-1)$$

where  $REPOW(t)$  is the steady state reactor power as a function of time:

$\overline{REPOW_M}(t)$  is the mean reactor power-to-melt for the considered pin (at nominal or  $0\sigma$  conditions) as a function of time;

$\sigma_{REPOW_M}(t)$  is the standard deviation about the mean  $\overline{REPOW_M}$ ;

K is the overpower factor.

If nominal conditions are used as the pin operating conditions in determining  $\overline{REPOW_M}$ , it is  $K = 1.15$ . However, if the pin is analyzed at  $0\sigma$ , i.e., the uncertainty on reactor power level (1.03, see Table 4.4-18.A) is already accounted for in the operating conditions representing the starting point for power-to-melt analysis, as in the present case, K is then equal to  $1.15/1.03$ , in order not to consider the 1.03 factor twice.

As shown by Table 4.4-31, substantial margin exists. When full power is first reached (108 hrs.), greater than 6% margin occurs. This is the time when the margin is the least; in fact, analyses performed at 158 hrs. indicated 20% increase in power-to-melt margin over the value at 108 hrs. A programmed startup for the fuel rods can thus be identified which ensures that the no-melting criterion can be satisfied. The programmed startup used was not an optimum one and further work will be performed in this area for FSAR analyses. An experimental program has been identified to characterize the startup procedure, namely duration of initial period during which power is held below the rated level and magnitude of the hold power as percentage of the rated full power, as well as to determine the corresponding power-to-melt. This program will help in defining the optimum startup procedure to be recommended for CRBRP.

For the blanket assemblies, inner blanket assembly 99 was investigated as the blanket assembly having the highest power in the first five years of CRBRP operation. Assembly 99 reaches its maximum power in the second core, at end-of-cycle 4 (see Figure 4.4-33). Inner blanket assemblies envelope with respect to power-to-melt conditions the longer residence time radial blanket assemblies.

Both the hot and the peak rods were investigated, since the peak pin has the highest linear power, while the hot pin has the highest cladding temperature. The cladding temperature has, in fact, a very significant effect on cladding swelling, hence on fuel/cladding gap size, hence gap conductance, fuel temperature and finally on power-to-melt. Thus, both the hot pin and the peak pin need to be investigated. Analysis of the hot pin was obviously not necessary for the fuel assemblies, since their critical time in life is at beginning-of-life, rather than end-of-life as for the blanket assemblies. Finally because the maximum power in blanket assemblies occur at end-of-life, the programmed start-up cannot affect the power-to-melt in the blanket.

The axial positions where the cladding temperature and the linear power rating are maximum were investigated in addition to intermediate positions between the two above. Also considered were: a) when the blanket pins go through a full overpower factor of 1.15 at EOL; and b) when the reactor power is increased to 115% of rated power from the top of the allowed variation, i.e., with an overpower factor of 1.15/1.03.

It was found that the no-melting criterion is fully satisfied in the worst case. The peak pin has 0.4% less margin than the hot pin. When the overpower excursion is a full 15% the margin is 0.4% less than for the case when the reactor power is ramped from 1.03% of the rated power. Substantial conservatism was implicit in the analyses (e.g., in cladding swelling evaluation, adopting a direct combination of nuclear uncertainties), thus, removal of the implicit conservatism and factoring of experimental data when available, would substantially improve the power-to-melt margin.

#### 4.4.3.3.7 Control Assemblies Thermal-Hydraulic Performance

The CRBRP has two control systems: primary and secondary control rod system (PCRS and SCRS) with nine (9) and six (6) control assemblies, respectively. Detailed design features of the systems are provided in Section 4.2.3 (Reactivity Control Systems).

The bases and methodology of the thermal-hydraulic analysis of the primary control assemblies followed that used in the homogeneous core design, reported in Reference 13. A summary of the principal operating parameter for the primary and secondary control assemblies are presented in Tables 4.4-32a and 4.4-32b, respectively. Values reported in Table 4.4-32 are for the row 7 corner assembly, which is the thermally limiting PCA.

Key hydraulic performance assessments relate to the assembly flow margin to control rod flotation and control rod scram dynamics. The PCA E-Spec. requires that the control assembly design shall assure that the control rod cannot be lifted (or floated) from the fully inserted position, under maximum assembly flowrate (and pressure drop) conditions, more than the distance causing a reduction in shutdown reactivity margin equal to the stuck rod

margin. This requirement shall apply to all 9 rods, either with the driveline connected to the control rod or to refueling conditions for which the driveline is disconnected and withdrawn to its refueling position.

Both experimental and analytical investigations were conducted to assure the PCA will not float under the worst possible conditions; the results of these investigations are summarized in Table 4.4-33. Data, analytical results and margin-to-flotation were expressed in terms of both assembly flowrate and pressure drop across the absorber bundle. Prototypic testing of the CRBR PCA provided experimental measurements of the PCA flotation characteristics; experimental uncertainties were directly superimposed over the observed values. On the other hand, the maximum flow through the PCA was calculated with the CATFISH code accounting for all the various effects causing a flow variation in the PCA. Specifically, the hydraulic resistance uncertainties in all core components were varied by their maximum value and, conservatively, the absolute variation in the PCA flow and  $\Delta P$  was taken as increasing the design value. The three leading causes for an increase in the PCA flow were found to be: primary pumps at their maximum speed resulting in a maximum reactor flow equal to 115% of the rated THDV value; PCA orifice resistance at its minimum; and LIM containing the PCA at its minimum resistance allowable.

As reported in Table 4.4-33, the individually induced variations in the PCA flowrate and  $\Delta P$  were combined at various levels of conservatism, ranging from 2 $\sigma$  and root sum of the squares to 3 $\sigma$  and absolute sum combination. Correspondingly, the flotation margin ranged from 15% to 3% in terms of  $\Delta P$  and from 9.5% to 5.5% in terms of flowrate. In all cases a large amount of conservatism was included, for example: a) by comparing the minimum experimental with the maximum predicted flotation characteristics, analytical and experimental uncertainties were superimposed rather than combined statistically; b) use of absolute rather than relative values of the PCA flow (and  $\Delta P$ ) variations does not take into account the variations causing decrease, rather than increase of the PCA flowrate and  $\Delta P$ . In spite of this conservatism, a positive margin to flotation resulted under the worst conditions, as shown in Table 4.4-33.

The secondary control rod system uses the concept of hydraulic scram-assist design with a net hydraulic force in the 150-250 lbs. range on the control rod when fully withdrawn from the core. The same magnitude of downward hydraulic force (in addition to the weight of the assembly) is also available under the abovementioned design conditions. Thus, it is concluded that the secondary control rods do not float at 100% flow (even when disconnected).

Predicted control rod scram performance of the primary control rod system is reported in Section 4.2.3 (Reactivity Control Systems).

Figures 4.4-54 and 4.4-55 show typical PCA absorber region temperature distributions under the minimum withdrawal and full withdrawal control rod conditions, respectively.

Figure 4.4-55a shows the maximum SGA absorber region axial temperature distributions at fully withdrawn position under the THDV conditions. The maximum absorber centerline temperatures were calculated based on the required 115% overpower with design uncertainties at 3 $\sigma$  confidence level. The highest absorber pin centerline temperature calculated in SCA is 1500°F.

#### 4.4.3.3.8 RRS Thermal-Hydraulic Analyses

The steady-state duct temperatures at PEOV conditions were calculated for a 30° sector of the RRS.

The region analyzed is partially shown in Figure 4.4-56. The model consists of all 29 RRSA's in a 30° sector, plus a corresponding section of fixed radial shielding (FRS), core barrel (CB) and core barrel/reactor vessel annulus (CB/RVA).

Radial blanket boundary temperatures were obtained from TRITON analyses summarized in Section 4.4.3.3.5. Assembly interstitial flow was conservatively not modeled.

58 | There are two orificing zones in the RRS, with the zone arrangement and nominal flow rates shown in Figure 4.4-56. This zoning utilizes 1.3% of reactor flow for the RRS.

The analyses showed that the highest RRS duct temperatures and cross duct temperature gradients occur when the outer row radial blanket boundary is at end-of-life conditions with plus  $2\sigma$  uncertainties on radial blanket temperatures.

58 | Uncertainties in RRS temperatures are given in Table 4.4-34. Results of the analysis at core midplane, ACLP and TLP at EOC5 with  $+2\sigma$  uncertainties applied to RRS input data are shown in Figures 4.4-57 through 4.4-59. The maximum RRS duct midwall temperature is 1052°F and occurs at the TLP at a RRS duct wall adjacent to a radial blanket assembly.

58 | Results of the analysis at EOC5 with  $-2\sigma$  uncertainties applied to RRS input data are shown in Figures 4.4-60 through 4.4-62. The maximum RRS cross-duct  $\Delta T$  is 207°F and occurs at the TLP for a first row RRS.

#### 4.4.3.4 Analytical Techniques

The reactor design presented in this PSAR represents the latest in a series of design iterations performed to optimize the CRBR design. Computerized techniques have been developed to expeditiously supply the information needs of design and analysis groups. The step-by-step flow of core thermal-hydraulic information and the computer codes used for the routine analyses in each step are outlined in Figures 4.4-63 and 4.4-64.

A brief description of the main features of the computer codes used in thermal-hydraulic analyses is presented in Appendix A. A comprehensive discussion of the analytical techniques used in evaluating the core thermal-hydraulics follows.

##### 4.4.3.4.1 Fuel and Blanket Assemblies

The fuel and blanket assemblies thermal-hydraulic performance



predictions begin with the determination of the optimum orificing scheme using the OCTOPUS code, as discussed in Section 4.4.2.5.

The OCTOPUS code determines the optimum flow distribution among orificing zones in the core of a reactor. The optimization is based on establishing the minimum possible flow rate in each orificing zone that does not cause the maximum cladding temperature in that zone to exceed a specified temperature limit (i.e., the most restrictive of the temperature constraints: SELT, DELT, TELT, see Section 4.4.2.5.1) while simultaneously minimizing the gradient between the outlet mixed mean coolant temperature of each flow zone. The first part of the solution is achieved through characterizing each core assembly, for which input is supplied by a subchannel analysis code (e.g., COTEC). By this means, the code can handle the proper axial power distributions in the assemblies and also indirectly account for the effects of interchannel heat and mass transfer on the coolant and cladding temperatures. Minimization of the outlet temperature gradients is obtained through the use of a least-squares optimization method on the exit coolant temperature utilizing previously calculated results. Grouping of the assemblies in a given number of orificing zones is done by choosing among all the various possible combinations the one yielding the minimum value of total core flow, thereby assuring optimum utilization of the allocated flow.

58 | Using the required flow ratios among orificing zones determined through OCTOPUS as input condition to be satisfied, the CATFISH code determines the individual assemblies flow by considering all the parallel flow paths in the reactor and the pump head as boundary condition. The effect of the LIM, which causes assemblies belonging to the same orificing zone, but to different LIMs to have slightly different flow rates, as discussed in Section 4.4.2.7.1, is properly accounted for. CATFISH thus calculates the orificing resistance required to yield the design flow rates in each orificing zone. Additionally, CATFISH  
51 | calculates the pressure drop in each component and in each flow path of the reactor. Individual flows and pressure drops are calculated under nominal conditions or accounting for uncertainties (root-mean square, at various levels of confidence; systematic superimposition of uncertainties in selected flow paths, etc.).

58 | Predictions of assembly flow rates and subchannel flow and temperature distributions at flow rates less than full flow, including natural circulation are performed with the CORINTH code and through sequential use of the COBRA-WC/FORE-2M codes as discussed in Section 4.4.2.6. CORINTH includes the capability to model the branched network of the lower inlet modules, the different transient power decay rates of fuel, blanket and structure and detailed assembly component hydraulic characteristics. As a transient code, the  
51 |

particular transient event of interest may be analyzed, thus avoiding the ambiguities inherent in quasi-steady state analyses as conducted in past studies.

The total assembly flow rates calculated by CATFISH and hardware and physics design information are input to the subchannel analysis codes. The subchannel analysis codes are used to predict the coolant flow and temperature distributions in the core assemblies. Of particular interest are the peripheral subchannel temperatures and flow rates which are used for duct temperature predictions and the peak subchannel coolant temperature which is used for hot channel/spot temperature predictions of the hot rod. The subchannel analysis codes all calculate solutions to the mass, momentum and energy transport equations describing heat and mass transfer in turbulent fluid flow. Since the governing systems of equations are very complicated, each code makes simplifying assumptions to expedite solutions.

The CØTEC and CØBRA subchannel analysis codes were used for fuel and blanket assemblies thermal-hydraulic performance predictions. The CØTEC code was routinely adopted for design since it features phenomenological models for sweeping (fluid following the wire under the projection of the wire wrap) and pumping (fluid forced from channel to channel by subchannel area changes due to wire wrap rotation), thus greatly simplifying the energy and momentum equations with very substantial savings in required computation time. The axial coolant flow distribution is calculated from either the equal velocity or from the subchannel hydraulic diameter flow split option as specified by the user; turbulent mixing and thermal conduction are included in the energy transport model. CØTEC assumes an adiabatic duct and does not include a density body force term in the momentum equation. Comparison and calibration of CØTEC with experimental data was discussed in Section 4.4.3.2.1. The CØBRA computer program computes the flow and enthalpy in rod bundle subchannels during both steady state and transient conditions. It uses a mathematical model that considers both turbulent and diversion cross flow mixing between adjacent subchannels. The equations of the mathematical model are solved using a semi-explicit finite difference scheme which gives a boundary-value flow solution for both steady state and transients where the boundary conditions are the inlet enthalpy, inlet mass velocity and exit pressure. An extended version of the COBRA code is COBRA-WC (COBRA-Whole Core) which predicts the detailed dynamic core-wide performance including inter- and intra-assembly flow and heat redistribution effects.

For detailed rod temperature distribution, the FATHØM-360 code is employed. A two-dimensional (radial and circumferential) analysis of the heat transfer between the rod and surrounding coolant and within the rod itself is performed, accounting for the proper boundary conditions around the entire rod circumference (as provided by the subchannel analysis codes). Performing these calculations at different axial levels (subchannel analysis codes calculate rod bundle lumped subchannel coolant temperatures over the whole length) provides the designer with the desired detailed three-dimensional mapping of rod temperatures throughout the core. The code has the capability of analyzing wire wrapped as well as bare rods.

Starting from the bulk velocity and temperature provided by the sub-channel analysis codes as boundary conditions, FATHOM-360 solves the momentum and energy equations to calculate in detail the coolant velocity and temperature distribution, radially and circumferentially, around the rod. The fundamental equations are solved via the finite difference technique through adoption of the Buleev (Ref. 48) formulation of the momentum eddy diffusivity and of a fixed ratio between the eddy diffusivities of heat and momentum, which is a function of channel geometry, Prandtl and Reynolds numbers (Ref. 49). While FATHOM-360 performs the above calculations for an inboard rod, the companion code FATHOM-360S analyzes side rods. FATHOM-360 S adds to the features of FATHOM-360 the capability of accounting for heat transfer across the duct wall into or from the side channel, with boundary conditions provided by the TRITON code.

58 | Following calculation of the detailed coolant temperature profile, the rod temperature profile is calculated (with particular emphasis in detailing the cladding temperature distribution) by solving the energy conservation equations in the cladding, wire wrap, pellet/cladding gap and pellet (Ref. 50). Comparison (Ref. 51) between FATHOM and bare rod analyses performed by Nijssing and Eifler (Ref. 52) and by Dwyer and Berry (Ref. 53) showed excellent agreement. A comparison (Ref. 71) between pre-  
58 | dictions by FATHOM-360/360S and wire wrapped rods velocity distribution obtained in the inboard (Ref. 54)/side (Ref. 55) channels of a large scale model of CRBRP fuel assembly showed good agreement, both qualitatively and quantitatively. A similar comparison against experimental data recently obtained for the large scale model of CRBRP blanket assembly (Ref. 72) will be performed. FATHOM-360 and -360S predictions have also been  
58 | favorably compared with experimental data obtained in the CRBRP prototypic blanket heat transfer tests conducted at ARD.

51 | Duct temperature calculations are performed using the TRITON code which solves the thermal-hydraulics of a cluster of seven adjacent assemblies. TRITON uses as a basic block the subchannel analysis code COTEC and simultaneously solves for the thermal-hydraulic field in the seven individual assemblies and for the inter-assembly heat transfer effect. Therefore, use of TRITON allows proper consideration of the two most important physical phenomena affecting the duct temperatures, i.e., wire wrapped assemblies hydraulics, especially at the periphery where swirl flow occurs, and interassembly heat transfer. All types of core assemblies, fuel, blanket, control and radial shield, are analyzed in TRITON. Effects of interstitial flow and gamma-heating in the ducts can be included. Even though emphasis is on calculation of duct temperatures, TRITON can provide assembly mixed mean temperature and individual subchannel/rod temperatures as modified from adiabatic conditions by the effect of inter-assembly heat transfer. TRITON has the capability to calculate temperatures under nominal conditions and to account for uncertainties.

Amend. 58  
Nov. 1980

58

It should be noted that effect of uncertainties is not superimposed on calculations; thus, TRITON accounts simultaneously for uncertainties and interassembly heat transfer effects, providing the most realistic calculation of assembly temperatures to be adopted in design. TRITON predictions have shown good agreement with the first set of data obtained in the ARD blanket heat transfer test in sodium (auxiliary ducts were located in the test on two sides of the blanket assembly to simulate inter-assembly heat transfer).

The fuel and blanket rod temperatures and fission gas plenum pressures are calculated in the NICER code. Uncertainties can be included to calculate component temperature distributions at different levels of confidence. NICER accepts input from OCTOPUS, CATFISH, COTEC, FATHOM-360 and FATHOM-360S and reproduces the results from these codes to present a comprehensive picture of the axial and radial temperature distributions in the fuel/blanket rod. The NICER calculations begin with the axial coolant temperature distribution predicted for any rod by the subchannel analysis codes. The code uses the assembly hardware geometry to calculate the subchannel hydraulic parameters and the resultant subchannel average flow rates and velocities by splitting the total assembly flow rate calculated in OCTOPUS and CATFISH. The circumferential average coolant to cladding film coefficient is calculated from the Nusselt number correlation (discussed in Section 4.4.2.8.2) using the subchannel geometric and hydraulic parameters calculated above. Direct and statistical hot channel factors are input for off-normal calculations. Local coolant and cladding temperatures under the wire wrap are calculated on the basis of results obtained from FATHOM-360 and FATHOM-360S. A discussion of the analytical approach to rod temperature calculations is reported in Section 4.4.2.2.

Fission gas plenum pressure calculations reported in Section 4.3.3.3.4 are performed by NICER on the basis of the correlations discussed in Section 4.4.2.8.16 and accounting for uncertainties as outlined in Section 4.4.3.2.4.

58

Rod bundle coolant pressure drops are estimated by NICER, at user's option, on the basis of the Novendstern correlation (Ref. 56), which provides a quick realistic estimate valuable in scoping analyses, or on the basis of the rod friction correlations reported in Tables 4.4-6 and 4.4-7. More detailed calculations of the pressure drops in the rod bundle and in every assembly component are performed by the CATFISH code, using the correlations reported in Section 4.4.2.7.2.

51

Transient core thermal-hydraulic performance predictions are carried out by the FØRE-2M computer code. FØRE-2M calculates detailed, transient, peak coolant, cladding and fuel temperatures using the same hot spot and uncertainty factors used in NICER. In fact, one of the verifications of FØRE-2M predictions is comparison of initial conditions with peak operating conditions predicted by NICER. FØRE-2M uses additional transient input and uncertainties specified by Plant Performance Analysis. Time varying coolant flow rates and reactor inlet temperatures are specified from the DEMØ code for the transient being analyzed.

The basic heat transfer model considers one-dimensional radial heat conduction, convection and radiation through the fuel and cladding to the coolant. Axial heat convection in the coolant is accounted for. The nuclear feedback model is of the point-kinetics type. A single fuel pin is divided into a maximum of seven axial nodes. Each axial node is divided into radial rings consisting of coolant, cladding, gap and fuel, with a maximum of ten fuel rings.

Finite difference techniques are used in FØRE-2M to calculate the temperature profile in the cladding and fuel for both steady state and transient predictions. A heat balance is set up for each node and the new temperature at the end of a time step is solved for in terms of the old temperature plus the energy change due to heat transfer and power generation. All of the temperature -dependent property values and temperature differences which establish the heat transfer rate are based on the known temperature profiles at the beginning of the time step. Node by node the new temperatures for the first step are calculated by using the property values and temperature differences that existed in steady state until a completely new temperature distribution is determined. This process is repeated for each time step using the property values and temperature difference from the previous step.

Uncertainty limits on FØRE-2M are based upon comparison with NICER steady state predictions and conservative evaluations.

#### 4.4.3.4.2. Primary Control Assemblies

The steady state and transient T&H analyses for the Primary Control Assemblies parallel that for the fuel and blanket assemblies, particularly as regards the methods for assembly subchannel and uncertainty analyses. The uniqueness of the control assemblies as compared to the other core assemblies lies with their special design functions (reactor reactivity control by neutron absorber) and their operational capability (rate of inserting negative reactivity). These unique characteristics call for special computer programs to account for such design features as the presence of the bypass channels, withdrawn position of the control rod bundle as well as the control rod scram dynamics analysis. Discussions provided herein are for each of the nine PCA's which as a group, is called the Primary Control Rod System. The six control assemblies of the Secondary Control Rod System follow a similar analytical procedure.

Figure 4.4-64 illustrates the flow diagram for the steady state T&H analysis of the PCA. Compared to the flow diagram for the fuel and blanket assemblies, the functions of OCTOPUS and NICER are replaced by the CRSSA code, and the usual subchannel analysis codes are replaced by a version of COBRA and THI-3D with bypass channels. THI-3D accounts

58

for the conservation of mass, energy and momentum subject to pressure drop boundary conditions and leads to a non-linear multi-point boundary value problem. The turbulent interchange, radial thermal conduction and forced flow due to the spacer system between the channels are explicitly taken into account. The computer program CRAB is used to predict the scram dynamics of a control rod from any parked position. The CATFISH code is still used to provide the control assembly flow rate and orificing pressure drop compatible with the reactor pump head and flow rates in other reactor components. This information when used with the CRAB code calculations will provide the margin to floatation.

The T&H conditions for each location of the primary control system are different due to combinations of conditions such as  $B_4C$  enrichment, time in core life, control rod parked position, heat transfer rate from the surrounding core assemblies, etc. Figure 4.4-64 illustrates how a limiting analysis to determine the design assembly flow rate is an iterative process as described in the following steps:

1. Based on initial assembly flow rate, the CRSSA code calculates the important nominal T&H conditions for the subsequent steps of the analytical process, e.g., bypass/pin bundle flow split, pin bundle pressure drop, average assembly coolant temperatures, etc.
2. Scram dynamics of the control rod as well as margin to floatation of a control rod with disconnected driveline is performed by the CRAB code. The subchannel flow and temperature distribution is performed by COBRA or THI-3D.
3. Nominal bypass channel conditions are fed to TRITON to calculate the assembly outer duct temperatures considering heat transfer with the adjacent fuel assemblies. COBRA or THI-3D subchannel T&H data are used in FATHOM-360 and FATHOM-360S for the determination of hot spot factors for calculating absorber pin peak cladding temperatures due to wire wrap.
4. The absorber pin temperatures and plenum pressures with and without uncertainties are calculated by CRSSA.
5. The beginning of core cycle absorber pin cladding midwall temperature (from step #4 based on  $2\sigma$  hot channel/spot factors) are now compared to the maximum allowable to remain within structural limitations. If the limiting temperature exceeds the maximum allowable temperature, the assembly flow rate must be increased in order to lower this limiting T&H hot channel/spot temperature, and thus, resulting in repeating steps 1 through 5 over again until acceptable flows and temperatures are obtained.

51

As discussed in Appendix A, the thermal section of the CRSSA code is an adaptation of the NICER thermal model, and hence, the discussions on calculations and uncertainties in NICER apply to CRSSA. Comparison between CRAB predictions and experimental data for the FFTF control assembly mockup showed very satisfactory agreement (References 57, 58). Transient T&H predictions for the PCA are performed with FØRE-2M and DEMØ as discussed for fuel and blanket assemblies.

#### 4.4.3.4.3 Secondary Control Assemblies

The steady state and transient T&H analyses for the Secondary Control Assemblies use similar analytical procedures as that for the Primary Control Rod System. However, there are some differences in hydraulic design between the two systems. The Secondary Control Rod System utilizes hydraulic forces to assist scram action. To accommodate this unique feature a three-way flow split in the Secondary Control Assemblies is provided. The total coolant flow in a secondary control assembly first splits into upflow to the upper outlet plenum and downflow to the low pressure plenum. The upflow further splits into absorber pin bundle flow and bypass flow in the annulus between the pin bundle and guide tube. Discussions that follow are for each of the six SCA's.

Figure 4.4-64A illustrates the flow diagram for the thermal-hydraulic analysis of the SCA. The SCA thermal-hydraulic performance predictions begin with the determination of the control assembly flow rate, flow split, pre-scram hydraulic scram assist force, and pressure drops in the SCA compatible with the reactor pump head and flow rates in other reactor components. The computer program STALSS is developed specifically to provide this information in detail. The DYNALSS code is used to predict the scram dynamics of the movable control rod from the fully withdrawn parked position. The control rod inserts into the reactor core by its own weight with the aid of hydraulic scram assist force at the beginning of the stroke. DYNALSS also provides steady state total flow rate, flow split, hydraulic scram assist force, and pressure drops in the SCA from pre-scram hydraulic calculation, but in a less detailed fashion compared to that computed by the STALSS code. The results from both codes are compared for verification purposes.

The pin bundle flow, by-pass flow, and down flow calculated by STALSS and physics design information are input to the CORTEM code. CORTEM consists of a unique module of three-way flow split including down flow in the SCA. The code treats steady state intra-assembly and interassembly heat transfer in a full 30-degree sector of the core. The intra-assembly heat transfer inside core assemblies is modeled based on application of the subchannel concept together with the use of bulk parameters for coolant velocity and coolant temperature within a subchannel. The inter-assembly heat transfer between assemblies is determined by heat transfer coefficient in the assembly gaps which is a function of interstitial flow and Peclet number in the coolant. The result from CORTEM provides two important data for other thermal-hydraulic analyses: 1) SCA duct wall temperature distribution for core restraint analysis, and 2) surrounding assemblies duct wall temperature distribution to be used as boundary conditions in detailed SCA pin bundle subchannel analysis.

Based on the SCA surrounding assemblies duct wall temperature distribution, the subchannel flow and temperature distribution is calculated by FULMIX which models the circular bundle of the SCA. The flow split uncertainties which are the major hot channel factors in the SCA are generated by STALSS and DYNALSS. Hot spot factors calculated by FATHOM based on secondary pin pitch/diameter ratio are used to calculate absorber pin peak cladding temperatures due to wire wrap. The absorber pin temperatures and plenum pressure with and without uncertainties are calculated by CONROD.

Transient thermal-hydraulic performance predictions for the SCA are performed with COBRA based on the reactor thermal-hydraulic transient data calculated by DEMO.

#### 4.4.3.5 Hydraulic Instability Analysis

To have a situation where hydraulic instability could occur generally requires the phenomenon of two-phase flow. Since two-phase flow is not permitted in CRBRP (sodium boiling is precluded, see Section 4.4.1) during normal operation or anticipated operating transients, hydraulic instability cannot be caused by this phenomenon. Therefore, no further evaluation of two-phase hydraulic instability will be included. No instability was observed to exist through the laminar to turbulent transition range in water tests on FFTF and CRBR fuel assemblies and in water and sodium tests on the CRBRP blanket assembly (Ref. 9).

#### 4.4.3.6 Temperature Transient Effects Analysis

The quantitative limit for evaluation of cladding integrity due to the effect of normal operation and reactor transients is given in Section 15.1.2. A discussion of the basis of these limits is also given in Section 15.1.2.1. In determining the allowable transients, the variation in the cladding effective thickness with lifetime, the loading mechanism acting on the cladding and the stress/strain properties are all important parameters. With respect to the variation of the cladding effective thickness, such effects as cladding defects, sodium corrosion and depletion effects, fission product chemical attack, fretting wear and manufacturing tolerances are all considered as discussed in Section 4.2.1.1. With respect to the various transient loading mechanisms and irradiated material properties, experimental programs are being heavily relied upon for information.

One of the principal loading components on the cladding is due to the internal gas pressure that develops in the rods due to gaseous fission products being released with irradiation exposure. This is discussed in Section 4.2.1.3.

The integrity limits specified in Table 15.1.2-2 represent the best current estimate by which the cladding performance potential can be evaluated and are largely based on data and/or extrapolations of data that are currently available.



The above discussion refers to demonstrating the ability of the rods to meet their design requirements when subjected to the various categories of design transients. Such topics as transient effects due to rod failures and continued operations with failed rods are presented in Section 15.4.

#### 4.4.3.7 Potentially Damaging Temperature Effects During Transients

In general, a single anticipated event is not damaging to the reactor structures; it is the total sum of all the occurrences (in this event classification) over the particular lifetime that may cause the structure to approach its design limit. As mentioned in Section 4.4.2.9, the current cladding requirement for fuel pins is that considering all normal and anticipated events, the cumulative cladding damage must not preclude the capability to survive at least one of the worst unlikely events without loss of cladding integrity.

Maximum 3 $\sigma$  fuel and blanket hot rod temperatures during various limiting core design events of the plant duty cycle which are described in Appendix B have been analyzed. Detailed temperatures for various axial and radial positions along the rods have been evaluated in determining the core design adequacy as described in Section 4.2.1. Conservative assumptions used in calculating these temperatures are described in Section 15.1.4. These assumptions include: full power operation, hot rod analyzed in highest power and temperature fuel assembly of all core conditions, worst case Doppler coefficient with uncertainties included, a 200 millisecond delay between trip signal and the start of control rod insertion, 3 $\sigma$  hot channel factors, the single most reactive control rod assumed to be stuck in the withdrawn position for both sets of control rods, highest core pressure drop, and the most rapid flow coastdown of the primary pumps following pump trip. In addition, Section 15.1.4 shows that of the safety related events, both of the overpower and undercooling type, the Safe Shutdown Earthquake (SSE) event (60% step reactivity insertion occurring under SSE conditions) results in the highest core temperatures. The conclusion of the Chapter 15.0 safety evaluations and the Section 4.2.1 design evaluations is that the design changes incurred in going from the homogeneous to the heterogeneous scheme are not expected to significantly change the design or safety capability of the core.

An evaluation has also been made to determine if expected levels of gas entrained in the sodium could impair heat transfer in the reactor. It was found that at the limiting value of one volume percent established for reactor neutronics effects (Section 4.3.2.3.2) there is no significant effect on heat transfer. The expected entrainment level (Section 4.4.4.1) is much lower than this limiting value.

#### 4.4.3.8 Thermal Description of the Direct Heat Removal Service (DHRS)

The thermal description of the Direct Heat Removal Service will be found in Section 5.6.2.

#### 4.4.4 Testing and Verification

At the present state-of-the-art in reactor design, scale model tests of reactor flow systems provide the most useful tool for studying reactor hydraulics. Pressure drop through complicated flow paths, thermal striping,

gas entrainment and flow induced vibration of reactor components are not amenable to analytical solution, and must be studied experimentally using scale models. Analytical methods are being developed to study mixing and transport time in plena; these methods require experimental verification.

In general, there are usually three types of model flow studies. The simplest tests are two-dimensional water table model tests. These types of tests are generally qualitative screening studies that look for potential problems and possible solutions, and are useful for the planning of three-dimensional tests. The second type of test deals with specific regions of the reactor, and are called feature model tests. These tests are three-dimensional, and provide qualitative design data. The third type of model is more comprehensive, and includes a hydraulic simulation of the entire reactor. This type of model is more complex, and provides more quantitative information useful in the reactor design. This type of model also provides information on the interaction of different regions of the reactor.

In each of the model studies, careful attention must be given to satisfying similitude requirements. A comprehensive study of the effects of geometric scale, fluid parameters, etc., was conducted in the FFTF program, and is directly applicable to CRBRP. The results of this study are presented in Reference 59.

#### 4.4.4.1 Feature Model Tests

The following provides a listing of the major tests planned or completed in the CRBRP reactor development program, and the purpose of each test.

##### Inlet Plenum Feature Model Test (1/4 Scale)

This test determined the hydraulic characteristics of a water flow model, which simulates the inlet plenum. The major areas that were investigated using the model included: 1) mixing; 2) core flow distribution; 3) pressure drop; 4) inlet plenum transport time; 5) inlet plenum flow patterns; 6) particle mobility in the plenum; and 7) inlet plenum gas dispersion. Geometric parameters varied were: 1) plenum height; 2) inlet nozzle angle; and 3) location of the elevation of the nozzles relative to the core support structure.

##### Inlet Plenum Model Flow Test (1/21 Scale)

A 1/21-scale Inlet Plenum Model (IPM) flow test simulating various plenum geometry and inlet nozzle concepts has been completed. The purpose of the IPM test was to visually observe and obtain qualitative information of the flow patterns and mixing of fluid in the inlet plenum as a function of the plenum

51

height, inlet nozzle discharge angle, and the elevation of the nozzles relative to the Core Support Structure. The test served a scoping purpose for use in designing the 1/4-scale IPFM test previously described.

The gross flow patterns were predictable and produced no unusual or unexpected results.

#### Integral Reactor Flow Model, Phase I Testing - Outlet Plenum Feature Flow and Vibration Test

This test: 1) measured the velocity pattern in the outlet plenum and in the vicinity of the major outlet plenum structures; 2) determined the pressure drop characteristics of the outlet plenum and major outlet plenum structures; 3) determined the mixing characteristics and transport times in the outlet plenum and at locations of probable hot/cold interfaces; 4) evaluated flow induced vibration characteristics of selected outlet plenum structures; and 5) evaluated the gas entrainment characteristics of the suppressor plate.

The gas entrainment tests were performed to determine the amount of cover gas that might be entrained at the free surface inside the CRBRP reactor vessel. Using conservative Weber Number modeling of the entrainment process, the average reactor vessel outlet void fraction when at normal liquid level and scaled to 115 percent of CRBRP average full flow is  $1.25 \times 10^{-4}$ . The maximum void fraction measured at any reactor vessel outlet nozzle for this same case and extrapolated to 115 percent flow was  $3.0 \times 10^{-4}$ .

In addition to determining primary entrainment phenomena within the reactor vessel, tests were run to determine the equilibrium PHTS void fraction that results for a given gas entrainment rate in the reactor vessel. These tests were based on the conservative assumption that all gas removal occurs in the outlet plenum of the reactor. This assumption results in the highest equilibrium void fraction in the PHTS.

Based on the entrainment rate that gave the void fraction of  $1.25 \times 10^{-4}$  and Weber Number modeling of the entrainment process, the equilibrium void fraction in the PHTS at 115 percent of rated flow is  $2.0 \times 10^{-3}$ . Gas removal by the IHX vent and the primary pump standpipe bubbler will reduce this level.

The test results, as well as a complete description of the subject testing, are presented in Reference 76.

#### Integral Reactor Flow Model, Phase II Testing

The purpose of this test which is in progress, is to verify the final design for hydraulic and vibration performance using the integral reactor flow model. Those components used in the Phase I testing, whose design has changed to the extent that hydraulic and vibration performance is influenced, will be modified in a subsequent Phase II.

#### Outlet Plenum Flow Stratification Test

The Outlet Plenum Flow Stratification Test was performed in a model of 0.55 scale simulating a 120° sector of the CRBRP reactor vessel outlet plenum, containing a portion of the UIS, and an outlet main coolant pipe.

Some important conclusions and observations derived from the evaluation of the test data (Ref. 60) are:

- 1) The transient temperature response at the outlet nozzle is less severe than that predicted by the plant simulation model in the DEMO code, thus demonstrating that this UIS design goal is satisfied.
- 2) The standard height UIS chimneys resulted in less severe transient temperature ramp rates at the outlet nozzle than shorter chimneys.
- 3) The nominal prototypic gap beneath the UIS skirt of 1.0 inch resulted in less severe outlet nozzle transient temperatures than either larger or smaller gaps.
- 4) Stratification definitely occurs in the outlet plenum following a reactor trip but does not cause significant design problems.
- 5) Large amplitude, low frequency oscillations were observed during the reactor trip transients at the hot/cold fluid interface, which is established above the UIS. These oscillations do not cause a fatigue problem due to the low range of temperature change and moderate number of total cycles.

#### ANL 1/10 Scale Outlet Plenum Tests

These tests have investigated conditions in the outlet plenum during steady-state and transient operation. The steady state tests (Refs. 61 and 62) measured the mixed mean temperatures and temperature fluctuations throughout the plenum. The transient tests (Refs. 63 and 64) measurements include the temperature response in the plenum to reactor transients and the temperature fluctuations as the hot/cold interface advanced following flow stratification.

#### ANL 1/15 Scale Outlet Plenum Tests

These tests (Ref. 65) investigated the transient behavior in the outlet plenum and compared results obtained using both water and sodium. Using both FFTF and CRBRP geometries, it was shown that water and sodium transients were in fairly good agreement; thus, water can be used to adequately simulate sodium.

#### Orifice Feature Tests

The purpose of this test, which is in progress, is to calibrate all types of orifices to be used in the CRBRP reactor. These may include orificing required for the module, fuel assembly, control assembly, radial shield assembly and blanket assembly.

#### 4.4.4.2 Reactor Assemblies T&H Testing

Several experiments have been conducted to characterize the thermal-hydraulic behavior of wire wrapped assemblies; the results of these tests have been used in calibrating the subchannel analysis codes. For example, tests performed at ORNL (19-pin bundle), ANL (91-pin bundle), HEDL (217-pin bundle) and WRL (11:1 scaled sector of a 217-pin bundle) were reviewed and the COTEC code was calibrated accordingly. A similar analysis and calibration was performed by

PNL and ANL for the COBRA and TH1-3D codes, respectively. Tests on a 5:1 scaled sector of a 61-pin blanket assembly have been concluded at WRL and are being factored into subchannel analysis codes calibration.

Further information on temperature distribution in wire wrapped assemblies were obtained from in-sodium tests on the THORS facility at ORNL, which are also intended to gather data for selected transient conditions, including initiation of boiling. Calibration of COTEC against 61-rod bundle steady-state heat transfer data has been accomplished.

Low flow heat transfer tests in sodium have been completed at HEDL in a full 217-pin fuel assembly (Ref. 66). The results from these tests have been used to calibrate analytical codes and to verify performance predictions in the natural circulation range of flow rates.

Blanket heat transfer tests using sodium on a full scale 61-rod assembly are being conducted at ARD to investigate the thermal-hydraulic behavior of blanket assemblies, with particular emphasis on conditions unique to blanket assemblies, such as low flow, high power skew, reduced pitch/diameter, large rod diameter, etc. Over 90% of the scheduled tests have been completed, covering uniform to 3:1 power skew across the assembly and flow ranges between 3 and 40% of prototypic radial blanket values (Refs. 73 to 75). Test results have been employed in preliminary calibration of the COTEC, TRITON, FATHOM-360 and FATHOM-360S codes. In addition to these steady-state tests, the natural circulation and transient tests have also been completed.

Extensive prototypic testing of components pressure drops in fuel, blanket and control assemblies have been concluded or are currently underway. Available results from these tests have been factored into a re-evaluation of assembly components pressure drops as discussed in Section 4.4.2.7.2.

The fuel pellet power-to-melt and thermal parameters (restructuring) characteristics, gap conductance and corresponding uncertainties) were determined at BOL conditions on the basis of the P-19 (Ref. 37) and P-20 (Ref. 38) irradiation tests in EBR-II.

The analytical correlation between fission gas release and fuel pin operating parameters (burnup, power rating, temperature) utilized in the NICER code for calculating the fission gas pressure has been compared with favorable results against a large amount of experimental data from mixed oxide irradiation tests in EBR-II (Refs. 39, 40, 41).

Steady-state hydraulic and scram dynamics behavior of control assemblies are predicted using the CRAB code. CRAB predictions were found in excellent agreement, both with HEDL steady-state tests (Ref. 57) and ARD scram dynamics tests (Ref. 58) performed for the FFTF control assembly. Tests are underway to characterize the CRBRP primary control rod scram performance. Hydraulic tests of the CRBRP primary control assembly have recently been completed. These tests included orificing characterization, flow split determination, detailed component pressure drop and inception of flotation measurements. Comparison of these data against CRAB predictions has been initiated.

A Natural Circulation Verification Program is underway to develop and validate computer codes capable of core-wide T&H transient analysis through the descent and during natural circulation operation. Validation will be accomplished by comparison to low flow steady state and transient test data, including the EBR-II natural circulation and FFTF Acceptance Test Phase startup testing.

A test of the performance of the fuel transfer and storage assembly is underway to verify the performance of that component.

As more data from the experimental efforts become available, the analytical techniques and computer codes (see Section 4.4.3.4) will be calibrated accordingly and the uncertainty analyses (see Section 4.4.3.2) revised to reflect such additional information.

#### 4.4.5 Core Instrumentation

The core instrumentation for the CRBR is core exit thermocouples. The bases for this selection are provided in Reference 67.

In-core instrumentation, specifically designed to monitor the detailed core power distribution, is not provided in CRBRP. Liquid Metal Fast Breeder Reactors have inherent differences relative to LWR's that permit operation without in-core power monitoring. In addition, selective CRBRP design features have been incorporated to eliminate possible perturbations caused by complicated fuel management schemes and control and movement. The rationale supporting this decision is provided below.

CRBRP, like FFTF, is instrumented with assembly-outlet thermocouples to monitor the coolant temperatures and to detect gross asymmetries in the radial or azimuthal power distribution. Nuclear control is provided by ex-vessel neutron detectors which view the core as a whole. The batch fuel management scheme incorporates a single fuel enrichment, and, since there is no scatter refueling or assembly shuffling, there is therefore minimal potential for refueling or loading errors to lead to unplanned power peaks. In addition, the power distribution is relatively flat, symmetric, and predictable in a fast neutron spectrum reactor like CRBRP. This power distribution has been thoroughly characterized in the ZPPR (Engineering Mockup Critical) program where extensive isotopic fission and capture rate distributions have been analyzed with CRBRP design calculational methodology and cross section data. The power shape is accurately predicted with an uncertainty in the fission rates of approximately  $\pm 2\%$  ( $1\sigma$ ).

Unlike an LWR, there is no power peaking caused by local moderating regions. Sodium is a relatively weak moderator, so the power shape is relatively insensitive to sodium channels and sodium density variations. In a light water reactor, the extremely high thermal absorption cross section for fission product daughters (particularly  $Xe^{135}$ ) can lead to power oscillations. However, in a fast reactor system, such as CRBRP, the fission product cross sections are relatively low so that Xe-induced power oscillations will not be present. To minimize azimuthal power perturbations, the CRBRP control rods are operated in a uniformly-inserted bank. The control rod bank position is monitored by two independent systems, and interlocks maintain relatively close

tolerances on the control rod banking. Selection of the R7C operating control rod bank location in the core was designed to minimize adverse global power peaking, and, in fact, the BOL control insertion tends to suppress the power peak in CRBRP. Because of the relatively long neutron mean free path in a fast reactor, the presence of this uniform absorber material does not cause severe local perturbations in the neutron flux (power).

As noted above, potential mechanisms for producing significant power perturbations, as in a light water reactor, do not exist in a fast reactor system. In addition, CRBRP has a well characterized flat, unperturbed power distribution which is the result of a simplified fuel management scheme. In addition, tight controls are exercised on control rod movement to insure symmetric control rod operation. Based on these observations and design features, it has been concluded that there is no need for in-core power monitoring in CRBRP.

#### 4.4.5.1 Design Bases

The functions identified for the core exit thermocouples located above the selected core assemblies are:

- o reactor control;
- o surveillance (primarily for assessment of cladding cumulative damage function);
- o design verification (verification of design margins, power distribution, symmetry, operational slow transients, assessment of uncertainty factors).

Core instrumentation (i.e., core exit thermocouples) is not required to perform any PPS function.

#### 4.4.5.2 Design Description

To provide these functions a single thermocouple is provided above each of the selected core assemblies as follows:

- o Fuel Assemblies: 148 positions out of a total of 156 are instrumented;
- o Inner Blanket Assemblies: 72 positions out of a total of 76 are instrumented;
- o Alternating Fuel/Inner Blanket Assemblies: all 6 positions are instrumented;
- o Radial Blanket Assemblies: 79 positions out of a total of 132 are instrumented. Almost the totality of radial blanket thermocouples are concentrated in the first row.

- o Control Assemblies: No thermocouples are provided for any control assemblies.
- o All thermocouples will be of the dry-well type;
- o 30 selected assemblies have one thermocouple each for control purposes;
- o Almost full coverage of fuel, inner blanket and first row radial blanket assemblies are provided for surveillance and design verification purposes. It should be noted that the thermocouples providing a signal to the reactor control system are also used for surveillance and design verification. Only a few thermocouples were selected for the second row blanket assemblies due to the very high measurement uncertainties in the core outermost periphery.

For the thermocouples selected for reactor control, a preset limit on the number of out-of-limit reading thermocouples will be established. It will be annunciated in the main control room in the event this preset limit is exceeded. For the CDF surveillance, a simplified and conservative trend calculation capability will be provided on the on-site computer for the determination of temperature trend and CDF history of assemblies experiencing a temperature higher than a preset value. This information will aid in enhancing optimum operation of the reactor core.

The thermocouple coverage is shown in Figure 4.4-65. Reference 67 contains a detailed discussion of the rationale leading to selection of the thermocouples coverage along with a comparison of measurement and design uncertainties in each position, and how the selected coverage satisfies the required functions. Even though the discussion in Reference 67 applies to the CRBRP homogeneous core, the philosophy and methodology do not depend on the particular core configuration and are still valid for the heterogeneous design. The only significant difference is in the selection of the positions used for reactor control purposes. This will be discussed in the following. A detailed discussion of the overall rationale and justification can be found in Reference 67.

#### 4.4.5.3 Design Evaluation of Reactor Control Thermocouples

In the selection of the assemblies monitored with thermocouples feeding the reactor control system, the optimum arrangement is reached when the following objectives are satisfied:

- 1) The arithmetic average of the thermocouple readings should remain constant as much as possible: a) throughout the cycle; and b) from cycle-to-cycle. Requirement (a) is more important than requirement (b), since at each refueling, the thermocouples can be recalibrated against the hot leg RTDs. It is not required that the average reading of the thermocouples be the same as (or close to) the core average temperature since such difference is removed by the calibration against the RTDs.



- 2) Assemblies which are limiting from the point of view of thermofluids and structural performance should be covered by control thermocouples. These assemblies are the ones with highest coolant temperature (transient limiting), highest cladding temperature and CDF (lifetime limiting), and highest power (power-to-melt limiting). Even though these assemblies will be monitored with surveillance thermocouples, it is highly desirable that their monitoring be directly fed into the control system. By doing so, the peak assemblies are automatically controlled.
- 3) Different types of assemblies should be monitored. This means assemblies belonging to different orificing zones and, in the case of the heterogeneous core, both fuel and blanket (inner and radial) assemblies. For a heterogeneous configuration, blanket assemblies are an integral part of the overall core performance. In fact, some blanket assemblies are even more limiting than the fuel assemblies from the point of view of thermofluids and structural performance. Also, in the heterogeneous core, almost all the fuel assemblies are decreasing in temperature as the residence time increases. Thus, temperature readings from blanket assemblies, which are continuously increasing with time, are necessary to minimize fluctuations in the average temperature.
- 4) Coverage should be scattered through a  $60^{\circ}$  symmetry sector as uniformly as possible; i.e., control thermocouples should not be clustered in one region of the reactor so that they will not all be affected by localized flow and/or power disturbances.
- 5) More than one symmetry sector should be monitored, again to avoid localized effects. Three symmetrical sectors  $120^{\circ}$  apart is a logical compromise between this requirement and the following.
- 6) The number of control thermocouples should be practical (the CRBRP homogeneous core adopted 27 control thermocouple positions).

Selected positions of thermocouples to be input to the reactor control system are shown in Figure 4.4-65. Table 4.4-35 reports the nominal outlet temperature of each of the 10 chosen assemblies in one of the three core symmetrical sectors throughout the first four cycles (first and second cores) which are the ones considered in CRBRP core thermal-hydraulics design. The arithmetic average of the 10 readings is also shown in Table 4.4-35. The overall deviation between the minimum and maximum is  $5^{\circ}\text{F}$ . The maximum over any given cycle is only  $2^{\circ}\text{F}$ . Thus, recalibration against the RTDs after each refueling can be avoided. Deviations are minimal during cycles 3 and 4 which can be construed as being representative of equilibrium conditions.

54 The recommended locations represent, for the heterogeneous configuration, the optimum arrangement from both the control and core performance monitoring standpoints.

Amend. 54  
May 1980

#### REFERENCES

1. M. D. Carelli, A.J. Friedland, C. W. Bach and R. A. Markley, "An Optimized Method for Orificing LMFBR Cores", Trans. Amer. Nucl. Soc., 26, pp. 437-438 (1977).
2. M. H. Fontana, R. E. MacPherson, P. A. Gnadt, and others, "Temperature Distribution in a 19-rod Simulated LMFBR Fuel Assembly in a Hexagonal Duct (Fuel Failure Mockup Bundle 2A): Record of Experimental Data", ORNL-TM-4113, September 1973. (Availability: US DOE Technical Information Center).
3. M. D. Carelli and C. W. Bach, "Predicted Steady State Thermal-Hydraulic Performance of the Fuel and Blanket Assemblies in the CRBRP Heterogeneous Core", WARD-D-0210, Rev. 1, January 1979.
4. "Covered Pressure Drop Flow Test/Crossflow Mixing Test", HEDL-TI-76049, November 1976. (Availability: US DOE Technical Information Center).
5. W. L. Thorne, "Pressure Drop Measurements in FFTF Fuel Vibration Tests", HEDL-TC-812, April 1977. (Availability: US DOE Technical Information Center).
6. W. L. Thorne, "Pressure Drop Measurements from Fuel Assembly Vibration Test II", HEDL-TC-824, April 1977. (Availability: US DOE Technical Information Center).
7. P. M. McConnell, "Clinch River Breeder Reactor Fuel Assembly Inlet/Outlet Nozzle Flow Tests", HEDL-TME-77-8, February 1977. (Availability: US DOE Technical Information Center).
8. H.M. Geiger, D.C. Mees, and D. K. Schmidt, "Radial Blanket Flow Orificing Testing: Calibration Tests", WARD-RB-3045-18, April 1977. (Availability: US DOE Technical Information Center).
9. F. C. Engel, R. A. Markley and A. A. Bishop, "Laminar, Transition and Turbulent Parallel Flow Pressure Drop Across Wire-Wrap-Spaced Rod Bundles", Nucl. Sci. Eng., 69, pp. 290-296 (1979).
10. M. R. Spiegel, Schaum's Outline of Theory and Problems of Statistics, p. 247, Schaum, New York, 1961.

56 | 541

54 | 51

11. I. E. Idel'chik, "Handbook of Hydraulic Resistance Coefficients of Local Resistance and of Friction", AEC-tr-6630 (1960).
12. L. F. Moody, "Friction Factors for Pipe Flow", Trans. Amer. Soc. Mech. Eng., pp. 671-684 (1944).
13. D. Y. Nee, "Clinch River Breeder Reactor Plant. Preliminary Thermal-Hydraulic Performance of CRBRP Primary Control Assemblies", CRBRP-ARD-0151, June 1977. (Availability: US DOE Technical Information Center).
14. Deleted.
15. G. H. Golden and J. V. Tokar, "Thermophysical Properties of Sodium", ANL-7323, August 1967.
16. M. S. Kazimi and M. D. Carelli, "Clinch River Breeder Reactor Plant. Heat Transfer Correlation for Analysis of CRBRP Assemblies", CRBRP-ARD-0034, November 1976. (Availability: US DOE Technical Information Center).
17. "Liquid Metal Fast Breeder Reactor Materials Handbook", HEDL-TME-71-32, June 1971.
18. "Nuclear Systems Materials Handbook", TID 26666. (Availability: Hanford Engineering Development Laboratory).
19. A. J. Friedland, "CRBRP Assemblies Hot Channel Factors Preliminary Analysis", WARD-D-0050, Rev. 3, September 1979.
20. "A Compilation of Boron Carbide Design Support Data for LMFBR Control Elements", HEDL-TME-75-19, March 1975. (Availability: US DOE Technical Information Center).
21. J. F. Hogerten and R. C. Grass, "The Reactor Handbook, Vol. 2, Engineering", AECD-3646, Government Printing Office, Washington, D.C., May 1955.
22. A. Biancheria, "The Effect of Porosity on Thermal Conductivity of Ceramic Bodies", Trans. Amer. Nucl. Soc., 15, pp. 9-10 (1966).
23. G. P. Marino, "The Porosity Correction Factor for the Thermal Conductivity of Ceramic Fuels", J. Nucl. Matl., 38, pp. 178-190 (1971).
24. R. L. Gibby, "Fabrication Microstructure and Thermal Conductivity in UO<sub>2</sub>- 25 Wt. Percent PuO<sub>2</sub> Sintered Pellets", HEDL-TME-72-88, May 1972.

56 |

51

25. G. Ondracek and B. Schultz, "The Porosity Dependence of the Thermal Conductivity for Nuclear Fuels", J. Nucl. Matl., 46, pp. 253-258 (1973).
26. L. A. Lawrence and R. L. Gibby, "Effects of Pore Structure on the Melting Heat Rating of Oxide Fuels", HEDL-TME-72-81, May 1972.
27. R. B. Baker, R. D. Leggett and D. S. Dutt, "Effect of Burnup on Heat Rating-to-Incipient Fuel Melting: HEDL P-20 Interim Report", HEDL-TME-75-63 (1975). (US DOE Technical Information Center).
28. B. F. Rubin, "Summary of (U,Pu)<sub>2</sub>O<sub>3</sub> Properties and Fabrication Methods", GEAP-13582, November 1970.
29. A. Biancheria, U. P. Nayak and M. S. Beck, "Effects of Burnup on Fuel Pin Thermal Performance", in Proceedings of the Conference on Fast Reactor Fuel Element Technology, pp. 361-381, American Nuclear Society, Hinsdale, IL. (1971).
30. U. P. Nayak and A. Biancheria, "Radial Blanket Power-to-Melt Analysis", Westinghouse Electric Corp., Advanced Reactors Division, Madison, PA, FMT-FI-AB-313, May 1973.
- 31a) E. A. Aitken and S. K. Evans, "Thermodynamic Data Program Involving Plutonia and Urania at High Temperatures. Quarterly Report No. 3", GEAP-5634, May, 1968.
- 31b) E. A. Aitken and S. K. Evans, "Thermodynamic Data Program Involving Plutonia and Urania at High Temperatures. Quarterly Report No. 4", GEAP-5672, October 1968.
32. J. L. Krankota and C. N. Craig, "Melting Point of Plutonia-Urania Mixed Oxides Irradiated to High Burnup", GEAP-13515, July 1969.
33. R. O. Meyer, E. M. Butler and D. R. O'Boyle, "Actinide Redistribution in Mixed-Oxide Fuels Irradiated in a Fast Flux", ANL-7929, May 1972.
34. R. O. Meyer, E. M. Butler and D. R. O'Boyle, "Actinide Redistribution in Mixed-Oxide Fuels Irradiated in a Fast Flux", ANL-7929 (Suppl. 1), July 1973.
35. R. O. Meyer, D. R. O'Boyle and E. M. Butler, "Effect of Oxygen-to-Metal Ratio on Plutonium Redistribution in Irradiated Mixed-Oxide Fuels", J. Nucl. Matl., 47, pp. 265-267 (1973).
36. M. Bober, C. Sari and G. Schumacher, "Redistribution of Uranium and Plutonium During Evaporation Processes in Mixed Oxide Fuel", J. Nucl. Matl., 40, pp. 341-345 (1971).

- 58 | 37. R. D. Leggett, E. O. Ballard, R. B. Baker and others, "Linear Heat Rating for Incipient Fuel Melting in  $UO_2$ - $PuO_2$  Fuel", Trans. Amer. Nucl. Soc., 15, pp. 752-753 (1972).
38. R. D. Leggett, R. B. Baker, D. S. Dutt and S. A. Chastain, "Influence of Burnup on Heat Rating-to-Melt for  $UO_2$ - $PuO_2$  Fuel", Trans. Amer. Nucl. Soc., 19, pp. 136-137 (1974).
39. D. S. Dutt, D. C. Bullington, R. B. Baker and L. A. Pember, "A Correlated Fission Gas Release Model for Fast Reactor Fuels", Trans. Amer. Nucl. Soc., 15, pp. 198-199 (1972).
40. R. F. Hilbert, K. J. Perry, W. K. Appleby and others, "Performance of Mixed Oxide Fuel Rods Irradiated to 13 Atom Percent Burnup in EBR-II", GEAP-13538, April 1973.
41. R. F. Hilbert, T. J. Black, K. D. Challenger and W. K. Appleby, "Performance of LMFBR Fuel Rods at High Cladding Temperatures", GEAP-13971, June 1973. (Availability: US DOE Technical Information Center).
42. M. E. Meek and R. F. Rider, "Compilation of Fission Product Yields", NEDO-12154-1, January 1974. (Availability: US DOE Technical Information Center).
43. ASME Boiler and Pressure Vessel Code, "Section III - Division 1, Nuclear Power Plant Components, Subsection NB, Class 1 Components", American Society of Mechanical Engineers, New York, 1974.
44. RDT Standard RDT-C-16-1-T, "Supplementary Criteria and Requirements for RDT Reactor Plant Protection Systems", December 1969. (Availability: Reactor Standards Office, Oak Ridge National Laboratory).
45. A. S. Hanson and N. E. Todreas, "Fluid Mixing Studies in a Hexagonal 61-Pin Wire Wrapped Rod Bundle", COO-2245-51TR, August, 1977.
46. H. Hoffmann and E. Baumgartner, "Experimental Investigation of the Thermodynamic Behavior of Fast Breeder Reactor Fuel Elements with Different Spacer Types", in Fuel and Fuel Element for Fast Reactors, Vol. 1, pp. 351-368, International Atomic Energy Agency, Vienna, 1974.
- 58 | 47. K. Takahashi and E. Ishibashi, "Experimental Study on Coolant Sodium Mixing Effect in JOYO Fuel Assembly with Spiral Wire Spacer. Experimental Results on Core Fuel Subassembly", SN 941-75-77, July 1975.
- 51 | 48. N. I. Buleev, K. N. Polosukhina and V. K. Ryshin, "Hydraulic Resistance and Heat Transfer in a Turbulent Liquid Stream in a Lattice of Rods", High Temp., 2. pp. 673-681 (1964).

49. W. T. Sha and M. D. Carelli, "A Model for Predicting Turbulent Transport in Subchannel Analysis", Trans. Amer. Nucl. Soc., 21, pp. 380-382 (1975).
50. M. C. Chuang, M. D. Carelli, C. W. Bach and J. S. Killimayer, "Three-Dimensional Thermal-Hydraulic Analysis of Wire-Wrapped Rods in Liquid Metal Fast Breeder Reactor Core Assemblies", Nucl. Sci. Eng., 64, pp. 244-257 (1977).
51. M. C. Chuang, R. E. Kothmann, M. J. Pechersky and R. A. Markley, "Cladding Circumferential Hot Spot Factors for Fuel and Blanket Rods", Nucl. Eng. Design, 35, pp. 21-28 (1975).
52. R. Nijssing and W. Eifler, "Analysis of Liquid Metal Heat Transfer in Assemblies of Closely Spaced Fuel Rods", Nucl. Eng. Design, 10, pp. 21-54 (1969).
53. O. E. Dwyer and H. C. Berry, "Turbulent Flow Heat Transfer for In-Line Flow through Unbaffled Rod Bundles: Molecular Conduction Only", Nucl. Sci. Eng., 46, pp. 284-303 (1971).
54. R. M. Roidt, T. G. Bartholet and L. J. Harper, "Experimental Determination of Interior Subchannel Crossflow and Axial Flow in a Model of the Clinch River Breeder Reactor Fuel Assembly Rod Bundle with Wire-Wrap Spacers", ASME Paper 76-WA/HT-83, December 1976 (Also CRBRP-ARD-Q108, January 1977).
55. T. G. Bartholet, R. M. Roidt and J. E. Romano, "Clinch River Breeder Reactor Plant. 11:1 Scale Wire Wrapped Rod Bundle Air Flow Test, Side Subchannels", CRBRP-ARD-Q129, January 1977. (Availability: US DOE Technical Information Center).
56. E. H. Novendstern, "Turbulent Flow Pressure Drop Model for Fuel Rod Assemblies Utilizing a Helical Wire Wrap Spacer System", Nucl. Eng. Design, 22, pp. 19-27 (1972).
57. M. D. Carelli, C. W. Bach and R. A. Markley, "Hydraulic and Scram Dynamics Analysis of LMFBR Control Rod Assemblies", Trans. Amer. Nucl. Soc., 16, pp. 218-219 (1973).
58. M. D. Carelli, H. W. Brandt, C. W. Bach and H. D. Kulikowski, "LMFBR Control Rods Scram Dynamics", Trans. Amer. Nucl. Soc., 18, pp. 278-279 (1974).
59. D. S. Trent, "Application of Geometric Models for the FFTF Hydraulic Core Mockup", BNWL-575, November 1967.

60. M. D. Woods and T.S. Andreychek, "Clinch River Breeder Reactor Plant. Test Evaluation Report on the CRBR Outlet Plenum Flow Stratification Study", CRBRP-ARD-0125, September 1976. (Availability: US DOE Technical Information Center).
61. J. J. Lorenz and P. A. Howard, "A Study of CRBR Outlet Plenum Thermal Oscillations during Steady State Conditions", ANL-CT-76-36, July 1976. (Availability: US DOE Technical Information Center).
62. P. A. Howard, "Steady State CRBR Outlet Plenum Mixing with an AFMS Core", ANL-CT-77-14, April 1977. (Availability: US DOE Technical Information Center).
63. P. A. Howard and J. J. Lorenz, "CRBR Outlet Plenum Thermal Behavior during Transient Conditions", ANL-CT-76-49, September 1976. (Availability: US DOE Technical Information Center).
64. P. A. Howard and J. J. Lorenz, "CRBR Outlet Plenum Mixing Studies: Suppressor Plate and Shear Web Tests", ANL-CT-77-7, November 1976. (Availability: US DOE Technical Information Center).
65. J. J. Lorenz, R. D. Carlson and P. A. Howard, "An Investigation of LMFBR Outlet Plenum Thermal-Hydraulic Behavior during Reactor Scram Transients", ANL-CT-76-18, September 1975. (Availability: US DOE Technical Information Center).
- 51 | 66. M. L. Millburg, J. A. Hassberger and C. J. Boasso, "Natural Circulation Heat Transfer Testing With a Simulated Full Scale LMFBR 217-Pin Electrically Heated Fuel Assembly", HEDL-TME-77-3, June 1977. (Availability: US DOE Technical Information Center).
67. M. D. Carelli, "Core Exit Instrumentation of the Clinch River Breeder Reactor Plant", Nuclear Technology, 37, pp. 261-273, 1978.
68. R. M. Singer and J. L. Gillette, "Measurements of Subassembly and Core Temperature Distributions in an LMFBR", AIChE Symposium Series, 73, p. 184, 1977.
69. A. K. Agrawal, et.al., "Dynamic Simulation of LMFBR Plant Under Natural Circulation", ASME Paper 79-HT-6, 1979.
- 54 | 70. M. Khatib-Rahbar and K. B. Cody, "Establishment of Buoyancy-Induced Natural Circulation in Loop-Type LMFBRs", ANS Transactions, Vol. 28, pp. 432-433, June 1978.
71. R. M. Roidt, M. D. Carelli and R. A. Markley, "Experimental Investigations of the Hydraulic Field in Wire Wrapped LMFBR Core Assemblies", to be published in special issue of Nuclear Engineering Design.
- 58 | 72. L. Patch, R. M. Roidt, M. D. Carelli and R. A. Markley, "Experimental Studies of Flow Distribution in a Wire Wrapped LMFBR Blanket Assembly", in Fluid Flow and Heat Transfer Over Rod or Tube Bundles symposium at ASME 1979 Winter Annual Meeting, pp. 55-65, December 1979.

73. F. C. Engel, R. A. Markley and B. Minushkin, "Buoyancy Effects on Sodium Coolant Temperature Profiles Measured In an Electrically Heated Mock-up of a 61-rod Breeder Reactor Blanket Assembly", ASME 78-WA/HT-25.
74. F. C. Engel, R. A. Markley and B. Minushkin, "Heat Transfer Test Data of a 61-rod Electrically Heated LMFBR Blanket Assembly Mockup and their use for Subchannel Code Calibration", in Fluid Flow and Heat Transfer Over Rod or Tube Bundles symposium of ASME 1979 Winter Annual Meeting, pp. 223-229, December 1979.
75. F. C. Engel, B. Minushkin, R. J. Atkins and R. A. Markley, "Characterization of Heat Transfer and Temperature Distributions in an Electrically Heated Model of an LMFBR Assembly, to be published in a special issue of Nuclear Engineering Design.
76. D. R. Dickson, "Final Tests of Entrainment and Equilibrium Void Fraction in the Integral Reactor Flow Model," Volume II of HEDL-TMC-80-59, November 1982, (Availability: U. S. DOE Technical Information Center).



TABLE 4.4-1

CRBRP CORE LOADING DURING CYCLES 1 THROUGH 5

CYCLE NUMBER	ASSEMBLY TYPE	TOTAL NUMBER OF ASSEMBLIES	REMARKS
1	Fuel	156	All Fresh Assemblies
	Inner Blanket	82	
	Radial Blanket	126	
2	Fuel	159	3 Fresh Fuel Assemblies
	Inner Blanket	79	
	Radial Blanket	126	
3	Fuel	156	All Fresh Fuel and Inner Blanket Assemblies
	Inner Blanket	82	
	Radial Blanket	126	
4	Fuel	162	6 Fresh Fuel Assemblies
	Inner Blanket	76	
	Radial Blanket	126	
5	Fuel	156	All Fresh Fuel and Inner Blanket Assemblies plus 60 Fresh Row 1 Radial Blanket Assemblies
	Inner Blanket	82	
	Radial Blanket	126	

TABLE 4.4-2

SUMMARY OF STRAIN EQUIVALENT LIMITING TEMPERATURE  
CALCULATIONS FOR SECOND CORE FUEL ASSEMBLIES

<u>ASSEMBLY</u>	<u>EOL STRAIN (%)</u>	<u>EOL PRESSURE (psi)</u>	<u>SELT (°F)</u>	<u>SET (°F)</u>
2	.003	816	1264	1180
3	.007	845	1260	1192
13	.068	875	1258	1232
15	.031	891	1254	1211
24	.037	781	1270	1227
25	.039	861	1258	1220
26	.025	725	1281	1235
27	.057	748	1277	1247
28	.13	771	1272	1264
29	.003	815	1265	1181
30	.004	828	1262	1184
33	.001	855	1259	1194
34	.0086	862	1258	1193
37	.096	921	1249	1233
43	.015	892	1254	1197
44	.18	930	1248	1247
45	.034	876	1256	1217
47	.13	914	1251	1241
48	.12	773	1272	1261
49	.06	750	1276	1249
50	.023	726	1281	1232
51	.04	862	1258	1221
10	.19	920	1250	1250
11	.34	941	1247	1259
14	.36	928	1249	1263
36	.33	943	1247	1259
68	1.37	966	1243	~1295
101	1.43	970	1242	~1295
62	.029	529	not a limit	
98	.018	488	not a limit	

51

TABLE 4.4-3

COOLANT LIMITING TEMPERATURES FOR TLT CALCULATIONS  
(TEMPERATURES IN °F)

TYPICAL WORST CASE FOR ASSEMBLY TYPE	HETEROGENEOUS CORE MAXIMUM TRANSIENT TEMP. (FORE-2M CALCULATED)	STEADY STATE TEMP. CORRESPONDING TO HETEROGENEOUS CORE MAXIMUM TRANSIENT TEMP. (FORE-2M)	STEADY STATE TEMP. CORRESPONDING TO 1550°F MAXIMUM TRANSIENT TEMP.	T M
Fuel Assembly	1571	1331	1316	1252 First Core 1261 Second Core
Inner Blanket Assembly	1498	1247	1282	1198 First Core 1207 Second Core
Radial Blanket Assembly	1580	1331	1310	1232

Temperatures at THDV, 3σ, 750°F Inlet

Temperatures for  
PEOV, 2σ

4.4-89

Amend. 73  
Nov. 1982

TABLE 4.4-4  
CORE ORIFICING ZONES FLOW ALLOCATION

ZONE	TYPE	NO. ASSYS/ ZONE	CYCLES		FLOW (lb/hr)		CYCLES	
			1,3,5,..	( )	CYCLE 2	( )	4,6,8,..	( )
1	Fuel	39	189,990	(201,900)	188,520	(200,340)	187,050	(198,780)
2	Fuel	54	176,790	(187,870)	175,420	(186,420)	174,060	(184,970)
3	Fuel	21	166,900	(177,360)	165,610	(175,990)	164,320	(174,620)
4	Fuel	18	153,400	(163,020)	152,220	(161,760)	151,030	(160,500)
5	Fuel	24	149,480	(158,850)	148,330	(157,630)	147,170	(156,400)
6	Fuel	0,3 or 6			178,590	(189,780)	177,190	(188,300)
	Inner Blanket	6,3 or 0	68,790	(73,100)	69,330	(73,680)		
7	Inner Blanket	57	88,790	(94,360)	88,110	(93,630)	87,420	(92,900)
8	Inner Blanket	19	78,030	(82,920)	77,420	(82,270)	76,810	(81,620)
9	Radial Blanket	12	62,300	(66,210)	61,820	(65,700)	61,340	(65,190)
10	Radial Blanket	36	48,300	(51,330)	47,930	(50,930)	47,550	(50,530)
11	Radial Blanket	48	35,090	(37,290)	34,820	(37,000)	34,540	(36,710)
12	Radial Blanket	30	25,740	(27,350)	25,540	(27,140)	25,330	(26,920)

NOTE: Flows are for THDV (PEOC) conditions.

CORE REGION FLOW FRACTIONS

REGION	CYCLES 1,3,5...	CYCLE 2	CYCLES 4,6,8...
Fuel	0.65	0.66	0.66
Inner Blanket	0.17	0.16	0.16
Radial Blanket	0.12	0.12	0.12
Total	0.94	0.94	0.94

A-1-00

Amend. 64  
Jan. 1982

TABLE 4.4-5

FUEL ASSEMBLY COMPONENT PRESSURE DROP DATA LINEAR REGRESSION ANALYSIS

COMPONENT	LINEAR REGRESSION FUNCTION	NO. OF DATA POINTS	MEAN OF $\ln(\text{Re})$	STANDARD DEVIATION ABOUT MEAN OF $\ln(\text{Re})$	MEAN OF $\ln(D)$	STANDARD DEVIATION ABOUT MEAN OF $\ln(D)$ **	STANDARD ERROR OF ESTIMATE
Inlet Nozzle	$\ln(K) = 0.9177 - .05289 \ln(\text{Re})$	222	13.64	0.3560			0.0841
Inlet Nozzle-Orifice-Shield:							
-- 1 Plate	$\ln(K)=2.352-.09211\ln(\text{Re})-1.452\ln(D)$	41	13.95	0.3763	-.1845	0.1256	0.0170
-- 2 Plates	$\ln(K)=1.708-.05022\ln(\text{Re})-3.293\ln(D)$	73	13.73	0.3684	-.3528	0.1057	0.0472
-- 3 Plates	$\ln(K)=2.240-.08226\ln(\text{Re})-3.891\ln(D)$	60	13.61	0.3560	-.4064	0.1165	0.0207
-- 4 Plates	$\ln(K)=2.293-.07141\ln(\text{Re})-4.032\ln(D)$	43	13.52	0.2982	-.4454	0.1040	0.0136
-- 5 Plates	$\ln(K)=2.225-.03072\ln(\text{Re})-3.651\ln(D)$	42	13.45	0.2589	-.4484	0.0997	0.0165
Shield	$\ln(K)=0.3988-.03879\ln(\text{Re})$	17	13.82	0.3768			0.0966
Rod Bundle:							
-- Inlet	$K = 0.370$	--					0.2(*)
-- Rod Friction	see Table 4.4-6	161	entire range				0.0524
		46	full flow				+0.0312, -0.0262
-- Outlet	$K = 0.178$	--					0.2(*)
Outlet Nozzle	$\ln(K) = .00495 - .04902 \ln(\text{Re})$	16	13.67	0.7483			0.0450

(\*) A 20% uncertainty was selected as a bounding value (not standard error), since no test data are available. This uncertainty is much greater than the values determined for other components, but the effect on flow rate calculations is negligible since the untested components account for only 1 to 2 psi of the 100 psi total assembly pressure drop.

\*\* D is the hydraulic diameter of the plate flow area.

4.4-91

51

TABLE 4.4-6

FUEL ASSEMBLY COMPONENT HYDRAULIC CORRELATIONS

COMPONENT	CORRELATION	REFERENCE AREA (IN <sup>2</sup> )	REFERENCE HYDRAULIC DIAMETER (IN)	REFERENCES
Inlet Nozzle	$K = 2.504 Re^{-0.0529}$	3.976	2.250	7
Inlet Nozzle-Orifice-Shield:				
-- 1 Plate	$K = 10.50 Re^{-0.0921} D^{-1.452}$	3.976	2.250	7
-- 2 Plates	$K = 5.519 Re^{-0.0502} D^{-3.293}$			
-- 3 Plates	$K = 9.396 Re^{-0.0823} D^{-3.891}$			
-- 4 Plates	$K = 9.909 Re^{-0.0714} D^{-4.032}$			
-- 5 Plates	$K = 9.253 Re^{-0.0307} D^{-3.651}$			
Shield	$K = 1.490 Re^{-0.0388}$	3.976	2.250	7
Rod Bundle:				
-- Inlet	$K = 0.370$	6.724	0.1281	11
-- Rod Friction	$f = 84/Re$ for $Re \leq 1000$ $f = [1.080 + 0.0927*(1000/Re)^2 + 0.1694 * (1000/Re)^4] f_c$ where $f_c^{(*)} = 4 \log_{10}(2.51/(Re \sqrt{f_c}))$	6.724	0.1281	4 - 6
-- Outlet	$K = 0.178$	6.724	0.1281	11
Outlet Nozzle	$K = 1.005 Re^{-0.0490}$	5.899	2.116	7

(\*)  $f_c$  is the Colebrook friction factor correlation<sup>[12]</sup> for a smooth tube.

4.4-92

51

TABLE 4.4-7  
BLANKET ASSEMBLIES COMPONENT HYDRAULIC CORRELATIONS

COMPONENT	CORRELATION	REFERENCE AREA (IN <sup>2</sup> ) <sup>(*)</sup>	REFERENCE HYDRAULIC DIAMETER (IN) <sup>(*)</sup>	REFERENCES
Inlet Nozzle	$K = 2.504 Re^{-0.0529}$	3.976 (1.767)	2.250 (1.500)	7
Inlet Nozzle Orifice Shield	$K = C Re^{-0.05}$	3.976 (1.767)	2.250 (1.500)	7,8
Shield	$K = 2.0$	2.405	1.750	11
Rod Bundle:				
-- Inlet	$K = 0.427$	3.956	0.1338	11
-- Rod Friction	$f = 110/Re$ for $Re \leq 400$ $f = (110/Re)\sqrt{1-\psi} + (.55/Re^{.25})\sqrt{\psi}$ where $\psi = (Re-400)/4600$ for $400 < Re < 5000$ $f = .55/Re^{.25}$ for $Re > 5000$	3.956	0.1338	9
-- Outlet	$K = 0.290$	3.956	0.1338	11
Outlet Nozzle	$K = 1.005 Re^{-0.0490}$	3.976	2.250	7

(\*) Number outside parentheses refers to inner blanket assemblies; inside parenthesis refers to radial blanket.

4.4-93

Amend. 51  
 Sept. 1979

TABLE 4.4-8  
BASES FOR REACTOR INTERNALS PRESSURE DROPS

COMPONENT	NOMINAL PRESSURE LOSS (psi)	LOSS COEFFICIENT	FLOW (lb/hr)10 <sup>6</sup>	FLOW AREA (ft <sup>2</sup> )	BASIS - LIMITATIONS
1) Reactor Vessel Inlet Plenum	4.25	K=1.19	41.446	8.655	Loss coefficient obtained from the inlet plenum feature model test. +9% uncertainty used in design. ( $\Delta P = K \bar{W}^2 / 2g\rho A_f^2$ )
2) Lower Inlet Module	8.66	$(K + \frac{fL}{D}) = 2.13$	1.096	0.214	Calculated; to be confirmed by radial blanket orificing test. +20% uncertainty used in design. ( $\Delta P = (K + \frac{fL}{D}) \bar{W}^2 / 2g\rho A_f^2$ )
3) Reactor Vessel Outlet Plenum:					
a) UIS	1.78	$(K + \frac{fL}{D}) = 2.01$	33.986 <sup>(*)</sup>	14.51	Loss coefficient obtained from the integral reactor feature model test. +3% uncertainty used in design. ( $\Delta P = (K + \frac{fL}{D}) \bar{W}^2 / 2g\rho A_f^2$ )
b) Exit Nozzle	0.43	K=0.29	41.446	13.77	Loss coefficient obtained from the integral reactor feature model test. +7% uncertainty used in design. ( $\Delta P = K \bar{W}^2 / 2g\rho A_f^2$ )

(\*) Based on a total reactor flow of 41.446 x 10<sup>6</sup> lb/hr with 82% flowing up the UIS chimneys.  
A<sub>f</sub> = flow area

f = friction factor

ρ = density ( $\frac{g}{cc}$ )

4.4-94

Amend. 56  
Aug. 1980



TABLE 4.4-9

DETAILED PRESSURE DROP BREAKDOWN FOR PLANT THDV  
CONDITIONS ( $41.446 \times 10^6$  lb/hr) AND MAXIMUM UNCERTAINTIES

Orificing Zone	1	2	3	4	5	6 F/A	6 IB/A	7	8	9	10C	10P	11	12
Average Zone Flow	187130	174130	164400	151090	147240	177270	69070	87450	76850	61360	47570	47570	34560	25360
Component $\Delta P$ (psi)														
Inlet Nozzle	8.7	7.6	6.8	5.8	5.5	7.9	1.3	2.0	1.6	4.9	3.0	3.0	1.6	0.9
Assembly Orifice	40.0	48.6	55.3	63.5	66.9	46.5	69.9	44.9	60.5	69.6	42.2	42.2	22.5	12.2
Shield	6.4	5.5	5.0	4.2	4.0	5.7	5.6	8.9	6.9	4.4	2.6	2.6	1.4	0.7
Rod Bundle Inlet	1.1	1.0	0.9	0.7	0.7	1.0	0.5	0.8	0.6	0.4	0.2	0.2	0.1	0.1
Rod Bundle	51.5	45.3	40.8	35.1	33.6	46.7	35.9	54.3	43.3	29.3	18.7	18.7	10.7	6.2
Rod Bundle Outlet	0.6	0.5	0.4	0.4	0.3	0.5	0.4	0.6	0.4	0.3	0.2	0.2	0.1	0.1
Outlet Nozzle	1.6	1.4	1.3	1.1	1.0	1.5	0.5	0.8	0.6	0.4	0.2	0.2	0.1	0.1
Total Assembly	109.9	109.9	110.5	110.8	112.0	109.8	114.1	112.3	113.9	109.3	67.1	67.1	36.5	20.3
LIM, Upper Portion and Orifice	2.9	2.5	2.3	1.9	1.8	2.6	0.4	0.6	0.5	5.7	47.3	48.8	79.6	95.5
LIM, Lower Portion	5.6	6.0	5.6	5.7	4.6	6.0	4.8	5.5	4.0	3.4	4.0	2.5	2.3	2.6
Inlet Plenum							5.8							
Outlet Plenum							2.2							
Vessel Nozzle-to- Nozzle							126.4							
Primary Loop							37.1							
Pump Head							163.5							

NOTES:

- All flows for cycle 4, except zone 6 IB/A which is for cycle 2;
- All flow resistance uncertainties at +3 $\sigma$  or maximum bounding value, whichever appropriate;
- Minimum pump head curve;
- Zone 1 through 8 and 10C are fed by central modules, zones 9, 10P, 11 and 12 by peripheral modules.

4.4-95

Amend. 51  
Sept. 1979

TABLE 4.4-10

MELTING TEMPERATURES FOR  
UNIRRADIATED MIXED URANIA-PLUTONIA  
 (from Nuclear Systems Materials Handbook)

<u>Mole Fraction</u> <u>PuO<sub>2</sub></u>	<u>Solidus</u> <u>°C</u>	<u>Liquidus</u> <u>°C</u>
0.0	2875	2875
0.2	2787	2855
0.4	2685	2745
0.6	2580	2627
0.8	2505	2545
1.0	2445	2445

51

TABLE 4.4-11

EFFECT OF BURNUP ON MELTING POINT OF MIXED URANIUM-PLUTONIA (\*)

(from Nuclear Systems Materials Handbook)

<u>Burnup MWD/MTM</u>	<u>Decrease in Observed Melting Point °C</u>
15,000	62
25,000	64
50,000	69
75,000	74
100,000	80

51

\*Applicable in the composition range of 20 to 25% PuO<sub>2</sub>

TABLE 4.4-12

PRINCIPAL PARAMETERS OF EBR-II IRRADIATED PINS  
USED TO CALIBRATE FISSION GAS RELEASE MODEL

PIN	PEAK BURNUP (a/o)	PEAK LINEAR POWER (kw/ft)	FUEL PELLET DENSITY (% THEORETICAL)	COLD DIAMETRAL GAP THICKNESS (mils)	PERCENT GAS RELEASE	
					MEASURED	PREDICTED
GE-F2-A	4.9	15.6	95.6	2.2	76.2	73.6
GE-F2-B	5.0	16.0	95.2	2.2	75.0	75.1
GE-F2-U	5.3	15.9	89.6	3.8	86.0	82.0
PNL-1-3	0.90	10.7	93.0	5.0	14.6	13.1
PNL-1-6	0.87	10.5	89.5	5.0	13.5	14.0
PNL-1-14	0.87	10.3	90.0	5.0	8.6	11.0
PNL-1-19	0.98	10.7	90.1	7.0	30.8	21.9
PNL-4-1	5.07	10.0	95.1	6.0	63.1	58.7
PNL-4-26	4.93	9.4	92.4	6.0	66.4	56.1
PNL-4-34	4.77	8.9	91.3	8.0	68.7	51.1
PNL-5-31	5.8	13.95	92.7	5.9	86.7	78.7
PNL-8-38	3.4	12.7	93.5	5.6	57.5	60.1
PNL-17-6	3.89	11.5	94.2	6.0	60.5	58.1

4.4-98

Amend. 51  
Sept. 1979

51

TABLE 4.4-13

PRINCIPAL PARAMETERS OF EBR-II IRRADIATED HIGH-BURNUP PINS  
USED TO VERIFY FISSION GAS RELEASE MODEL

PIN	PEAK BURNUP (a/o)	BOL PEAK LINEAR POWER (kw/ft)	PELLET DENSITY (% T.D.)	COLD DIAMETRAL GAP THICKNESS (mils)	PERCENT GAS RELEASED	
					MEASURED	PREDICTED
GE-F2-C	7.2	16.2	94.7	3.2	78.0	84.2
GE-F2-R	7.1	16.2	95.4	1.5	70.1	82.6
GE-F2-H	7.3	16.9	96.1	3.3	80.7	85.4
GE-F2-T	7.4	17.0	96.1	3.0	70.0	84.6
GE-F2-G	12.7	16.3	95.6	3.5	100	91.4

4.4-99

51

Amend. 51  
 Sept. 1979

TABLE 4.4-14

PRINCIPAL PARAMETERS OF EBR-II IRRADIATED PINS AT HIGH  
CLADDING TEMPERATURE USED TO VERIFY FISSION GAS RELEASE MODEL

PIN	PEAK BURNUP (a/o)	BOL PEAK LINEAR POWER (kw/ft)	PELLET DENSITY (% T.D.)	AVERAGE COLD DIAMETRAL GAP THICKNESS (mils)	BOL PEAK CLADDING ID TEMP. (°F)	PERCENT GAS RELEASED	
						MEASURED	PREDICTED
GE-F5-F	6.23	16.1	94.0	4.1	1165	95.8	86.8
GE-F5-H	6.34	16.3	94.1	6.0	1168	~100	89.0
GE-F5-Q	6.21	16.1	94.3	6.0	1163	91.7	88.7

4.4-100

51

Amend. 51  
Sept. 1979

TABLE 4.4-15

ENDF/B-IV FISSION YIELDS (GASEOUS Xe + Kr)  
 (Number of rare gas atoms per 100 fissions)

	U-235 Fission	U-238 Fission	Pu-239 Fission
Kr	3.791	2.486	1.879
Xe	21.732	21.351	23.165
<b>Total</b>	<b>25.523</b>	<b>23.837</b>	<b>25.044</b>

51

TABLE 4.4-16

EVENT CLASSIFICATION AND CLADDING DAMAGE SEVERITY LIMIT

Event Classification (*)	Severity Level	
ASME Code Section III (Article NR-3113)	RDT Standard C-16-1	RDT Standard C-16-1
<p><b>Normal:</b></p> <p>Any condition of system startup, design range operations, not standby, or shutdown other than an upset, emergency, faulted or testing conditions.</p> <p><b>Upset:</b></p> <p>Any abnormal incident not causing a forced outage or causing a forced outage for which the corrective action does not include any repair of mechanical damage.</p> <p><b>Emergency:</b></p> <p>Infrequent incident requiring shutdown for correction of the condition or repair of damage in the system. No loss of structural integrity.</p> <p><b>Faulted:</b></p> <p>Postulated event and consequences where integrity and operability may be impaired to the extent that considerations of public health and safety are involved.</p>	<p><b>Normal Operation:</b></p> <p>Normal operation includes steady power operations and those departures from steady operation which are expected frequently or regularly in the course of power operations, refueling, maintenance, or maneuvering of the plant.</p> <p><b>Anticipated Faulted:</b></p> <p>An off-normal condition which individually may be expected to occur once or more during the plant lifetime.</p> <p><b>Unlikely Faulted:</b></p> <p>An off-normal condition which individually is not expected to occur during the plant lifetime; however, when integrated over all plant components, events in this category may be expected to occur a number of times.</p> <p><b>Extremely Unlikely Faulted:</b></p> <p>An off-normal condition of such extremely low probability that no events in this category are expected to occur during the plant lifetime, but which nevertheless represents extreme or limiting cases of failures which are identified as design bases.</p>	<p><b>No Damage:</b></p> <p>No damage is defined as 1) no significant loss of effective fuel lifetime; 2) accommodations within the fuel and plant operating margins without requiring automatic or manual protective action; and 3) no planned release of radioactivity.</p> <p><b>Operational Incident:</b></p> <p>An operational incident is defined as an occurrence which results in 1) no reduction of effective fuel lifetime below the design values; 2) accommodation with, at most, a reactor trip that assures the plant will be capable of returning to operation after corrective action to clear the trip cause; and/or 3) plant radioactivity releases that may approach the 10CFR20 guidelines.</p> <p><b>Minor Incident:</b></p> <p>A minor incident is defined as an occurrence which results in 1) a general reduction in the fuel burn-up capability and, at most, a small fraction of fuel rod cladding failures; 2) sufficient plant or fuel rod damage that could preclude resumption of operation for a considerable time and/or 3) plant radioactivity releases that may exceed 10CFR20 guidelines, but does not result in interruption or restriction of public use of areas beyond the exclusion boundary.</p> <p><b>Major Incident:</b></p> <p>A major incident is defined as an occurrence which results in 1) substantial fuel and/or cladding melting or distortion in individual fuel rods, but the configuration remains coolable; 2) plant damage that may preclude resumption plant operations, but no loss of safety functions necessary to cope with the occurrence; and/or 3) radioactivity release that may exceed the 10CFR20 guidelines but are well within the 10CFR100 guidelines.</p>

(\*) ASME code and RDT Standard given below define events somewhat differently. Equivalent event classifications are shown here.



TABLE 4.4-17

SUMMARY OF PRELIMINARY DESIGN CRITERIA

<u>Event Classification</u>	<u>Severity Level</u>	<u>Criterion**</u>
Emergency  (Unlikely Faults)	Minor Incident	The total cumulative damage function is to be less than 1.0.  The accumulated plastic and thermal creep strain is to be less than 0.3%.
Faulted  (Extremely Unlikely)	Major Incident	No cladding melting (temperature less than 2475°F) and  *No sodium boiling (temperature less than saturation temperature at the existing pressure).

\*Sodium boiling temperature is quoted as a guideline to establish that no cladding melting can occur.

\*\*The emergency criteria are limits.  
The faulted criteria are guidelines.

TABLE 4.4-18.A

CRBR FUEL ASSEMBLIES ROD TEMPERATURE ENGINEERING UNCERTAINTY FACTORS

	<u>COOLANT</u>	<u>FILM</u>	<u>CLADDING</u>	<u>GAP</u>	<u>FUEL</u>	<u>HEAT FLUX</u>
<u>DIRECT</u> (o)						
Power Level Measurement and Control System Dead Band	1.03(1.0)					1.03
Inlet Flow Maldistribution	1.05	} -----1.022				
Flow Distribution Computational Uncertainty (Simulation Bias)	1.03					
Cladding Circumferential Temperature Variation		1.0(+)	1.7(*)	1.0(+)		
<u>STATISTICAL</u> (3o) (o)						
Reactor ΔT Variation	1.0(1.144)					
Wire Wrap Orientation	1.01					
Subchannel Flow Area	1.028	1.0				
Film Heat Transfer Coefficient		1.12				
Pellet-Cladding Eccentricity		1.15	1.15			
Cladding Thickness and Conductivity			1.12			
Gap Conductance				1.48(±)		
Fuel Conductivity					1.10	
Coolant Properties	1.01					
Flow Distribution Computational Uncertainty (Calibration)	1.054	-----1.015				

(\*) For cladding midwall temperature calculations. Applies to the nominal temperature drop between cladding midwall and bulk coolant.

(+) For fuel temperature calculations.

(±) Applies to BOL conditions.

(o) Nuclear Uncertainty Factors are given on Table 4.4-18.B.

NOTE: Same values of subfactors apply to both Plant T&H and Expected Operating conditions except when two values are given; in this case, the parenthesized values apply to Plant Expected Operating conditions while the non-parenthesized values apply to T&H Operating conditions.

4.4-104

Amend. 51  
Sept. 1979

TABLE 4.4-18.B

CRDR FUEL ASSEMBLIES ROD TEMPERATURE NUCLEAR UNCERTAINTY FACTORS  
WITH AND WITHOUT CONTROL ASSEMBLY INFLUENCE

	<u>COOLANT</u>	<u>HEAT FLUX</u>
<u>DIRECT</u> (o)		
Physics Modeling	1.02(1)	(*)1.02 (1.10)(1)
Control Rod Banking	1.02(2)	1.02(2)
ZPPR-7 Flux Tilt	1.0(4)	1.0(4)
<u>STATISTICAL</u> (3o)(o)		
Nuclear Data	1.07	1.07
Criticality	1.01(3)	1.01(3)
Fissile Fuel Maldistribution	1.03	1.03

If assembly is influenced by adjacent control rod, replace with:

		<u>COOLANT</u>		<u>HEAT FLUX</u>			
		<u>BOL</u>	<u>EOL</u>	<u>"PEAK POWER POSITION"</u>		<u>"TOP OF CORE"</u>	
				<u>BOL</u>	<u>EOL</u>	<u>BOL</u>	<u>EOL</u>
1) Physics Modeling	Adjacent	1.04	1.02	1.03	1.02	1.15	1.15
	Far Side	1.01	1.02	.95	1.02	1.30	1.15
2) Control Rod Banking	Adjacent	1.04	1.02	1.04	1.02	1.01	1.02
	Far Side	1.02	1.02	1.02	1.02	1.01	1.02
3) Criticality	Adjacent	1.04	1.04	1.04	1.04	1.0	1.0
	Far Side	1.01	1.01	1.01	1.01	1.03	1.03

4) ZPPR-7 Flux Tilt - Assy's. 9, 10, 13, 14, 15, 16, 17, 23, 25, 37, 38, 41, 42, 43, 44, 45, 51, 53 (0.97 @ BOL, 1.0 @ EOL). Assy's. 8, 11, 19, 36, 39, 47, 65, 68, 101, 104 (0.99 @ BOL, 1.0 @ EOL). Assys. 62, 98 (0.99 @ BOL, 1.0 @ EOL).

(\*) Non-parenthesized value applies at the peak power position (i.e., core midplane). Parenthesized value applies at the core lower/upper axial blanket interface except as superseded by note (1).

(o) Engineering Uncertainty Factors are given on Table 4.4-18.A.

4.4-105

58

51

Amend. 58  
 NOV. 1980

TABLE 4.4-19.A

CRBR FUEL ASSEMBLIES MIXED MEAN EXIT TEMPERATURE  
ENGINEERING UNCERTAINTY FACTORS

	<u>ASSEMBLY EXIT</u>
<u>DIRECT</u> <sup>(o)</sup>	
Power Level Measurement and Control System Dead Band	1.03(1.0)
Inlet Flow Maldistribution	1.05
<u>STATISTICAL</u> $(3\sigma)$ <sup>(o)</sup>	
Reactor $\Delta T$ Variation	1.0(1.144)
Coolant Properties	1.01

<sup>(o)</sup> Nuclear Uncertainty Factors are given on Table 4.4-19.B.

NOTE: Same values of subfactors apply to both plant T&H and expected operating conditions except when two values are given; in this case, the parenthesized values apply to plant expected operating conditions while the non-parenthesized values apply to T&H operating conditions.

TABLE 4.4-19.B

CRBR FUEL ASSEMBLIES MIXED MEAN EXIT TEMPERATURE NUCLEAR UNCERTAINTY FACTORS

	<u>ASSEMBLY EXIT</u>
<u>DIRECT</u> <sup>(o)</sup>	
Physics Modeling	(*) 1.01(1.02 @ BOL, 1.01 @ EOL)
Control Rod Banking	(*) 1.02(1.03 @ BOL, 1.02 @ EOL)
ZPPR-7 Flux Tilt	1.0 (4)
<u>STATISTICAL</u> (3 $\sigma$ ) <sup>(o)</sup>	
Nuclear Data	1.07
Criticality	(*) 1.01(1.02)
<u>Fissile Fuel Maldistribution</u>	1.03

(4) ZPPR-7 Flux Tilt - Assy's. 9, 10, 13, 14, 15, 16, 17, 23, 25, 37, 38, 41, 42, 43, 44, 45, 51, 53 (0.97 @ BOL, 1.0 @ EOL). Assy's. 8, 11, 19, 36, 39, 47, 65, 68, 101, 104 (0.99 @ BOL, 1.0 @ EOL). Assy's. 62, 98 (0.99 @ BOL; 1.0 @ EOL).

(\*) Non-parenthesized values are applied for assemblies not adjacent to control assemblies. Parenthesized values are applied for the control assembly effect for assemblies adjacent to control assemblies.

(o) Engineering uncertainty factors are given on Table 4.4-19.A.

4.4-107

Amend. 51  
Sept. 1979

TABLE 4.4-20.A

CRBR FUEL ASSEMBLIES PLENUM PRESSURE  
ENGINEERING UNCERTAINTY FACTORS

	<u>PLENUM TEMPERATURE</u>	<u>BURNUP</u>
<u>DIRECT</u> (o)		
Power Level Measurement and Control System Dead Band	1.03(1.0)	1.02
Inlet Flow Maldistribution	1.05	
Flow Distribution Computational Uncertainty (Simulation Bias)	1.03	
<u>STATISTICAL</u> (3 $\sigma$ ) (o)		
Reactor $\Delta T$ Variation	1.0(1.144)	
Wire Wrap Orientation	1.01	
Coolant Properties	1.01	
Flow Distribution Computational Uncertainty (Calibration)	1.085	

(o) Nuclear Uncertainty Factors are given on Table 4.4-20.B.

NOTE: Same values of subfactors apply to both plant T&H and expected operating conditions except when two values are given; in this case, the parenthesized values apply to plant expected operating conditions while the non-parenthesized values apply to T&H operating conditions.

4.4-108

Amend. 51  
Sept. 1979

TABLE 4.4-20B

CRBRP FUEL ASSEMBLIES PLENUM PRESSURE NUCLEAR UNCERTAINTY FACTORS  
WITH AND WITHOUT CONTROL ASSEMBLY INFLUENCE

<u>DIRECT</u> (o)	<u>PLENUM TEMPERATURE</u>	<u>BURNUP</u>
Physics Modeling	1.02 (1)	1.02 (1)
Control Rod Banking	1.02 (2)	1.02 (2)
ZPPR-7 Flux Tilt	1.0 (4)	1.0 (4)
<u>STATISTICAL</u> (3u) (o)		
Nuclear Data	1.07	1.07
Criticality	1.01 (3)	1.01 (3)
Fissile Fuel Maldistribution	1.03	1.03

If assembly is influenced by adjacent control rod, replace with:

		BOL	EOL
1) Physics Modeling	Adjacent	1.04	1.02
	Far Side	1.01	1.02
2) Control Rod Banking	Adjacent	1.04	1.02
	Far Side	1.02	1.02
3) Criticality	Adjacent	1.04	1.04
	Far Side	1.01	1.01

(4) ZPPR-7 Flux Tilt - Assy's. 9, 10, 13, 14, 15, 16, 17, 23, 25, 37, 38, 41, 42, 43, 44, 45, 51, 53 (0.97 @ BOL, 1.0 @ EOL). Assy's. 8, 11, 19, 36, 39, 47, 65, 68, 101, 104 (0.99 @ BOL, 1.0 @ EOL). Assy's. 62, 98 (0.49 @ BOL; 1.0 @ EOL)

(o) Engineering Uncertainty Factors are given on Table 4.4-20.A.

TABLE 4.4-21.A

CRBR INNER/RADIAL BLANKET ASSEMBLIES ROD TEMPERATURES ENGINEERING UNCERTAINTY FACTORS

	<u>COOLANT</u>	<u>FILM</u>	<u>CLADDING</u>	<u>GAP</u>	<u>FUEL</u>	<u>HEAT FLUX</u>
<u>DIRECT</u> <sup>(o)</sup>						
Power Level Measurement and Control System Dead Band	1.03(1.0)					1.03
Inlet Flow Maldistribution	1.07	} ----- 1.03				
Flow Distribution Computational Uncertainty (Simulation Bias)	1.03					
Cladding Circumferential Temperature Variation		1.0(+)	2.2(*)	1.0(+)		
<u>STATISTICAL</u> (3 <sub>o</sub> ) <sup>(o)</sup>						
Reactor ΔT Variation	1.0(1.144)					
Wire Wrap Orientation	1.01					
Subchannel Flow Area	1.035	1.0				
Film Heat Transfer Coefficient		1.21				
Pellet-Cladding Eccentricity		1.15	1.15			
Cladding Thickness and Conductivity				1.12		
Gap Conductance					1.48(ϕ)	
Fuel Conductivity						1.10
Coolant Properties	1.01					
Flow Distribution Computational Uncertainty (Calibration)	1.199/1.1(ϕ)	1.056				

(\*) For cladding midwall temperature calculations. Applies to the nominal temperature drop between cladding midwall and bulk coolant.

(+) For fuel temperature calculations

(ϕ) Applies to BOL conditions.

(o) Nuclear Uncertainty Factors are given on Table 4.4-21.B.

(◇) Inner/radial blanket.

NOTE: Same values of subfactors apply to both Plant T&I and Expected Operating conditions except when two values are given; in this case, the parenthesized values apply to Plant Expected Operating conditions while the non-parenthesized values apply to T&I Operating conditions.



TABLE 4.4-21.B

CRBR INNER/RADIAL BLANKET ASSEMBLIES ROD TEMPERATURE NUCLEAR UNCERTAINTY FACTORS

	<u>INNER BLANKET</u>		<u>RADIAL BLANKET</u>			
	<u>COOLANT</u>	<u>HEAT FLUX</u>	<u>Row 1</u>		<u>Row 2</u>	
			<u>COOLANT</u>	<u>HEAT FLUX</u>	<u>COOLANT</u>	<u>HEAT FLUX</u>
<u>DIRECT (EOL)<sup>(a)</sup></u>						
Physics Modeling	1.06	(*)1.07(1.11)	1.03	(*)1.07(1.02)	1.03	(*)1.07(0.99)
Control Rod Banking	1.02	(*)1.02	1.02	(*)1.02	1.02	(*)1.02
Nuclear Data	1.12	(*)1.10(1.17)	1.13	(*)1.11(1.18)	1.27	(*)1.24(1.32)
Criticality	1.02	1.02	----	----	----	----
Heavy Metal	1.01	1.01	1.01	1.01	1.01	1.01
U-235	1.01	1.01	1.01	1.01	1.01	1.01
<u>DIRECT (EOL)<sup>(a)</sup></u>						
Physics Modeling	1.02	(*)1.04(1.12)	1.01	(*)1.07(1.05)	1.01	(*)1.07(1.02)
Control Rod Banking	1.02	(*)1.02	1.02	(*)1.02	1.02	(*)1.02
Nuclear Data	1.03	(*)1.00(1.07)	1.05	(*)1.03(1.10)	1.15	(*)1.13(1.21)
Criticality	1.01	1.01	----	----	----	----
Heavy Metal	1.01	1.01	1.01	1.01	1.01	1.01
U-235	1.0	----	----	----	----	----

(\*) Non-parenthesized values apply at the peak power position (i.e., near core midplane). Parenthesized values apply at core upper/lower axial extension interface.

(a) Engineering Uncertainty Factors are given on Table 4.4-21.A:

4.4-111

58

Amend. 58  
Nov. 1980

51

TABLE 4.4-22.A

CRBR INNER/RADIAL BLANKET ASSEMBLIES MIXED MEAN EXIT TEMPERATURE  
ENGINEERING UNCERTAINTY FACTORS

<u>DIRECT</u> <sup>(o)</sup>	<u>ASSEMBLY EXIT</u>
Power Level Measurement and Control System Dead Band	1.03(1.0)
Inlet Flow Maldistribution	1.07
<u>STATISTICAL</u> <sup>(3σ)</sup> <sup>(o)</sup>	
Reactor ΔT Variation	1.0(1.144)
Coolant Properties	1.01

<sup>(o)</sup> Nuclear Uncertainty Factors are given on Table 4.4-22.B.

NOTE: Same values of subfactors apply to both plant T&H and expected operating conditions except when two values are given; in this case, the parenthesized values apply to plant expected operating conditions while the non-parenthesized values apply to T&H operating conditions.

51

TABLE 4.4-22.B

CRBR INNER/RADIAL BLANKET ASSEMBLIES MIXED MEAN EXIT TEMPERATURE NUCLEAR UNCERTAINTY FACTORS

	<u>INNER BLANKET</u>		<u>RADIAL BLANKET</u>	
	<u>ASSEMBLY EXIT</u>	<u>Row 1</u>	<u>Row 2</u>	<u>ASSEMBLY EXIT</u>
		<u>ASSEMBLY EXIT</u>	<u>ASSEMBLY EXIT</u>	<u>ASSEMBLY EXIT</u>
<u>DIRECT (BOL)<sup>(o)</sup></u>				
Physics Modeling	1.01	1.02	1.02	1.02
Control Rod Banking	1.02	1.02	1.02	1.02
Nuclear Data	1.12	1.13	1.13	1.27
Criticality	1.02	----	----	----
Heavy Metal	1.01	1.01	1.01	1.01
U-235	1.01	1.01	1.01	1.01
<u>DIRECT (EOL)<sup>(o)</sup></u>				
Physics Modeling	1.01	1.02	1.02	1.02
Control Rod Banking	1.02	1.02	1.02	1.02
Nuclear Data	1.03	1.05	1.05	1.15
Criticality	1.01	----	----	----
Heavy Metal	1.01	1.01	1.01	1.01
U-235	----	----	----	----

<sup>(o)</sup> Engineering uncertainty factors are given on Table 4.4-22.A.

4.4-113

Amend. 51  
Sept. 1979

TABLE 4.4-23.A

CRBR INNER/RADIAL BLANKET ASSEMBLIES PLENUM PRESSURE  
ENGINEERING UNCERTAINTY FACTORS

<u>DIRECT</u> (o)	<u>PLENUM TEMPERATURE</u>	<u>BURNUP</u>
Power Level Measurement and Control System Dead Band	1.03(1.0)	1.02
Inlet Flow Maldistribution	1.07	
Flow Distribution Computational Uncertainty (Simulation Bias)	1.03	
<u>STATISTICAL (3σ) (o)</u>		
Reactor ΔT Variation	1.0(1.144)	
Wire Wrap Orientation	1.01	
Coolant Properties	1.01	
Flow Distribution Computational Uncertainty (Calibration)	1.299/1.1 (o)	

(o) Nuclear Uncertainty Factors are given on Table 4.4-23.B.

(o) Inner/radial blanket

NOTE: Same values of subfactors apply to both plant T&H and expected operating conditions except when two values are given; in this case, the parenthesized values apply to plant expected operating conditions while the non-parenthesized values apply to T&H operating conditions.

4.4-114

Amend. 51  
Sept. 1979

TABLE 4.4-23.B

CRBR INNER/RADIAL BLANKET ASSEMBLIES PLENUM PRESSURE NUCLEAR UNCERTAINTY FACTORS

	<u>INNER BLANKET</u>		<u>RADIAL BLANKET</u>			
	<u>PLENUM TEMPERATURE</u>	<u>BURNUP</u>	<u>Row 1</u>		<u>Row 2</u>	
			<u>PLENUM TEMPERATURE</u>	<u>BURNUP</u>	<u>PLENUM TEMPERATURE</u>	<u>BURNUP</u>
<u>DIRECT (BOL) (o)</u>						
Physics Modeling	1.06	1.06	1.03	1.03	1.03	1.03
Control Rod Banking	1.02	1.02	1.02	1.02	1.02	1.02
Nuclear Data	1.12	1.12	1.13	1.13	1.27	1.27
Criticality	1.02	1.02	----	----	----	----
Heavy Metal	1.01	1.01	1.01	1.01	1.01	1.01
U-235	1.01	1.01	1.01	1.01	1.01	1.01
<u>DIRECT (EOL) (o)</u>						
Physics Modeling	1.02	1.02	1.01	1.01	1.01	1.01
Control Rod Banking	1.02	1.02	1.02	1.02	1.02	1.02
Nuclear Data	1.03	1.03	1.05	1.05	1.15	1.15
Criticality	1.01	1.01	----	----	----	----
Heavy Metal	1.01	1.01	1.01	1.01	1.01	1.01
U-235	----	----	----	----	----	----

4.4-115

Amend. 51  
Sept. 1979

51 (o) Engineering uncertainty factors are given on Table 4.4-23.A.

TABLE 4.4-24

CRBRP PRIMARY CONTROL ASSEMBLIES PIN TEMPERATURES HOT CHANNEL/SPOT FACTORS

DIRECT (+)	Coolant	Film	Cladding	Gap	Absorber	Heat Generation						
						Absorber	Cladding	Coolant				
Power Level Measurement and Control System Dead Band	1.03											
Inlet Flow Maldistribution	1.08					1.03	1.03	1.03				
Subassembly Flow Maldistribution	1.08 } 1.10 }	1.075										
Calculational Uncertainties												
Bundle/Bypass Flow Split												
Cladding Circumferential Temperature Variation		1.0(0)	1.0(0)									
			(Note 1)									
<u>STATISTICAL (3σ) (0)</u>												
Inlet Temperature Variation	1.02 (+)											
Reactor ΔT Variation	1.04 (+)											
Absorber Maldistribution and Conductivity	1.02				1.10	1.03						
Wire Wrap Orientation	1.01											
Subchannel Flow Area	1.09	1.0										
Film Heat Transfer Coefficient		1.21							1.0			
Pellet-Cladding Eccentricity		1.37 (*)										
Cladding Thickness and Conductivity	1.01		1.39 (*)									
Gap Thickness and Conductivity			1.10					1.04				
Coolant Properties	1.01				1.13							
TOTAL	2σ 3σ	1.413 (+) 1.458 (+)	1.404 (+) 1.445 (+)	1.23 (0) 1.30 (0)	1.38 (*) 1.53 (*)	1.07 (0) 1.10 (0)	1.27 (*) 1.40 (*)	1.09 1.13	1.07 1.10	1.051 1.061	1.057 1.071	1.03 1.03

(+) Uncertainties due to physics analysis calculational methods (15% on coolant enthalpy rise and on absorber, cladding and coolant heat generation) are applied directly on nuclear radial peaking factors.

(\*) For local cladding temperature calculations.

(0) For average cladding, absorber temperature calculations.

(o) In addition, the assembly inlet temperature will be increased by 16°F, to account for primary loop temperature coolant uncertainties.

(+) Applies to Plant Expected Operating Conditions.

(t) Applies to Plant T&H Design Conditions.

(Note 1) Under the wire wrap local hot spot factors are 3.17, 1.40 and 1.20, for the cladding OD, midwall and ID, respectively.

4.4-116

Amend. 51  
Sept. 1979

TABLE 4.4-25

CR8RP PRIMARY CONTROL ASSEMBLIES MIXED MEAN EXIT TEMPERATURE HOT CHANNEL FACTORS

	<u>Assembly Exit</u>	<u>Chimney Exit</u>
<u>DIRECT (+)</u>		
Power Level Measurement and Control System Dead Band	1.03	1.02
Inlet Flow Maldistribution	1.08	1.07
<u>STATISTICAL (3<math>\sigma</math>) (o)</u>		
Inlet Temperature Variation	1.03( $\phi$ )1.0(+)	
Reactor $\Delta T$ Variation	1.04( $\phi$ )1.0(+)	
Absorber Maldistribution	1.02	1.02
Cladding Thickness	1.01	1.01
Coolant Properties	1.01	
TOTAL	1.154( $\phi$ )1.130(+)	1.111
	3 $\sigma$ 1.175( $\phi$ )1.140(+)	1.116

(+) Uncertainties due to physics analysis calculational methods (15% for both assembly and chimney exit) are applied directly on nuclear radial peaking factors.

( $\phi$ ) Applies to Plant Expected Conditions.

(+) Applies to Plant T&H Design Conditions.

(o) In addition, the assembly inlet temperature will be increased by 16°F (assembly exit) or 10°F (chimney exit), to account for primary loop temperature control uncertainties.

TABLE 4.4-26

CRBRP PRIMARY CONTROL ASSEMBLIES PLENUM PRESSURE  
HOT CHANNEL FACTORS

	<u>Plenum Temperature</u>	<u>Burnup</u>
<u>DIRECT (+)</u>		
Power Level Measurement	1.02	1.02
Inlet Flow Maldistribution	1.08	
Subassembly Flow Maldistribution Calculational Uncertainties	1.08	
Bundle/Bypass Flow Split	1.10	
<u>STATISTICAL (3σ) (o)</u>		
Inlet Temperature Variation	1.02 <sup>(ϕ)</sup> 1.0 <sup>(†)</sup>	
Reactor ΔT Variation	1.04 <sup>(ϕ)</sup> 1.0 <sup>(†)</sup>	
Absorber Maldistribution	1.02	1.02
Cladding Thickness	1.01	
Wire Wrap Orientation	1.01	
Coolant Properties	1.01	
TOTAL		
	2σ	1.034
	3σ	1.040
	1.354 <sup>(ϕ)</sup> 1.332 <sup>(†)</sup>	
	1.376 <sup>(ϕ)</sup> 1.356 <sup>(†)</sup>	

(+) Uncertainties due to physics analysis calculational methods (15% on both plenum temperature and burnup) are applied directly on nuclear peaking factors.

(ϕ) Applies to Plant Expected Operating Conditions.

(†) Applies to Plant T&H Design Conditions.

(o) In addition, the assembly inlet temperature will be increased by 16°F to account for primary loop temperature control uncertainties.

51



TABLE 4.4-27  
CRBRP SECONDARY CONTROL ASSEMBLIES PIN TEMPERATURES HOT CHANNEL/SPOT FACTORS

	<u>Coolant</u>	<u>Film</u>	<u>Cladding</u>	<u>Gap</u>	<u>Absorber</u>	<u>Heat Generation</u>		
						<u>Absorber</u>	<u>Cladding</u>	<u>Coolant</u>
<u>DIRECT (+)</u>								
Power Level Measurement and Control System Dead Band	1.03					1.03	1.03	1.03
Inlet Flow Maldistribution	1.05	} -1.12						
Subassembly Flow Maldistribution								
Calculational Uncertainties	1.10							
Bundle/Bypass Flow Split	1.06							
Cladding Circumferential Temperature Variation		1.58	2.53 (*)					
<u>STATISTICAL (3σ) (o)</u>								
Absorber Maldistribution and Conductivity	1.02				1.10	1.03		
Subchannel Flow Area	1.08							1.0
Film Heat Transfer Coefficient		1.40	1.37 (*)	1.38 (*)				
Pellet-Cladding Eccentricity								
Cladding Thickness and Conductivity	1.01		1.10	1.13			1.04	
Gap Thickness and Conductivity	1.01							
Coolant Properties								
TOTAL	2σ	1.54	2.25 3.85 (*)	1.07 1.26		1.05	1.06	1.03
	3σ	1.58	2.48 4.36 (*)	1.10 1.39 (*)	1.13 1.10	1.06	1.07	1.03

(+) Uncertainties due to physics analysis calculational methods (15% on coolant enthalpy rise and on absorber, cladding and coolant heat generation) are applied directly on nuclear radial peaking factors.

(o) in addition, the assembly inlet temperature will be increased by 16°F, to account for primary loop temperature control uncertainties.

(\*) For maximum local cladding midwall temperature calculations only.

4.4-119

57

Amend. 51  
 Sept. 1979

TABLE 4.4-28

CRBR EXPECTED OPERATING CONDITIONS DURING PLANT LIFETIME

Parameter	Clean & Unplugged Heat Exchangers (New Plant)				Estimated (2 Year Fouling)				Fouled & Plugged Heat Exchangers (30 Year Fouling)			
	Nominal	Mean	$\sigma$	T <sub>97.7</sub>	Nominal	Mean	$\sigma$	T <sub>97.7</sub>	Nominal	Mean	$\sigma$	T <sub>97.7</sub>
	Primary Hot Leg Temperature (°F)	943	946	13	968	950	954	13	976	960	964	13
Primary Cold Leg Temperature (°F)	698	697	13	722	705	704	11	725	714	714	12	736
Primary $\Delta T$ (°F)	245	249	12	273	245	250	12	274	246	250	12	275
Power (Mwt)	975	975		1004	975	975		1004	975	975		1004

NOTE: Design and control uncertainties are included.

4.4-120

51

56

Amend. 56  
Aug. 1980

TABLE 4.4-29

PLANT EXPECTED CONDITIONS AND ASSOCIATED UNCERTAINTIES  
CONSIDERED ON CRBRP CORE THERMOFLUIDS ANALYSES

	<u>First Core</u>	<u>Second Core</u>
Nominal Inlet Temperature (°F)	704	711
Nominal Reactor $\Delta T$ (°F)	250	250
Reactor $\Delta T$ Uncertainty Factor ( $3\sigma$ ) <sup>(*)</sup>	1.144	1.144
Inlet Temperature Uncertainty ( $3\sigma$ ) (°F)	33	36
Loop-to-Loop Imbalance ( $3\sigma$ ) (°F)	4.6	4.6
Combined Uncertainty on Inlet Temperature ( $2\sigma$ ) (°F) - (Additive to Nominal)	22.2	24.6

(\*) To be combined with other uncertainties on  $F_{\Delta H}$

NOTE: Power Level Measurement/Control Dead Band Uncertainty is  
 Already Included in Above Uncertainties

TABLE 4.4-30

CENTER TEMPERATURES AND POWERS-TO-MELT OF INCIPIENT  
MELT SECTIONS AS COMPUTED BY LIFE-3

Pin No.	Calculated T		Calculated Power-to-Melt		Observed Power-to-Melt	
	°F	(°C) <sup>max</sup>	kw/ft	(kw/m)	kw/ft	(kw/m)
P19-35	5009	(2765)	16.62	(54.5)	16.69	(54.6)
P19-02	4978	(2748)	16.04	(52.6)	15.89	(52.1)
P19-24R	5024	(2773)	15.44	(50.6)	15.59	(51.1)
P19-27R	4990	(2754)	19.23	(63.1)	19.16	(62.8)
P19-28	4966	(2741)	19.02	(62.4)	18.82	(61.8)
P19-30	5070	(2799)	17.22	(56.5)	17.79	(58.3)
P19-08	5006	(2763)	15.36	(50.4)	15.40	(50.5)
P20-07	5004	(2762)	15.72	(51.7)	15.75	(51.7)
P20-30	4985	(2752)	16.82	(55.2)	16.70	(54.8)
P20-33	4982	(2750)	19.07	(62.5)	18.98	(62.2)

Average T =  $5001 \pm 28^{\circ}\text{F}$   
( $2761 \pm 16^{\circ}\text{C}$ )

r.m.s error  
= 0.21 kw/ft (.69 kw/m)

std. dev.\*  
= 0.24 kw/ft (.77 kw/m)

51

\*Two degrees of freedom lost in calibrating LIFE-III parameters.

TABLE 4.4-31  
COMPARISON OF 3 $\sigma$  MINIMUM POWER-TO-MELT TO POWER AT 15% OVERPOWER

ASSEMBLY	t(hrs)	$Q_1 =$ POWER AT START OF JUMP NFP*	$\frac{1.15}{1.03} Q_1$	$Q_2 = \overline{\text{REPOW}}_M$	$Q_3 = 3\sigma \text{REPOW}_M$	$Q_4 = Q_2 - Q_3$	MARGIN = $Q_4 - \frac{1.15}{1.03} Q_1$
F/A 101	8	0.70	0.782	1.111	0.234	0.877	0.095
F/A 101	58	0.90	1.005	1.315	0.180	1.135	0.130
F/A 101	108	1.00	1.117	1.390	0.210	1.180	0.063
F/A 14	8	0.70	0.782	1.172	0.234	0.938	0.156
F/A 14	58	0.90	1.005	1.350	0.180	1.170	0.165
F/A 14	108	1.00	1.117	1.442	0.210	1.232	0.115

(\*) NFP = Nominal full power.

4.4-123

51

Amend. 51  
 Sept. 1979

TABLE 4.4-32a

## PRIMARY CONTROL ASSEMBLY OPERATING PARAMETERS

o Number of orificing zones	1
o PCA's total flow allocation (fraction reactor flow)	0.01
o Flowrate (PEOC, lb/hr)	49,500
o Flow split (bundle/total assembly flow)	0.62
o Maximum bundle flow velocity (ft/sec)	8
o Maximum hot rod midwall cladding temperature (PEOC, $2\sigma$ , °F)	1006
o Maximum fission gas pressure ( $2\sigma$ , psia)	3600 @ 275 fpd
o Maximum linear power rating ( $3\sigma$ + overpower, Kw/ft)	16 Bottom 1.4 Top
o Maximum absorber temperature (THDV nominal, °F)	3367
o Maximum mixed mean exit temperature (THDV nominal, °F)	853
o Maximum exit gradient (nominal, °F)	246

TABLE 4.4-32b

SECONDARY CONTROL ASSEMBLY OPERATING PARAMETERS

Flow Rate (THDV, 1b/hr)	
Control Rod Flow	9,130
Bypass Flow	9,330
Total Upflow	18,460
Downflow	50,710
Total Assembly	69,170
Hydraulic Scram Assist Force at Full Flow (lbs)	148 - 248
Peak Linear Power (kw/ft)	4.0
Outlet Temperature (THDV, Nominal, °F)	
Control Rod Bundle	829
Assembly	854
Maximum Cladding Midwall Temperature (°F)	
Nominal, THDV	853
Hot Spot (THDV, 2σ)	895
Maximum Absorber Temperature (°F)	
Nominal, THDV	1054
Hot Spot (THDV, 3σ)	1188

TABLE 4.4-33

## SUMMARY OF FLOTATION EVALUATION

	<u>Rod Bundle Pressure Drop (Psi)</u>	<u>Flow Rate (Lb/Hr)</u>
1. Test observed flotation conditions	7.5	57,500
2. Above, accounting for test uncertainties	7.2	55,000
3. PCA operation conditions, nominal, PEOC	5.94	49,600
4. Total effect of core components hydraulic resistance uncertainties:		
o r.s.s. combination $2\sigma/3\sigma$	0.35/0.52	687/976
o Absolute sum combination $2\sigma/3\sigma$	0.73/1.06	1932/2696
5. Maximum design conditions (3+4):		
o r.s.s. combination $2\sigma/3\sigma$	6.29/6.46	50287/50576
o Absolute sum combination $2\sigma/3\sigma$	6.67/7.0	51532/52296
6. Margin-to-flotation (2-5):		
o r.s.s. combination $2\sigma/3\sigma$	0.91/0.74 (15/12)*	4713/4424 (9.5/9)*
o Absolute sum combination $2\sigma/3\sigma$	0.53/0.2 (9/3)*	3468/2704 (7/5.5)*

\*In percentage of nominal conditions.



TABLE 4.4-34

RRSA POWER AND FLOW UNCERTAINTY FACTORS

HEAT GENERATION<sup>(c)</sup>

DIRECT

Bias <sup>(a)(b)</sup>	0.8731
Non-Statistical SOC-to-EOC and Assembly-to-Assembly	1.08
Cycle-to-Cycle Bias <sup>(a)</sup>	1.02
	0.88 (Cycle 1)
	1.05 (Cycle 5)
Power Level Measurement and Control System Dead Band	1.03 <sup>(d)(g)</sup>

STATISTICAL (3 $\sigma$ )

Statistical	1.12
-------------	------

FLOW<sup>(c)</sup>

DIRECT

Inlet Flow Maldistribution	1.02
BPFM Leakage <sup>(e)</sup>	1.069

STATISTICAL (3 $\sigma$ )

Inlet Flow Maldistribution	1.122
Loop Temperature Imbalance	1.030 (for $\Delta T = 250^{\circ}F$ )
Coolant Properties	
Reactor $\Delta T$ and Inlet Temperature Variation	1.156 <sup>(f)(g)</sup> (for $\Delta T = 250^{\circ}F$ )

- (a) Biases are always in direction indicated. Remaining factors are  $\pm$ .
- (b) Bias on stainless steel heating is weighted for combined stainless steel and sodium heating, and applied to unbiased heating rates.
- (c) A factor greater than unity increases temperatures; i.e., heat generation rate is multiplied by the factor and flow rate is divided by the factor.
- (d) THDV conditions.
- (e) For RRSA's in BPFM.
- (f) PEOV conditions.
- (g) Affects all RRSA and core assemblies in same direction.

TABLE 4.4-35

LIFETIME VARIATION OF NOMINAL MIXED MEAN TEMPERATURE OF SELECTED  
ASSEMBLIES AND AVERAGE TEMPERATURE USED FOR REACTOR CONTROL

ASSEMBLY NO.	ASSEMBLY TYPE	BOC1	EOC1	BOC2	EOC2	BOC3	EOC3	BOC4	EOC4
101	Fuel	1104	1081	1076	1041	1091	1048	1047	1010
99	Inner Blanket	842	893	887	956	834	928	946	1030
201	Radial Blanket	848	874	877	914	926	965	953	982
14	Fuel	1092	1077	1081	1063	1069	1045	1021	1010
24	Fuel	1095	1073	1078	1050	1093	1050	1032	1008
2	Fuel	1057	1059	1075	1068	1040	1045	1067	1054
44	Fuel	1120	1103	1064	1056	1094	1068	1043	1030
50	Fuel	1073	1051	1029	1008	1076	1032	1020	992
12	Inner Blanket	896	938	939	990	894	972	967	1021
34	Fuel	1067	1062	1074	1058	1048	1042	1061	1040
Average of above		1019	1021	1018	1020	1017	1019	1016	1018

NOTE: All temperatures in °F.

TABLE 4.4-36

EXPERIMENTAL DATA REFERENCES FOR FLOW DISTRIBUTION  
CALCULATIONS AT LOW FLOW (SECTION 4.4.2.6)

1. PRESSURE DROP DATA - FLOW REDISTRIBUTION FOR FIGURES 4.4-66 & 67
  1. "Covered Pressure Drop Flow Test/Cross Flow Mixing Test", HEDL-TI-76049, November 1976. (Availability: US/DOE Technical Information Center).
  2. W. L. Thorne, "Pressure Drop Measurements In FFTF Fuel Vibration Tests", HEDL-TC-812, April 1977. (Availability: US/DOE Technical Information Center).
  3. W. L. Thorne, "Pressure Drop Measurements from Fuel Assembly Vibration Test II", HEDL-TC-824, April 1977. (Availability: US/DOE Technical Information Center).
  4. P. M. McConnell, "Clinch River Breeder Reactor Fuel Assembly Inlet/Outlet Nozzle Flow Tests", HEDL-TME-77-8, February 1977. (Availability: US/DOE Technical Information Center).
  5. H. M. Geiger, D. C. Meess and D. K. Schmidt, "Radial Blanket Flow Orificing Testing: Calibration Tests", WARD-RB-3045-18, April 1977. (Availability: US/DOE Technical Information Center).
  6. F. C. Engel, R. A. Markley and A. A. Bishop, "Laminar, Transition and Turbulent Parallel Flow Pressure Drop Across Wire Wrap Spaced Rod Bundles", Nucl. Sci. Eng., 69, pp. 290-296 (1979); 74, p. 226 (1980).
  7. I. E. Idel'chik, "Handbook of Hydraulic Resistance - Coefficients of Local Resistance and of Friction", AEC-TR-6630, 1960.
  8. L. F. Moody, "Friction Factors for Pipe Flow", Trans. Amer. Soc. Mech. Eng., 66, pp. 671-684 (1944).
  9. R. G. White and M. D. Simmons, "CRBRP Fuel Assembly Flow and Vibration Tests in Water", HEDL-TME-78-106, October 1979.
  10. P. M. McConnell, "Interim Report on CRBRP Fuel Assembly Cavitation Tests in Water", HEDL-TC-967, October 1977.
  11. C. Chiu, et al., "Pressure Drop Measurements in LMFBR Wire Wrapped Blanket Assemblies", MIT COO-2245-42TR Report (1977).
  12. "Radial Blanket Design and Development Quarterly Progress Report for Period Ending August 31, 1977", WARD-RB-3045-21 (1977).
  13. J. G. Akey and H. O. Lagally, "Primary Control Assembly Hydraulic Test", WARD-D-0263, July 1980.

TABLE 4.4-36 (Cont'd)

14. D. R. Dickinson and F. H. Nunamaker, "Measurement of Outlet Plenum Velocity Profiles, Pressure Drops and Flow Splits in the IRFM of CRBRP", HEDL-TC-1015, December 1979.
  15. P. M. McConnell, et al., "Inlet Plenum Feature Model Flow Tests of the CRBRP; Addendum V-Results", HEDL-TME-76-33, March 1976.
  16. P. M. McConnell, "CRBRP Removable Radial Shielding Orifice Pressure Drop Test Results, DRS 31.14.37", HEDL-TC-958, September 1977.
11. HEAT TRANSFER AND OTHER DATA USED FOR VALIDATION OF COBRA-WC (PNL-4128) AND FORE-2M (Nucl. Eng. & Des., 68, No. 3, pp. 323-336, April 1982) CODES FOR FIGURE 4.4-68
1. Bates, J. M., and E. U. Khan. 1980. "Investigation of Combined Free and Forced Convection in a 2 x 6 Rod Bundle During controlled Flow Transients." AIChE Symposium Series: Heat Transfer - Orlando, 1980, American Institute of Chemical Engineers, New York, New York, Series No. 199, Vol. 76, pp. 215-230.
  2. Bates, J. M., and E. U. Khan. 1980. Investigation of Combined Free and Forced Convection in a 2 x 6 Rod Bundle During controlled Flow Transients. PNL-3135, Pacific Northwest Laboratory, Richland, Washington.
  3. Chen, Y. B., K. Ip and N. E. Todreas. 1974. Velocity Measurements in Edge Subchannels of Wire-Wrapped LMFBR Fuel Assemblies. COO-2245-11TR, Department of Nuclear Engineering, Massachusetts Institute of Technology, Cambridge, Massachusetts.
  4. Chiu, C., et al. 1978. Flow Split Measurements in LMFBR Blanket Assemblies. COO-2245-41TR, Massachusetts Institute of Technology, Cambridge, Massachusetts.
  5. Engel, F. C., R. A. Markley, and B. Minushkin, 1978. "Buoyancy Effects on Sodium coolant Temperature Profiles Measured in an Electrically Heated Mockup of a 61-Rod Breeder Reactor Blanket Assembly." ASME paper 78-WA/HT-25; American Society of Mechanical Engineers, New York, New York.
  6. Fontana, M. H. 1973. Temperature Distribution in the Duct Wall and at the Exit of a 19-Rod Simulated LMFBR Fuel Assembly (FFM Bundle 2A). ORNL-4852, Oak Ridge National Laboratory, Oak Ridge, Tennessee.
  7. Gillette, J. L., R. M. Singer, J. V. Tokar and J. W. Sullivan. 1979. "Experimental Study of the Transition from Forced to Natural Circulation in EBR-11 at Low Power and Flow." Paper No. 79-HT-10, American Society of Mechanical Engineers, New York, New York.

TABLE 4.4-36 (Cont'd)

8. C. W. Hoth. 1981. "Fuel Open Test Assembly (FOTA) Data Obtained During the FFTF, 75% and 100% Natural Circulation Tests." HEDL-TC-1940, Hanford Engineering Development Laboratory, Richland, Washington.
9. Juneau, J., and E. U. Khan. 1979. Analysis of Steady-State Combined Forced and Free Convection Data in Rod Bundles. FRA-TM-116, Argonne National Laboratory, Argonne, Illinois.
10. Lafay, J., B. Menant and J. Barrois. 1975. "Influence of Helical Wire-Wrap Spacer System in a 19-Rod Bundle." Presented to the 1975 Heat Transfer Conference, April 1975, San Francisco, California.
11. Lorenz, J. J., T. Ginsberg and R. A. Morris. 1974. Experimental Mixing Studies and Velocity Measurements with a Simulated 91-Element LMFBR Fuel Assembly. ANL-CT-74-09, Argonne National Laboratory, Argonne, Illinois.
12. Lorenz, J. J., D. R. Pedersen and R. D. Pierce. 1973. Peripheral Flow Visualization Studies in a 91-Element Bundle. ANL-RAS-73-14, Argonne National Laboratory, Argonne, Illinois.
13. Milburg, M. L., J. A. Hassberger and C. J. Boasso. 1977. Natural Circulation Heat Transfer Testing with a Simulated Full-Scale LMFBR 217-Pin Electrically Heated Fuel Assembly. HEDL-TME-77-3, Hanford Engineering Development Laboratory, Richland, Washington.
14. Morris, R. H. et al. 1980. Single-Phase Sodium Tests in 61-Pin Full-Length Simulated LMFBR Fuel Assembly-Record of Phase 1 Experimental Data for THORS Bundle 9. ORNL/TM-7313, Oak Ridge National Laboratory, Oak Ridge, Tennessee.
15. Novendstern, E. H. 1972a. Mixing Model for Wire-Wrapped Fuel Assemblies. WARD-5915, Westinghouse Advanced Reactor Division, Madison, Pennsylvania.
16. Novendstern, E. H. 1972b. "Turbulent Flow Pressure Drop Model for Rod Assemblies Utilizing a Helical Wire-Wrap Spacer System." Nuclear Engineering and Design. 22:19-27.
17. Wang, S. and N. E. Todreas. 1981. "Computer Model for MIT Correlations for Friction Factors, Flow Splits and Mixing Parameters in LMFBR Wire-Wrapped Rod Assemblies." DOE/ET/37240-87TR, Massachusetts Institute of Technology, Cambridge, Massachusetts.
18. Cheung, A. C., et al., "Verification of the CRBRP Natural Circulation Core Analyses Methodology with Data from FFTF Natural Circulation Tests", CRBRP-ARD-0310, June 1982.
19. Coffield, R. D., R. A. Markley and E. U. Khan, "Natural Circulation Analyses and Verification for LMFBR Cores", Nucl. Engrg. Des., 62, (1980) pp. 181-198.

TABLE 4.4-36 (Cont'd)

20. Billone, M. C., et al., "LIFE-III Fuel Element Performance Code User's Manual", ERDA-77-56, July 1977.
21. Henderson, J. M., S. A. Wood and D. D. Knight, "Sodium Boiling and Mixed Oxide Fuel Thermal Behavior in FBR Undercooling Transient", W-1 SLSF experimnts results.
22. Freeman, D. D., "SEFOR Experimental Results and Applications to LMFBRs", GEAP-13929, January 1979.
23. Bishop, A. A., R. D. Coffield and R. A. Markley, "Review of Pertinent Thermal-Hydraulic Data for LMFBR Core Natural Circulation Analyses", AIChE Symposium, Series 76, (1980), pp. 193-204.
24. Coffield, R. D., et al., "Buoyancy-Induced Flow and Heat Redistribution During LMFBR Core Decay Heat Removal", Proc. of Specialists Meeting on Decay Heat Removal and Natural Convection in FBRs., Brookhaven National Laboratory, New York, February 1980.
25. Gillette, J. L., D. Mohr, R. Singer and R. Smith, "A Flow Coastdown to Natural Convection Conditions in EBR-II", ANS Trans. 22 (1975) p. 394.
26. Singer, R. M. and J. L. Gillette, "Measurements of Subassembly and Core Temperature Distribution in an LMFBR", AIChE Symposium, Series 73, (1977), p. 97.
27. Stover, R. L., et al., "FFTF Natural Circulation Tests", Presented at ANS Winter Meeting at San Francisco, California, 1981.

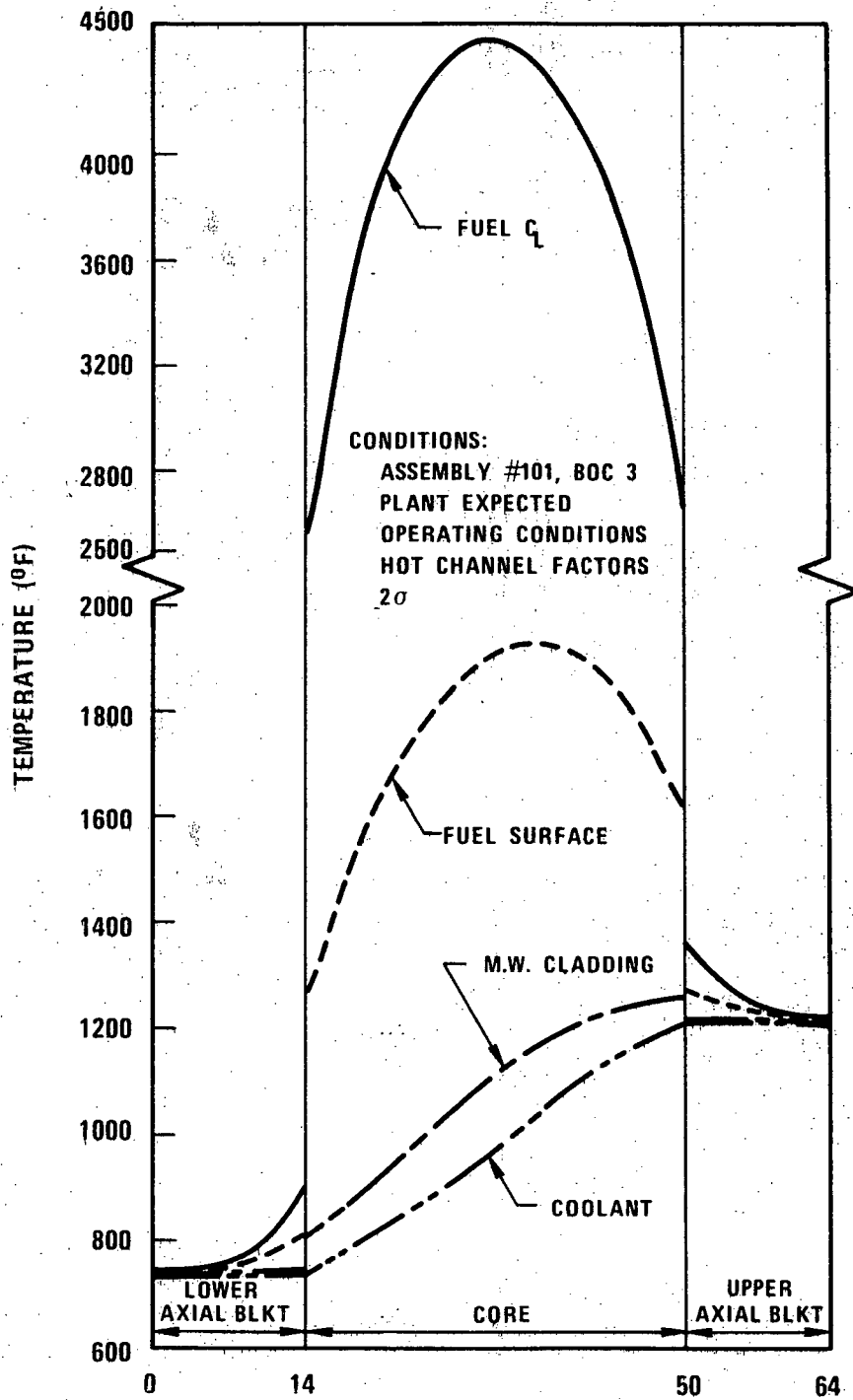
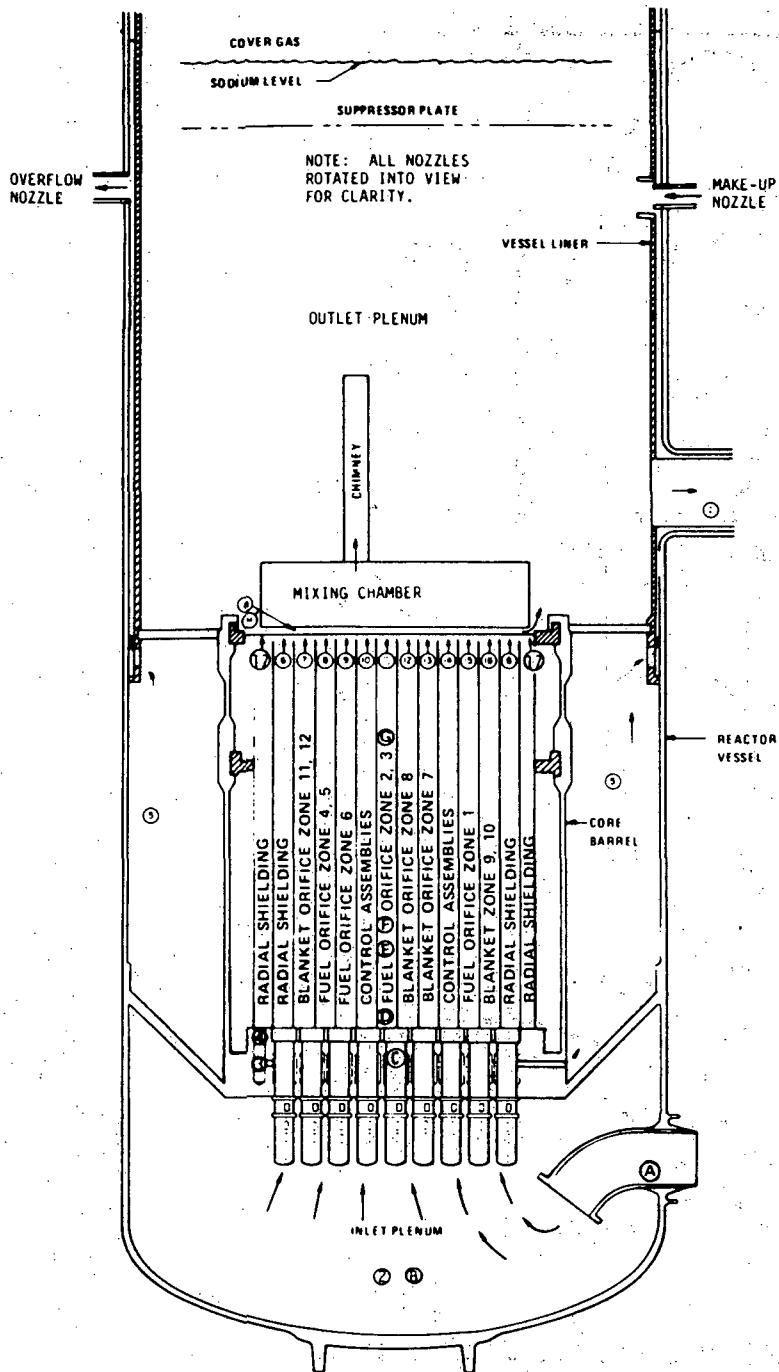


Figure 4.4-1. Typical Axial Temperature Profile in CRBRP Fuel Rod



CRBR FLOW ALLOCATION  
 HETEROGENOUS CORE - CYCLE 4  
 REACTOR ΔT = 265°F TOTAL FLOW = 41,448 × 10<sup>3</sup> LB/HR

COMPONENT	LOCATION	NUMBER OF ASSEMBLIES	FLOW		
			LB/HR × 10 <sup>3</sup>	% TOTAL	
1. FUEL ZONE	1	2-15	39	7.296	17.60
	2	2-11	54	3.380	22.09
	3	2-11	21	3.451	8.33
	4	2-8	12	2.710	6.54
	5	2-8	24	3.532	8.52
	6	2-8	6	1.863	2.54
2. TOTAL FUEL		182	27.460		66.25
3. INNER BLANKET	7	2-13	57	4.883	12.02
	8	2-12	16	1.450	2.52
4. TOTAL INNER BLANKET		78	6.442		15.54
5. OUTER BLANKET	9	2-18	12	0.742	1.79
	10	2-18	36	1.720	4.17
	11	2-7	40	1.672	4.03
	12	2-7	36	0.829	2.22
6. TOTAL OUTER BLANKET		126	5.860		12.21
7. RADIAL SHIELD ASSEMBLIES	a) INNER	2-8	48	0.129	0.29
	b) OUTER	2-17	294	0.435	1.05
8. TOTAL RADIAL SHIELD		312	0.555		1.34
9. CONTROL ASSEMBLIES	a) PRIMARY	2-10	9	0.424	1.02
	b) SECONDARY, UPFLOW	2-14	6	0.101	0.24
	c) SECONDARY, DOWNFLOW	2-3	1	0.328*	0.79*
10. TOTAL CONTROL ASSEMBLIES (UPFLOW)		15	0.525		1.26
11. BYPASS & LEAKAGE	a) AROUND CORE		---	0.433	2.35
	b) THROUGH CORE		---	0.872	1.05
	c) THROUGH CORE		---	1.405	3.40
12. TOTAL BYPASS & LEAKAGE					
13. REACTOR VESSEL/THERMAL LINER				0.829*	2.00*
14. TOTAL				41,448	100.0

\*DO NOT INCLUDE IN FLOW TOTAL (INCLUDED IN ITEM 11)

CRBRP REACTOR COMPONENT  
 LOADS AT TBN DESIGN CONDITIONS

COMPONENT	LOCATION	HYDRAULIC LOAD, LB.
INLET NOZZLE	A-B	2623
CORE SUPPORT STRUCTURE	B-D	7.37 × 10 <sup>8</sup>
HORIZONTAL BAFFLE PLATE	S-W	33,127
INLET MODULE	B-C	810
INLET NOZZLE	C-D	1831
SHIELD AND ORIFICE	D-E	515
ROD BUNDLE INLET	E-F	20
ROD BUNDLE	F-G	820
ROD BUNDLE EXIT	G-H	55
OUTLET NOZZLE	H-I	6650

††† THE MAXIMUM HYDRAULIC LOAD OCCURS DURING STEADY STATE OPERATION. LOADS DURING UPSET, EMERGENCY AND FAULTED EVENTS ARE LESS SEVERE.

FIGURE 4.4-2. CRBRP Flows and Hydraulic Loads



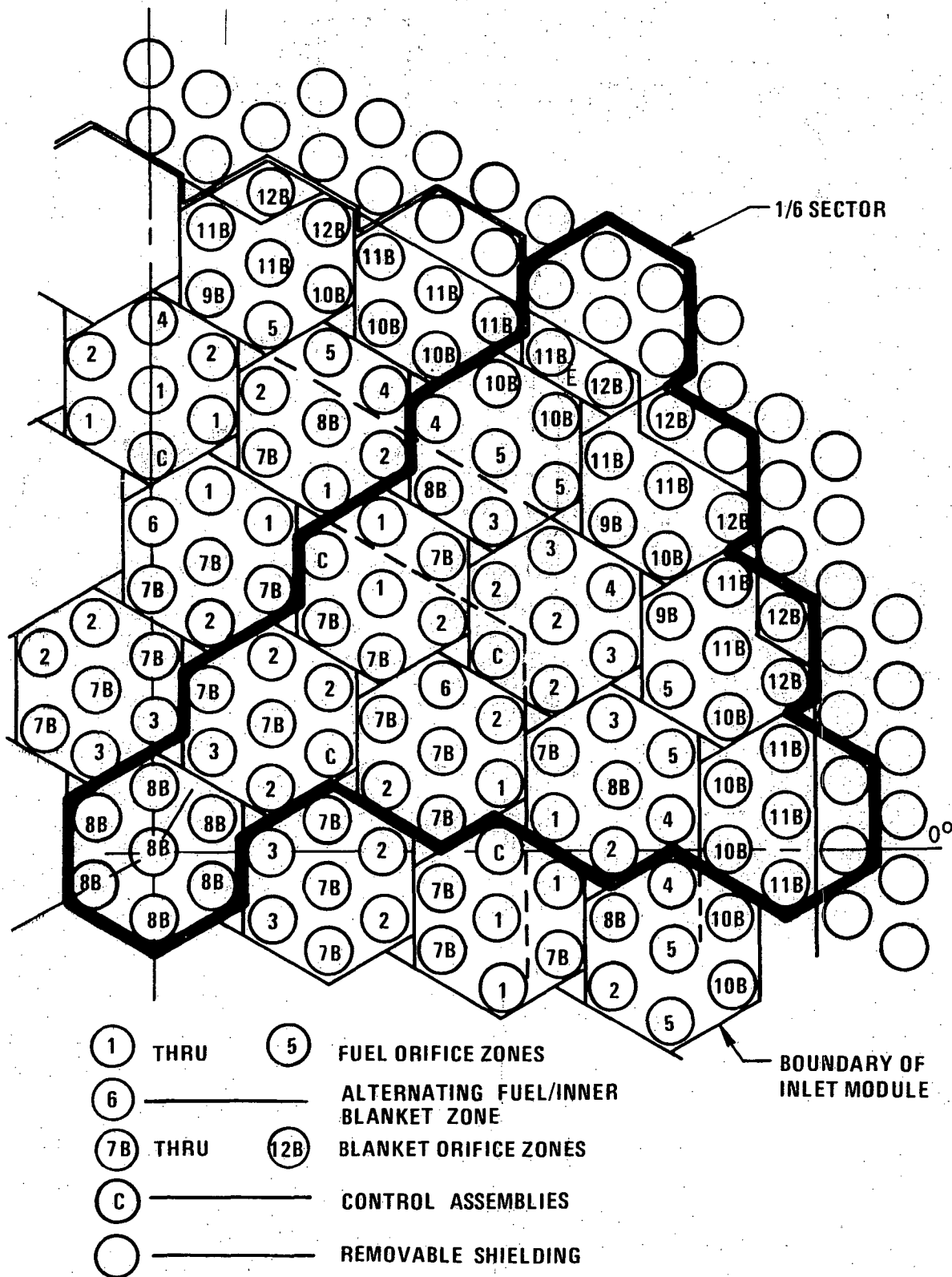


FIGURE 4.4-3. Inlet Module Map, Showing Orificing Requirements of Reactor Assemblies 5894-23

1668-1

4.4-130

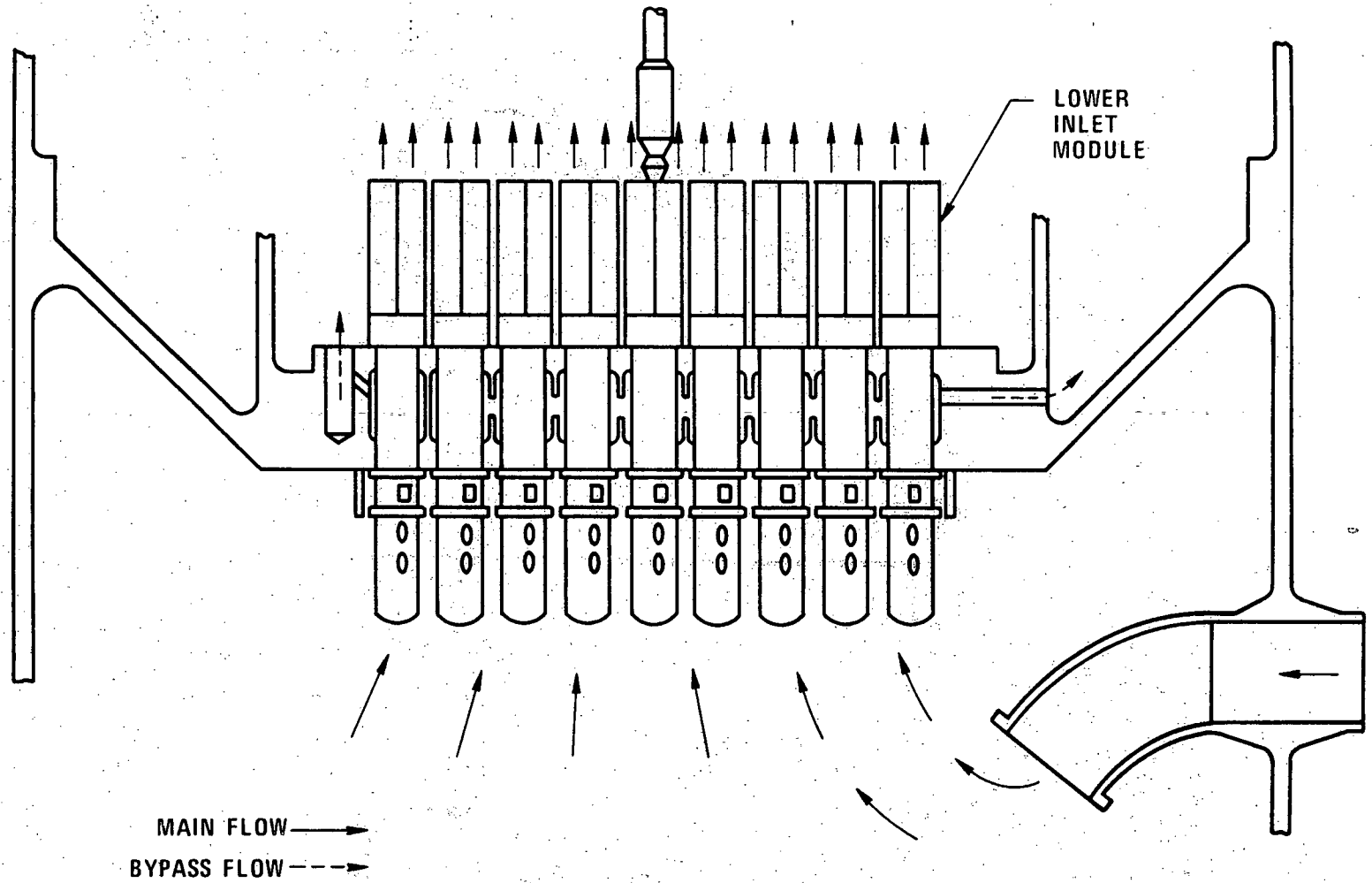
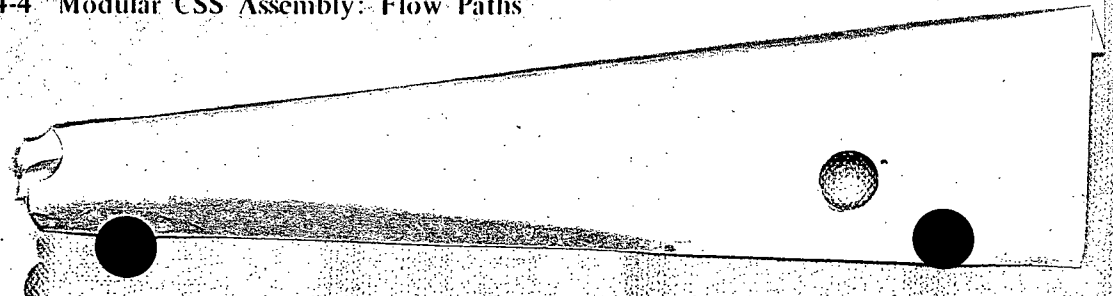


Figure 4.4-4 Modular CSS Assembly: Flow Paths

Amend. 51  
Sept. 1979



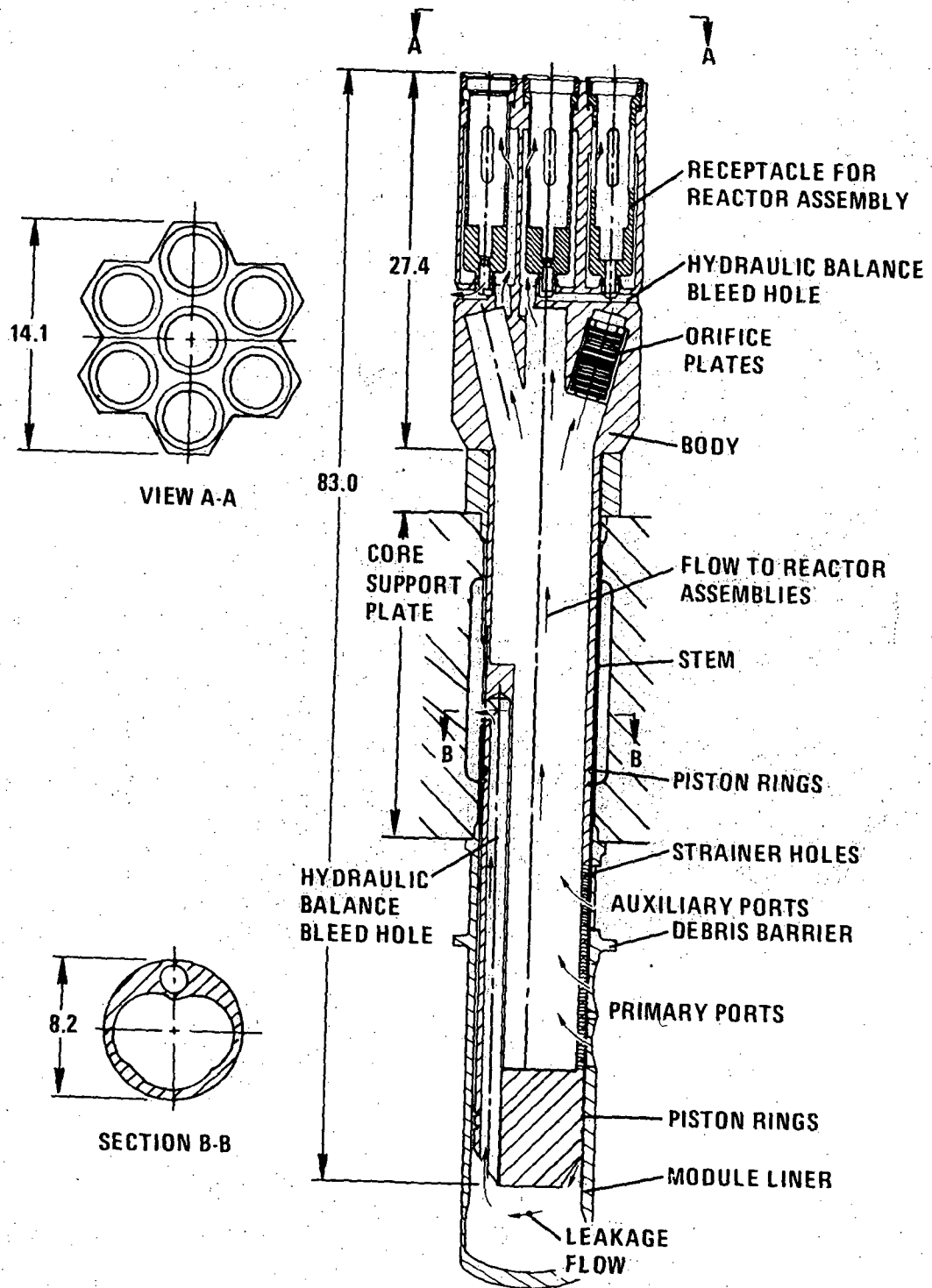


Figure 4.4-5 Elevation of Typical Lower Inlet Module

1668-70

4.4-132

Amend. 51  
Sept. 1979

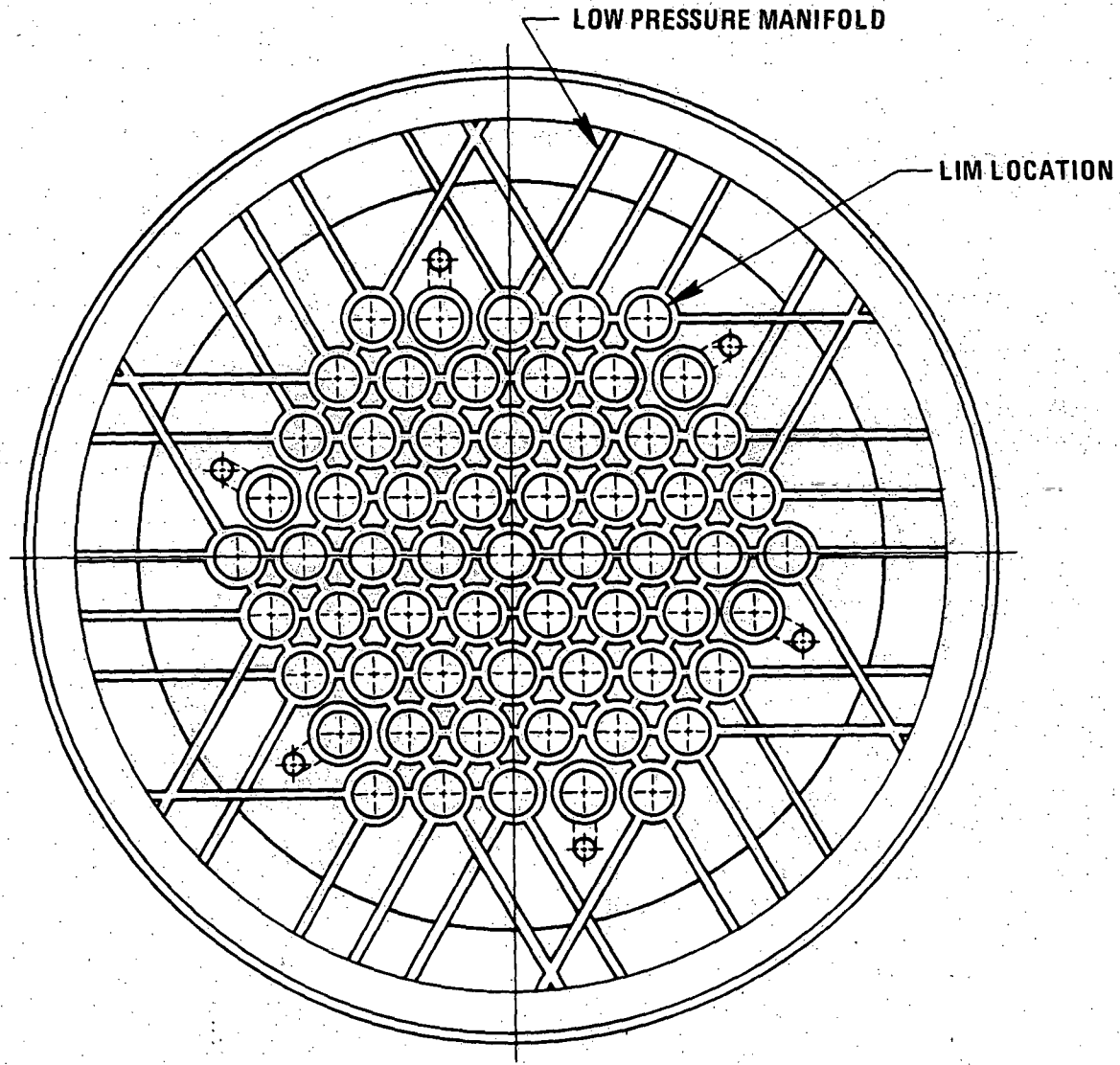


Figure 4.4-6 Lower Core Support Plate Low Pressure Manifold System

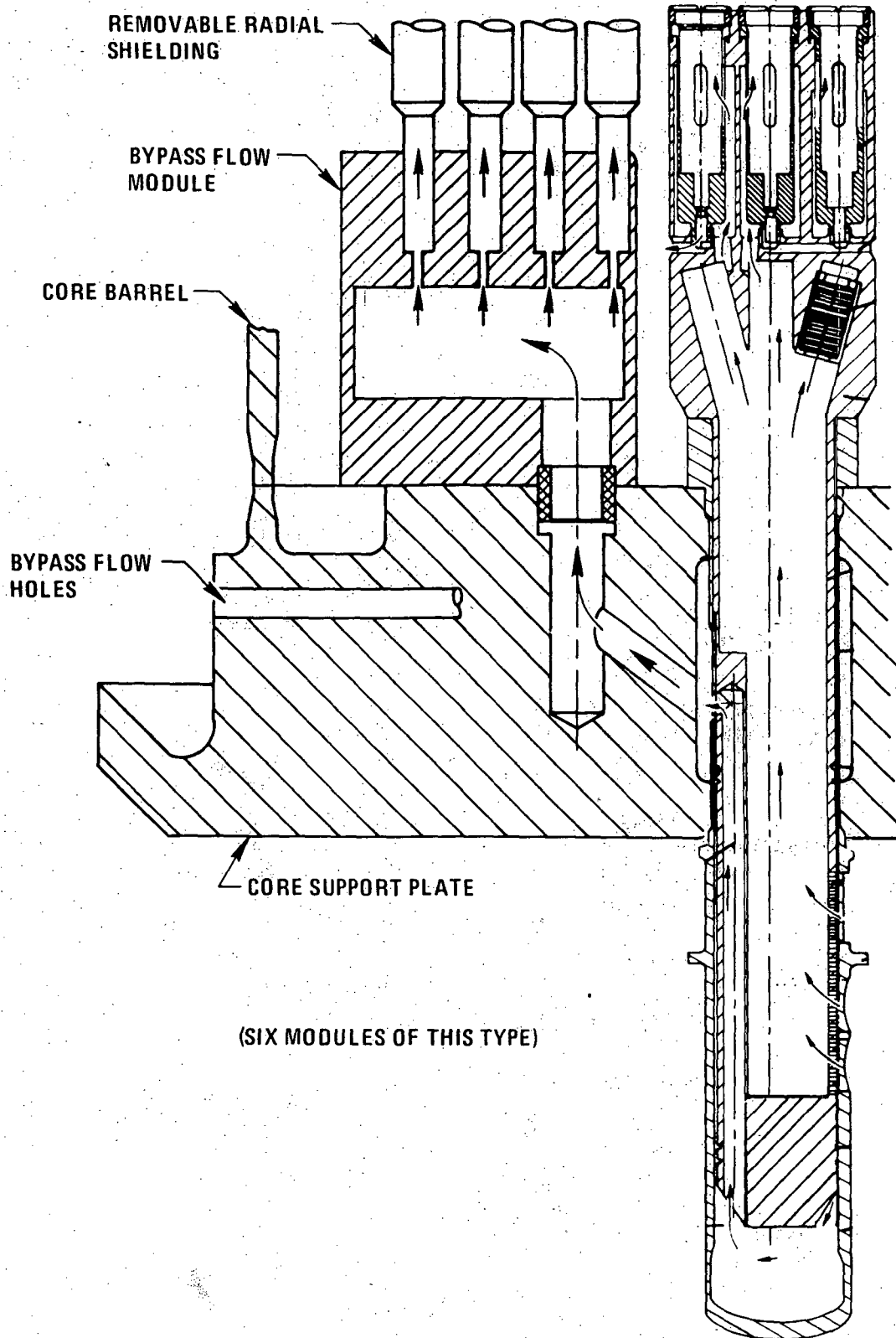


Figure 4.4-7. Radial Shield Orificing Flow Path

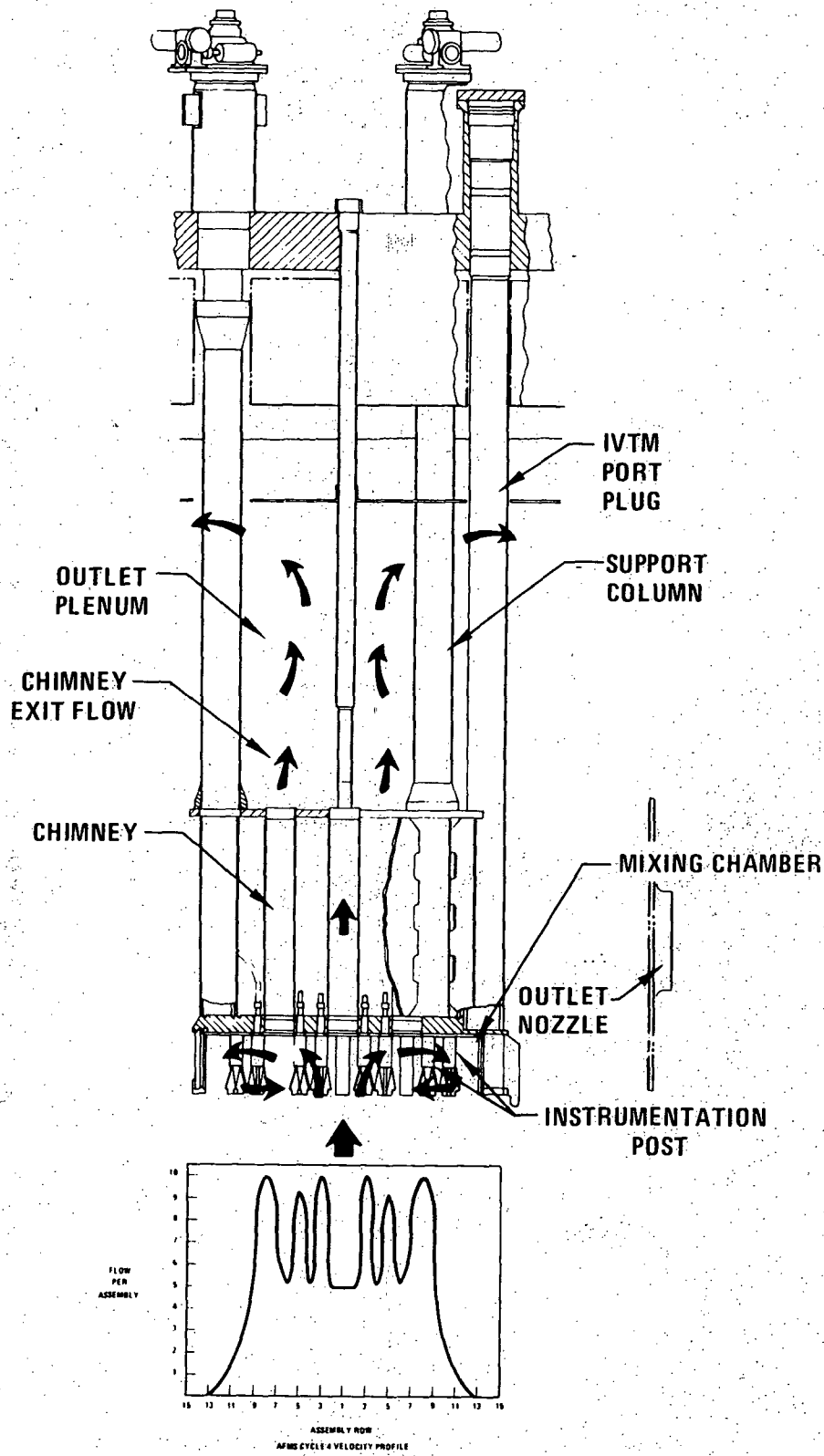
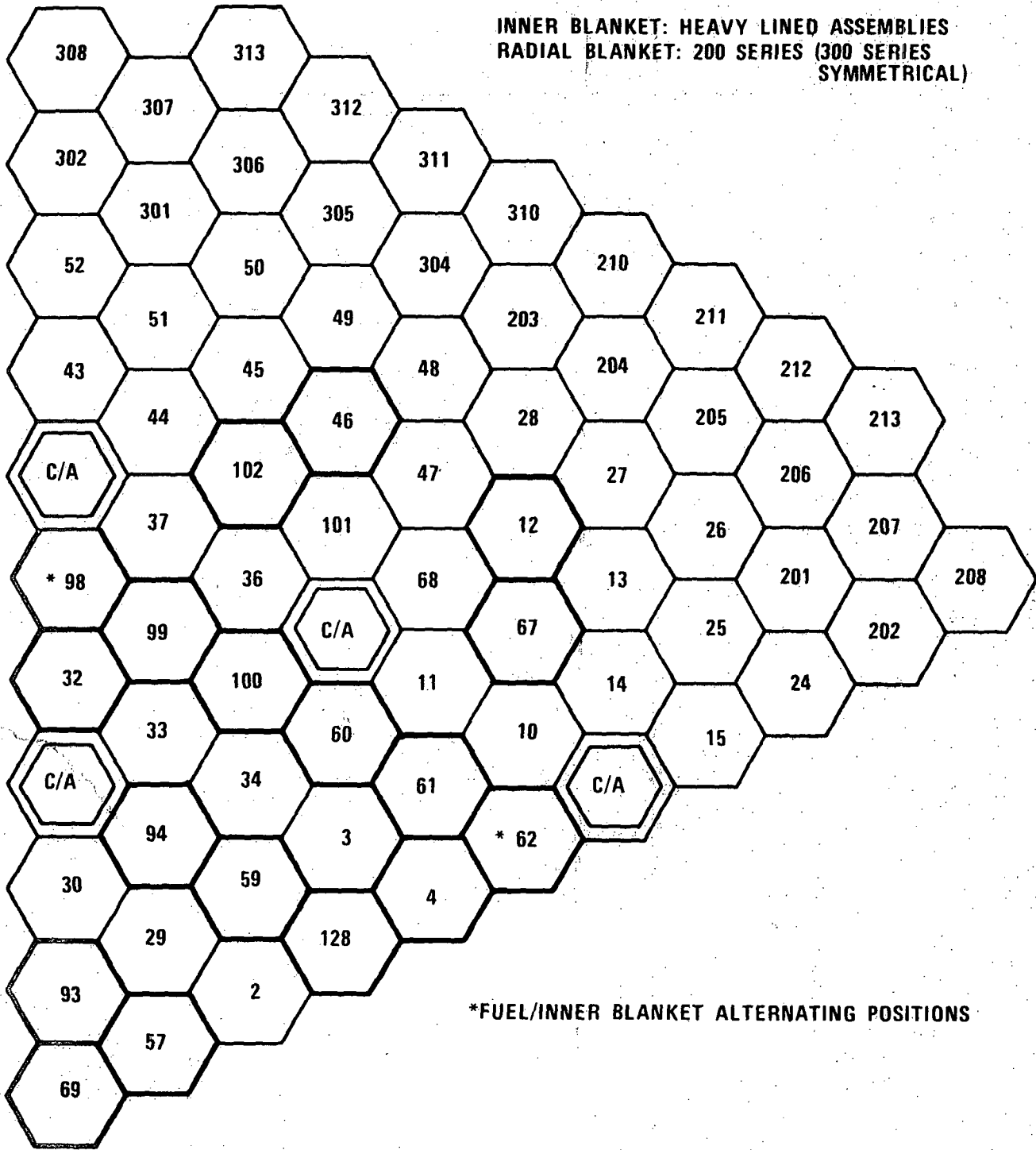


Figure 4.4-8. Upper Internals Structure Concept Feature



**\*FUEL/INNER BLANKET ALTERNATING POSITIONS**

FIGURE 4.4-9. CRBRP Core 60° Symmetry Sector and Assemblies Numbering Scheme

5894-11

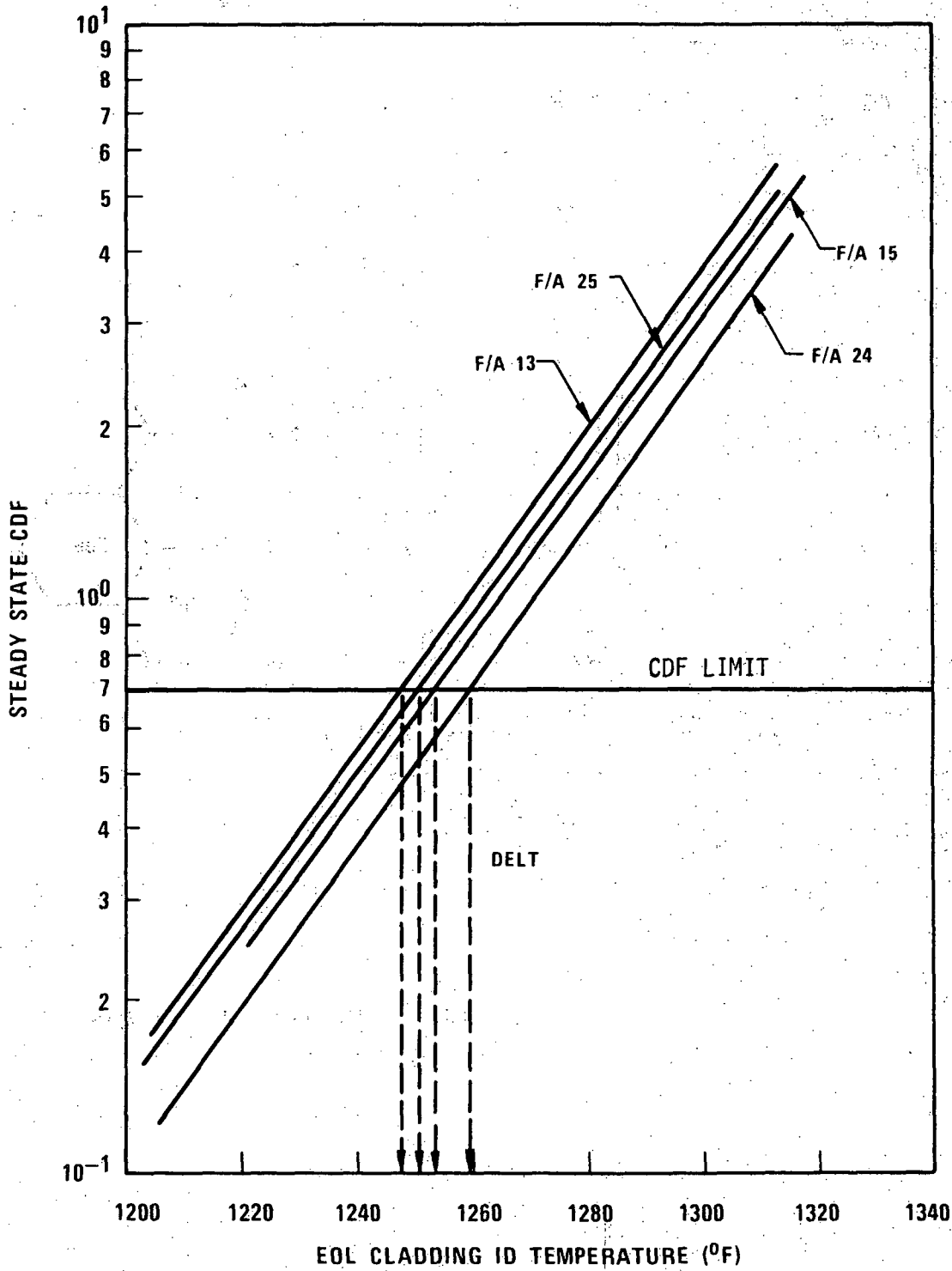


Figure 4.4-10 Typical DELT Determination for First Core Fuel Assemblies

1668-67



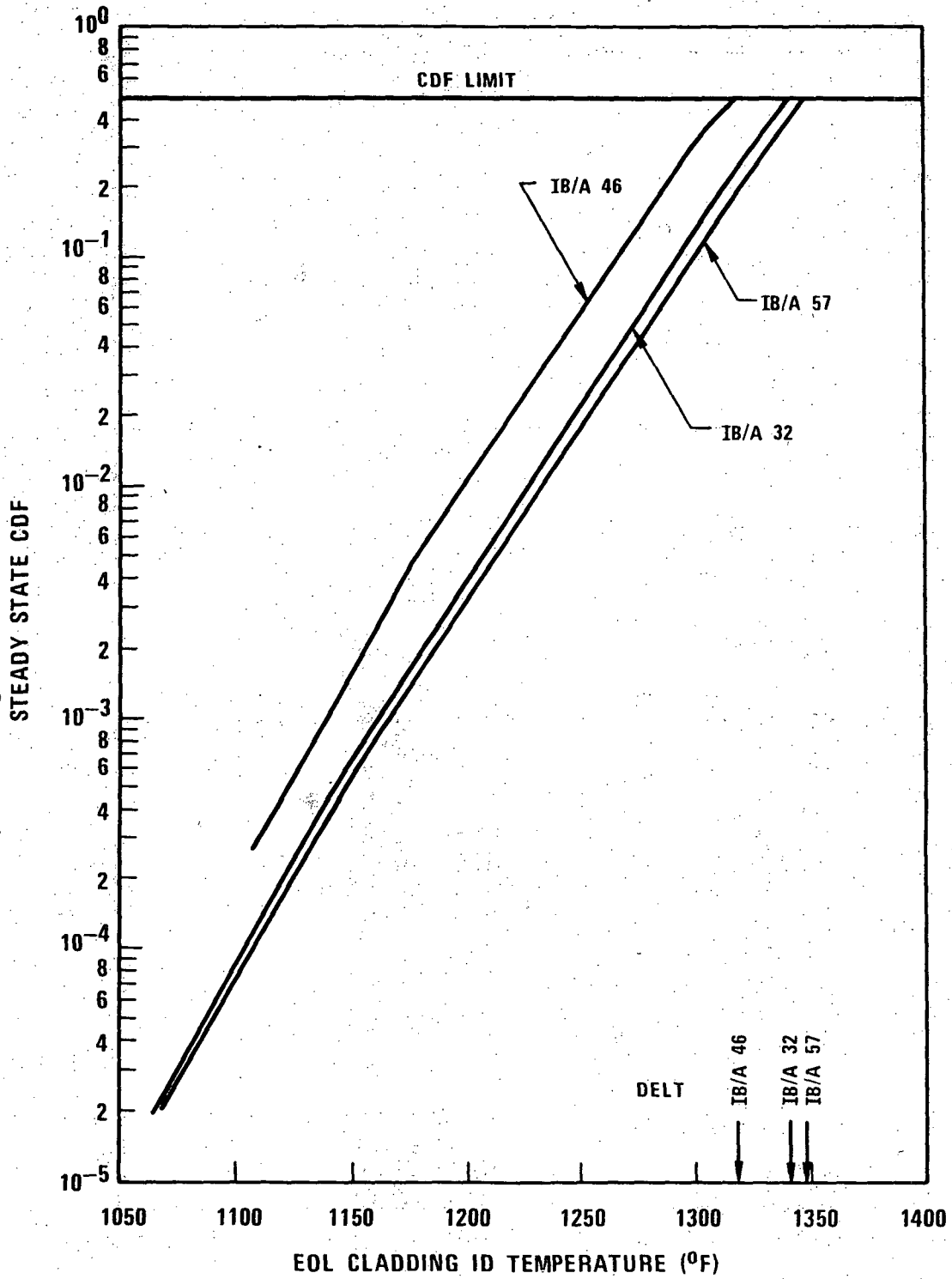


Figure 4.4-11 Typical DELT Determination for First Core Inner Blanket Assemblies

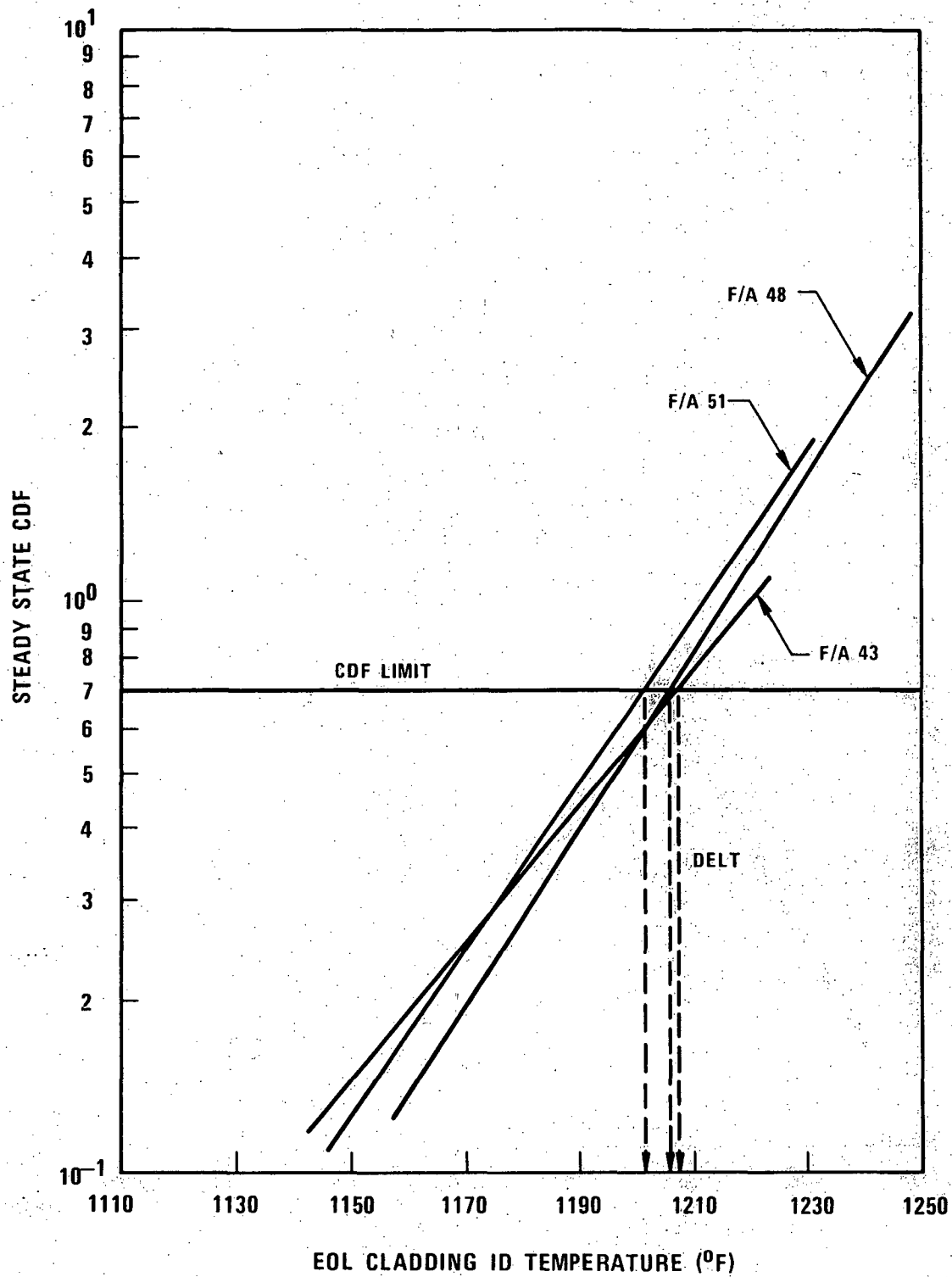


Figure 4.4-12 Typical DELT Determination for Second Core Fuel Assemblies

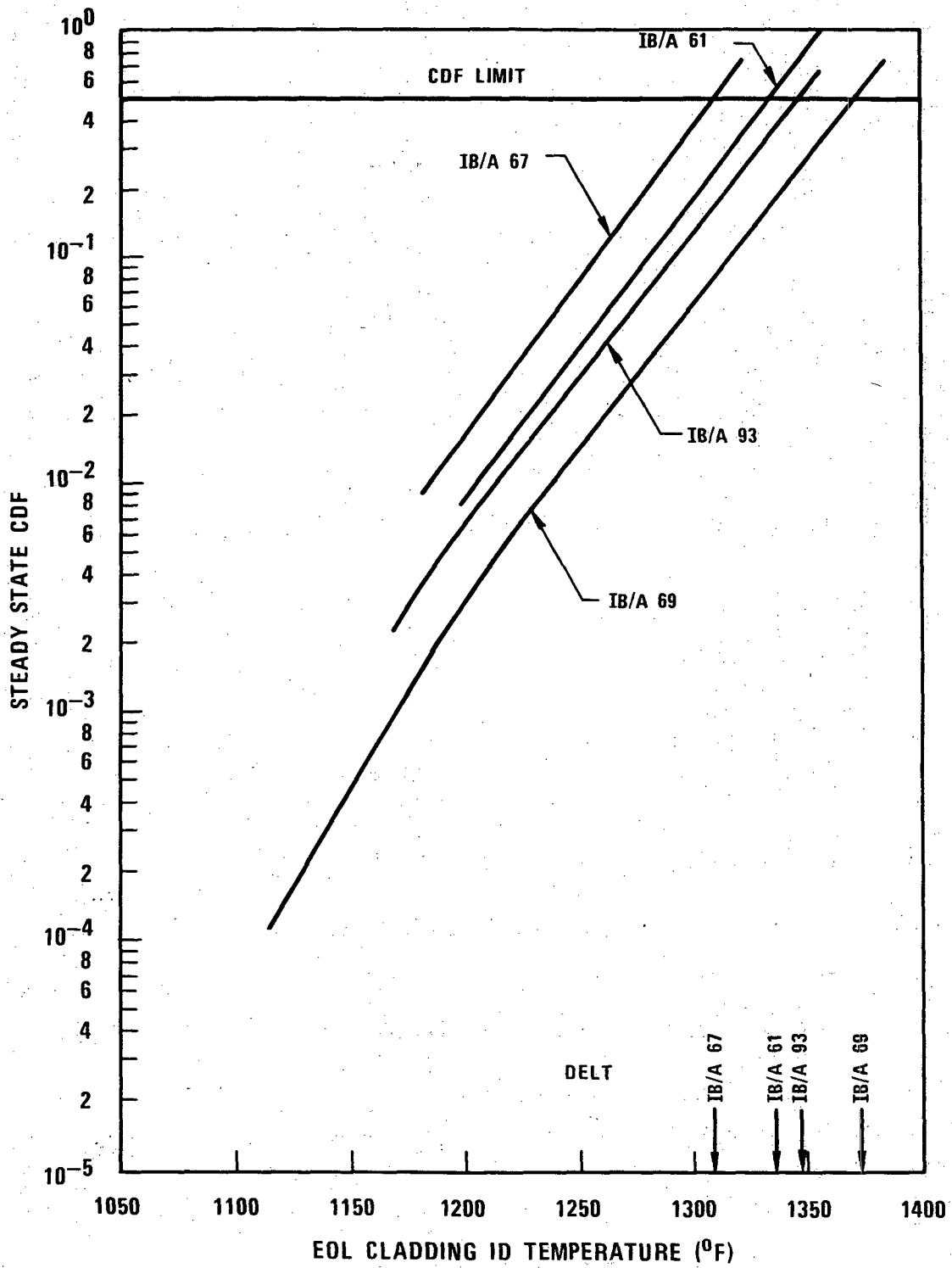


Figure 4.4-13 Typical DELT Determination for Second Core Inner Blanket Assemblies

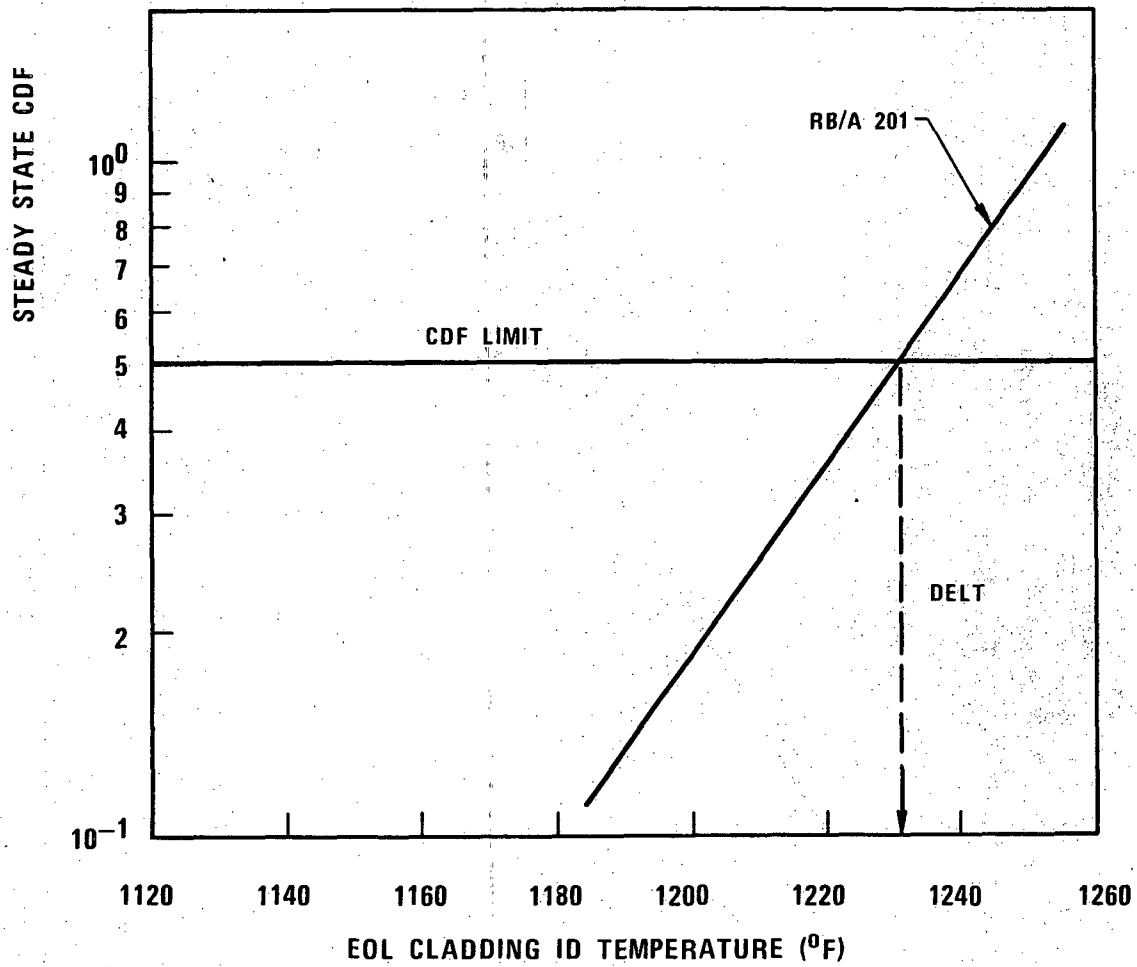


Figure 4.4-14 Typical DELT Determination for Radial Blanket Assemblies

1668-63

4.4-140

Amend. 51  
Sept. 1979

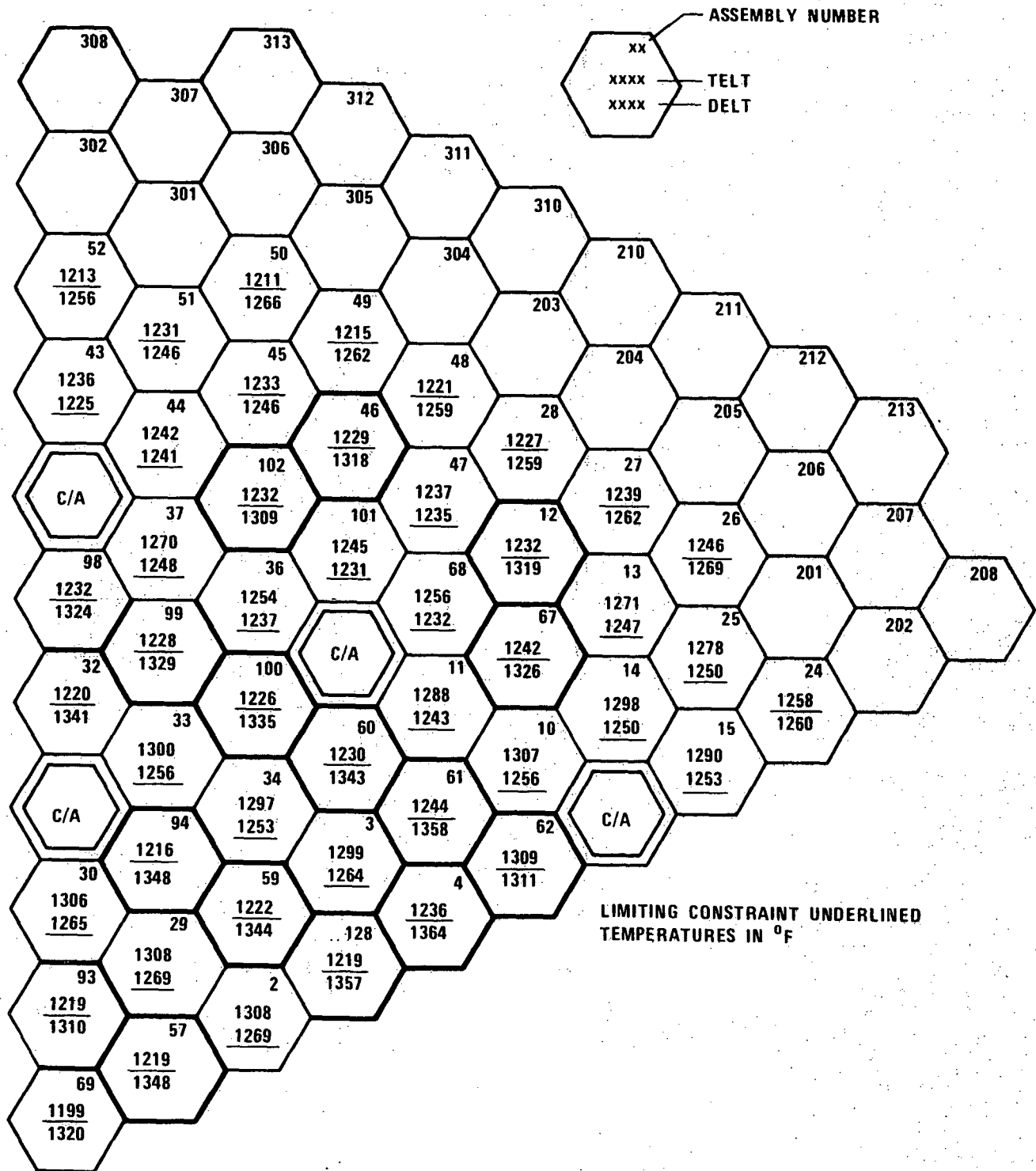


FIGURE 4.4-15. Individual Assemblies Limiting Temperatures at First Core

5894-9

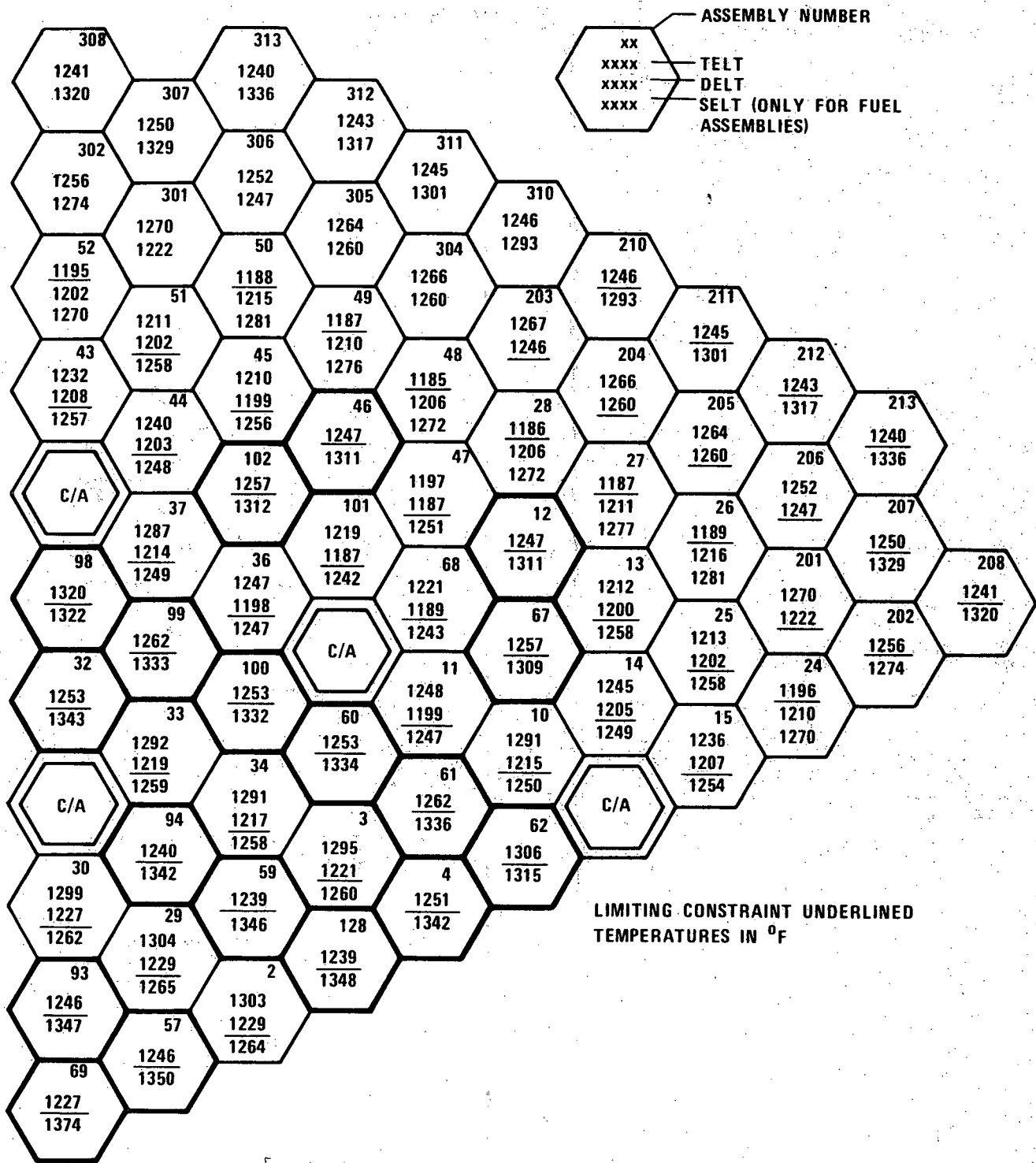


FIGURE 4.4-16. Individual Assemblies Limiting Temperatures at Second Core

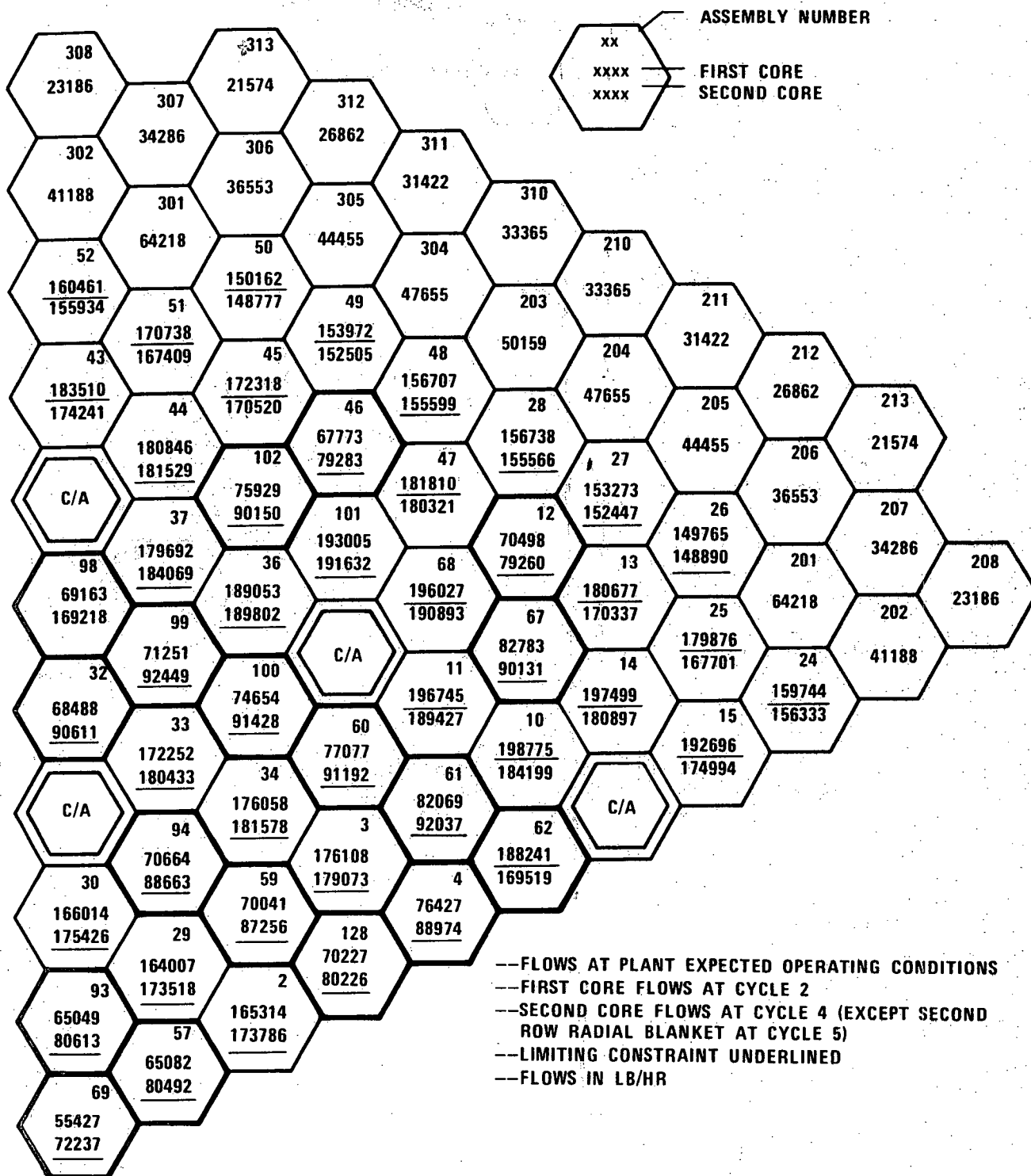


FIGURE 4.4-17. Individual Assemblies Minimum Flow Rates at First and Second Core Necessary to Satisfy the Constraints

5894-17

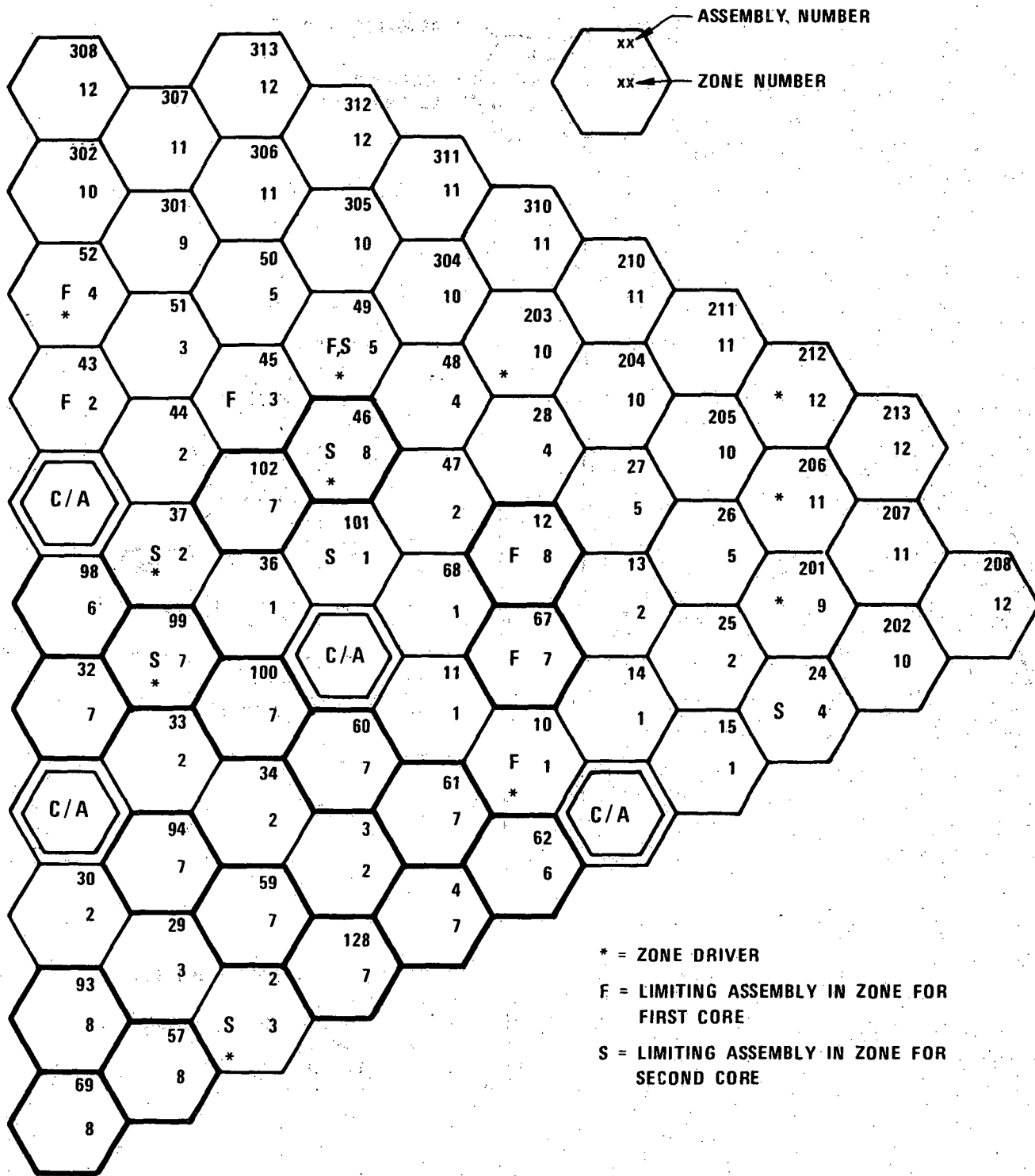


FIGURE 4.4-18. Core Orificing Scheme

5894-21



Figures 4.4-19 thru 4.4-23 DELETED

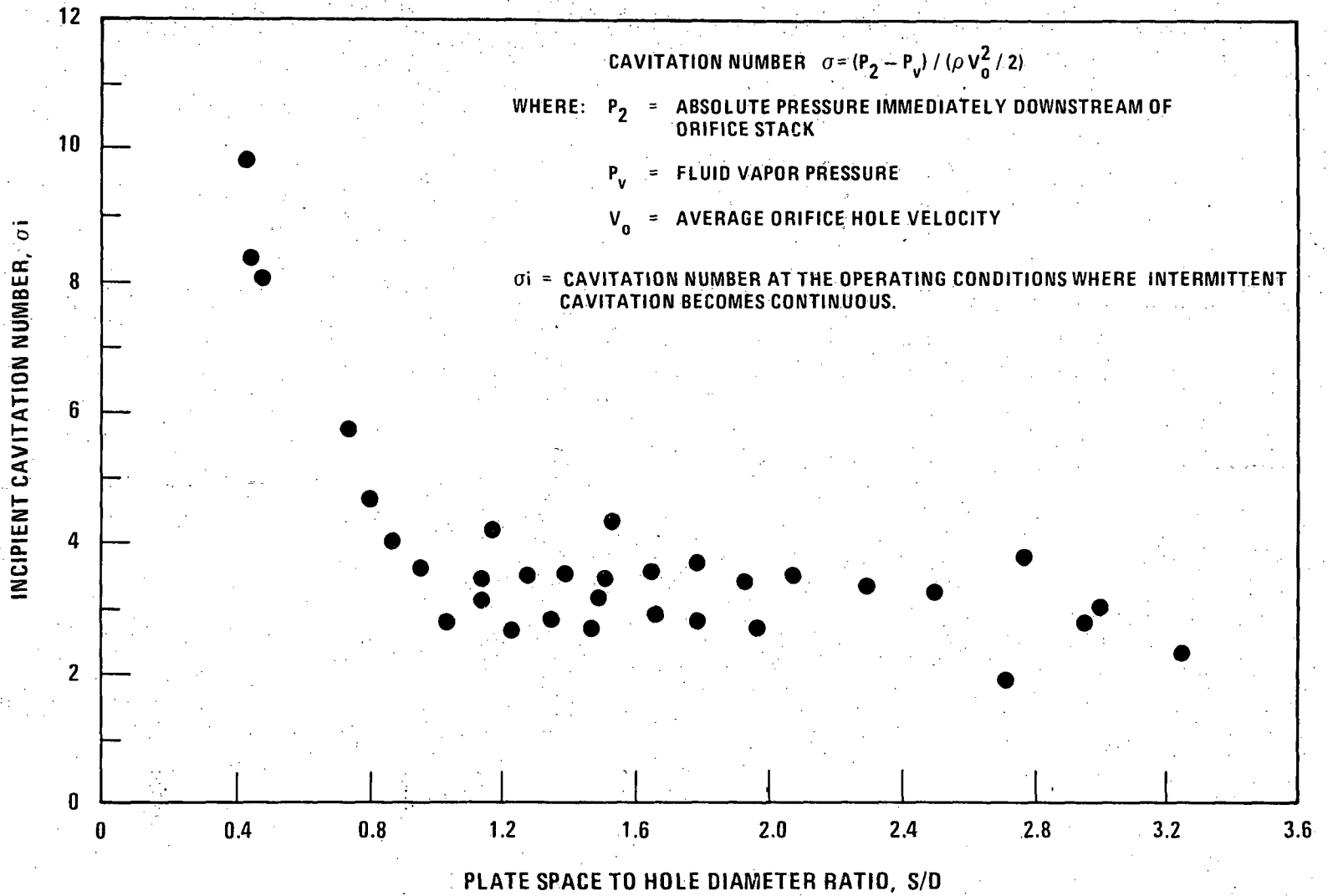


Figure 4.4-24 Typical CRBR Fuel Assembly Orifice Stack Cavitation Data

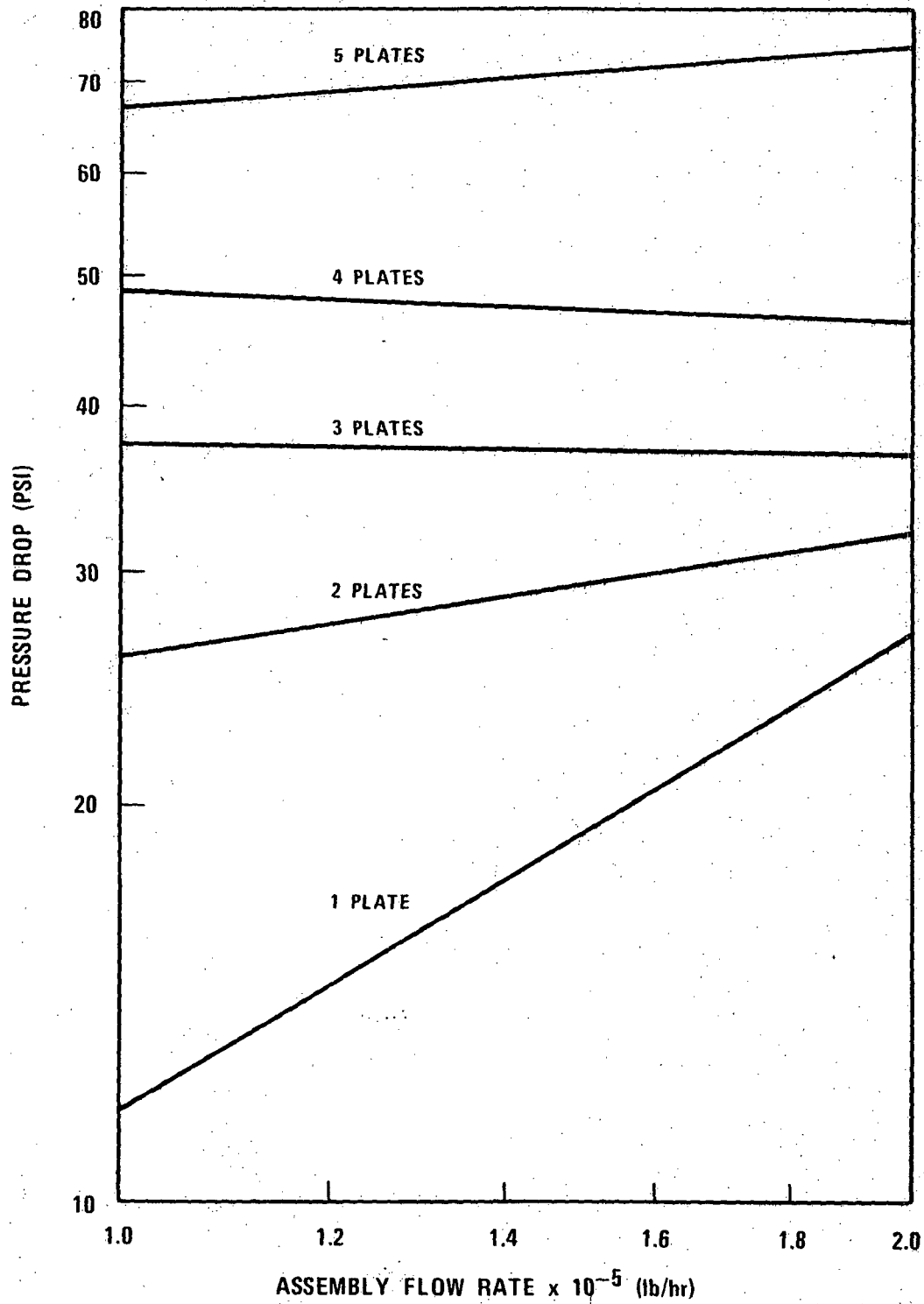


Figure 4.4-25 Fuel Assembly Inlet Nozzle-Orifice-Shield Pressure Drop for Orifice Hole Velocity Limit of 40 Ft/Sec

NOTES:  
 EACH CIRCLE REPRESENTS AN ASSEMBLY  
 WHEN TWO NUMBERS ARE GIVEN, THE FIRST  
 ONE IS THE ORIFICING ZONE  
 S INDICATES SHIELD ASSEMBLY  
 MODULES E2 TO E9 ARE PERIPHERAL  
 MODULES, REMAINING ARE CENTRAL  
 ONLY 1/3 OF MODULE A1 MODELED  
 IN CATFISH TO RETAIN 1/3 SYMMETRY

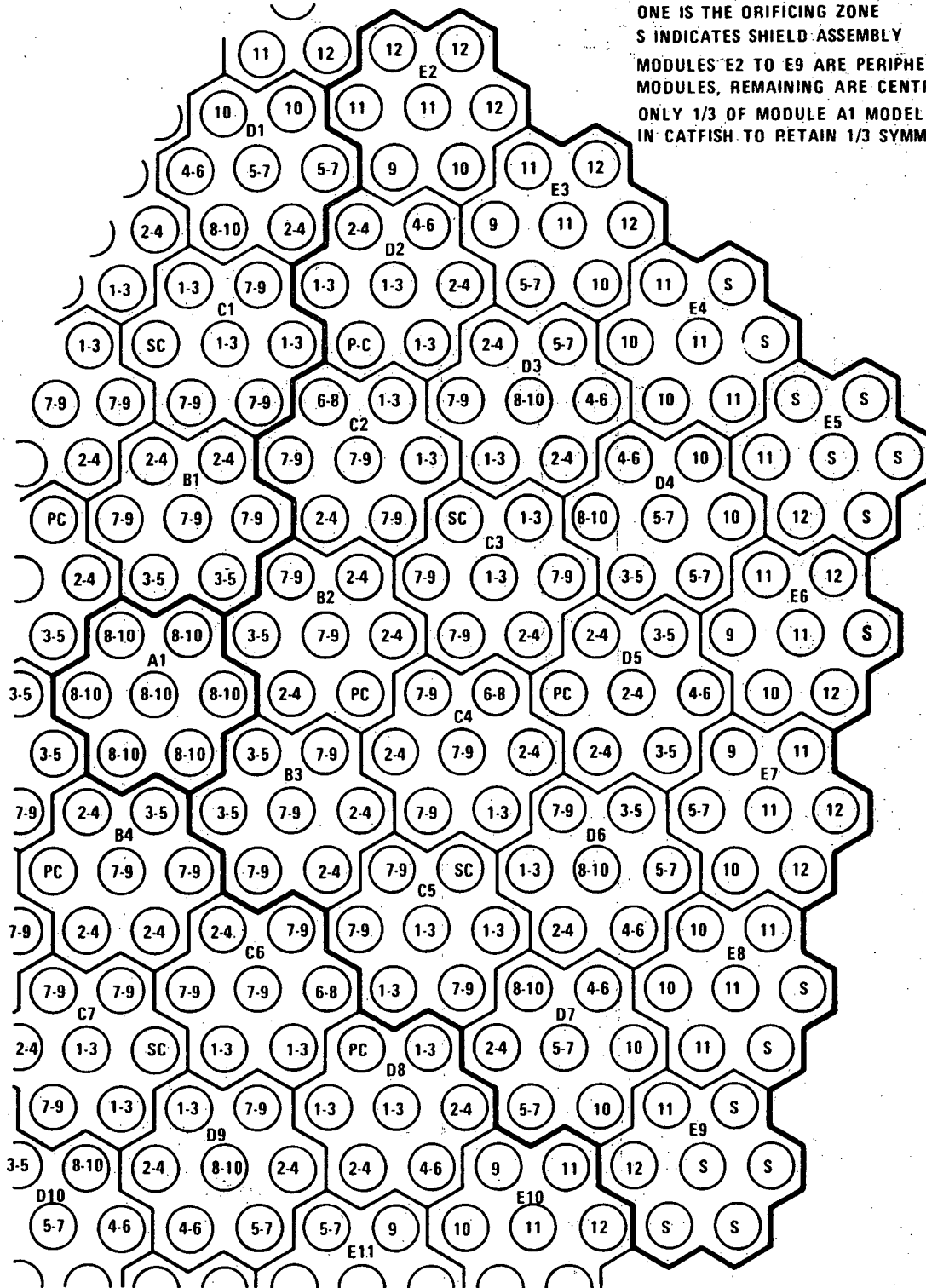


FIGURE 4.4-26. Map of CRBRP Lower Inlet Modules (1/3 Symmetry Sector)

5894-16

1668-10

4.4-153

Amend. 56  
Aug. 1980

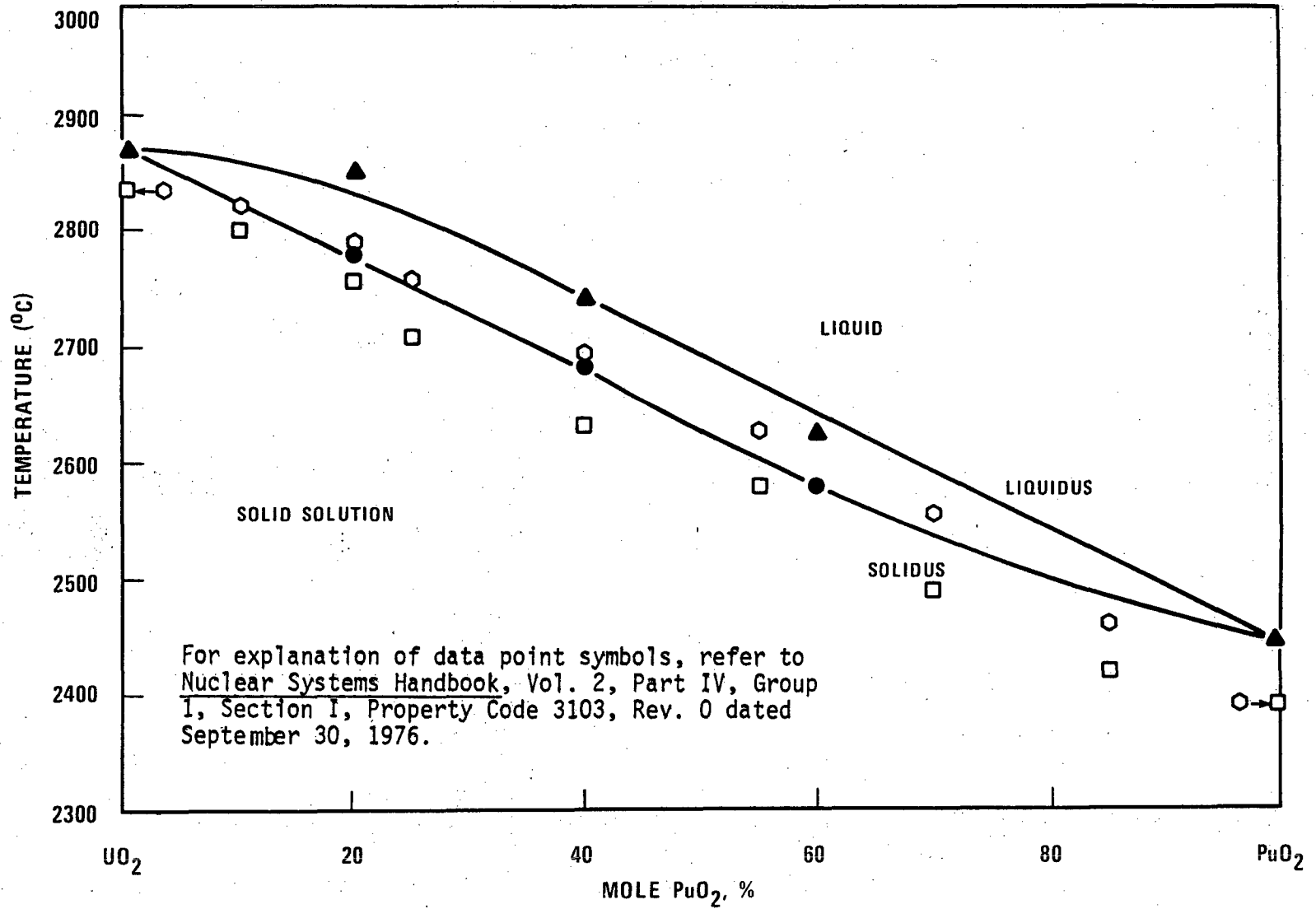


Figure 4.4-27 Phase Diagram for UO<sub>2</sub>-PuO<sub>2</sub>

1668-9

4.4-154

Amend. 51  
Sept. 1979

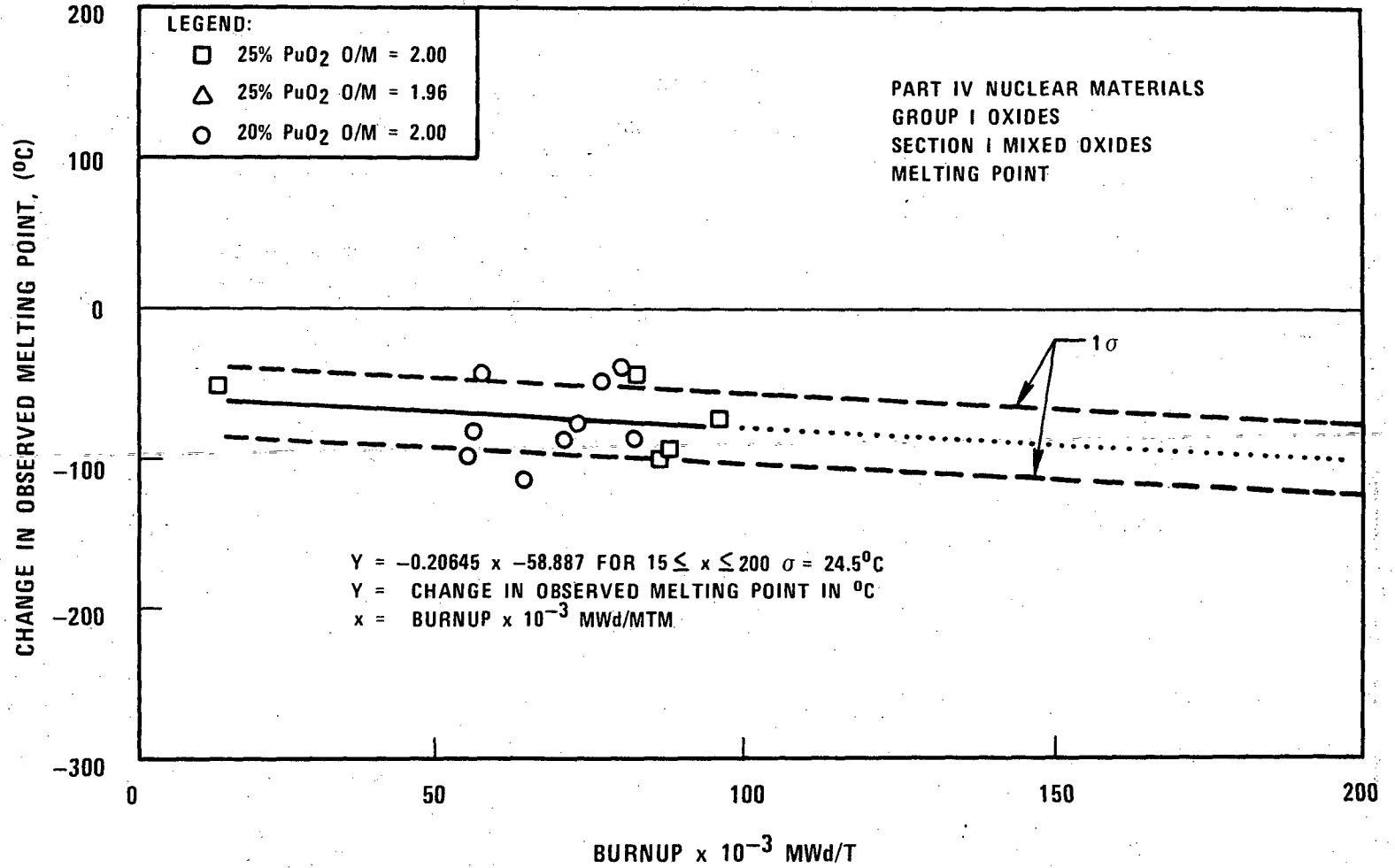


Figure 4.4-28 Effect of Burnup On Melting Point of (U,Pu) O<sub>2-x</sub>

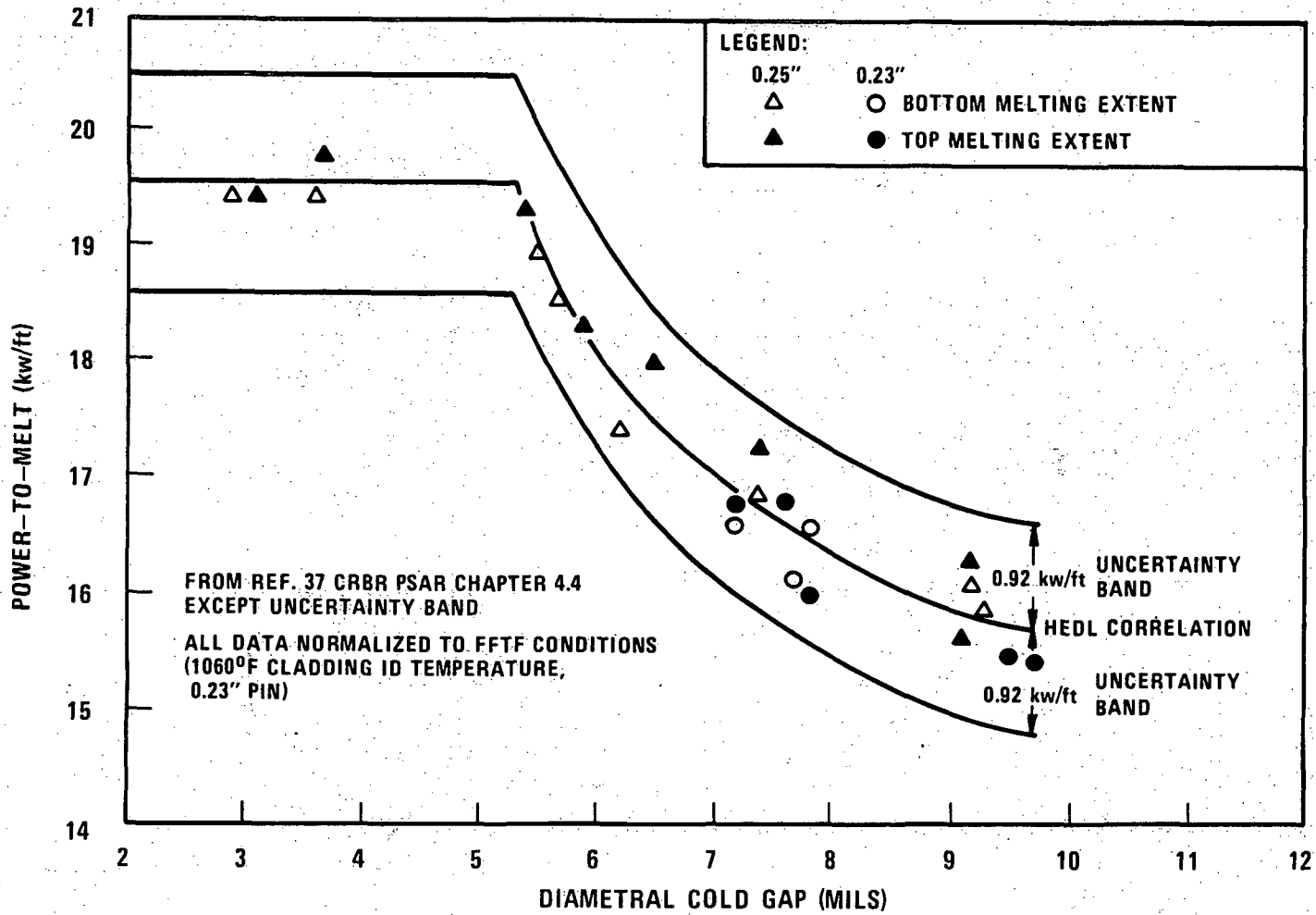


Figure 4.4-29 Power- to-Melt/Cold Gap Size Relationship from P-19 Data and Uncertainty Band

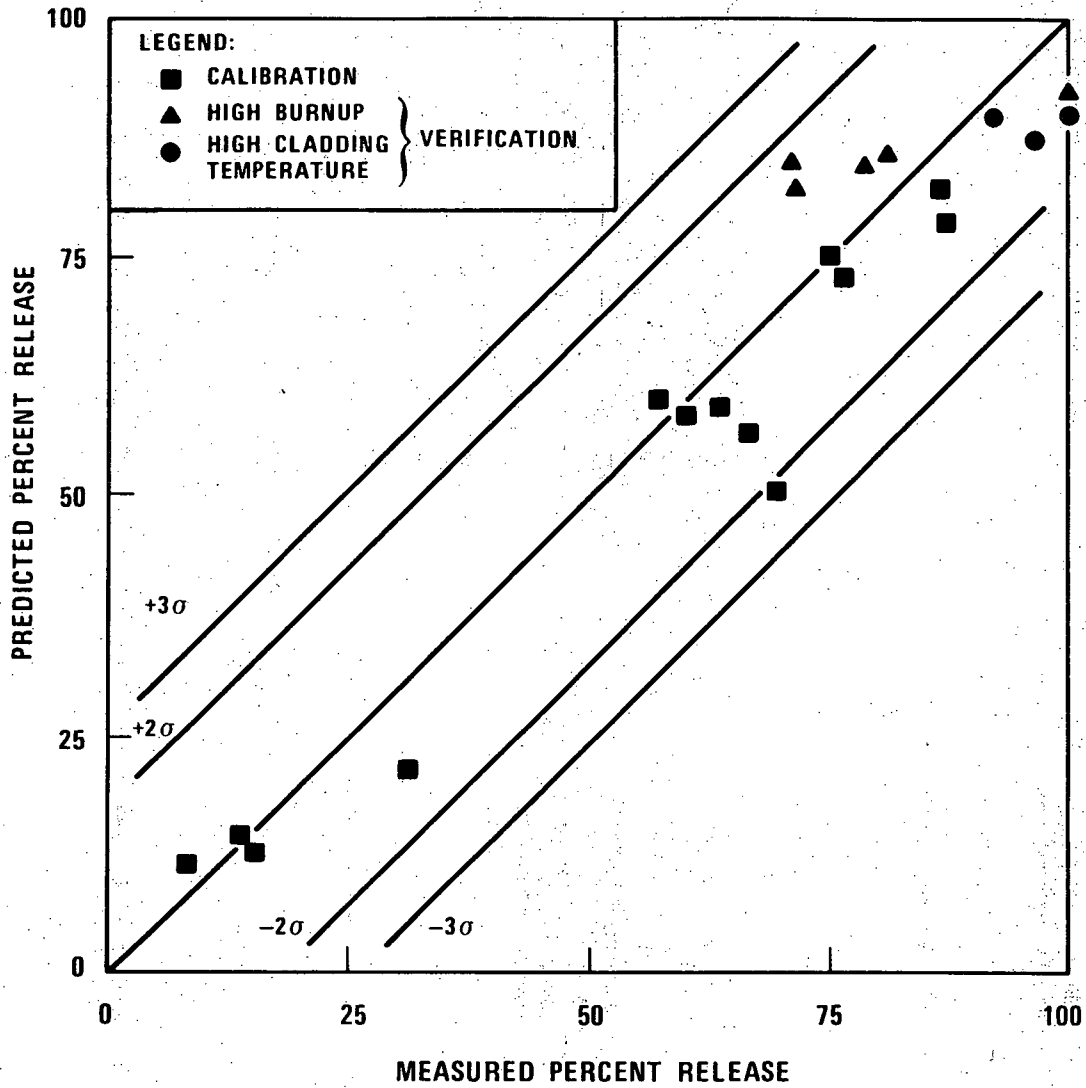


Figure 4.4-30 Comparison of Measured and Predicted Fission Gas Release



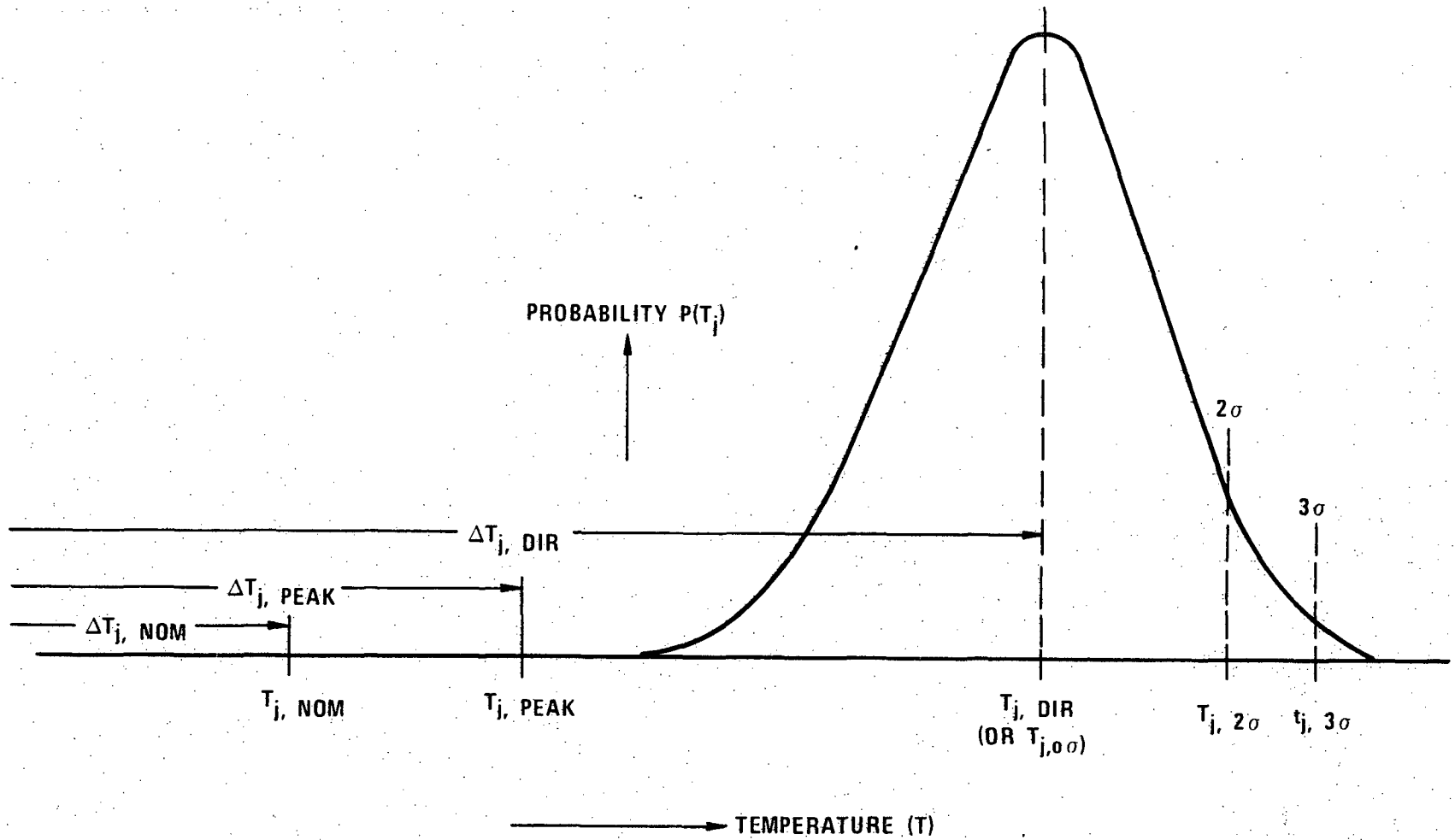


Figure 4.4-31 Graphical Illustration of Semi-Statistical Method

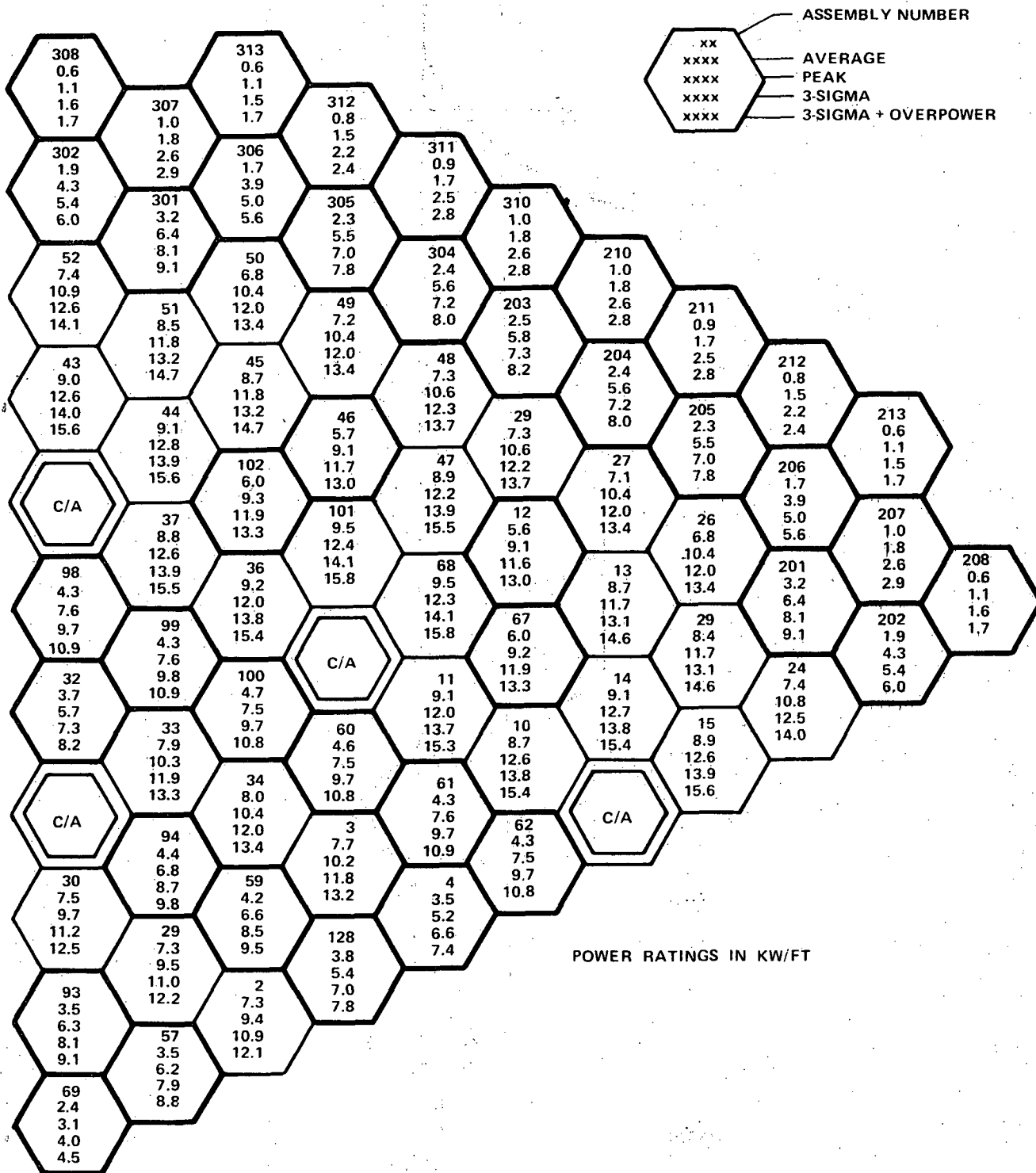


FIGURE 4.4-32. Core Assemblies Linear Power Ratings @ BOC1

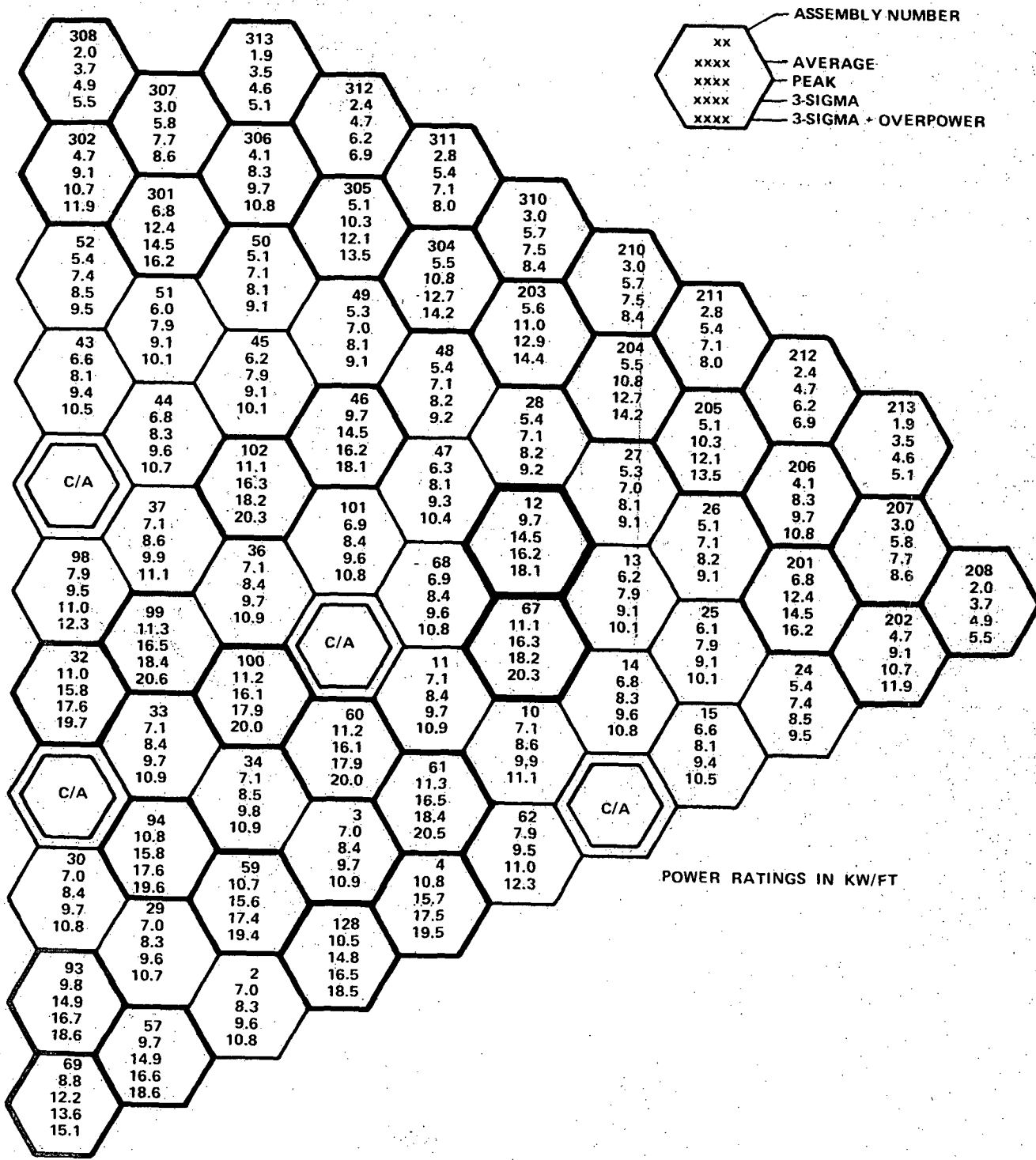


FIGURE 4.4-33. Core Assemblies Linear Power Ratings at EOC4

5894-14

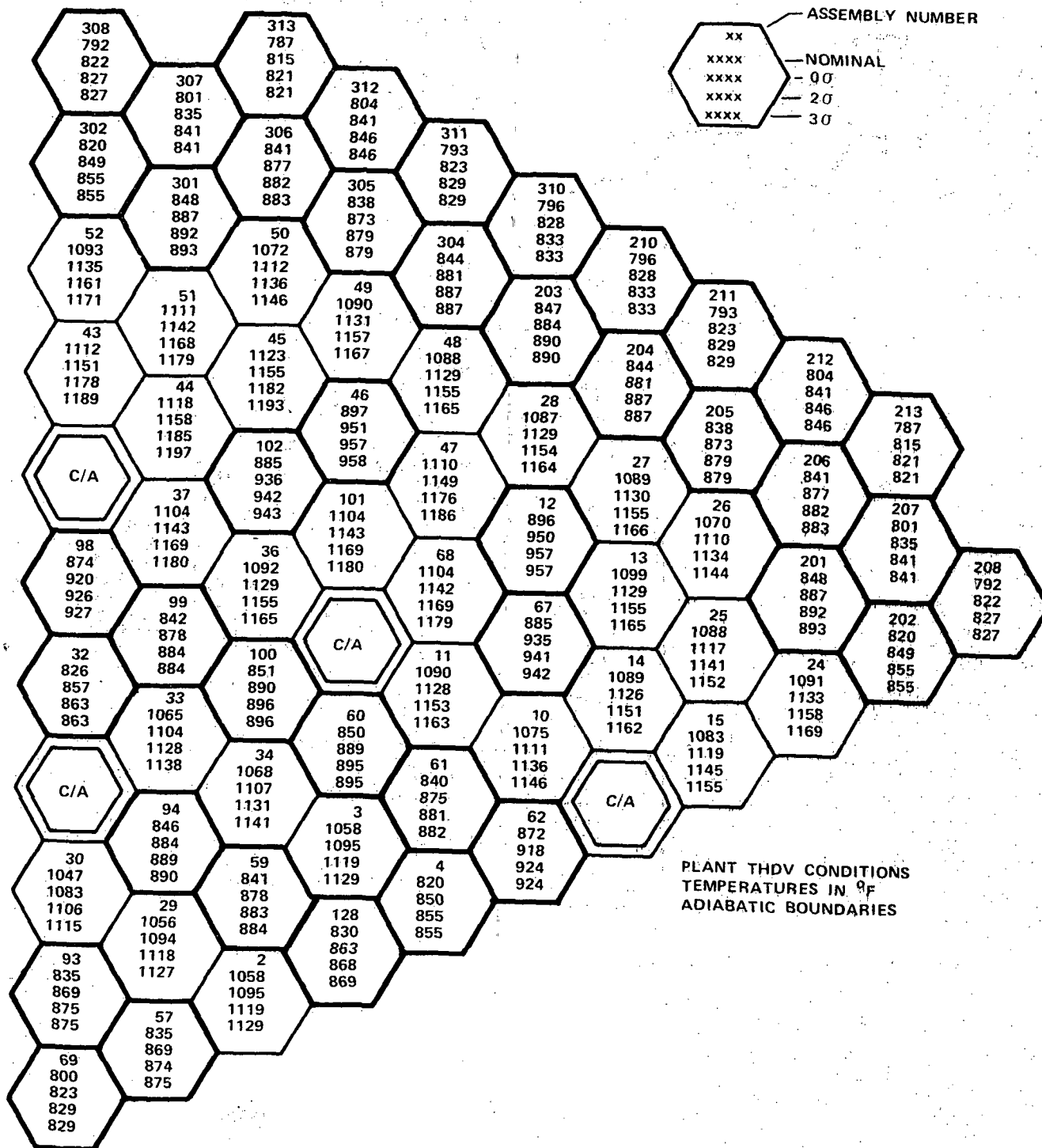


FIGURE 4.4-34. Core Assemblies Mixed Mean Outlet Temperatures at BOC1

5894-13

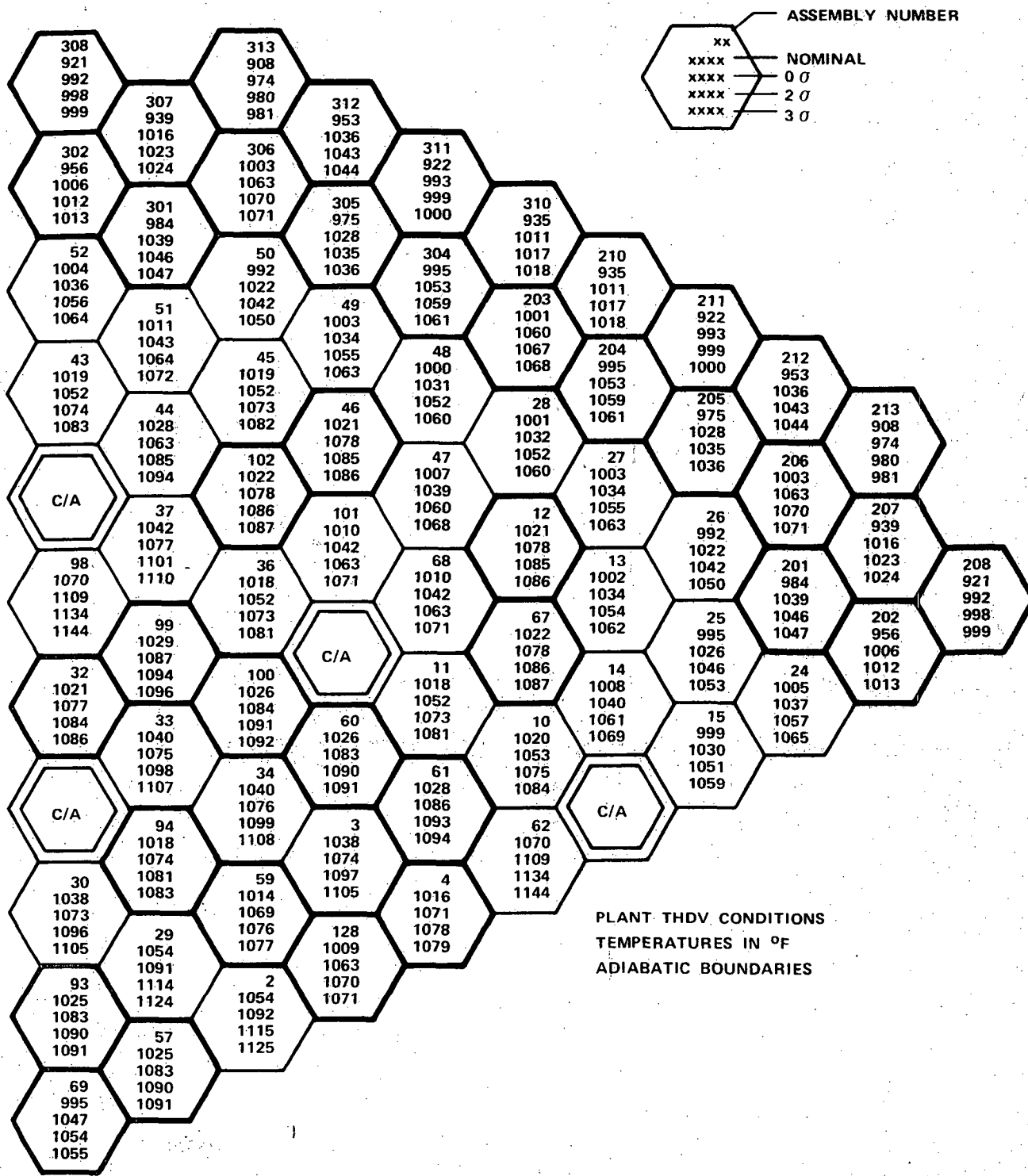


FIGURE 4.4-35. Core Assemblies Mixed Mean Outlet Temperatures at EOC4

5894-12

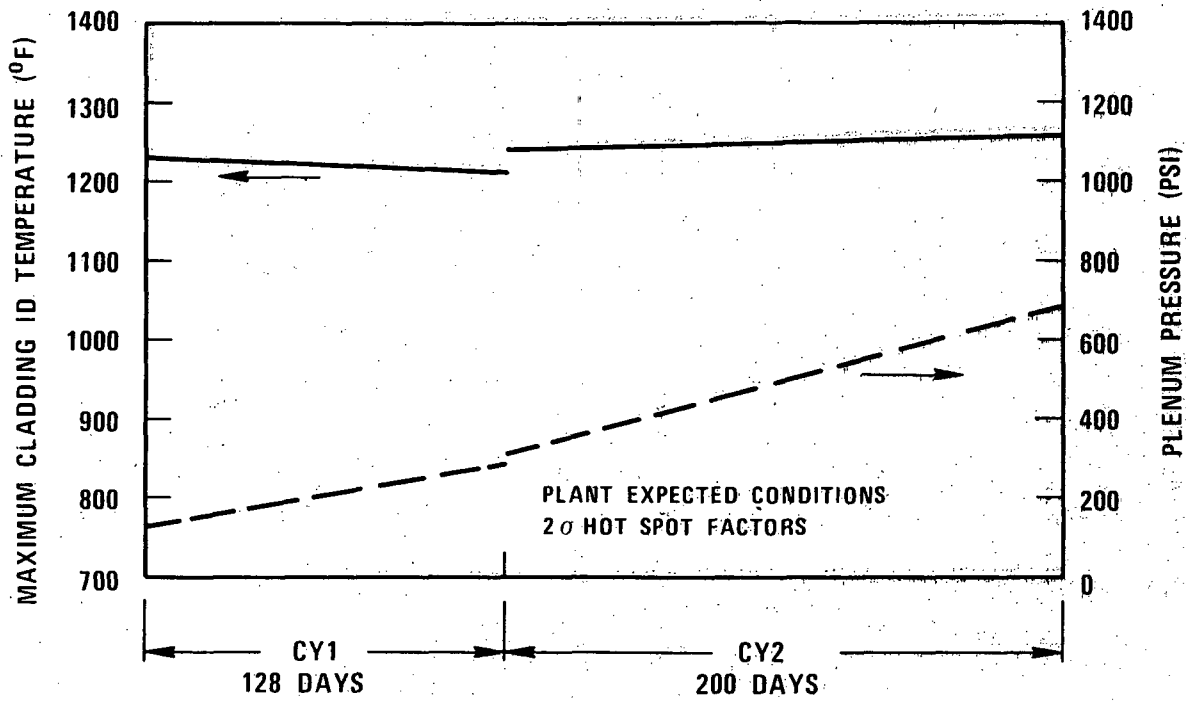


Figure 4.4-36 Lifetime Cladding Temperature/Pressure History in Fuel Assembly #10, First Core, Orificing Zone 1

1668-32

4.4-162

Amend. 51  
Sept. 1979

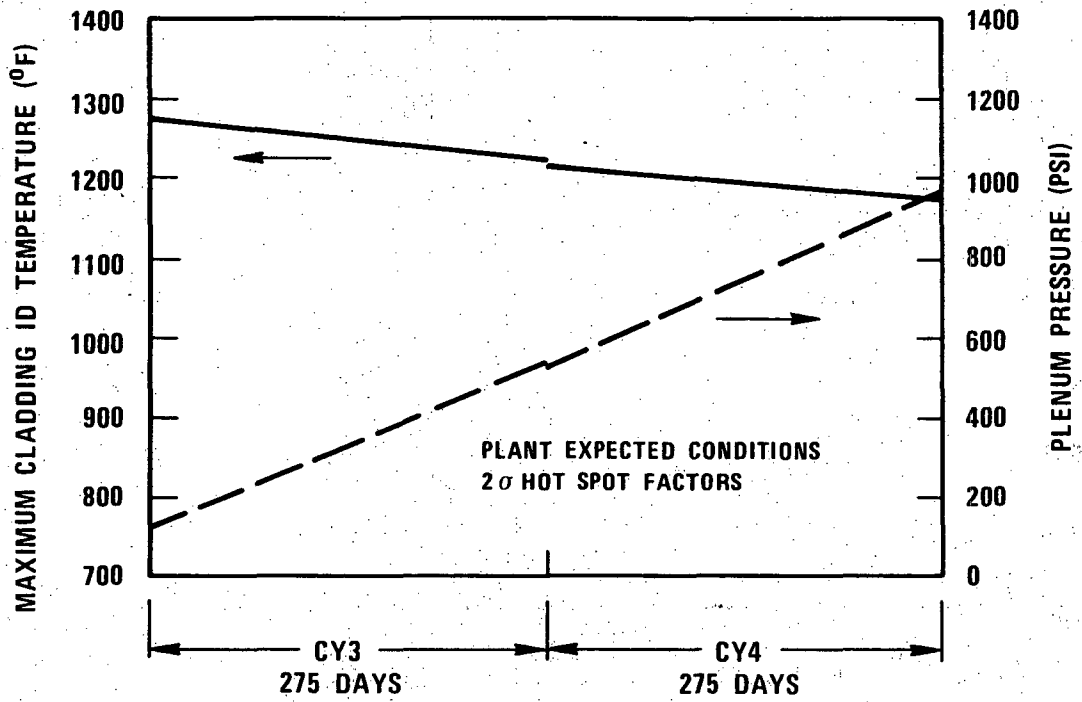


Figure 4.4-37 Lifetime Cladding Temperature/Pressure History in Fuel Assembly #101, Second Core, Orificing Zone 1

1668-33

4.4-163

Amend. 51  
Sept. 1979

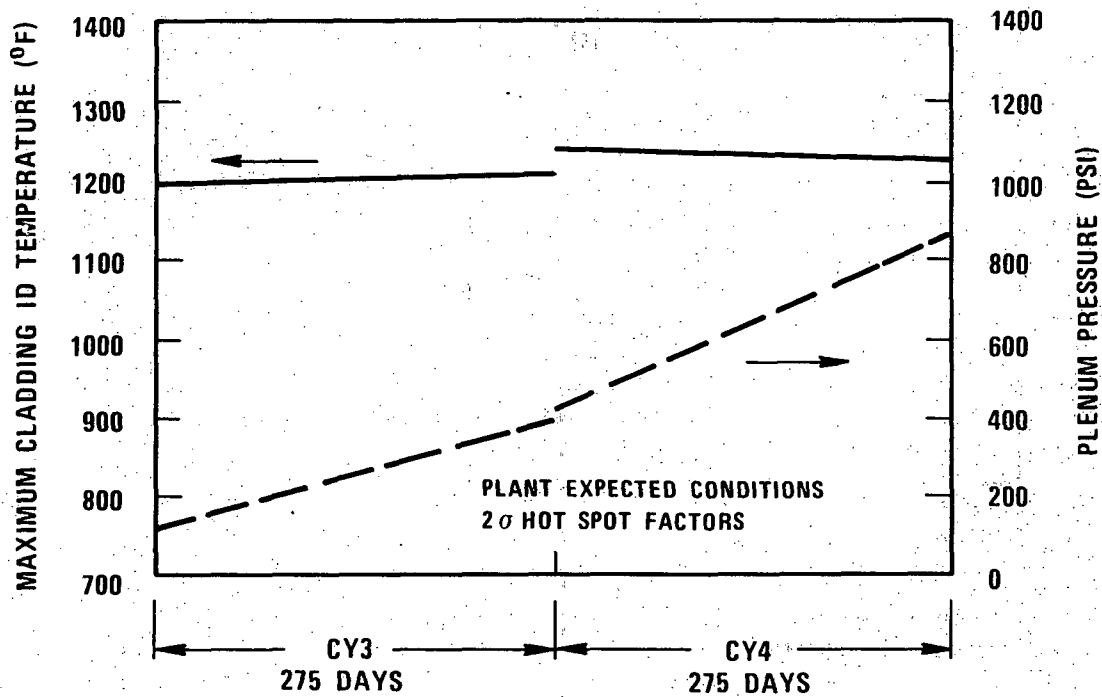


Figure 4.4-38 Lifetime Cladding Temperature/Pressure History in Fuel Assembly #2, Second Core, Orifing Zone 3

1668-34

4.4-164

Amend. 51  
Sept. 1979



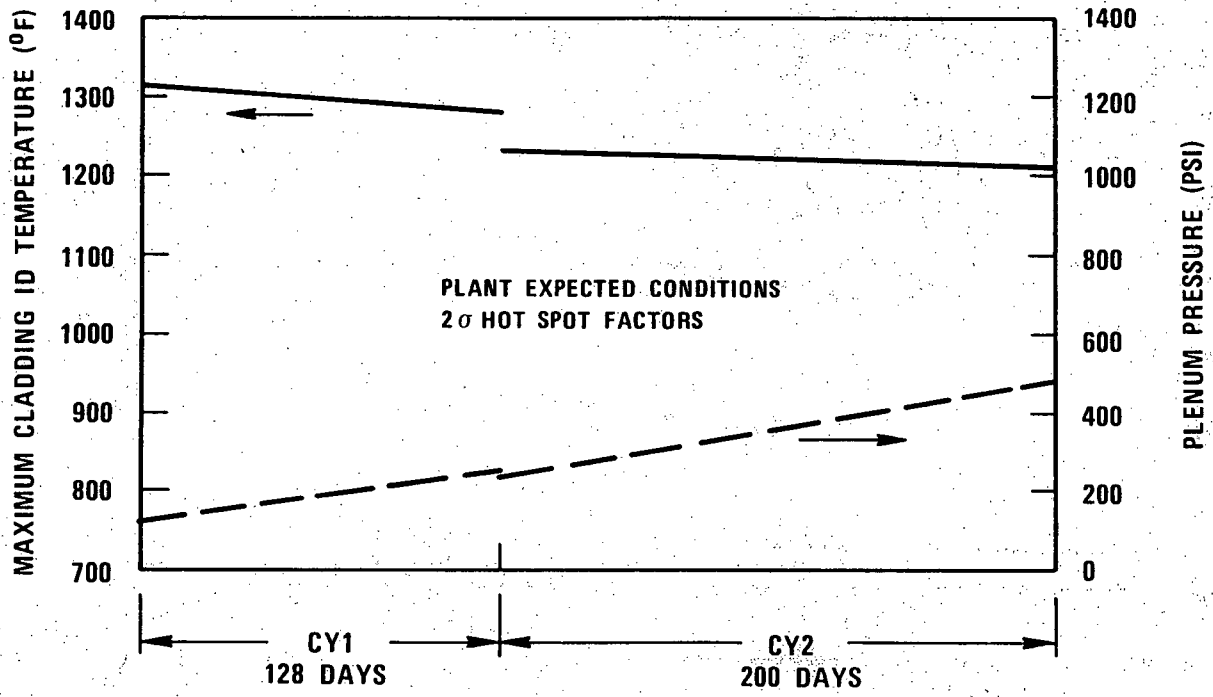


Figure 4.4-39 Lifetime Cladding Temperature/Pressure History in Fuel Assembly #52, First Core, Orificing Zone 4

1668-35

4.4-165

Amend. 51  
Sept. 1979

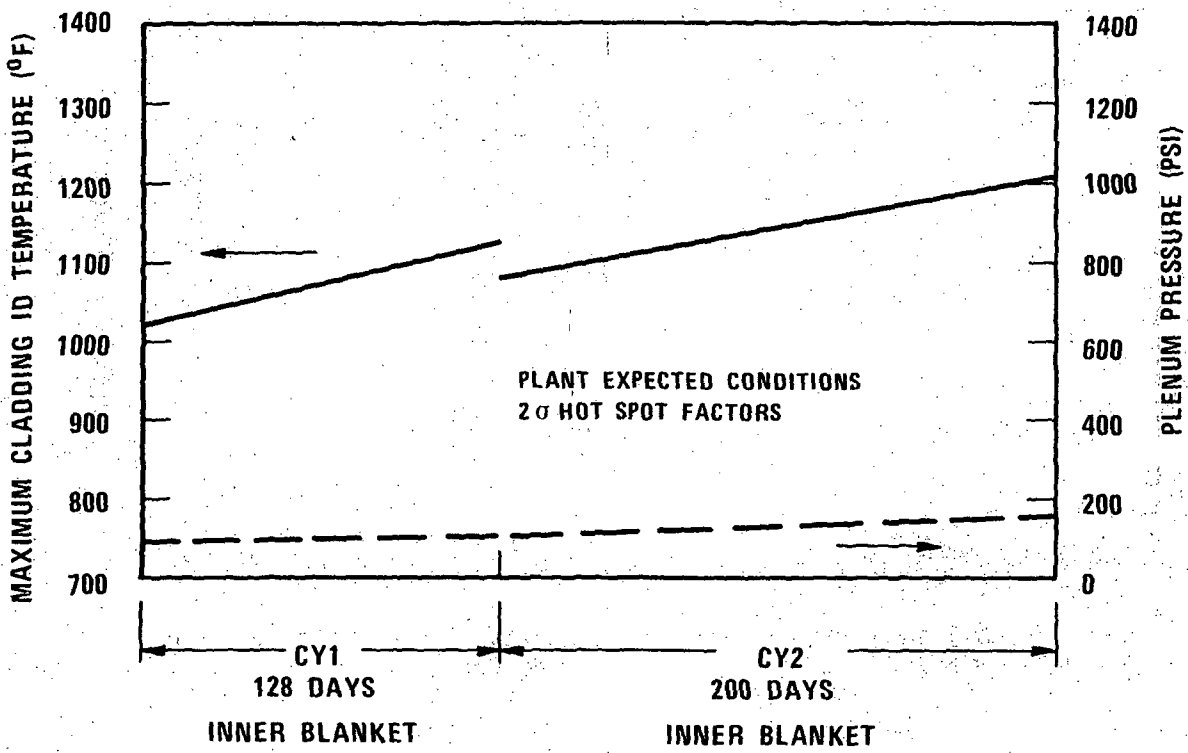


Figure 4.4-40 Lifetime Cladding Temperature/Pressure History in Assembly #98, First Core, Orificing Zone 6, Row 6 Alternating Position

1668-36

4.4-166

Amend. 51  
Sept. 1979

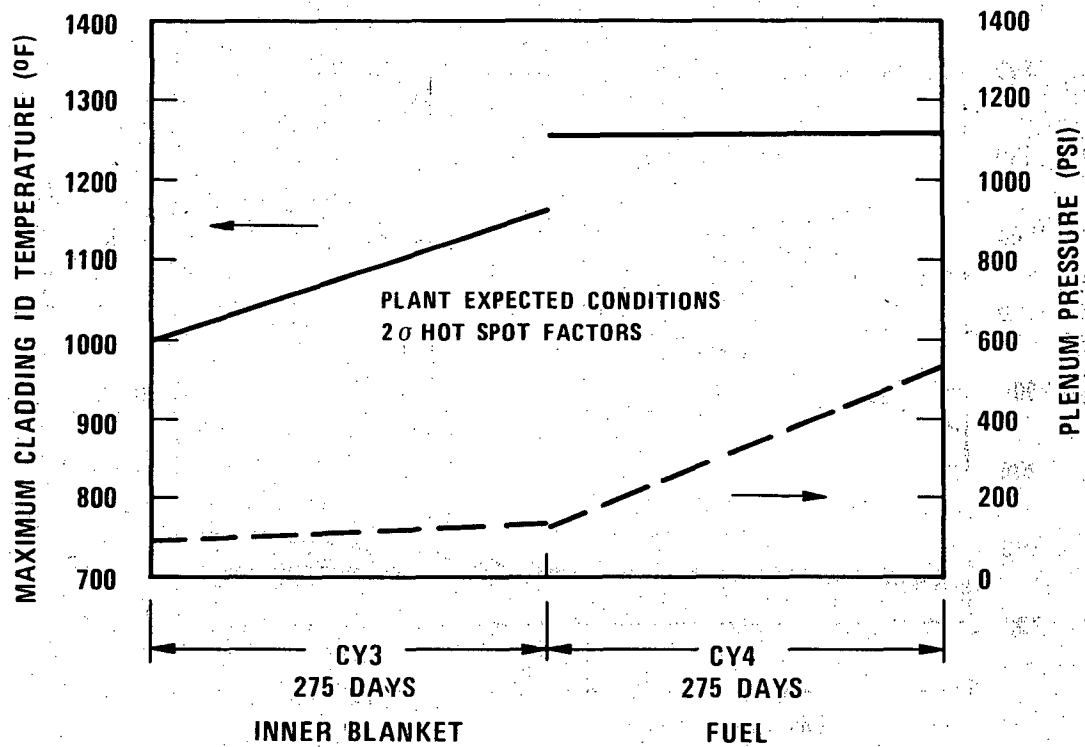


Figure 4.4-41 Lifetime Cladding Temperature/Pressure History in Assembly #62, Second Core, Orificing Zone 6, Row 6 Alternating Position

1668-37

4.4-167

Amend. 51  
Sept. 1979

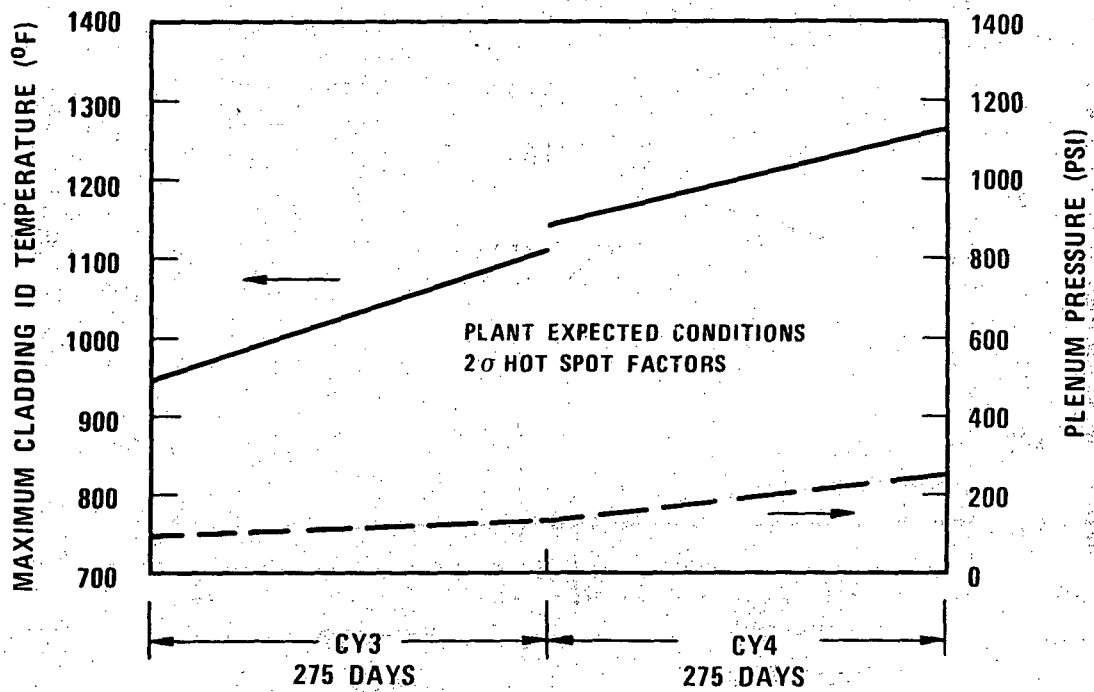


Figure 4.4-42 Lifetime Cladding Temperature/Pressure History in Inner Blanket Assembly #99, Second Core, Orificing Zone 7

1668-2

4.4-169

Amend. 51  
Sept. 1979

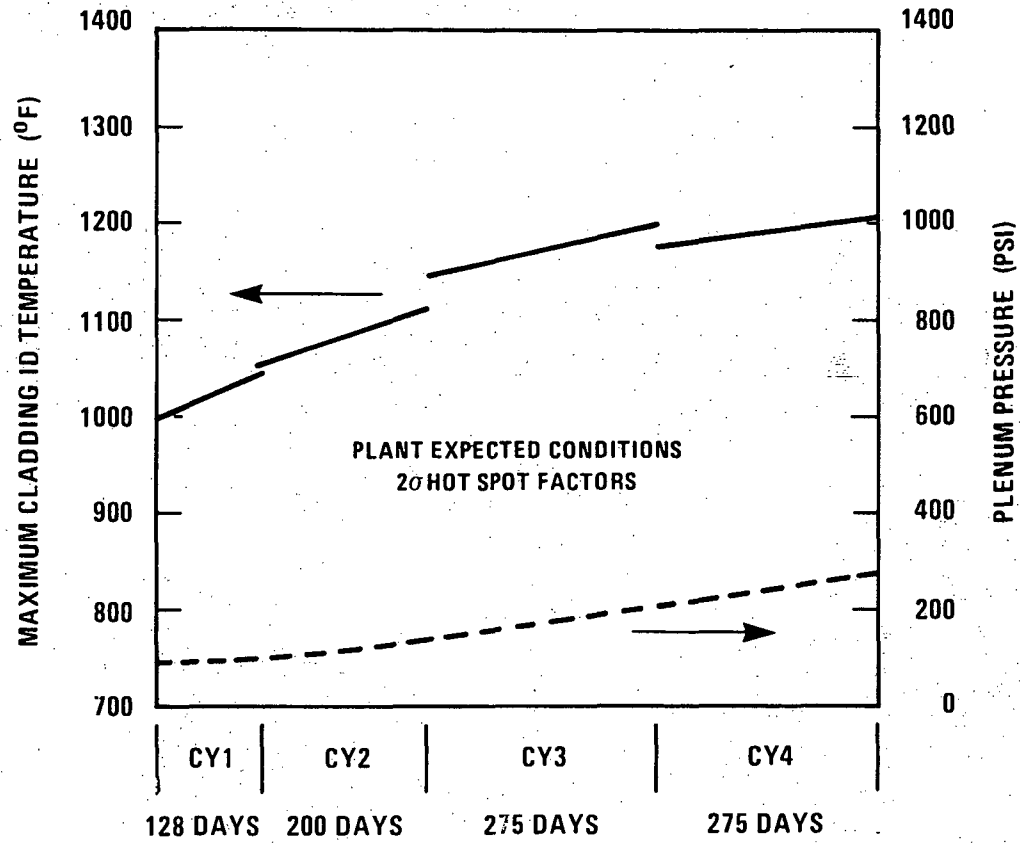


Figure 4.4-43. Lifetime Cladding Temperature/Pressure History in Radial Blanket Assembly #201, Orifing Zone 9

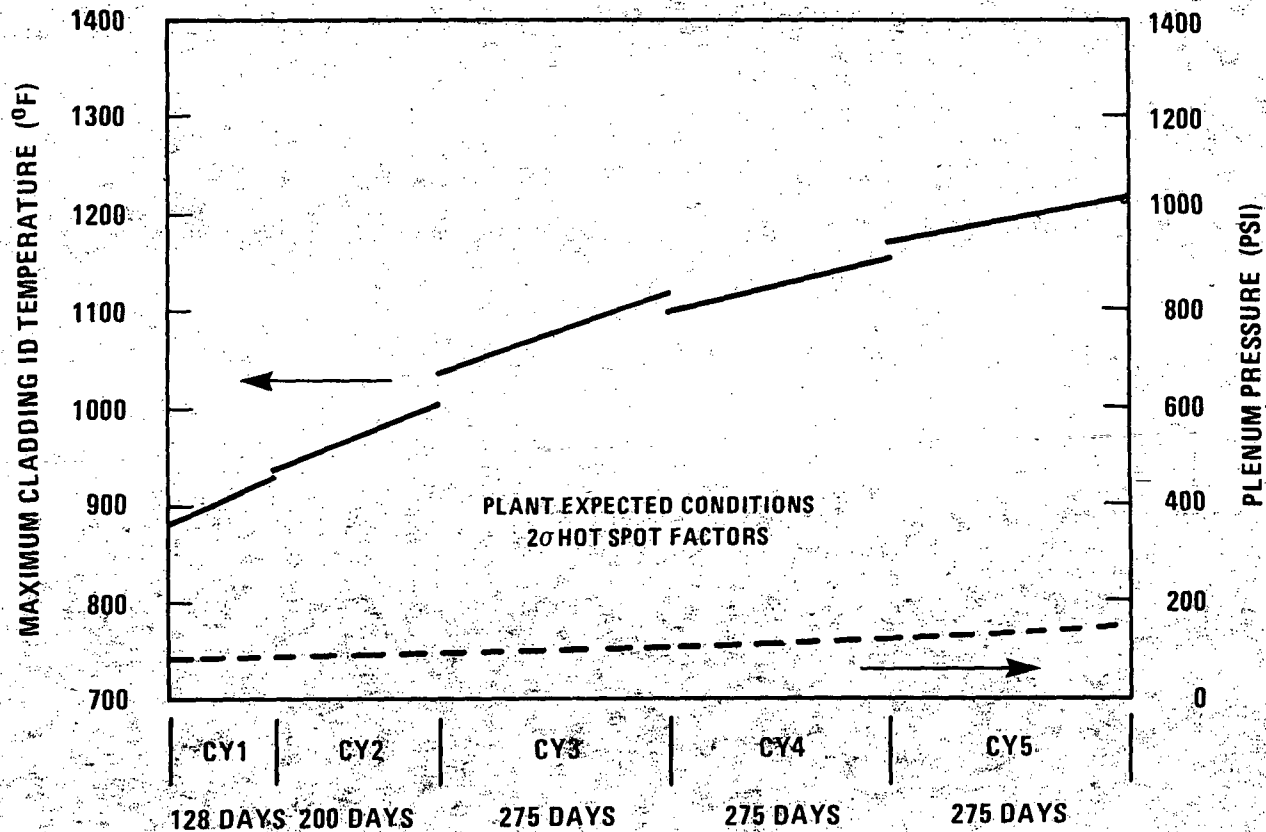


Figure 4.4-44. Lifetime Cladding Temperature/Pressure History in Radial Blanket Assembly #212, Orificing Zone 12

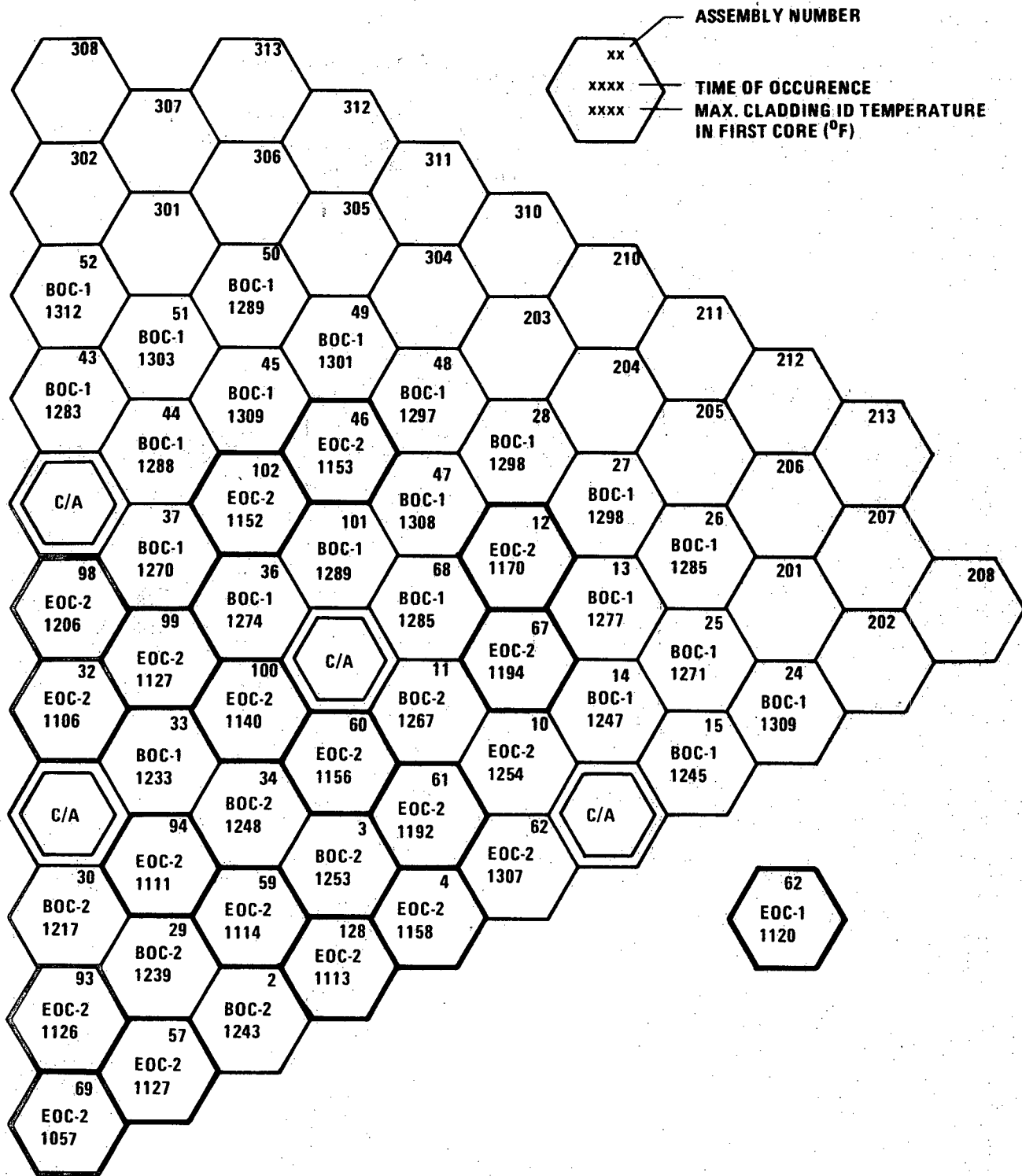


FIGURE 4.4-45. Envelope of Assemblies Maximum Cladding ID Temperature at Plant Expected Conditions During the First Core and Time Occurrence

5894-10

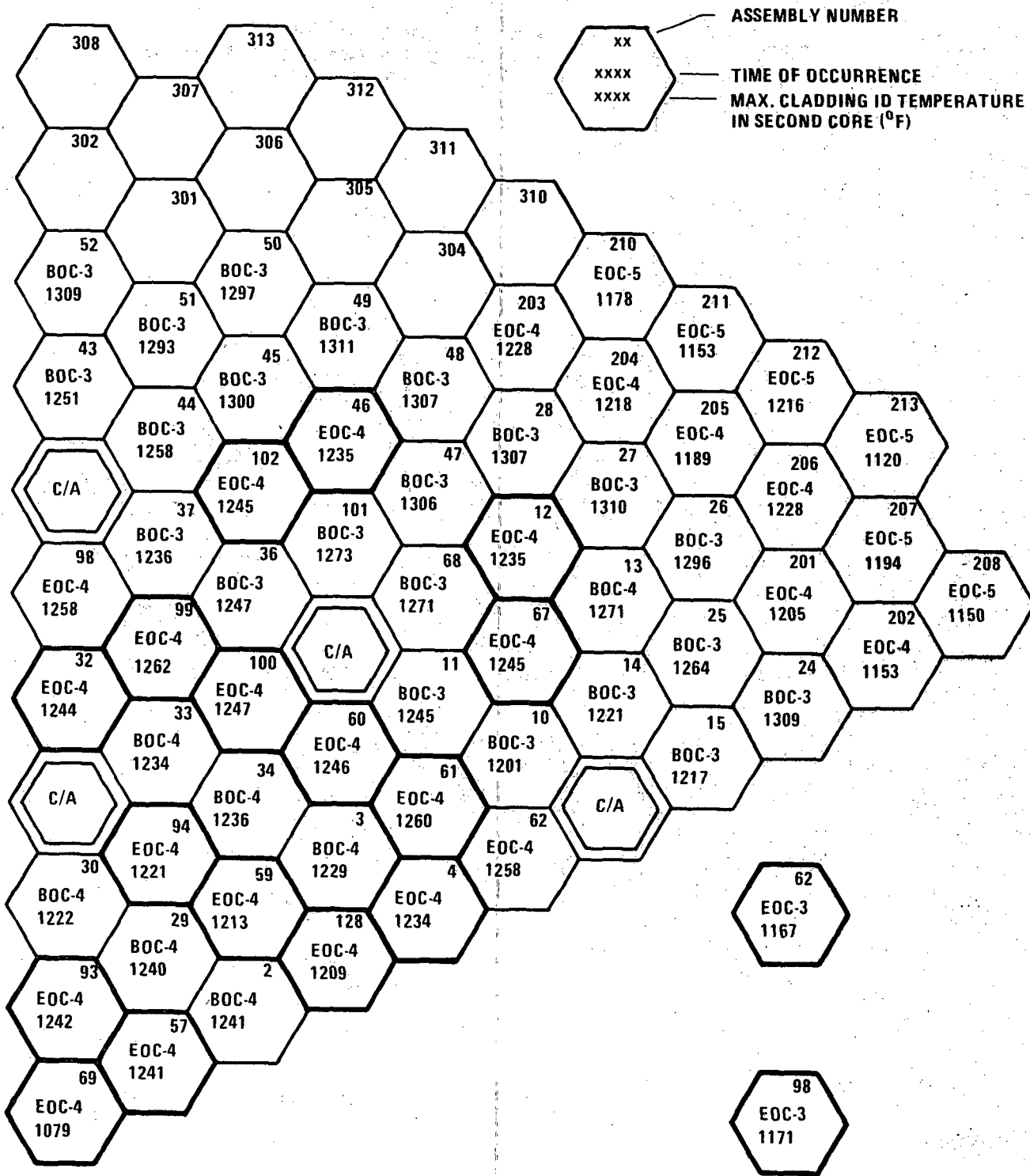
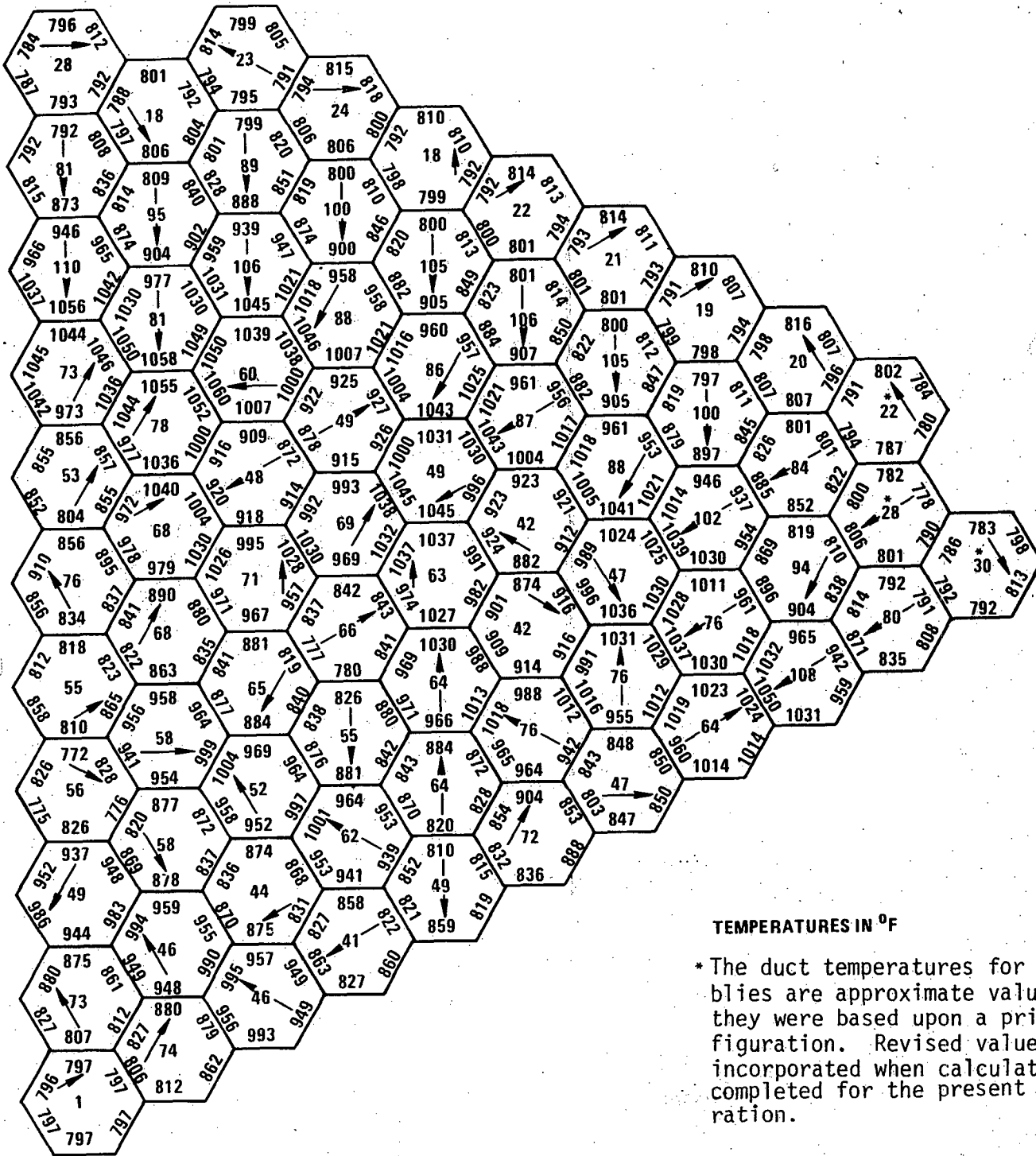


FIGURE 4.4-46. Envelope of Assemblies Maximum Cladding ID Temperature at Plant Expected Conditions During the Second Core and Time of Occurrence

5894-20

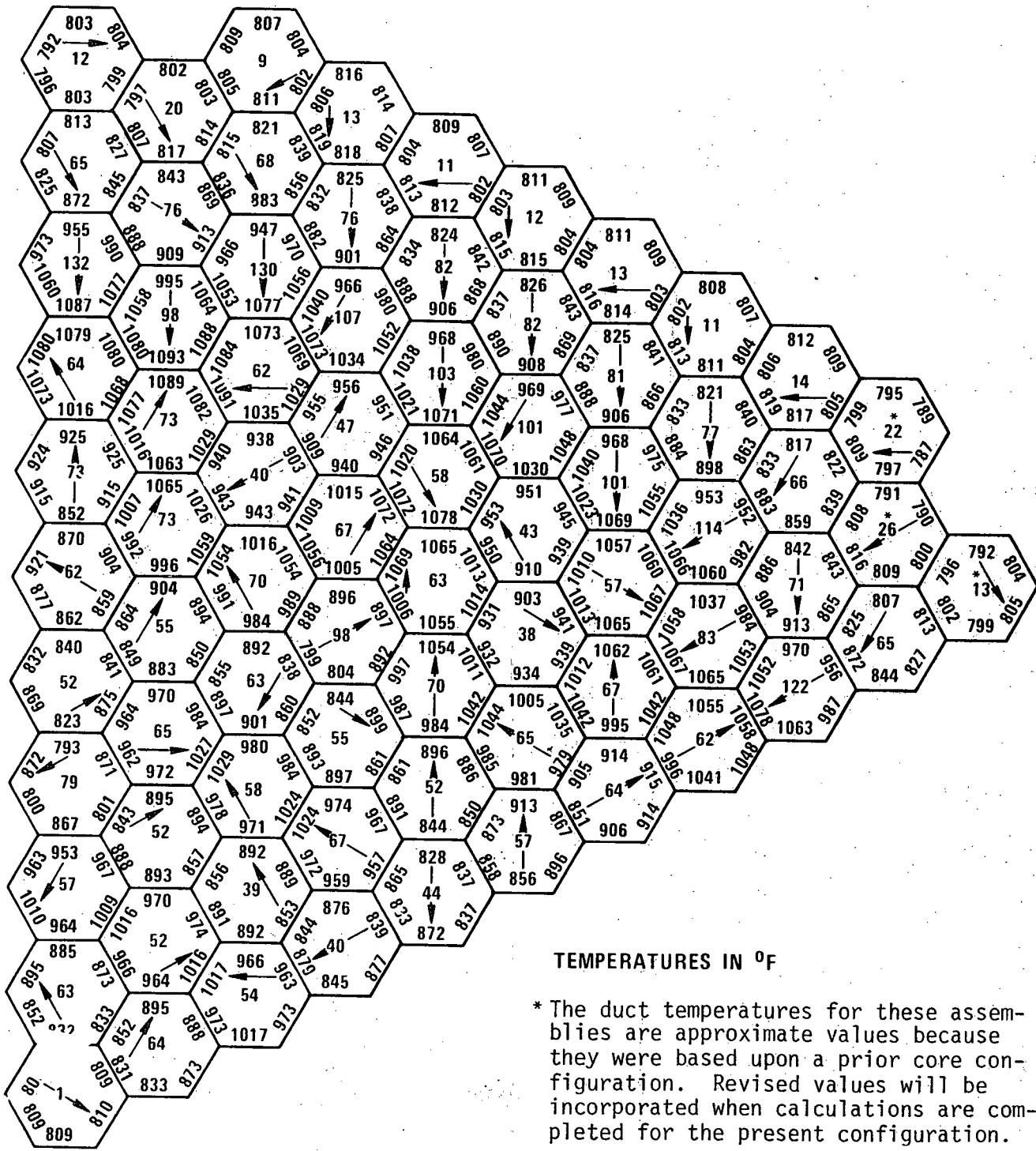




TEMPERATURES IN °F

\* The duct temperatures for these assemblies are approximate values because they were based upon a prior core configuration. Revised values will be incorporated when calculations are completed for the present configuration.

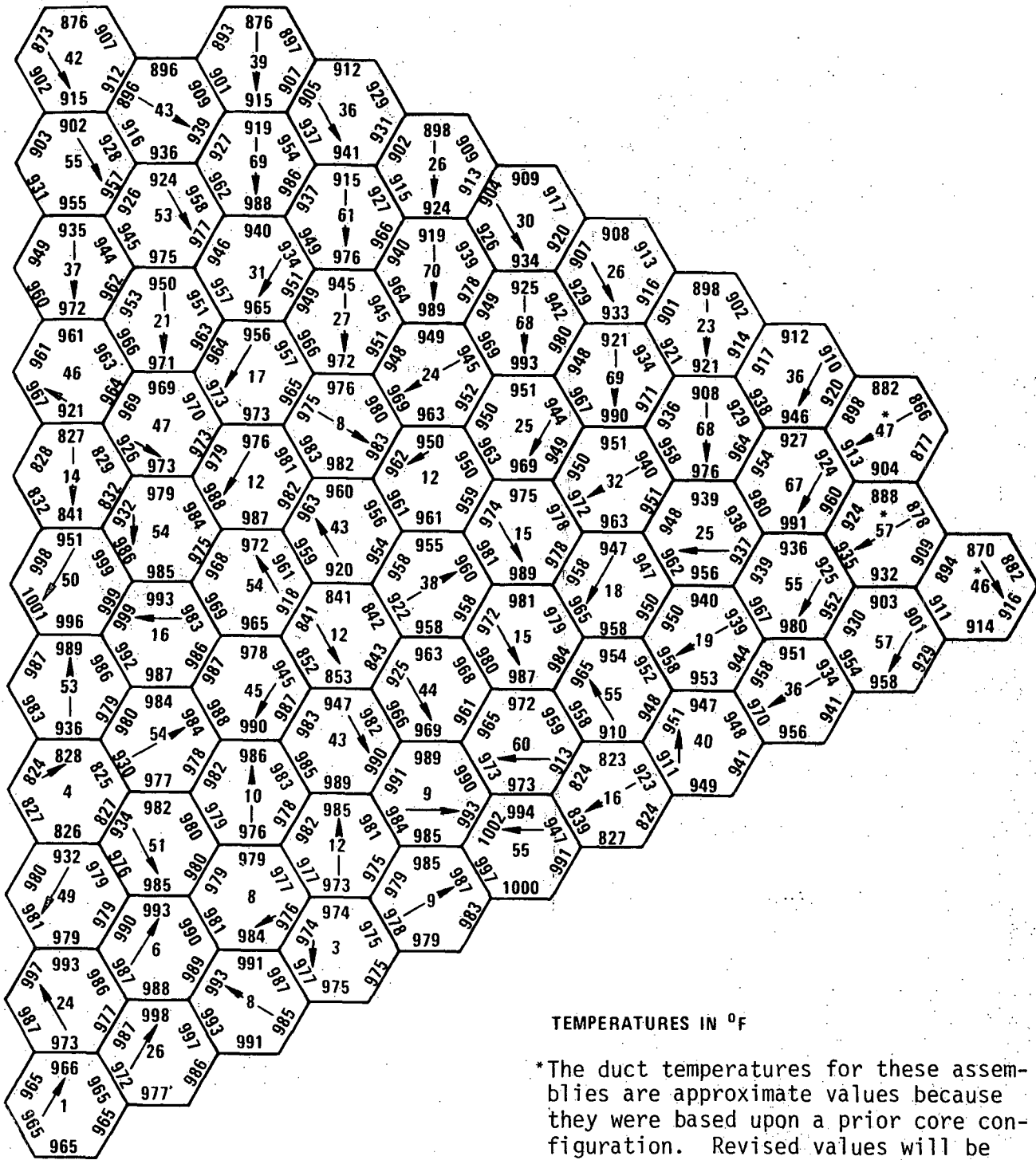
FIGURE 4.4-47. Core Wide Duct Midwall Temperatures at 60" Elevation BOC1, Under Nominal Conditions



TEMPERATURES IN °F

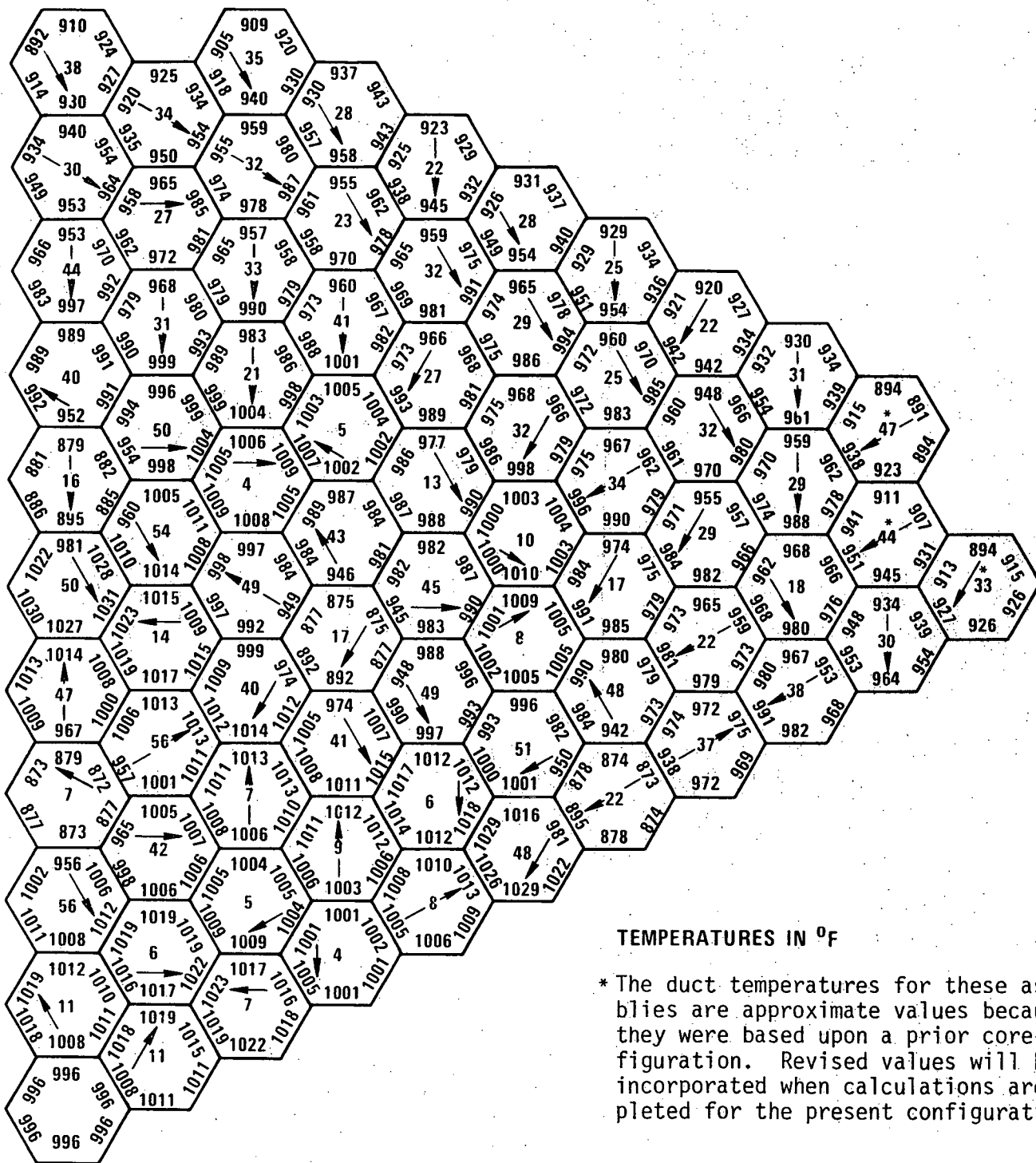
\* The duct temperatures for these assemblies are approximate values because they were based upon a prior core configuration. Revised values will be incorporated when calculations are completed for the present configuration.

5894-19 FIGURE 4.4-48. Core Wide Duct Midwall Temperatures at 112" Elevation BOC1, Under Nominal Conditions



5894-3

FIGURE 4.4-49. Core Wide Duct Midwall Temperatures at 60" Elevation, EOC4, Under Nominal Conditions



TEMPERATURES IN °F

\* The duct temperatures for these assemblies are approximate values because they were based upon a prior core configuration. Revised values will be incorporated when calculations are completed for the present configuration.

FIGURE 4.4-50. Core Wide Duct Midwall Temperatures at 112" Elevation, EOC4, Under Nominal Conditions

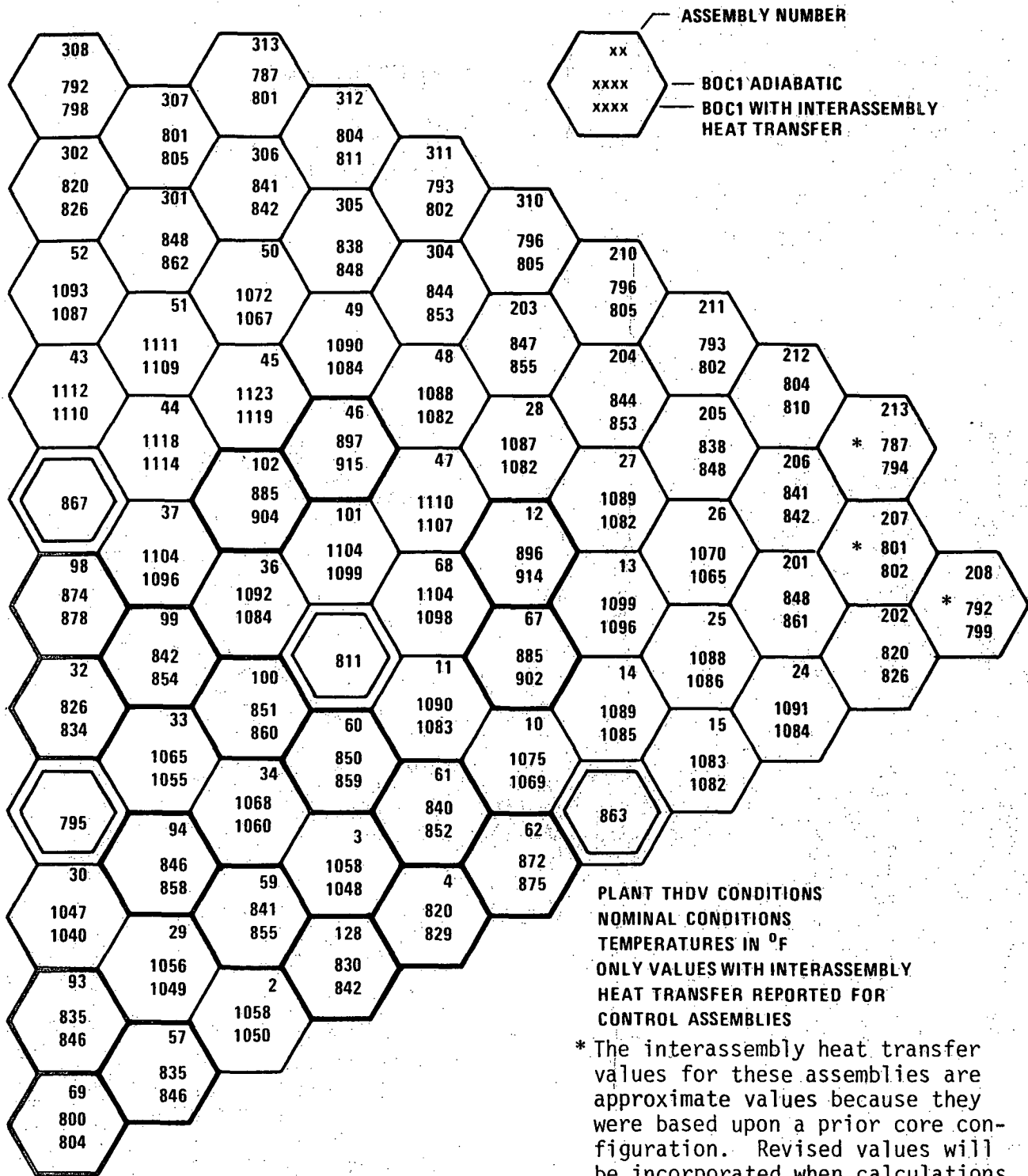


FIGURE 4.4-51. Comparison of Assemblies Mixed Mean Exit Temperatures Under Adiabatic Conditions and Including Inter-Assembly Heat Transfer Effects at BOC1

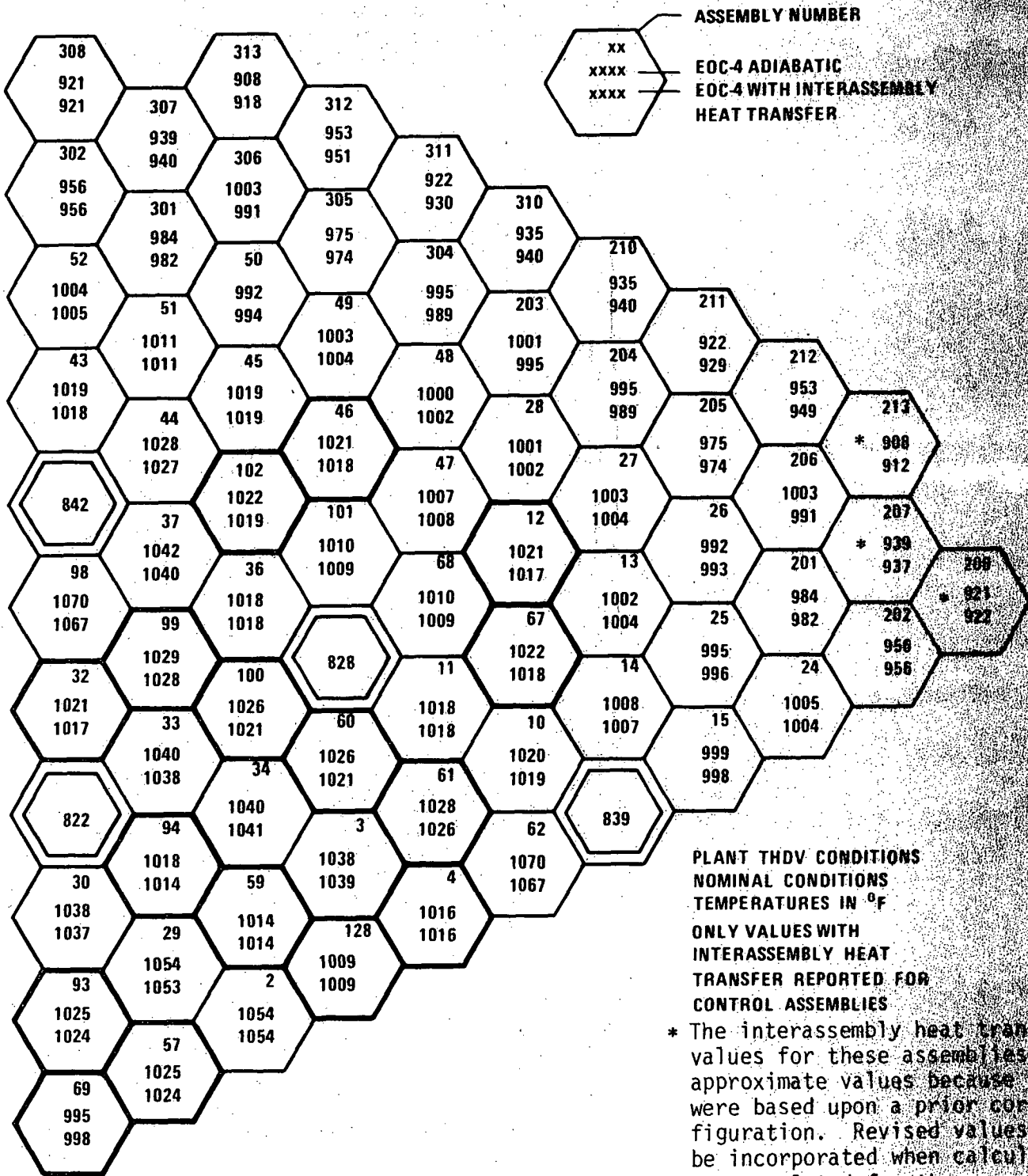


FIGURE 4.4-52. Comparison of Assemblies Mixed Mean Exit Temperatures Under Adiabatic Conditions and Including Inter-Assembly Heat Transfer Effects at EOC4

5894-2

1668-2

4.4-179

Amend. 51  
Sept. 1979

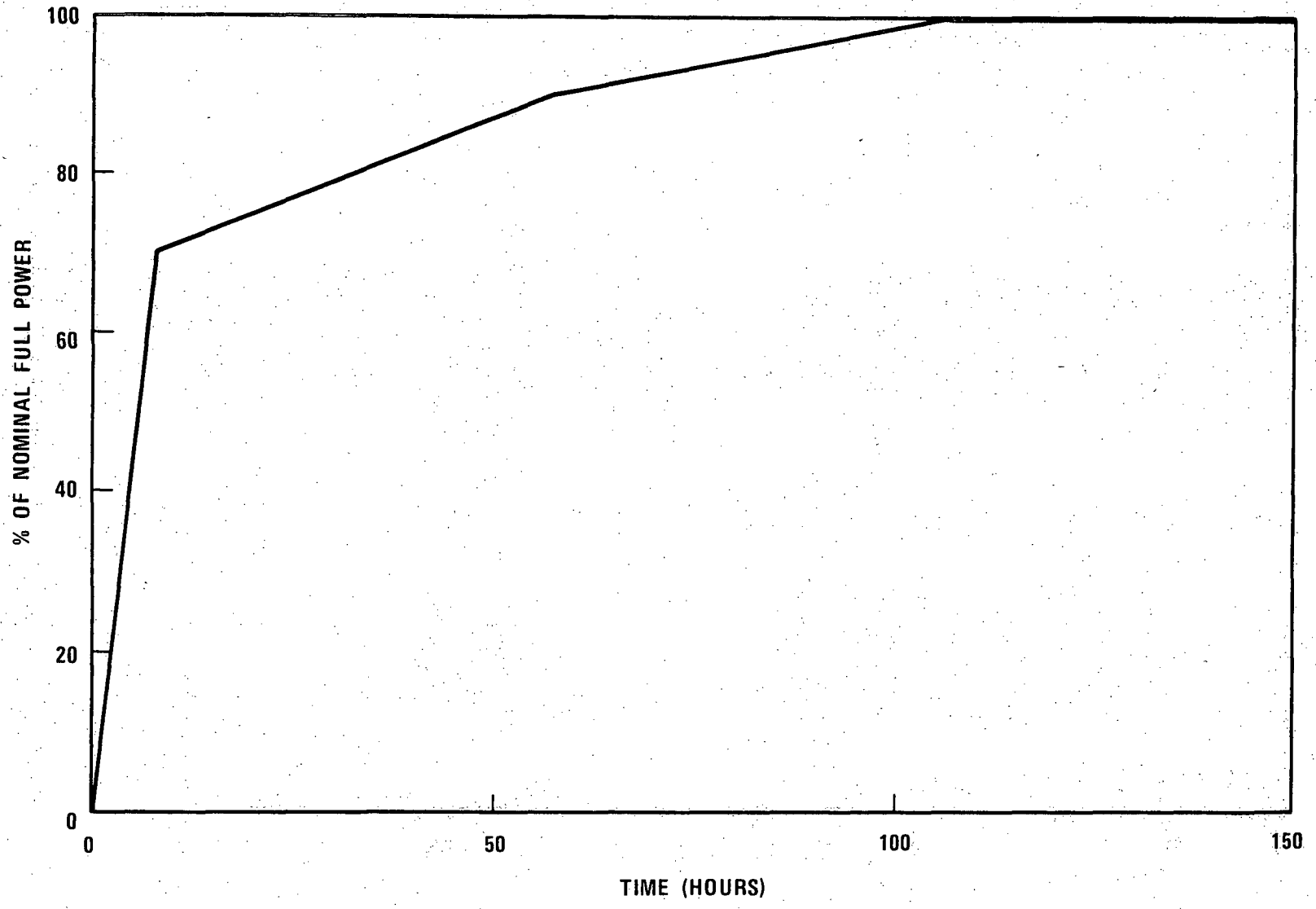


Figure 4.4-53 Power History (Programmed Startup) Used in Fuel Assemblies  
Power-to-Melt Analyses

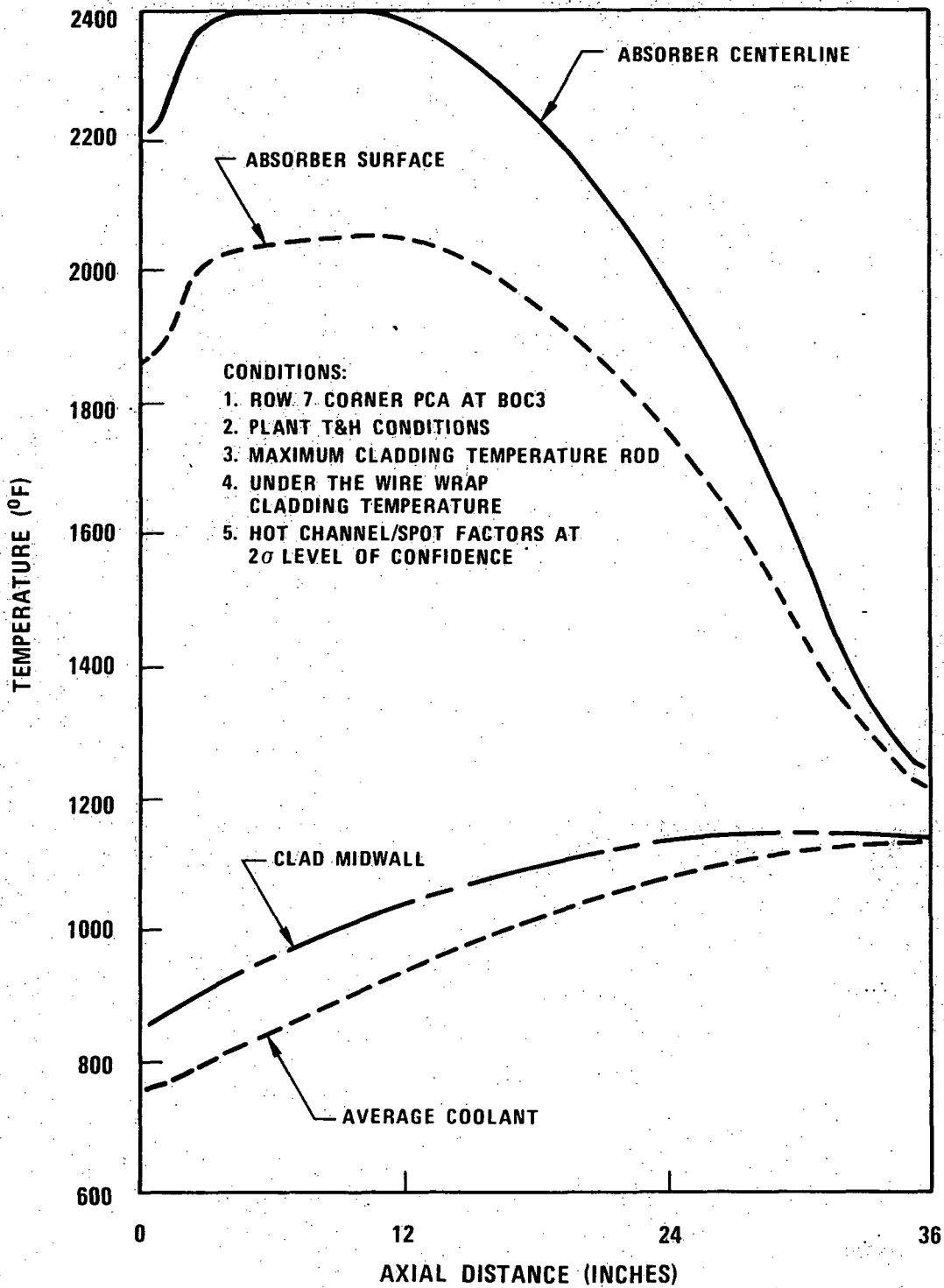


Figure 4.4-54 Typical 10.5-Inch Withdrawn C/R Absorber Axial Temperatures



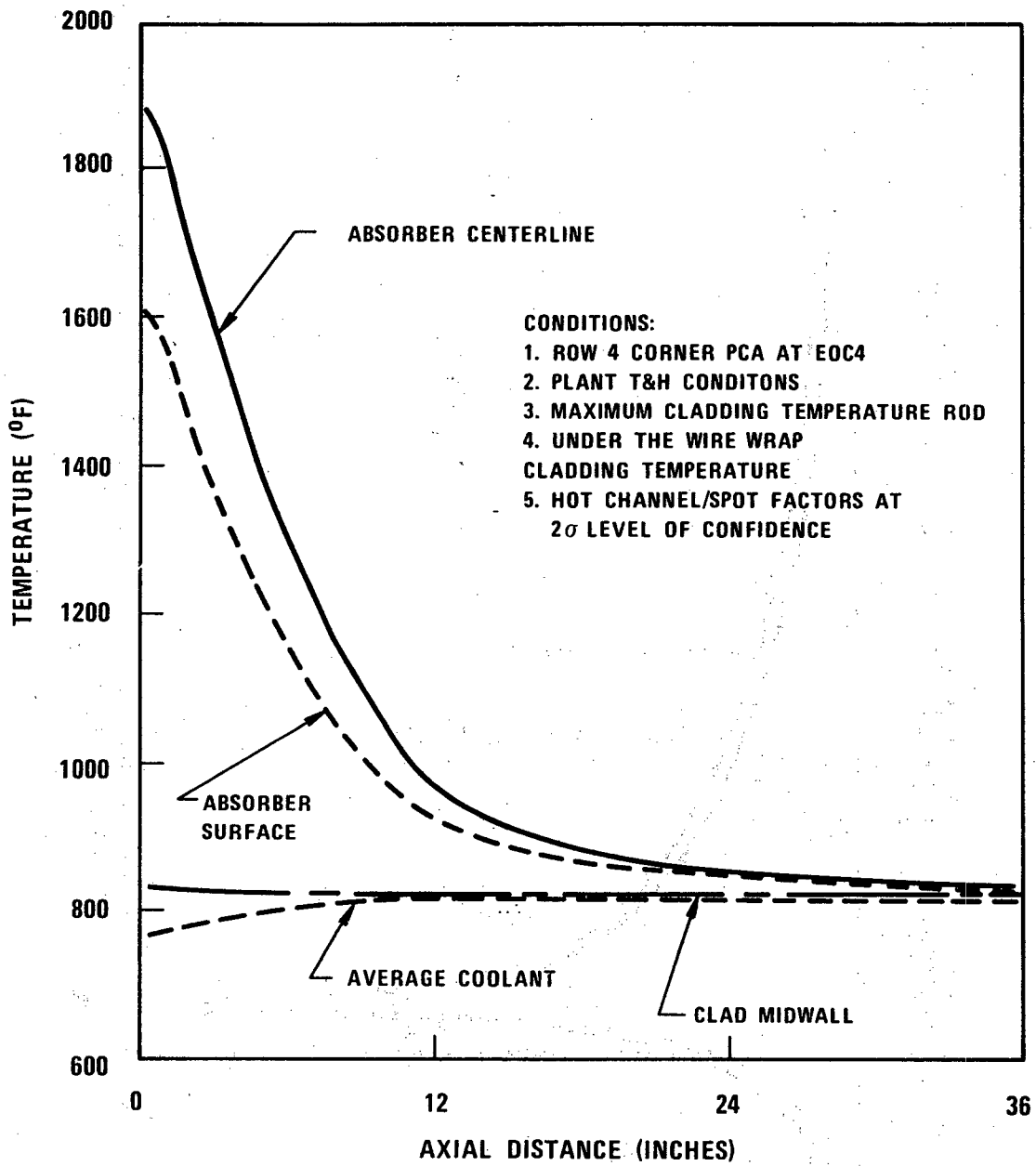
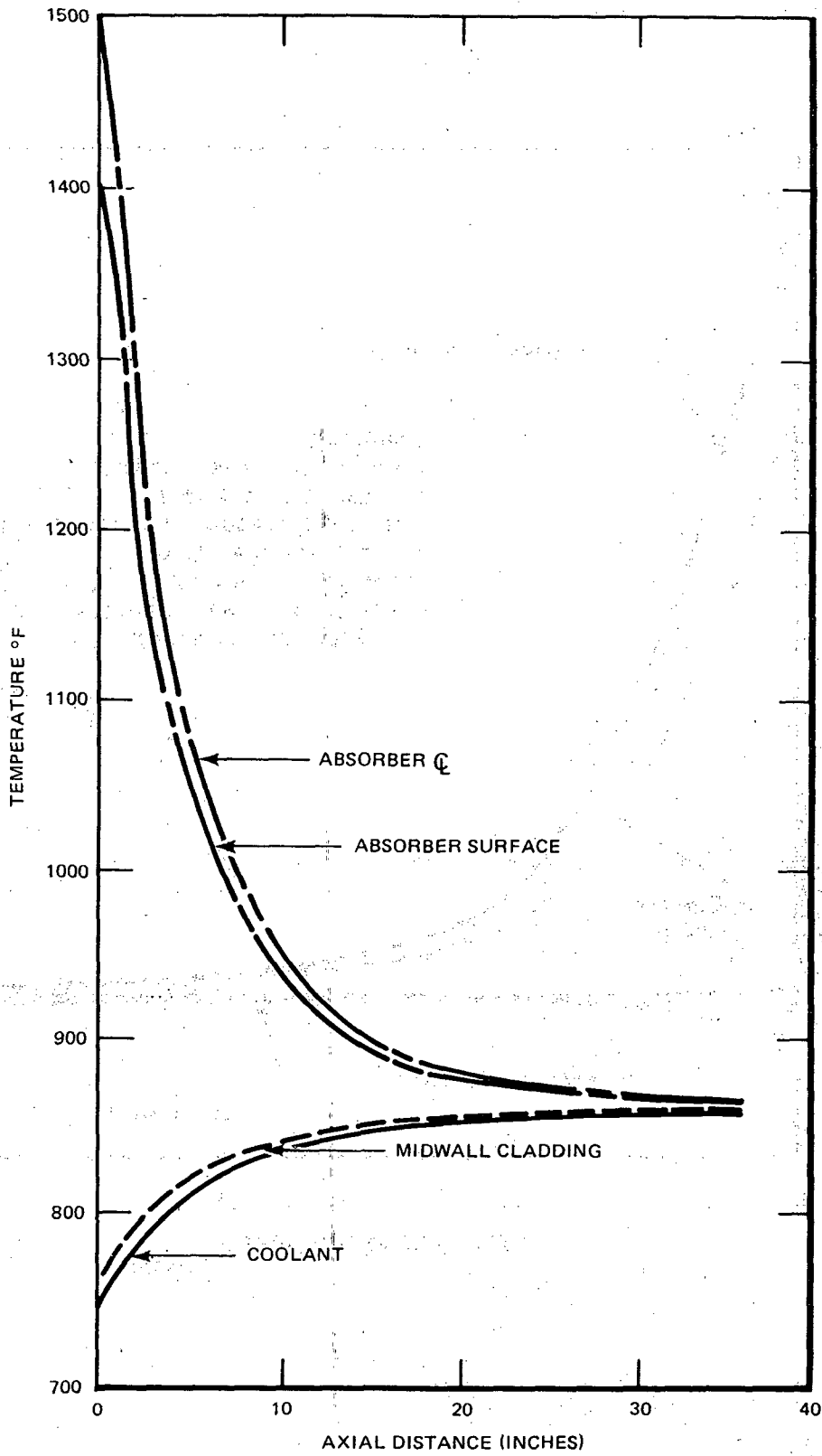


Figure 4.4-55 Typical 36-Inch Withdrawal C/R Absorber Axial Temperatures

1668-11

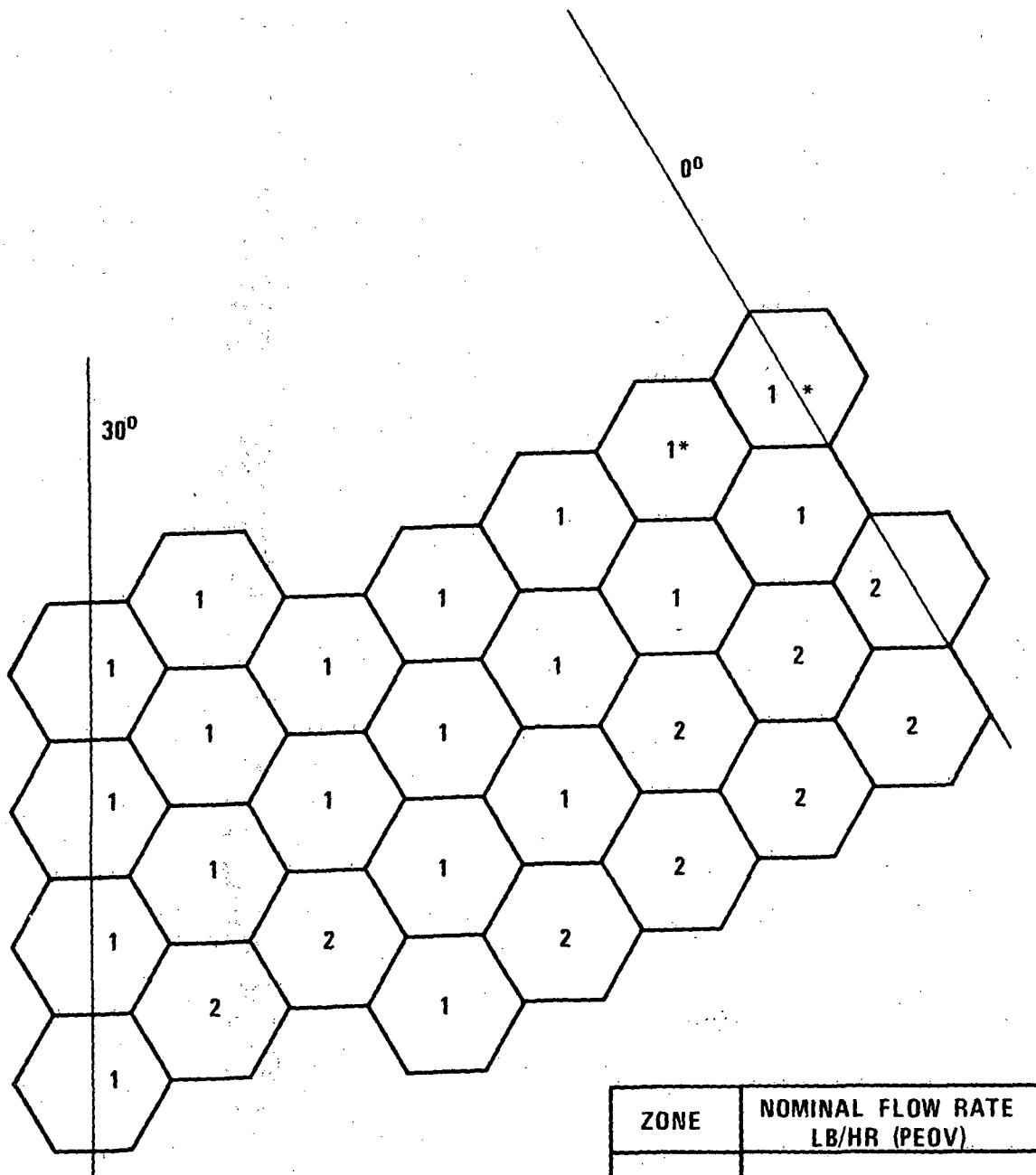
4.4-181

Amend. 51  
Sept. 1979



83-031-03

Figure 4.4-55a TYPICAL FULLY WITHDRAWN SECONDARY CONTROL ROD ABSORBER AXIAL TEMPERATURES UNDER THDV CONDITIONS AT 115% OVERPOWER



ZONE	NOMINAL FLOW RATE LB/HR (PEOV)
1	1626
2	2275

\*ASSEMBLIES WITHIN LIM FOR THIS SECTOR (SEE ALSO FIGURE 4.4-26)

Figure 4.4-56 Two Zone Orificing Scheme of Removable Radial Shield Assemblies

4482-4

CONDITIONS: PLANT EXPECTED OPERATING CONDITIONS  
 EOC5, 714°F INLET TEMPERATURE  
 +2σ UNCERTAINTIES ON RADIAL BLANKET  
 BOUNDARY TEMPERATURES  
 +2σ UNCERTAINTIES ON REMOVABLE  
 RADIAL SHIELD TEMPERATURES

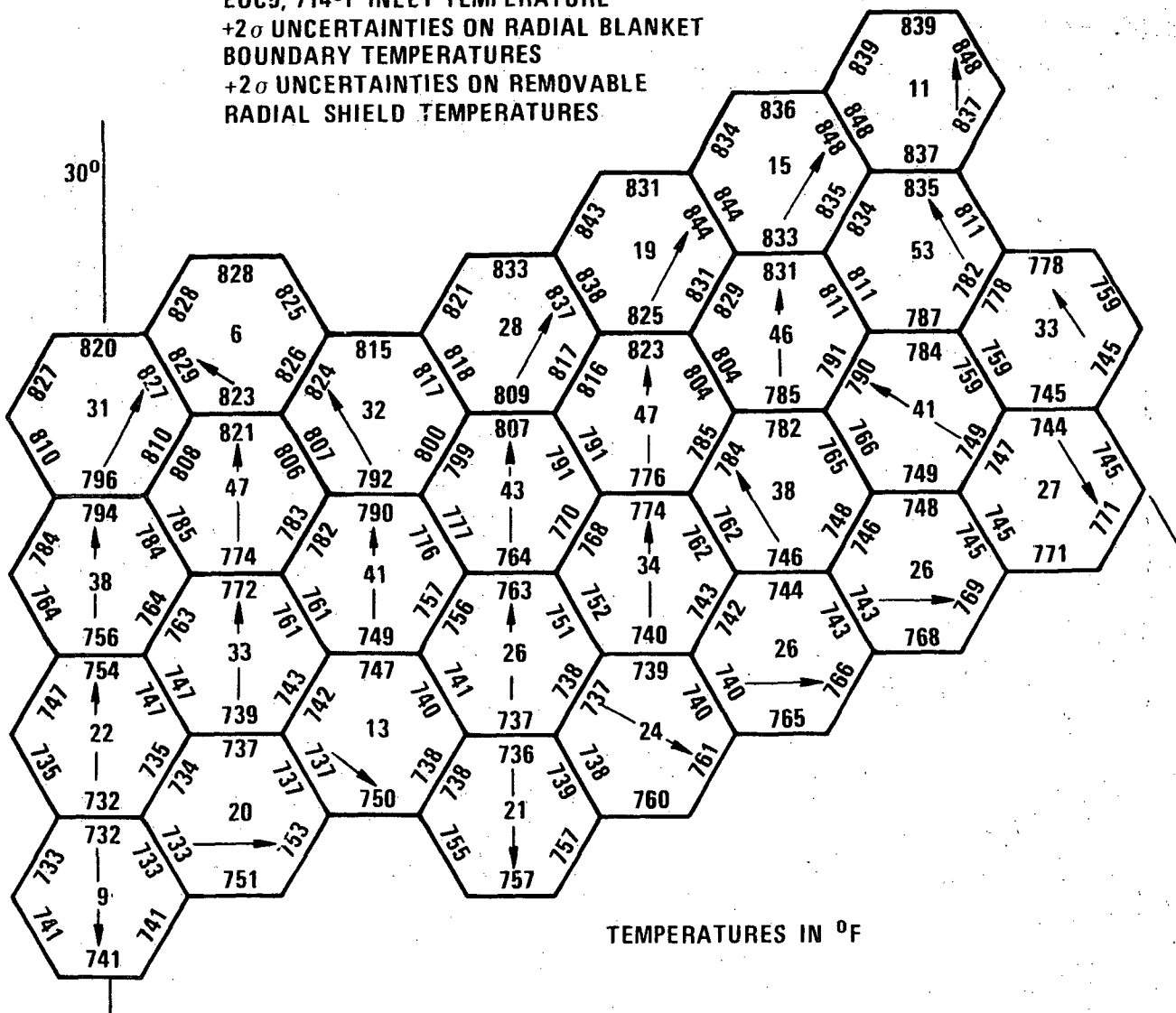


Figure 4.4-57 Removable Radial Shield Duct Midwall Temperature at Core Midplane (+2σ RRS Uncertainties)

**CONDITIONS: PLANT EXPECTED OPERATION CONDITIONS**  
**EOC5, 714°F INLET TEMPERATURE**  
**+2 $\sigma$  UNCERTAINTIES ON RADIAL BLANKET BOUNDARY TEMPERATURES**  
**+2 $\sigma$  UNCERTAINTIES ON REMOVABLE RADIAL SHIELD TEMPERATURES**

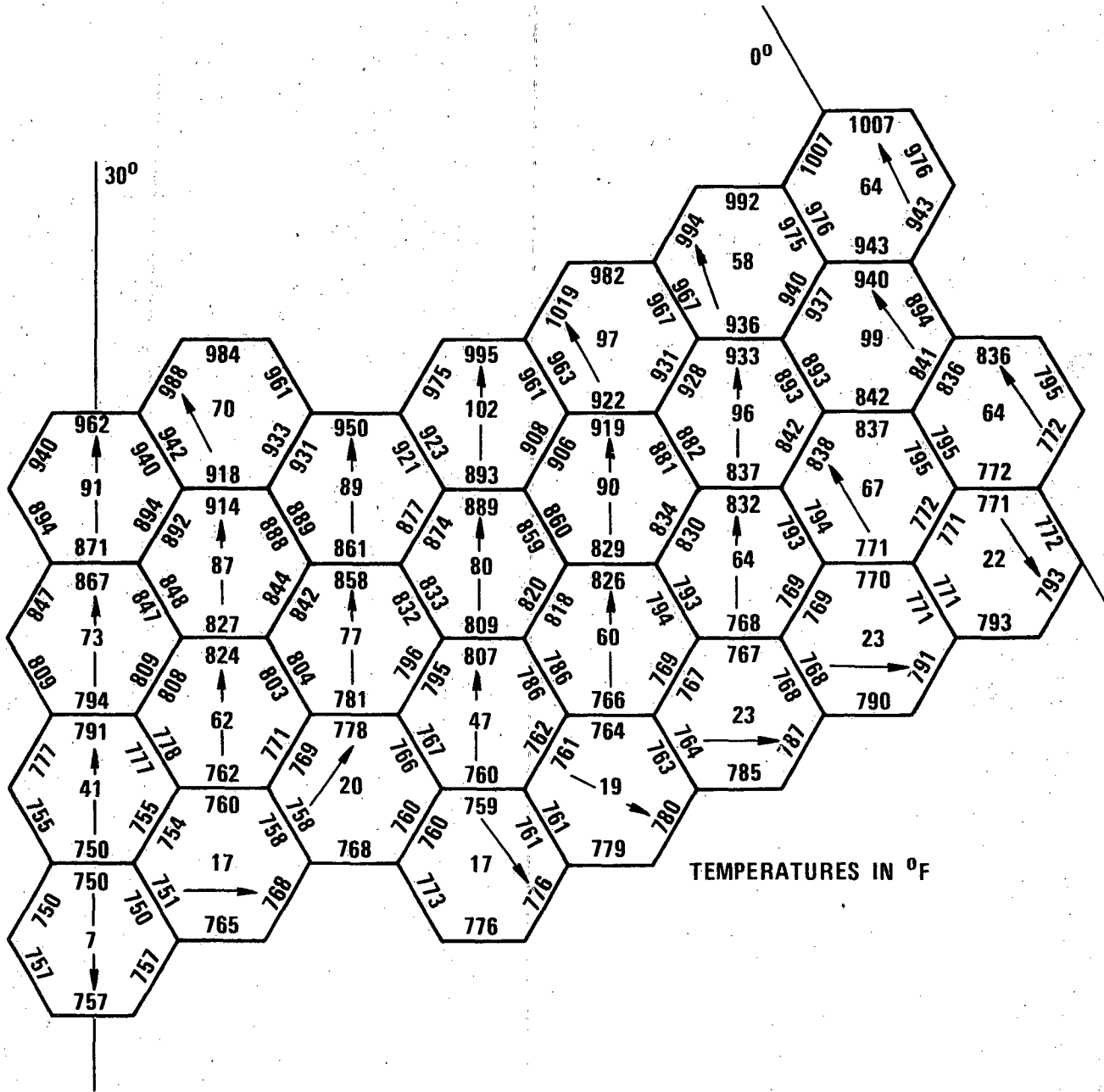


Figure 4.4-58 Removable Radial Shield Duct Midwall Temperatures at Above Core Load Pad (+2 $\sigma$  RRS Uncertainties)

**CONDITIONS: PLANT EXPECTED OPERATING CONDITIONS**  
**EOC5, 714°F INLET TEMPERATURE**  
**+2 $\sigma$  UNCERTAINTIES ON RADIAL BLANKET BOUNDARY TEMPERATURES**  
**+2 $\sigma$  UNCERTAINTIES ON REMOVABLE RADIAL SHIELD TEMPERATURES**

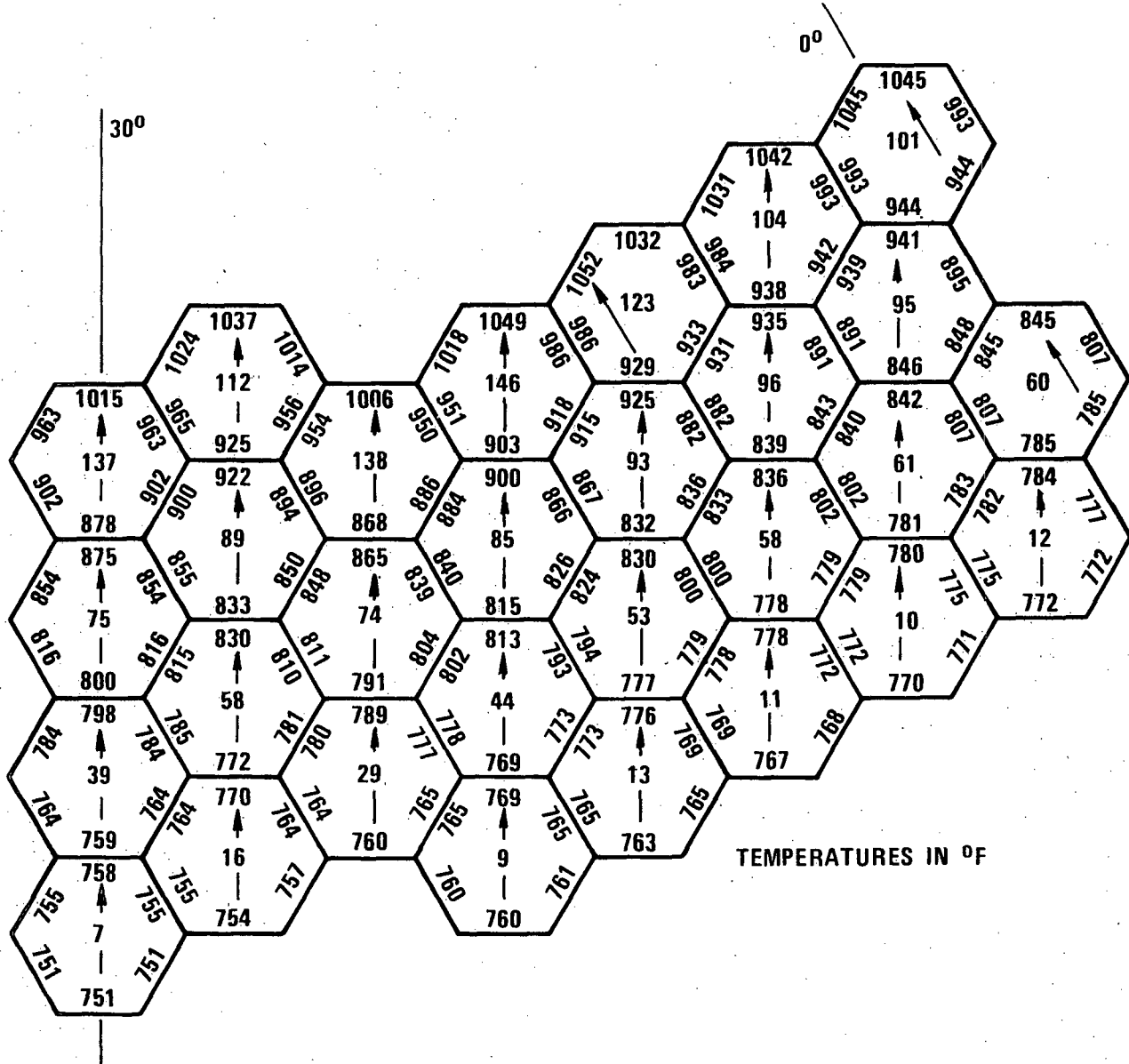


Figure 4.4-59 Removable Radial Shield Duct Midwall Temperatures at Top Core Load Pad (+2 $\sigma$  RRS Uncertainties)

**CONDITIONS: PLANT EXPECTED OPERATING CONDITIONS**  
**EOC5, 714°F INLET TEMPERATURE**  
**+2 $\sigma$  UNCERTAINTIES ON RADIAL BLANKET BOUNDARY TEMPERATURES**  
**-2 $\sigma$  UNCERTAINTIES ON REMOVABLE RADIAL SHIELD TEMPERATURES**

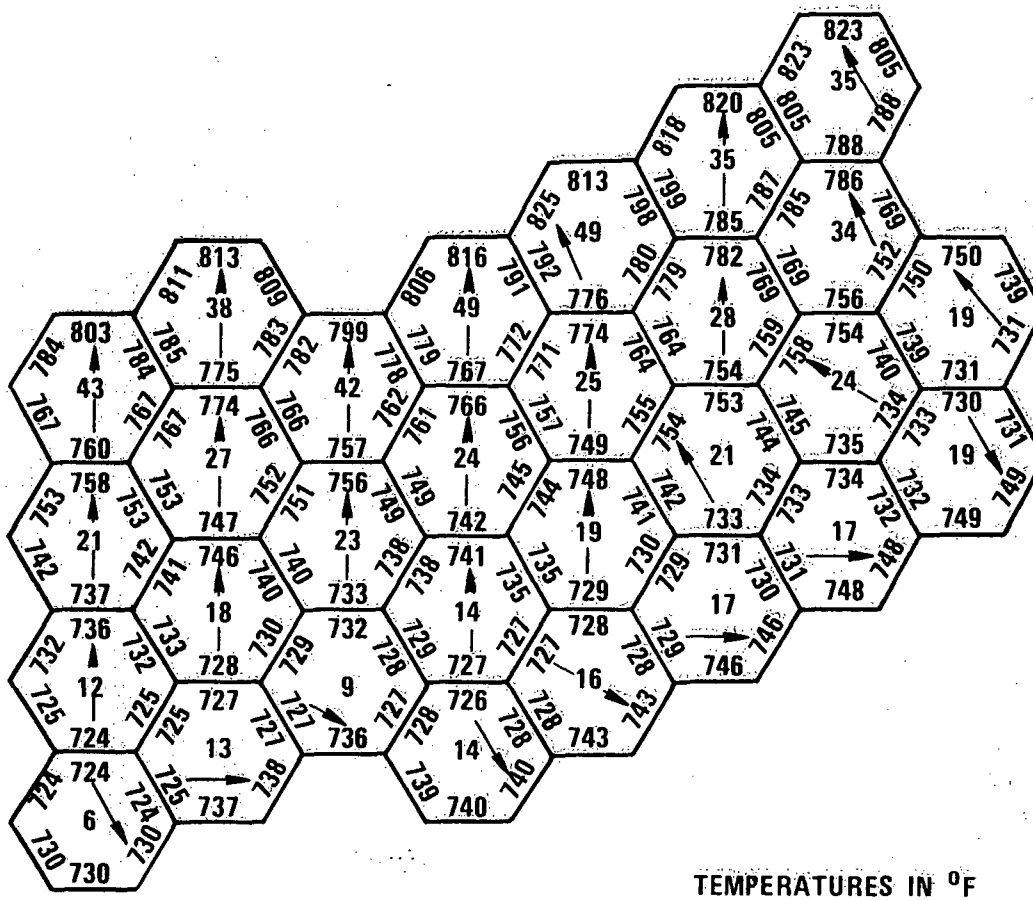


Figure 4.4-60 Removable Radial Shield Duct Midwall Temperatures at Core Midplane (-2 $\sigma$  RRS Uncertainties)

CONDITIONS: PLANT EXPECTED OPERATING CONDITIONS

EOC5, 714°F INLET TEMPERATURE

+2σ UNCERTAINTIES ON RADIAL BLANKET BOUNDARY TEMPERATURES

-2σ UNCERTAINTIES ON REMOVABLE RADIAL SHIELD TEMPERATURES

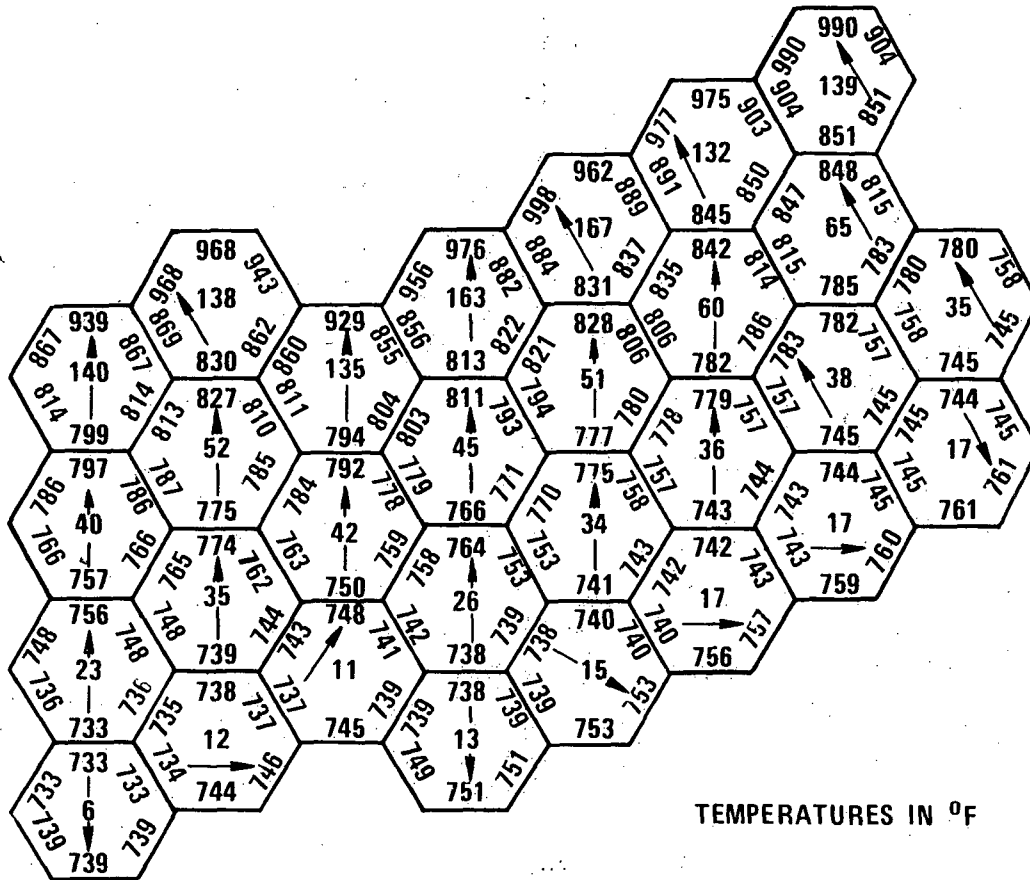


Figure 4.4-61 Removable Radial Shield Duct Midwall Temperatures at Above Core Load Pad (-2σ RRS Uncertainties)

4482-3



CONDITIONS: PLANT EXPECTED OPERATING CONDITIONS  
 EOC5, 714°F INLET TEMPERATURE  
 +2σ UNCERTAINTIES ON RADIAL BLANKET BOUNDARY TEMPERATURES  
 -2σ UNCERTAINTIES ON REMOVABLE RADIAL SHIELD TEMPERATURES

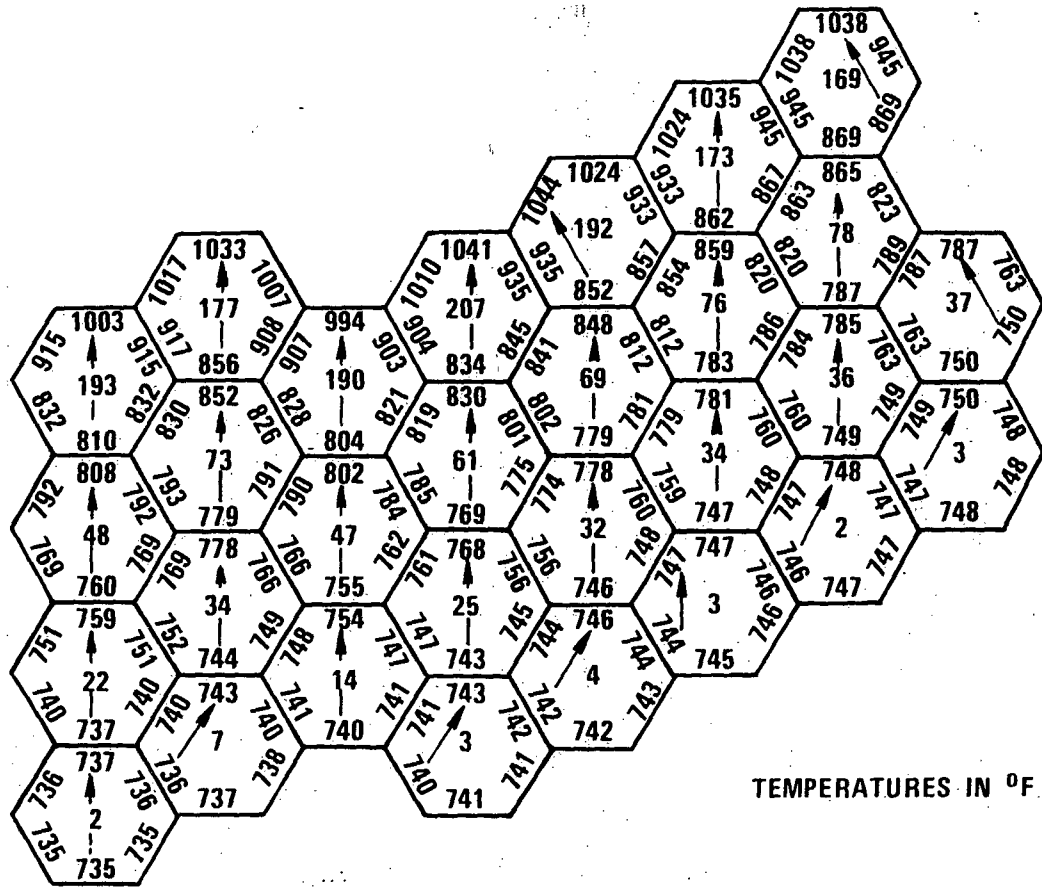


Figure 4.4-62 Removable Radial Shield Duct Midwall Temperatures at Top Core Load Pad (-2σ RRS Uncertainties)

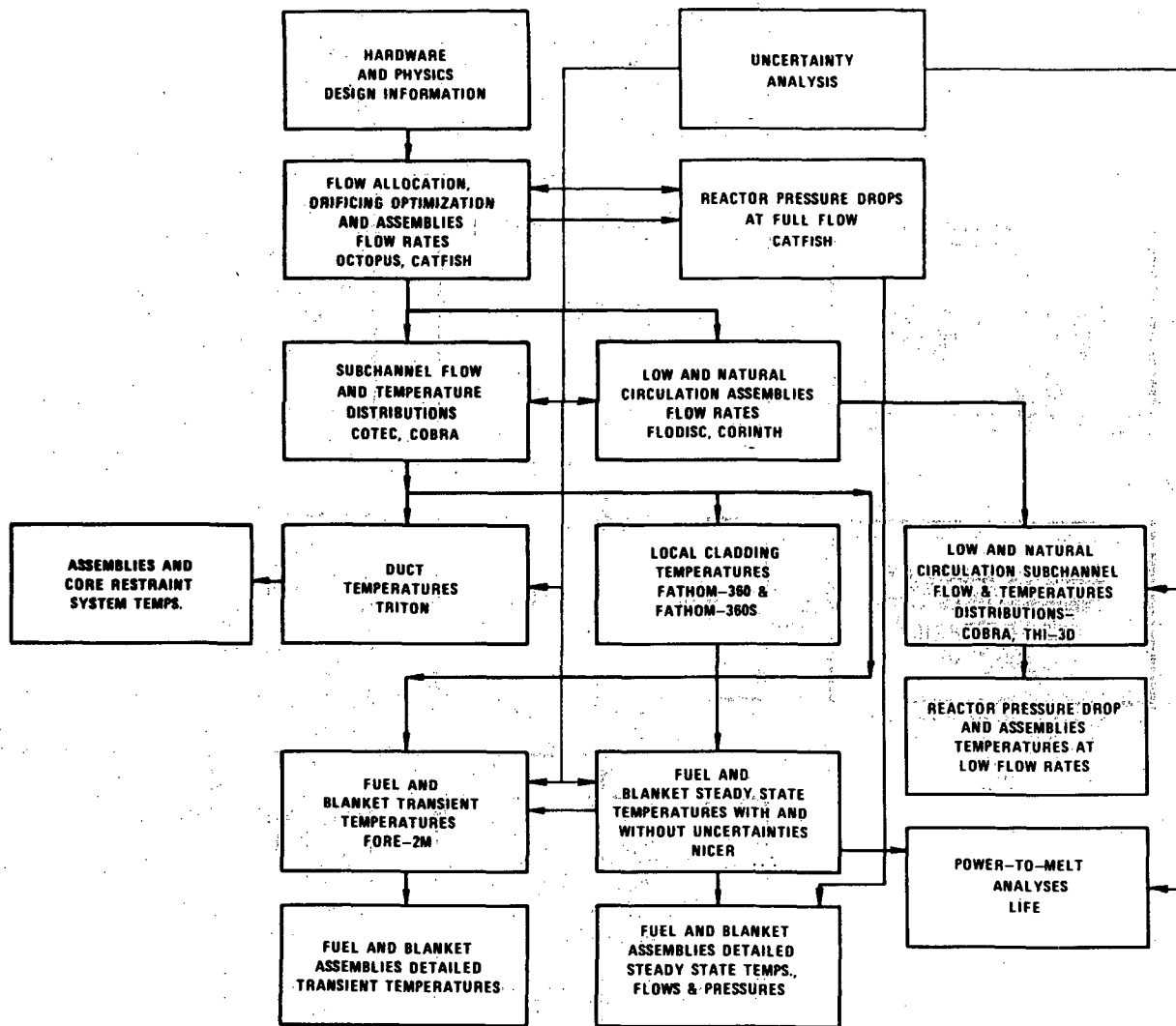


Figure 4.4-63 Fuel and Blanket Assemblies Thermal-Hydraulic Analysis Flow Diagram

1668-13

4.4-189

Amend. 51  
Sept. 1979

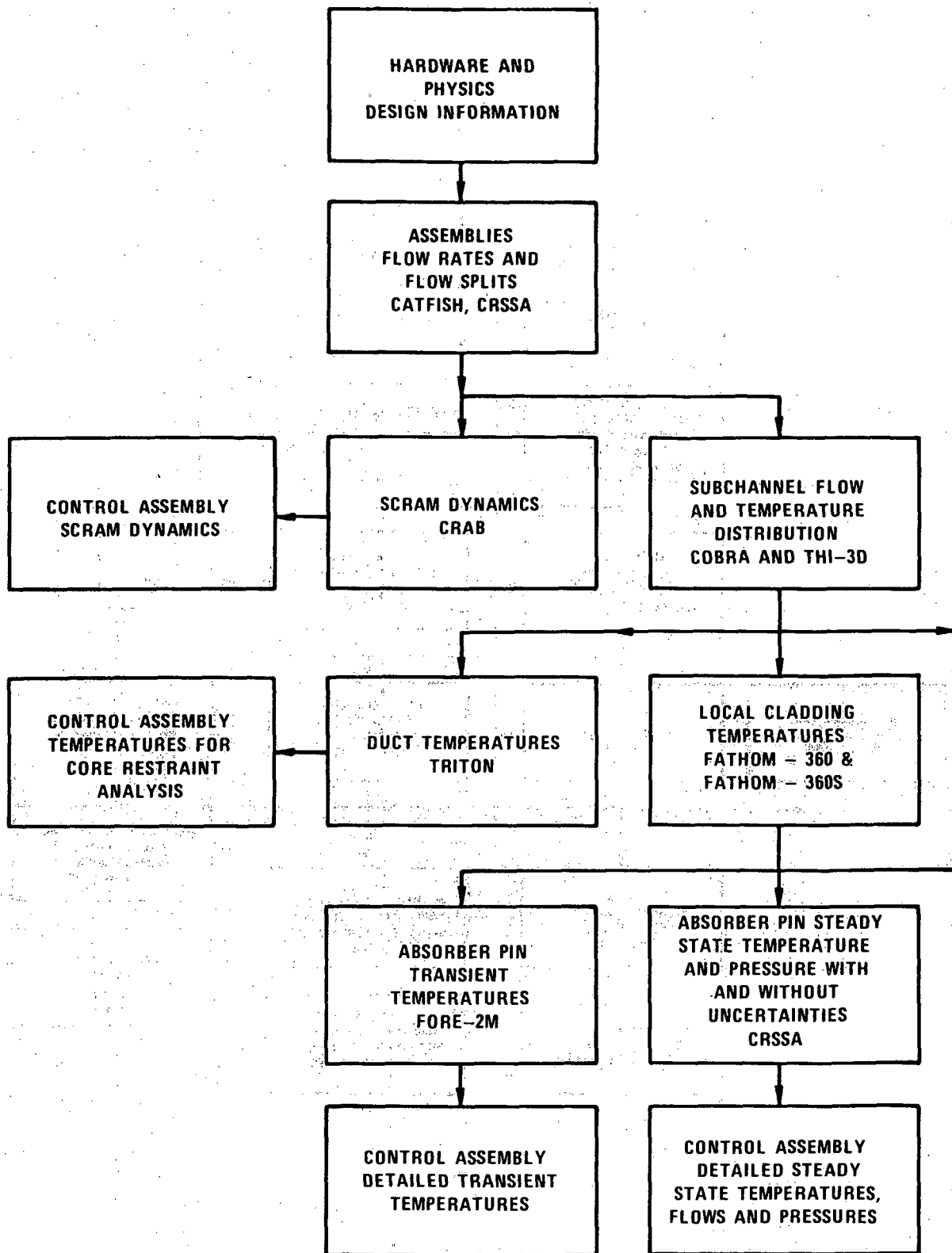
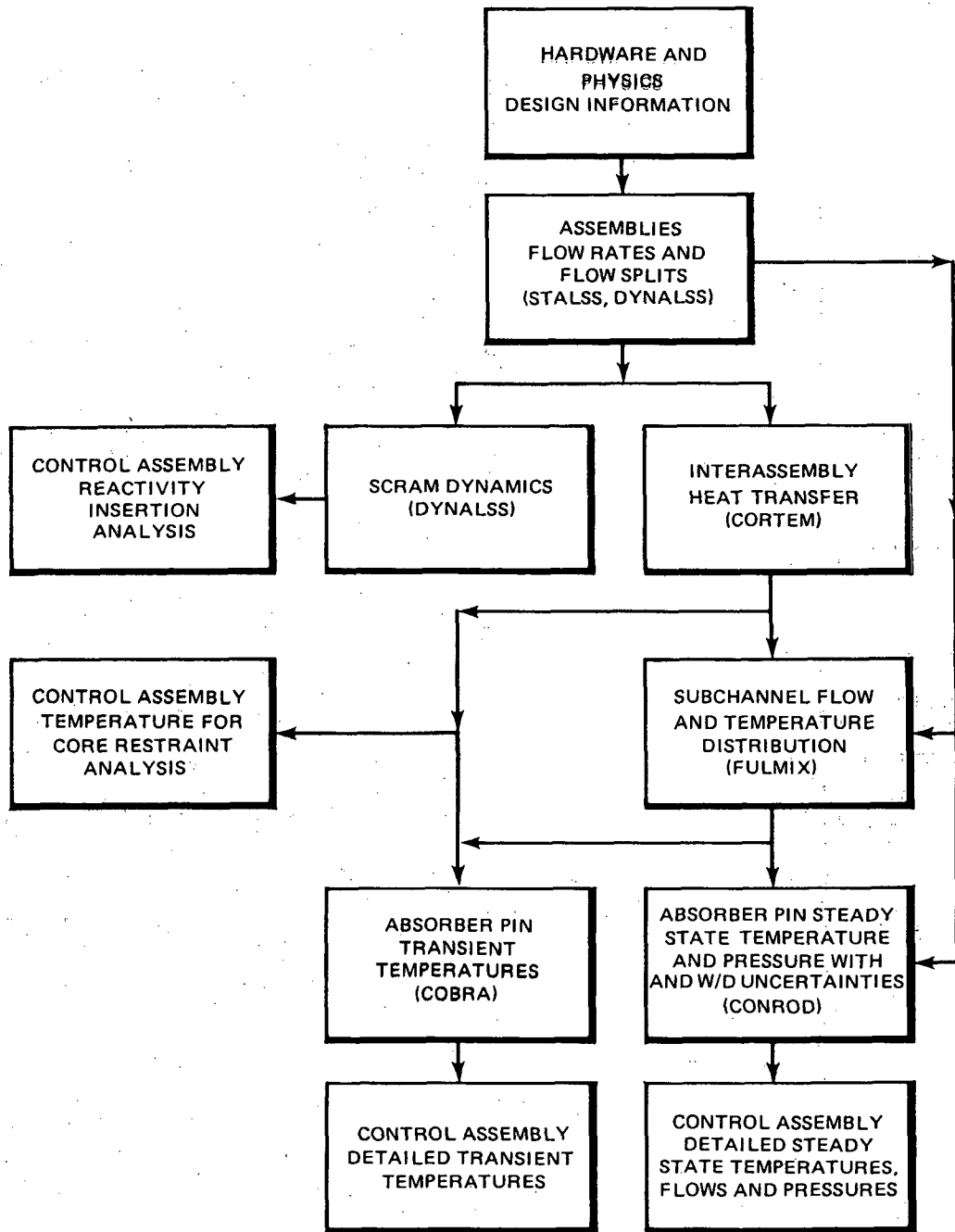


FIGURE 4.4-64 Primary Control Assembly and Absorber Pin Thermal-Hydraulic Analysis Flow Diagram



83-031-02

Figure 4.4-64a SECONDARY CONTROL ASSEMBLY AND ABSORBER PIN THERMAL-HYDRAULIC ANALYSIS FLOW DIAGRAM

3457-1a

**ASSEMBLIES**



**FUEL**



**FUEL/INNER BLANKET  
ALTERNATING POSITION**



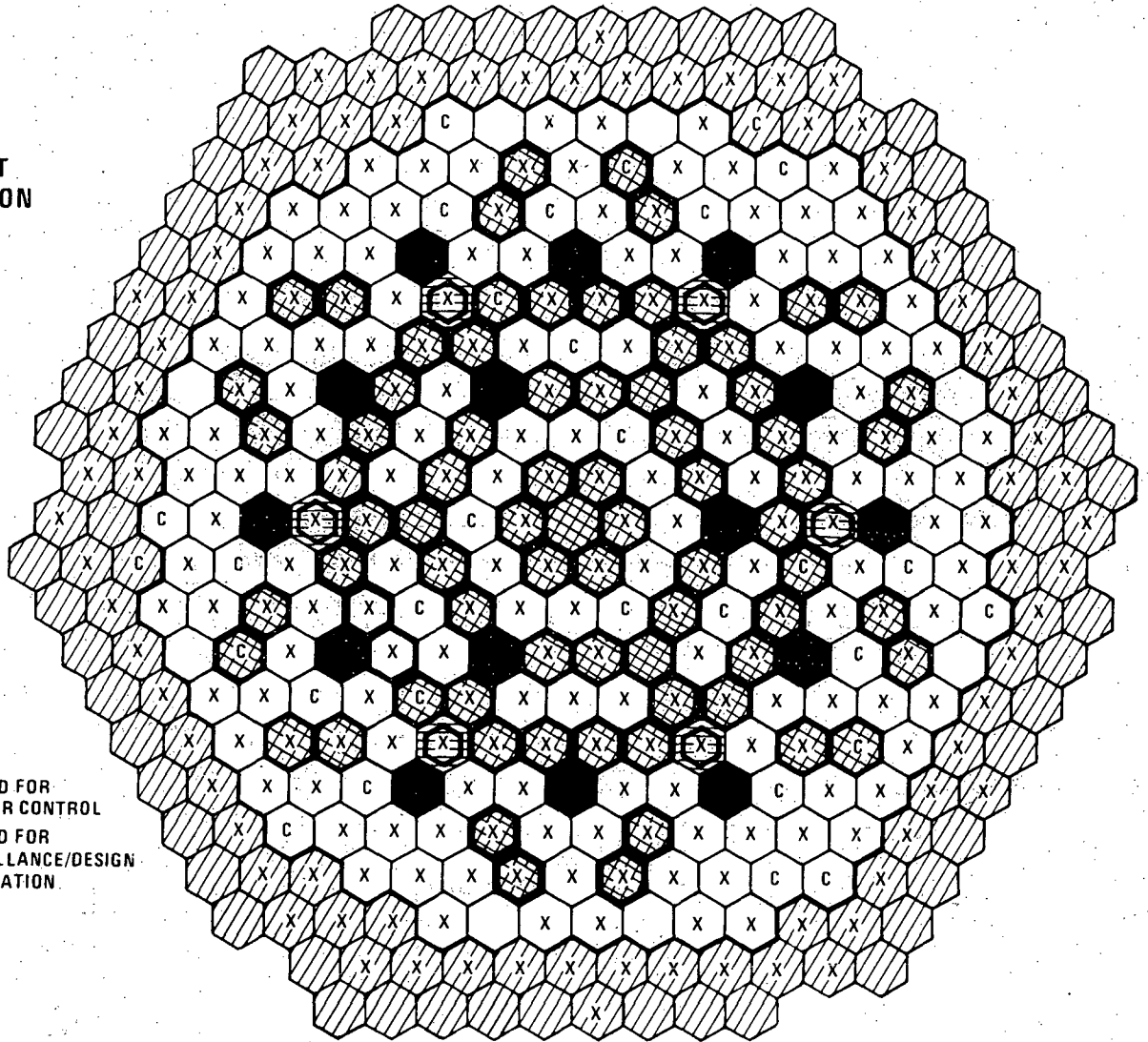
**CONTROL (NOT  
INSTRUMENTED)**



**INNER BLANKET**



**RADIAL BLANKET**



**LEGEND**

**C = T/C USED FOR  
REACTOR CONTROL**

**X = T/C USED FOR  
SURVEILLANCE/DESIGN  
VERIFICATION**

4.4-191

Amend. 54  
May 1980

Figure 4.4-65. CRBRP Heterogeneous Core Exit Thermocouples Coverage

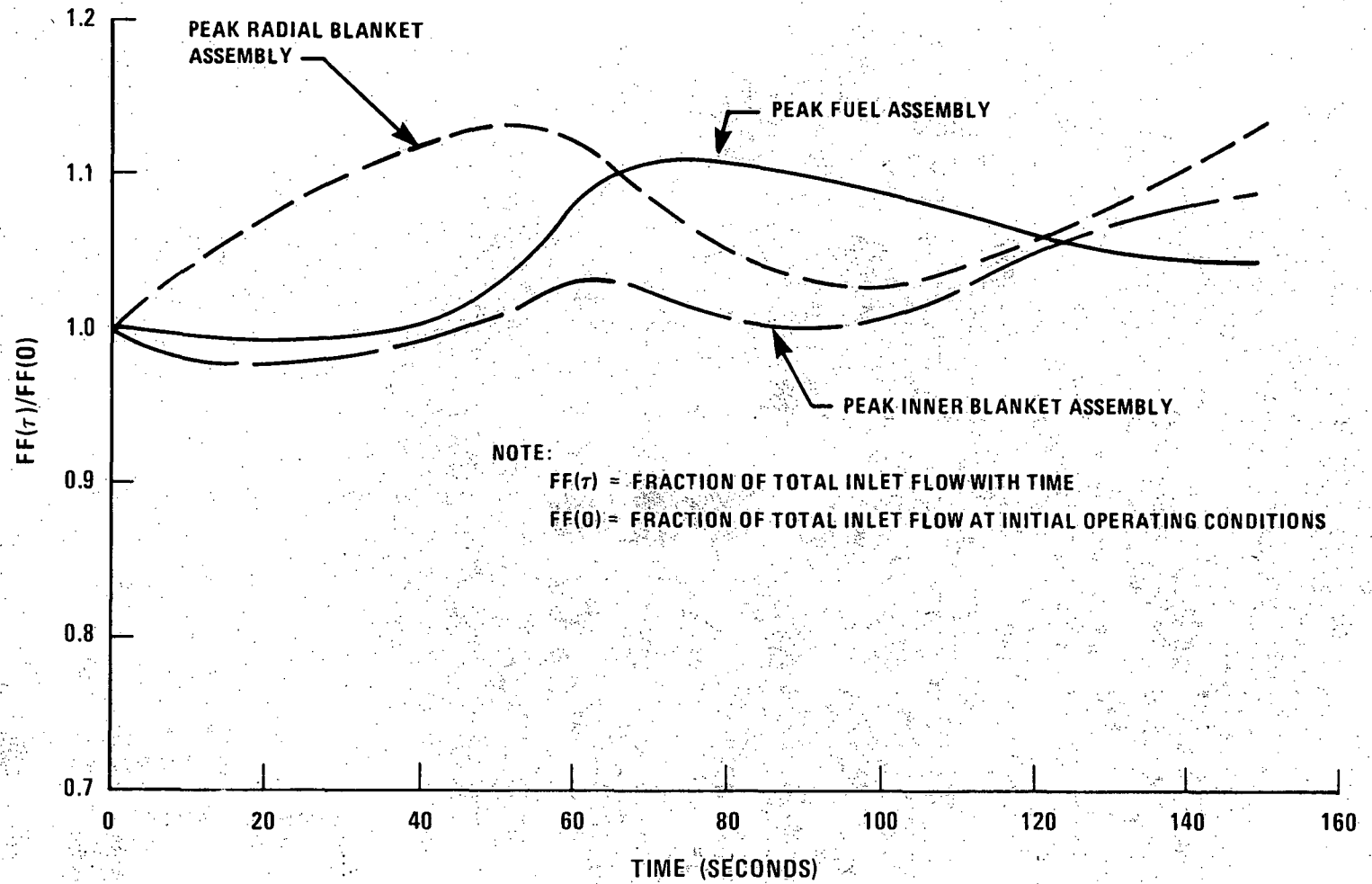


Figure 4.4-66. Typical Inter-Assembly Flow Redistribution for Peak Fuel, Inner Blanket and Radial Blanket Assemblies During Natural Circulation Transient

**ASSEMBLIES**



FUEL



FUEL/INNER BLANKET  
ALTERNATING POSITION



CONTROL (NOT  
INSTRUMENTED)



INNER BLANKET



RADIAL BLANKET

**LEGEND**

C = T/C USED FOR  
REACTOR CONTROL

X = T/C USED FOR  
SURVEILLANCE/DESIGN  
VERIFICATION

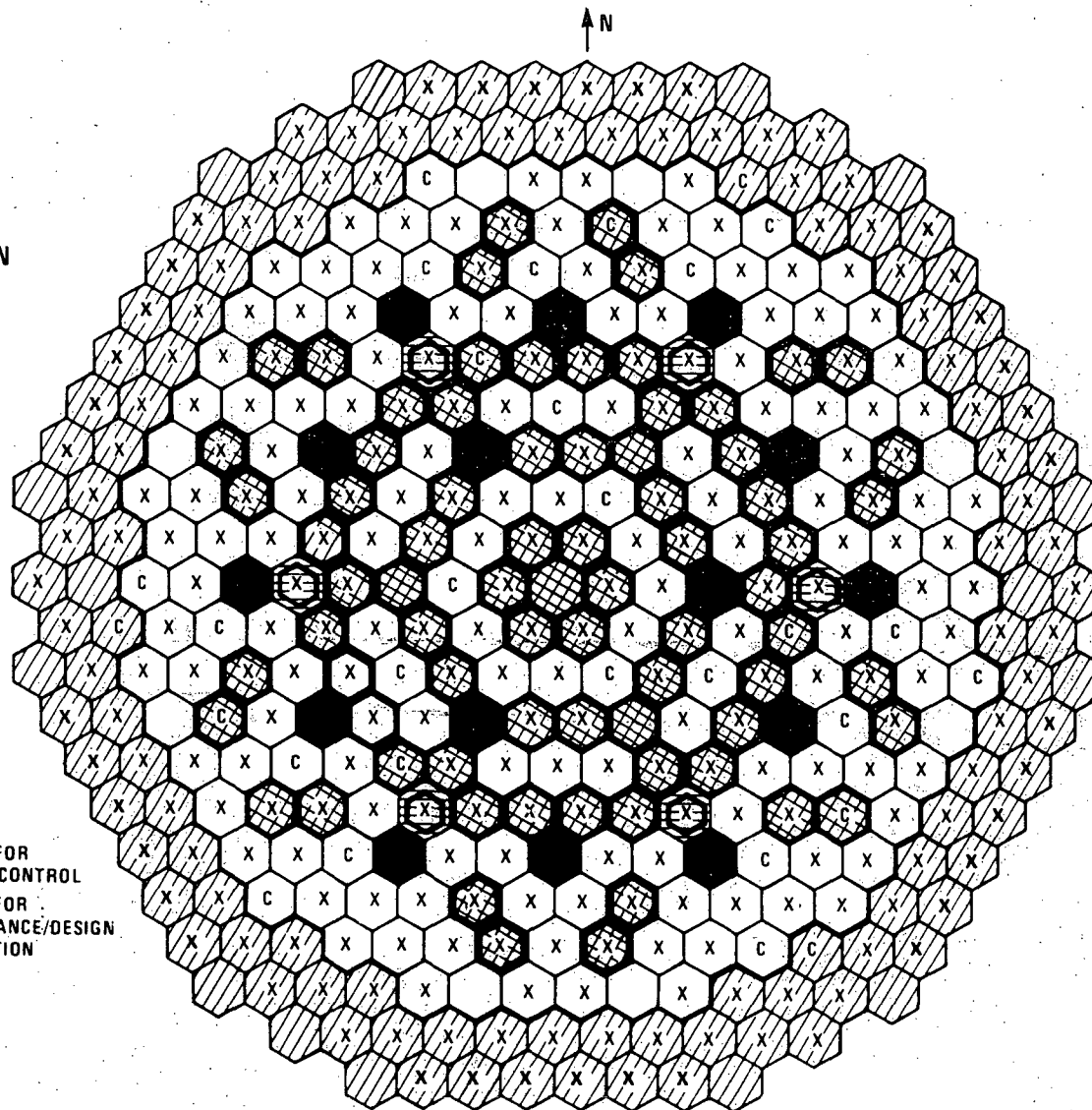


FIGURE 4.4-65. CRBRP Heterogeneous Core Exit Thermocouples Coverage

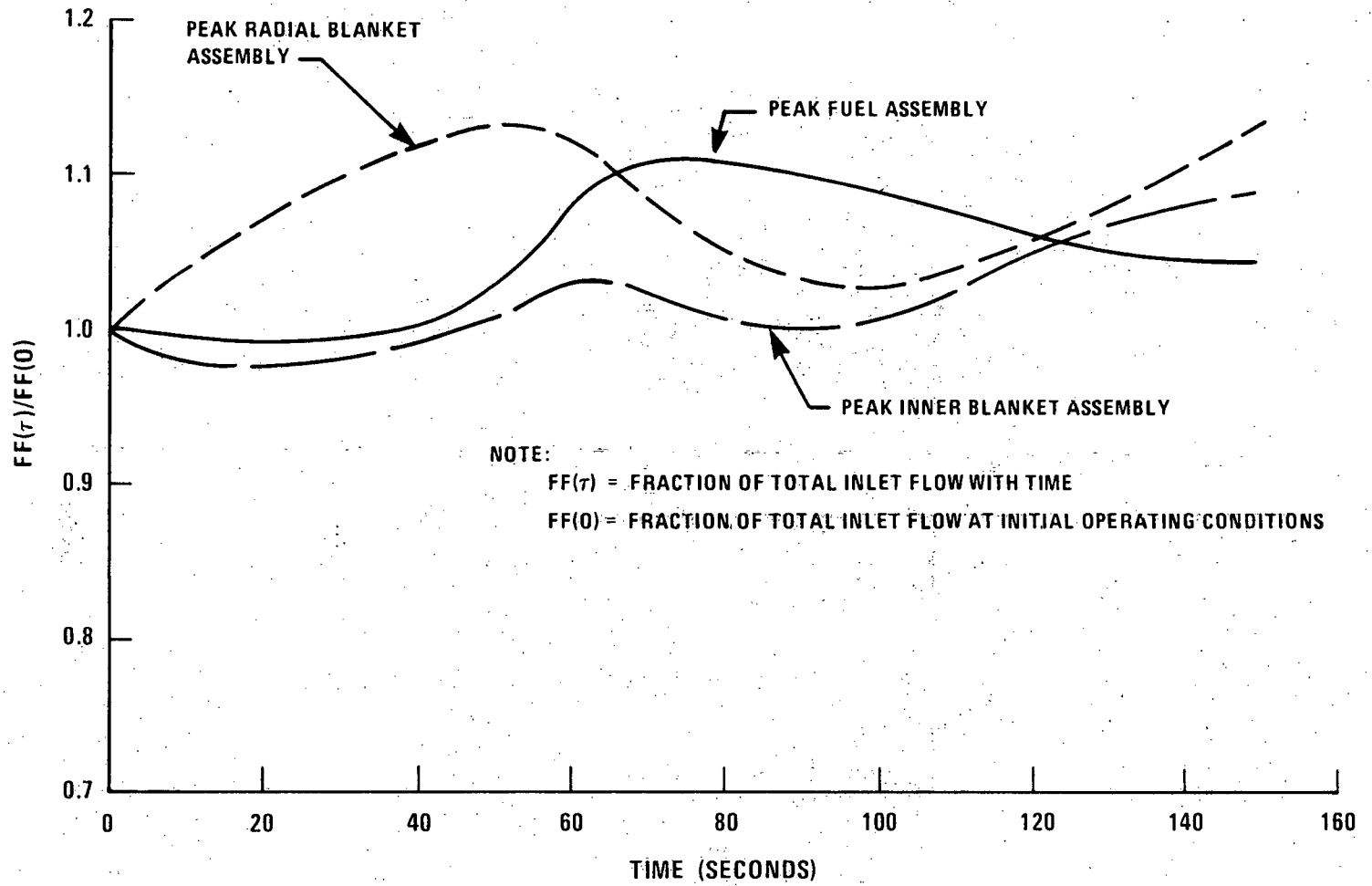


Figure 4.4-66. Typical Inter-Assembly Flow Redistribution for Peak Fuel, Inner Blanket and Radial Blanket Assemblies During Natural Circulation Transient



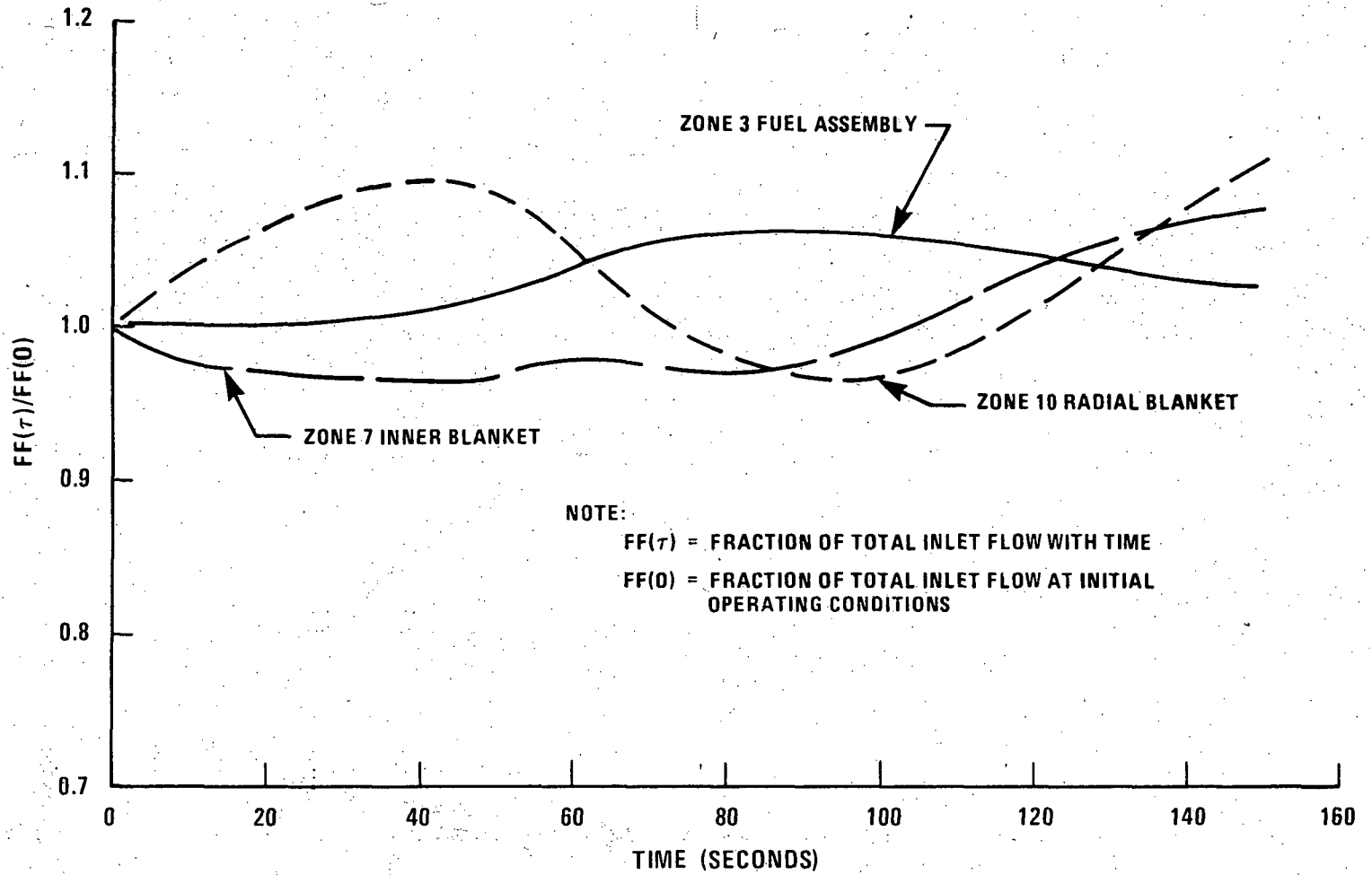


Figure 4.4-67. Typical Inter-Assembly Flow Redistribution for Several Core Orificing Zones During Natural Circulation Transient.

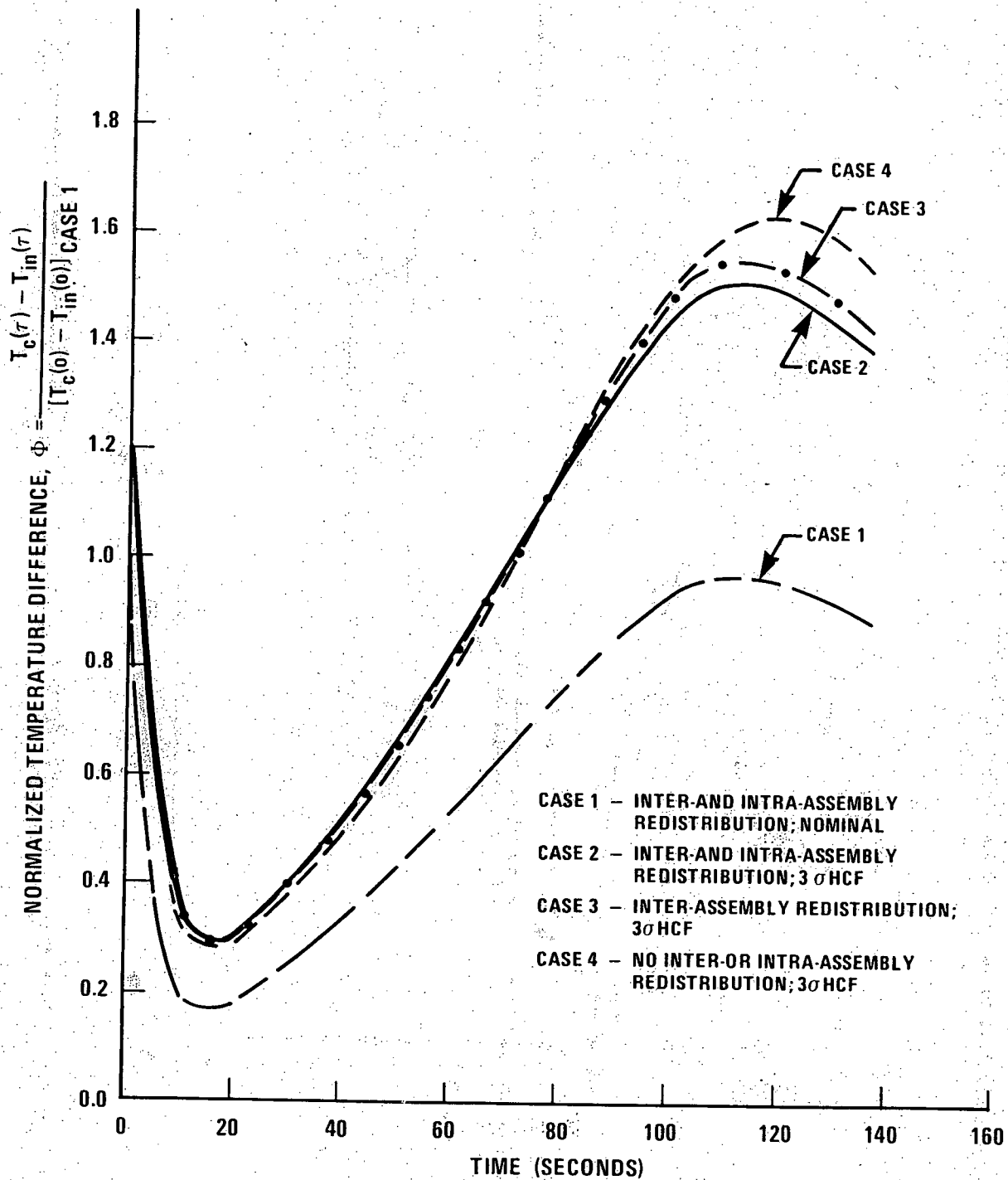


Figure 4.4-68. Typical Effect of Uncertainties and Inter-/Intra-Assembly Flow Heat Redistribution on F/A Peak Coolant Temperatures During Natural Convection Cooling